Photoproduction of η and η' Mesons using CLAS at JLAB

by

Zebulun A. Krahn

A dissertation submitted in partial fulfillment of the requirements
for the degree of

Doctor of Philosophy

in the Department of Physics

Carnegie Mellon University

October 29, 2007

Abstract

The focus of this analysis is photoproduced η and η' mesons. The data were obtained in Hall B at Jefferson Lab using a photon beam at an endpoint energy of 4.016 GeV in the spring and summer of 2004. The Hall B photon tagging system and the CLAS spectrometer were used to collect the data.

From this data, and in the course of analysis of the $N\eta$ and $N\eta'$ systems, measurements were made of the differential cross sections for η and η' photoproduction. The differential cross section measurements for the η improve the statistics and slightly improve the kinematic range for world data. The results for the η' represents an almost entirely new dataset which will allow for further analysis of the η' meson. The results of this measurement for the η' extend the statistics and kinematic range of world data dramatically.

Dedication

This work is dedicated to the memory of my father, Donald Robert Krahn.

Acknowledgements

While the list of people who deserve my thanks is quite long, I will endeavor to keep this list as brief as possible. I want to thank my wife, Krista, for all of her support and love for almost my entire graduate career. I want to thank my mother, Betina, brother Nathan, and sister-in-law Kristine for all of their support. I want to acknowledge all of my grandparents, Dors Maynard in particular. A special thank you to my grandparent-in-laws, who treat me like their own grandson. Thank you to all of my aunts, uncles, and cousins. My nephews Nicholas and Michael, and my niece Kate. Thank you to Jeanne and Joe for reminding me how to have a good time. Thank you to Rita and Shorty, for always having a beer ready at 9:00 AM, and the hospitality to serve it with a bowl of cashews.

I need to thank all of the people who helped me through the past years of my life at CMU. Mike Williams, Adam Lichtl, Dan Bock, Matt Bellis, Curtis Meyer, Gregg Franklin, Reinhard Schumacher, and Brian Quinn. I need to especially thank Brian Quinn for not getting too upset about a broken scintillator bar. Special thanks to Gary Wilkin, for being one seriously cool dude. Additional thanks go out to Mike McCraken, Seamus Riordan, Ryan Dickson, Diana Seymour, and Kei Moriya. Additional thanks go to Dr. Steve Dytman for serving on my thesis committee.

I want to thank some of the people who have been the most helpful to me at CMU. Special thanks to Mary Jane, Hilary, and Karey. You keep the department running, the cookies available, and you always emailed me first to inform me of left-over food.

Thank you to Kevin Bandura for always being around to talk about sports, and occasionally work. Special thanks go to Tom, Diana, and Maria Bajzek, who are clearly the best landlords a tenant could ever hope for. I want to thank Sam AbTech for all of the extra manual labor and free T-shirts. A special thanks to all of those who spend time inside a kitchen on wheels, just so I can get something to eat on campus at a reasonable price. Mr. and Mrs. Sarit Tasit, my thanks to you for all the spicy fried rice and curry.

For all of my work and struggle, I would still not have made it here without the support of several other professors along the way. For my first introduction to physics, in a classroom, my thanks go to Mr. Mark Brandt. When I chose to continue with physics in college, I had a wonderful group of professors. My thanks go to Dr. Jim Cederberg, Dr. David Nitz, Dr. Robert Jacobel, Dr. Amy Kolan, Dr. David Dahl, and Dr. Amy Larson. Every one of you inspired and taught, and for that you deserve my thanks and the thanks of all of my classmates.

Contents

Chapter 1

Introduction and Motivation

Experiments are becoming more advanced, and achieving higher energies than ever before. They are in search of new particles, new states of matter, and a new understanding of the physics of the universe. While new experiments are absolutely essential to any physics program, there are still holes in the current knowledge. As an example, consider the nucleon resonance spectrum. There are many experimentally observed states in the spectrum, but to date there is little theoretical understanding of the dynamics which define the known spectrum. Quantum Chromodynamics(QCD) is the theory of the nuclear strong force. The interactions occurring within a nucleon are no doubt complex, but a study of these interactions through the mapping of the nucleon resonance spectrum is essential science. An experimental study of the lower energy nucleons may shed light on some of the fundamental questions still unanswered in QCD, like confinement.

Theorists have different models which each propose certain dynamics upon the interactions within the nucleon. Through a series of iterative steps theorists and experimentalists have attempted to refine models and improve data to yield a better understanding of the nucleon resonance spectrum. To that end, this analysis is an experimental study of the nucleon resonance spectrum for states which may couple to the $N\eta$ and $N\eta'$ final states. Experimental observation of any new states may allow for a more complete nucleon resonance spectrum upon which to build theories. Additionally, this analysis will utilize a real photon beam as a probe of the nucleon structure. This is in contrast to the majority of experiments which utilized pion beams. This analysis should therefore be complimentary to previous analyses.

A Partial Wave Analysis (PWA) will be used to search for nucleon resonances within a high statistics η and η' photoproduction dataset from Jefferson Lab(JLAB). A thorough experimental mapping of the nucleon resonance spectrum will allow for more refined models, which in turn will allow for a greater insight into the nature of quarks bound within baryons.

1.1 Theoretical Motivation

This section describes the principle scientific motivation for this analysis, the missing baryon resonance problem. The missing baryon resonance problem is the title given to the discrepancy between the number of observed and theoretically predicted nucleon resonances in quark models. The Constituent Quark Model(CQM) is based on the dynamics of the three valence quarks within the baryon, and predicts a spectrum richer in resonance states than has been experimentally observed.

There are two proposed solutions which bear consideration. The first potential solution is that the "missing" resonance states exist but have not been seen because they decouple from the Nπ final state. Since a majority of the scattering data for baryon resonance analysis comes from $N\pi$ scattering experiments, looking for resonances in other channels may yield interesting results. The

second possible solution is called the diquark model. In the diquark model two of the three valence quarks form a tightly bound subsystem, which interacts with the remaining quark.

A brief description of the constituent quark model will be presented here. Additionally, the motivation behind the two possible solutions to the missing baryon resonance problem will be described.

1.1.1 Quark Models

In 1961 Gell-Mann proposed an ordering scheme, called the Eight-fold Way, to explain the growing chaos that was particle physics. At that time, particle physics was experiencing a huge surge of discovery, and there was a clear need to organize the new particles in some fundamental way. This explosion in detected particles became known as the "subatomic particle zoo". The Eight-fold Way organizes hadrons into geometrical patterns according to charge and hypercharge. Hypercharge is related to strangeness, and organization according to charge and strangeness is now more common.

The groups of mesons and baryons can be separately organized into a hexagonal pattern with strangeness changing in integer steps, as shown in Figure 1.1. Electric charge runs from $q = -1 \rightarrow 1$ in integer steps as well. This organization scheme also yielded some predictive power, since there were particles which had not been discovered which should fit into the geometric organization. For example, the Ω^- at the edge of the first baryon decuplet, was observed until after its existence and mass was predicted by Gell-Mann.

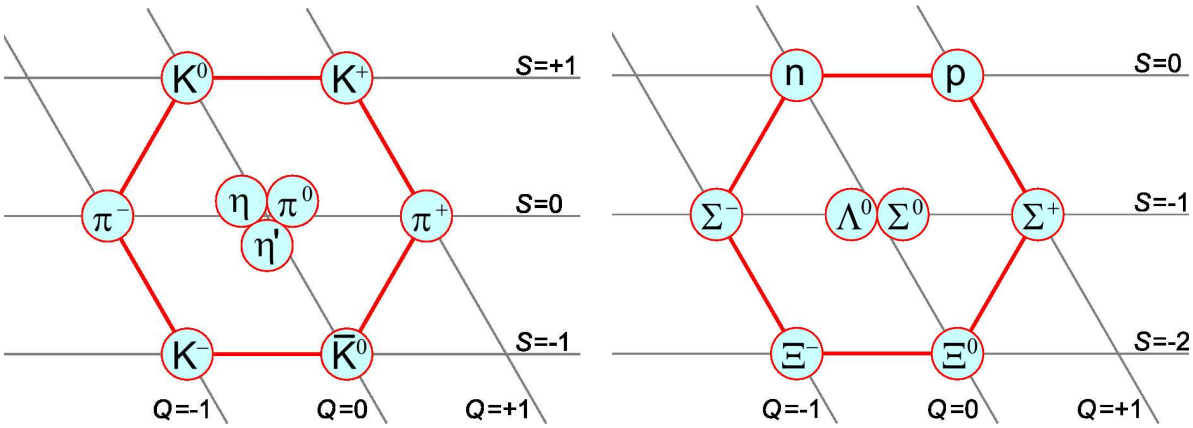

Figure 1.1: Left: Diagram of the meson nonet labeled according to electric charge and strangeness. Right: Diagram of the octet of lightest $s = \frac{1}{2}$ baryons also labeled by strangeness and charge. Note that the η and η' occupy the same location, due to having the same quantum numbers.

The predictive power of the Eight-fold Way was clearly evident, but questions remained as to why this organizational scheme was so successful. In 1964 Gell-Mann and Zweig each proposed the theory that hadronic matter was composed of other, more fundamental particles. These constituent particles were dubbed quarks by Gell-Mann. Gell-Mann proposed the existence of three flavors of quarks to account for the known particles, and their behavior. Each flavor of quark was assigned a fractional electric charge, an isospin, and strangeness.

As an added complication, the quarks were spin $\frac{1}{2}$ particles, meaning that they are fermions. As such, quarks should obey the Pauli Exclusion Principle that states that no two identical fermions can reside in the same quantum state. With only three flavors of quarks with which to compose many baryons, each requiring three quarks or anti-quarks, there were states which contained multiple u, d, or s quarks. In order for multiple quarks of the same flavor to exist within a baryon, and not violate the exclusion principal, there must be an additional degree of freedom. This additional freedom was

determined to be three-fold, because that satisfied the exclusion requirements for baryons composed of three quarks of identical flavor. This new freedom was dubbed "color", and because it is three fold, there are three colors available. The available colors are red, blue, and green, along with their anti-colors, anti-red, anti-blue, and anti-green. Bare color, much like a bare quark has never been observed, and current theory along with experimental evidence indicates that all physical particles are colorless objects. A baryon with one quark of each color, or one quark of each anti-color, is a colorless object. Additionally, for a meson to be colorless, the quark/anti-quark pair must be color/anti-color pair as well. All observed particles are colorless objects by construction. Color, as a new degree of freedom for hadronic matter, allowed for satisfaction of the Pauli Exclusion Principle.

Quark models describe hadronic particles in terms of their valence quarks. The valence quarks give rise to the quantum numbers of the hadronic particle. For baryons, there are the 3 valence quarks or anti-quarks. The term valence is used to emphasize their prominence in the baryonic structure, as well as to distinguish them from the "sea" quarks present in all hadronic matter. "Sea" quarks are usually quark/anti-quark pairs which pop in and out of the QCD vacuum. The quantum numbers of the valence quarks define the quantum numbers of the baryon, which then identifies the baryon. The principle quantum numbers of interest here are: J^{PC}, where J is the total angular momentum, P is the intrinsic parity, and C is the charge conjugation parity. Additionally, other quantum numbers, such as isospin(I), aid in the determination of a baryon's identification. For the purposes of this analysis however, the initial state is I = $\frac{1}{2}$, and the η and η' are I = 0, so only I = $\frac{1}{2}$ baryons are accessible. Thus, the η and η' reaction channels are referred to as isospin filters.

While the CQM allowed for an understanding of hadrons in terms of their valence quarks, there are additional components which are added to more accurately predict the masses, characteristics, and spectrum of baryons. In the model from Capstick and Roberts[1], a three dimensional harmonic oscillator potential is used as the starting point for the interactions between the valence quarks within the baryon. Various corrections are then applied, representing either further theoretical knowledge or experimental result, which modify the potential, and thus the calculated spectrum.

1.1.2 Decoupling of Resonances from Nπ

Starting with Koniuk and Isgur[2] in 1980, theorists have postulated that the missing resonances are not really missing, but do not couple strongly to the $N\pi$ system, which comprises the bulk of scattering data for baryon spectroscopy. A nucleon resonance state that does not couple strongly to the $N\pi$ system may not be observed in a $N\pi$ production experiment despite any theoretical motivation for the existence of such a state. This could lead to that resonance state being labeled as "missing".

There are several possible probes with which we can explore the structure of the nucleon, and the one chosen for this analysis is the photon. There are several theoretical indications that photoproduction may be a promising avenue for discovery of these "missing" resonance states. The principle reason for photoproduction to be a unique place to observe baryon resonance states, is simply that it has not been done before with statistically significant datasets. While the baryon resonance states will be photoproduced, the decays of such states that are of interest here are the Nη and Nη' decay modes. Clearly, a systematic study of photoproduced final states would provide significant insight into the baryon spectrum.

1.1.3 The Diquark Model

There is an alternate model that was thought to be a possible solution to the missing baryon resonance problem. In 1968 Lichtenberg et al.[3] proposed a model of the baryon in which two of the three quarks form a tightly bound subsystem. This two quark subsystem, referred to as a diquark, is then free to interact with the remaining quark. While not the original motivation behind the model, diquark model proponents believe it could provide insight into the missing baryon resonance

problem. The diquark model effectively turns a three-body problem into a two-body problem thereby reducing the number of degrees of freedom of the quark system. The fewer the degrees of freedom, the less populated the spectrum is expected to be. Many of the states which this model removes are states which have not been experimentally observed, and thus it is considered a promising solution to the missing baryon resonance problem. Currently there is no experimental evidence from deep inelastic scattering to indicate this quark-diquark structure within the baryon.

1.2 Baryon Resonances and $N\eta/N\eta'$

To construct a starting point for this analysis the current state of baryon resonances will be reviewed. There are several known resonances which couple to the Nη system. The η and η' mesons have the same quantum numbers so they should couple to the same resonances. They are significantly different in mass, however, so some states may not be observable in the $\eta'(mass = 958MeV[4])$ which are observable in the $\eta(mass = 547MeV[4])$ channel. The Nη and Nη' decays only couple to the isospin $= \frac{1}{2}$ nucleon resonances, and as such provides an isospin filter for the analysis.

Table 1.1 summarizes the resonance states which couple to Nη and Nη'. The states listed by the Particle Data Group (PDG)[4] with 3 or 4 star ratings are considered to be experimentally verified. There are also a few resonance states in the table with 1 or 2 star ratings, which list measured branching fractions to Nη. These states are considered "indications" but are not to be fully trusted. There exist numerous resonance states which are listed that do not have a measured branching fraction to Nη and so are not listed in 1.1.

Table 1.1: Resonance states for nucleons in the $N = 1$ and $N = 2$ bands which couple to Nη. This table comes from Capstick and Roberts [5]. The predicted states listed are ones which are expected to couple to the $N\eta$ and/or $N\eta'$ final states, and are indicated by the lack of star-rating from the PDG[4]. There are more states at higher mass in the $N = 3$ band of this model. The branching fraction $(\Gamma_i/\Gamma_{total})$to $N\eta$ is listed where possible. Where Γ_i is the width of the decay to the *ith* channel, and Γ_{total} is the total decay width.

Resonance	J^P	Status	Γ_i/Γ_{total}
$N(1520)D_{13}$	$\frac{3}{2}^-$	****	$(2.3 \pm 0.4) \times 10^{-3}$
$N(1535)S_{11}$	$\frac{1}{2}^-$	****	45-60%
$N(1650)S_{11}$	$\frac{1}{2}^-$	****	3-10%
$N(1675)D_{15}$	$\frac{5}{2}^-$	****	0.0±1.0
$N(1680)F_{15}$	$\frac{5}{2}^+$	****	0.0±1.0
$N(1700)D_{13}$	$\frac{3}{2}^-$	***	0.0±1.0
$N(1710)P_{11}$	$\frac{1}{2}^+$	***	6.2±1.0%
$N(1720)P_{13}$	$\frac{3}{2}^+$	****	4.0±1.0%
$N(1900)P_{13}$	$\frac{3}{2}^+$	**	14±5%

As previously mentioned, a large majority of the known baryon resonance states come from an $N\pi$ production mechanism. This analysis focuses on data taken with γp production, and as such, offers the advantage of looking in places where large data samples have not been available until recently. With this in mind, Table 1.2 lists calculated photocouplings to the known resonance states

from the PDG [4]. The important thing to note is the relative scale of the photocoupling amplitudes to each other, as this allows for comparison between the known states and the "missing" states. The predicted photocouplings are listed from a relativized quark model from Capstick and Roberts[5].

Table 1.2: Known and calculated resonance photocouplings to $p\gamma$. Known values come from the PDG[4] while the calculated values come from Capstick and Roberts[5].

Resonance	J^P	Status	PDG[4]	Capstick[5]
$N(1520)D_{13}$	$\frac{3}{2}^-$	****	-0.024 ± 0.009	-0.022 ± 0.010
$N(1535)S_{11}$	$\frac{1}{2}^-$	****	+0.90 ± 0.030	+0.073 ± 0.014
$N(1650)S_{11}$	$\frac{1}{2}^-$	****	+0.053 ± 0.016	+0.048 ± 0.016
$N(1675)D_{15}$	$\frac{5}{2}^-$	****	+0.019 ± 0.008	+0.019 ± 0.012
$N(1680)F_{15}$	$\frac{5}{2}^+$	****	-0.015 ± 0.006	-0.017 ± 0.010
$N(1700)D_{13}$	$\frac{3}{2}^-$	***	-0.018 ± 0.013	-0.022 ± 0.012
$N(1710)P_{11}$	$\frac{1}{2}^+$	***	+0.009 ± 0.022	+0.005 ± 0.016
$N(1720)P_{13}$	$\frac{3}{2}^+$	****	+0.018 ± 0.030	+0.052 ± 0.039
$N(2080)D_{13}$	$\frac{3}{2}^-$	**	-0.20 ± 0.008	

Quark model predictions indicate that several of the "missing" resonance states may couple to the $N\eta$ and $N\eta'$ final state. To produce these states with a photon beam, they must also couple to $N\gamma$. Table 1.3 contains photocouplings for known states and was compiled from predictions by Capstick and Roberts[5] and from the PDG[4] for known states that couple to $N\eta$ final state. The Capstick and Roberts model is a relativized quark model which includes some spin-orbit effects. It is considered to be one of the best models available for baryon resonance calculations.

Table 1.3: Predicted "Missing" Resonances that couple to $N\eta$ and $N\eta'$ from Capstick and Roberts[5]. The states listed here are from the $N = 1$ and $N = 2$ bands of their oscillator potential. These are the lower lying states. There are additional, higher mass, $N = 3$ band states which are predicted as well.

Resonance	J^P	$N\eta$	$N\eta'$
$N(1880)P_{11}$	$\frac{1}{2}^+$	$-3.7^{+0.5}_{-0.0}$	$+0.0^{+0.0}_{-2.5}$
$N(1975)P_{11}$	$\frac{1}{2}^+$	$+0.1^{+0.2}_{-0.1}$	
$N(1870)P_{13}$	$\frac{3}{2}^+$	-4.6±0.3	$+0.0^{+0.0}_{-3.3}$
$N(1910)P_{13}$	$\frac{3}{2}^+$	-0.9±0.1	$-0.2^{+0.2}_{-0.6}$
$N(2030)P_{13}$	$\frac{3}{2}^+$	+0.4±0.1	$+0.2^{+0.1}_{-0.2}$
$N(1980)F_{15}$	$\frac{5}{2}^+$	-0.8±0.2	$-0.1^{+0.1}_{-0.2}$

Clearly there are a number of states that are predicted to couple to $N\eta$ which have not been seen experimentally and there are no reported results for a resonance decay to $N\eta'$. This discrepancy

provides the motivation for this experimental analysis. A large statistical sample of photoproduced η and η' mesons is used to search for missing baryon resonances that couple to $N\eta$ and $N\eta'$. This experiment provides a unique opportunity to contribute in a meaningful way to the deeper understanding of QCD and the structure of the nucleon.

1.2.1 Previous Resonance Analysis of Nη and Nη'

There exist several previous analyses which performed a search for indications of baryon resonances in photoproduced η and η' mesons. There are results from Dugger et al.[6][7] for both η and η' photoproduction. Additionally, there are results from Anisovich et al.[8] which combine η meson photoproduction data with π meson data. These previous analyses will be summarized briefly in this section.

Previous JLAB η Results

An analysis was performed by Dugger et al.[6] on photoproduced η mesons in the CLAS detector at JLAB. Differential cross sections measured for the η meson as a function of $cos(\theta_{CM})$ were compared with several models. The models used for comparison were an isobar model for η photo- and electroproduction (ETA-MAID), as well as a chiral constituent quark model (χQM). ETA-MAID was also used to extrapolate the differential cross sections into regions where there is no acceptance in the CLAS detector. It is estimated that the extrapolated regions constitute 15%-30% of the total cross section depending upon the center of mass energy.

The ETA-MAID model includes the following resonances: $D_{13}(1520)$, $S_{11}(1535)$, $S_{11}(1650)$, $D_{15}(1675)$, $F_{15}(1680)$, $D_{13}(1700)$, $P_{11}(1710)$, and $P_{13}(1720)$. The measured differential cross sections were added into the ETA-MAID fit to provide further kinematic coverage, and new parameters were obtained (refit ETA-MAID). The refit ETA-MAID model described the new cross sections well, except it fell below measured values at $W = 1.85$ GeV. The χQM used the same base resonances as ETA-MAID but added the $P_{11}(1440)$, $P_{13}(1900)$, and $F_{15}(2000)$ resonances. Agreement between the new measured cross sections and the χQM required an additional S_{11} resonance at $W = 1.7-1.8$ GeV.

It is important to note that the analysis by Dugger was not a partial wave analysis. The measured cross sections were compared with existing models with known resonance structure to determine if the models would reproduce the newly measured differential cross sections.

There are some preliminary differential cross section measurements from another set of photoproduction data at JLAB from Ball et al.[9]. While preliminary, these results can be used to provide an additional dataset with which to compare the measured differential cross sections.

Previous JLAB η' Results

A similar analysis was done by Dugger et al.[7] on photoproduced η' mesons in CLAS at JLAB. The measured differential cross sections of the η' meson were compared with a relativistic meson-exchange model from Sibirtsev et al[55], as well as a relativistic meson-exchange description from Nakayama and Haberzettl(NH)[11]. In both cases s-, t-, and u-channel contributions were included. Both models also included the $S_{11}(1535)$ and the $P_{11}(1710)$ resonances which are known to decay strongly to the Nη channel. The NH model also includes 2 additional S_{11} and P_{11} resonances with small couplings. It was found that additional J=3/2 resonances were required in the NH model to fit the data, and the $P_{13}(1940)$, $D_{13}(1780)$, and $D_{13}(2090)$ were added. Since the NH model is in better agreement with the measured differential cross sections than the Sibirtsev model it is concluded that the J=3/2 resonances are important inclusions. This was the first analysis to include the known η resonances in an η' analysis. As this was the first set of data to allow comparison between differential cross sections of the η' and models, the use of η results to influence the η' results is unsurprising. The experimental data and models also allowed for the extraction of the η'-nucleon-nucleon coupling constant, $g_{\eta' NN}$. While its value is highly model dependent, the reported value of $g_{\eta' NN} = 1.3 - 1.5$ is consistent with previous theoretical estimates.

CB-ELSA η Results

A partial wave analysis was carried out by Anisovich et al.[8] on data taken using the Crystal Barrel detector at the ELectron Stretcher Accelerator (CB-ELSA)[12]. The η was reconstructed through the neutral channels $\gamma p \to p\gamma\gamma$ and $\gamma p \to p3\pi^0$. Combining both channels, there were approximately 100,000 η mesons reconstructed. Additional data was combined in the fit, and the analysis fit several final states in the data simultaneously. The Nη final state differential cross sections were fit along with the Nπ differential cross sections. Measurements of beam polarization asymmetry from GRAAL were also included in the fit.

The fit includes 11 N* resonances which couple to the Nη final state. The analysis of the Nη final state reproduced known resonances in reasonable agreement with the PDG. There were also indications of two new resonances, the $N(2070)D_{15}$ and $N(2200)P_{13}$, which couple to Nη. The $N(1535)S_{11}$ and the $N(1650)S_{11}$ resonances amplitudes were combined into a K-matrix formalism and fit together because they are so strongly overlapping, and both strongly coupled to Nη.

1.3 Analysis Goals

The goal of this analysis was to search for the "missing" nucleon resonance states in Nη and Nη' photoproduction. If resonances are observed in the analysis, then determining the properties of those resonances is also a goal. The possibility does exist however that no such resonances will be found, and a strong negative result could have implications on the present quark models. This makes a PWA of photoproduced η and η' mesons an extremely interesting study.

This analysis also serves as a proof of principle for the development of an event based PWA, in contrast to all of the previous analyses which fit or compared to measured differential cross sections to determine which resonances are required to describe the data. The formalism for this method of analysis will be discussed in a later chapter.

1.3.1 Event Based Analysis Method

An event-based partial wave analysis will be used as the method to search for the missing baryon resonance states in Nη and Nη' photoproduction. A full description of the partial wave analysis method and formalism will be given in a later chapter, but a brief description is given here.

A partial wave analysis is a technique in which the data is fit with a set of quantum mechanical amplitudes to determine what best represents the physics in the dataset. The power of the partial wave analysis is that all of the angular distributions are fit at the same time which maintains any correlations which may exist. Additionally, mass dependence can be implemented, or left out to let the fit itself determine where a partial wave is required to fit the data.

There is freedom in how the amplitudes used in fitting can be constructed. This analysis utilizes a covariant tensor formalism in writing amplitudes with different spin-parities. With the amplitudes available, an un-binned likelihood fit is used to fit complex parameters in the amplitudes to the data. The fit results extract the contributions of the different spin-parity amplitudes. While the fit is un-binned, the data has been binned in center-of-mass energy(W,$\sqrt{s}$) for the ease of running the fit, and interpreting the results. The fit is run independently in each bin of W. The independent solutions are then plotted as a function of W to map out the contribution of each partial wave.

1.4 Summary

The "missing" baryon resonance problem has been known to exist for many years, but only in recent years have the data and computing resources become available to truly examine the problem. This analysis examines the problem of these "missing" states by searching for nucleon resonances in Nη and Nη' photoproduction. The formalism and methodology utilized in this analysis will also be employed in analyzing other photoproduced reactions including Nω, KΛ, KΣ, Nπ, and N$\pi\pi$. A definitive statement about the existence of these states could have serious implications on the current theoretical models of baryon quark structure.

Table 1.4: Table of CB-ELSA PWA Results[8]

Resonance	M(MeV)	Γ(MeV)	Branching Fraction
$N(1520)D_{13}$	1523 ± 4	105^{+6}_{-18}	0.020
PDG	1520^{+10}_{-5}	120^{+15}_{-10}	
$N(1535)S_{11}$	1501 ± 5	215 ± 25	
PDG	1505 ± 10	170 ± 80	0.430
$N(1650)S_{11}$	1610 ± 10	190 ± 20	(total)
PDG	1660 ± 20	160 ± 10	
$N(1675)D_{15}$	1690 ± 12	125 ± 20	0.001
PDG	1675^{+10}_{-5}	150^{+30}_{-10}	
$N(1680)F_{15}$	1669 ± 6	85 ± 10	0.005
PDG	1680^{+10}_{-5}	130 ± 10	
$N(1700)D_{13}$	1740 ± 12	84 ± 16	0.004
PDG	1700 ± 50	100 ± 50	
$N(1720)P_{13}$	1775 ± 18	325 ± 25	0.300
PDG	1720^{+30}_{-70}	250 ± 50	
$N(2000)F_{15}$	1950 ± 25	230 ± 45	0.007
$N(2070)D_{15}$	2068 ± 22	295 ± 40	0.171
$N(2080)D_{13}$	1943 ± 17	82 ± 20	0.011
$N(2200)P_{13}$	2214 ± 28	360 ± 55	0.051

Chapter 2

Experimental Setup

The data that form the basis of this analysis were taken as part of the g11a run period in the summer of 2004 at the Thomas Jefferson National Accelerator Facility in Newport News, VA. While the original purpose of the g11a data run was to provide greater statistics for a pentaquark search, it also provided a high statistics data set for reactions with multiple charged tracks like $\gamma p \to p\eta \to p\pi^+\pi^-(\pi^0)$ and $\gamma p \to p\eta' \to p\pi^+\pi^-(\eta)$. The parenthetical notation used here indicates that the π° and the η are not directly detected, but are reconstructed from the other detected particles.

The run conditions called for a photon beam incident on a proton target. The photon beam was produced via a bremsstrahlung technique which produces photons with a spectrum of energies. To distinguish between available photons, the photon tagger was used in this analysis. For the g11a dataset, the endpoint electron beam energy used was 4.016 GeV. The CEBAF Large Acceptance Spectrometer (CLAS) was used for charged particle detection and identification in this experiment. CLAS provides a large acceptance for the detection of multi-particle charged final states. The large acceptance of CLAS, along with good beam quality, and a trigger optimized for multiple charged tracks has produced the largest dataset of photoproduced multi-particle final states in the world.

This chapter will describe the details of the accelerator, photon tagger, and the CLAS detector. Additionally, the run conditions specific for the g11 data taking run will be described, including the trigger conditions.

2.1 JLAB

Thomas Jefferson National Accelerator Facility (TJNAF,JLAB) previously known as the Continuous Electron Beam Accelerator Facility (CEBAF), is located in Newport News, Virginia. There are currently 3 experimental halls at JLAB, labeled Hall A, Hall B, and Hall C. Each hall has significant control over its own endpoint beam energy. Hall B, the smallest of the experimental halls, is the location of the CEBAF Large Acceptance Spectrometer (CLAS) and is the hall in which this experiment was conducted.

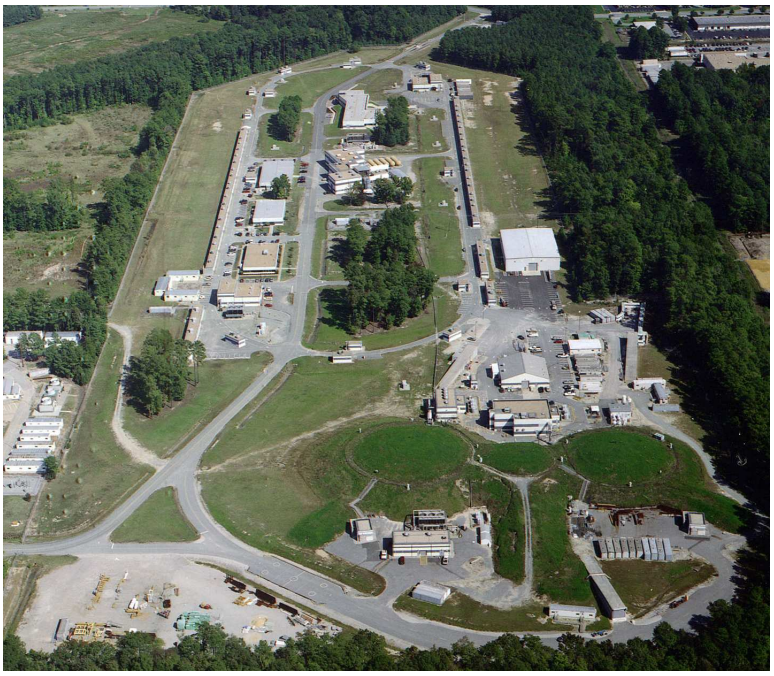

Figure 2.1: An aerial view of JLAB with the three experimental halls in the foreground.

2.2 The Continuous Electron Beam Accelerator Facility

The Continuous Electron Beam Accelerator Facility (CEBAF) began delivering beam for physics experiments in 1996 and is the essential feature of JLAB. The accelerator is a racetrack configuration with two sets of Linear Accelerators (LINACs), through which the beam is recirculated to provide up to 5 full passes prior to extraction to experimental end stations.

The biggest advance in accelerator technology employed at CEBAF is the superconducting radio frequency (RF) cavity used to provide the accelerating gradient. Traditional copper RF cavities are resistive and require a significant time to cool between beam spills. The superconducting cavities at CEBAF are non-resistive, resulting in an accelerator that achieves a duty factor of 100%. The constant delivery of electrons allows for the acquisition of high statistics datasets quickly, even at relatively low instantaneous currents. This makes CEBAF the ideal accelerator for running coincidence experiments, which are complicated by higher peak currents.

The production of the electron beam at CEBAF begins at the injector. The injector's basic components consist of a photo-emission electron gun, an RF accelerating cavity, and a chopper. The CEBAF electron gun uses three lasers, one for each experimental end-station. The three-laser arrangement permits each experimental hall to have independent control of its current and beam polarization. The lasers are independently pulsed at 499 MHz, 120° out of phase. The laser pulses are synchronized to give the accelerator an overall frequency of 1497 MHz, with a frequency of 499 MHz to any one experimental station [13]. To users in a given experimental hall, this means that they receive electrons in bunches, called beam buckets, approximately every 2 ns.

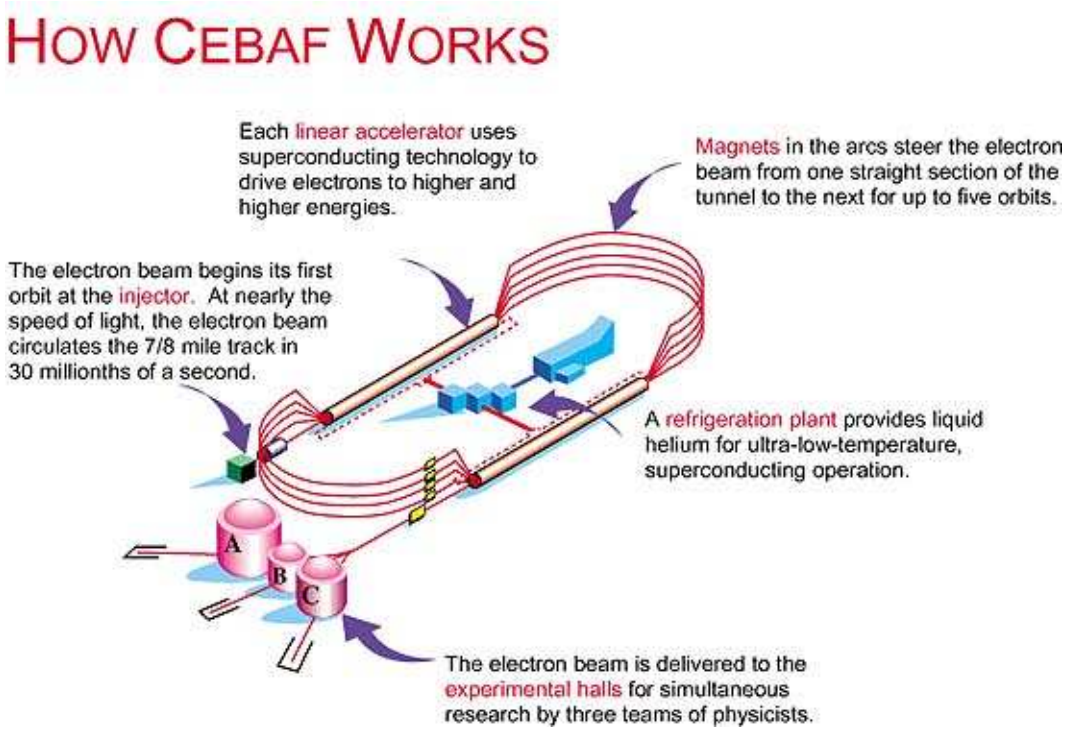

Figure 2.2: Beam starts at the injector before making an integral number of passes through the recirculating linear accelerators. Beam of the desired energy is extracted independently for each experimental hall. Graphic taken from [14].

Laser pulses are temporally 60-80 ps, FWHM [15]. The combined laser pulses are then used to illuminate a GaAs photocathode, which produces the bunches of electrons. The resulting electron bunches are accelerated to 45 MeV [16] by two superconducting radio-frequency cavities and packaged by an chopper before being sent to the recirculating linacs of CEBAF.

A picture of a typical RF cavity assembly is shown in Figure 2.3. The cavities were constructed of niobium and chilled to ≈ 2 K, a temperature at which they were superconducting [17]. Klystrons are used to set up radio frequency standing waves in these cavities, providing the accelerating gradient for the electron beam. The RF waves in the cavity had a frequency of 1497 MHz and were in phase with the beam's electron bunches so that there was always an electric force on an electron bunch providing acceleration as it passed through an RF cavity.

A diagram indicating how this works is given in Figure 2.4. Each RF cavity has its own klystron and control package to allow optimal tuning of phase and accelerating gradient [16].

Figure 2.3: Pair of typical CEBAF superconducting RF cavities. The cavities, shown here with supporting hardware and beam pipe, were marked by the elliptical cavities perpendicular to the beam pipe. Once assembled, the cavities are immersed in liquid helium inside a cryomodule. The liquid helium chills the cavities to a superconducting temperature of $-271°$C. The accelerator consists of 338 such superconducting cavities [17].

CEBAF's linacs are each composed of 168 RF cavities. There were two linacs laid out in parallel along the "straightaways" of CEBAF's 7/8 mile racetrack course [17]. The linear accelerators were connected by nine recirculation arcs, allowing the beam to make a total of five passes through each linac, for a maximum achievable energy of ≈ 6.0GeV. A graphic presenting an overview of the major accelerator components is given in Figure 2.2.

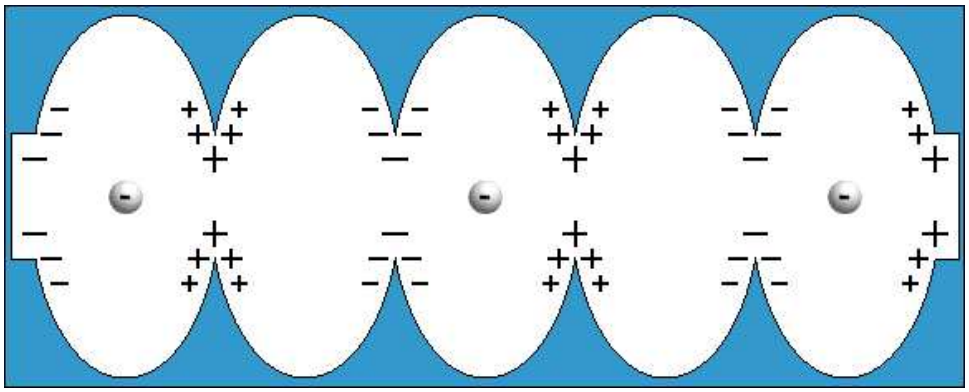

Figure 2.4: Microwave radiation supplied from klystrons is fed into the RF cavities to establish a standing wave. The frequency and phase of the waves are set so that there was always an electric force on an electron bunch as it propagates through an RF cavity [17].

Beam for the experimental halls was extracted by RF separator cavities. All three halls can run at the five-pass energy, or individual halls could choose to have their beam extracted after fewer passes through the accelerator.

2.3 Hall B and CLAS

Hall B is the smallest of the three experimental halls at JLAB. It is most well known for housing the CLAS detector, but Hall B also contains a photon tagger system, and various beam measurement tools. With the exception of the RADΦ experiment, every experiment in Hall B has utilized CLAS. Upon entering the experimental hall, the electron beam is directed toward the photon tagger. In the case that the run conditions call for an electron beam, the tagger system is not used. When run conditions call for a photon beam, the photon tagger uses the electron beam to produce a beam of photons via the bremsstrahlung process. This photon beam then goes on to interact with the CLAS cryotarget positioned within CLAS. The products of the resulting interactions are then tracked by CLAS and, if the trigger conditions are met, recorded by data acquisition. This section will provide an overview of the photon tagger, CLAS detector, beamline devices, and data acquisition system used for the collection of the g11a dataset.

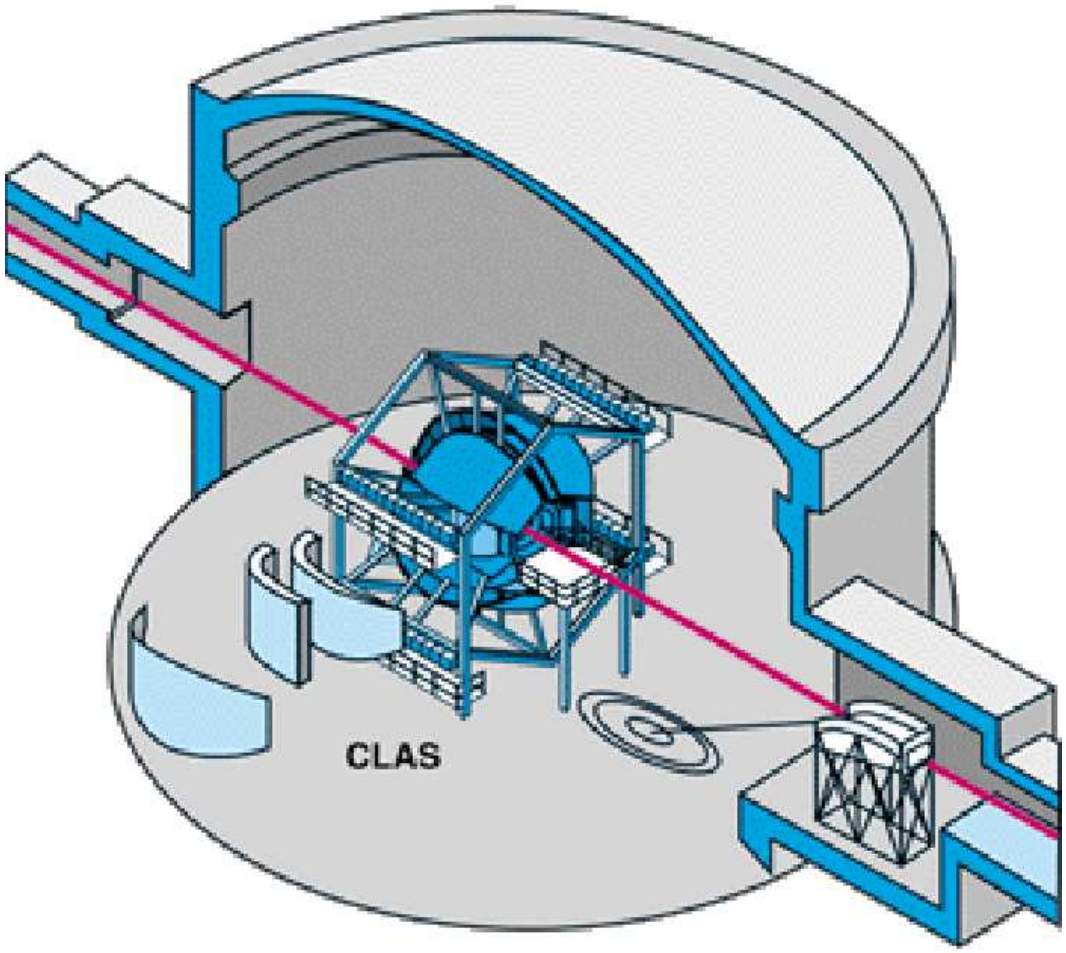

Figure 2.5: This is an exploded schematic of Hall B and the CLAS detector. Beam travel from right to left in this diagram. Also seen here is the relative position of the CLAS photon tagging system to the CLAS. Source: [57].

2.3.1 The Photon Beamline

The purpose of the photon beamline is to produce, and determine the energy of, photons incident on the CLAS cryotarget. There are several parts to the photon tagger system including, a radiator, a magnetic spectrometer, and collimators. The relative position of the radiator and magnetic spectrometer can be seen in Figure 2.6. A detailed description of these parts of the photon tagger system will be presented here.

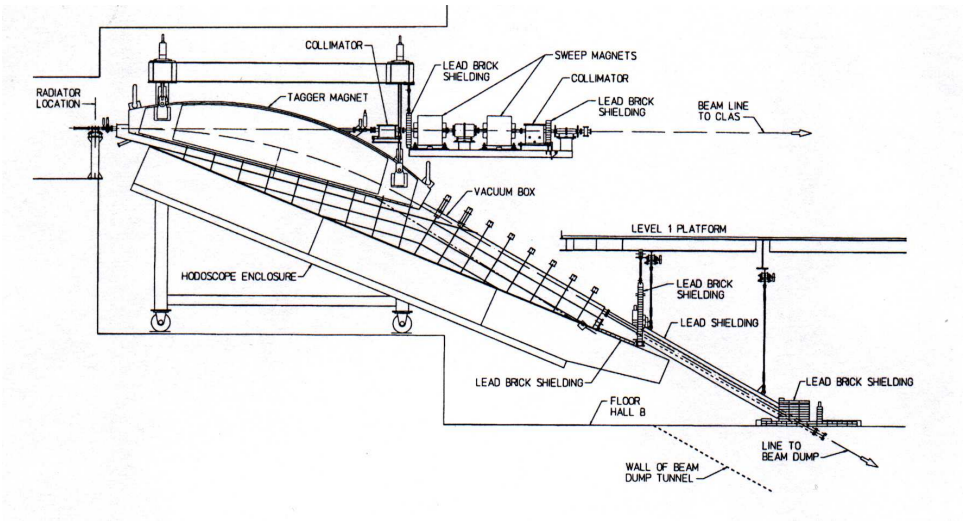

Figure 2.6: The foil radiator and the magnetic spectrometer of the CLAS photon tagging system. Beam travels from left to right in this diagram. Image taken from [38].

Radiator

The bremsstrahlung radiator target ladder is based on a modification of a HARP design used throughout the CEBAF accelerator as an electron beam position monitor. Radiators of high atomic number (Z) were used in order to minimize the effects from electron-electron bremsstrahlung in the spectrum.

The foils are prepared through deposition onto standard 2.54×7.62 cm^2 microscope slides treated with a release agent. The thinner radiators are combination films of gold on a backing of carbon made with one of two methods; (1) carbon deposition by carbon-arc discharge followed by gold deposition by electron beam, or (2) carbon and gold both deposited by electron beam in one vacuum cycle. The thicker radiators are free standing gold films.

The g11a run conditions called for a radiator with a thickness of 1×10^{-4} radiation lengths.

Tagger Spectrometer

After hitting the gold foil radiator, the beam is a mix of electrons which did not interact in the radiator, scattering electrons, and photons. The tagger magnet sweeps the electrons out of the beam, allowing photons to continue toward the CLAS cryotarget. The tagger magnet is a normal-conducting dipole that produces a maximum field of 1.75 T. The magnet was designed to provide momentum resolution of 2×10^{-4}, although the overall tagger e^- momentum resolution was ultimately limited to be $.001 \times E_\gamma$ by the hodoscope planes. The magnet was tuned to direct full-energy

Table 2.1: Table of Available Radiators for the Photon Tagging System. Source:[38]

Radiation Length	Composition
1×10^{-6}	$4\mu g/cm^2$ Au, on $15\mu g/cm^2$ C
2×10^{-6}	$10\mu g/cm^2$ Au, on $15\mu g/cm^2$ C
5×10^{-6}	$30\mu g/cm^2$ Au, on $15\mu g/cm^2$ C
1×10^{-5}	$62\mu g/cm^2$ Au, on $15\mu g/cm^2$ C
2×10^{-5}	$129\mu g/cm^2$ Au free standing
5×10^{-5}	$323\mu g/cm^2$ Au free standing
1×10^{-4}	$646\mu g/cm^2$ Au free standing

electrons (those which did not interact with the radiator) toward a beam dump, while lower-energy scattering electrons were bent at greater angles toward the two hodoscope planes of the spectrometer for measurement.

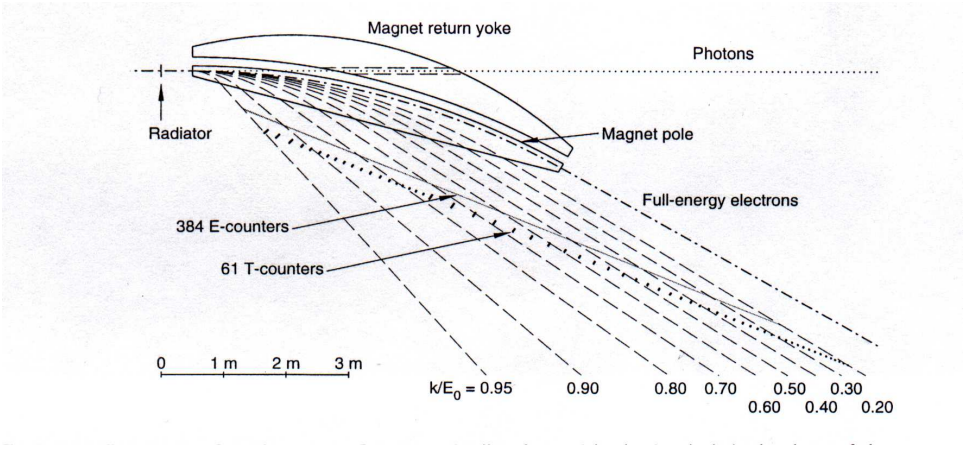

Figure 2.7: The path of electrons and photons as they pass through the magnetic spectrometer of the CLAS photon tagging system. The location of the E-counter plane and T-counter plane is also indicated. Image taken from [38].

There are two hodoscope planes which are similar in construction, but serve different purposes. The scintillators were positioned so that their surfaces were normal to the local trajectory of a scattering electron. The first scintillator plane is the "E-plane" and is used for momentum determination of the scattering particles. It contains 384 individual scintillator paddles that are 20 cm long, 4 mm thick, and from 6 to 18 mm wide. Because the trajectory of a scattering electron in the magnetic field is a function of the electron's momentum, different regions in space along the hodoscope plane corresponded to differing electron energies. So if an electron passes through a given paddle, its momentum is determined. The E-plane scintillators are arranged in an overlapping configuration which then creates 767 logical paddles, providing an energy resolution of 0.1% of the incident electron energy.

The function of the second plane, or "T-plane" is to obtain accurate timing measurements of the recoiling electrons. The T-plane had 61 plastic scintillator paddles 2 cm thick and from 9 to 20 cm wide. The widths of these paddles are varied so that counting rates in the paddles are

uniform, considering the $1/E_\gamma$ drop-off of the energy spectrum of bremsstrahlung photons. The timing resolution of the tagger spectrometer is 110 ps. The spectrometer is capable of tagging photons of 20% to 95% of the incident electron beam energy. A diagram of the tagger, showing trajectories for scattering electrons of various fractional energies is given in Figure 2.7.

Signals from the scintillator paddles are read out by photomultiplier tubes (PMTs). The T-counter PMT signals were sent to a Phillips 715 constant fraction discriminator. Signals satisfying the discriminator were then fed to the "Master OR" (MOR) and an array of FASTBUS TDC's. The Master OR is a large "OR" gate which accepts input from all 61 T-counters. The MOR is one of the main inputs of the g11a trigger and will be discussed later in Section 2.6. A TDC array was used to count the total number of hits registering in the tagger for the purpose of computing the photon normalization. Timing information provided by the T-counters was also used to associate the correct electron with an event, as multiple electrons per event were typically recorded during readout. The E-counter signals were discriminated by a Phillips 6816 amplifier discriminator unit and then sent to a multi-hit TDC. The timing signals from the E- and T-counters were recorded during event readout and used during offline data analysis to establish coincidence between the signals. A schematic diagram of the tagger front-end electronics is given in Figure 2.8.

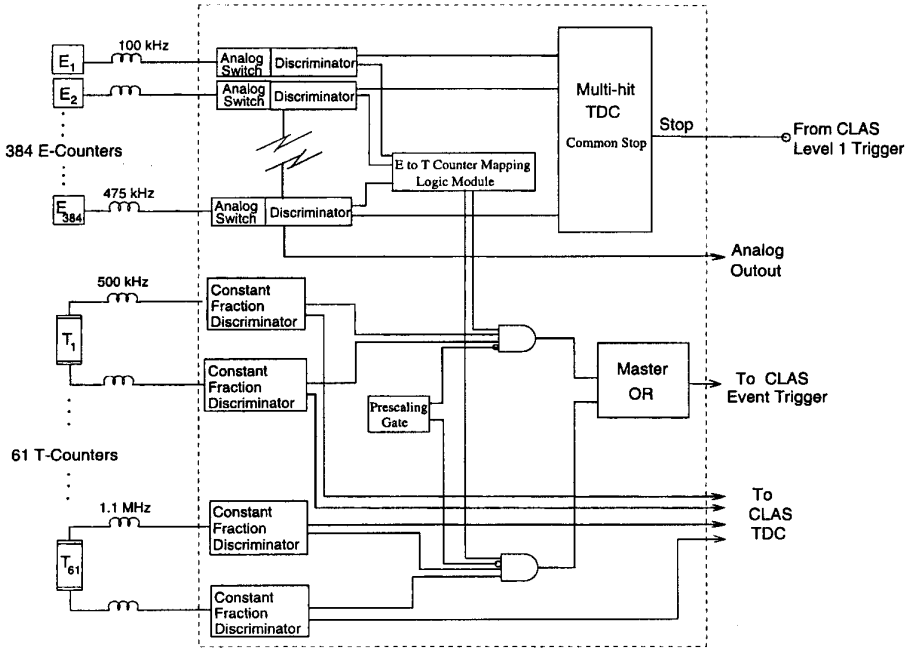

Figure 2.8: A block diagram of the tagger electronics. Image taken from [38].

While the energy of the scattering electron yields a measure of photon energy, the tagger timing information is used during offline analysis to produce an accurate determination of the event start time. The tagger time signal is used to correctly identify the beam bucket to which a given event corresponds; the 110 ps resolution of the tagger is adequate to uniquely identify a beam bucket. The accelerator RF signal is the most accurate time signal in the experimental setup, so the "RF time" is recorded by a TDC within Hall B for each event. Once an event is correlated with the proper beam bucket, the RF time is propagated to the event's interaction vertex to yield the event's "vertex time".

During data collection for g11a, only the 40 of the 61 T-counters (covering 40% to 95% of the photon energy range) of the tagger were active as part of the trigger, though all of the tagger

recorded data when the trigger requirements were met. Additional detail about the tagging system and spectrometer can be obtained from [18].

Collimators

The photon beam passes through a pair of collimators on the way toward the CLAS cryotarget. Between the first and second collimator, the beamline is equipped with sweeping magnets to remove charged particles created in the first collimator as photons interact with the collimator walls. For the g11a data run, the first collimator was 8.6 mm in diameter and was positioned 5.8 m from the radiator. The second collimator was 17.3 mm in diameter and was positioned 8.84 m from the radiator. The primary function of the collimators is to reduce beam halo.

2.4 CEBAF Large Acceptance Spectrometer

The CLAS detector was used to track and detect reaction products. To accomplish this, the detector utilized several detector subsystems. There was an inner start counter, three layers of drift chambers, an outer scintillator shell for time-of-flight measurements, and a Cherenkov detector and two electromagnetic calorimeter packages in the forward direction. A superconducting toroidal magnet enabled measurements of track momentum.

This particular analysis made use of the start counter, the drift chambers, and the time of flight, while ignoring the Cherenkov detector and the calorimeters. Described in this section are the apparatus used for this analysis at JLAB, as pictured in Figure 2.9.

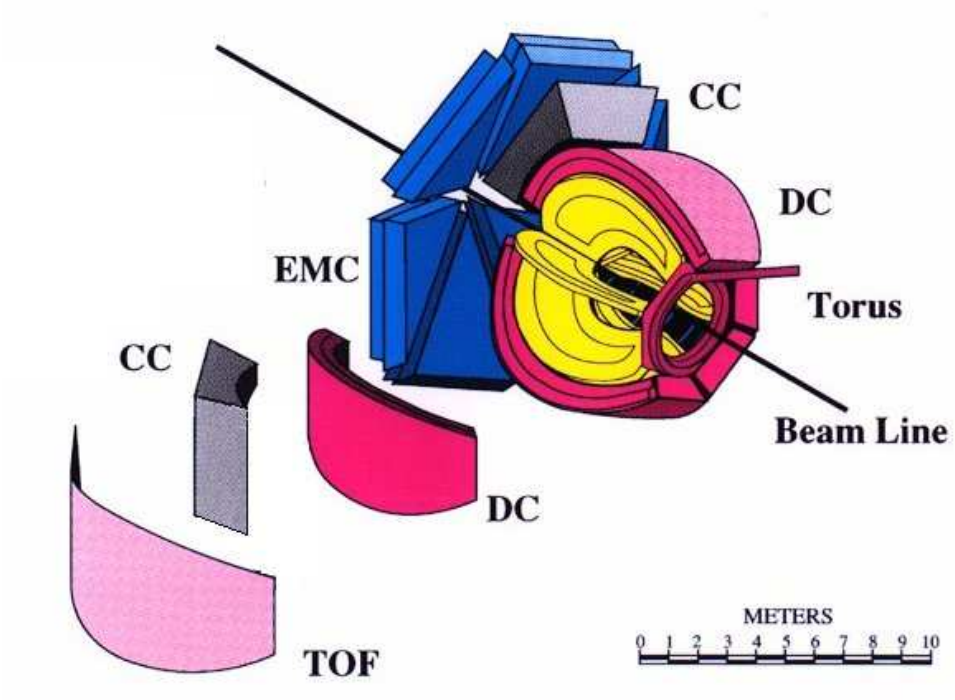

Figure 2.9: A exploded view of the CLAS detector. Source: [58]

2.4.1 The Target

The target material for the g11a run period was liquid hydrogen. The target cell was a cylindrically shaped Kapton shell that was designed by CLAS technician Steve Christo. To maintain the liquid state of the hydrogen, the target was cryogenically cooled. The length of the g11a target was 40.00 cm and roughly 5cm in diameter. The target was positioned slightly upstream -10.0cm with respect to the center of the CLAS detector. The location is measured from the center of the target to the center of CLAS. The negative sign is used to denote the upstream direction of the placement. The upstream position was chosen to improve the acceptance of positively charged tracks in the forward direction. An image of the target is presented in Figure 2.10.

Figure 2.10: The CLAS g11a target. The target is 40cm in length and slightly conical in shape. Additional details, and a detailed diagram can be located at: [19].

2.4.2 The Start Counter

For the g11a run period a new start counter was installed. It was designed to provide full acceptance coverage as defined by the CLAS detector and based on a target length of 40.0 cm. There are a total of 24 paddles divided into 6 sectors in ϕ. Each sector couples 4 scintillators together through an acrylic light guide. The central scintillators bend inward around the downstream end of the target to provide forward coverage, while the scintillator on either edge of the sector, taper to a triangular piece to accommodate the limited space at the nose of the start counter. See Figure 2.11

Scintillators which are very long and thin provide a technical challenge in that it is difficult to produce enough useful light for the detector to be effective. This challenge led to the use of a different wrapping material for the scintillator. A radiant mirror film called VM-2000 from 3M was used, instead of more traditionally used aluminized Mylar.

The acrylic light guides taper to meet a 15mm Hamamatsu 10-stage R4125HA photomultiplier tube. The PMT signals from the 24 start counter paddles are sent to ADCs and CAMAC C207 discriminators. The discriminated outputs are then sent to both the VME V775 TDC modules and to the trigger logic.

The hermiticity of the new start counter was estimated by direct measurements to be no less that 98 percent. Each of the six sectors were assembled separately, and then mounted on a hexagonal support shell made of high-strength foam. The sag at the downstream end of the start counter when fully assembled was measured and was less that 0.1mm. The base with the flange, the light guides, PMTs, and housings were completely outside of the useful acceptance of the CLAS detector. Testing of the start counter using CLAS was done and for events with several charged tracks. Testing indicated that, presuming a Gaussian timing distribution, the start counter achieved its design goals of standard deviation < 388 ps.

This analysis did not use the start counter for tracking, but the start counter was implemented as part of the Level 1 trigger for the data acquisition, so a description of the start counter hardware was warranted. For additional detail regarding the start counter, see [20].

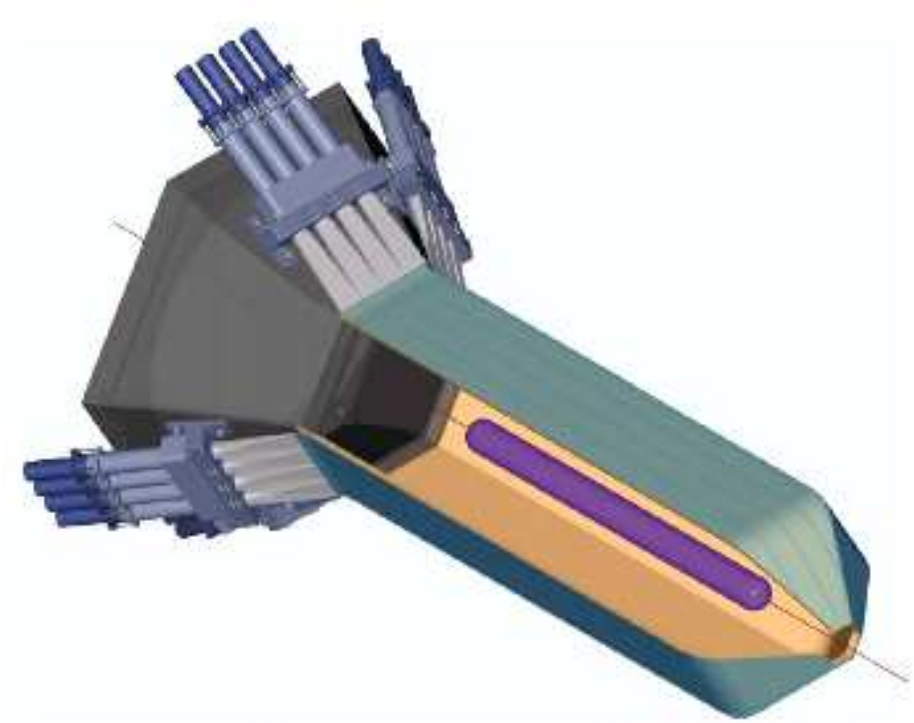

Figure 2.11: The CLAS start counter. Here the target is the cylindrical purple piece in the center of the cut-away. The scintillator paddles are indicated in the dull blue-green color, and the light guides and PMTs are indicated in gray and blue. Image source: [20].

2.4.3 The Superconducting Toroidal Magnet

The superconducting toroidal magnet was one of the most important systems in the spectrometer, both structurally and scientifically. The magnetic field, combined with the tracking system, is used for momentum determination of charged particles traveling through CLAS. The toroidal magnet also drove the overall geometry of the CLAS detector. A picture of the bare torus coils is shown in Figure 2.12.

The magnet is made up of six superconducting coils arranged around the beam-line, separated azimuthally by 60°. The magnet as a whole is approximately 5 m in length, and 5 m in diameter.

The magnet has a peak current of 3861 A and produces a peak field of 3.5 T. The magnetic field points in the azimuthal direction around the beam. The default or "normal field" configuration is set such that negatively charged particles are bent inward toward the beam pipe while positively charged particles are bent away from the beam pipe. By reversing the current direction, the opposite field configuration is achievable, and is referred to as "reverse field". Each of the 6 coils have 4 layers of 54 turns of aluminum stabilized NbTi/Cu conductor. The magnet is cooled to an operating temperature of 4.4 K using helium supplied by the central CEBAF helium refrigerator.

The torus coils were structurally important in the design and construction of the detector. Drift chambers were mounted directly to the cryostats. The torus cryostats also defined the geometry of the fiducial region of the detector. The coils determined the sector boundaries; electronics and other non-sensing components of other detector systems were constrained to fit in the shadow regions created by the torus cryostats.

During the g11a data run, the torus was run in "normal field" mode with a nominal current of 1920 A. More details of the torus are given in [21].

Figure 2.12: The bare coils for the CLAS toroidal magnet in place on the carriages that hold the detector. The cross members were actually thin carbon-fiber posts. Image source: [22].

2.4.4 The Drift Chambers

Tracking of charged particles in the fiducial region radially outward from the start counter is provided by three layers of drift chambers. These layers are also referred to as "regions". Region 1 is the inner-most drift chamber layer and is positioned inside the torus cryostats. Region 2 is mounted directly to the cryostats and sits in the region of high magnetic field. Region 3 is the furthest out from the target and is in a region of low magnetic field. Figure 2.13 gives a cutaway of CLAS showing the positions of the drift chambers relative to the torus cryostats. Each region is divided into 6 "sectors" to match the geometry of the coils of the torus magnet.

Each region is also divided radially into two "superlayers", one superlayer with the wires oriented axially with respect to the magnetic field direction, and the second superlayer having the wires tilted

off-axis at a 6° stereo angle. In Region 1, the stereo superlayer is closer to the beam, while Regions 2 and 3 have the axial layers closer. Within each superlayer, there were typically six layers of drift cells, with neighboring layers being offset by half a cell width to provide an overlap of the cells allowing for more precise tracking.

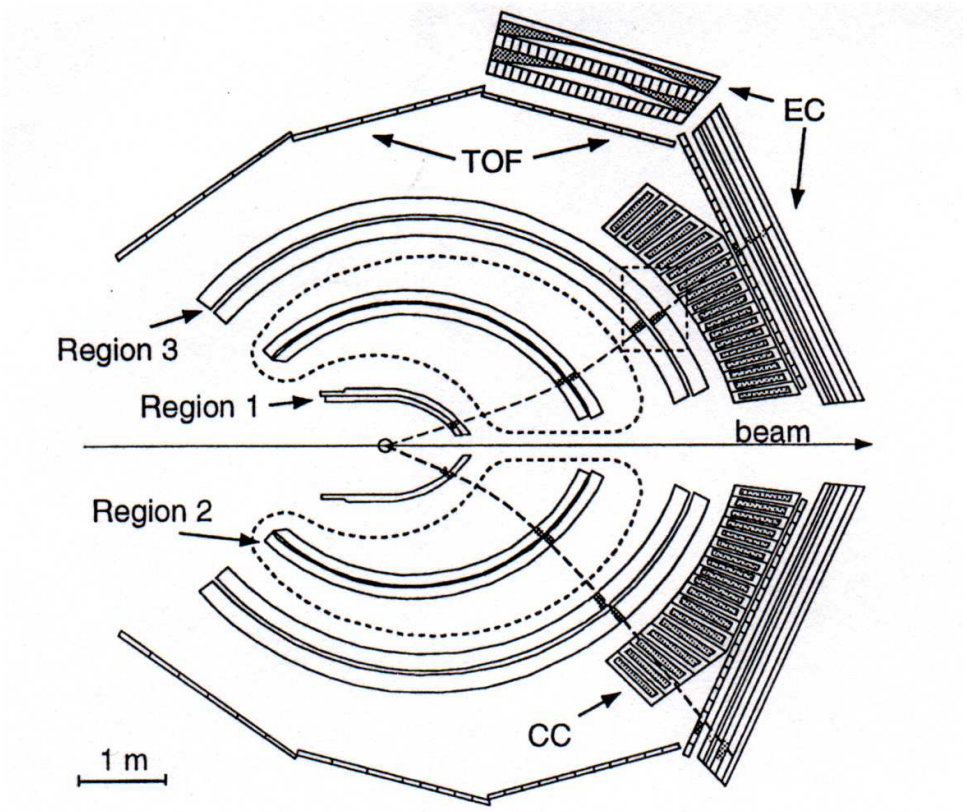

Figure 2.13: A Cut-away diagram of CLAS showing the positions of the various detector packages. The drift chambers are labeled as "Region 1", "Region 2", and "Region3". The "TOF" is the outer scintillator time-of-flight detector. Image source: [23].

Each sector contains 5,858 individually-instrumented hexagonal drift cells. The sense wires are made of 20 μm gold-plated tungsten and are located at the center of the hexagonal cells. Six field wires, made of 140 μm gold-plated aluminum alloy wire, surrounded each sense wire. The field wires are held at negative high voltage while the sense wires are maintained at a positive potential. The drift gas chosen for the CLAS drift chambers is a 90%-10% Argon-CO_2 mixture. This particular mixture was chosen because it has a relatively high saturated drift velocity ($> 4cm/\mu s$), as well as an operating voltage plateau of several hundred volts before breakdown. Additionally, as a safety measure, it was required that the drift chamber gas be non-flammable.

Signals from the sense wires are first sent to Signal Translation Boards (STBs). The STBs decouple the signal from the high voltage and then the signals are routed to single in-line package (SIP) transimpedance preamplifiers. From here, the differential amplified signals are sent to amplifier discriminator boards (ADBs) located on the CLAS support frame. The discriminated signals are then go to the timing electronics, which is comprised mainly of LeCroy 1877 TDCs.

More information about the construction and performance of the drift chambers is given in [23, 24, 25, 26].

2.4.5 TOF

The outer layer of the CLAS is a segmented scintillator shell that resides roughly four meters from the cryotarget. Each sector has 57 scintillator bars mounted in four panels as shown in Figure 2.14. In order to simplify the electronics, the 18 scintillator bars at the largest lab angle were paired together to create 9 effective bars. In CLAS the TOF scintillator bars are numbered from 1 through 48. The scintillators in the most forward direction, where counting rates are the greatest, are 15 cm wide, while counters corresponding to a scattering angle greater than 45° are then 22 cm wide. The bars vary in length from 32 to 445 cm and mounted so that their lengths projected perpendicularly onto the beamline. All bars are 2 inches thick in order to provide 100% detection of minimum-ionizing particles.

The scintillators are each instrumented with a photo-multiplier tube at each end of the bar. The PMT's are mounted in the shadow of the magnet's cryostats, to keep them out of the fiducial region of the detector. The PMT's interface the scintillator bars with the help of short lightguides made of lucite.

The timing resolution of the scintillator shell ranges from 80 to 160 ps and is a function of the counter lengths; longer counters have poorer resolution. More details on the construction and performance of the TOF system may be found in [27].

The time-of-flight shell provides a vital timing measurement for each track as it leaves the CLAS detector. Signals from the TOF scintillators may be collected quickly, so the time-of-flight shell is a key input to the CLAS trigger. Offline, the TOF signal is a key component of the particle identification that has been implemented in this analysis.

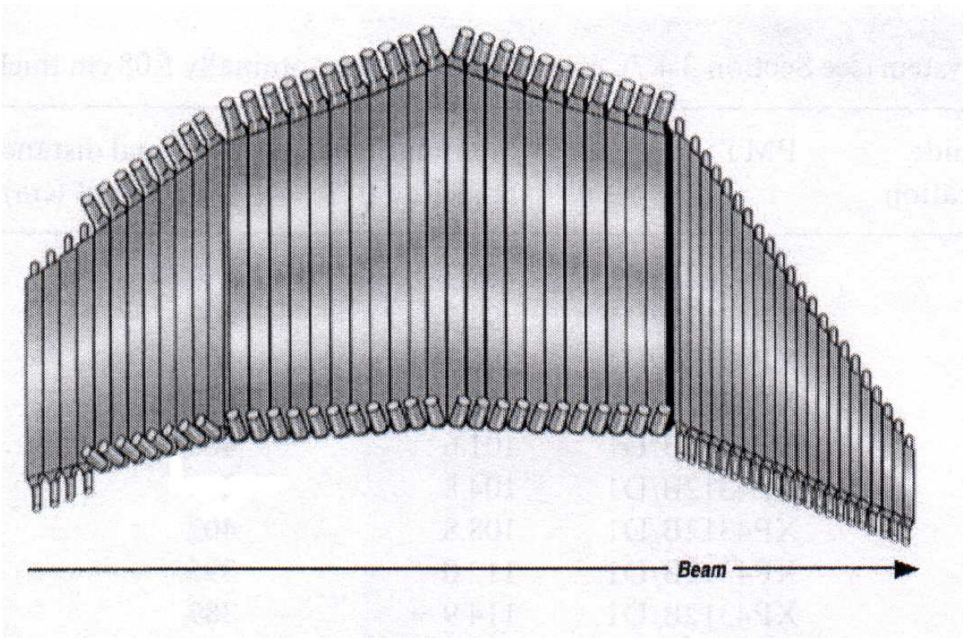

Figure 2.14: Scintillator shell for one CLAS sector. The scintillator bars are mounted in four panels that cover scattering polar angles from 8° in the forward direction to 142°. The PMT's shown lie in the shadow of the cryostats for the toroidal magnet. In the forward direction and extreme backward direction, smaller PMT's and straight lightguides were used. Elsewhere, the light guides were bent 90° to accommodate larger PMT's. Image source: [27].

2.5 Beamline Devices

Aside from the main CLAS detector, the physics program in Hall B requires the use of numerous beamline devices. Upstream from CLAS, beam position monitors, harps and current measuring devices are used to monitor beam quality. Downstream, the total absorption shower counter (TASC), pair spectrometer (PS), and pair converter (PC) are used to measure photon flux for normalization.

2.5.1 Beam Position Monitors

The pickup for the beam position monitors (BPM's) was a normal-conducting RF cavity operating at 1497 MHz. The beam position monitors provided an x and y position measurement with a resolution of less than 0.1 mm and a current measurement. The BPM's were capable of monitoring beam over a current range from 1 to 100 nA. The BPM's reported at a rate of 1Hz [28]. Signals from the BPM's were used in continuous feedback loops to constantly ensure acceptable beam positions during data acquisition.

Three BPM's are installed on the beamline, at 36.0, 24.6, and 8.2 m upstream from the target. During photon experiments, only the first two BPM's were functional [29].

2.5.2 Harps

Harps provided a means of studying the beam profile. The harps in Hall B consisted of a pair of wires oriented to scan the beam profile in orthogonal directions. Electrons scattered by the harp wires could be detected by just about any detector element in the Hall, but the standard device was an array of PMT detectors located downstream from the harps. The wires in the harp were made of both tungsten and iron. Three harps were located at 36.7m, 22.1m, and 15.5m upstream from the target. The PMT array was placed at 6.8m. Harp scans would disrupt the beam and could only be performed while the data acquisition system was not running [29].

2.5.3 Total Absorption Shower Counter

The total absorption shower counter (TASC) consisted of four lead glass blocks assumed to have perfect detection efficiency for photons. The glass was made of 55% PbO and 45% SiO_2 and had a radiation length of 2.36 cm. The blocks were each 10 cm $\times$ 10 cm $\times$ 40 cm and were mounted in a 2 $\times$ 2 array with the longest dimension positioned parallel to the beam. Each block was individually instrumented with a Philips XP4312B phototube.

Although the TASC was used to obtain an absolute measure of the photon flux, it could only be used at beam currents lower than 100 pA. During production data taking, the TASC was removed from the beamline. It was inserted periodically during lower-intensity "normalization" runs. More details about the TASC can be found in [18] and [29].

2.5.4 Pair Spectrometer

The pair spectrometer (PS) consisted of a large aperture dipole magnet, an aluminum converter and an array of eight scintillator paddles. The converter resided within the field of the dipole magnet. As photons struck the converter, they produced e^+e^- pairs, which the magnetic field swept out of the beamline and directed toward the scintillator paddles. Two converters were made of aluminum and had thicknesses of 1% or 2% of a radiation length. The scintillators were positioned so that the PS would detect e^+e^- pairs over the full energy range of the tagger spectrometer. The segmentation of the counters gives the spectrometer a degree of energy discrimination.

The pair spectrometer was used to measure the photon flux at higher beam intensities than was possible with the TASC. The PS was cross calibrated against the TASC during low-intensity runs, but then remained in the beamline during higher intensity runs of several nano-amps.

2.6 Triggering and Data Acquisition

The previous sections mentioned the first level of readout electronics applied to each detector system; each system had its unique package of electronics to monitor active components, discriminate, and collect signals. Above this level of electronics, the readout was controlled by the trigger and data acquisition system. The trigger looks at the preliminary signals from the faster detector elements to decide which events should be recorded. Events passing this hardware trigger are then packaged and recorded by the data acquisition system.

The initial hardware trigger (also called Level 1 trigger) provides a gate for the readout electronics based on signals from the tagger, start counter, and time-of-flight scintillators as they are the fastest detector systems in CLAS. The specific details of the g11a production trigger will be described elsewhere.

Tracks are identified by comparing signals from the detectors to pre-defined patterns. The trigger required three memory lookups. The first two lookups correlated information from the start counter and the time-of-flight scintillators within a single sector (all 6 sectors being processed in parallel). The third memory lookup then attempted to correlate a possible event with a hit in the tagger and further information from all six sectors. The average time it took to process an event with the Level I trigger was 90 ns.

CLAS has a Level 2 software trigger which was implimented on a few test runs for the g11a dataset. It was not used when collecting the g11a dataset.

The data acquisition and readout is shown schematically in Figure 2.15. Once an event satisfies the Level I trigger, the data acquisition is gated and begins to read out the event. Signals from the individual detector elements within CLAS are digitized and then read out by 24 VME readout controllers (ROC's). Data tables from the various systems were then sent to the CLAS online acquisition computer in the control room. The Event Builder (EB) running on the acquisition computer collects the data tables. The EB associates the tables into banks, and packaged the event into its final form before depositing it in a shared memory bank on the online computer. The Event Transport (ET) system manages the shared memory and makes events available to a number of online monitoring processes. It is also from this shared memory that the Event Recorder took delivery of events and wrote them to magnetic tape on the Jefferson Lab tape silo system [29].

Events are collected in "runs" and individual events within a run were tagged with a unique event number. Although run sizes vary greatly, a typical run contained 20 million triggers. Ideally, the length of a data run is determined by the shift workers in the control room, however runs often ended prematurely due to unforeseen troubles, such as the DAQ system crashing. Once written to tape, runs were saved as a collection of sequentially-numbered 2 GB files, a typical run comprising 30 files.

Assuming perfect running conditions would be naive. Systems are bound to fail during data acquisition, and the shift workers are expected to monitor and correct such problems. At all times during data taking, the control room was staffed by at least two workers. Workers were expected to maintain an online logbook, noting unforeseen troubles and detailing their solutions. Workers also were given the opportunity to record comments at the beginning and end of a run. These comments, with notes about the performance and difficulties encountered at run time allow for a better understanding of the data taken for analysis.

2.7 The g11a Run Conditions

In this section the g11a run conditions will be described. The original purpose of the g11a data run was to collect a large statistics data sample for a pentaquark study. The run conditions were thus set up to maximize efficiency for pentaquark production and detection in CLAS. This meant optimizing the run conditions and trigger for multi-track events, and maximizing the DAQ rate to record as much data as possible. While these run conditions were advantageous for study of the

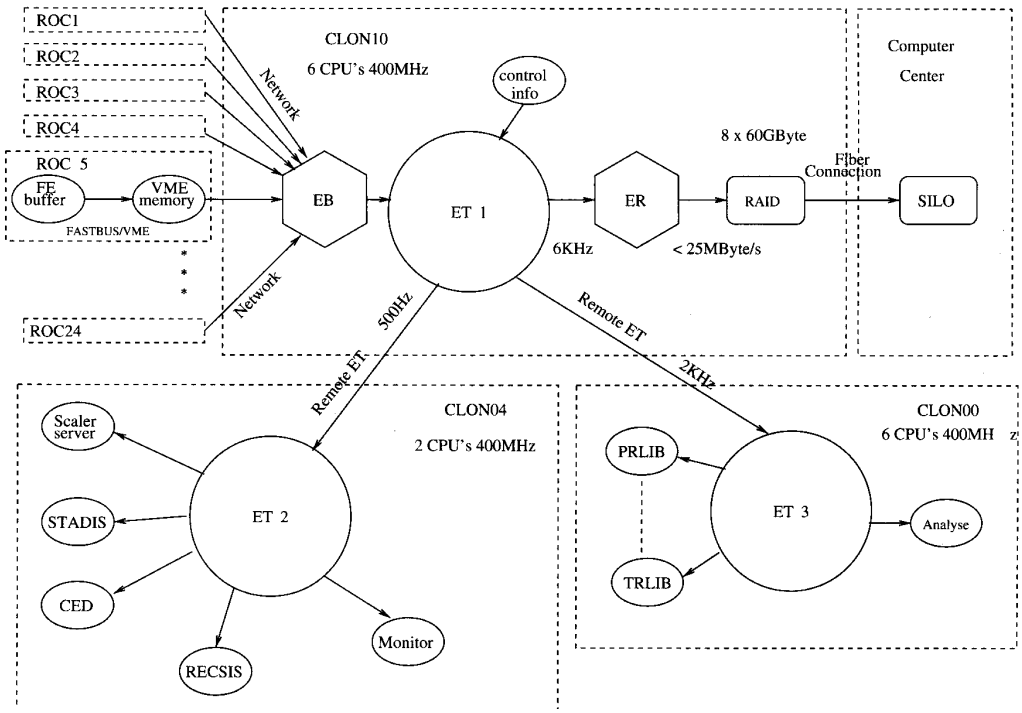

Figure 2.15: Signals from the detector subsystems were assembled by readout controllers (ROC's) and arranged into fragments. These fragments are packaged into an event by the Event Builder (EB). Event Transport (ET1) makes the events accessible to a variety of online subprocesses and monitors (managed by ET2 and ET3) from a bank of shared memory. The Event Recorder (ER) is responsible for writing the data to tape. Image source: [29].

purported pentaquark, it also provided a large data sample for multi-track events which has allowed for the study of η and η' photoproduction in this analysis with greater statistics than previously recorded.

2.7.1 The Beam Energy and Beam Current

The electron beam energy for the g11a data run was 4.017 GeV. This value was chosen to maximize coverage of the kinematic region where the pentaquark state was purported to exist. At the end of the run period, there were 26 runs which were collected with an endpoint electron beam energy of 5.021 GeV. These runs were not included in this analysis due to possible differences in systematics, but these runs comprised only $\approx$ 4% of the total data collected in the g11 run period.

2.7.2 The Target Requirements

The target material was selected for two reasons. The primary reason was due to the reaction channel of the purported pentaquark observation, which was $\gamma p \to \bar{K}^0\Theta^+$ and $\gamma p \to K^*\Theta^+$. The secondary reason for utilizing a proton target was to provide a complimentary experiment to the g10 data run which used a deuterium target for photoproduction off of neutrons.

2.7.3 The Magnet Settings

The g11a run period called for the main toroidal magnet to be at $0.5 \times B_{max}$. So the current was set to 1920 A for the duration of the data run. The magnitude of the magnetic field has an effect on two competing aspects of charged particle detection. The acceptance of small-angle negative particles is severely reduced by using a large magnetic field because they are bent strongly back into the beamline where they are not detectable. Alternately, the larger the B-field the better the resolution for missing-mass and invariant-mass plots. Selecting a B-field magnitude is a balance between the competing factors of detection efficiency and resolution. It was found that a reasonable compromise was to run at half of the available magnetic field magnitude.

2.7.4 The g11a Trigger

The g11a Level 1 trigger had several requirements specifically chosen to maximize multi-track event detection in CLAS. The trigger required 2 charged tracks in different sectors of the TOF of CLAS within a 100 ns timing coincidence window. It also required 2 hits in the Start Counter, matching the sectors of the TOF hits, within a 15ns coincidence timing window. Finally, the MOR from the Photon Tagger was required as well. The photon tagger was only triggered on the first 40 of the 61 T-counters, which biased the overall trigger towards events originating from higher energy photons. Figure 3.15 indicates the triggered and untriggered portions of the tagger as a function of photon energy.

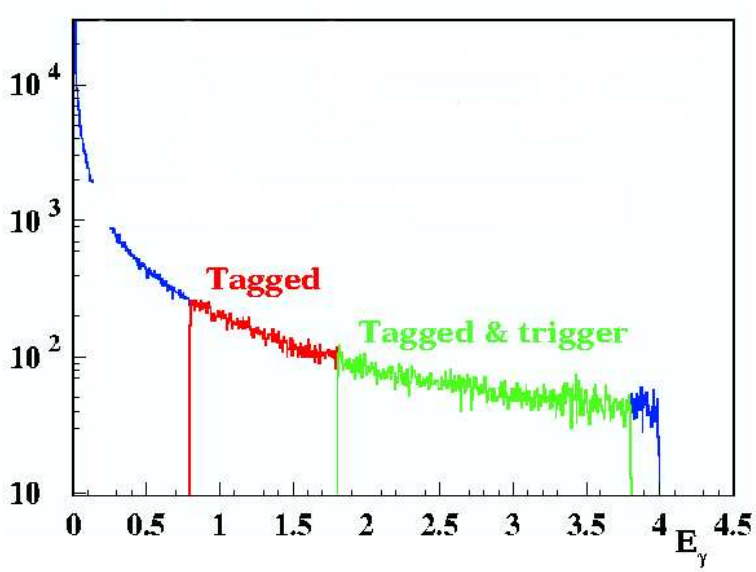

Figure 2.16: Plot of photon energy in the tagger. The Green area at higher energy indicates where hits in the tagger fired the trigger. In Red, are photons in the tagger which were not included in the trigger. The Blue points were outside of the range of the tagger for the given run conditions. Image source: [29].

So, to summarize in a symbolic mathematical form, the trigger condition is the following:

$$DAQTrigger = (PhotonTagger) \cdot (StartCounter(2sectors)) \cdot (TOF(2sectors)) \qquad (2.1)$$

Where the sectors of the TOF and the Start Counter are required to match.

The g11a run conditions yielded a trigger rate would be 4.1 kHz. The determining factors being beam current, radiator selection, and trigger condition. The total trigger rate is affected by the rates in separate parts of the trigger, as well as accidental triggers in CLAS and the tagger. The MOR×ST rate is affected by two accidentals. First, are hadronic events coming from photons of below the minimum tagger triggering energy of 1.6 GeV. The second is hits in the start counter from electromagnetic background. If there is a 10ns coincidence window between the Start Counter and the MOR from the tagger, then the accidental rates are calculated to be: $R^{acc_1}_{(MOR\times ST)\times CLAS} = 1.8kHz$ and $R^{acc_2}_{(MOR\times ST)\times CLAS} = 200Hz$ [30]. Combining these accidental rates with the true hadronic rate modified by the acceptance of CLAS, we arrive at the following expression for the total rate:

$$R_{trigger} = R^{true}_{hadronic} \times \epsilon_{CLAS} + R^{acc_1}_{(MOR\times ST)\times CLAS} + R^{acc_2}_{(MOR\times ST)\times CLAS} = 4.1kHz \tag{2.2}$$

This event rate was within the available DAQ rates for CLAS at the time the data were collected.

2.8 Summary

This analysis relies on the high statistics dataset produced during the g11 run period at CLAS. The experimental apparatus which allowed for the collection of that data has been described in this chapter. The particular conditions under which this data was collected was also described, as the run conditions contribute significantly to making this dataset one of the largest sets of photoproduction data available.

Chapter 3

Data Selection and Acceptance Determination

This chapter describes the CLAS g11a dataset used in this analysis, and the steps taken to select the $\gamma p \to \eta p$ and $\gamma p \to \eta' p$ reactions. The determination of the acceptance of CLAS for photoproduction of the η and η' mesons will be presented, along with any corrections to the data or Monte Carlo. The measurement of the photon flux and the overall normalization will be presented in this section as well.

The CLAS g11a data production runs were taken between May 17^{th} and July 29^{th} of 2004. There were a total of 20 billion triggers recorded in 421 production runs. There are a total of 10,500 BOS files of data, which, at 2GB per file, makes the total g11a dataset 21TB in size. The run numbers for this dataset begin with commissioning at run #43490 and end with higher beam energy runs at run #44133. This 21 TB dataset was the starting point for constructing the dataset eventually used for the analysis.

3.1 Preliminary Data Skim

The data was initially skimmed according to the number of charged tracks in the event. Events were selected that contained at least 2 positive and 1 negative charged track. This skim of the dataset was about 11 TB in size prior to being compressed using the Carnegie Mellon University data compression scheme. Post-compression the 2-positive/1-negative track skim was held on a 600 GB RAID disk, providing immediate access for analysis. The initial skim was made at the charged track level to allow for multiple analyses of several different photoproduction reactions using the same starting data set.

3.2 Channel Selection

Once the data has been skimmed according to the number of charged tracks, the particular reaction channels of interest must be selected. Additionally, some corrections must be made to the data to account for detector problems prior to event selection. These corrections include corrections to the tagger energy, momentum corrections, and energy loss corrections. Once the appropriate corrections are made, a very loose mass cut is made to save time in the more calculationally intensive cuts. As an example, in selecting the η a cut was made on the missing mass off of the proton to keep all events within 30.0MeV of the η mass of 547 MeV. The width of the η is known to be 1.3 keV, so a window of 30.0MeV in either direction should contain the entirety of the η peak. For the η', the cut was similarly broad, keeping all events within 50.0MeV of its 957MeV mass. The width of the η' is

listed as 203keV, so a cut at ±50MeV is reasonable way to begin selecting the particle of interest without losing signal.

The data is then kinematically fit to the missing particle for the reaction of interest. The η is identified by a kinematic fit to a missing π^0 coming from the $\eta \to \pi^+\pi^-(\pi^\circ)$ decay. The η' is identified by a fit to the missing η in the $\eta' \to \pi^+\pi^-(\eta)$ decay. Kinematic fitting will be described in a following section. Once the kinematic fit is complete a 1% confidence level cut is made, and a simple timing cut is made to select the dataset. The timing cut requires that at least one of the detected particles (p, π^+, π^-) have a vertex time within 2 nanoseconds of the photon vertex time. This timing cut is purposefully loose to retain signal, and select events for further scrutiny. Described in this section are the corrections made to the data, the kinematic fitting, and the cuts on the data to select the reactions of interest. Cuts made beyond the initial selection of the reactions will be described elsewhere. With a rough version of the data selected, the data is then binned into center-of-mass energy bins (W,$\sqrt{s}$). In each of these bins, the data will be analyzed. In order to facilitate the possible coupling of the η and η' analyses at a later time, the binning for the two datasets was set up equivalently. The binning scheme is shown in Table 3.1.

Table 3.1: The binning scheme used for the η and η' analyses.

W(MeV)	bin width (MeV)
$threshold \to 2100$	10
$2100 \to 2360$	20
$2360 \to 2680$	40
$2680 \to 2880$	50

Plots of the binned data are shown in Figures 3.1 and 3.2. The structure evident in the plots is mostly a binning artifact. When discretely changing from one bin width to another, there are jumps in the number of events in a given bin. This explains a majority of the discrete structure, however there is no change of bin width below 2000MeV. The discrete jump located there, and particularly well seen in the binned η data (Figure 3.1) is due to a triggering artifact. In this case the tagger was only triggered on the higher energy photons, which means there is a systematic drop in the number of events collected in the lower energy range.

3.3 Kinematic Fitting

Kinematic fitting is a mathematical process that uses physical constraints, such as energy and momentum conservation, to improve event measurements. A description of kinematic fitting and its uses is also given in a CLAS analysis note from M. Williams and C Meyer[31]. The initial step of the kinematic fitting process is construction of the full tracking covariance matrix. During tracking a covariance matrix is produced containing the resolution errors and correlation coefficients of the tracking parameters for each track. Energy loss and multiple scattering effects must be added to improve the accuracy of the covariance matrix.

Next, the kinematic fitting itself is done. The process uses the method of Lagrange multipliers to handle physical constraints, and a least squares fitting method. Essentially the kinematic fit uses energy and momentum conservation to determine what the best values of the track momentum should be. The tracking parameters are varied within their errors to yield a kinematically consistent fit to the hypothesized production and decay sequence. The amount that the tracking parameters need to be adjusted yields a confidence level of the fit for that event. The confidence level is a standard formula for determining the goodness of fit to a hypothesis. This confidence level can later be used to determine which events to cut, in an attempt to remove background events. Background

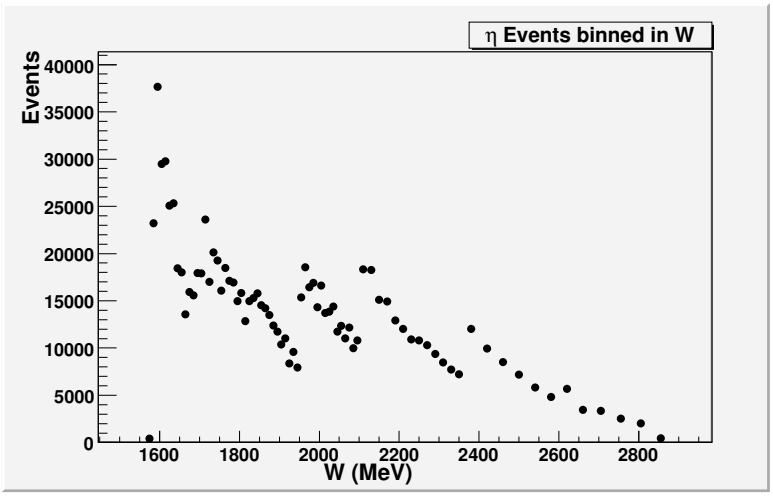

Figure 3.1: A plot of the binned η events which passed the original reaction channel skim as binned in center-of-mass energy, W. This plot is made without the use of the more specific cuts which more cleanly define the dataset. The structure seen is a combination of effects. The larger number of events at threshold, followed by drop-offs is a function of the photoproduction cross section. The discrete jumps at $2100, 2360, 2680$MeV originate in the difference in binning widths from one region in W to another. The discrete jump located just below 2000MeV is caused by the trigger conditions, which indicated that only the higher energy portion of the tagger is included in the trigger. This caused a systematically lower number of events to appear in the lower bins.

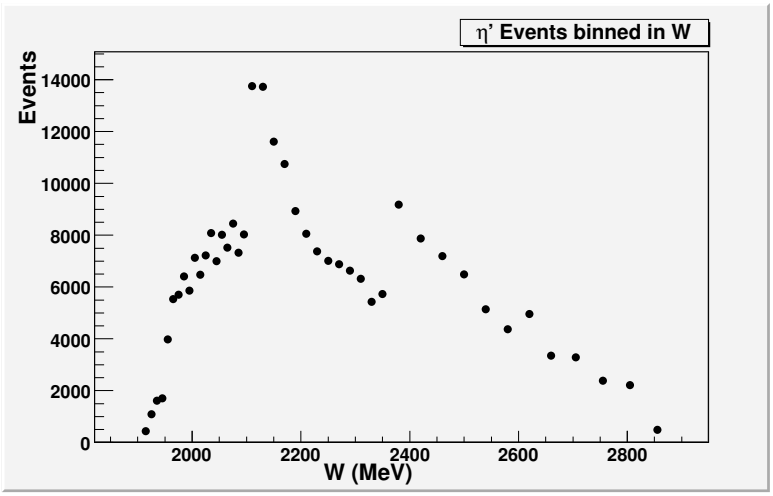

Figure 3.2: A plot of the η' events which passed the original reaction channel skim as binned in center-of-mass energy, W. This plot is made without the use of the more specific cuts which more cleanly define the dataset. The discrete jumps at $2100, 2360, 2680$MeV originate in the difference in binning widths from one region in W to another.

events generally do not satisfy the kinematic constraints placed on them by the kinematic fit, thus producing a confidence level which is very low, allowing them to be removed via a cut.

At this point, a smaller subset of the original data set has been selected for analysis.

3.4 Acceptance and Monte Carlo

In order to fully understand the acceptance of CLAS for this analysis the CLAS GSIM simulation package was used. GSIM is a GEANT-based simulation of the CLAS detector and is the collaboration's standard simulation package [34].

For the η reaction there were 150 million simulated events run through the simulated CLAS detector. For the η' reaction 50 million Monte Carlo events were generated. In order to determine the most efficient distribution in which to throw the Monte Carlo events, the data events were plotted as a function of incident photon energy. This distribution was used as the template for the generated distribution of the Monte Carlo. This assured that there would be enough Monte Carlo for each W bin, while not requiring excess computing time. It is important to note that while the photon energy distribution for events thrown was not flat, the events themselves were thrown flat in $p\eta$ and $p\eta'$ phase space. The decay of the η in the Monte Carlo was an input, specifying the $\eta \to \pi^+\pi^-\pi^\circ$ decay. The decay of the η' was specified to be be $\eta \to \pi^+\pi^-\eta$, with the η then free to decay to according to physics..

Once generated, the events were processed by GSIM, which propagated the particle tracks from their vertex positions through the CLAS detector and generated a simulated set of detector signals for the tracks. GSIM included the effects of particle decays, multiple scattering, and scattering from structures within CLAS. Output from GSIM was packaged in the standard CLAS data file structure.

The GSIM output was then processed with a code called "GPP". The GSIM code assumes that CLAS has perfect timing resolution, which it clearly does not have. The GPP code provides for several corrections which are required for an accurate simulation of the detector. It takes into account the holes in the drift chambers and paddles, as well as allowing for the smearing of the timing resolution. For this analysis however, GPP was only used to account for drift chamber holes and help correct for time of flight inefficiencies. The smearing itself was accounted for separately by Mike Williams based on the momentum corrections[41].

Monte-Carlo events processed by GSIM and GPP were the equivalent of actual data read from the detector and immediately written to tape. The Monte-Carlo still needed to be cooked and treated by all of the code normally used in the offline data processing. The cooking was handled by the code called "RECSIS". To ensure that the acceptance calculations accurately reflected any software bugs or biases affecting the data, the same versions of the CLAS software were run on the Monte Carlo simulation that had been used during the cooking of the g11a data. Additionally, it was vital to maintain consistency between the different analyses which are a part of the CMU PWA program. To this end, all of the g11a Monte Carlo was generated by Dr. Curtis Meyer using the same set of control files, with the same smearing and scale factors.

After being cooked the Monte Carlo was processed by the CMU data compression code, to put it in the same format as the data. From there corrections were determined to assure that the Monte Carlo accurately represented the data that had been collected in the g11a data production runs. When there were errors in the Monte Carlo, there were two ways to correct it. The first option was to regenerate the Monte Carlo, assuming the inconsistencies could be solved in that way. An example of this might be an adjustment to the amount of smearing in the simulation. The second option was to correct the Monte Carlo after it was generated. These corrections made post-generation will be enumerated in a later section. The Monte Carlo was binned identically in W to the data, and any applicable cuts on the data were also applied to the Monte Carlo.

3.5 Energy and Momentum Corrections

This section documents the energy and momentum corrections used to improve the data. Both the tagger and momentum corrections were derived using the $\gamma p \to p\pi^+\pi^-$ channel and the kinematic fitting procedure. The only requirement is that the events used for determining the corrections are actually $\gamma p \to p\pi^+\pi^-$. For this stage of the analysis, the standard CLAS particle identification scheme is used. It is strict enough to ensure that the background leakage from misidentified particles is negligible, and it is easy to implement.

The procedure used to calculate the tagger and momentum corrections is as follows. First we obtain the tagger corrections. These corrections are then applied when obtaining the momentum corrections. To reduce the likelihood of a drastic effect from one correction affecting the other correction, an iterative process is used.

For each iteration the previous iteration's momentum corrections are applied. The tagger corrections are then recalculated, and used to then recalculate the next iteration of momentum corrections. When the corrections are stable after iterations the process is finished. The particulars of calculating each correction will be described.

3.5.1 Energy Loss Corrections

The momentum vectors of the proton, π^+ and π^- were each corrected for energy lost as they passed through material in the detector.

At the energies used in the CLAS detector, charged particles lose energy in matter primarily through atomic excitation and ionization [4]. Corrections were made to account for energy lost in the target material (liquid hydrogen) and target walls, the beam pipe, the start counter and the air gap located between the start counter and the Region 1 drift chambers. The corrections were applied by the "eloss" software package written by Eugene Pasyuk for the CLAS detector [35].

3.5.2 Tagger Corrections

Gravitational sag in the photon tagger's focal plane were first discovered in 2003 [36, 37, 38]. This leads to an inaccurate photon energy constructed from the raw tagger information. We can obtain an empirical correction for this effect using the $\gamma p \to p\pi^+\pi^-$ channel.

To start, events are selected with only one proton, π^+ and π^- and no other charged tracks. Energy loss and momentum corrections are then applied, to the final state particles. Then each event is kinematically fit to an event hypothesis of $(\gamma)p \to p\pi^+\pi^-$ while ignoring the measured photon energy. A 10% confidence level cut from the kinematic fit excludes event which are not consistent with the event hypothesis. For each event included in calculating the correction, the kinematic fit produces a calculated photon energy(E_γ^{kfit}) for the photon in the event. This can then be compared to the measured value of the photon energy(E_γ^{meas}) to determine what, if any, correction is required. Further details regarding the tagger correction is given in Appendix 10.

3.5.3 Momentum Corrections

Discrepancies in the toroidal magnetic field map and/or in the drift chamber survey information can lead to inaccuracies in the reconstructed momenta. Following the procedure described for the determination of the tagger correction, the inclusive channel $\gamma p \to p\pi^+\pi^-$ is used to empirically obtain corrections for the reconstructed momenta. Events are selected which contain only a single proton, π^+ and π^-. Energy-loss corrections are applied to the particles, along with the tagger corrections from the previous iteration. The event is kinematically fit to the series of hypotheses $\gamma p \to p\pi^+(\pi^-)$, $\gamma p \to p(\pi^+)\pi^-$ and $\gamma p \to (p)\pi^+\pi^-$. The parenthetical notation used here indicates a particle which is reconstructed, instead of directly measured.

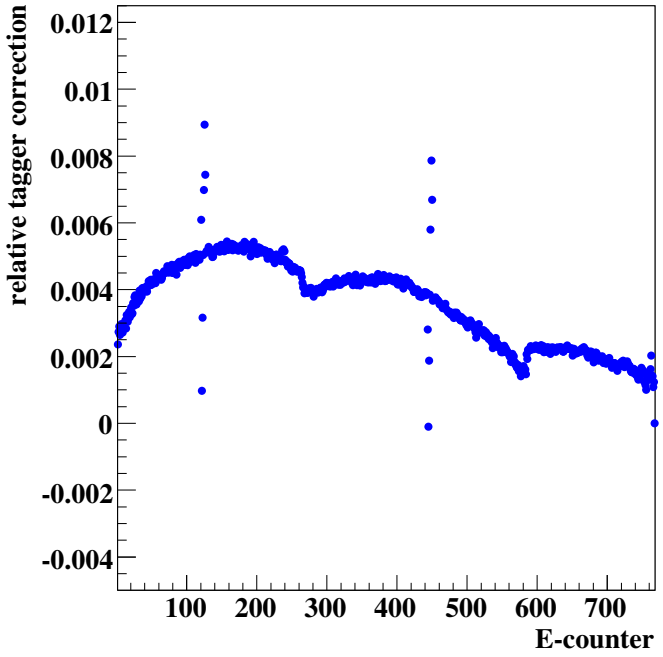

Figure 3.3: The tagger energy correction as a function of tagger E-counter. The two sets E-counter corrections which do not fall on the curve are the result of swapped cables during cooking.

The series of hypotheses systematically checks each particle, allowing for the comparison between a reconstructed "missing" particle and the detected measured particle. As with the tagger correction, only events with a confidence level of greater than 10% are used for determining the momentum corrections. For a more detailed description of the momentum corrections see Appendix 10 or Williams et al. [37].

3.6 Data and Monte Carlo Selection Cuts

A variety of cuts were made on both the data and Monte Carlo to select the reaction channels of interest. For this analysis, the term cut, is used to describe any events that are removed from either the experimental data sample, or the accepted Monte Carlo sample. As with any experiment the effects of the detector must be separated from the physics that is to be extracted. The cuts used for this analysis have been described in a CLAS analysis note by Applegate et al.[39]. This section will detail the cuts used to present a complete description of the data analysis. There are cuts and corrections which are applicable only to the experimental data, others are applicable only to the Monte Carlo data, and some apply to both datasets. The general purpose of cutting events from a dataset is to reduce background, and improve signal. Additionally, there are cuts and corrections required for the Monte Carlo data, to make it as representative as possible of the experimental data. After the cuts and the corrections, the experimental data and the Monte Carlo data should be very similar to one another.

3.6.1 Run Trip Periods

Data taken immediately before and after the "beam trips", periods where beam delivery is interrupted, are removed from the dataset due to the lack of ability to calculate an accurate photon flux during those periods. These groups of events are stored in a file to facilitate their removal from the dataset at a later time. The events cut due to beam trips are only in the experimental data, as there are no simulated beam trips.

3.6.2 Bad Runs

In the process of analyzing the g11a dataset, it was determined that some of the data runs should be excluded from analysis. There were normalization runs, and calibration runs which were not included in the analysis. There were some systematic runs with different trigger conditions, which were excluded from analysis. There is a selection of run numbers which were excluded due to hardware and software problems during data taking. Additionally, there were runs at the end of the run period which used a higher beam energy. These higher-energy runs were excluded as well. This cut is made only for the data, since there is no "bad run" analogue for the Monte Carlo. Table 3.2 lists the runs removed from the analysis.

Table 3.2: G11 cooked runs which have been excluded from this analysis.

Run	Description
43490-43525	Commissioning Runs
43675-43676	Different Trigger Configuration
43777-43778	Different Trigger Configuration
43981-43982	Logbook Lists DC Problems
43989-43991	Logbook Lists DAQ Problems
44108-44133	$5.021 GeV$ Beam Energy

3.6.3 Bad Time-of-Flight Paddles

Some of the Time-Of-Flight(TOF) scintillator paddles in the CLAS detector are either non-functional or non-efficient. Particles which hit these paddles are either not read out, or are only occasionally read out. This inefficiency is not problem as long as the same inefficiency exists in the simulated Monte Carlo data. Unfortunately this is not always the case, and there exist some discrepancies

Table 3.3: TOF paddles by sector, which are excluded in this analysis.

Sector 1	Sector 2	Sector 3	Sector 4	Sector 5	Sector 6
18		11	26	20	25
26		23			30
27					34
33					

between the Monte Carlo and the data from paddle to paddle. Any paddle which is found to be inefficient in either the data or the Monte Carlo, but not both, must be removed from both the experimental and Monte Carlo datasets. TOF paddle efficiency studies were conducted by Dr. Matthew Bellis[40] to determine which paddles needed to be cut.

In his studies Dr. Bellis used events of the type $\gamma p \to p\pi^+\pi^-$ where all three final state particle were detected to determine the efficiency of the each time of flight paddle in detecting either the proton or the pions. To analyze the efficiency of the TOF paddles to detect protons, a comparison was made between an event where to proton was detected versus an event where the pions were detected, and a proton was reconstructed. Ideally, the number of detected protons hitting a particular TOF paddle will be equivalent to the number of protons reconstructed to have hit that paddle, and that would be a paddle efficiency of 100%. In practice, TOF paddles are not 100% efficient. The process to determine the efficiency is repeated twice more to determine the efficiency of the detecting each of the pions. Figure 3.4 shows the paddle occupancy for negative particles in the various sectors of CLAS. There are clearly paddles which are not occupied, for example paddle 33 in sector 1.

TOF paddles are included in the simulation of the detector with some set efficiency. To determine that efficiency, the whole process is repeated for protons and pions in the Monte Carlo as well. If the efficiency of the Monte Carlo is equivalent to the efficiency of the experimental data, then any inefficiency will be accounted for in the acceptance determination using the Monte Carlo. However, if there are significant differences between the efficiencies of the data and the Monte Carlo, then the events which hit those paddles must be removed from the dataset for both the data and the Monte Carlo. Overall, the TOF paddle cut is applied to both the data and the Monte Carlo due to discrepancies between the two, which need to be resolved. Table 3.3 lists the TOF paddles which are cut in each sector.

3.6.4 Particle Identification(PID) and Vertex Timing Cut

Particle identification is always an experimental challenge within a physical analysis of a given dataset. While CLAS has preexisting particle identification schemes, this analysis utilized a timing cut within the context of the event-based analysis to determine particle identification.

The primary limitation of the pre-packaged PID schemes is that they attempt to determine the species of particle on a track-by-track basis. The identification is then determined on the basis of the calculated mass from the timing information in the TOF wall. For lower momentum particles, this is a reasonable means for determining PID, but for high momentum tracks ($P > 1.5$GeV) there are often ambiguities as seen in Figure 3.5.

While PID on a track-by-track level may allow for ambiguities, there is a solution to the problem. Examine the event as a whole, instead of track by track. For a given event, the total energy and momentum are fixed, so if one track is very high momentum the other tracks will be of a lower momentum. On an event level, the identification of the lower momentum track, can determine the identification of the higher momentum track. Suppose we are trying to identify $\gamma p \to p\pi^+\pi^-$ exclusive events. We initially select events based on charge and the number of tracks. Events are chosen which contain two positive-charge tracks, and one negative-charged track. All combinations for a given event are looped over, along with all of the available photons. A PID hypothesis, in this

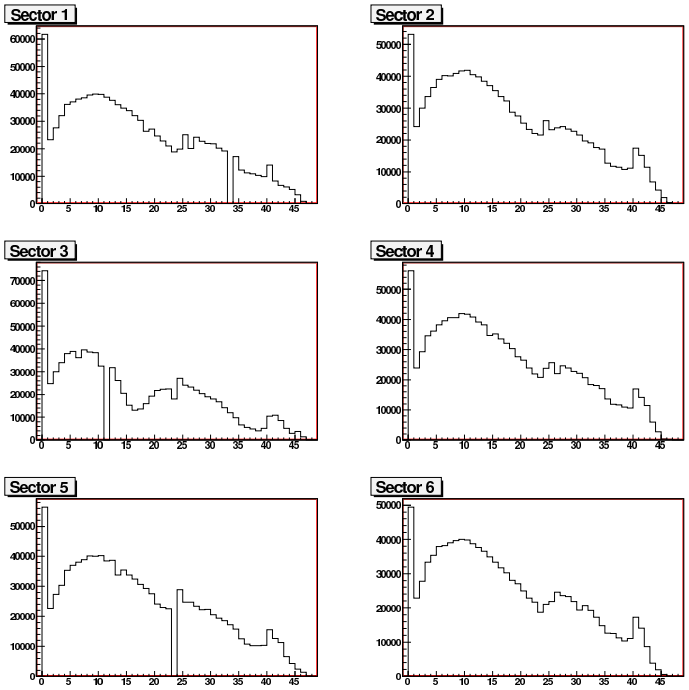

Figure 3.4: Time of flight (TOF) paddle occupancy for negative particles as a function of sector and paddle number. There are clearly paddles with either zero, or limited occupancy.

case $p\pi^+\pi^-$, is imposed upon the event, and a kinematic fit is performed.

Timing cuts are used to remove background events due to out of time photons. There are events in which the photon associated with the event may have been switched with a photon from another beam bucket. To eliminate these photons from other beam buckets, a timing cut is made such that the particles detected in CLAS originated at the same vertex time. For the purposes of this analysis, an "iron cross" cut as shown in Figure 3.6 is used to constrain the timing between the proton and π^+ meson. The cut is made on the difference between a constructed vertex time and the photon vertex time. The photon vertex time comes from the tagger timing signal, which is then propagated forward to the center of the target. The constructed vertex time is the difference between the scintillator time which comes from the time of flight wall propagated back to the vertex, and the calculated time from the particle path length.

The "iron cross" shape of this cut allows for a more relaxed cut when the timing of both particles are close to the photon vertex time. When one or more of the particles is further away from the photon vertex time, then the cut has a tighter restriction on the remaining particle. This cut is made for both the data and the Monte Carlo.

As with any cut on the data, care must be taken to remove background events while keeping a maximum of signal events. To this end, Mike Williams[41] made a Feldman-Cousin's estimate of the signal removed when this cut is made. In the analysis of ω photoproduction he determined an upper limit on the amount of signal removed by the cut to be $\approx 0.3\%$. As the cut in the $N\omega$ analysis is equivalent to the cut in this analysis, the cut will have a similar effect in the η and η' analyses. A plot of the cut events as a function of missing mass off of the proton reveals no structure around the mass of the η justifying the belief that the signal cut is negligible. To demonstrate this, Figure

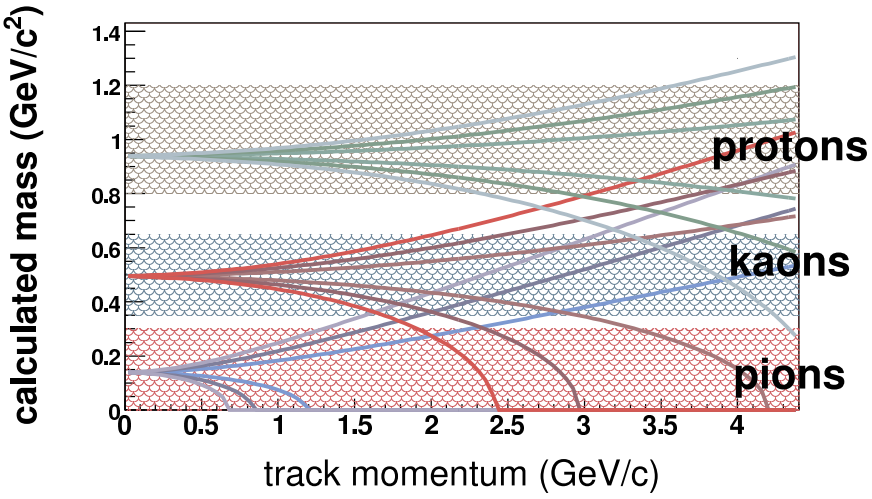

Figure 3.5: This plot reflects the PART particle identification scheme. Assuming $\sigma = 120$ps for a given TOF paddle. Momentum of a track is plotted against its calculated mass. The shaded regions are the cuts made to identify the hadrons detected in CLAS with the PART identification scheme. The curved lines show the effects of $1\sigma, 2\sigma$ and 3σ timing resolution on the mass calculation.

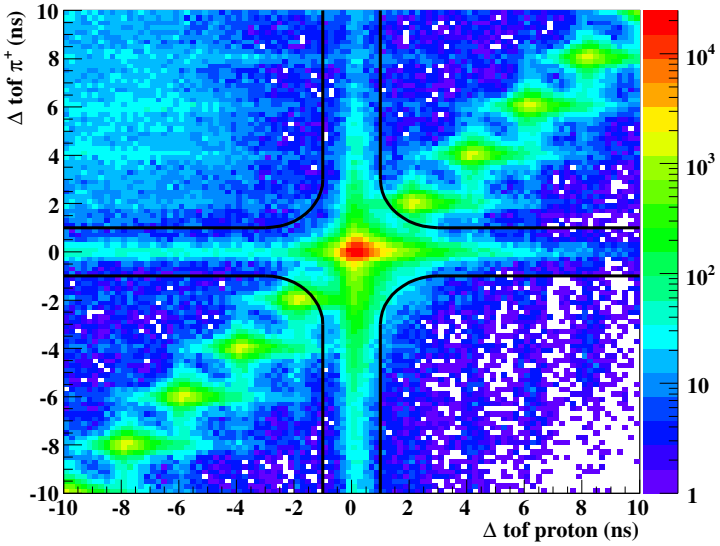

Figure 3.6: The Δ vertex timing cut for the pi^+ versus the proton used to determine η events. The cut is indicated by the black lines in the "iron cross" configuration.

3.7 shows the missing mass off of the proton for events passing the cut, and events excluded(shaded histogram). There is clearly a signal in the events passing the cut, while the events failing the cut lacks significant structure.

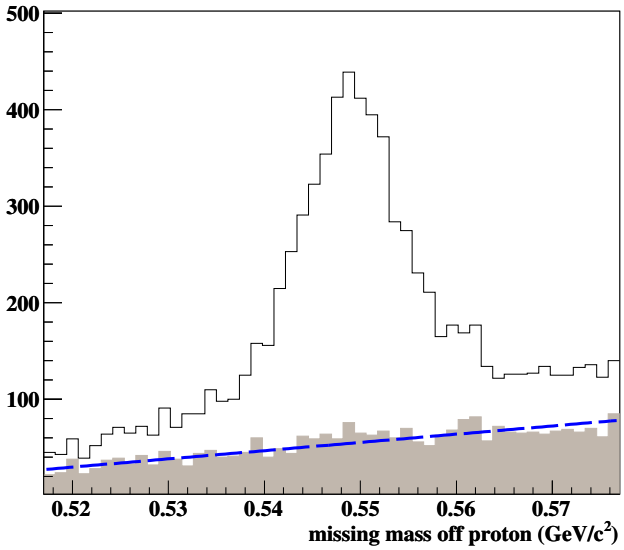

Figure 3.7: Plot of the missing mass off of the proton for events in run number 43582, with the very basic channel selecting cuts. The vertex timing cut is applied, and the events which do not pass the cut are shown in gray on this plot. Note the lack of peak near the η mass in the events cut.

3.6.5 Fiducial Cuts

In every experimental apparatus there are areas of the detector in which measurements can not be made well. In CLAS there are several areas where events are cut due to geometry, or functionality of the detector in that physical space. In the far forward and backward direction, there is no coverage, and thus events in which particles enter these regions are cut, unless that particle is the reconstructed missing particle required for the channel of interest. Likewise, since CLAS is segmented into 6 sectors in ϕ, there are regions between the sectors where the toroidal magnets exist, which are also cut. The phi cut is 4 degrees from 30° and -30° in each sector to make the active region from -26° to 26° in ϕ. This cut is made in both the data and the Monte Carlo to keep the acceptance between the two consistent. Figure 3.8 indicates the whole region where data appears in the detector. Figure 3.9 indicates the regions kept by the fiducial cut. Clearly, the most efficient and occupied areas of the detector are kept.

3.6.6 Confidence Level Cut

When the reaction channel of interest is selected from the 2-plus/1-minus skim, there is a 1% confidence level cut made on the kinematic fit to the missing particle. The confidence level is based on the amount of adjustment to the particle momentum required to produce the kinematically fit hypothesis. If the momentum of the particles had to change significantly to construct a missing $\pi°$ or missing η, then it was very unlikely that this event was kept. To further reduce background, a more severe cut is made on the confidence level of the kinematic fit to the missing particle. A 10% confidence level cut is made on the kinematic fit to a missing $\pi°$ for the η analysis. A 10% confidence level cut is made on the kinematic fit to a missing η for the η' analysis. The 10% confidence level cut was utilized for both the data and Monte Carlo for the η and η' channels.

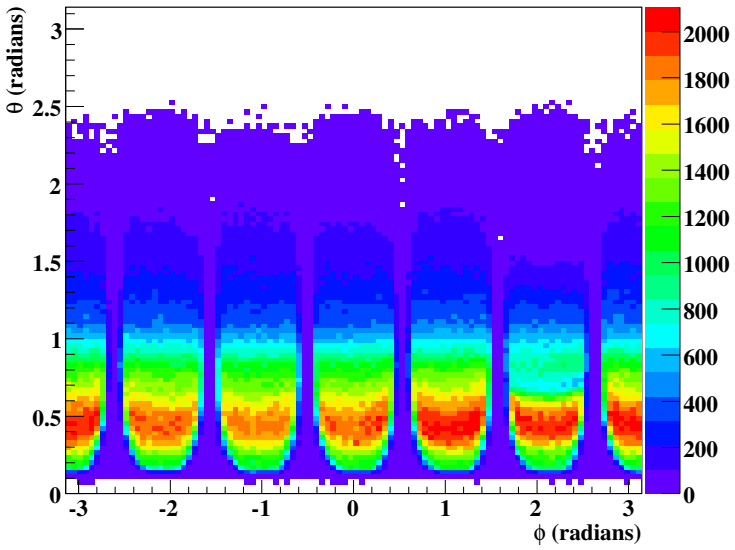

Figure 3.8: The total fiducial regions of the detector. The higher efficiency regions in the middle of the detector sectors are clearly visible.

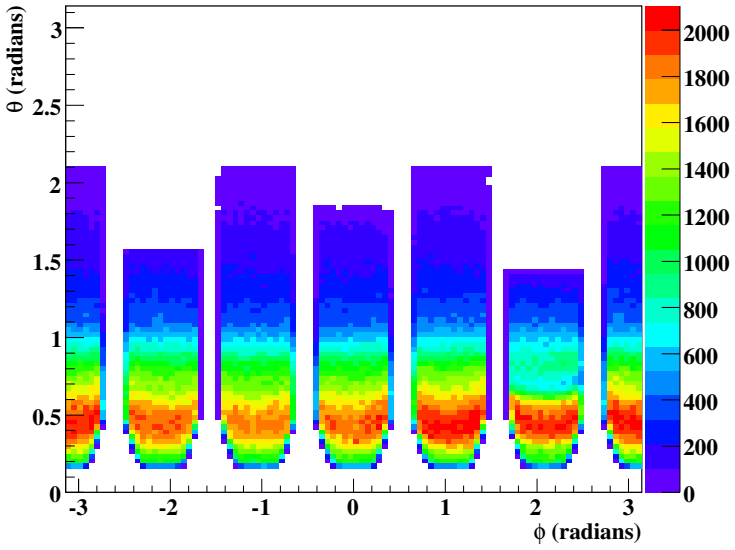

Figure 3.9: The fiducial regions in which events are kept. Outside of these regions of the detector, only particles which are assumed to be missing, and then reconstructed continue into the analysis.

3.6.7 Low Momentum Proton Scaling

Low momentum protons have long been difficult to deal with in CLAS. The added scattering and energy loss as they pass through material in the detector creates challenges when trying to analyze

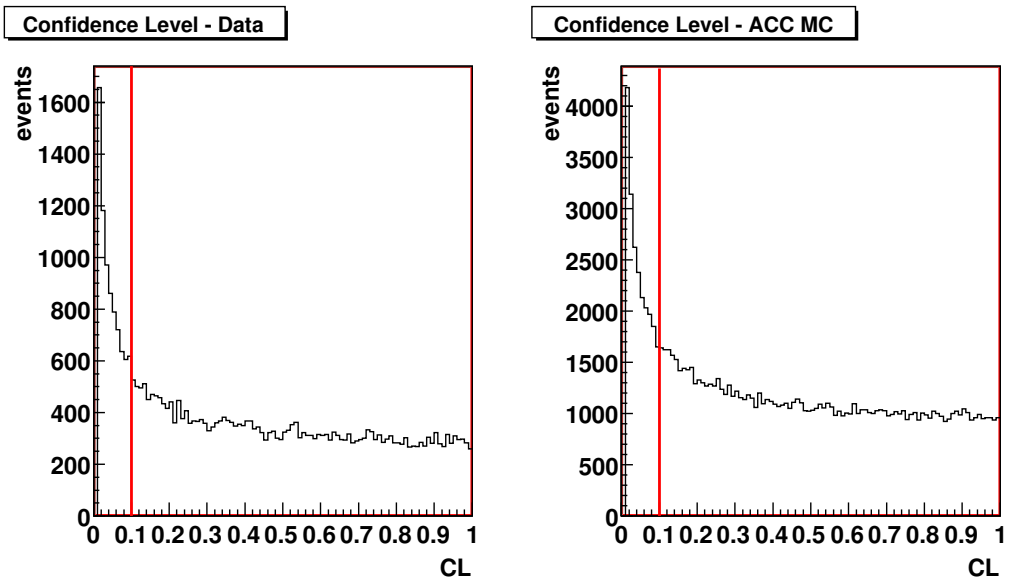

Figure 3.10: The confidence level of η events without any other cuts. A cut is made at the 0.1 (10%) level and everything greater than that is kept.

this subset of events. There are discrepancies with the detection efficiency of these low momentum proton between the Monte Carlo and the data. In order to correct for the efficiency discrepancy a scaling map was developed in order that the Monte Carlo could be corrected to match the data. The scaling of proton begins at an energy of 425 MeV, and protons are scaled down to an energy of 375 MeV. Events that contain protons with momenta below 375 MeV are removed from the dataset used in this analysis.

3.6.8 Trigger Simulation

The multiple track nature of the trigger for the g11a run period combined with triggering inefficiencies due to TOF paddles create a discrepancy between the data and Monte Carlo. The easiest way to view this discrepancy is to look at the TOF paddles, and the efficiency with which they set the trigger. Figures 3.11 and 3.12 show the trigger efficiency for positively, and negatively charged tracks. A systematic study of the trigger efficiency was done for the g11a dataset. The starting point for this study was the set of $\gamma p \to p\pi^+\pi^-$ where each of the final state particles were detected. The trigger condition for the experiment required at least two charged tracks in two different sectors. To study the efficiency of that process, events were used in which the three charged tracks were all in different sectors.

To determine negative-particle trigger efficiencies, events were selected for which the proton and π^+ both set the trigger in their respective sectors. For a given sector and TOF paddle number, a ratio of the number of π^- which set the trigger in its sector to the total number of π^- detected was constructed. This ratio is the trigger efficiency for the π^- for that given sector, TOF paddle, and position in sector ϕ.

The process was essentially the same for the positive particles. Events were selected for which the π^- and either the proton or the π^+ set the trigger in their respective sectors. This condition satisfied the overall trigger requirement, so the remaining positive particle is independent of the trigger. For

each sector and each TOF paddle the ratio of the number of times the remaining positive particle set the trigger to the number of detected particles yields the efficiency of the trigger for positive particles.

The calculated efficiencies for a given sector are compiled into a map which is binned in the azimuthal angle within the sector and TOF paddle number. This map is used as part of the trigger simulation. Knowing the likelihood of a particle setting the trigger for a given charge, azimuthal angle within the sector, and TOF paddle number allows for a correction to be made to the Monte Carlo. As a numerical example, if there is a 90% triggering efficiency for a given proton, and an 80% triggering efficiency for a given pion, then the overall efficiency of those particles setting the trigger for a given event is 72%. This trigger efficiency is the most important for final states in which only two particles are detected, as they both are required to set the trigger. In the case of the η and η' analysis there are three detected particles, the proton, π^+, and the π^-. With three detected particles, only two of the three must set the trigger. Extending the previous numerical example to the three particle case, there would be a $\approx$97% efficiency for the trigger to be set with that final state.

The trigger simulator used the trigger efficiency map as a function of azimuthal angle within a sector, for a given TOF paddle number and sector to determine if a Monte Carlo event would have satisfied the trigger conditions. For each event in the Monte Carlo, the TOF paddle the simulated particle hit and the ϕ in the sector are determined. Then, on the basis of charge, the efficiency is obtained from the map for that track. A random number is then thrown in the range of $0 \rightarrow 1$, and if that thrown number is lower than the efficiency, then the track has set the "trigger" for the Monte Carlo event. From there, the trigger simulator reproduces the trigger conditions from the experimental trigger. If at least two of the tracks set the trigger in different sectors, then the overall event is kept. If not, then that event will be cut from the Monte Carlo.

The trigger simulation is a critical correction to the Monte Carlo for events with only two charged tracks. For the final states of primary interest in this analysis, with three charged tracks, this is a small correction. The novelty of this approach should not be lost however considering that this was one of the first experimental datasets in CLAS which required more than one charged track for the trigger. In future, any experiment run at CLAS with similar trigger requirements will need some sort of correction for the Monte Carlo to account for the more complex trigger.

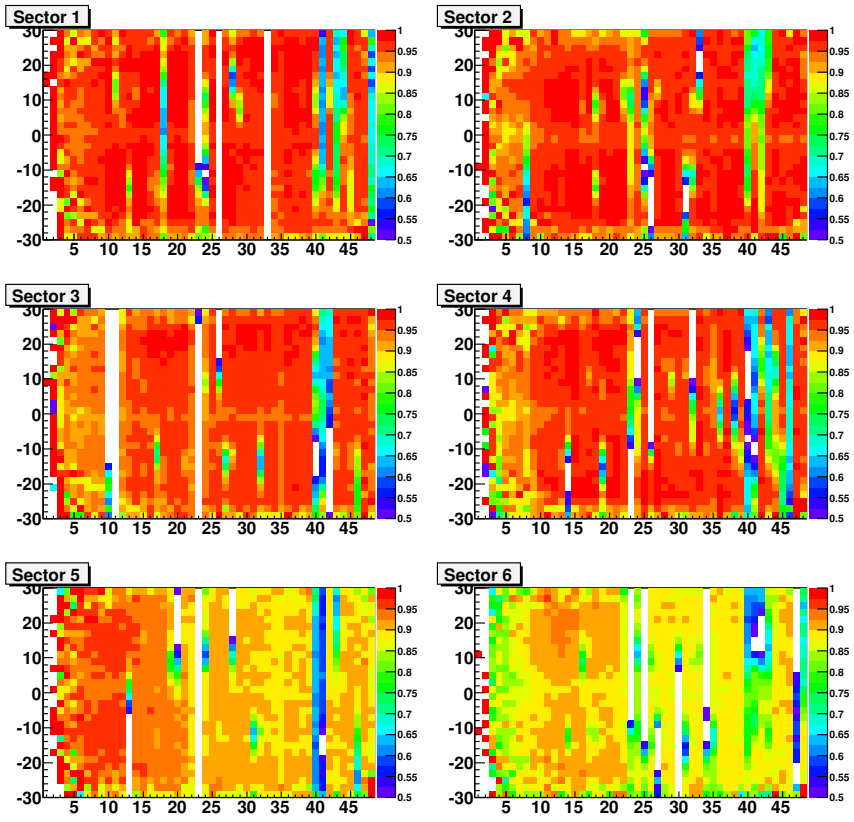

Figure 3.11: Trigger efficiency as a function of sector, paddle number, and azimuthal angle within the sector for positively charged tracks. Note the non-functional paddles are clearly visible, and even slight inefficiencies in the midst of paddles due to the threshold settings in the electronics are visible.

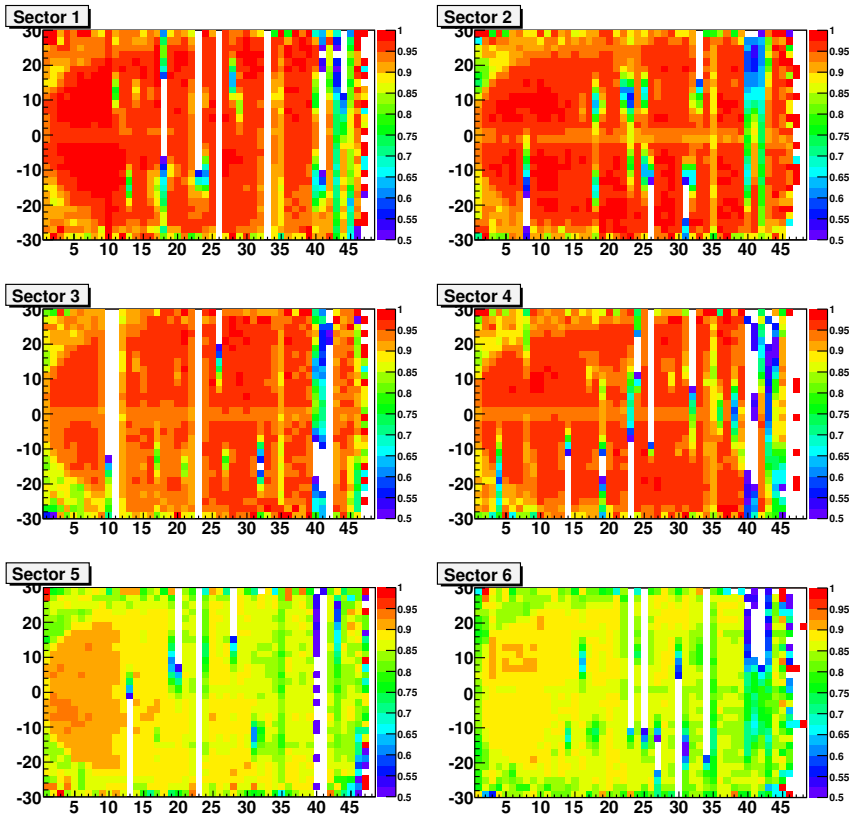

Figure 3.12: Trigger efficiency as a function of sector, paddle number, and azimuthal angle within the sector for negatively charged tracks. Note the non-functional paddles are clearly visible, and even slight inefficiencies in the midst of paddles due to the threshold settings in the electronics are evident.

3.6.9 Missing Particle $cos(\theta)$ Cut

In an effort to reduce the background, a cut was made on the $cos(\theta_{CM})$ of the missing particle. So, for the η photoproduction dataset, the cut removed π° mesons of $\cos(\theta_{CM}) > 0.99$. For the η' photoproduction dataset the cut removed η mesons of $\cos(\theta_{CM}) < -0.96$. In terms of geometry these cuts essentially remove events in which the missing particle is traveling almost directly along the beamline.

The events removed in this cut arise from selection of the photon for a given event. It is possible for an event which has no missing particle to be associated with the wrong photon. If the photon energy then does not line up with the given event, energy and momentum can only be adjusted in the "missing" particle which does not exist. Additionally, with nearly all of the transverse momentum accounted for, the only direction which the "missing" particle can go is either up or down the beamline. These anomalous events are thus removed from the dataset. In the η analysis there is a very forward peak in the $cos(\theta_{CM})$ of theπ°, which is removed. This peak can be seen clearly in Figure 3.13.

In the case of the η' there is an anomalous peak in the backward direction of the missing η, which is removed. The plot of this distribution can be seen clearly in Figure 3.13. There is also a forward peak in the $cos(\theta_{CM})$ of the η which is not removed in this analysis. This peak, while present, is more difficult to separate from the other events, and is not cut.

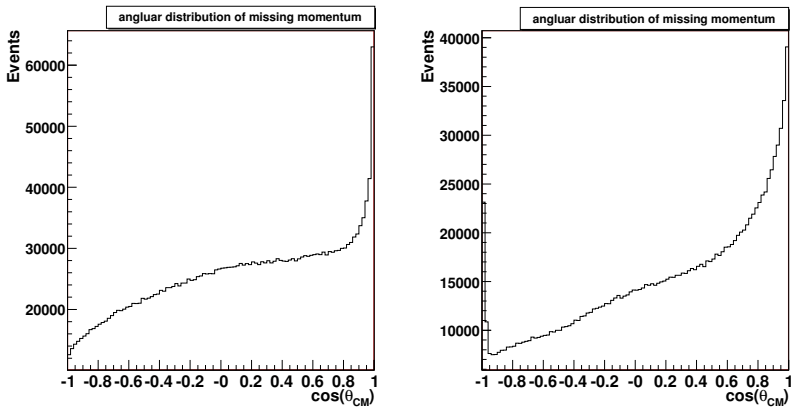

Figure 3.13: Plots of the $\cos(\theta_{CM})$ of the missing particle for the η and η' channels. Left: In the very forward direction there is a peak in $cos(\theta_{CM})$ of the π°, the events in the very forward direction are removed from the η analysis. Right: At very backward angles for the $cos(\theta_{CM})$ of the η there is a spike which is removed from the η' analysis.

3.6.10 Missing Mass Cut

One of the standard experimental cuts for both the data and the Monte Carlo is a cut on the missing mass off of the proton to select the particle of interest. For both the η and the η' the cut on the missing mass off of the proton was determined bin by bin in W. The width of the mass peak was somewhat dependent upon the center-of-mass energy of the reaction, and as such, it was prudent to construct the cut in each bin. An example of the missing mass cut is shown in 3.14. The cut itself was made at $2.5\times\sigma$ on either side of a Gaussian fit to the mass peak on top of a linear background. A table has been compiled with the mean and sigma for each bin as it was used in the analysis. These tables are available in an appendix.

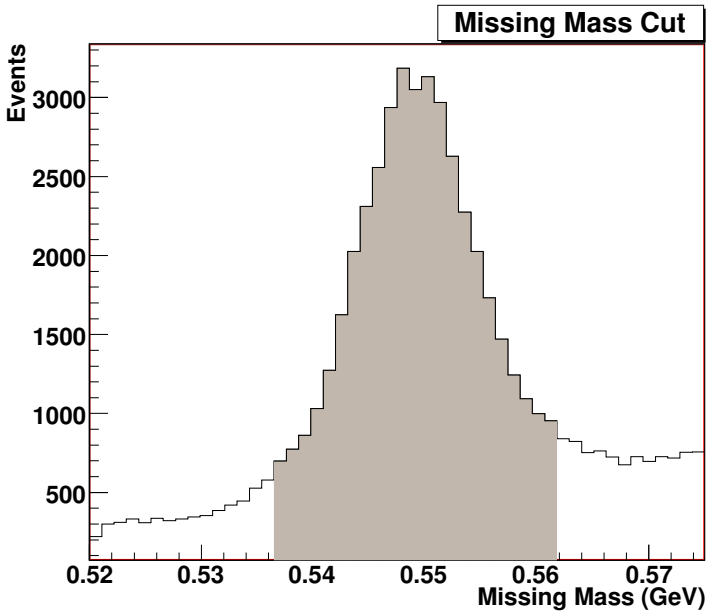

Figure 3.14: Plot of the missing mass off of the proton for η photoproduction in the $W = 1700 - 1710 MeV$. The gray region denotes the events which are kept, while outside this region, the events are cut.

3.7 Normalization

Normalization is a term used to describe a calculated factor which directly scales the measured differential cross section in an experiment. The principle component to the normalization is the number of photons incident on the target for a given energy. The greater(smaller) the number of photons, the lower(higher) the measured differential cross section. Along with the number of incident photons, the Live-Time of the detector and data acquisition also affects the normalization. The Live-Time is the term used to describe the amount of time the detector is ready to acquire data when triggered. The principle components of the normalization will be described in this section.

3.7.1 Photon Flux

The photon flux at the target N_{flux} is calculated by the "gflux" program developed by Eugene Pasyuk for the CLAS collaboration. The procedure by which the flux is calculated is described in an analysis note from Ball and Pasyuk[42] but will be briefly described here. Determination of the photon flux is equivalent to counting the "good" electrons in the tagger hodoscope and then comparing this number with the number of photons on the target measured by a high efficiency detector. The detector used in the case of CLAS is the total absorption counter(TAC). The TAC will be overloaded if the beam intensity is too high, so a lower beam intensity beam is used to determine the normalization. The ratio of the "good" electrons in the tagger to the number of photon on the target is called the tagging ratio. The assumption is made that the tagging ratio is independent of photon flux intensity.

With the tagging ratio determined through normalization runs, there task becomes determining the number of "good" electrons in the tagger hodoscope when running at higher beam intensities. This is done by sampling the "out-of-time" electron hits in the T-counters. An "out-of-time" electron

is any "good" electron detected in the tagger which was not involved in a physics event trigger. A "good" electron is measured when both the left and right TDC hits of a given T-counter match in time along with a matched hit in time for one E-counter. The "good" electron rate on each T-counter in the tagger is measured by assuming that the "out-of-time" electron hits follow Poisson statistics.

The product of the tagging ratio and the number of "good" electrons yields the photon flux. There is a small correction included in the calculation to account for the loss of photons from the target to the TAC. A photon attenuation factor,α, is included to account for the fractional loss of photons from the target to the TAC. This attenuation factor was motivated by Schumacher [43].

Hence the number of tagger photons per T-counter is given by the following:

$$N_{\gamma}^{T} = \frac{N_{e^-}^{T} \times \epsilon^{T}}{1 - \alpha} \tag{3.1}$$

Where $N_{e^-}^{T}$ is the number of "good" electrons in a given T-counter, ϵ^{T} is the tagging ratio, and α is the fractional attenuation factor. Determining the photon flux for a given experiment is a several step process. There are numerous normalization runs which utilize the TAC and a lower beam intensity to determine the tagging ratio as a function of T-counter. Then, during the data runs, the out of time electrons are sampled to determine the number of good electrons in a given T-counter. These two pieces are combined by the gflux program to determine the photon flux as a function of T-counter.

There are several corrections to the flux which are required. The first correction accounts for the fact that the trigger for the g11a data runs only included a portion of the tagger. The un-triggered portion of the tagger needs to be corrected for in the flux. Additionally, there is a correction to be made for the Live-Time. These corrections will be discussed in this section.

Tagger Correction(trigger)

A correction is required to the flux as measured by the tagger due to the fact that the entire tagger was not included in the trigger. In bins below $W = 1940MeV$, a scaling of the flux is required because these events were caused by photons which were not in the energy regime to trigger the data acquisition. These events exist in the data due to higher-energy photons triggering the tagger, but are not associated with the physics event. The correction is a constant multiplicative factor determined by Mike Williams[41]. The correction factor was calculated to be ≈ 2.0. Figure 3.15 shows the portion of the photon energy spectrum which was tagged(red), and the section that was both tagged and triggered(green). There are regions at the very top and bottom of the spectrum for which the tagger has no coverage, and these are indicated in blue.

Live Time

The Live-Time is a correction factor which scales the normalization factor up to take into account that while the data acquisition system was busy recording events, there were still events going through the detector which were lost. This correction must be made, due to the fact that the flux was still measured during data collection. Thus, yielding the correct number of photons, but missing the events which occurred while the data acquisition was busy. The construction of the live time correction is described in detail in the analysis note from Applegate et al.[39] but the process will be described here.

To determine the Live-Time, the flux normalized yields for ρ and ω photopoductions was measured as a function of beam current. The flux normalized yield demonstrated a current dependence, and to investigate further the Faraday cup measurement was used. The Faraday cup is not used in photoproduction experiments and was in no way tied to the data acquisition making it independent

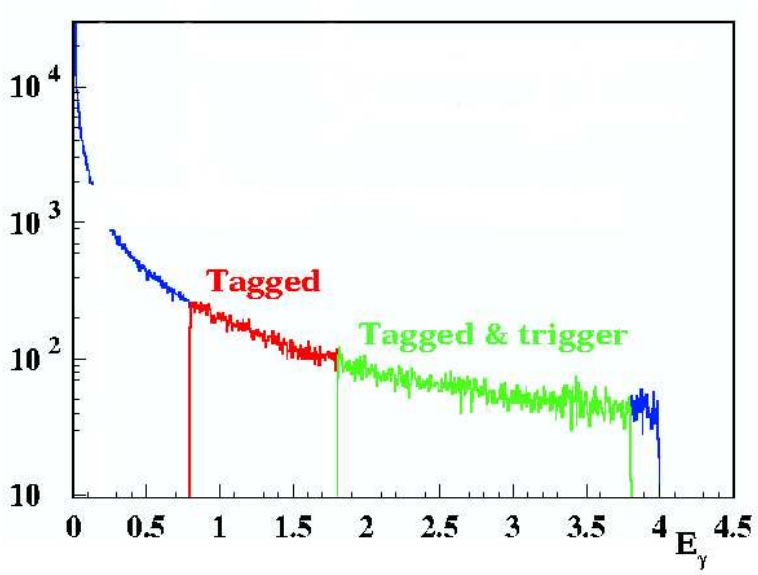

Figure 3.15: Plot of photon energy in the tagger. The Green area at higher energy indicates where hits in the tagger fired the trigger. In Red, are photons in the tagger which were not included in the trigger. The Blue points were outside of the range of the tagger for the given run conditions. Source: [30]

of the trigger. Analysis by Mike Williams [41] indicated that the Live-Time previously determined and used for flux determination was actually the $\sqrt{\text{Live-Time}}$.

The live time was modified by a correction factor of the Live-Time as determined from the Faraday cup divided by the clock live time.

3.8 Background Parameterization

Regardless of the how carefully the cuts are determined, it is impossible to eliminate the presence of background events within the η and η' datasets. Since these events can not be cut, their contribution to measured quantities must be removed. To this end, a background parameterization technique was developed for this analysis. With no interest in extraction of the background physics, this technique employs a polynomial parameterization to the background. The procedure for background parameterization will be described here.

3.8.1 Basic Kinematic Variables

The starting point of this procedure is to produce plots of the relevant kinematic variables. These variables include, but are not limited to, $\cos(\theta_{CM})$, ϕ_{CM}, missing mass off of the Nucleon, and a 2-dimensional plot of $\cos(\theta_{CM})$ against the missing mass off of the Nucleon. These plots are made for each W bin because the shape of the background and the width of the mass peak can depend on W. See Figure 3.16 for an example of these plots.

Plots of the kinematic variables are made using all of the standard cuts developed by Carnegie Mellon University for the g11a dataset, except for the cut on the missing mass off of the Nucleon.

Table 3.4: Binning scheme used for background parameterization.

$\cos(\theta_{CM}) =$	-1.0	$\rightarrow$	-0.8
$\cos(\theta_{CM}) =$	-0.8	$\rightarrow$	-0.6
$\cos(\theta_{CM}) =$	-0.6	$\rightarrow$	-0.4
$\cos(\theta_{CM}) =$	-0.4	$\rightarrow$	-0.2
$\cos(\theta_{CM}) =$	-0.2	$\rightarrow$	0.0
$\cos(\theta_{CM}) =$	0.0	$\rightarrow$	0.2
$\cos(\theta_{CM}) =$	0.2	$\rightarrow$	0.4
$\cos(\theta_{CM}) =$	0.4	$\rightarrow$	0.6
$\cos(\theta_{CM}) =$	0.6	$\rightarrow$	0.8
$\cos(\theta_{CM}) =$	0.8	$\rightarrow$	1.0

The missing mass cut is determined, but not applied until later in the procedure in order to facilitate the best possible measurement of the background in each W bin.

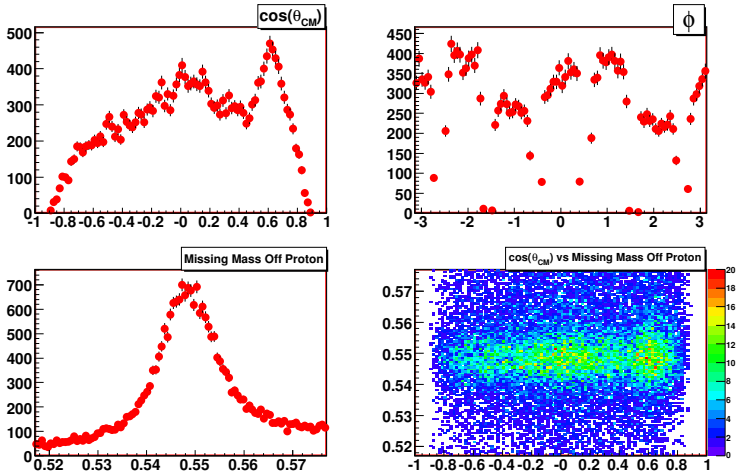

Figure 3.16: Basic kinematic variables for $W = 2100 - 2120 MeV$ for the η reaction channel. Upper left is the $\cos(\theta_{CM})$. Upper Right is ϕ_{CM}. Lower left is the missing mass off of the proton. Lower right is the $\cos(\theta_{CM})$ plotted against the missing mass off of the proton.

3.8.2 Generating Signal/Background Plots

In each W bin the $\cos(\theta_{CM})$ is divided into 10 equal sub-bins. Table 3.5 shows the slices selected for the $p\eta$ and $p\eta'$ photoproduction reactions.

For the events in each slice of $\cos(\theta_{CM})$ a plot of the missing mass off of the proton is made. Demonstrated in Figure 3.17.

The missing mass plots for each slice are then fit to some functional form. For the η reaction channel a Gaussian with a linear background is used. Which is given by the following functional form:

$$(b_0 + b_1 * m) + A * \frac{1}{\sqrt{2\pi}\sigma} * e^{-(m-m_0)^2/2*\sigma^2} \tag{3.2}$$

Table 3.5: Binning scheme used for background parameterization.

$\cos(\theta_{CM})$ =	-1.0	$\rightarrow$	-0.8
$\cos(\theta_{CM})$ =	-0.8	$\rightarrow$	-0.6
$\cos(\theta_{CM})$ =	-0.6	$\rightarrow$	-0.4
$\cos(\theta_{CM})$ =	-0.4	$\rightarrow$	-0.2
$\cos(\theta_{CM})$ =	-0.2	$\rightarrow$	0.0
$\cos(\theta_{CM})$ =	0.0	$\rightarrow$	0.2
$\cos(\theta_{CM})$ =	0.2	$\rightarrow$	0.4
$\cos(\theta_{CM})$ =	0.4	$\rightarrow$	0.6
$\cos(\theta_{CM})$ =	0.6	$\rightarrow$	0.8
$\cos(\theta_{CM})$ =	0.8	$\rightarrow$	1.0

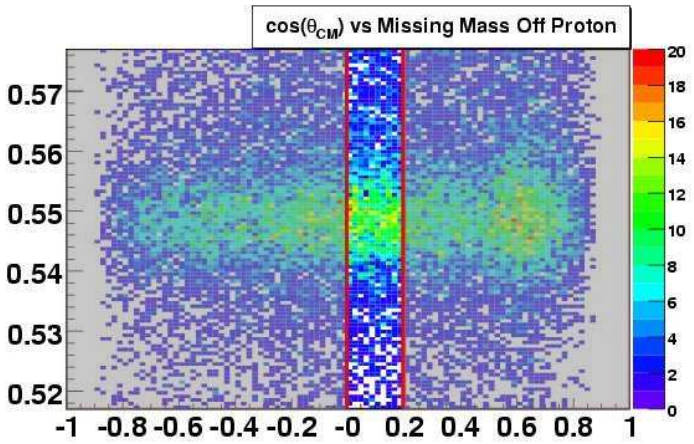

Figure 3.17: A slice is selected from the 2-Dimensional $\cos(\theta_{CM})$ vs missing mass off of the proton. Here the slice selected is $0.0 < \cos(\theta_{CM}) < 0.2$ for the $W = 2100 \rightarrow 2120 MeV$ bin.

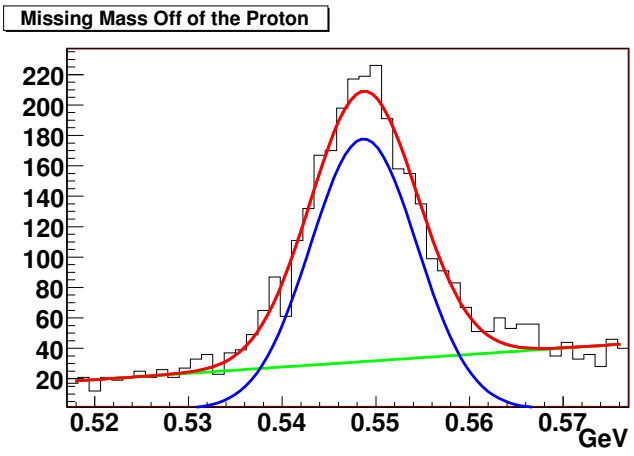

Figure 3.18: The $0.0 < \cos(\theta_{CM}) < 0.2$ slice projected onto the missing mass axis for the $W = 2100 \rightarrow 2120 MeV$bin. This projection is fit to a Gaussian (blue) with a linear background (green).

Integrating the linear background over a range of $\pm 2.5 \times \sigma_{masscut}$ yields the total number of background events under the peak for that $\cos(\theta_{CM})$ slice. A fit to the mass peak for the whole W bin determines $\sigma_{masscut}$ and determines the mass cut to select the particle of interest. Defining this $\sigma_{masscut}$ across the whole center-of-mass energy bin provides consistency between the range where background events are counted, and the range where data is used for the fits. The following equation is used to determine the number of background events in a missing mass plot for each slice of $\cos(\theta_{CM})$:

$$N_{background} = \frac{1}{BW}\int_{m_l}^{m_h}(b_0 + b_1 m)dm = \frac{b_0(m_h - m_l) + \frac{1}{2}b_1(m_h^2 - m_l^2)}{BW} \tag{3.3}$$

Where:

$$\begin{array}{rcc} BW & = & \text{Bin Width} \\ m_l & = & \text{Low Edge of Mass Cut} \\ m_h & = & \text{High Edge of Mass Cut} \end{array}$$

Nominally, one could compute the error on $N_{Background}$ by getting the errors on the linear background parameters b_0 and b_1. However, it turns out that b_0 and b_1 are highly correlated, and to extract the actual error we need the full covariance matrix.
The square of the error is given by the following expression:

$$\sigma^2_{bkgd} = \left(\frac{\partial f}{\partial b_0}, \frac{\partial f}{\partial b_1}\right) \begin{pmatrix} \sigma^2_{b_0} & \rho\sigma_{b_0}\sigma_{b_1} \\ \rho\sigma_{b_1}\sigma_{b_0} & \sigma^2_{b_1} \end{pmatrix} \begin{pmatrix} \frac{\partial f}{\partial b_0} \\ \frac{\partial f}{\partial b_1} \end{pmatrix} \tag{3.4}$$

Where f is the linear function which describes the background. The 2×2 matrix is the covariance matrix returned by Minuit for the linear fit to the background. The errors on the individual parameters are given by the diagonal elements of the covariance matrix. The off-diagonal elements are the correlated errors, where ρ sets the scale for the amount of correlation between the b_0 and b_1 parameters. Expanding this linear equation we find:

$$\sigma^2_{bkgd} = \sigma^2_{b_0}\left(\frac{\partial f}{\partial b_0}\right)^2 + \sigma^2_{b_1}\left(\frac{\partial f}{\partial b_1}\right)^2 + 2\rho\sigma_{b_0}\sigma_{b_1}\left(\frac{\partial f}{\partial b_0}\right)\left(\frac{\partial f}{\partial b_1}\right) \tag{3.5}$$

Plugging in for the partial derivatives, we arrive at the following equation for the square of the error on $N_{Background}$:

$$\begin{aligned} \sigma^2_{N_{Background}} = \left(\frac{1}{BW^2}\right)(&\sigma^2_{b_0}(m_h - m_l)^2 + \frac{\sigma^2_{b_1}}{4}(m_h^2 - m_l^2)^2 \\ &+(\rho\sigma_{b_0}\sigma_{b_1})(m_h^2 - m_l^2)(m_h - m_l)) \end{aligned} \tag{3.6}$$

With errors established for the integrated background measurement, this fitting and integrating process is repeated for the other slices in $\cos(\theta_{CM})$. The measured background count from each slice is then pieced back together to yield the background in each W bin as a function of $\cos(\theta_{CM})$, an example of which can be seen in Figure 3.19.

The background shape as a function of $\cos(\theta_{CM})$ is then acceptance corrected. Acceptance correction assures that the parameterization is of the background physics, and not the background physics weighted by the CLAS detector. When measuring a differential cross section, the raw background shape, like Figure 3.19 can be used to subtract the background contribution. However,

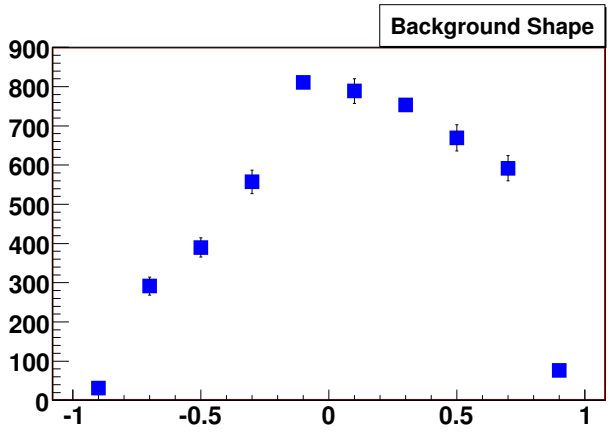

Figure 3.19: The shape of the background as a function of $\cos(\theta_{CM})$ for the $W = 2100 \rightarrow 2120 MeV$ bin.

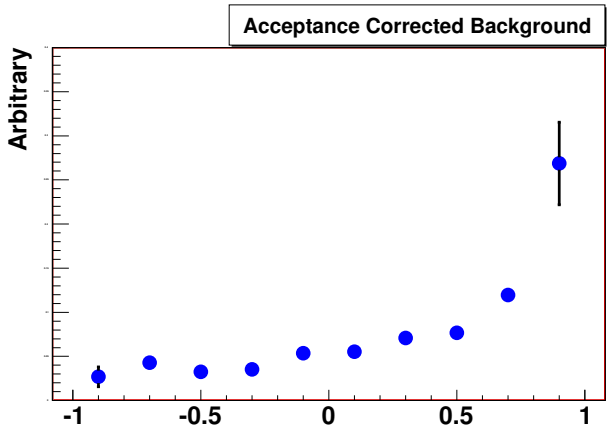

Figure 3.20: The shape of the acceptance corrected background as a function of $\cos(\theta_{CM})$ for the $W = 2100 \rightarrow 2120 MeV$bin.

for the purposes of the PWA, the acceptance corrected background is used. Figure 3.20 shows the acceptance corrected background for the given example bin.

Comparing the non-acceptance corrected distribution to the acceptance corrected distribution demonstrates that the acceptance is generally backward peaked at this center of mass energy. The acceptance causes the parameterized background to be forward peaked at this center-of-mass energy. Were the background contributions not correctly taken into account, measurements in the forward region would likely be incorrect.

3.8.3 Background Polynomial Generation

A polynomial is now fit to the acceptance corrected background shape in $\cos(\theta_{CM})$. An example of the polynomials fit to the acceptance corrected background is shown in Figure 3.21. It is important to note that the polynomials have been scaled arbitrarily so the differences in polynomial shape from bin to bin may be observed. Clearly the bottom-most line is the fit to the data points, while the others presented are from neighboring bins. The lower peak in the forward direction of the second polynomial from the bottom is indicative of a statistical limitation. In the most forward bin, the

acceptance is very low, and as such the statistics are not as high as would be preferable.

This polynomial will serve as the parameterization of the background for this W bin. While determining the polynomial which best describes the background, the total number of background events in that W bin is also determined. Armed with the shape of the background, and the total yield of the background in a given W bin, the background is completely determined.

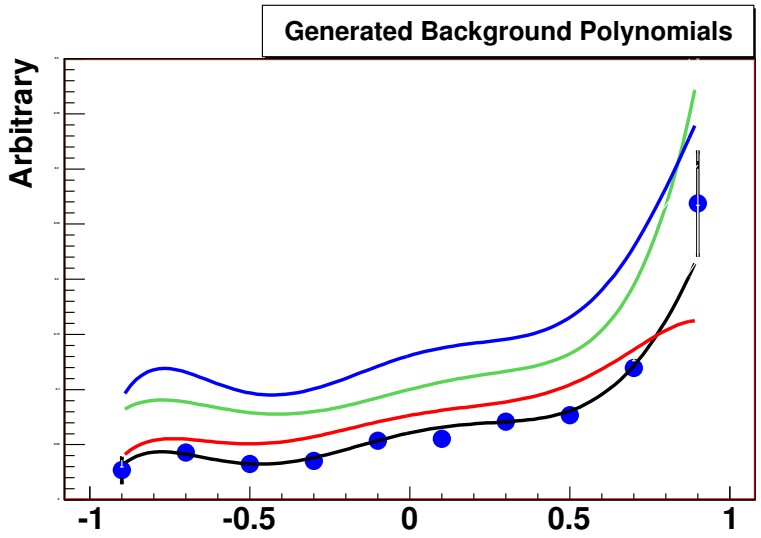

Figure 3.21: The lowest line is the polynomial fit to the points which is the acceptance corrected background as a function of $\cos(\theta_{CM})$ in $W = 2100 \rightarrow 2120$ MeV bin. The other lines are the polynomial fits to the $2120 \rightarrow 2140$, $2140 \rightarrow 2160$, and $2160 \rightarrow 2180$ MeV W bins in increasing order. These have been arbitrarily scaled in order to observe differences in polynomial shape from bin to bin.

The covariance matrix from the polynomial fit to the acceptance corrected data is recorded, so that it may be used to properly determine the errors. The procedure for calculating errors on the polynomial using the covariance matrix is the same as was used to calculate the errors on the integrated linear background fit earlier. A complication is that the covariance matrix is now $n \times n$ because a $(n-1)^{th}$ order polynomial is used to parameterize the background. Additionally, using the covariance matrix, the error can be computed for any given binning in $\cos(\theta_{CM})$. Equation 3.9 is a general form for the determination of the errors of a polynomial function f of $(n+1)^{th}$ order.

$$\sigma^2_{polynomial} = \left(\frac{\partial f}{\partial a_0}, ..., \frac{\partial f}{\partial a_n}\right) \begin{pmatrix} \sigma^2_{a_0} & . & . & \rho\sigma_{a_0}\sigma_{a_n} \\ . & . & . & . \\ . & . & . & . \\ . & . & . & . \\ \rho\sigma_{a_n}\sigma_{a_0} & . & . & \sigma^2_{a_n} \end{pmatrix} \begin{pmatrix} \frac{\partial f}{\partial a_0} \\ . \\ . \\ . \\ \frac{\partial f}{\partial a_n} \end{pmatrix} \tag{3.7}$$

This fitting procedure is repeated for all W bins in the reaction channel dataset. Once the polynomials are generated for all W bins, they are averaged, or smoothed, with neighboring W bins to reduce statistical fluctuations, as previously seen in Figure 3.21. The algorithm of the weighted average for W bin X with its neighbors is the following:

$$
\begin{aligned}
bin = \quad & X \quad && \Longrightarrow \quad weight = 1 \\
bin = \quad & X \pm 1 && \Longrightarrow \quad weight = \tfrac{1}{2} \\
bin = \quad & X \pm 2 && \Longrightarrow \quad weight = \tfrac{1}{3} \\
bin = \quad & X \pm 3 && \Longrightarrow \quad weight = \tfrac{1}{4} \\
bin = \quad & X \pm 4 && \Longrightarrow \quad weight = \tfrac{1}{5} \\
bin = \quad & X \pm 5 && \Longrightarrow \quad weight = \tfrac{1}{6}
\end{aligned}
$$

If a bin is near the edge of a boundary, it is smoothed with the available bins that meet the criteria of the algorithm. For example, the first bin of the dataset is averaged only with the 5 bins above it. The second bin is averaged with the five above it, and the one bin below it, and so on. The weighting and the number of neighboring bins with which a bin is averaged, was chosen somewhat arbitrarily. Prior to the current version, a smoothing algorithm was used which incorporated only the two nearest bins on either side, and the was no noticeable difference in the overall results.

For example, a 6^{th} order raw polynomial fit to the acceptance corrected data for bin X would have the following general form:

$$f(z) = a_0^X + a_1^X z + a_2^X z^2 + a_3^X z^3 + a_4^X z^4 + a_5^X z^5 + a_6^X z^6 \tag{3.8}$$

When averaged, or smoothed, with neighboring bins according to the stated algorithm, the explicit form of the polynomial for W bin X becomes the following:

$$
\begin{aligned}
f(z) \quad = \tfrac{1}{norm} \quad & ((a_0^X + \frac{1}{2}a_0^{X\pm1} + \frac{1}{3}a_0^{X\pm2} + \frac{1}{4}a_0^{X\pm3} + \frac{1}{5}a_0^{X\pm4} + \frac{1}{6}a_0^{X\pm5}) \\
& +(a_1^X + \frac{1}{2}a_1^{X\pm1} + \frac{1}{3}a_1^{X\pm2} + \frac{1}{4}a_1^{X\pm3} + \frac{1}{5}a_1^{X\pm4} + \frac{1}{6}a_1^{X\pm5})z \\
& +(a_2^X + \frac{1}{2}a_2^{X\pm1} + \frac{1}{3}a_2^{X\pm2} + \frac{1}{4}a_2^{X\pm3} + \frac{1}{5}a_2^{X\pm4} + \frac{1}{6}a_2^{X\pm5})z^2 \\
& +(a_3^X + \frac{1}{2}a_3^{X\pm1} + \frac{1}{3}a_3^{X\pm2} + \frac{1}{4}a_3^{X\pm3} + \frac{1}{5}a_3^{X\pm4} + \frac{1}{6}a_3^{X\pm5})z^3 \\
& +(a_4^X + \frac{1}{2}a_4^{X\pm1} + \frac{1}{3}a_4^{X\pm2} + \frac{1}{4}a_4^{X\pm3} + \frac{1}{5}a_4^{X\pm4} + \frac{1}{6}a_4^{X\pm5})z^4 \\
& +(a_5^X + \frac{1}{2}a_5^{X\pm1} + \frac{1}{3}a_5^{X\pm2} + \frac{1}{4}a_5^{X\pm3} + \frac{1}{5}a_5^{X\pm4} + \frac{1}{6}a_5^{X\pm5})z^5 \\
& +(a_6^X + \frac{1}{2}a_6^{X\pm1} + \frac{1}{3}a_6^{X\pm2} + \frac{1}{4}a_6^{X\pm3} + \frac{1}{5}a_6^{X\pm4} + \frac{1}{6}a_6^{X\pm5})z^6))
\end{aligned}
$$

Where the normalization factor at the beginning of the expression returns the smoothed polynomial to its native scale. This is important because the scale of the polynomial when originally fit, defines the covariance matrix, which in turn defines the errors. If the polynomial is scaled, either up or down, then the covariance matrix must be scaled to match. In this case, it is easier to re-normalize the smoothed polynomials to their native scale. The effect of the smoothing on the polynomials is indicated in Figure 3.23. Here, both the raw and smoothed polynomials have been scaled to observe differences in the structure.

The same weighted average algorithm is used to smooth the covariance matrices from the polynomial fit. When smoothing the covariance matrices however, a few additional steps are required. Here a covariance matrix M_X for bin X is inverted. This inverted matrix is then put into a weighted

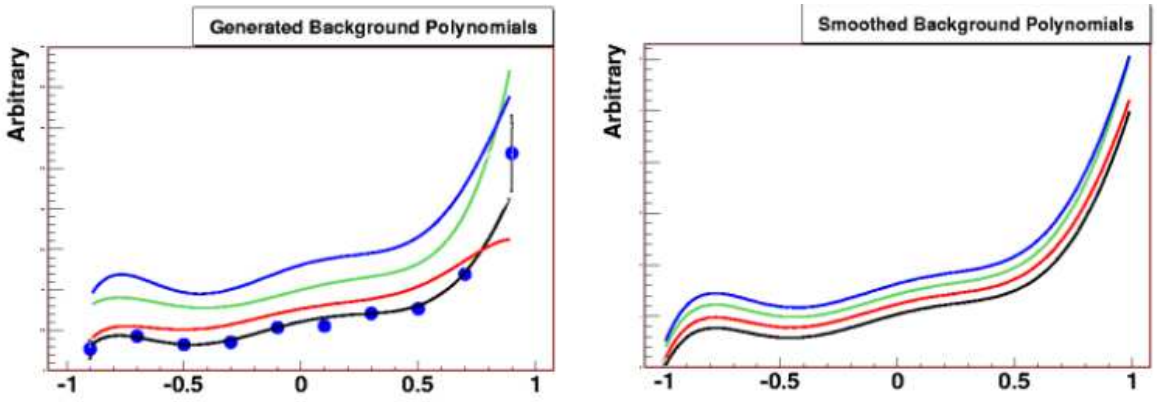

Figure 3.22: Right: Examples of the smoothed polynomials of the fit to the $2100 \rightarrow 2120$, $2120 \rightarrow 2140$, $2140 \rightarrow 2160$, and $2160 \rightarrow 2180 MeV$ W bins. These have been arbitrarily scaled in order to observe differences in polynomial shape from bin to bin. Left: The raw plot is reproduced for comparison.

sum with neighboring inverted matrices, and the normalization is taken into account. This weighted sum is equal to the inverted smoothed covariance matrix S_X^{-1}. The matrix S_X^{-1} is then inverted to return the averaged covariance matrix S_X.

$$M_X \longrightarrow M_X^{-1}$$

$$S_X^{-1} = \frac{1}{norm}(M_X^{-1} + \frac{1}{2}M_{X\pm1}^{-1} + \frac{1}{3}M_{X\pm2}^{-1} + \frac{1}{4}M_{X\pm3}^{-1} + \frac{1}{5}M_{X\pm4}^{-1} + \frac{1}{6}M_{X\pm5}^{-1})$$

$$S_X^{-1} \longrightarrow S_X$$

By inverting the covariance matrices prior to averaging, fits with low errors are weighted more heavily than fits with large errors. This means more weight is given to the solutions in which we have more confidence. Clearly checks must be made to ensure the covariance matrix is not singular, and if so, it is excluded from the smoothing and the normalization factor is adjusted accordingly.

If there are regions where an n^{th} order polynomial is used, and another region where an m^{th} order polynomial is used, these are treated separately, and the boundary is preserved between them. There is no smoothing across a boundary of this type.

Armed with the smoothed polynomial background parameterizations, the smoothed covariance matrices, as well as the total number of background events, we can now effectively subtract the background and correctly propagate the errors through to a differential cross section measurement.

While the total number of measured background events in a given W bin is fixed, the polynomial smoothing does push events around a bit as a function of $\cos(\theta_{CM})$. To illustrate this, Table 3.6 was constructed for the $W = 1990 - 2000 MeV$ bin of the η reaction. The values in the N_b^s column in Table 3.6 were determined by using the smoothed polynomials as the input to the reverse of the process just described in this section 3.8 . The smoothed polynomial was weighted by the acceptance, to return a number of counts per bin in $\cos(\theta_{CM})$. The total number of events was then normalized to the total background count in the bin.

The averaging of the polynomials is justified physically by claiming that the background shape

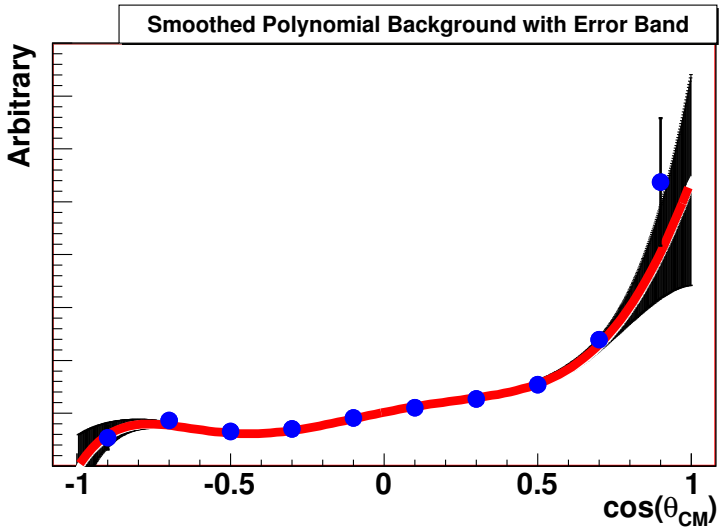

Figure 3.23: The round points are the measured acceptance corrected background determined for the $W = 2100 \rightarrow 2120$MeV bin. The curve through the points is the smoothed polynomial fit to the points. The black band structure indicate the error on the smoothed polynomial. Note the significance of the errors in the very forward and backward directions, while in the middle of the distribution the errors are small.

$\cos\theta_{cm}$	N_s	ΔN_s	N_b^r	ΔN_b^r	N_b^s	ΔN_b^s
-0.90	76	8.7	29.4	12.4	27.3	8.7
-0.70	558	23.6	153.8	18.2	163.4	14.7
-0.50	1166	34.1	317.5	21.0	306.9	17.2
-0.30	1833	42.8	487.2	25.8	496.4	20.0
-0.10	2460	49.6	617.4	27.7	643.4	22.2
0.10	2779	52.7	818.7	32.0	762.4	23.5
0.30	2149	46.4	659.2	28.8	664.5	22.9
0.50	1926	43.9	596.2	27.9	627.6	24.0
0.70	1566	39.6	489.7	30.1	482.6	25.2
0.90	158	12.6	56.2	8.8	50.6	9.1
Total			4225.3		4225.3	

Table 3.6: The number of events and various background estimates in each $\cos\theta$ bin. N_s is the number of signal events. The N_b^r is the number of background events as determined by the fit of the Gaussian plus linear polynomial in each bin. The N_b^s is the background as estimated using the smoothed polynomial fit to the backgrounds across all the $\cos\theta$ bins.

does not vary significantly from W bin to W bin. Considering the average width of the W bins is on the order of 10's of MeV this is clearly reasonable. This claim is also generally supported by the non-averaged polynomial shapes for the acceptance corrected background.

3.9 Summary

This chapter has described the cuts and corrections involving the data and Monte Carlo events used for this analysis. The dataset compiled during the g11 run period in Hall B at JLAB is high-

statistics, and has allowed for analysis of significant sets of photoproduction data. As with any experiment, corrections and calibrations must be done to have confidence in the data underlying the analysis. The data and Monte Carlo, where possible, were treated identically in order to assure that any introduced systematics would appear in both sets of data. Considerable effort has been made to fully understand the detector and how well it functioned at the time the data was recorded. Newer developments include the trigger simulation for multi-track triggers, as well as the background parameterization technique. The next chapter will describe the results of the differential cross section measurements.

Chapter 4

Differential Cross Section Results

This chapter describes the results of the differential cross section measurements made for η and η' photoproduction. The measurement of the differential cross section follows naturally within the context of a partial wave analysis. This chapter reviews the previous measurements, the construction of the differential cross sections for this analysis, and reports the measured results. There are two good sets of measurements of the η differential cross sections, but this analysis extends the available measurements in kinematic range. The best previous measurements made for η' photoproduction is considerably extended in kinematics.

Differential cross sections are used extensively to compare experimental results between experiments. Additionally, differential cross section measurements are used to drive theory by providing an input for models. Before reporting the results of the differential cross section measurements for η and η' photoproduction, a review of previous results and their construction will be presented.

4.1 Previous Differential Cross Section Results

In order to put the results of this analysis in context, the previously published differential cross section measurements will be summarized here. There have been several analyses which are relevant to this analysis. For η photoproduction there are results from Dugger et al.[6] and Crede et al.[12]. For η' photoproduction the results are more sparse, but results from Dugger et al.[7] are worth mention. To avoid any confusion, the analysis which is the thrust of this dissertation will be referred to as the Krahn analysis and the others will be referred to by name of lead author.

4.1.1 Previous η Results

There have been several analyses which produced differential cross section measurements for the η meson photoproduction. The two results with the greatest statistics will be reviewed here. First, the previous CLAS result from Dugger et al. [6] will be discussed, and then the CB-ELSA result from Crede et al. [12].

Previous CLAS Result

The results from Dugger et al.[6] come from an experiment using CLAS at JLAB just like the Krahn analysis. Since the measurement of the differential cross sections from the Dugger analysis comes from the CLAS detector, the acceptance, and many of the systematics are equivalent to the Krahn analysis. The data for the Dugger analysis was taken much earlier in the running of CLAS, and utilized some slightly different components. Additionally, there were corrections, like the tagger energy correction, which were not made at that time.

The most significant difference between the Dugger analysis and the Krahn analysis is in the reaction channel selection. Since the Krahn analysis concentrated only on the $\gamma p \rightarrow p\pi^+\pi^-(\pi^\circ)$ reaction, the Dugger analysis utilized a less specific approach. While the approach did not specify the decay of the η meson, the background under the peak was considerably larger. The η was extracted from the $\gamma p \rightarrow pX$ spectrum, with the background subtracted assuming a mixture of two- and three-pion contributions. In the Dugger analysis there were 24 bins of ≈ 50 MeV in E_γ, covering a range from 750 MeV to 1950 MeV. The differential cross section was reported as a function of $\cos(\theta_{CM})$ of the η meson.

Also presented are some preliminary results from Ball et al.[9] which come from a different run period than the Dugger results. These are preliminary and unpublished, and are being used only for a systematic comparison to another CLAS result. The Ball results are binned more finely in $\cos(\theta_{CM})$ than the Dugger results, while the binning in W is approximately equivalent. The data covers a kinematic range of $1.0 \rightarrow 2.3$ GeV.

Previous CB-ELSA Result

The results from Crede et al.[12] come from an experiment using Crystal Barrel at ELSA in Germany. That analysis measured the η photoproduction cross section through the neutral decay modes of $\eta \rightarrow \gamma\gamma$ and $\eta \rightarrow \pi^0\pi^0\pi^0$. The acceptance of the CB-ELSA detector is considerably different from that of CLAS, and as such makes for an important comparison to the measurement made in the Krahn analysis. Additionally, the neutral channel detection of the decay particle of the η meson is relatively free of background contamination. The overall normalization was set by utilizing a previous analysis of $\gamma p \rightarrow p\pi^\circ$. Differential cross sections were reported as a function of $cos(\theta_{CM})$ for bins in E_γ. A total of 36 bins in E_γ were reported with bins varying in width from 50 MeV to 200 MeV. The majority of the bins are 50 MeV in width, and range from 750 MeV to 2300 MeV. Beyond $E_\gamma = 2300$ MeV, the bins are 100 MeV wide up to $E_\gamma = 2600$ MeV. The range of $E_\gamma = 2600 \rightarrow E_\gamma = 3000$ MeV is broken into two bins each of 200 MeV in width.

4.1.2 Previous η' Results

There are very few previous results for the photoproduction of the η' meson. The best measurement of η' differential cross sections to date were made by Dugger et al [7] using CLAS at JLAB. Data were reported for 15 bins in E_γ covering the range of 1.527 to 2.227 GeV. In each of these bins, which were about 50 MeV in width, results were reported as a function of $\cos(\theta_{CM})$ of the η meson. The Krahn analysis concentrated on the $\eta' \rightarrow \pi^+\pi^-(\eta)$, while the Dugger analysis took a less restrictive approach which increased the total background under the η' peak. The η' mesons were extracted from the $\gamma p \rightarrow pX$ spectrum. The background subtraction assumed a mixture of two-, three-, and four-pion contributions, along with ρ meson production. There were $\approx$ 200,000 η' events in the Dugger analysis dataset. This is comparable to the number of η' events present in the Krahn analysis, but the Krahn analysis utilized only a single decay mode of the η' meson. The Dugger results represent the first exploitable differential cross section results for η' photoproduction.

4.2 Differential Cross Section Construction

4.2.1 General Construction

This section will report the general method of measurement of the differential cross sections for η and η' photoproduced mesons. Additionally, the general calculation of the error on the differential cross section will be presented.

For the reaction $\gamma p \to pX$, the standard formula for evaluating the differential cross section is the following:

$$\frac{d\sigma}{d\Omega} = \frac{N_{observed}}{N_\gamma \cdot N_{targ}} \cdot \frac{1}{b_w} \tag{4.1}$$

where $N_{observed}$ is the number of observed events in a particular (W,cos(θ_{CM})) bin, N_γ is the number of incident photons in the given W bin, N_{targ} is the number of scattering centers in the target per unit area, and b_w is the bin width in Ω given as $2\pi\Delta\cos(\theta_{CM})$.

In order to account for the finite acceptance of the detector, one needs to correct for the experimental acceptance ϵ in each (W,cos(θ_{CM})) bin. It is also necessary to correct for decays of the η or η' particles. In particular, there are known branching fractions b for the observed final state of $\eta \to \pi^+\pi^-\pi^\circ$, or $\eta' \to \pi^+\pi^-\eta$. The number of observed events must be modified with this factor to yield the correct number of η or η' mesons actually produced. Using $N_{observed} = N_{evts}/b_w$, along with the acceptance, the general formula Eqn. 4.1 is modified to yield:

$$\frac{d\sigma}{d\Omega} = \frac{N_{evts}}{N_\gamma \cdot N_{targ}} \cdot \frac{1}{b_w} \cdot \frac{1}{b \cdot \epsilon} \tag{4.2}$$

This is the formula that will be used to calculate the differential cross sections for this analysis. Each of the pieces in this formula needs to be obtained to produce a differential cross section. At this point, there is an important note to be made about the acceptance. In the case of the $\eta \to \pi^+\pi^-\pi^\circ$ or the $\eta' \to \pi^+\pi^-\eta$ the decay of the η or η' have been integrated over in computing the acceptance. The decays of the η and η' lead to flat distributions in its decay particles, so this integration is straightforward.

Determining differential cross sections in the context of a PWA is done by throwing a large set of partial waves to fit the data as well as possible. The partial waves used do not need to accurately represent the physics involved in the process, only allow the fit to match the data. The results of this fit can then be used to weight the two Monte Carlo data sets, raw and accepted, in computing the acceptance. Recall that the Monte Carlo data sets are generated uniformly in the appropriate phase space. The determination of the acceptance (ϵ) is one of the pieces required to construct the differential cross section.

Regardless of the cuts made in the course of selecting the reaction channel of interest, there are background events among the signal events in the data collected. These background events must be accounted for, and subtracted to obtain an accurate differential cross section measurement. If we have $N_{observed}$ events which pass all of our cuts, and $N_{background}$ of these observed events are known to be background, then we have that the number of signal events is

$$N_{evts} = N_{observed} - N_{background}$$

The determination of the number of background events, and their distribution in $cos(\theta_{CM})$ is described in Section 3.8. With this parameterization we have determined the background as a function of W and $cos(\theta_{CM})$, which can then be subtracted from the number of events as a function of the same variables.

Putting all of the pieces together, we can construct the differential cross section as a function of both W and $cos(\theta_{CM})$. With the differential cross sections constructed, the errors must be determined. The error on the cross section, $\Delta\left(\frac{d\sigma}{dt}\right)$ is given in terms of known errors by standard formulas from which we find

$$\frac{\Delta\left(\frac{d\sigma}{d\Omega}\right)}{\left(\frac{d\sigma}{d\Omega}\right)} = \sqrt{\left(\frac{\Delta N_{evts}}{N_{evts}}\right)^2 + \left(\frac{\Delta N_\gamma}{N_\gamma}\right)^2 + \left(\frac{\Delta N_{targ}}{N_{targ}}\right)^2 + \left(\frac{\Delta b}{b}\right)^2 + \left(\frac{\Delta\epsilon}{\epsilon}\right)^2 + \left(\frac{\Delta b_w}{b_w}\right)^2} \tag{4.3}$$

The error on the number of events is given as

$$\Delta N_{evts} = \sqrt{(\Delta N_{observed})^2 + (\Delta N_{background})^2}$$

Assuming purely statistical errors for the acceptance error ($\Delta N = \sqrt{N}$), we find that acceptance is given by the ratio of accepted Monte Carlo events to thrown Monte Carlo events in a given bin.

$$\epsilon = \frac{N_{acc}}{N_{raw}}$$
$$\frac{\Delta(\epsilon)}{\epsilon} = \sqrt{\frac{1}{N_{acc}} + \frac{1}{N_{raw}}}$$

4.2.2 Construction within a PWA

This section will describe the slightly more specific topic of the construction of the differential cross section within the context of a partial wave analysis. This section will also point out more specifically where the values used for calculating the differential cross section come from.

Each of the pieces required to construct the cross section are present in the infrastructure needed to carry out a partial wave analysis. The event four-vectors have been divided up into bins in W ($\sqrt{s}$), with the number of incident photons in a given W bin known. In addition to the data, there is a set of Monte Carlo four-vectors which have been thrown uniformly in the correct phase space (raw), and a second set of Monte Carlo which consists of those events from the raw set which have been run through the detector GEANT Monte Carlo and then reconstructed and passed through the same physics cuts as in the analysis. This second set is known as the accepted Monte Carlo (acc).

Since the four vectors of these data sets are available, the data in a given W bin can be binned in t or $\cos(\theta_{CM})$. This allows for the calculation of the acceptance in a given bin. This is done by running a PWA fit using a large set of waves to describe the data. In the case of this analysis, the set of waves chosen included $J^P = \frac{1}{2}^{\pm}, \frac{3}{2}^{\pm}, \frac{5}{2}^{\pm}, \frac{7}{2}^{\pm}$. The physical meaning of these waves will be described in Chapter 5. For now, consider that they possess a large set of free parameters, with which the data can be well fit. A maximal set of waves is used to describe the data as well as possible, with no interest in extracting physically meaningful information from the PWA at this time. The fit results, which match the data very well, are then used to weight the raw and accepted Monte Carlo. In each W bin, the accepted Monte Carlo is divided by the raw Monte Carlo to determine the acceptance. The acceptance in a given bin is then known as a function of $\cos(\theta_{CM})$. As an example of the weighting, Figure 4.1 contains histograms of the data events in black, accepted Monte Carlo events in gray, and the accepted Monte Carlo weighted by the fit results in red. When both the raw and accepted Monte Carlo as weighted by the fit results, the accepted can be divided by the raw to determine the acceptance.

The total number of events, N_{evts} in that bin is known from the data. The background in a given bin is determined by a polynomial fit to appropriate side-bands as described in Section 3.8 Subtracting the background events from the observed events yields the number of signal events for that W and $\cos(\theta_{CM})$ bin. The known branching fractions for the observed final state of $\eta \to \pi^+\pi^-\pi^\circ$, or $\eta' \to \pi^+\pi^-\eta$. The PDG[4] lists the branching ratio for $\eta \to \pi^+\pi^-\pi^\circ$ as $22.6 \pm 0.4\%$. The $\eta' \to \pi^+\pi^-\eta$ branching ratio is given as $44.3 \pm 1.5\%$[4]. Additionally, the target factor is comprised of known quantities, such as target density, target material, and target length. The flux is determined through a program called "gflux" and applying systematic corrections to determine the actual number of photons that were incident on the target. Combining all of these pieces together the differential cross section for η and η' photoproduction can be constructed.

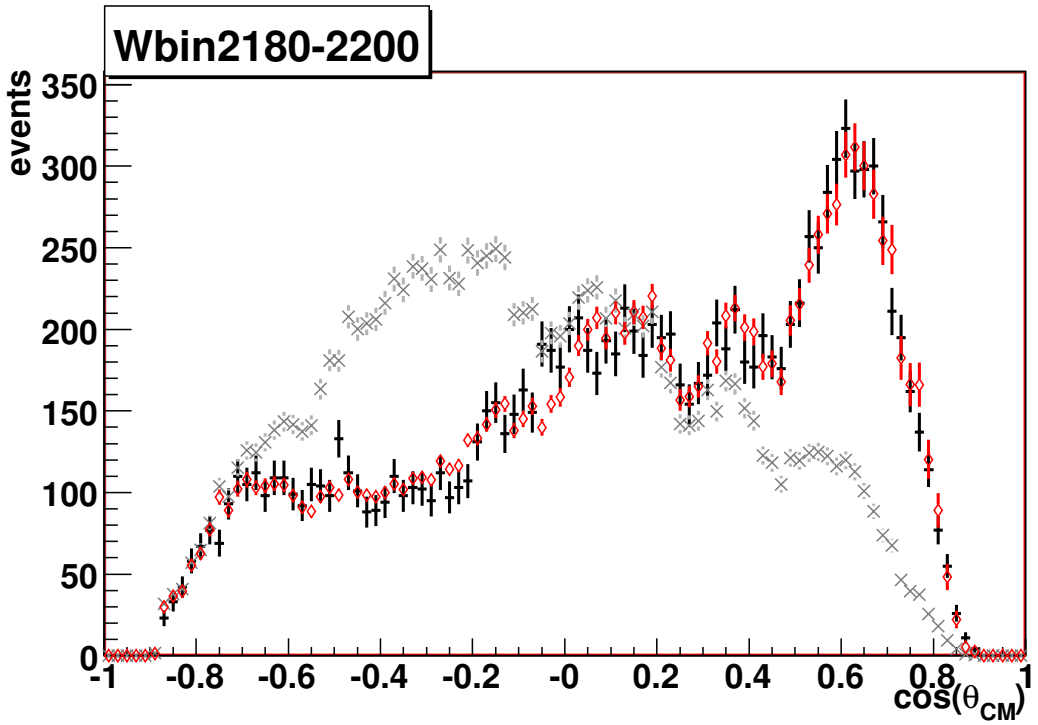

Figure 4.1: Plots of the data, accepted Monte Carlo, and the accepted Monte Carlo weighted by the fit results as a function $cos(\theta_{CM})$ for the η in a particular W bin. The black markers indicate the data. The grey criss-cross markers indicate the accepted Monte Carlo. The red diamonds indicate the accepted Monte Carlo events weighted by the fit results.

4.3 Errors on Differential Cross Sections

The general formula for the calculated error is given as Eqn. 4.3. A determination of the errors is a vital exercise in the construction of the differential cross section for a given reaction. The error on acceptance and the error on the number of events must both be calculated for each point of the measured differential cross section. Other errors, which fall under the category of normalization errors, are calculated globally for the entire dataset. Global values are used for the errors on the flux and the target length and density. The values of the global errors, as well as typical values for the kinematically dependent errors are given in Table 4.3. The dominant error is the error on the number of events for a given W and $cos(\theta_{CM})$ bin. This error is the combination of the statistical errors from the number of events detected, as well as the error on the number of background events which are subtracted through the parameterization.

It should be noted, that a different procedure was used for the determination of the overall normalization in the analysis of the same data for the $p\omega$ final state by CMU graduate student Mike Williams[41]. In the determination of the normalization, he determined that the combined error from factors like flux, target density, and acceptance, to be below 1.7%. The overall errors in this analysis are larger, and as such should provide a very conservative estimate of the error.

$\frac{\Delta\sigma}{\sigma}$	6.8%
$\frac{\Delta N_e}{N_e}$	6%
$\frac{\Delta\epsilon}{\epsilon}$	2%
$\frac{\Delta N_\gamma}{N_\gamma}$	2%
$\frac{\Delta N_{targ}}{N_{targ}}$	1%
$\frac{\Delta b}{b}$	1.76%

Table 4.1: The relative error on the measured cross section by component. N_e is the number of events, ϵ is the acceptance, N_γ is the photon flux, N_{targ} is the target factor, and b is the branching ratio.

4.4 Example Construction of Differential Cross Section

As a concrete example of the construction of the differential cross section, the individual numbers can be determined point by point for a given W bin in the η dataset. To this end, the $W = 1990 \rightarrow 2000$ MeV bin will be used as an example of differential cross section construction.

The flux of incident photons for a given bin is a known quantity, as is the target density, target length and branching fraction. The events which have passed the cuts are plotted as a function of $cos(\theta_{CM})$ because the differential cross sections for η and η' are typically reported as a function of $cos(\theta_{CM})$. With the background parameterized in $cos(\theta_{CM})$, the number of background events are known with the same binning as the number of events which passed the cut, allowing for the calculation of the number of signal events.

For the purposes of this example, 10 bins in $cos(\theta_{CM})$ will be used from -1.0 to 1.0. Table 4.2 demonstrates the binning chosen for this example, as well as the number of events, background events, and signal events with errors. Here, N_s is the number of observed events, N_b is the determined number of background events, and N_e is the number of signal events.

$\cos\theta_{cm}$	N_s	ΔN_s	N_b	ΔN_b	N_e	ΔN_e	$\frac{\Delta N_e}{N_e}$
−0.90	76	8.7	29.4	12.4	46.6	15.1	0.324
−0.70	558	23.6	153.8	18.2	404.2	29.8	0.0737
−0.50	1166	34.1	317.5	21.0	848.5	40.0	0.0471
−0.30	1833	42.8	487.2	25.8	1345.8	50.0	0.0372
−0.10	2460	49.6	617.4	27.7	1842.6	56.8	0.0308
0.10	2779	52.7	818.7	32.0	1960.3	61.7	0.0315
0.30	2149	46.4	659.2	28.8	1489.8	54.6	0.0366
0.50	1926	43.9	596.2	27.9	1329.8	52.0	0.0391
0.70	1566	39.6	489.7	30.1	1076.3	49.7	0.0462
0.90	158	12.6	56.2	8.8	101.8	15.4	0.151

Table 4.2: The number of events in each $cos(\theta_{CM})$ bin for a given W bin of the η dataset. N_s are observed events, N_b is the determined background, and N_e is the number of signal events.

With the number of events known, the next hurdle to the calculation of the differential cross

section is a determination of the acceptance as a function of $cos(\theta_{CM})$. This is determined through the use of Monte Carlo, and a simulation of the detector. Following all of the same cuts which are used on the data, and a few corrections to the Monte Carlo, which have been previously described, the raw and accepted events can be used to determine the acceptance. Table 4.3 demonstrates the calculation of the acceptance as a function of the binning used for this example. Where N_a is the number of accepted Monte Carlo events, N_r is the number of raw Monte Carlo events, and ϵ is the acceptance and is the ratio of the two.

$\cos\theta_{cm}$	N_a	ΔN_a	N_r	ΔN_r	ϵ	$\Delta\epsilon$	$\frac{\Delta\epsilon}{\epsilon}$
−0.90	617	24.8	89721	898.6	0.00688	0.000285	0.0414
−0.70	3530	59.4	90540	902.7	0.0390	0.000763	0.0196
−0.50	6954	83.4	88677	893.4	0.0784	0.00123	0.0157
−0.30	9476	97.3	90657	903.3	0.105	0.00150	0.0143
−0.10	8952	94.6	89703	898.5	0.0998	0.00145	0.0143
0.10	8453	91.9	91611	908.0	0.0923	0.00136	0.0147
0.30	6190	78.7	89631	898.2	0.0691	0.00112	0.0162
0.50	5167	71.9	89955	899.8	0.0574	0.000984	0.0171
0.70	3095	55.6	89775	898.9	0.0345	0.000709	0.0206
0.90	205	14.3	89739	898.7	0.00228	0.000161	0.0706

Table 4.3: The acceptance in each $cos(\theta_{CM})$ bin for a given W bin of the η dataset.

With the acceptance determined, the pieces can be put together to construct the differential cross section for the $W = 1990 \rightarrow 2000$MeV bin. Table 4.4 puts the pieces of the error together as a function of $cos(\theta_{CM})$ for the given W bin.

$\cos\theta_{cm}$	$\frac{\Delta\sigma}{\sigma}$	$\frac{\Delta N_e}{N_e}$	$\frac{\Delta\epsilon}{\epsilon}$	$\frac{\Delta N_\gamma}{N_\gamma}$	$\frac{\Delta N_{targ}}{N_{targ}}$	$\frac{\Delta b}{b}$
−0.90	0.328	0.324	0.0414	0.020	0.010	0.0176
−0.70	0.0814	0.0737	0.0196	0.020	0.010	0.0176
−0.50	0.0572	0.0471	0.0157	0.020	0.010	0.0176
−0.30	0.0490	0.0372	0.0143	0.020	0.010	0.0176
−0.10	0.0443	0.0308	0.0143	0.020	0.010	0.0176
0.10	0.0449	0.0315	0.0147	0.020	0.010	0.0176
0.30	0.0491	0.0366	0.0162	0.020	0.010	0.0176
0.50	0.0513	0.0391	0.0171	0.020	0.010	0.0176
0.70	0.0580	0.0462	0.0206	0.020	0.010	0.0176
0.90	0.169	0.151	0.0706	0.020	0.010	0.0176

Table 4.4: The relative errors of each individual piece going into the differential cross section calculation as determined in $cos(\theta_{CM})$.

Using these errors, and the events and acceptances already determined, the differential cross section can be calculated point by point. The numbers are reported for this given bin in center-of-mass energy in Table 4.5.

$\cos\theta_{cm}$	$\frac{d\sigma}{d\Omega}$	$\Delta\left(\frac{d\sigma}{d\Omega}\right)$	$\frac{\Delta\sigma}{\sigma}$
	$W = 1.995$		
-0.90	0.0341	0.0088	0.258
-0.70	0.0488	0.0038	0.078
-0.50	0.0528	0.0029	0.055
-0.30	0.0614	0.0029	0.047
-0.10	0.0877	0.0038	0.043
0.10	0.105	0.0045	0.043
0.30	0.104	0.0050	0.048
0.50	0.109	0.0056	0.051
0.70	0.151	0.0085	0.056

Table 4.5: The measured differential cross sections for $\gamma p \to p\eta$ at $1.990 \leq \sqrt{s} \leq 2.000\, Gev/c^2$. The cross section at $\cos\theta = 0.90$ is not reported due to binning issues.

With an example of the construction of the differential cross section for a given W bin reviewed, the measurement results will be presented.

4.5 η Differential Cross Sections Results

The results of the differential cross section measurements for η photoproduction will be presented in this section. These results represent an improvement upon the existing world data, and should provide theorists with a reasonable measurement with which to compare their models. The numerical values of the measured differential cross sections for the η are reported in Appendix 12. The differential cross section results will be presented in two ways. First, the results are binned in W, and presented as a function of $\cos(\theta_{CM})$ of the η meson. Second, the results will be binned in $\cos(\theta_{CM})$ of the η meson, and displayed as a function of W. In both cases, the results are plotted along with the available previous measurements from Dugger[6] and Crede[12]. The preliminary results from an on-going analysis by Ball[9] will be presented as well.

4.5.1 η Photoproduced Differential Cross Sections as Function of $\cos(\theta_{CM})$

The differential cross section results for photoproduced η mesons. The black crosses are the results from this, the Krahn, analysis. The blue circular markers are the results from Dugger et al.[6] using CLAS at JLAB. The red criss-cross markers are the results from Crede et al.[12] using the Crystal Ball at ELSA. The preliminary results from an additional CLAS analysis, for Ball[9] will be compared to as well, and will be denoted by green empty cross markers in the plots. These preliminary results are only being used as a comparison to another CLAS analysis. The results from Dugger, Crede, and Ball are all binned in 25 MeV bins in E_γ. The results of this analysis are binned in W, but in bins of varying widths. Thus, the results of this analysis will be compared to the results of Dugger and Crede in the W bin which most closely matches the middle of the available bins. The results are reported as $\cos(\theta_{CM})$ of the η versus $\frac{d\sigma}{d\Omega}$ for each bin in W. The plots are displayed on a log-scale. Figures 4.2 $\to$ 4.6 present the results of the differential cross section measurement. The highest W bin is not presented in the figures, but is reported with the other results in Appendix 12.

The differential cross sections reported in this analysis for η photoproduction are generally consistent with previously reported measurements. There are discrepancies however that should be noted.

While the new measurements do not contain the leading edge of the η threshold due to kinematics, it is worth comparing the lowest couple of bins to determine if any discrepancies exist. In the lowest bins, as seen in 4.2, the new measurement is systematically high in comparison to the previous

results from both Dugger[6] and Crede[12]. This discrepancy appears only in the first few W bins, from $W \approx 1640$ MeV on the differential cross sections appear to agree quite well.

The most obvious discrepancy appears in the higher W bins ($2400 \rightarrow 2600$ MeV region) in the forward $\cos(\theta_{CM})$ of the η meson. The results from Crede[12] are systematically higher than that of the Krahn measurement. The error bars present on the measurement from Crede grow to be quite large in the forward direction, much like the error bars on the Krahn measurement, indicating a growing lack of confidence in the forward most points. When comparing the differential cross sections as a function of W, binned in $\cos(\theta_{CM})$ of the η, the discrepancy becomes very clear. In the forward direction, the cross section from Crede flattens out as a function of W, while the Krahn result continues to fall. This is most clear in Figures 4.5 and 4.6. The preliminary Ball[9] results from CLAS indicate a closer agreement to the Krahn results than the Crede results in this region.

There is also a smaller discrepancy in the $W = 2000 \rightarrow 2200$ MeV region in the vicinity of $cos(\theta_{CM}) = 0.0 \rightarrow 0.2$. While the new measurement shows a possible enhancement in this region, the Crede result appears to have a systematically higher differential cross section in this region. There is currently no explanation for this discrepancy as the measured points on either side of this region are typically in pretty good agreement.

At the higher W range for the Dugger results, which are around $W \approx 2000$ MeV, the Krahn measurement is systematically low by comparison. In some cases, the error bars are quite large, and so the results are still consistent within those errors, but there is a clear discrepancy between the two measurements. Currently, the nature of the systematic discrepancy between the Krahn and Crede/Dugger results is unknown, but the relative agreement between the Krahn and preliminary Ball results is encouraging.

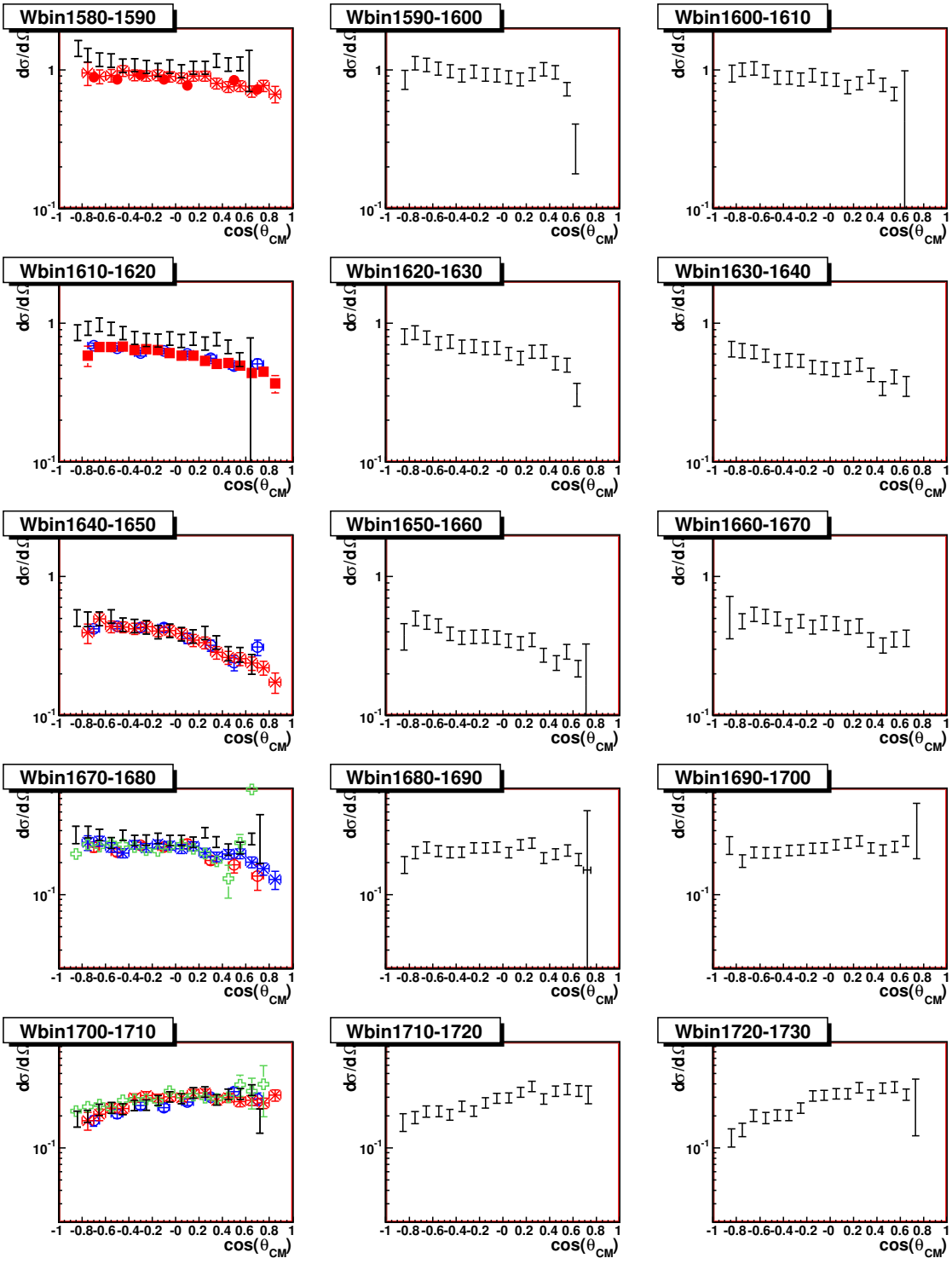

Figure 4.2: Differential cross section results for η photoproduction. The bins presented here run from top left to bottom right in increasing W. The black crosses are the Krahn results, the red criss-cross markers are the Crede[12] results, the blue circles are the Dugger[6] results, and the green empty crosses are the preliminary Ball[9] results. At threshold the Krahn results appear to be systematically high, in comparison to the Crede and Dugger measurements, this appears in the first few bins only.

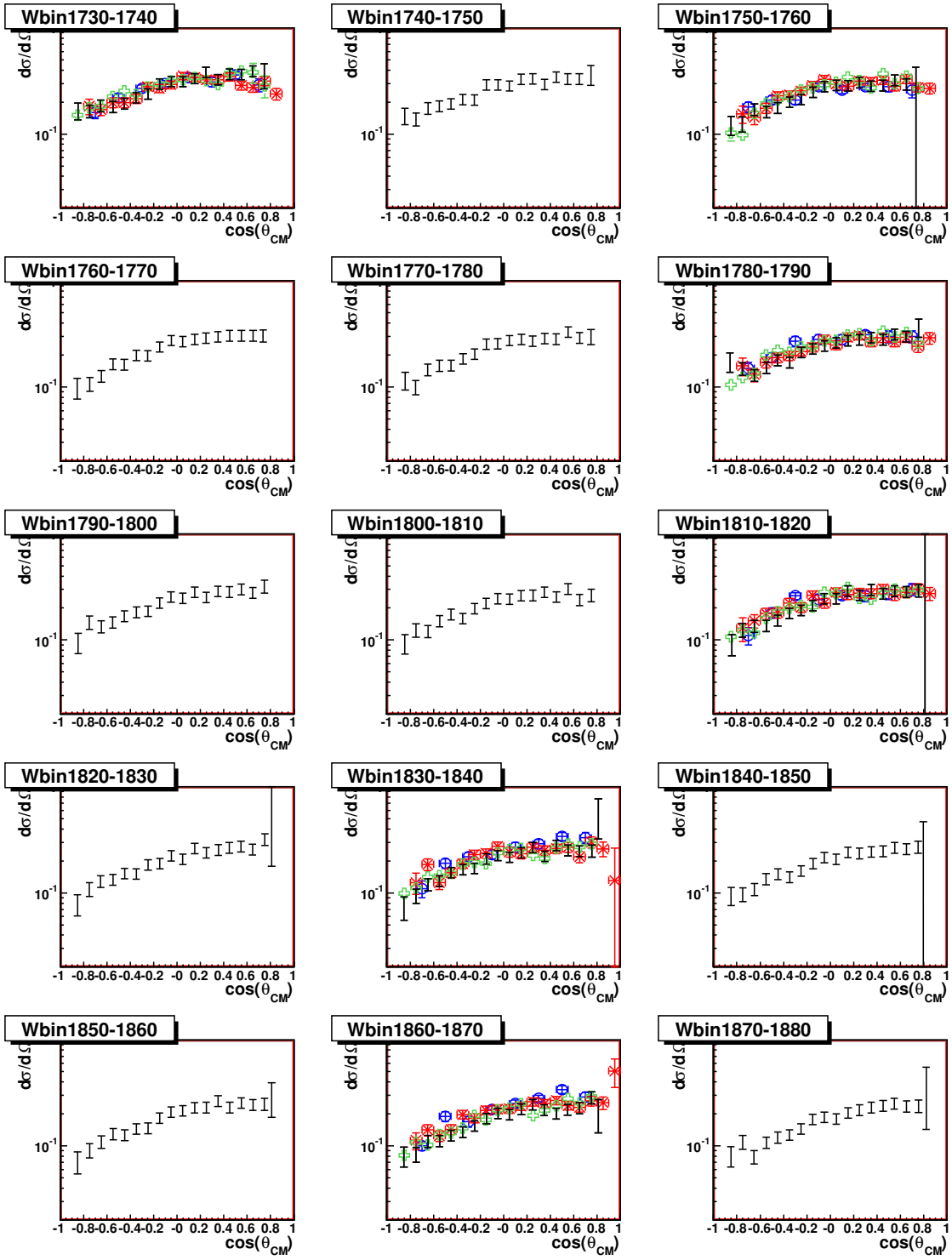

Figure 4.3: Differential cross section results for η photoproduction. The bins presented here run from top left to bottom right in increasing W. The black crosses are the Krahn results, the red criss-cross markers are the Crede[12] results, the blue circles are the Dugger[6] results, and the green empty crosses are the preliminary Ball[9] results. In this region in W there appears to be general agreement between all of the analyses.

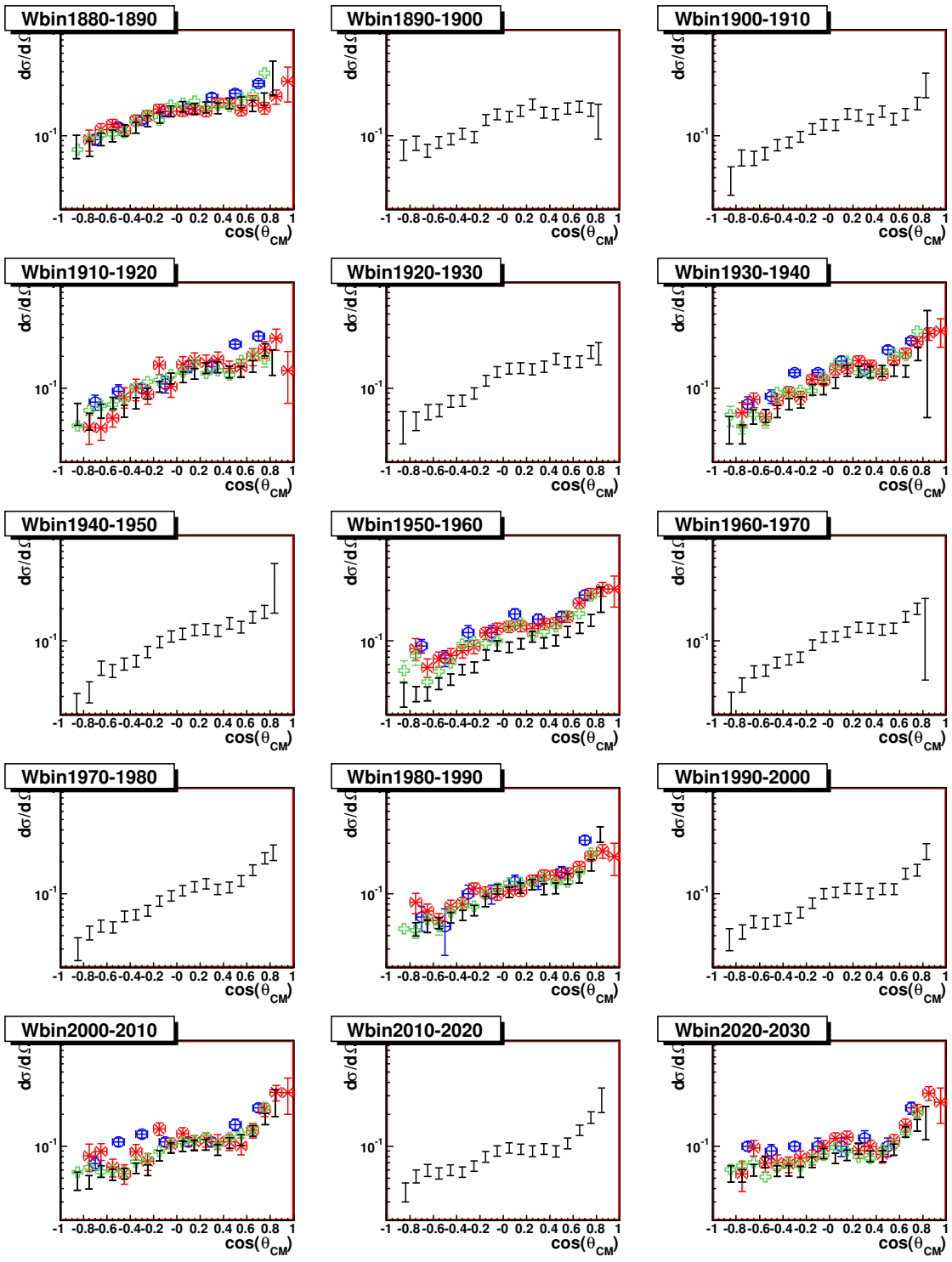

Figure 4.4: Differential cross section results for η photoproduction. The bins presented here run from top left to bottom right in increasing W. The black crosses are the Krahn results, the red criss-cross markers are the Crede[12] results, the blue circles are the Dugger[6] results, and the green empty crosses are the preliminary Ball[9] results.

4.5.2 η Photoproduced Differential Cross Sections as Function of W

The differential cross section results for photoproduced η mesons are presented in this section as a function of center-of-mass energy, W. The results are binned in W equally spaced bins in $\cos(\theta_{CM})$, with results reported for 18 of the 20 bins due to lack of events in the very forward and backward regions. The black crosses are the results from the Krahn analysis. The blue circular markers are the results from Dugger et al.[6] using CLAS at JLAB. The red criss-cross markers are the results from Crede et al.[12] using the Crystal Ball at ELSA. The green empty cross markers denote the preliminary results from Ball[9] using the CLAS detector. The results from Krahn, Crede[12], and Ball[9] are all binned into 20 equally spaced bins in $\cos(\theta_{CM})$. The Dugger[6] results are binned in 10 equally spaced bins. Rather than re-bin to accommodate this, the Dugger[6] results are simply plotted twice each. For example, the results from Dugger[6] for the $-0.2 < \cos(\theta_{CM}) < 0.0$ bin will be plotted in both of the Krahn and Crede bins which intersect this larger bin, $-0.2 < \cos(\theta_{CM}) < -0.1$ and $-0.1 < \cos(\theta_{CM}) < 0.0$. The results are displayed on log scale for ease of comparison. The results are reported as $\frac{d_\sigma}{d_\Omega}$ as a function of W for each bin in $\cos(\theta_{CM})$.

In the most forward 6 bins, there are two additional curves presented. The curved magenta line present in Figure 4.9 represents the Regge t-channel contribution to the differential cross section in a given bin as determined in the Krahn analysis. The overall scale of this t-channel was set by the highest few points in W. The curved blue line is the result from a fit to DESY[53] data by Chiang[54]. The purpose of including models in the plots is to allow for further comparisons to be made regarding the shape of the differential cross sections as a function of W. See Section 5.2.1 for a description of the models.

As was evident in the results binned in W, there is a high-W forward-direction discrepancy between the results of the Krahn analysis and the results from Crede[12] and Dugger[6]. The Ball results appear to agree more with the Krahn results than with the Crede results. The results from Ball, while unpublished, are in reasonably good agreement across the whole range in W. Comparing the Krahn results to the Dugger[6] results demonstrates that, where comparable, the results from the Krahn analysis start systematically high by $\approx 20\%$ then progress to being systematically low by $\approx 20\%$. The results from Krahn and Crede line up quite well at low W, and in the more backward $\cos(\theta_{CM})$ bins, but deviate by as much as a factor of @ in the high-W forward-angle region.

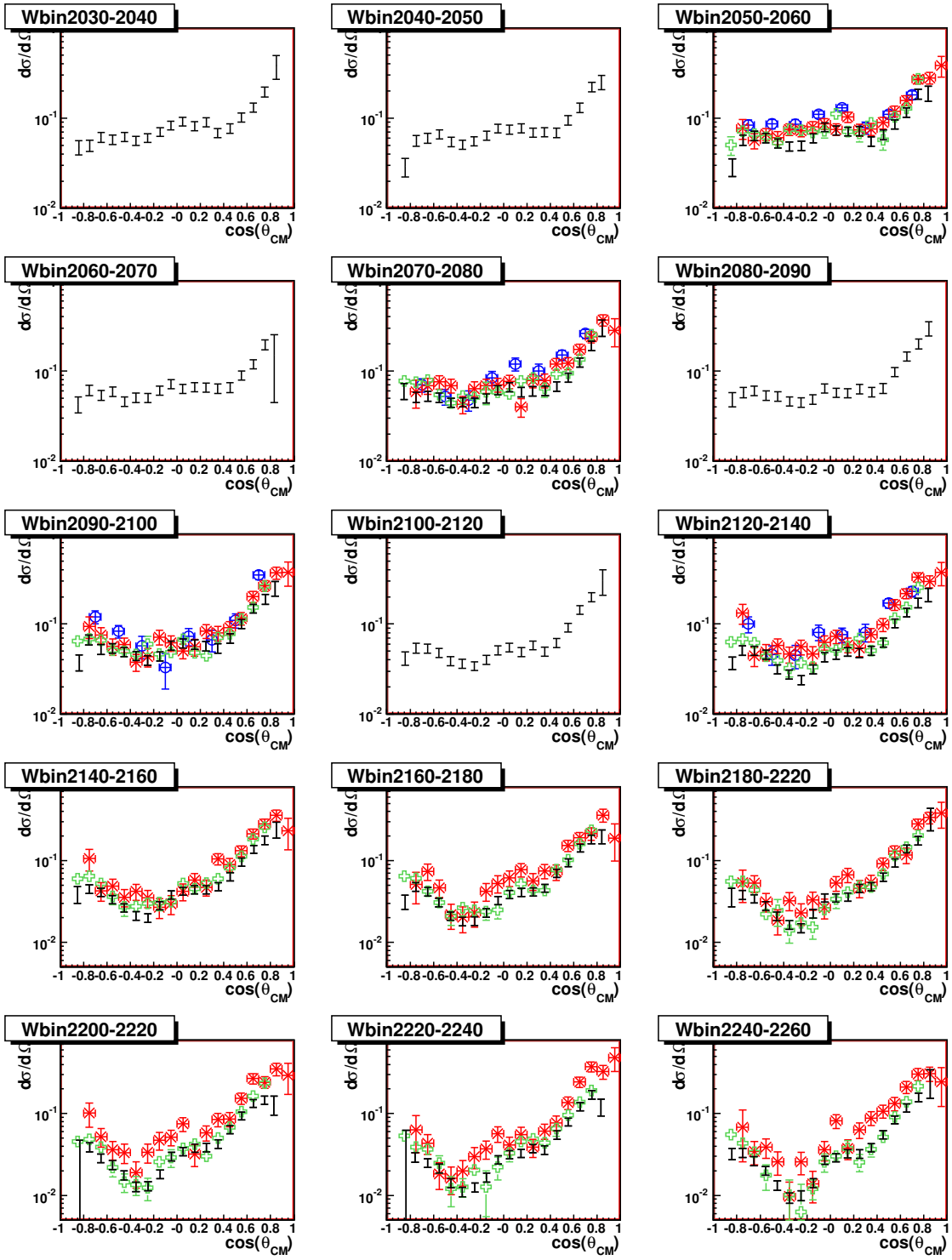

Figure 4.5: Differential cross section results for η photoproduction. The bins presented here run from top left to bottom right in increasing W. The black crosses are the Krahn results, the red criss-cross markers are the Crede[12] results, the blue circles are the Dugger[6] results, and the green empty crosses are the Ball[9] preliminary results. The differential cross sections are becoming more forward peaked in this region of W and there begins to be a hint of a discrepancy at forward angles. The Krahn result appears to systematically fall below the Crede and Dugger results, while remaining in good agreement with the Ball result.

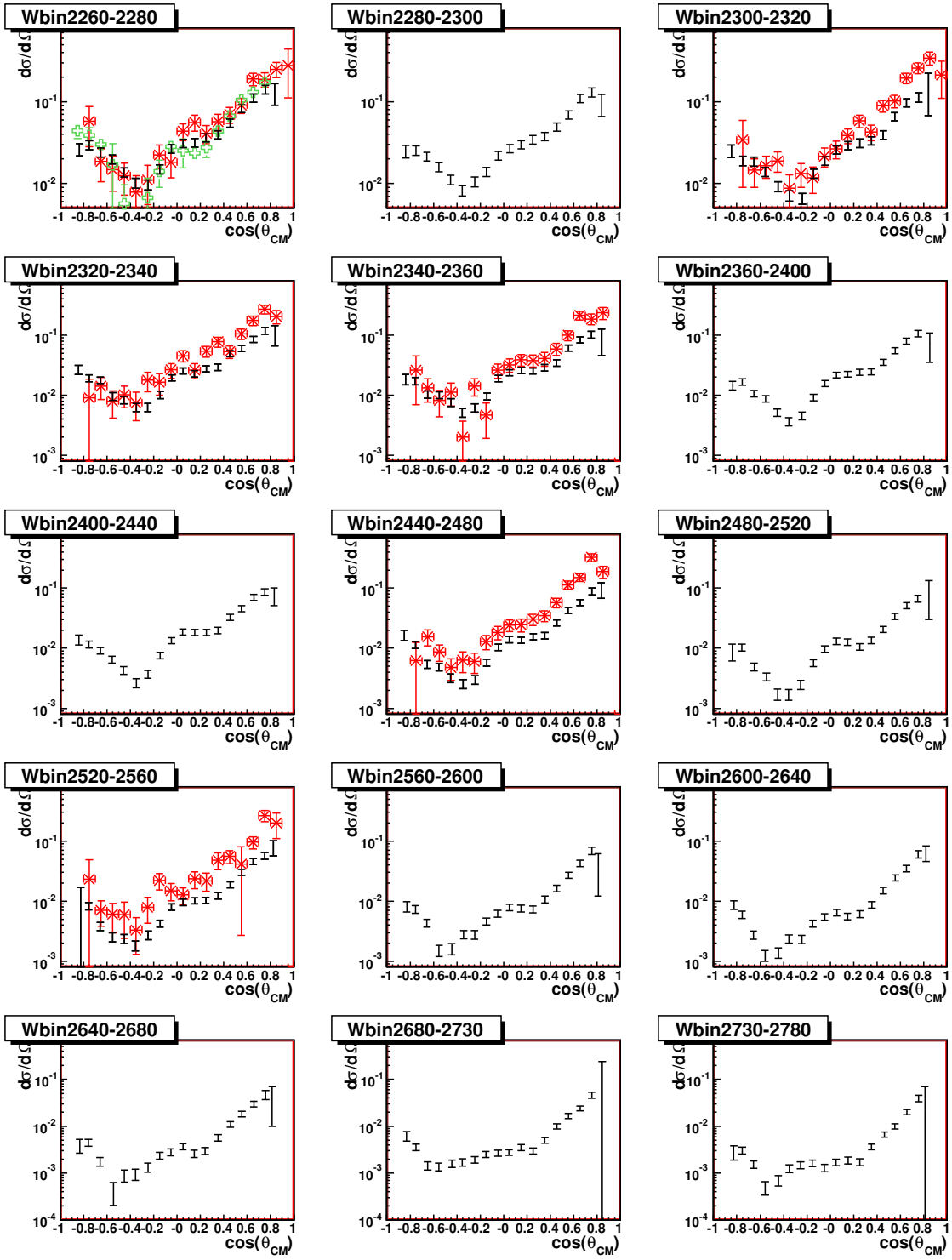

Figure 4.6: Differential cross section results for η photoproduction. The bins presented here run from top left to bottom right in increasing W. The black crosses are the Krahn results, the red criss-cross markers are the Crede[12] results, the blue circles are the Dugger[6] results, and the green empty crosses are the preliminary Ball[9] results. In these plots all of the results appear to have regions of agreement and disagreement. The Krahn result is typically lower than both Crede and Dugger, but in fair agreement with the preliminary Ball results.

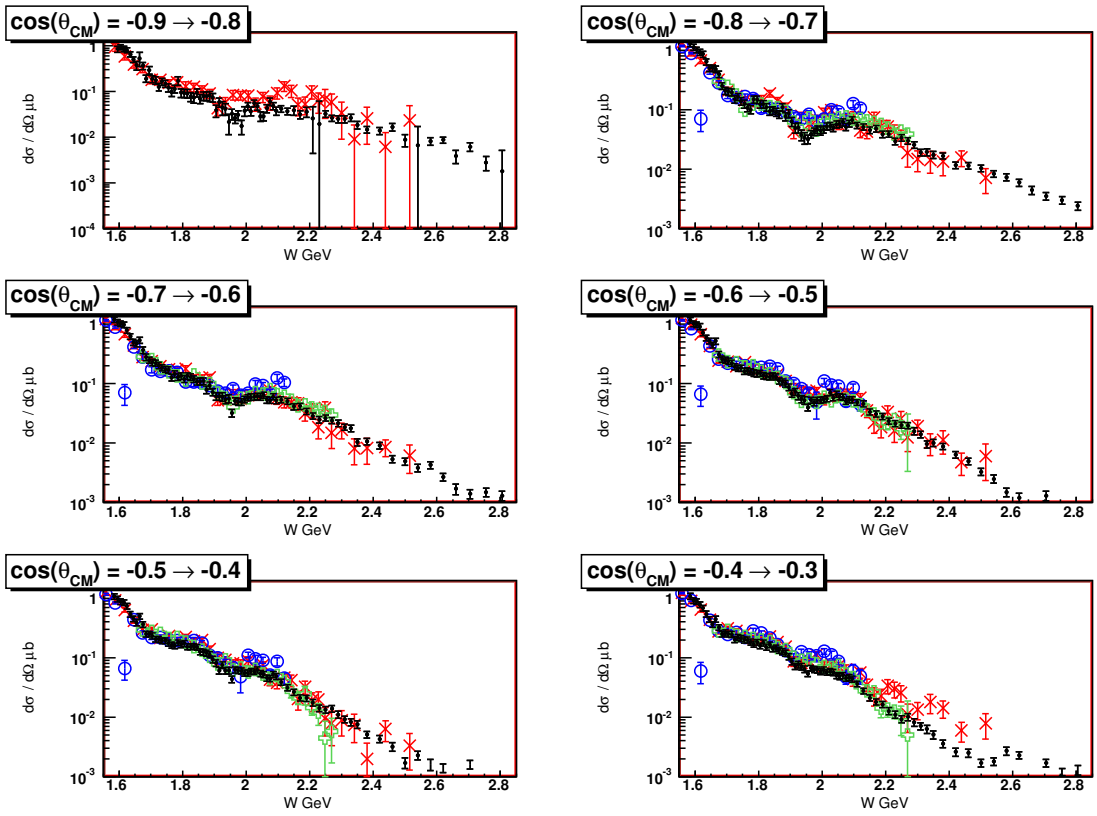

Figure 4.7: Differential cross section results for η photoproduction. The bins presented here are in $\cos(\theta_{CM})$, with results plotted as a function of W. The width of the bins is $\cos(\theta_{CM}) = 0.1$. The black points are the Krahn results. The red criss-cross markers are the Crede[12] results, the blue circles are the Dugger[6] results, and the green empty cross markers are the Ball[9] results. Through most of the backward angles, across W the results from the Krahn analysis and the Crede, Dugger, and Ball analyses appear to be in good agreement. Maximal disagreement appears to occur around $W = 2000 \rightarrow 2200$ MeV.

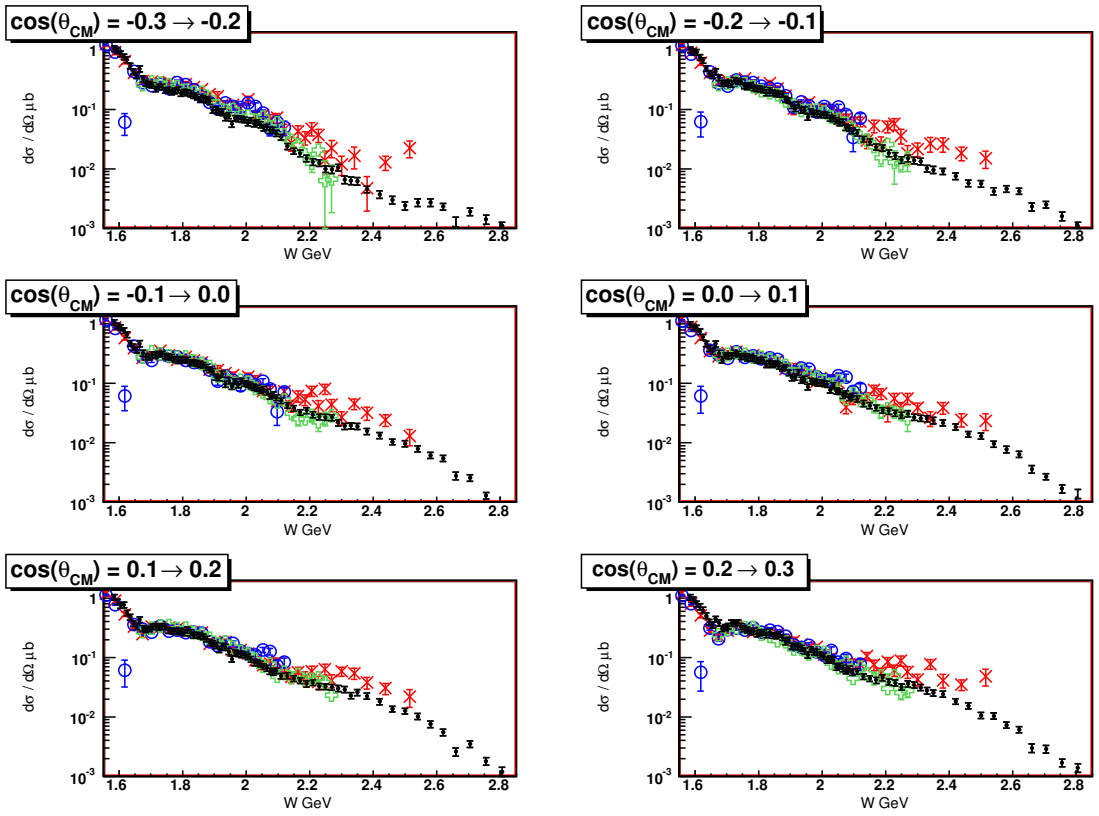

Figure 4.8: Differential cross section results for η photoproduction. The bins presented here are in $\cos(\theta_{CM})$, with results plotted as a function of W. The width of the bins is $\cos(\theta_{CM}) = 0.1$. The black points are the Krahn results. The red criss-cross markers are the Crede[12] results, the blue circles are the Dugger[6] results, and the green empty crosses denote the preliminary Ball[9] results. Up to $\approx$ 2000 MeV the agreement at these angles is good between the three results. Above this W range, however, the Krahn result appears systematically low in comparison to the Dugger and Crede results. Worth noting however, is that the Ball results and the Krahn results still appear to be in good agreement.

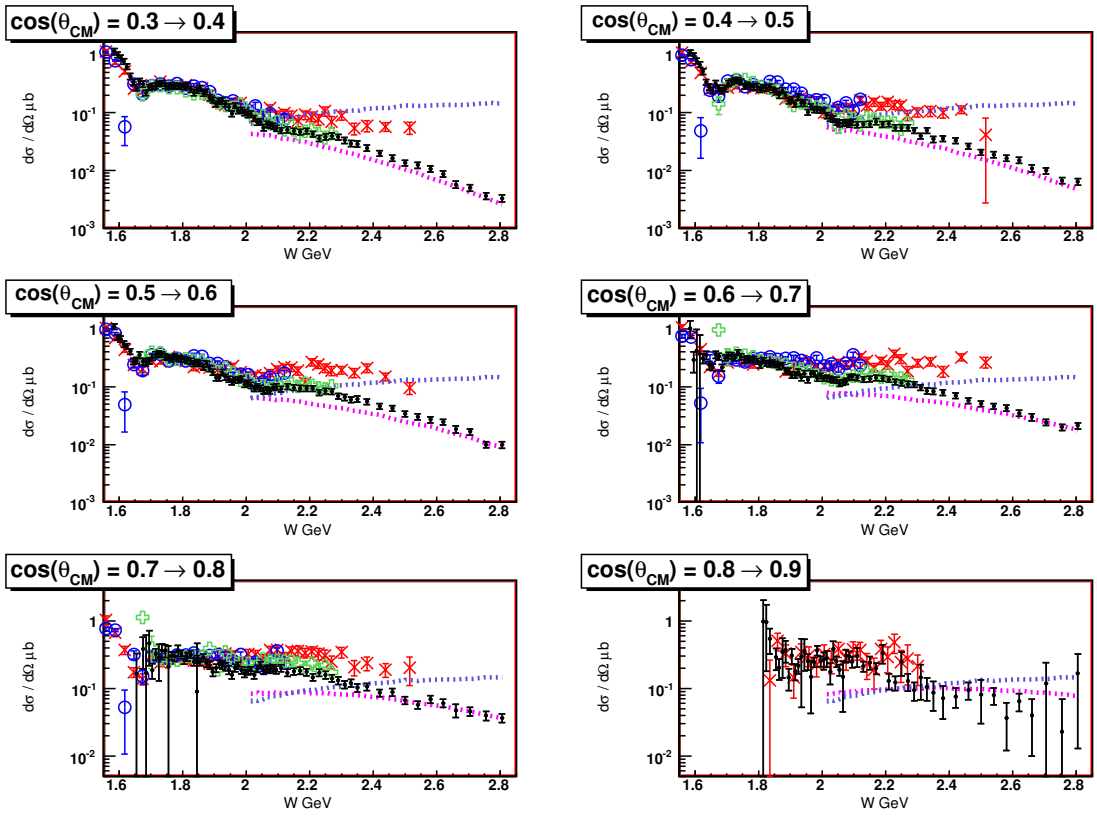

Figure 4.9: Differential cross section results for η photoproduction. The bins presented here are in $\cos(\theta_{CM})$, with results plotted as a function of W. The width of the bins is $\cos(\theta_{CM}) = 0.1$. The black points are the Krahn results. The red criss-cross markers are the Crede[12] results, the blue circles are the Dugger[6] results, and the green empty cross markers indicate the Ball[9] preliminary results. Again, for $W < 2000$ MeV the agreement between the results appears to be pretty good, while above this value the results diverge with the Krahn result systematically low. Again, the Ball result and the Krahn result appear to agree fairly well, despite the divergence from the Crede and Dugger results.

4.5.3 Average Ratios of η Results

The average ratio of the differential cross section measurements between the Krahn and Crede, Krahn and Dugger, and Krahn and Ball is presented in this section. The differential cross section measurements are divided point by point as a function of $cos(\theta_{CM})$. In a given W bin, for a given point in $cos(\theta_{CM})$, the ratio, R, is determined:

$$R = \frac{\frac{d\sigma}{d\Omega}(Krahn)}{\frac{d\sigma}{d\Omega}(Other)} \tag{4.4}$$

This ratio is now defined as a function of $cos(\theta_{CM})$ for a given W bin. A horizontal line is then fit to the ratio in each bin to determine the average ratio for a given W bin. The average ratio, R_{AVE} is defined as:

$$R_{AVE} = \frac{(\sum R)}{\#points} \tag{4.5}$$

This is the value reported as a function of W in Figure 4.10. This plot is only suggestive of the ratio, as the angular dependence is somewhat washed out. Additionally, the kinematics are a little different from bin to bin between the Krahn and other results. This is a result of the Dugger and Crede measurements binning in E_γ, instead of in W which is done in the Krahn analysis. The Crede and Ball results are reported similarly in $cos(\theta_{CM})$ to the Krahn results allowing for a point by point ratio to be determined. The Dugger results are reported more coarsely in $cos(\theta_{CM})$, requiring that an average be taken between the two overlapping bins in the Krahn analysis, prior to determining the ratio.

This average ratio allows for some of the gross features to be examined from a global perspective. The average ratio between the Krahn values and the Crede[12] values is depicted in the red criss-cross markers. The green empty cross markers indicate the ratio with the preliminary results from Ball[9], and the open blue circles are the ratio between Krahn and Dugger[6]. The Crede[12] results are clearly much higher at higher W, while they appear systematically lower in the low-W region. The Dugger[6] results follow the Crede results. The preliminary results from Ball[9] are more promising. On average, the Ball results and the Krahn results appear to be very comparable, as seen in Figure 4.10.

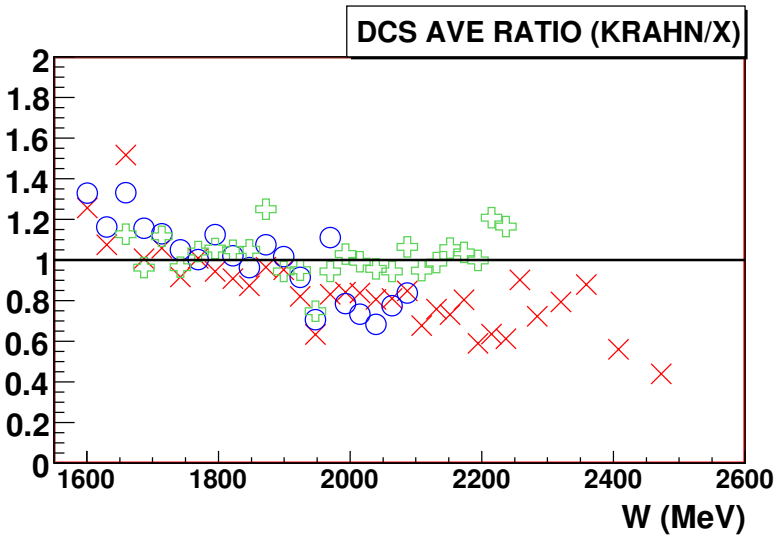

Figure 4.10: Plot of the average ratio between differential cross sections for Krahn compared to Crede[12], Dugger[6], and the preliminary results from Ball[9]. The average ratio is determined in each W bin, and then results are displayed as a function of W. The average ratio between the Krahn values and the Crede[12] values is depicted in the red criss-cross markers. The green empty cross markers indicate the ratio with the preliminary results from Ball[9], and the open blue circles are the ratio between Krahn and Dugger[6]. There is some clear systematic change in the ratio between the Krahn results and the Dugger and Crede results. The preliminary Ball results appear to be systematically similar to the Krahn results in W.

4.5.4 η Systematics

As indicated in previous sections, there are discrepancies between the Krahn results and the previously reported Crede[12] and Dugger[6] η results, particularly at high-W and forward-angles. Due to the W and angular dependence of the discrepancy, the possibility of a simple normalization issue is effectively excluded. Further analysis was done to determine if various changes in the fiducial cuts could account for this discrepancy. Three new variations on the fiducial cuts allowed for a systematic check of the differential cross section measurement, and the results are presented in this section. At this point, the issue remains unresolved, as none of the changes to the fiducial cuts could account for such a sizable discrepancy.

First, a more severe forward angle cut in the lab frame was made on the inward-bending π^- meson coming from the η decay to $\pi^+\pi^-\pi^\circ$. The forward going η and the inward-bending path of the π^- in the magnetic field of CLAS could cause the acceptance for events in that region to be inaccurately determined. A cut was placed to remove any π^- mesons in the data and Monte Carlo for which $\cos(\theta_{LAB}) > 0.94$. The measurement of the differential cross section was made in one of the high-W bins where a discrepancy has been noted. The results of this measurement are shown in Figure 4.11 in magenta. Additionally, Table 4.6 displays the values measured on a point by point basis for the $W = 2440 \rightarrow 2480$ MeV bin. It is clearly evident that while there is a slight change in the measurement, it would not account for the significant discrepancy in the forward region which exists between the Krahn and Crede results.

Second, the effect of increasing the momentum threshold to cut low-momentum protons was investigated. A low-momentum backward angle proton, corresponds to a higher-momentum η meson. A cut was made eliminating all protons which had a magnitude of momentum of less that 475 MeV. This is an increase of 100 MeV over the cut made in the standard fiducial cuts. Again, as seen in the previous investigation, there was little change in the measured differential cross section. The red points in Figure 4.11 show the measured values for the $W = 2440 \rightarrow 2480$ MeV bin. See Tables 4.6 and 4.7 for the numerical values. A ratio of the solutions is shown in Figure 4.12, to indicate the effect of each change in the cuts. Bear in mind that the systematic error determined in this study is not included in the error values listed in Tables 4.6 and 4.7.

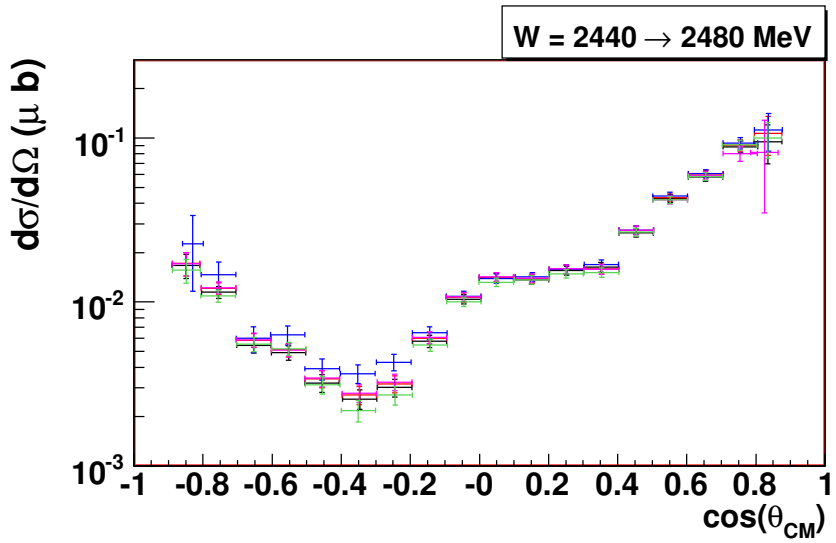

Figure 4.11: Differential cross section results for η photoproduction. There are five measurements presented for a single bin in W. The black crosses are the originally reported results, while the other results (see text for colors) are determined from alternate cuts on the data and Monte Carlo. There is generally very good agreement between the five reported results. Clearly, none of the cuts which have been altered provide for a correction to account for the systematic discrepancy between the Krahn and Crede[12] results in the forward region at high W.

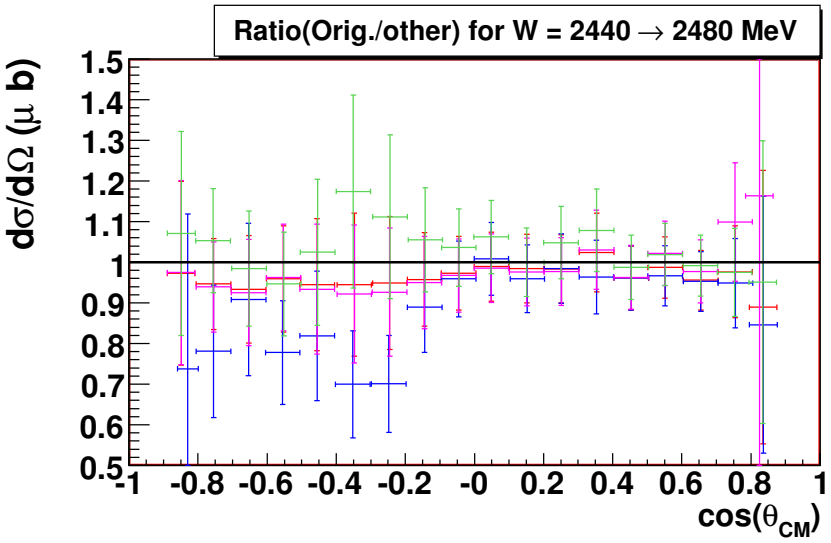

Figure 4.12: Ratios of the differential cross section results for η photoproduction with different cuts. There are four measurements presented for a single bin in W. The magenta markers indicate angular cut on the π^-. The red markers indicate a higher mass cut on the low momentum protons. The blue markers indicate a cut on the minimum momentum of the π^-. The green markers indicate the effect of reducing the confidence level cut. Clearly, none of the cuts which have been altered provide for a correction large enough to account for the systematic discrepancy between the Krahn and Crede[12] results in the forward region at high W.

Third, a cut was made on the magnitude of the momentum for the π^- meson, requiring that it have at least 375 MeV of momentum. The blue points in Figure 4.11 indicate that the measured values of the differential cross section are not significantly effected by the addition of this cut. Table 4.6 reports the measure values point by point for the $W = 2440 \rightarrow 2480$ MeV bin.

Fourth, as an additional check, the confidence level cut was reduced from a 10% cut, to a 2% cut, to determine what effect it may have on the differential cross section measurements. The results of this investigation are presented in green in Figure 4.11, and the numerical values are presented in Tables 4.6 and 4.7.

It is important to note that none of the changes to the cuts resulted in a systematic shift to higher differential cross sections in the forward direction which are significant enough to account for the discrepancy between the Krahn and Crede results. The discrepancy in the very forward regions reaches a factor of 2, or even 3, between the Krahn and Crede results. None of the cuts made or investigated here, provided a factor of 2 or 3 in the differential cross section measurement.

Attempting to define an additional global systematic error on the differential cross section measurements, the ratios determined in creating Figure 4.12 were histogrammed, and fit to a Gaussian. While the distribution is not expected to yield a Gaussian distribution, it will yield some idea of the spread of the ratios for this bin. Figure 4.13 presents this histogram, and the Gaussian fit which has determined the spread in the ratio values. Additionally, it is important to note, that while systematic changes in the differential cross section measurement were achieved, the changes made to the fiducial cuts were not minor tweaks. The fiducial cuts used here were made specifically to chop into the acceptance of the detector, where particles are clearly detected, in order to observe as large of an effect as possible. The goal was to make significant cuts to determine if they could account for the discrepancy in the forward region at high-W, from which it was clearly determined

that even severe cuts could not account for the discrepancy.

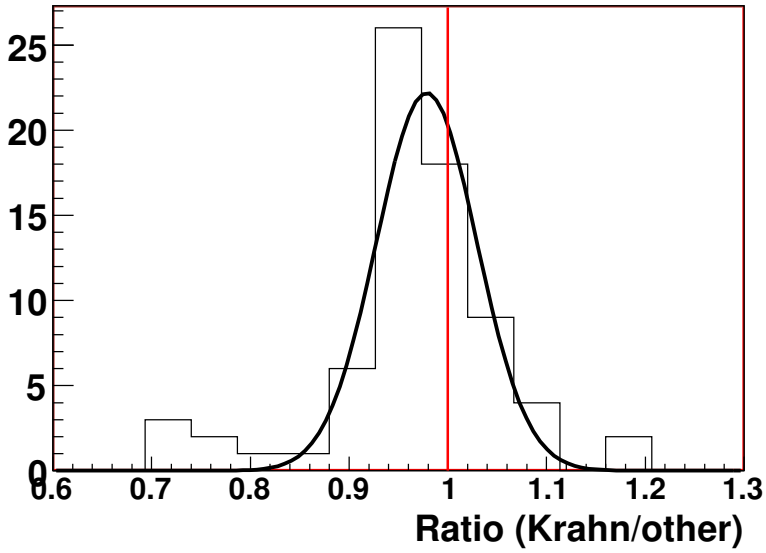

Figure 4.13: Ratios of the differential cross section results for η photoproduction with different cuts from W bin 2440 $\rightarrow$ 2480 MeV are histogrammed and fit to a Gaussian. The Gaussian fit can yield a quantitative measure of the spread created in the measurements of the differential cross sections when determined with alterations in the cuts.

The fit represented in Figure 4.12 yields a mean of 0.97 and a sigma of 0.05. So, for this W bin, the overall ratio of the alternate measurements to the original measurement are in relatively good agreement. At this point in time, it is prudent to include a systematic error of 10% on all points to account for the shifts in measurement with the changing cuts. This additional systematic error should be included in the values of the error listed in Tables 4.6 and 4.7.

The discrepancy between in the high-W and at forward-angles between the Krahn and Crede results remains unresolved. The preliminary results from Ball indicate a relatively good agreement of the differential cross section measurements with another on-going CLAS analysis. There may be some slight discrepancy in this same forward-angle, high-W region between Krahn and Ball, but the discrepancy is considerably smaller that between Krahn and Crede. One promising area of investigation lies in the background parameterization used for the η. The original skim selecting the η excluded events which were more than 30 MeV away from the mass of the η. While this was sufficient to select the η, it may be insufficient to allow for the best determination of the background, which requires side-bands around the η peak. This is compounded by the fact that the exact shape of the peak varies somewhat with W and $cos(\theta_{CM})$. It is possible that a discrepancy of 10-20% could be accounted for in this effect. This is, however, too small to account for the discrepancy between the Krahn and Crede results. Even if every event was determined to be signal, which is unlikely, it may account for $\approx$ 50%, not the factor of 2.

$\cos\theta_{CM}$	$\frac{d\sigma}{d\Omega}$ orig.	$\frac{d\sigma}{d\Omega}$ error orig.	$\frac{d\sigma}{d\Omega}$ $cos(\theta_{LAB}(\pi^-)) < 0.94$	$\frac{d\sigma}{d\Omega}$ error $cos(\theta_{LAB}(\pi^-)) < 0.94$	$\frac{d\sigma}{d\Omega}$ $P_{proton} > 475MeV$	$\frac{d\sigma}{d\Omega}$ error $P_{proton} > 475MeV$
-0.85	0.0167	0.0027	0.0171	0.0027	0.0226	0.0110
-0.75	0.0114	0.0009	0.0121	0.0010	0.0146	0.0028
-0.65	0.0054	0.0005	0.0058	0.0005	0.0060	0.0010
-0.55	0.0049	0.0004	0.0051	0.0004	0.0063	0.0008
-0.45	0.0032	0.0004	0.0033	0.0004	0.0039	0.0005
-0.35	0.0025	0.0003	0.0027	0.0003	0.0036	0.0004
-0.25	0.0030	0.0003	0.0031	0.0003	0.0042	0.0004
-0.15	0.0057	0.0004	0.0060	0.0005	0.0064	0.0005
-0.05	0.0104	0.0006	0.0106	0.0006	0.0108	0.0007
0.05	0.0140	0.0008	0.0141	0.0008	0.0132	0.0008
0.15	0.0136	0.0008	0.0138	0.0008	0.0142	0.0008
0.25	0.0155	0.0009	0.0158	0.0009	0.0158	0.0009
0.35	0.0163	0.0011	0.0159	0.0010	0.0169	0.0011
0.45	0.0263	0.0015	0.0274	0.0015	0.0274	0.0015
0.55	0.0427	0.0023	0.0433	0.0023	0.0442	0.0023
0.65	0.0576	0.0031	0.0607	0.0032	0.0605	0.0032
0.75	0.0883	0.0073	0.0905	0.0072	0.0931	0.0074
0.85	0.0949	0.0255	0.1067	0.0283	0.1121	0.0290

Table 4.6: Calculated DCS for different cut conditions in the $W = 2440 \rightarrow 2480$ MeV bin. A plot of these results is shown in Figure 4.11.

$\cos\theta_{CM}$	$\frac{d\sigma}{d\Omega}$ orig.	$\frac{d\sigma}{d\Omega}$ error orig.	$\frac{d\sigma}{d\Omega}$ $P_{\pi^-} > 375MeV$	$\frac{d\sigma}{d\Omega}$ error $P_{\pi^-} > 375MeV$	$\frac{d\sigma}{d\Omega}$ $CL > 0.02$	$\frac{d\sigma}{d\Omega}$ error $CL > 0.02$
-0.85	0.0167	0.0027	0.0171	0.0027	0.0156	0.00255
-0.75	0.0114	0.0009	0.0122	0.0010	0.0108	0.00094
-0.65	0.0054	0.0005	0.0058	0.0008	0.0055	0.00055
-0.55	0.0049	0.0004	0.0050	0.0004	0.0051	0.00047
-0.45	0.0032	0.0004	0.0034	0.0004	0.0031	0.00038
-0.35	0.0025	0.0003	0.0029	0.0003	0.0021	0.00032
-0.25	0.0030	0.0003	0.0032	0.0003	0.0027	0.00035
-0.15	0.0057	0.0004	0.0060	0.0004	0.0054	0.00046
-0.05	0.0104	0.0006	0.0105	0.0006	0.0100	0.00064
0.05	0.0140	0.0008	0.0142	0.0008	0.0132	0.00077
0.15	0.0136	0.0008	0.0140	0.0008	0.0136	0.00079
0.25	0.0155	0.0009	0.0159	0.0009	0.0148	0.00087
0.35	0.0163	0.0011	0.0158	0.0014	0.0151	0.00098
0.45	0.0263	0.0015	0.0273	0.0015	0.0266	0.00148
0.55	0.0427	0.0023	0.0418	0.0023	0.0419	0.00218
0.65	0.0576	0.0031	0.0590	0.0034	0.0581	0.00305
0.75	0.0883	0.0073	0.0803	0.0083	0.0906	0.00663
0.85	0.0949	0.0255	0.0815	0.0466	0.0998	0.02471

Table 4.7: Calculated DCS for different cut conditions in the $W = 2440 \rightarrow 2480$ MeV bin. A plot of these results is shown in Figure 4.11.

4.6 η' Differential Cross Sections Results

The results of the differential cross section measurements for η' photoproduction will be presented in this section. These results represent a significant improvement upon the existing world data, and should provide theorists with a reasonable measurement with which to compare their models. The numerical values of the measured differential cross sections for the η' are reported in Appendix 13. The differential cross section results will be presented in two ways. First, the results are binned in W, and presented as a function of $\cos(\theta_{CM})$ of the η meson. Second, the results will be binned in $\cos(\theta_{CM})$ of the η meson, and displayed as a function of W. In both cases, the results are plotted along with the available previous measurements from Dugger[7].

4.6.1 η' Photoproduced Differential Cross Sections as Function of $\cos(\theta_{CM})$

The differential cross section results for η' photoproduction are reported here. The black crosses shown in the following figures are the results of this analysis. The red triangular markers are the results from the Dugger et al.[7] analysis from the CLAS collaboration. The Dugger results were published in bins of E_γ which were 25 MeV wide. To facilitate comparison, the results of this analysis are compared with the Dugger results only in the bin which most closely matches the "middle" of the Dugger bin. Like the Dugger results, the results of this analysis are reported as $\frac{d\sigma}{d\Omega}$ versus $\cos(\theta_{CM})$ of the η' meson for each bin in W. The results are displayed on a log scale. Figures 4.14 $\rightarrow$ 4.16 present the η' results as a function of $\cos(\theta_{CM})$ of the η meson.

Comparing the measured differential cross sections to the results from Dugger[7] indicate how limited the previous experimental measurements have been. Comparisons can only be made in a handful of W bins, and each with a limited number of data points. Across all of W the Krahn results are in good agreement with the Dugger results to within errors. There are occasionally individual data points which disagree, yet the overall agreement is good.

Despite some small discrepancies, the results of the differential cross section measurements for η' photoproduction are in generally in agreement with previous results where comparisons can be made. No source of error or systematic correction has been found that may remove the small discrepancies between the two results.

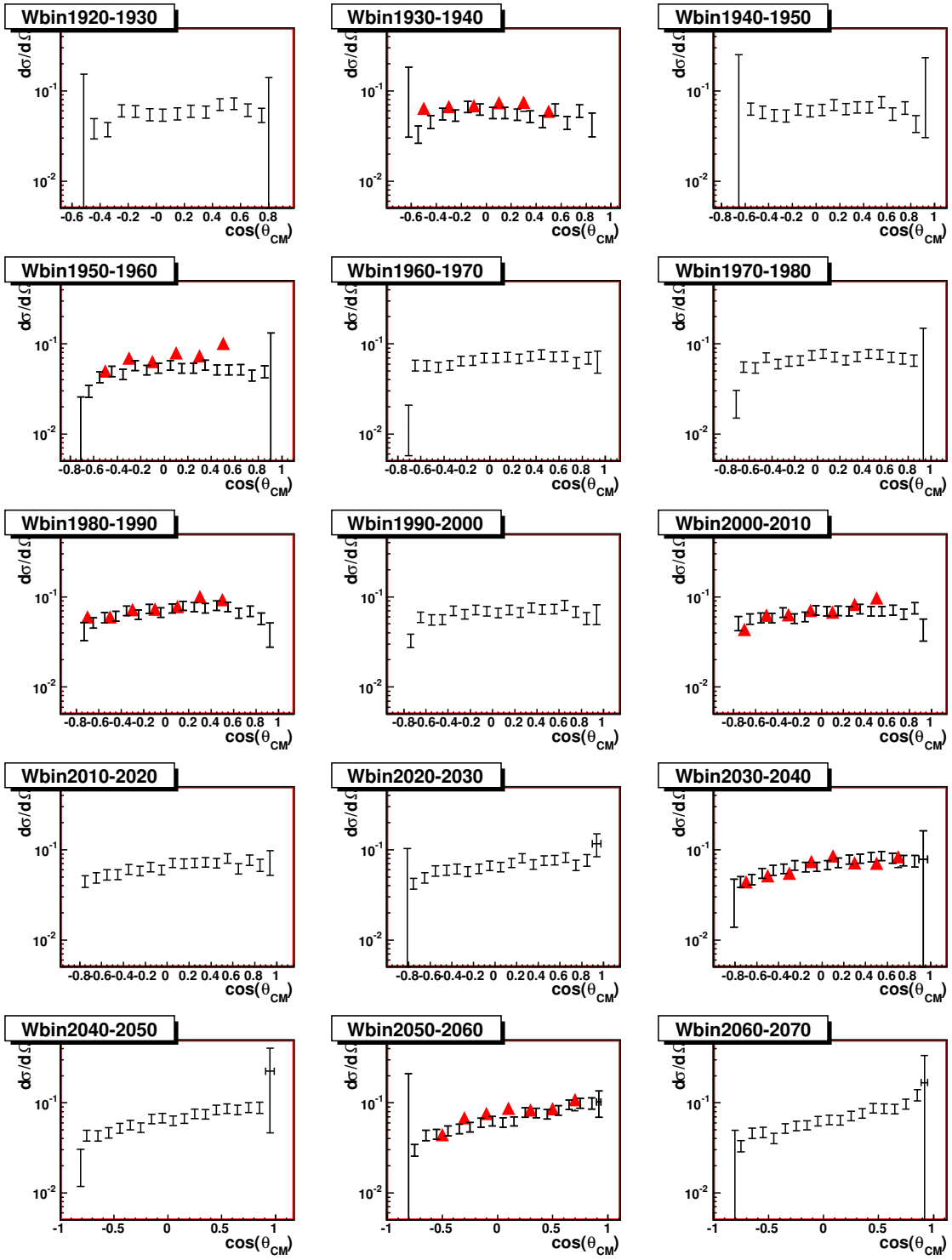

Figure 4.14: Differential cross section results for η photoproduction. The bins presented here run from top left to bottom right in increasing W. The black crosses indicate the Krahn results, while the red triangular markers indicate the Dugger[7] results. At threshold there is agreement within the errors between the two analyses.

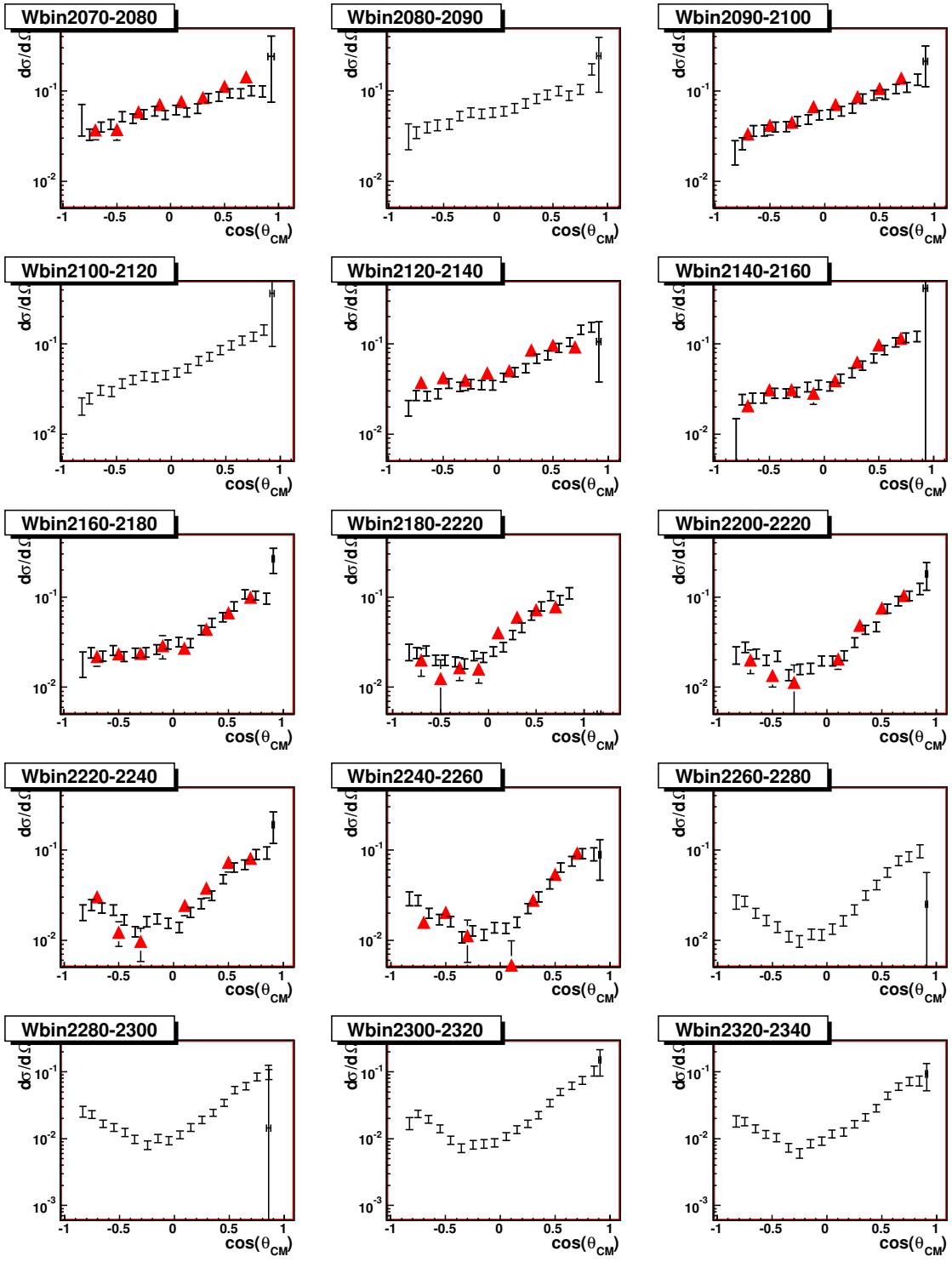

Figure 4.15: Differential cross section results for η' photoproduction. The bins presented here run from top left to bottom right in increasing W. The black crosses indicate the Krahn results, while the red triangular markers indicate the Dugger[7] results. At this range in W the agreement between the Krahn and Dugger results is quite good. There is perhaps a point of disagreement in the very forward most Dugger point with respect to the Krahn result at a similar $\cos(\theta_{CM})$.

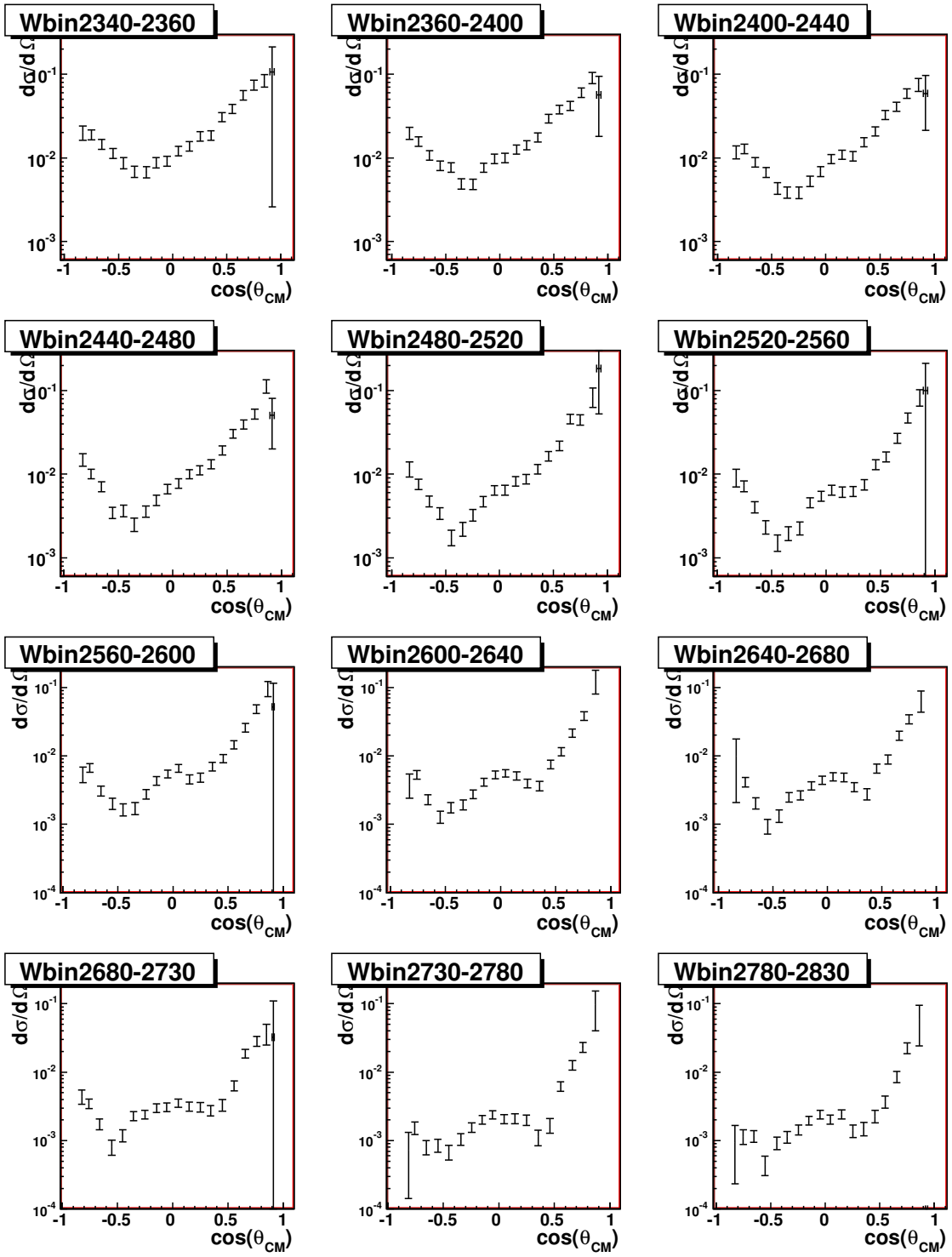

Figure 4.16: Differential cross section results for η' photoproduction. The bins presented here run from top left to bottom right in increasing W. The black crosses indicate the Krahn results, while the red triangular markers indicate the Dugger[7] results. In this W range the agreement between the two analyses is pretty good, and they appear to be reproducing similar results.

4.6.2 η' Photoproduced Differential Cross Sections as Function of W

The differential cross section results for photoproduced η mesons presented binned in $\cos(\theta_{CM})$ as a function of W. The black crosses are the results from the Krahn analysis, while the red triangular points are the results from Dugger[7]. The Dugger results are binned in 10 equally spaced bins incos(θ_{CM}) of the η' meson. Rather than re-bin to accommodate this, the Dugger results are simply plotted twice each. For example, the results from Dugger for the $-0.2 < \cos(\theta_{CM}) < 0.0$ bin will be plotted in both of the Krahn bins which intersect this larger bin, $-0.2 < \cos(\theta_{CM}) < -0.1$ and $-0.1 < \cos(\theta_{CM}) < 0.0$. The results are displayed on log scale for ease of comparison. The results are reported as $\frac{d\sigma}{d\Omega}$ as a function of W for each bin in $\cos(\theta_{CM})$. Figures 4.17 $\rightarrow$ 4.19 present the η' results.

Figure 4.17 presents the differential cross section measurements as a function of W for the backward angles. At the highest points in W where comparison is possible, around $W = 2.2$ GeV, the Krahn results are systematically high in comparison to the Dugger results. At the lower W region, the agreement is very good between the two results.

Figure 4.18 presents the results from the more central angular bins. There is very good agreement across most of W in these bins.

Figure 4.19 contains the most forward angular bins for the η' results. There are clearly a few points which are not in agreement to within errors, but the small discrepancies do not appear to be systematic in nature. Overall, the two results are fairly consistent. The highest angular bin is not presented in the Figures, but the results are present in Appendix 13.

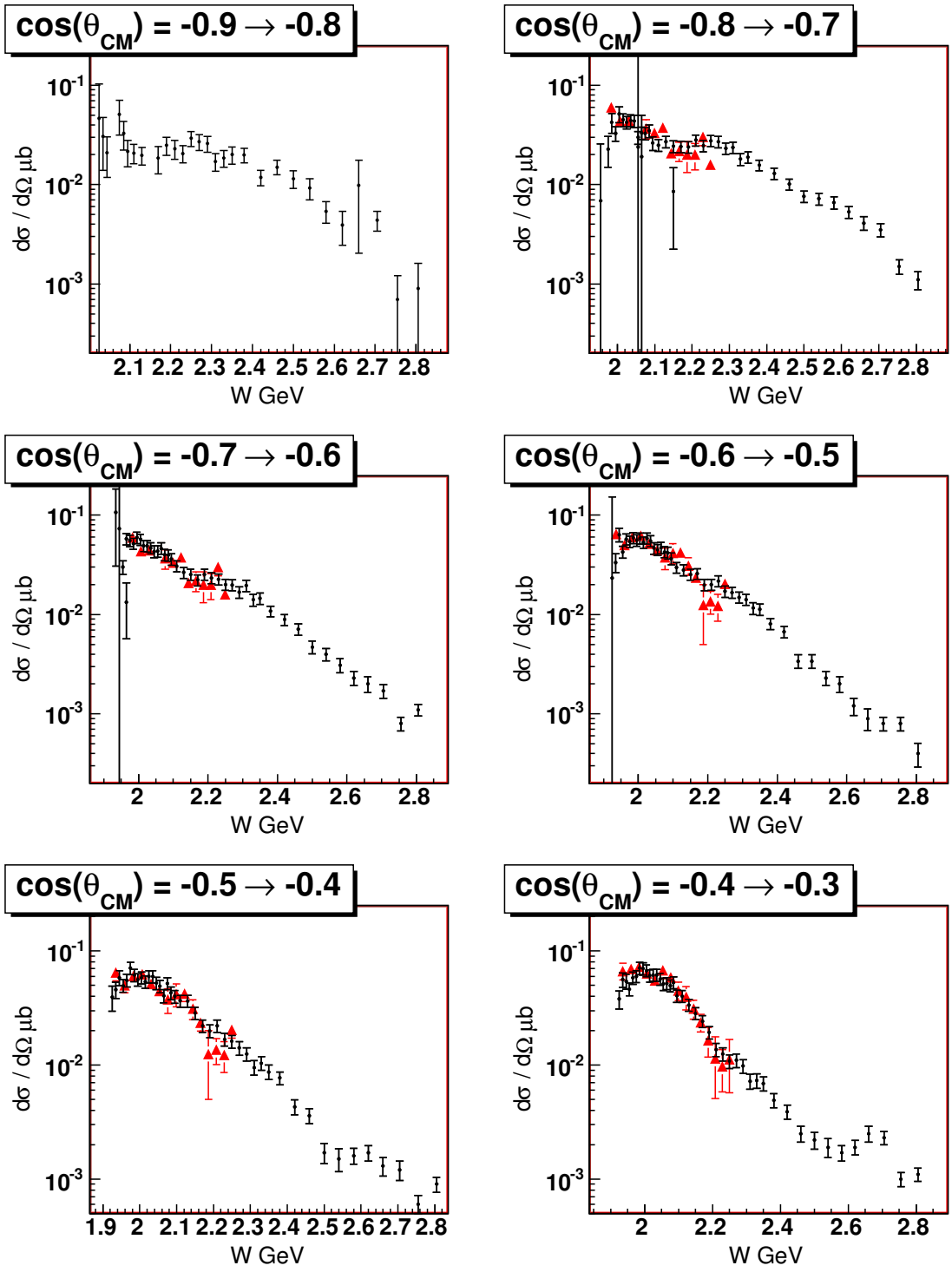

Figure 4.17: Differential cross section results for η' photoproduction. The bins presented here are in $\cos(\theta_{CM})$, with results plotted as a function of W. The width of the bins is $\cos(\theta_{CM}) = 0.1$. The black points are the Krahn results, and the red triangular markers are the Dugger[7] results. The Krahn results appear to line up reasonably well with the Dugger results as a function of W. These bins are in the most backward angles.

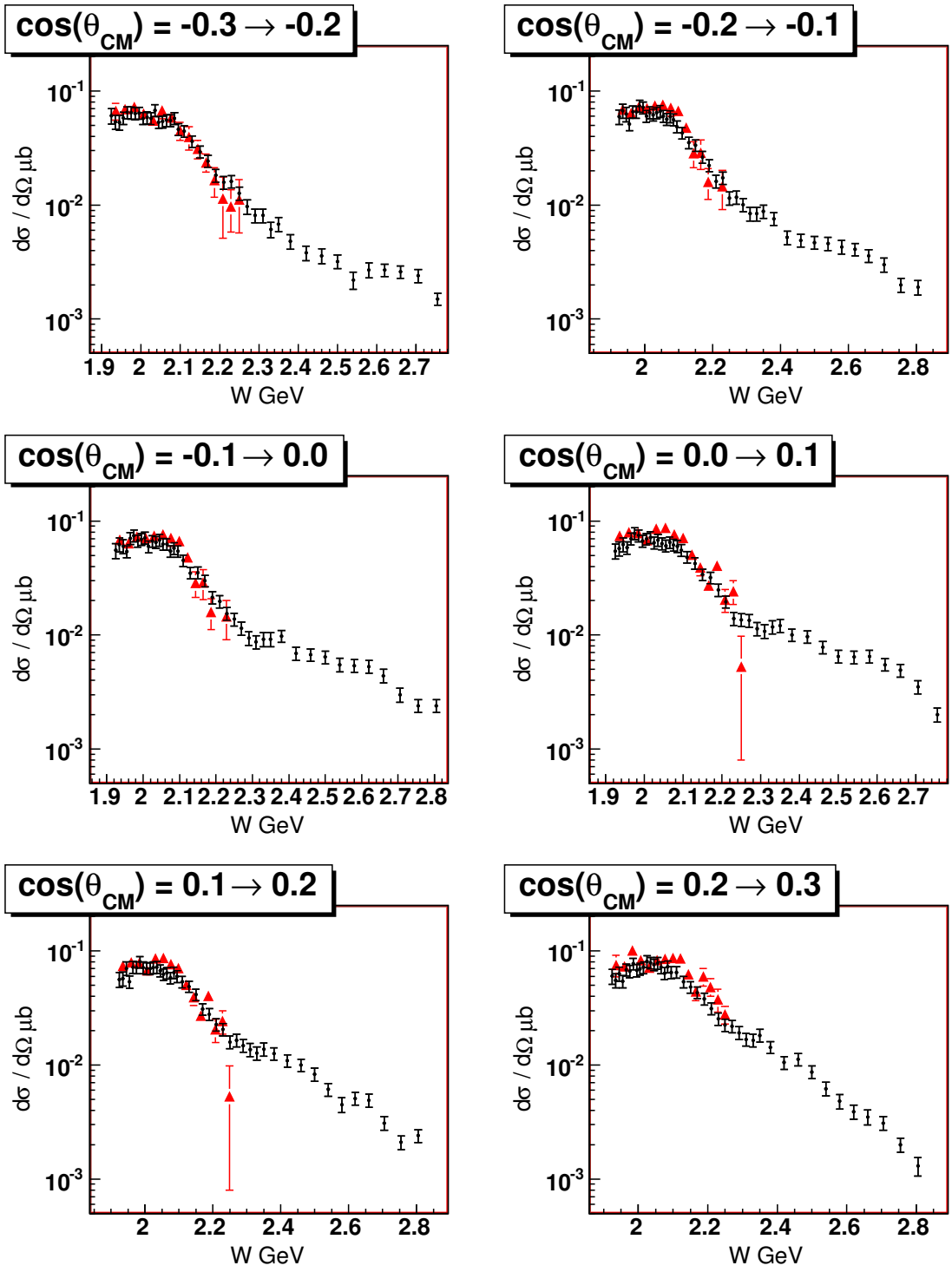

Figure 4.18: Differential cross section results for η' photoproduction. The bins presented here are in $\cos(\theta_{CM})$, with results plotted as a function of W. The width of the bins is $\cos(\theta_{CM}) = 0.1$. The black points are the Krahn results, and the red triangular markers are the Dugger[7] results. The results from the Krahn and Dugger analyses appear to be consistent within errors. These bins are in backward angles.

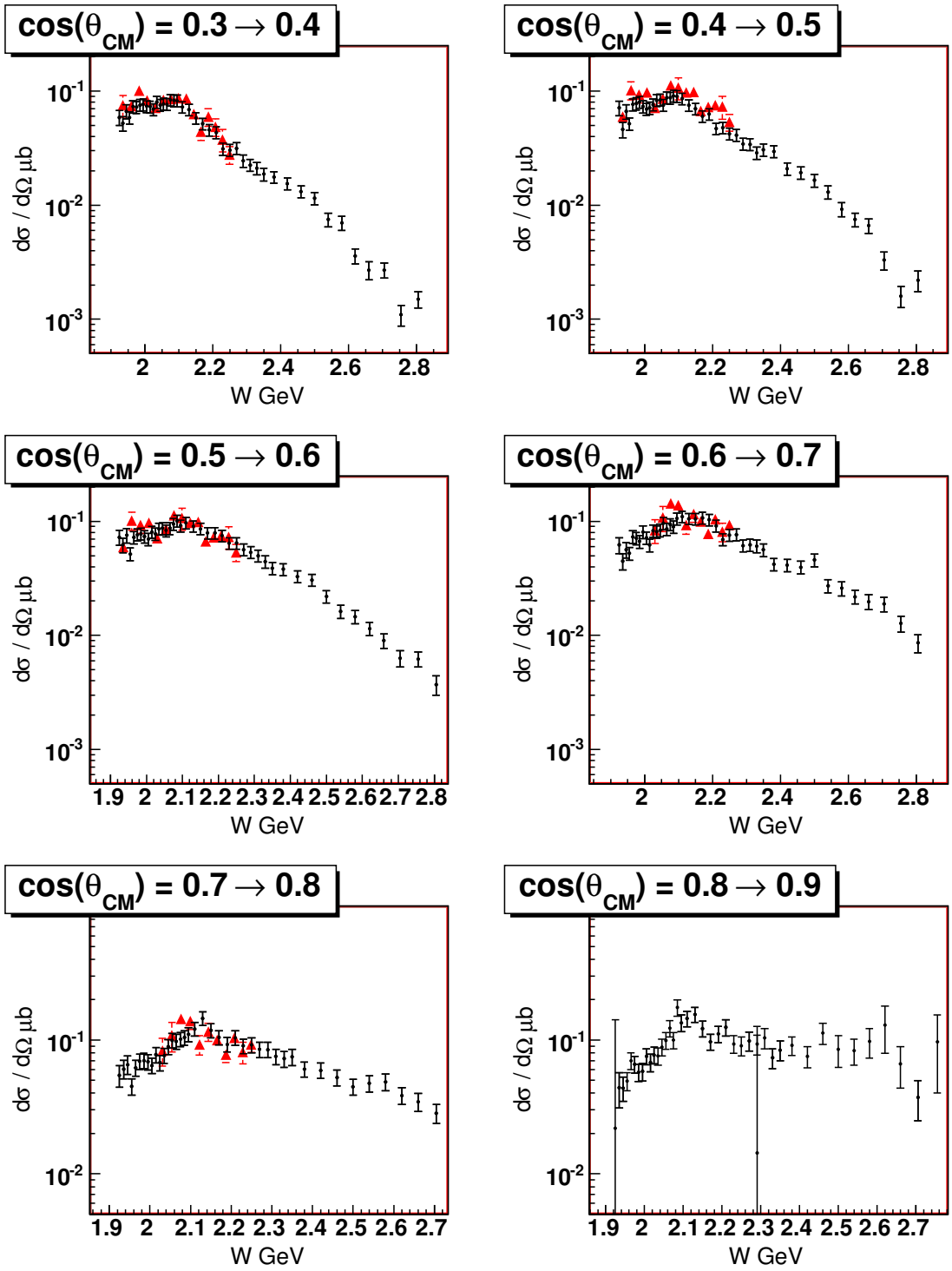

Figure 4.19: Differential cross section results for η' photoproduction. The bins presented here are in $\cos(\theta_{CM})$, with results plotted as a function of W. The width of the bins is $\cos(\theta_{CM}) = 0.1$. The black points are the Krahn results, and the red triangular markers are the Dugger[7] results. In the middle of the angular binning, the results from Krahn and Dugger appear here to be reasonably consistent. These bins are in the middle of the angular binning.

4.6.3 η' Systematics

While the discrepancies in the η analysis were clearly evident, there is painfully little data with which to compare the η' results. The cuts used in the η analysis are basically the same as were used in the η' analysis. As such, the lack of significant change to the differential cross section measurements in the η when those cuts were altered, is likely to translate to the η'. When the cuts were changed significantly, there were shifts in the differential cross section measurement for the η, and it is reasonable to believe that with severe cuts the measurement for the η' could be affected as significantly as for the η. Overall, a 10% systematic error was determined for the η, and that may apply here as well.

The issue of the background parameterization which may be present in the η should actually be less of an issue in the η' analysis. The original cut to select the events for the η' kept all events whose missing mass off the proton was ± 50 MeV from the peak. With a considerably wider window, it is much less likely that the background is incorrectly parameterized.

4.7 Summary

This chapter presents the results of the differential cross section measurements for η and η' photoproduction. The results for η photoproduction extend both the statistics and the kinematic range where data has previously been reported. The differential cross section measurement made in this analysis appears to be systematically low in comparison to the results from Crede[12] at high-W and forward-angle kinematics. The results compare to within $\approx 20\%$ with the results from Dugger[6], where comparable. Comparison of the results from this analysis with the preliminary results from Ball[9] are more encouraging, as there is reasonable agreement between this result and the Ball result. Systematic checks of various cuts were analyzed to try and determine the source of the discrepancy. In the process of this analysis, an additional 10% systematic error was determined, and added to the differential cross section measurement for the η. While shifts of the differential cross section within $10-20\%$ of measured the values were possible, there were no cuts or corrections found which would provide the factor of 2 which would resolve the discrepancy. The nature of the systematic discrepancy between the Crede result and this result remains unknown.

The η' results for photoproduction are a significant improvement over previous results, extending the statistics and kinematic range considerably. There is little available data with which comparisons can be made. The previous CLAS results from Dugger[7] are in good agreement with the new measurements. With no other data with which to compare, there is no way to know if the systematic discrepancies noted in the η measurement are present in the η' measurement. While systematics were not checked as thoroughly for the η' as for the η, it is assumed that the systematic error of 10% should be applied to the η' results as well.

Chapter 5

PWA Formalism and Fitting

This chapter describes the formalism used for the partial wave analysis. There are a number of pieces that have to come together to run a PWA fit. The amplitudes themselves are of enormous importance, as they contain the physics that is being put into the fit. If the amplitudes are either wrong, or incorrectly generated, then the physics coming out of the fit will be incorrect as well. Generation of the amplitudes will be described in this chapter. The development of the formalism is described fully in the Ph.D. thesis of Mike Williams[44]. For greater detail regarding the Covariant Tensor formalism from which the amplitudes used in this analysis came, see Appendix 11.

Once the amplitudes are generated, the likelihood fit is run Wbin by Wbin, to determine the contributions from each of the amplitudes. Likelihood fitting will also be described in this chapter. With the amplitudes and fitting generally described, the particulars of this analysis will be presented. The process of locking non-resonant contributions, such as the t- and u-channels, to the fit will be described.

5.1 Covariant Tensor Formalism

In this section, the construction of the amplitudes used in this analysis will be described. The construction of the amplitudes is primarily based on the work of W. Rarita and J. Schwinger[45]. Who utilized a covariant framework where all amplitudes are required to be Lorentz invariant. This allowed for the evaluation of all amplitudes in the same frame, and greatly reduced the amount of bookkeeping that was required to properly deal with final state particles.

5.2 Non-Resonant Amplitudes

There are several non-resonant contributions which are important for the analysis of η and η' photoproduction. Aside from background contributions, which must be subtracted from the dataset, there are prominent t-channel vector meson exchange diagrams which contribute. As the η and η' mesons are both $J^P = 0^-$, the amplitudes which are constructed are the same for the η and the η' with the exception of kinematic factors. In order to extract the resonant, or s-channel, contributions as accurately as possible, the non-resonant contributions must be accurately accounted for. The t-channel, u-channel, and background contributions will be described in this section.

5.2.1 t-channel Amplitudes

In the high W regions, η photoproduction is dominated by t-channel processes. In constructing t-channel amplitudes, several options were tried. Eventually, however, based on work by Anisovich

et al.[8], a Regge model was used to describe ρ and ω meson exchange in the t-channel. Anisovich built upon the work of Guidal and Laget[49] in constructing these amplitudes for the η. In the Anisovich analysis, the Regge trajectories used for the ρ and ω exchange were averaged together, and then put into the fit as a single exchange. While the Regge trajectories of the two mesons are indeed similar, this analysis chose to utilize the two exchanges individually, rather than to average them. The ρ trajectory is $\alpha_\rho(t) = 0.55 + 0.8t$, while the ω trajectory is given as $\alpha_\omega(t) = 0.44 + 0.9t$.

$$A^{Vector}_{\gamma p \to p\eta} = R(s,t)\bar{u}(p_f, m_f)\epsilon^*_\mu(q, m_\eta)(k_\alpha \gamma^\alpha g^{\mu\nu} - k^\mu \gamma^\nu)\epsilon_\nu(k, m_\gamma)u(p_i, m_i) \tag{5.1}$$

$R(s,t)$ is the Regge parameterization, and has the general form:

$$R(s,t) = F(t,m,\Lambda)\frac{1 + \xi exp^{-i\pi\alpha(t)}}{sin(\pi\alpha(t))}\left(\frac{s}{s_0}\right)^{\alpha(t)} \tag{5.2}$$

Where, $\alpha(t)$ is the Regge trajectory of the vector meson family, and F(t,m,Λ) is a monopole form factor meant to account for the finite size of the particles.

$$F(t,m,\Lambda) = \frac{\Lambda^2 - m^2}{\Lambda^2 - t}, \tag{5.3}$$

where Λ is the cutoff mass for the interaction.

While the basic form of the Regge parameterization is given in Eqn. 5.2, there are variations that can be made on this parameterization. First, the ξ in the Regge parameterization is referred to as the "signature", which can take the value of either 1 or -1. As an additional variation, linear combinations of the $1 + \xi exp^{-i\pi\alpha(t)}$ term can be used to parameterize the t-channel. When these linear combinations are used, they are referred to as "degenerate" trajectories. These degenerate combinations are made by adding or subtracting two $1 + \xi exp^{-i\pi\alpha(t)}$ terms with opposite signatures. When adding the two, this factor reduces to a simple factor of 2, and is referred to as a non-rotating parameterization due to the lack of the $exp^{-i\pi\alpha(t)}$ term. Alternately, when the two are subtracted with opposite signatures, the remaining piece is $2exp^{-i\pi\alpha(t)}$, which is referred to as a "rotating" parameterization.

In the course of this analysis, many t-channel parameterizations were investigated. Eventually, the "rotating-degenerate" t-channel was selected. So the Regge parameterization function, $R(s,t)$, is given by:

$$R(s,t) = F(t,m,\Lambda)\frac{2exp^{-i\pi\alpha(t)}}{sin(\pi\alpha(t))}\left(\frac{s}{s_0}\right)^{\alpha(t)} \tag{5.4}$$

Once the t-channel contribution was locked at high-W, the fact that a phase existed in the t-channel provided a reference phase for the rest of the analysis. There is some question as to how meaningful the phase may be if there is a very little strength in the parameterization. For example, at low-W the t-channel contribution is minimal. The effect of the reference phase established at high-W by the t-channel is questionable at very low-W.

5.2.2 Direct and Crossed Nucleon Exchange

To build the proton-exchange amplitudes, the appropriate effective Lagrangians are written,

$$\mathcal{L}_{\gamma pp} = -e\bar{\psi}(\gamma^\mu - \frac{\kappa_p}{2m_p}\sigma^{\mu\nu}\partial_\nu)A_\mu\psi \tag{5.5}$$

$$\mathcal{L}_{\eta pp} = -g_{\eta pp}\bar{\psi}(\gamma^\mu - \frac{\kappa_\eta}{2m_p}\sigma^{\mu\nu}\partial_\nu)\eta_\mu\psi. \tag{5.6}$$

From these Lagrangians two types of proton exchange amplitudes can be constructed. The u-channel crossed nucleon exchange amplitudes are given by,

$$\begin{aligned} A^{crossed-p-ex}_{\gamma p\to p\eta} &= eg_{\eta pp}\bar{u}(p_f,m_f)(\gamma^\alpha + i\frac{\kappa_p}{2m_p}\sigma^{\alpha\beta}k_\beta)\epsilon_\alpha(k,m_\gamma)\frac{(p_i-q)\cdot\gamma+m_p}{u-m_p^2} \\ &\quad\times(\gamma^\mu - i\frac{\kappa_\eta}{2m_p}\sigma^{\mu\nu}q_\nu)\epsilon^*_\mu(q,m_\eta)u(p_i,m_i). \end{aligned} \tag{5.7}$$

This processes can also proceed through an s-channel, or direct, exchange given by,

$$\begin{aligned} A^{direct-p-ex}_{\gamma p\to p\eta} &= eg_{\eta pp}\bar{u}(p_f,m_f)(\gamma^\mu - i\frac{\kappa_\eta}{2m_p}\sigma^{\mu\nu}q_\nu)\epsilon^*_\mu(q,m_\eta)\frac{(p_i+k)\cdot\gamma+m_p}{s-m_p^2} \\ &\quad\times(\gamma^\alpha + i\frac{\kappa_p}{2m_p}\sigma^{\alpha\beta}k_\beta)\epsilon_\alpha(k,m_\gamma)u(p_i,m_i). \end{aligned} \tag{5.8}$$

$$\tag{5.9}$$

The u-channel contributions to the η and η' photoproduction appear to be fairly limited. Generally speaking, u-channel processes tend to appear in differential cross section measurements as enhancements in the backward direction. It is clear from the results in Chapter 4, that in the η there is perhaps a slight enhancement in the backwards region in the highest W bins. This is however, a small portion of the cross section for a given bin.

5.2.3 Background Amplitudes

Though considerable effort was expended in reducing the background under the peak of the η and η' mesons in their respective datasets, there is still a background from which the signal can not be separated. In the $\gamma p \to p\eta$ channel, there is no way to separate non-η $p\pi^+\pi^-\pi^0$ events from the signal events. Likewise, for $\gamma p \to p\eta'$, there is no way to separate non-η' $p\pi^+\pi^-\eta$ events.

In order to proceed in the analysis, the assumption was made that these background events do not interfere with the $\gamma p \to p\eta$ and $\gamma p \to p\eta'$ amplitudes. This assumption is supported by the relatively long mean free path of the $\eta(\approx 150$ pm) and $\eta'(\approx 0.75$ pm) mesons in comparison to the length scale of the strong interaction(≈ 1 fm).

The process of background parameterization has been described in Section 3.8. The background was parameterized as a polynomial for a given Wbin and the yield of the background is known from the parameterization procedure. An amplitude is generated with the shape of the polynomial as a function of t. The contribution of this amplitude is fixed to the determined yield for the bin and reaction of interest.

As an example, in the η analysis, take Wbin $W = 2100 \to 2120$MeV. In this bin, the polynomial which described the background can be seen in Figure 5.1.

The total number of background events for this particular bin, is known from the parameterization procedure, and for this bin is 4225.3 events. As a reminder, the parameterization computes a calculated number of background for each bin, so the value is not necessarily an integer. When the amplitude is generated for this non-resonant background wave, the proper value of the fit parameter is determined such that the total yield of background for this bin will yield 4225.3 events.

5.3 Locking Non-Resonant Amplitudes

In the course of analyzing the η and η' it became clear that as the center-of-mass energy, W, increased, there was an increased contribution from non-resonant sources. Specifically, these sources were t- and u-channel diagrams. This was especially true for the η as it is considerably lower in mass than the η' and thus has a greater kinematic range in this experiment.

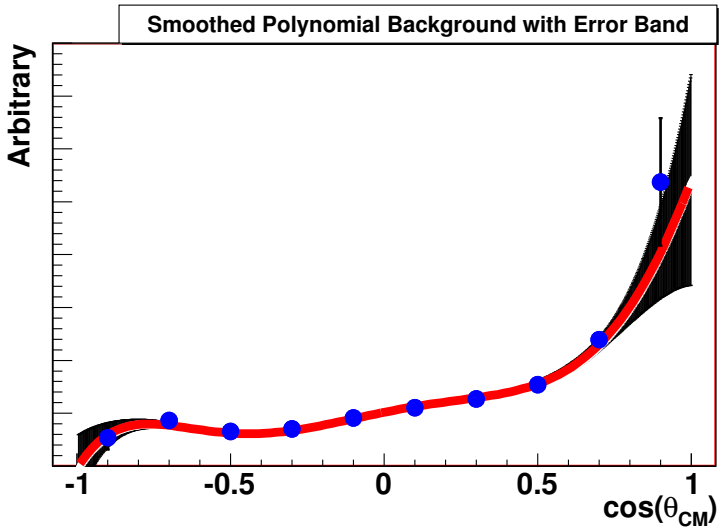

Figure 5.1: The round points are the measured acceptance corrected background determined for the $W = 2100 \rightarrow 2120$MeV bin in the η analysis. The curve through the points is the smoothed polynomial determined for this bin. The black band structure indicate the error on the smoothed polynomial.

As mentioned in a previously, the goal of this analysis was to observe resonant(s-channel) processes, the t- and u-channel contributions were locked at fit time. These contributions were locked using data in the high W region. The kinematic dependence in the amplitude allows for the contributions of the amplitudes to be extrapolated down to threshold.

To determine the contributions of the t-channel, the measured differential cross sections were used. The points available in the few highest W bins and at $t > -1.2$ were fit using a chi-square minimization to the Regge t-channel parameterization. Some of the available factors were locked to theoretical values, and some of the couplings are known from radiative decays. The unknown couplings were fit using the data. With the ρ and ω Regge trajectories being so similar, the choice was made to lock two of the parameters, $\kappa_{\rho NN}$ and $\kappa_{\omega NN}$, to the theoretical values, to restrict the freedom present in the fit. Without this step, the fit tended to push the values to competing extremes where the values would blow up, but essentially cancel each other. The values used came from Chiang[54], and are represented in Table 5.1. These values were determined using only the η dataset due to the more limited kinematic spectrum of the η'.

The values to which these contributions are locked will be presented here, along with plots of the strength of the contribution as a function of center-of-mass energy. Results for the η and η' will both be presented.

Table 5.1: t-channel parameter values for fits to the η and η'

V	$m_V(MeV)$	$g_{VNN}(theory)$	κ_{VNN}	$\lambda_{V\eta\gamma}$	$\lambda_{V\eta'\gamma}$	$\alpha_V(t)$
ρ	770	1.19(2.4)	3.7	0.81	1.24	$0.55 + 0.8t/GeV^2$
ω	782	5.53(9)	0.0	0.29	-0.43	$0.44 + 0.9t/GeV^2$

The values in Table 5.1 come from two different sources. The first source is a paper from Chiang et al.[54], from which the κ_{VNN} and λ values are taken. The couplings g_{VNN} come from a fit in

this analysis with the Regge amplitudes to the high energy data in these datasets. The values in the parentheses are the theoretical values as determined by Chiang[54]. Fits were run with the determined differential cross sections, using a standard chi-square fitting technique to fit only the data in the forward direction at high W.

The values determined in this analysis are about half the values of the ones determined by Chiang[54]. This is perhaps unsurprising as there is a known discrepancy between previous results and the results from this analysis in the differential cross sections at high-W and forward-angles. This is precisely the region where these fits are run, and the parameters are determined. The data used to constrain the fits from Chiang[54] comes from a photoproduction experiment run at DESY[53] in 1970. The DESY data has photon energies of $4.0GeV$ and $6.0GeV$. Only the very highest W bins, and most forward points of the differential cross section measurement will overlap with the lowest energy bin of DESY. Comparing the overall scale of the differential cross section measurements, in the small region of overlap, indicates that the results from the DESY analysis are $\approx 20\%$ higher than those presented in this analysis.

The u-channel fits determined two values concurrently for each of the η and η' reactions. The two factors are a form-factor value, and the coupling value. The two are much related, and between the two parameters, there may be several combinations of factors which produce the same overall physical phenomena. The parameters as determined in the fits to the backwards, high W cross sections are listed in Table 5.2. It is likely that including the u-channel in the fit does not have a significant impact on the overall results. Figure 5.2 indicates that even at high W the u-channel contributes a very small amount to the total yield.

Table 5.2: u-channel parameter values for fits to the η

Parameter	Value
$g_{\eta NN}$	0.477
$\Lambda_{\eta NN}$	1.08

The results for the η' are listed in Table 5.3. In the case of the η' the form-factor piece was arbitrarily locked, to a value, and the χ^2 fit to the differential cross section determined the value of the coupling $g_{\eta' NN}$. It is likely that the inclusion of the u-channel pieces does not have a significant impact on the overall results of the fits. Figure 5.3 indicates that even at high W the u-channel contributes a very small amount to the total yield.

Table 5.3: u-channel parameter values for fits to the η'

Parameter	Value
$g_{\eta' NN}$	5.47
$\Lambda_{\eta' NN}$	0.5

To demonstrate the influence of the t- and u-channel contributions to the η and the η' PWA results, the total strength of the contributions must be considered. The plot in Figure 5.2 shows the yield of the two non-resonant contributions to the total yield of the η. Clearly, there is a significant contribution to the yield coming from the t-channel. The t-channel was established at the high W region of this dataset and as such, it makes sense that it would be a significant portion of the yield in this region. The u-channel was also established at high center-of-mass energy in this dataset, but

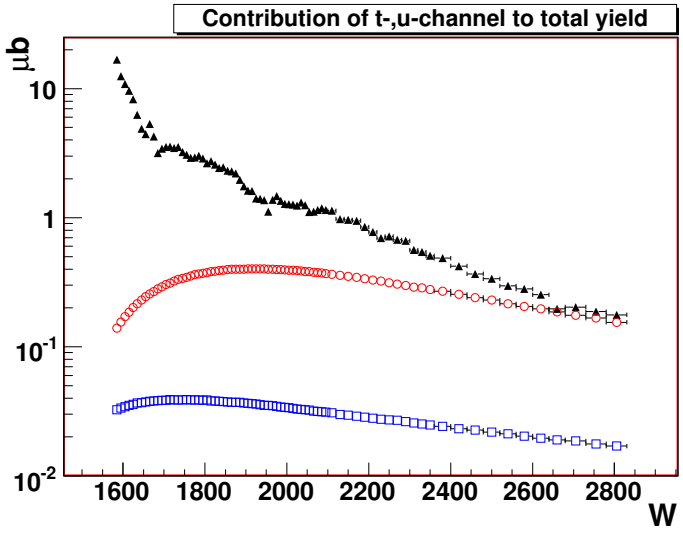

Figure 5.2: The contributions of the t- and u-channels to the η total yield. The t-channel is in the hollow circles, while the hollow squares denote the u-channel contribution. Note that this is plotted on a log scale. At high W the t-channel accounts for a large amount of the total η yield. This is not surprising, as this is where the contribution of the t-channel was determined. Note that in general, the u-channel does not make a significant contribution to the total yield.

it is clearly less influential on the overall results as it contributes so little to the total yield. See Figure 5.2.

The contributions to the total yield of the η' which come from the t- and u-channels are similar to those in the η. The u-channel contributes very little to the total yield of the η'. The t-channel on the other hand appears to contribute to a majority of the total yield at high W. See Figure 5.3.

As previously mentioned the values chosen for the t-,u-channel pieces have locked the contribution of these amplitudes in the fits. These values have been used for all of the fits which will be presented in an upcoming chapter. When observing differences between one fit and another, the contributions of these pieces should effectively cancel, allowing for the resonant contributions to the yield in the fits to be explored.

5.4 Resonant Amplitudes

The thrust of this analysis is the exploration of possible resonant structures present in η and η' photoproduction off of a proton target. The general construction of these s-channel amplitudes under a covariant tensor formalism was done by CMU graduate student Mike Williams[41], and is described fully in his thesis[44]. There are some particular features which bear pointing out. First, by binning in W, there is no need to impose any energy dependent shapes into the resonant amplitudes. This is an important distinction because a majority of previous analysis utilized an energy dependence as an input to the fit. Second, each of the W bins represents an independent fit to the data present in that bin. This allows for a check of the consistency of the fits ability to both reproduce the data, and extract results.

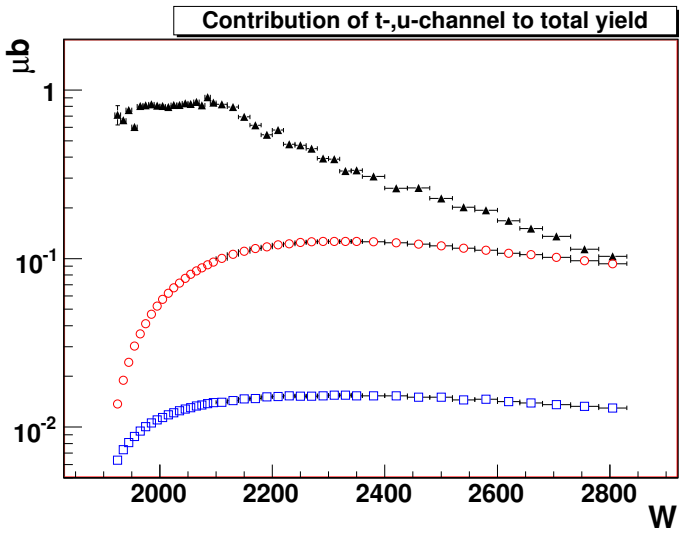

Figure 5.3: The contributions of the t- and u-channels to the η' total yield. The t-channel is in the hollow circles, while the hollow squares denote the u-channel contribution. Note that this is plotted on a log scale. At high W the t-channel accounts for a large amount of the total η' yield. This is not surprising, as this is where the contribution of the t-channel was determined and locked. This is further justified by the results from the differential cross section measurement, which clearly indicates at high W a vary forward asymmetric peak, which is indicative of a t-channel process. For examples, see Section 4.5 .Note that in general, the u-channel does not make a significant contribution to the total yield.

5.5 Notation

In all of the work that follows, p_i, p_f, q and k will be used for the initial proton, final proton, η and photon 4-momenta. The z-axis in the overall center-of-mass frame, defined by $\hat{k}$, is used as the angular momentum quantization axis. We denote particle spin projections as m_x and particle masses as w_x for any particle x. The Mandelstam variables are defined as,

$$s = (p_i + k)^2 = (p_f + q)^2 \quad (5.10)$$
$$t = (q - k)^2 = (p_i - p_f)^2 \quad (5.11)$$
$$u = (p_i - q)^2 = (p_f - k)^2. \quad (5.12)$$

The fit parameters are denoted as $\vec{x}$. The set of all independent kinematic variables will be X and the Lorentz invariant phase space element $d\Phi(X) = \phi(X)dX$. The detector acceptance is given by $\eta(X)$. The Lorentz invariant transition amplitude, $\mathcal{M}$, which takes γp to $p\pi^+\pi^-\pi^\circ$ for the η analysis, can be written as:

$$|\mathcal{M}(\vec{x}, X)|^2 = \sum_{m_i, m_\gamma, m_f} |\sum_a \alpha_a(\vec{x}, X)\mathcal{A}_a(X)|^2, \quad (5.13)$$

where $\mathcal{A}_a$ are the partial wave amplitudes, α_a are complex functions built from the fit parameters (and possibly the kinematic variables X) and m_i, m_γ, m_f are the initial proton, incident photon and final proton spin projections. The general form is the same for the η' analysis.

The fit parameters for the t- and u-channel amplitudes are fixed for the fits. The s-channel fit parameters depend upon the amplitude itself. For example, there are two parameters for the

$J^P = \frac{1}{2}^{\pm}$ partial waves, while there are three parameters for the higher-spin partial waves. This is due to the lack of both an electric and magnetic multipole in the $J = \frac{1}{2}$ waves. The additional term is a angle which represents the ratio of the electric and magnetic multipoles. Writing out a sum of amplitudes symbolically for a fit with non-resonant terms as well as two s-channel partial waves (in this case $J^P = \frac{1}{2}^-, \frac{3}{2}^+$):

$$\mathcal{A} = \mathcal{A}_{t-chan.} + \mathcal{A}_{u-chan} + r_{\frac{1}{2}} e^{i\phi_{\frac{1}{2}}} \mathcal{A}_{\frac{1}{2}} + (cos(\theta_{EM})\mathcal{A}^{mag}_{\frac{3}{2}} + sin(\theta_{EM})\mathcal{A}^{elec}_{\frac{3}{2}}) r_{\frac{3}{2}} e^{i\phi_{\frac{3}{2}}} \tag{5.14}$$

The fit parameters in this example are $r_{\frac{1}{2}}$, $r_{\frac{3}{2}}$, $\phi_{\frac{1}{2}}$, $\phi_{\frac{3}{2}}$, and θ_{EM}. The t- and u-channel amplitudes are locked at fit time, and so have no free parameters, but are added coherently to allow for interference. For the $J^P = \frac{3}{2}^+$ partial wave there are separate amplitudes for the electric and magnetic multipoles, which are denoted by the superscript.

5.6 Extended Maximum Likelihood Method

This section details the formulas necessary for performing event-based likelihood fits. This term is used to describe fits where no binning, except in W, is done. The work detailed in this section is based on that of Chung [50], however, the normalizations used here differ from his work.

The goal is to find estimators $\hat{x}$ for the set of parameters $\vec{x}$ in a W bin with n detected events. To begin, the likelihood function is defined as,

$$\mathcal{L} = \left(\frac{\bar{n}^n}{n!} e^{-\bar{n}} \right) \prod_i^n \mathcal{P}(\vec{x}, X_i), \tag{5.15}$$

where the term in parentheses is the Poisson probability of obtaining n events given the expected number is $\bar{n}$, X_i represents the kinematics of event i, and $\mathcal{P}(\vec{x}, X)$ is the probability density function. $\bar{n}$ will be further defined in a subsequent section.

The probability density for an event with acceptance $\eta(X_i)$, phase space element $\phi(X_i)$ and Lorentz invariant transition amplitude $\mathcal{M}(\vec{x}, X_i)$ is,

$$\mathcal{P}(\vec{x}, X_i) = \frac{|\mathcal{M}(\vec{x}, X_i)|^2 \eta(X_i) \phi(X_i)}{\mathcal{N}(\vec{x})}. \tag{5.16}$$

where $\mathcal{N}(\vec{x})$ is defined such that the probability density function is properly normalized,

$$\int \mathcal{P}(\vec{x}, X) dX = 1. \tag{5.17}$$

From left to right, (5.16) accounts for the relative strength of the transition amplitude, the detection probability and the available phase space for the i-th event. The estimators $\hat{x}$ are then determined by maximizing $\mathcal{L}$.

5.6.1 Normalization

In order to maximize the likelihood, the expected number of events, $\bar{n}$, needs to be calculated. To begin, the concept of a cross section must be introduced.

A cross section for a reaction, in this case $\gamma p \to p\eta$ or $\gamma p \to p\eta'$, is defined as the transition rate per unit incident flux per target particle [59]. For photoproduction, the cross section for a particular reaction, σ, can be defined in terms of measurable quantities as,

$$\sigma = \frac{N}{\mathcal{F} \rho_{target} \ell_{target} N_A / A_{target}}, \tag{5.18}$$

where N is the number of scattering events of that reaction, $\mathcal{F}$ is the time-integrated incident photon flux, ρ_{target} ,ℓ_{target} and A_{target} are the target density, length and atomic weight and, N_A is Avogadro's number.

The cross section, in any W bin, can also be related to the transition amplitude $\mathcal{M}$ by [4],

$$\sigma = \frac{1}{4}\frac{(2\pi)^4}{2(s-w_p^2)}\int |\mathcal{M}(\vec{x},X)|^2 d\Phi(X), \tag{5.19}$$

where the factor of $1/4$ comes from averaging over the initial spin states.

Thus, for a given set of parameters $\vec{x}$, (5.18) and (5.19) can be used to get the number of expected scattering events as,

$$N = (\mathcal{F}\rho_{target}\ell_{target}N_A/A_{target})\,\frac{(2\pi)^4}{8(s-w_p^2)}\int |\mathcal{M}(\vec{x},X)|^2 d\Phi(X). \tag{5.20}$$

To obtain the expected number of data events $\bar{n}$, the detector acceptance must be taken into account in (5.20),

$$\bar{n} = (\mathcal{F}\rho_{target}\ell_{target}N_A/A_{target})\,\frac{(2\pi)^4}{8(s-w_p^2)}\int |\mathcal{M}(\vec{x},X)|^2 \eta(X) d\Phi(X). \tag{5.21}$$

The integral in (5.21) must be done numerically due to the lack of an analytic expression for the detector acceptance $\eta(X)$. The numerical integration is done using Monte Carlo.
To start, N_{raw} events are randomly generated according to $\gamma p \to p\eta$, $\eta \to \pi^+\pi^-\pi^0$ phase space for center-of-mass energy W. The same process is utilized for the $\gamma p \to p\eta'$, except that $\eta' \to \pi^+\pi^-\eta$ is used to determine the phase space kinematics. The integral can then be approximated by,

$$\int |\mathcal{M}(\vec{x},X)|^2 \eta(X) d\Phi(X) \approx \frac{\int d\Phi(X)}{N_{raw}} \sum_i^{N_{raw}} |\mathcal{M}(\vec{x},X_i)|^2 \eta(X_i). \tag{5.22}$$

To obtain the values of $\eta(X_i)$, each event is run through a detector simulation package(GSIM), which is standard for CLAS analyses and is specifically determined for a given dataset. This procedure simulates the acceptance of the detector by rejecting events that would not have survived to be part of the data analysis. For each event, the acceptance factor is $\eta(X_i) = 0$ or 1, according to whether the event was accepted. The number of Monte Carlo events which are accepted is labeled N_{acc}. Rewriting (5.22) as,

$$\int |\mathcal{M}(\vec{x},X)|^2 \eta(X) d\Phi(X) \approx \frac{\int d\Phi(X)}{N_{raw}} \sum_i^{N_{acc}} |\mathcal{M}(\vec{x},X_i)|^2. \tag{5.23}$$

Notice that (5.23) requires the value of the phase space integral $\int d\Phi(X)$. In this analysis, the $\eta \to \pi^+\pi^-\pi^0$ phase space is factored into the η decay amplitude. Thus, at this point, only the phase space integral value for $p\eta$ must be computed.

$$\begin{aligned}
\int d\Phi(X) &= \int \delta^4(p_i + k - p_f - q)\frac{d^3\vec{p_f}}{(2\pi)^3 2E_f}\frac{d^3\vec{q}}{(2\pi)^3 2E_\eta} \\
&= \frac{1}{4(2\pi)^6}\int \delta(\sqrt{s} - E_f - E_\eta)\frac{|\vec{p}_f|^2 d\eta}{E_f E_\eta} \\
&= \frac{1}{4(2\pi)^6}\int \frac{|\vec{p}_f| d\eta}{\sqrt{s}} \\
&= \frac{\left[(s-(w_p+w_\eta)^2)(s-(w_p-w_\eta)^2)\right]^{1/2}}{8(2\pi)^5 s},
\end{aligned} \tag{5.24}$$

making use of the identity $\delta(f(x)) = \delta(x - x_0)/|f'(x_0)|$ with x_0 being the root of $f(x)$.
Using (5.23) and (5.24), (5.21) can be rewritten as,

$$\bar{n} \approx \frac{\mathcal{S}(s)}{N_{raw}} \sum_{i}^{N_{acc}} |\mathcal{M}(\vec{x}, X_i)|^2, \tag{5.25}$$

where,

$$\mathcal{S}(s) = \frac{\mathcal{F}\rho_{target}\ell_{target}N_A}{A_{target}} \frac{\left[(s - (w_p + w_\eta)^2)(s - (w_p - w_\eta)^2)\right]^{1/2}}{64\pi s(s - w_p^2)}. \tag{5.26}$$

To conclude, extraction of the total cross section, given a set of estimators $\hat{x}$, will be described. Removing the effects of detector acceptance from (5.22) and using (5.24), yields

$$\int |\mathcal{M}(\hat{x}, X)|^2 d\Phi(X) \approx \frac{\left[(s - (w_p + w_\eta)^2)(s - (w_p - w_\eta)^2)\right]^{1/2}}{8(2\pi)^5 s} \frac{1}{N_{raw}} \sum_{i}^{N_{raw}} |\mathcal{M}(\hat{x}, X_i)|^2. \tag{5.27}$$

Then, using (5.19) the total cross section is given by,

$$\sigma = \frac{\left[(s - (w_p + w_\eta)^2)(s - (w_p - w_\eta)^2)\right]^{1/2}}{64\pi s(s - w_p^2)} \frac{1}{N_{raw}} \sum_{i}^{N_{raw}} |\mathcal{M}(\hat{x}, X_i)|^2. \tag{5.28}$$

5.6.2 Log Likelihood

Since the natural logarithm is a monotonically increasing function, it is sure that the estimators which minimize $-\ln(\mathcal{L})$ will also maximize $\mathcal{L}$.
From (5.15) the log likelihood can be written as,

$$-\ln \mathcal{L} = -n \ln \bar{n} + \ln n! + \bar{n} - \sum_{i}^{n} \ln \mathcal{P}(\vec{x}, X_i). \tag{5.29}$$

Using (5.21) and (5.17), the probability density normalization factor $\mathcal{N}(\vec{x})$ can be written as,

$$\mathcal{N}(\vec{x}) = \mathcal{C}(s)\bar{n}, \tag{5.30}$$

where,

$$\mathcal{C}(s) = \frac{8(s - w_p^2)}{(2\pi)^4} \frac{A_{target}}{\mathcal{F}\rho_{target}\ell_{target}N_A}. \tag{5.31}$$

The log likelihood then becomes,

$$-\ln \mathcal{L} = -\sum_{i}^{n} \ln |\mathcal{M}(\vec{x}, X_i)|^2 \eta(X_i)\phi(X_i) + \bar{n} + \ln n! + n \ln \mathcal{C}(s). \tag{5.32}$$

The actual value of $-\ln \mathcal{L}$ is not relevant to the analysis, just the fact that it has been minimized properly. Thus, any terms which do not depend on the parameters $\vec{x}$, can be disregarded.

$$-\ln \mathcal{L} = -\sum_{i}^{n} \ln |\mathcal{M}(\vec{x}, X_i)|^2 + \bar{n} + const. \tag{5.33}$$

Finally, using (5.25) allows (5.33) to be rewritten as,

$$-\ln \mathcal{L} = -\sum_{i}^{n} \ln |\mathcal{M}(\vec{x}, X_i)|^2 + \frac{\mathcal{S}(s)}{N_{raw}} \sum_{i}^{N_{acc}} |\mathcal{M}(\vec{x}, X_i)|^2 + const. \tag{5.34}$$

Examination of the expected number of events $\bar{n}$ for the parameter estimators $\hat{x}$ will conclude this section. Assuming that a suitable set of parameters has been found that maximize $\mathcal{L}$. Then, the set of functions $\{\alpha'\}$ is defined such that,

$$\alpha_a(\hat{x}, X) = c \cdot \alpha'_a(\hat{x}, X) \tag{5.35}$$

where c is a constant independent of X. Using (5.13), define,

$$\begin{aligned} |\mathcal{M}'(\vec{x}, X)|^2 &= \sum_{m_i, m_\gamma, m_f} |\sum_a \alpha'_a(\vec{x}, X)\mathcal{A}_a(X)|^2 \\ &= \frac{1}{c^2}|\mathcal{M}(\vec{x}, X)|^2. \end{aligned} \tag{5.36}$$

For the estimators $\hat{x}$,

$$\frac{\partial}{\partial c^2}\ln\mathcal{L} = \frac{\partial}{\partial c^2}\left(\sum_i^n \ln c^2|\mathcal{M}'(\hat{x}, X_i)|^2 - \frac{\mathcal{S}(s)}{N_{raw}}\sum_i^{N_{acc}} c^2|\mathcal{M}'(\hat{x}, X_i)|^2\right) \tag{5.37}$$

$$= \frac{n}{c^2} - \frac{\bar{n}}{c^2} \tag{5.38}$$

$$= 0. \tag{5.39}$$

Therefore, the best estimate for $\bar{n}$ is n as should be expected. It indicates that the number of events that should have been detected, was indeed the number that were detected.

5.7 The Method of Least Squares

There are times when it is advantageous to perform fits to binned data. These fits are considerably faster than the event based fits. They are, however, working from less information which provides somewhat less confidence in their results. These fits are used for two main purposes. First, when an amplitude(s) has an $\alpha(\vec{x}, X)$ which is known to be a function of X. These can be extracted using the event-based fit, however, for technical reasons the fits are extremely cpu intensive and it is more convenient in this case to fit to binned data. An example of this is found in trying to fit to determine a form-factor which contains a W dependence.

Secondly, fitting to binned data can be used to guide the event-based fits. Regions of the data can be quickly scanned and tested to determine whether certain waves appear to contribute at a level which warrants further investigation in an event-based fit. Additionally, good starting values for the event based fit, can be determined through the use of a binned fit.

Estimators $\hat{x}$ must be determined for a set of parameters $\vec{x}$ in a W bin with n data points. The data is binned in t and the differential cross section $\frac{d\sigma}{dt}$ is used as the quantity which is fit to. The estimators are then found by minimizing,

$$\chi^2 = \sum_i^n \frac{(\frac{d\sigma_i}{dt} - \frac{d\sigma}{dt}(\vec{x}, X_i))^2}{\sigma_i^2}, \tag{5.40}$$

where $\frac{d\sigma_i}{dt}$, σ_i are the measured differential cross section and its error for point i, X_i are the kinematic variables at the bin center, and

$$\frac{d\sigma}{dt}(\vec{x}, X) \propto |\mathcal{M}(\vec{x}, X)|^2, \tag{5.41}$$

is the differential cross section built from the partial waves and fit parameters.
To calculate $\frac{d\sigma}{dt}(\vec{x}, X)$, begin by rewriting (5.19) as,

$$d\sigma = \frac{1}{4}\frac{(2\pi)^4}{2(s - w_p^2)}|\mathcal{M}(\vec{x}, X)|^2 d\Phi(X). \tag{5.42}$$

From (5.24),

$$d\Phi(X) = \frac{1}{4(2\pi)^6}\frac{|\vec{p}_f|d\eta}{\sqrt{s}}. \tag{5.43}$$

Then, using $dt = \frac{s-w_p^2}{\sqrt{s}}|\vec{p}_f|d\cos(\theta_{CM})$,

$$d\Phi(X) = \frac{dt}{(2\pi)^5 4(s-w_p^2)}, \tag{5.44}$$

and,

$$\frac{d\sigma}{dt}(\vec{x},X) = \frac{|\mathcal{M}(\vec{x},X)|^2}{64\pi(s-w_p^2)^2}. \tag{5.45}$$

5.8 MINUIT

The CERNLIB package MINUIT is used to minimize $-\ln\mathcal{L}$. MINUIT was written by Fred James while at CERN in the late 1960's. It has been revised several times over the years with the most extensive revision coming in 1989. The current package is written entirely in FORTRAN 77 [52]. MINUIT's main field of usage is in statistical analysis of experimental physics data, however it is also used in other fields as well.

5.8.1 MIGRAD and the DFP Algorithm

The minimization algorithm used for this analysis is called MIGRAD. It uses a variation of the Davidson-Fletcher-Powell (DFP) variable metric method (VMM). This method is suited for minimizing a function $F(\vec{x})$ of n variables $\vec{x}^T = (x_1, x_2, \ldots, x_n)$ where the gradient vector $\nabla_x F = \vec{g}(\vec{x})$ can be obtained explicitly, but the Hessian G ($G_{ij} = \partial^2 F/\partial x_i \partial x_j$) can not be explicitly obtained.

The DFP method uses an iterative approach to minimizing $F(\vec{x})$. Each iteration starts at some point $\vec{x}$ with gradient $\vec{g}(\vec{x})$. The goal is to find another point, $\vec{y}$, for which $F(\vec{y}) < F(\vec{x})$. This procedure is then repeated until the convergence criteria, $\delta F \equiv F(\vec{x}) - F(\vec{y}) < tolerance$, is met. The main feature of the DFP method is that an approximation to G^{-1}, denoted H, is kept and updated at each iteration. There are two formulas for updating H which arise in the DFP method,

$$H_y = H_x + \frac{\vec{\delta}\vec{\delta}^T}{\vec{\delta}^T\vec{\gamma}} - \frac{H_x\vec{\gamma}\vec{\gamma}^T H_x}{\vec{\gamma}^T H_x \vec{\gamma}} \tag{5.46}$$

$$H_y = \left(1 - \frac{\vec{\delta}\vec{\gamma}^T}{\vec{\delta}^T\vec{\gamma}}\right) H_x \left(1 - \frac{\vec{\gamma}\vec{\delta}^T}{\vec{\gamma}^T\vec{\delta}}\right) + \frac{\vec{\delta}\vec{\delta}^T}{\vec{\delta}^T\vec{\gamma}} \tag{5.47}$$

where H_y is the Hessian to be used at $\vec{y}$, H_x is the Hessian at $\vec{x}$ (current position), $\vec{\delta} = \vec{y} - \vec{x}$ and $\vec{\gamma} = \vec{g}(\vec{y}) - \vec{g}(\vec{x})$.

Both (5.46) and (5.47) can, under certain circumstances, cause the minimization process to diverge. In particular, updating H_y using only (5.46) is more likely to lead to singularities than (5.47). However, updating using only (5.47) is more likely to cause H_y to become unbounded. This lead Fletcher to develop what is referred to as the switching method. This method tests the criteria $\vec{\delta}^T\vec{\gamma} \leq \vec{\gamma}^T H_x \vec{\gamma}$ during each iteration. If true, then the updating scheme (5.47) is used, otherwise H_y is updated using (5.46).

To find the correction to the current position, $\vec{\delta}$, the direction of search is defined as $\vec{s} = -H_x\vec{g}(\vec{x})$. Then,

$$\vec{\delta} = \alpha\vec{s} = -\alpha H_x\vec{g}(\vec{x}), \tag{5.48}$$

where α minimizes $F(\vec{x}+\alpha\vec{s})$. This method of minimizing F along the direction of search is known as linear searching. From $\vec{\delta}$, $\vec{y}$ is easily obtained as $\vec{y} = \vec{x} + \vec{\delta}$ and the fit moves to the next iteration if $F(\vec{y})$ doesn't meet the convergence criteria. For more information on the DFP method see [60] and the references within.

5.8.2 Derivatives of the Log Likelihood

The MIGRAD routine, since it uses the DFP method, requires accurate knowledge of the gradient vector. For this analysis MIGRAD will be supplied with:

$$\frac{\partial(-\ln\mathcal{L})}{\partial x_j} = \frac{\partial}{\partial x_j}\left(-\sum_i^n q_i \ln|\mathcal{M}(\vec{x},X_i)|^2 + \frac{\mathcal{S}(s)}{N_{raw}}\sum_i^{N_{acc}}|\mathcal{M}(\vec{x},X_i)|^2\right) \tag{5.49}$$

for each parameter x_j. The only term in (5.49) that depends on $\vec{x}$ is $|\mathcal{M}|^2$. Thus, (5.49) becomes,

$$\frac{\partial(-\ln\mathcal{L})}{\partial x_j} = -\sum_i^n q_i\left(\frac{1}{|\mathcal{M}(\vec{x},X_i)|^2}\frac{\partial|\mathcal{M}(\vec{x},X_i)|^2}{\partial x_j}\right) + \frac{\mathcal{S}(s)}{N_{raw}}\sum_i^{N_{acc}}\frac{\partial|\mathcal{M}(\vec{x},X_i)|^2}{\partial x_j}. \tag{5.50}$$

Use (5.13) to write, $\partial|\mathcal{M}(\vec{x},X_i)|^2/\partial x_j$ as,

$$\begin{aligned}
\frac{\partial|\mathcal{M}(\vec{x},X_i)|^2}{\partial x_j} &= \frac{\partial}{\partial x_j}\left(\sum_{m_i,m_\gamma,m_f}|\sum_a \alpha_a(\vec{x},X_i)\mathcal{A}_a(X_i)|^2\right) \\
&= \sum_{m_i,m_\gamma,m_f}\sum_a\left(\frac{\partial\alpha_a(\vec{x},X_i)}{\partial x_j}\mathcal{A}_a(X_i)(\alpha_a(\vec{x},X_i)\mathcal{A}_a(X_i))^* + \frac{\partial\alpha_a^*(\vec{x},X_i)}{\partial x_j}\mathcal{A}_a^*(X_i)(\alpha_a(\vec{x},X_i)\mathcal{A}_a(X_i))\right) \\
&= \sum_{m_i,m_\gamma,m_f}\sum_a 2Re\left(\frac{\partial\alpha_a(\vec{x},X_i)}{\partial x_j}\mathcal{A}_a(X_i)(\alpha_a(\vec{x},X_i)\mathcal{A}_a(X_i))^*\right)
\end{aligned} \tag{5.51}$$

The only constraint which is placed on the functions $\alpha(\vec{x},X)$ is that analytical differentiation with respect to the parameters x_j is possible.

5.8.3 Derivatives of χ^2

Similar to the log likelihood case in the previous section, the least-squares fits also requires that MIGRAD is supplied with,

$$\frac{\partial\chi^2}{\partial x_j} = \frac{\partial}{\partial x_j}\left(\sum_i^n\frac{(\frac{d\sigma_i}{dt} - \frac{d\sigma}{dt}(\vec{x},X_i))^2}{\sigma_i^2}\right) \tag{5.52}$$

for each parameter x_j. The only term in (5.52) that depends on $\vec{x}$ is $\frac{d\sigma}{dt}(\vec{x},X)$. Thus,

$$\frac{\partial\chi^2}{\partial x_j} = \sum_i^n\frac{2}{\sigma_i^2}\left(\frac{d\sigma}{dt}(\vec{x},X_i) - \frac{d\sigma_i}{dt}\right)\frac{\partial}{\partial x_j}\frac{d\sigma}{dt}(\vec{x},X), \tag{5.53}$$

where,

$$\frac{\partial}{\partial x_j}\frac{d\sigma}{dt}(\vec{x},X) = \frac{1}{64\pi(s-w_p^2)^2}\frac{\partial|\mathcal{M}(\vec{x},X)|^2}{\partial x_j}, \tag{5.54}$$

and $\partial|\mathcal{M}(\vec{x},X)|^2/\partial x_j$ is defined in (5.51).

5.8.4 HESSE and the Covariance Matrix

The HESSE routine calculates the matrix of second derivatives of the log likelihood with respect to the parameters and inverts it to obtain the covariance matrix. The second derivatives are calculated numerically using the method of finite differences. The technique of using the inverse of the matrix of second derivatives relies on the assumption that the curvature at the minimum follows a parabolic shape.

5.9 Coupling Multiple Datasets

There are times when it is necessary to couple multiple datasets into a single fit. These datasets may be combining two W bins to fit them simultaneously, or may be coupling the η and η' to fit them at the same time. This is done to constrain the estimators $\hat{x}$, or some subset of them, to be the same for each of the coupled datasets. This is accomplished by minimizing,

$$\psi = \sum_{d}^{N_d} \psi_d, \tag{5.55}$$

where ψ_d is the quantity which is minimized for dataset d and N_d is the number of coupled datasets.

Then, the derivatives of the parameters $\vec{x}$ are just,

$$\frac{\partial \psi}{\partial x_j} = \sum_{d}^{N_d} \frac{\partial \psi_d}{\partial x_j}. \tag{5.56}$$

As a more concrete example, consider a likelihood fit with two datasets. The joint likelihood for the data sets 1 and 2 is simply the product of the two likelihoods $\mathcal{L}_1$ and $\mathcal{L}_2$. Let $\eta_1(\tau)$ and $\eta_2(\tau)$ be the corresponding acceptances, and the 'log' of the joint likelihood is then given by:

$$ln\mathcal{L} = \sum_{i}^{n_1+n_2} ln|\mathcal{M}(\vec{x}, X_i)|^2 - \int |\mathcal{M}(\vec{x}, X)|^2 \left[\frac{N_1}{N}\eta_1(X) + \frac{N_2}{N}\eta_2(X)\right] dX$$

Where $n_1(n_2)$ is the number of experimental events for the data sample 1(2) and $N_1(N_2)$ is the predicted number of events for sample 1(2). The key ingredient incorporated in the formula above is that the parameter sets $\vec{x}$ for samples 1 and 2 have the normalizations N_1 and N_2 that each must be renormalized by $\sqrt{N_1/N}$ and $\sqrt{N_2/N}$ in order that a common set of $\vec{x}$ can be used in the minimization process. Where N is the total number of predicted events in the combined dataset.

5.10 Running PWA Fits at CMU

This section will describe the more specific details of running the PWA fit for this analysis. Given the general structure of likelihood fitting with calculated amplitudes as input, there are many practical ways to put all of the pieces together. The specific way that the PWA was implemented in this analysis will be described in this section. The approach taken in this analysis was to utilize different files for many of the individually calculated quantities. For example, a given amplitude of a given projection was calculated and stored in a single file for each W bin. While the shear number of files then used to run a PWA fit was not insignificant, there were advantages to this approach. Primarily, if a small subset of files were corrupted or lost, they could generally be reconstructed in a timely

fashion. Similarly, if a new amplitude must be generated, it can be done on an individual basis, so that the other amplitudes are not effected. A description of the various files used for this analysis will be given here.

5.10.1 Amplitude Files

With the amplitude generation described, the amplitudes which were calculated were stored in separate amplitude files. For a given amplitude, and a given projection of that amplitude, the complex value for each event in each W bin is recorded in an amplitude file in the order of events in the data file. The alignment of the data events and their corresponding amplitudes allows for a more efficient memory management while the fit is running. At fit time, the amplitude files corresponding to the partial waves included in the fit are read by the fit program for use. Amplitude files are generated for all of the events in a given W bin, for the data, the accepted Monte Carlo, and the raw Monte Carlo datasets.

5.10.2 Normalization Integral Files

As mentioned in the description of likelihood fitting, the normalization is a critical piece to the likelihood fitting process. Pieces of the normalization are calculated prior to fit time. Due to the fact that they are calculated ahead of time, these normalizations are calculated for all of the amplitudes available to the fit. The pieces required for a given fit with a given set of partial waves, will be pulled out of the normalization file at fit time. Normalization integral files are constructed for both the raw and accepted Monte Carlo datasets.

5.10.3 Event Cut Files

In order to alter the selection of events which are cut from the dataset, a file, called an event cut file, is used. The entries in the cut file are integers, which tell the code which events to ignore, and which to include in the fit. Cut files are generated for the data and the accepted Monte Carlo datasets for each W bin. Considerable effort is put into understanding both the experimental and simulated datasets, and having the capacity to systematically alter cuts is critical.

To construct a cut file, each event is run through code for each of the cuts used on the data and accepted Monte Carlo datasets. For a particular event, for each cut, a bit of the integer is set to 0(1) indicating whether it passed(failed) the particular cut. If an event has passed all of the cuts, and is to be used in the PWA fit, then all of the bits will have been set to 0, and thus the integer will be 0. If any other bits are set, then the integer for a given event will not be equal to 0, and the corresponding event will be left out of the fit.

The primary advantage to the use of cut files, is that events can be selectively removed from the fit, amplitudes and all. This means that if a change is made in the cuts on the data, amplitudes which are generated once, do not have to be regenerated. Amplitude generation takes a considerable amount of computer time, so a system to remove events without regenerating amplitudes provides a time savings.

5.10.4 Fitting Code and Minuit

With the amplitude files, normalization integral files, and cut files described, all that is left is the fit itself. Computer programs were written which call Minuit, as earlier described in 5.8. The fit code uses Minuit to minimize the negative of the $ln(\mathcal{L})$, thereby maximizing the likelihood. Once the minimization is complete, an output file is written which records the initial and final parameters, the number of calls to minimize, the negative $ln(\mathcal{L})$, and the error matrix for the fit. As the fit is run individually in each bin, the output file with fit results are written out into different files for each bin.

5.10.5 Result Extraction

The results from the fit are recorded in output files for each bin where the fit was run. The fit results include the modulus and phase of the complex values used as the propagator for the s-channel resonances, along with ratios of the electric and magnetic multipoles. The modulus parameter of the fit, if plotted against W, should map out the modulus of a Breit-Wigner if a Breit-Wigner resonance is present. The phase result, likewise, should map out the phase of a Breit-Wigner. Additionally, these results when combined with the kinematic factors can be used to calculate differential yields from a particular partial wave. The results from the fit will be presented in a subsequent chapter.

5.11 Summary

The formalism and fitting methodology was described in this chapter. From amplitude generation to fitting with either binned or un-binned methods, the process involved in PWA fitting is complex. A brief description of the CMU PWA procedure was outlined as well.

Chapter 6

PWA Results

This chapter presents the results obtained from a PWA of η and η' photoproduction data using CLAS at JLAB. As a precursor to the presentation of the PWA results, a short review of previous results will be presented. The PWA results from this analysis will then be presented. There were numerous PWA fits run using the formalism previously described, and only the results from a subset of those fits will be presented here.

The results of the PWA will be previewed here, prior to further discussion. The η analysis indicates a $J^P = \frac{1}{2}^-$ at threshold, and a $J^P = \frac{5}{2}^-$ near 2.0 GeV. Additionally, the fit appears to require a $J^P = \frac{5}{2}^+, \frac{7}{2}^+$ wave around 2.2 GeV. There is also some evidence for a $J^P = \frac{3}{2}^+$ partial wave near 1.8 GeV.

The η' analysis indicates a threshold $J^P = \frac{1}{2}^-$ partial wave, and a $J^P = \frac{7}{2}^+$ partial wave at 2.2 GeV. There are also hints of a $J^P = \frac{3}{2}^+$ around 2.0 GeV. Due to the preference of the $J^P = \frac{7}{2}^+$ in the η' analysis, the coupled fit indicates the higher spin positive parity wave is the $J^P = \frac{7}{2}^+$.

6.1 Previous Results

Before delving into the results from the PWA, prior results for baryon resonance states coupling to Nη will be reviewed. This review will yield some expectation for what is likely to be seen in the results of the PWA. There are several previous analyzes which should be reviewed to put this analysis in perspective. As mentioned previously, there are results from Anisovich et al.[8] and Dugger et al.[6] for Nη coupled resonances. While the Dugger et al.[7] work is the only available analysis of the Nη' reaction channel. Each of these analyses will be briefly reviewed and their results compiled into a table for comparison.

6.1.1 Anisovich η Results

A partial wave analysis was carried out on data taken at the Crystal Barrel at the ELectron Stretcher Accelerator (CB-ELSA). The Nη final state differential cross sections were fit along with the Nπ differential cross section data. Measurements of beam polarization asymmetry from GRAAL were also included in the fit to maximize the data input to the fit.

The fit includes numerous N^* resonance states which couple to the $N\eta$ final state. The analysis of the $N\eta$ final state reproduced known resonances in reasonable agreement with the PDG. There were also indications of two new resonances, the N(2070)D_{15} and N(2200)P_{13}, which couple to Nη. See Table 2.1 for results from the Anisovich analysis.

6.1.2 Dugger η Results

An analysis was performed by Dugger et al.[6] on photoproduced η mesons using the CLAS detector at JLAB. Differential cross sections measured for the η meson as a function of $cos(\theta_{CM})$ were compared with several models. The models, their general contents and a compiled table of the previous results for η photoproduction was given in Section 1.2.1. The kinematic range of the Dugger measurements are relatively limited in comparison to the available kinematic range present for both Crede[12] and this analysis.

6.1.3 Dugger η' Results

Dugger et al.[7] performed an analysis of photoproduced η' mesons using the CLAS detector at JLAB. The measured differential cross sections of the η' meson were compared with a relativistic meson-exchange model from Sibirtsev et al.[55], as well as a relativistic meson-exchange description from Nakayama and Haberzettl(NH)[56]. In both cases contributions from s-, t-, and u-channels were included. Both models also included the $S_{11}(1535)$ and the $P_{11}(1710)$ resonances which are known to decay strongly to the Nη channel. The NH model also includes 2 additional S_{11} and P11 resonances with small couplings. It was found that additional J=3/2 resonances were required in the NH model to fit the data, and the $P_{13}(1940)$, $D_{13}(1780)$, and $D_{13}(2090)$ were added. Since the NH model fits is in better agreement with the measured differential cross sections than the Sibirtsev model it is concluded that the J=3/2 resonances are important inclusions. This was the first analysis to include the known η resonances in an η' analysis. A majority of the resonances included in this fit were below η' threshold, indicating that the tails of these resonances contribute significantly.

6.2 Partial Wave Analysis Results

In presenting the PWA results, there are several parts to consider. Of primary interest is determining which set of partial waves best describes the data. From all of the PWA fits that were run, a subset must be selected which describe the data as well as possible. From this subset of fits, the potential resonance contributions are then examined to determine if any resonance structures are present. The section will begin with the determination of a proper subset of partial waves which describe the data as well as possible. Once established, the resonance structure of the partial waves from these fits will be presented.

In determining the best partial wave sets for the description of the data, the difference of $ln(\mathcal{L})$ between two fits will be the criteria. As there is no standard goodness of fit prescription for maximum likelihood fits, the case will be made for the use of this criterion. A subset of the best fits will be determined and then utilized for further analysis.

Once a subset of the best fits has been established, the resonances characteristics of the partial waves present in the fit are examined. Recall that the amplitudes for the s-channel processes utilize a complex number for the propagator instead of a Breit-Wigner shape. This complex value is the piece which is being determined in the likelihood fitting. Since this propagator is a complex number, both the modulus and the phase of that value can be extracted for a particular partial wave.

The modulus of the partial wave can then be plotted as a function of $W(\sqrt{s})$. If a resonance has a Breit-Wigner structure, then the modulus plotted against W should map out the shape of the modulus of a Breit-Wigner. This shape can then be fit with a Breit-Wigner to determine both the mass and the width of a particular resonance structure.

Additionally, the phase information is also useful in determining resonance structure. Much like the modulus, the phase can be plotted as a function of W and can be compared to the shape of the phase of a Breit-Wigner resonance. The value that is actually plotted is not the phase of the Breit-Wigner, but the phase difference between two Breit-Wigners in the fit. Allowing the resonances to beat against each other provides a reference to the observed phase information.

6.3 Best Fits

While many PWA fits were run, only a subset will be presented here. Eventually, an even smaller subset of these fits will be determined to describe the data well, and scrutinized for resonance structures. In order to refer to them with as little confusion as possible, Table 6.1 assigns a number to each fit and describes what partial waves are in each fit for the η analysis. These fits vary only in the s-channel partial waves inputs. The non-resonant contributions from t-,u-channel and background are all locked as previously described. As there are some known resonances which decay to Nη there are some hints as to where to start with the analysis. The most obvious and well known of the baryon resonances which couple to Nη is the $S_{11}(1535)$, which is a $J^P = \frac{1}{2}^-$ state. Thus a majority of the partial wave sets include this wave, and where it is not present, a $J^P = \frac{1}{2}^+$ partial wave will be present.

Table 6.1: PWA fits for η photoproduction

Fit #	$\frac{1}{2}^-$	$\frac{1}{2}^+$	$\frac{3}{2}^-$	$\frac{3}{2}^+$	$\frac{5}{2}^-$	$\frac{5}{2}^+$	$\frac{7}{2}^-$	$\frac{7}{2}^+$
001	X			X	X			
002	X			X				
003	X				X			
004	X			X	X	X		
005	X			X	X			X
006	X					X		
007	X		X					
008		X	X			X		
009	X				X	X		
010	X				X			X
011	X		X		X			

Similarly, Table 6.2 assigns a fit number to the presented subset of fits, and indicates which partial waves were included in the fits run for the η' analysis. Again, a smaller subset will be selected for further scrutiny. The fit inputs only vary in the s-channel partial wave contributions. The non-resonant contributions from t-,u-channel and background are all locked as previously described. There are no known PWA results for baryon resonances coupling to Nη', so a starting point is more difficult to locate. The comparison of differential cross section measurements to models made by Dugger[7] indicated that the resonances which were important in the $N\eta$ analysis were contributing significantly to $N\eta'$. Additionally, the quantum numbers of the η and η' are equivalent, and as such if a resonance couples to $N\eta$ it should also couple to $N\eta'$. To this end, the starting point for the η' analysis will utilize a similar partial wave set to that of the η.

Table 6.2: PWA fits for η' photoproduction

Fit #	$\frac{1}{2}^-$	$\frac{1}{2}^+$	$\frac{3}{2}^-$	$\frac{3}{2}^+$	$\frac{5}{2}^-$	$\frac{5}{2}^+$	$\frac{7}{2}^-$	$\frac{7}{2}^+$
101	X			X	X			
102	X			X				
103	X				X			
104	X			X	X	X		
105	X			X	X			X
106	X					X		
107	X		X					
108		X	X			X		
109	X				X	X		
110	X				X			X
111	X		X		X			

With a reasonable subset of fits for both the η and η' reaction channels, the task becomes determining which fits are better than others. Typically, a goodness of fit test is used to determine which fit most closely matches the data. One of the added challenges with maximum likelihood fitting is that it does not lend itself well to a measurement of its goodness of fit. The standard means for determining whether one fit is better than the other is to look at the difference in the $-ln(\mathcal{L})$ between the two fits. This is the preferred method for this analysis as well. Fortunately,

there is an added simplification in the case of the η and η' analyses. For these analyses, the only angle of interest is the $cos(\theta_{CM})$ of the η or η'. With only one principle angle of interest, a standard χ^2 can be constructed to allow a comparison of the fit to the data. This is considerably more time consuming that observing differences in the $-ln(\mathcal{L})$ between the two fits, so the preferred method of comparing fits will remain a likelihood difference.

In order to demonstrate that the difference in likelihood remains a legitimate means of comparing two fits, a comparison will be made between the likelihood difference, and a total χ^2 difference between two fits. For two particular fits, the likelihood difference as a function of W will be constructed. Additionally, the difference in the total χ^2 between the fits as a function of W will be calculated independently of the value of the likelihood. The total χ^2 is constructed in each W bin by the comparison of the fit results and the data in the $cos(\theta_{CM})$ of the η. The χ^2 for each bin in $cos(\theta_{CM})$ is then added to determine the total χ^2 for a given W bin. Comparing these distributions it is clear that the likelihood difference is a reasonable means to compare one fit to another. See Figure 6.1.

The likelihood difference is obtained directly from the best likelihood fit in each bin in W. The χ^2 must be constructed from a comparison of the fit results to the data. Since the η and η' mesons are pseudoscalars, and have no spin, there is only one angle of physical interest which is the $\cos(\theta_{CM})$ of the η or η'. The χ^2 will be constructed in each bin in W and when combined, the χ^2 as a function of W will be assembled. To calculate the χ^2 of each Wbin a comparison of the fit results and the data must be obtained. The accepted Monte Carlo is weighted by the fit results in that particular bin, scaled to match the number of data events, and then are plotted on top of the data.

The χ^2 for each of the bins in the $\cos(\theta_{CM})$ distribution is calculated using the standard formula:

$$\chi^2 = \sum_{n}^{i=1} \frac{(x_i - \mu_i)^2}{\sigma^2} \tag{6.1}$$

Where x is the fit value, μ is the value from the data, and σ is the variance of the data value. This value is calculated for each of the points in the $cos(\theta_{CM})$ for a given bin in W. The χ^2 values in each bin of $\cos(\theta_{CM})$ are then summed to obtain a total χ^2 for that Wbin. The calculation of the total χ^2 is repeated for all of the bins in W and then the results are plotted as a function of W to compare to the analogous plot of the difference in $ln(\mathcal{L})$.

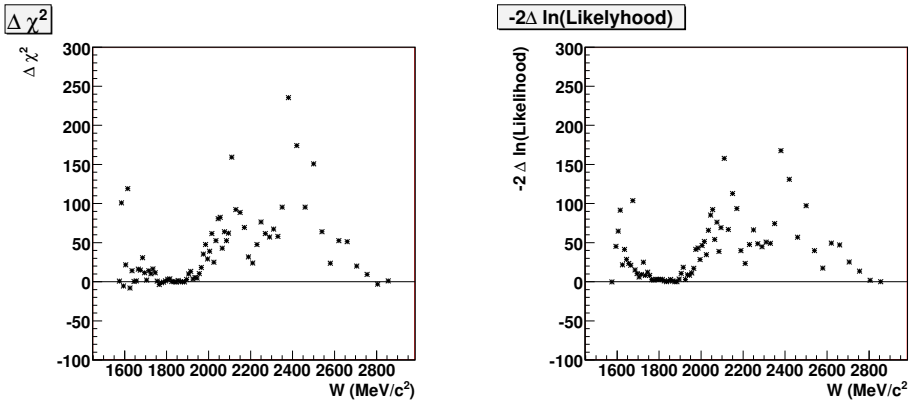

Figure 6.1: On the left, a plot of the difference in total χ^2 between two differing fits for the η is presented. On the right, a plot of the difference in $-2ln(\mathcal{L})$ between the same two fits for the η. Note that the general structures and scales are very similar.

With the change in $\ln(\mathcal{L})$ demonstrated to be a reasonable criteria for observing the goodness of fit, plots of the likelihood differences as a function of W will be presented. The likelihood difference plots allow for the systematic addition and/or subtraction of partial waves from a given wave set. With each partial wave that is included in the dataset, there are additional free parameters which the fit can use to describe the data as well as possible. Therefore, the goal of the analysis is to describe the data as well as possible with as few partial waves as possible. There is a point at which additional partial waves do not significantly improve the likelihood of the fit. Conversely, if the addition of a partial wave improves the likelihood in a significant way, then the fit clearly indicates that an additional wave is required to fit that region of W.

6.3.1 $\Delta ln(\mathcal{L})$ of η Fits

With a few known resonances which couple to the Nη final state there was some indication of where to start in constructing a wave set which would describe the data. The resonance which couples the most strongly to Nη is the $S_{11}(1535)$ which is a $J^P = \frac{1}{2}^-$ state. There are other known resonances, but as a starting point the inclusion of a $J^P = \frac{1}{2}^-$ partial wave seems obvious at low W.

Partial waves were then systematically added or subtracted to determine the best set of partial waves to describe the data. To determine what effect the addition or subtraction of a partial wave has on the fit, plots were made of the difference in $ln(\mathcal{L})$ from one fit to another as a function of W. With these plots of the likelihood difference constructed, the question becomes what amount of $\Delta(ln(\mathcal{L}))$ is significant. As a quick guide, a $\Delta(ln(\mathcal{L})) \approx 0 \rightarrow 30$ is considered in this analysis to be essentially insignificant. Typically, the claim that a partial wave benefits a fit in a significant way is indicated by a $\Delta(ln(\mathcal{L})) >\approx 75$. With these general guidelines in mind, the plots of the $\Delta(ln(\mathcal{L}))$ will be presented for a selection of different wave sets. Keep in mind that these are only rough guidelines for determining the significance of the inclusion or exclusion of a partial wave. In the comparison of partial wave sets it is important to make reasonable comparisons. A comparison of two fits which differ by a single partial wave would be considered a reasonable comparison, allowing for a determination to be made regarding the importance of the differing partial wave. However, in order to make reasonable comparisons, the number of partial waves included in the fits to be compared can only differ by a maximum of one. For example, a comparison between a fit with three waves and a fit with two waves is acceptable, while a comparison between a fit with four waves and a fit with two waves is not. As long as the number of waves in the fits being compared follows that pattern, the additional freedom of occasionally flipping the parity of a given wave in a given fit can be used to help determine the best wave set for the fit.

It is important to note that the addition of partial waves in general will improve the fit. The cause of which essentially is the addition of more fit parameters. The number of fit parameters for a given partial waves depends upon the wave itself. The $J = \frac{1}{2}$ partial waves each contribute two free parameters to the fit when included. These are a modulus and a phase. The higher-spin partial waves contribute three free parameters, including a modulus, phase, and an additional angle which parameterizes the ratio of electric to magnetic multipole. The addition of more free parameters should improve the ability of the fit to describe the data. This is the reason why there must be some relative minimum threshold on the size of likelihood change which is called "significant". Additionally, the improvement is required to be systematic. Since all of the bins are fit independently, the systematic improvement of a number of bins across a range of W is considered more significant that the improvement of a single isolated bin.

Starting with a comparison of the first two fits in the η analysis which differ by the inclusion of a $J^P = \frac{5}{2}^-$ partial wave. The $-(ln(\mathcal{L}))$ from a fit with $J^P = \frac{1}{2}^-, \frac{3}{2}^+, \frac{5}{2}^-$(fit #001) is subtracted from that of a fit with $J^P = \frac{1}{2}^-, \frac{3}{2}^+$(fit #002). A positive(negative) result indicates that the fit with the $J^P = \frac{5}{2}^-$ partial wave is a better fit to the data, and any significant structure may indicate where the $J^P = \frac{5}{2}^-$ wave contributes in W. It is clearly seen in Figure 6.2(A), there is a significant structure in the positive direction around $\approx$ 2200MeV. This plot clearly indicates that the additional $J^P = \frac{5}{2}^-$ allows the fit to more accurately represent the data in that region of W. Of additional interest is that below $W = 2000MeV$ the $J^P = \frac{5}{2}^-$ does not appear to influence the fit, which means that the fit reproduces the data just as well with only the $J^P = \frac{1}{2}^-, \frac{3}{2}^+$ partial waves.

The $-ln(\mathcal{L})$ from fit a fit containing $J^P = \frac{1}{2}^-, \frac{3}{2}^+, \frac{5}{2}^-$(fit #001) is subtracted from the $-ln(\mathcal{L})$ from a fit containing the $J^P = \frac{1}{2}^-, \frac{5}{2}^-$(fit #003) waves. A positive results indicates that the fit containing the $J^P = \frac{3}{2}^+$(fit #001) is a better description of the data than the fit without. As clearly shown in Figure 6.2(B), there is considerable positive structure across much of the W range. The scale of the improvement is not obviously significant, but it is consistently positive. Additionally,

the importance of the $J^P = \frac{3}{2}^+$ wave can also be determined through the comparisons of other fits.

Figure 6.2(C) shows the $\Delta(ln(\mathcal{L}))$ between a fit with $J^P = \frac{1}{2}^-, \frac{3}{2}^+, \frac{5}{2}^-$(fit #001) and a fit with $J^P = \frac{1}{2}^-, \frac{3}{2}^+, \frac{5}{2}^-, \frac{5}{2}^+$(fit #004). The effect of the additional $J^P = \frac{5}{2}^+$ partial wave is shown as an overall negative value in the $\Delta(ln(\mathcal{L}))$. The negative value indicates that the $J^P = \frac{5}{2}^+$ partial wave improves the fit. Note, however that the improvement only appears in the $W = 2100 \rightarrow 2500MeV$ region. Outside of this region there is no demonstrated improvement in the fit, indicating that the wave set with only three partial waves describes the data in that region.

Along a similar vein, the $\Delta(ln(\mathcal{L}))$ has been calculated between two fits which differ by the addition of a $J^P = \frac{7}{2}^+$ partial wave. The $-ln(\mathcal{L})$ of a fit with $J^P = \frac{1}{2}^-, \frac{3}{2}^+, \frac{5}{2}^-$(fit #001) is subtracted from the $-ln(\mathcal{L})$ of a fit with $J^P = \frac{1}{2}^-, \frac{3}{2}^+, \frac{5}{2}^-, \frac{7}{2}^+$(fit #005). The clear negative result across the entire W range indicates that the fit with the additional $J^P = \frac{7}{2}^+$ partial wave better describes the data. The real improvement in the fit appears to be limited to the region of $W = 2100 \rightarrow 2500MeV$. Both above and below this region the inclusion of the $J^P = \frac{7}{2}^+$ appears to have little effect on the overall fit.

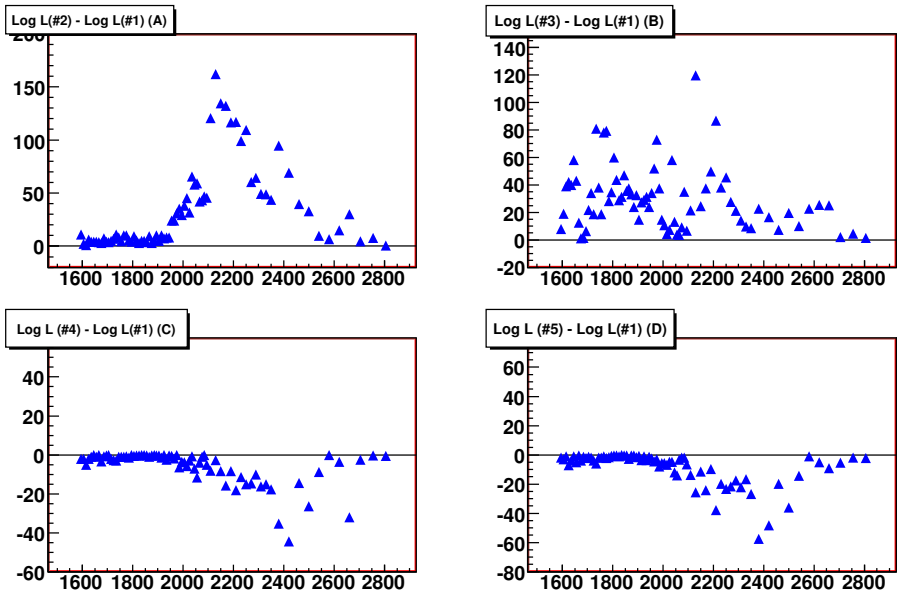

Figure 6.2: Plots of the difference in $-ln(\mathcal{L})$ for pairs of η fits. A fit containing $J^P = \frac{1}{2}^-, \frac{3}{2}^+, \frac{5}{2}^-$(fit #001) is used as a reference for these likelihood differences, so the value of the $-ln(\mathcal{L})$ for this fit is subtracted Wbin by Wbin from the fits which are being compared to. The x-axis is center-of-mass energy (W, $\sqrt{s}$), while the y-axis is the difference in the $-ln(\mathcal{L})$ between the two fits. If the value of the $\Delta(ln(\mathcal{L}))$ is positive, it means that the reference fit provides a better description of the data than the other fit in the comparison. If the value is negative, then the opposite is true. The large positively valued peak in the likelihood difference seen in (A) indicates the importance of the $\frac{5}{2}^-$ partial wave in describing the physics in the data. Similarly, the positively valued nature of the likelihood difference seen in (B) shows the value of the inclusion of a $J^P = \frac{3}{2}^+$ partial wave. Plots (C) and (D) both demonstrate the potential for including a higher-spin positive parity wave in the higher mass region. From the two plots there is no way to determine if the fit would prefer a $J^P = \frac{5}{2}^+$ or $J^P = \frac{7}{2}^+$ partial wave in that region.

To summarize the conclusions drawn from Figure 6.2 the $J^P = \frac{1}{2}^-, \frac{3}{2}^+, \frac{5}{2}^-$ partial wave set appears necessary to describe the physics present in the η analysis. Additionally, there is an indication in the high W region that either the $J^P = \frac{5}{2}^+$ or $J^P = \frac{7}{2}^+$ partial waves may be present in the fit. Unfortunately, there is currently no way to distinguish between the two higher-spin partial waves in the η analysis.

Additional fit comparisons can be done to further define the appropriate partial wave set for the η analysis. Adding or subtracting a single wave is an informative test, but there is also the possibility of simply replacing one wave with another. In a more extreme case, there is also the possibility of switching the parities of all of the waves present in the fit. The effects of these tests can be seen in Figure 6.3.

Figure 6.3(A) is a plot of the $-ln(\mathcal{L})$ of a fit containing $J^P = \frac{1}{2}^-, \frac{3}{2}^+, \frac{5}{2}^-$(fit #001) subtracted from the $-ln(\mathcal{L})$ of a fit with the $J^P = \frac{1}{2}^-, \frac{5}{2}^+$ (fit #006) partial waves. The removal of the $J^P = \frac{3}{2}^+$ is likely to have an effect on the fit, and the parity has been flipped to make the $J^P = \frac{5}{2}^-$ into a $J^P = \frac{5}{2}^+$. Bear in mind, however, that there were positive indications for the $J^P = \frac{5}{2}^+$ partial wave from previous comparisons. A positive result, which is clearly evident, indicates that the $J^P = \frac{1}{2}^-, \frac{3}{2}^+, \frac{5}{2}^-$ fit is still superior to the more limited two-wave fit. Some of the structure appears similar to that which was seen in Figure 6.2(B) when the $J^P = \frac{3}{2}^+$ partial wave was removed. This may indicate that the effect of switching the parity on the $J = \frac{5}{2}$ wave does not make a significant difference in the fit.

Turning attention to Figure 6.3(B) there is a plot of the $\Delta(-ln(\mathcal{L}))$ between a $J^P = \frac{1}{2}^-, \frac{3}{2}^+, \frac{5}{2}^-$(fit #001) fit and $J^P = \frac{1}{2}^-, \frac{3}{2}^-$(fit #007) fit. The positive result in the plot of $\Delta(-ln(\mathcal{L}))$ indicates the superiority of the three-wave reference fit across a significant range in W. The $J^P = \frac{1}{2}^-, \frac{3}{2}^-$(fit #007) fit's lack of ability to fit the data is likely due to the lack of a higher-spin partial wave, along with the limits of a two-wave set with which to fit the data. The previously compared results indicated that either $J = \frac{5}{2}$ or $J = \frac{7}{2}$ waves are important to the fit's ability to accurately represent the data.

Figure 6.3(C) is an interesting fit comparison. The two fits compared here differ only by a global parity flip. There is a $J^P = \frac{1}{2}^+, \frac{3}{2}^-, \frac{5}{2}^+$(fit #008) fit compared to a $J^P = \frac{1}{2}^-, \frac{3}{2}^+, \frac{5}{2}^-$(fit #001) fit. Nominally the two fits, differing only by a parity flip, would produce the same angular distributions for fixed photon energy. Due to different factors of momentum in the covariant amplitudes, and a finite bin width in photon energy, there is sufficient momentum variation to strongly favor the $J^P = \frac{1}{2}^-$ over the $J^P = \frac{1}{2}^+$ at threshold. This appears as the very large positively valued spike at threshold. While the plot is mostly positive, there is a small negative dip which may be indicating the preference of a $J^P = \frac{5}{2}^+$ at higher W. The small negative structure is in the same location as the fit showed benefit with the addition of a higher-spin positive parity wave in previous comparisons as seen in Figure 6.2(A),(B).

Figure 6.3(D) is a plot of the $\Delta(-ln(\mathcal{L}))$ between a fit containing $J^P = \frac{1}{2}^-, \frac{5}{2}^-, \frac{5}{2}^+$(fit #009) and a fit with $J^P = \frac{1}{2}^-, \frac{3}{2}^+, \frac{5}{2}^-$(fit#001) partial waves. Replacing the $J^P = \frac{3}{2}^+$ in one fit with the higher-spin $J^P = \frac{5}{2}^+$ partial wave in the other fit. It was shown that removing the $J^P = \frac{3}{2}^+$ partial wave completely had an adverse effect on the fit, now the wave will be replaced by another partial wave which has the same parity, and is one step higher in spin. It is evident in the plot of the $\Delta(-ln(\mathcal{L}))$ that this has a mixed effect on the fit. At low W the positive result indicates that the fit can not compensate for the lack of the $J^P = \frac{3}{2}^+$ by using the $J^P = \frac{5}{2}^+$. At higher W however, there is a clear negative result which indicates that the fit can do a better job at $W \approx 2400 MeV$ with the $J^P = \frac{5}{2}^-$ and the $J^P = \frac{5}{2}^+$ partial waves. This is consistent with the results from previous comparisons of fits.

As a summary to the description of Figure 6.3 there are clear indications that there are waves which are absolutely required by the fit. The $J^P = \frac{1}{2}^-, \frac{3}{2}^+, \frac{5}{2}^-$ all appear to be required to best

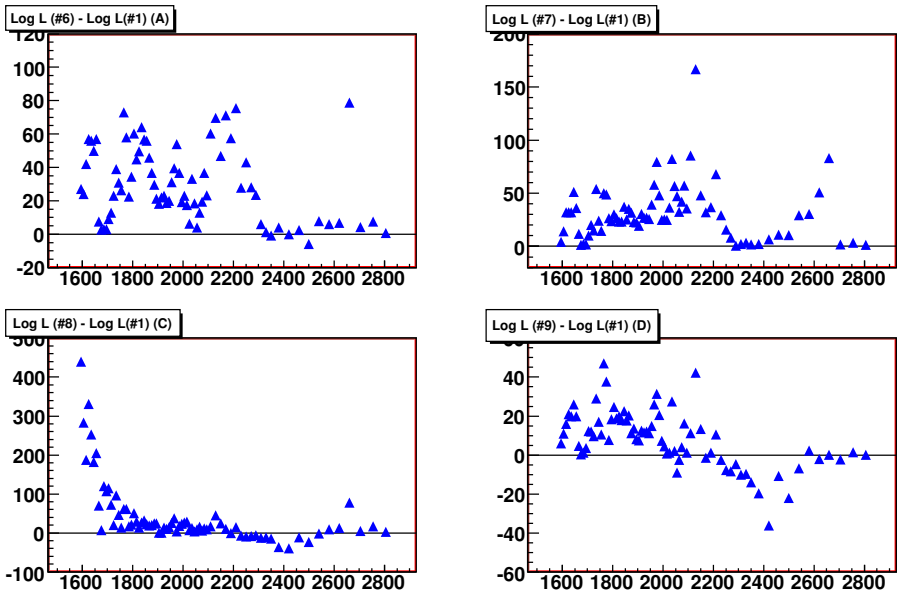

Figure 6.3: Plots of the difference in $-ln(\mathcal{L})$ for pairs of η fits. A $J^P = \frac{1}{2}^-, \frac{3}{2}^+, \frac{5}{2}^-$(fit #001) fit is used as a reference for these likelihood differences, so the value of the $-ln(\mathcal{L})$ for this fit is subtracted Wbin by Wbin from the fits which are being compared to. The x-axis is center-of-mass energy (W, $\sqrt{s}$), while the y-axis is the difference in the $-ln(\mathcal{L})$ between the two fits. If the value of the $\Delta(-ln(\mathcal{L}))$ is positive, it means that the $J^P = \frac{1}{2}^-, \frac{3}{2}^+, \frac{5}{2}^-$(fit #001) fit is a better description of the data than the other fit in the comparison. If the value is negative, then the opposite is true. Plots (A) and (B) are exclusively positive indicating that those wave sets provide an inferior description of the data to the reference wave set. Plot (C) provides a very interesting result, as the fit is capable of distinguishing between the $J^P = \frac{1}{2}^-$ and the $J^P = \frac{1}{2}^+$ partial waves. The fit very clearly prefers the $J^P = \frac{1}{2}^-$ partial wave at threshold. Plot (D) demonstrates that while the $J^P = \frac{3}{2}^+$ appears to be required at low W, there are benefits from including a $J^P = \frac{5}{2}^+$ at higher W.

describe the data. Additionally, there are several indications of the fit benefiting from the inclusion of a higher-spin positive-parity partial wave such as the $J^P = \frac{5}{2}^+$. There is also the very clear preference for a $J^P = \frac{1}{2}^-$ partial wave at threshold. This matches well with the known resonance states at threshold, as there are two resonance states which have significant branching ratios to $N\eta$ at threshold. They are the $S_{11}(1535)$ and the $S_{11}(1650)$ both of which are $J^P = \frac{1}{2}^-$ states.

Continuing the comparison of $-ln(\mathcal{L})$ for different η fits to determine which fits best represent the data, attention is now turned to Figure 6.4(A). Shown is a plot of the $\Delta(-ln(\mathcal{L}))$ bin by bin for a $J^P = \frac{1}{2}^-, \frac{5}{2}^-, \frac{7}{2}^+$(fit #010) fit and a $J^P = \frac{1}{2}^-, \frac{3}{2}^+, \frac{5}{2}^-$(fit #001) fit. The results of switching the $J^P = \frac{3}{2}^+$ wave for a $J^P = \frac{7}{2}^+$ wave are mixed. Similar to Figure 6.3(D), the lower W region suffers for lack of the $J^P = \frac{3}{2}^+$ wave, while the fit in the higher W region appears to benefit from the additional high-spin positive parity wave. Again, the peak of benefit appears to be around $W = 2400MeV$, which is where the high-spin wave has shown previous influence.

Figure 6.4(B) is a plot comparing the $-ln(\mathcal{L})$ of a $J^P = \frac{1}{2}^-, \frac{3}{2}^-, \frac{5}{2}^-$(fit #011) fit and a $J^P = \frac{1}{2}^-, \frac{3}{2}^+, \frac{5}{2}^-$(fit#001) fit. These fits are very similar, the only difference being the parity of the $J = \frac{3}{2}$ wave. The generally positive result indicates that the positive parity $J = \frac{3}{2}$ provides a better

representation of the data than the negative parity wave when accompanied by two identical partial waves.

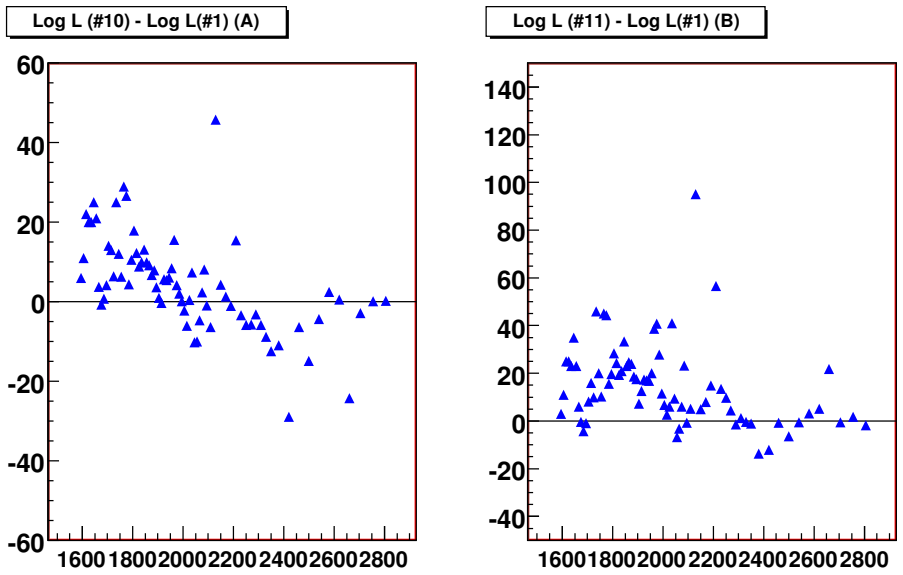

Figure 6.4: Plots of the difference in $-ln(\mathcal{L})$ for pairs of η fits. A $J^P = \frac{1}{2}^-, \frac{3}{2}^+, \frac{5}{2}^-$(fit #001) fit is used as a reference for these likelihood differences, so the value of the $-ln(\mathcal{L})$ for this fit is subtracted Wbin by Wbin from the fits which are being compared to. The x-axis is center-of-mass energy (W, $\sqrt{s}$), while the y-axis is the difference in the $-ln(\mathcal{L})$ between the two fits. If the value of the $\Delta(-ln(\mathcal{L}))$ is positive, it means that the reference fit is a better description of the data than the other fit in the comparison. If the value is negative, then the opposite is clearly true. Plot (A) indicates that the higher-spin positive parity waves may be beneficial to the fit at high W, but can not compensate for the removal of the $J^P = \frac{3}{2}^+$ wave. Plot (B) shows that the positive parity $J = \frac{3}{2}$ provides a better representation of the data than the negative parity wave.

$J^P = \frac{3}{2}^-$

To summarize the description of Figure 6.4, there is continuing support for the $J^P = \frac{1}{2}^-, \frac{3}{2}^+, \frac{5}{2}^-$ wave set with continued indications of a positive parity higher-spin wave which improves the fit at high W. There is a definitive preference in the fit for the $J^P = \frac{3}{2}^+$ partial wave over the $J^P = \frac{3}{2}^-$ partial wave. Removal of, or substitution for, the $J^P = \frac{3}{2}^+$ partial wave has thus far shown to be detrimental to the fit's ability to describe the data.

Having compared all of the reported fits to a "reference" fit containing $J^P = \frac{1}{2}^-, \frac{3}{2}^+, \frac{5}{2}^-$(fit #001), it is now prudent to make comparisons with reference to a different fit. This allows for another perspective in determining which partial waves should be included in the analysis. Figure 6.5 contains four plots of $\Delta(-ln(\mathcal{L}))$ which use a fit that contains $J^P = \frac{1}{2}^-, \frac{5}{2}^-$(fit #003) as a reference. With only two partial waves in the fit being used as a reference, it is likely that additional waves will be required to successfully describe the data. On the other hand, both of the waves present in the new reference fit $J^P = \frac{1}{2}^-, \frac{5}{2}^-$ have been shown to be very significant in describing the physics in the data.

Figure 6.5(A) shows the difference in $-ln(\mathcal{L})$ between the fit containing $J^P = \frac{1}{2}^-, \frac{5}{2}^-$ and a fit with $J^P = \frac{1}{2}^-, \frac{3}{2}^+$. There is clearly a mixed result in the case of this comparison. The negative

result near threshold indicates the importance of the $J^P = \frac{3}{2}^+$ in that W region. Moving higher in W, from $W = 2000 \rightarrow 2500 MeV$ the importance of the $J^P = \frac{5}{2}^-$ partial wave appears obvious.

The plot shown in Figure 6.5(B) shows the difference in $-ln(\mathcal{L})$ bin by bin between a fit with $J^P = \frac{1}{2}^-, \frac{5}{2}^+$(fit #006) and a fit with $J^P = \frac{1}{2}^-, \frac{5}{2}^-$(fit #003). In previous comparisons the importance of the $J^P = \frac{5}{2}^-$ in the $W = 2000 \rightarrow 2400 MeV$ range has been demonstrated. Alternatively, other comparisons have also indicated the improvement in the fit with the inclusion of the $J^P = \frac{5}{2}^+$ partial wave. A comparison of these two fits allows for a direct determination of the preference of the fit for either the positive or negative parity $J = \frac{5}{2}$ wave. The plot clearly shows there are regions in W where the $\Delta(-ln(\mathcal{L}))$ appears positive, and thus indicates a preference for the $J^P = \frac{5}{2}^-$ over the $J^P = \frac{5}{2}^+$. There are also regions which are negative, and on the whole the difference in the likelihood appears centered around zero. The bumps which appear in the positive or negative direction only involve a few W bins. Were these indicative of resonance states, the states would be quite narrow, and not on the order of $100 \rightarrow 300$ MeV in width which is typical for such states. It would be a reasonable conclusion to say that the data is described equally well by both fits.

Figure 6.5(C) contains a plot of the $\Delta(-ln(\mathcal{L}))$ for a fit containing $J^P = \frac{1}{2}^-, \frac{3}{2}^-$(fit #007) and a fit with $J^P = \frac{1}{2}^-, \frac{5}{2}^-$(fit #003). With the inclusion of a $J = \frac{5}{2}$ partial wave more or less established at this point, and without much evidence for the $J^P = \frac{3}{2}^-$, it is expected that the $J^P = \frac{1}{2}^-, \frac{5}{2}^-$(fit #003) fit will be a better description of the data. The positive values at $W = 2000 \rightarrow 2200 MeV$ indicate the importance of the $J^P = \frac{5}{2}^-$ partial wave. Near threshold however, the $J^P = \frac{3}{2}^-$ appears to help provide a slightly better description of the data. Bear in mind that the overall size of these likelihood differences near threshold is on the order of ≈ 25. The dip from $W = 2200 \rightarrow 2400 MeV$ appears to indicate that at higher mass the inclusion of the $J^P = \frac{3}{2}^-$ wave may be beneficial. Again, the overall size of the change in $-ln(\mathcal{L})$ along with the lack of previous evidence for its inclusions leads to the conclusion that the $J^P = \frac{3}{2}^-$ wave is not likely to be critical to the fit.

Figure 6.5(D) shows a plot of the difference in $-ln(\mathcal{L})$ as a function of W between a fit containing $J^P = \frac{1}{2}^+, \frac{3}{2}^-, \frac{5}{2}^+$(fit #008) and a fit with $J^P = \frac{1}{2}^-, \frac{5}{2}^-$(fit #003). The fit has demonstrated a preference for one parity chain over the other in a previous comparison, and this fit will again allow for a test of the importance of the parity chain. The plot clearly indicates a strong positive value at threshold. This demonstrates the preference the fit has for the $J^P = \frac{1}{2}^-$ over the $J^P = \frac{1}{2}^+$. This result is very consistent with the previous comparison. Alternatively, from $W = 1800 \rightarrow 2000$ MeV there is a slightly negative value indicating a better description of the data in the fit containing a $J^P = \frac{3}{2}^-$ wave. Beyond $W = 2000 MeV$, there is a clear indication that the $J^P = \frac{1}{2}^+, \frac{3}{2}^-, \frac{5}{2}^+$ fit is a better representation of the data than the $J^P = \frac{1}{2}^-, \frac{5}{2}^-$ fit. This result is generally consistent with the previously compared results, as there has been evidence for improvement in the fit at high W with the addition of a $J^P = \frac{5}{2}^+$ wave in several of the fits which have been compared. The improvement may also be principally rooted in the ability of a three-wave set to better describe the data than a simpler two-wave set.

On the whole, the conclusions to be drawn from the plots in Figure 6.5 are very similar to the ones which have been drawn from the other likelihood comparisons. There is further support for the inclusion of the $J^P = \frac{1}{2}^-, \frac{3}{2}^+, \frac{5}{2}^-$ waves. Similarly, there is support for the inclusion of a higher-spin positive parity wave like the $J^P = \frac{5}{2}^+$. There is again a strong indication that the $J^P = \frac{1}{2}^+$ partial wave can't replace the $J^P = \frac{1}{2}^-$ wave at threshold. Additionally, it can be concluded that there is a region in W above threshold and below ≈ 2000 MeV which is not generally described well by the partial waves in the $J^P = \frac{1}{2}^-, \frac{5}{2}^-$(fit #003) fit. These results are in agreement with the previous comparisons of likelihoods between fits.

Figure 6.6 compares the likelihood values from a $J^P = \frac{1}{2}^-, \frac{5}{2}^-$(fit #003) fit to several other fits run in the process of the η analysis. Figure 6.6(A), is a plot of the difference in $-ln(\mathcal{L})$ of a

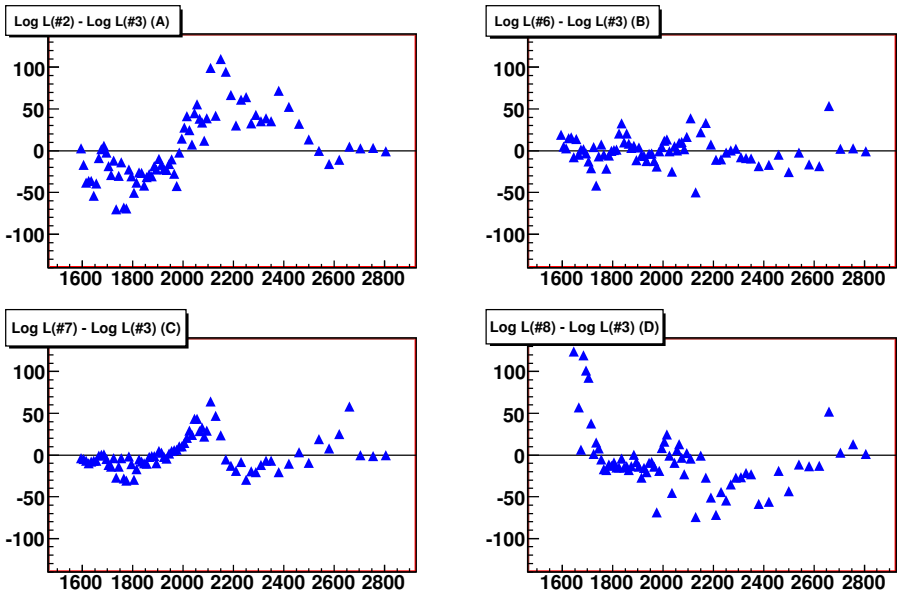

Figure 6.5: Plots of the difference in $-ln(\mathcal{L})$ for η fits. A fit containing $J^P = \frac{1}{2}^-, \frac{5}{2}^-$(fit #003) is now used as the reference for these likelihood differences. This means that for each Wbin in a given fit, the value of the $-ln(\mathcal{L})$ is subtracted by the value of the $-ln(\mathcal{L})$ for this new reference fit. The y-axis is the $\Delta(-ln(\mathcal{L}))$ between the two fits for a given Wbin, while the x-axis is W. A positive value indicates that the reference fit provides a better description of the data than the fit with which it is being compared. A negative value clearly indicates the opposite. Plot (A) clearly indicates that at low W the fit with the $J^P = \frac{3}{2}^+$ partial wave is better, while at higher W the fit with the $\frac{5}{2}^-$ partial wave is a better description of the data. Plot (B) shows that there is little difference across most of W between the use of the $J^P = \frac{5}{2}^-$ and $J^P = \frac{5}{2}^+$ partial waves when there is very little else included in the fit. Plot (C) demonstrates the need for the $J^P = \frac{5}{2}^-$ partial wave once again. Plot (D) again shows that the $J^P = \frac{1}{2}^-$ wave is preferred over the positive parity analogue at threshold. It also indicate that the description of the data is insufficient with only the $J^P = \frac{1}{2}^-, \frac{5}{2}^-$ partial waves.

$J^P = \frac{1}{2}^-, \frac{5}{2}^-, \frac{5}{2}^+$(fit #009) fit and the $J^P = \frac{1}{2}^-, \frac{5}{2}^-$(fit #003) reference fit. While both of these fits contain the $J^P = \frac{1}{2}^-, \frac{5}{2}^-$ waves, the additional $J^P = \frac{5}{2}^+$ partial wave improves the fit across much of the W range. The benefits of a higher-spin positive parity wave like the $J^P = \frac{5}{2}^+$ have been seen in other comparisons, and as such are not surprising here. The benefits to the fit at lower W are most likely caused by the fit utilizing the extra $J^P = \frac{5}{2}^+$ to mock-up the lower-spin $J^P = \frac{3}{2}^+$ which is not present in either fit. Note that the entire range is of negative value, indicating that an extra partial wave allows the fit to improve the description of the data across the whole range in W.

Along a similar line, Figure 6.6(B), is a plot of the difference in $-ln(\mathcal{L})$ of a $J^P = \frac{1}{2}^-, \frac{5}{2}^-, \frac{7}{2}^+$(fit #010) fit and the $J^P = \frac{1}{2}^-, \frac{5}{2}^-$(fit #003) reference fit. Both of these fits contain the $J^P = \frac{1}{2}^-, \frac{5}{2}^-$ partial waves, but the additional $J^P = \frac{7}{2}^+$ partial wave improves the fit across much of the W range. The negative values indicate that the three-wave fit is a superior description of the data than the more basic two-waves of the reference fit. This is consistent with the result seen in Figure 6.6(A) as well. The higher-spin positive parity wave benefits the fit across the whole W range. Comparing

plots Figure 6.6(A) and Figure 6.6(B) is further evidence for the benefits of a higher-spin wave, but also demonstrates the inability of the analysis of the η to distinguish between the $J^P = \frac{5}{2}^+$ and $J^P = \frac{7}{2}^+$ waves.

Figure 6.6(C) contains a plot of the difference in $-ln(\mathcal{L})$ between the $J^P = \frac{1}{2}^-, \frac{5}{2}^-$(fit #003) reference fit and a $J^P = \frac{1}{2}^-, \frac{3}{2}^-, \frac{5}{2}^-$(fit #011) fit. Both fits contain the now ubiquitous $J^P = \frac{1}{2}^-, \frac{5}{2}^-$ partial waves. The addition of an extra $J^P = \frac{3}{2}^-$ wave will help determine if that wave should be included in the standard fits. As can be observed in the plot, the additional wave provides a benefit across the whole range in W. Again, structure exists in the $W = 2200 \rightarrow 2400$ MeV region. and there is benefit all the way down to threshold. The benefits to the likelihood at center-of-mass energies below 2000 MeV are relatively small, ≈ 20. Combining this result with previous comparisons, the fit clearly prefers the positive parity $J = \frac{3}{2}$ wave to the negative parity version.

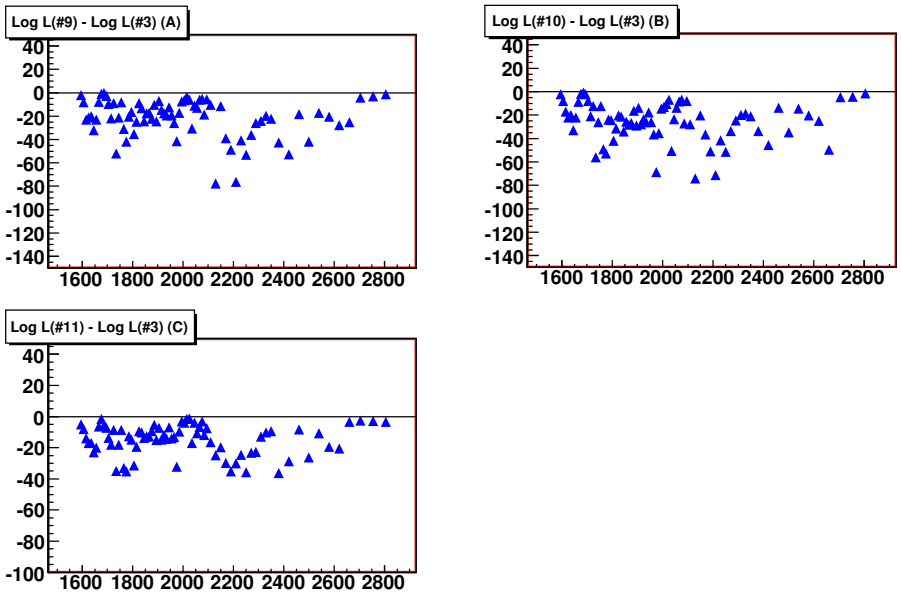

Figure 6.6: Plots of the difference in $-ln(\mathcal{L})$ for η fits. A $J^P = \frac{1}{2}^-, \frac{5}{2}^-$(fit #003) fit was used as the reference for these likelihood differences. The y-axis is the value of $\Delta(-ln(\mathcal{L}))$, while the x-axis is center-of-mass energy(W). A negative value indicates that the reference fit does an insufficient job at describing the data in comparison to the alternate fit. All of the plots in this figure contain negative values of $\Delta(-ln(\mathcal{L}))$. This indicates that two partial waves, however essential to the fit they may be, can not describe the physics in the data alone. The addition of a $J^P = \frac{5}{2}^+$(A), a $J^P = \frac{7}{2}^+$(B), or a $J^P = \frac{3}{2}^-$(C) all significantly improve the description of the data by the fit.

The overriding conclusion to be drawn from Figure 6.6 is that a bare-bones wave set consisting solely of the $J^P = \frac{1}{2}^-, \frac{5}{2}^-$ is insufficient for describing the data. Almost every partial wave that was added to this wave set had a systematically better likelihood. There is structure in all three of these plots in the $W \approx 2200 \rightarrow 2400$ MeV region, which indicates the need for an extra wave in that energy range. Additionally, there is a slightly smaller yet important effect at lower W in the $W \approx 1800 \rightarrow 2000$ MeV region. This is likely a product of the lack of $J^P = \frac{3}{2}^+$ partial wave in the fit, which has already been shown to be beneficial to the likelihood.

A large variety of structures appear in plots of the $\Delta(-ln(\mathcal{L}))$ as a function of W. The trick is determining which wave set best describes the physics of the data events which were collected in the experiment. There are regions, like threshold, where a single partial wave, the $J^P = \frac{1}{2}^-$, will describe the physics. There are other regions in W which might require three or even four partial waves to accurately describe the data.

With so many different fits compared to each other, there are several stand-out conclusions which can be drawn from these results. First, the threshold region in W absolutely requires the $J^P = \frac{1}{2}^-$ partial wave. This is not a surprising conclusion as there is a well known, very strong, resonance present at threshold with a large branching ratio to Nη called the $S_{11}(1535)$ which is $J^P = \frac{1}{2}^-$.

Second, the inclusion of the $J^P = \frac{5}{2}^-$ appears to improve the fit, particularly above $W = 2000$ MeV. Across all of the fits run, there benefit of the inclusion of this wave is clear. When removed from a set off partial waves there is a considerable effect on the likelihood of the fit. Including this partial wave, a base set of waves can be constructed, which now includes: $J^P = \frac{1}{2}^-, \frac{5}{2}^-$.

Third, the effect of including the $J^P = \frac{3}{2}^+$ improves the likelihood in the $W = 1700 \rightarrow 2000$ MeV region. Other waves appear to have mocked-up the effect of this wave in different fits, but the $J^P = \frac{3}{2}^+$ appears to consistently improve the fit. Additionally, there is another well known $J^P = \frac{3}{2}^+$ resonance at ≈ 1720 MeV called the $P_{13}(1720)$ which is known to couple to Nη. This increases the base wave set to three partial waves: $J^P = \frac{1}{2}^-, \frac{3}{2}^+, \frac{5}{2}^-$.

Fourth, as the two lower plots in Figure 6.2 demonstrate, there is a benefit in the likelihood if a higher-spin positive parity wave is included in the fit. All of the additional and different fits which included either a $J^P = \frac{5}{2}^+$ or $J^P = \frac{7}{2}^+$ partial wave showed a benefit to the likelihood at higher W, around ≈ 2400 MeV. There is currently no way to distinguish between these two partial waves, so both options will have to be studied further. The addition of one of these higher spin waves to the wave set would increase the base wave set to four partial waves. While the plots of the likelihood encourage the inclusion of these higher spin waves, it is a relatively small change in likelihood and as such it is prudent to maintain the base set of three waves: $J^P = \frac{1}{2}^-, \frac{3}{2}^+, \frac{5}{2}^-$. The addition of these higher spin waves will be studied further to determine what, if any, structure exists in the yields and phase difference results for individual partial waves.

There are five fits which have been selected for further study on the basis of the partial waves that they contain. The first is the $J^P = \frac{1}{2}^-, \frac{3}{2}^+, \frac{5}{2}^-$(fit #001) fit which has served as a basis for many of the likelihood comparisons. Next is the $J^P = \frac{1}{2}^-, \frac{3}{2}^+, \frac{5}{2}^-, \frac{5}{2}^+$(fit #004) and $J^P = \frac{1}{2}^-, \frac{3}{2}^+, \frac{5}{2}^-, \frac{7}{2}^+$(fit #005) fits which each incorporate an additional high-spin positive parity wave. Finally, are the $J^P = \frac{1}{2}^-, \frac{5}{2}^-, \frac{5}{2}^+$(fit #009) and $J^P = \frac{1}{2}^-, \frac{5}{2}^-, \frac{7}{2}^+$(fit #010) fits, which replace the $J^P = \frac{3}{2}^+$ with a higher-spin positive parity wave. These fits were selected because of the consistency of the results in their likelihood comparisons, and because they provide a comprehensive look at several available solutions.

6.3.2 $\Delta ln(\mathcal{L})$ of η' Fits

There is very little data on baryon resonance states which couple to Nη', so the most reasonable starting point in this analysis is to follow the sequence established by the Nη analysis. The η and η' have the same quantum numbers, and as such it is assumed that they couple to the same resonances if it is allowed kinematically. Presented in this section are plots of the $\Delta(-ln(\mathcal{L}))$ between differing fits run in the η' analysis. The difference is constructed bin by bin as a function of W so structures seen are correlated to where one fit is better than another. The difference in $-ln(\mathcal{L})$, as previously described, is a means of comparing one fit to another and determining which better describes the data. The fits will be described by their partial wave content, and a will also be referred to by fit number. See Table 6.2 for fit numbers and their wave content.

Starting with the first two fits in the η' analysis the two wave sets differ by the inclusion of a $J^P = \frac{5}{2}^-$ partial wave. In this comparison, the $-ln(\mathcal{L})$ from a $J^P = \frac{1}{2}^-, \frac{3}{2}^+, \frac{5}{2}^-$(fit #101) fit is subtracted from the $-ln(\mathcal{L})$ from a $J^P = \frac{1}{2}^-, \frac{3}{2}^+$(fit #102) fit. The result of this comparison is the shown in Figure 6.7(A). The generally positive result indicates that the $J^P = \frac{1}{2}^-, \frac{3}{2}^+, \frac{5}{2}^-$(fit #101) fit is a better description of the data, that the alternate fit. The significant structure around $W = 2400 \rightarrow 2600$ MeV shows the importance of the $J^P = \frac{5}{2}^-$ partial wave. The inclusion of the $J^P = \frac{5}{2}^-$ partial wave does not appear to have a significant effect on the threshold region. This is a promising indication as it means that the fit only appears to require the $J^P = \frac{5}{2}^-$ partial wave in a certain range of W which may indicate a resonance structure.

A $J^P = \frac{1}{2}^-, \frac{5}{2}^-$(fit #103) fit will now be used to determine the importance of the $J^P = \frac{3}{2}^+$ partial wave within the $J^P = \frac{1}{2}^-, \frac{3}{2}^+, \frac{5}{2}^-$(fit #101) reference fit. The $-ln(\mathcal{L})$ from the reference fit is subtracted from the $-ln(\mathcal{L})$ of the $J^P = \frac{1}{2}^-, \frac{5}{2}^-$(fit #103) fit. A positive value for $\Delta(-ln(\mathcal{L}))$ indicates that the reference fit provides a better description of the data than the opposing fit in the comparison. Figure 6.7(B) clearly indicates the overall positive nature of the $\Delta(-ln(\mathcal{L}))$. It is clear from this plot that the inclusion of the $J^P = \frac{3}{2}^+$ partial wave allows for a better description of the data. The large peak around $W = 2150 MeV$ may be indicative of a resonance structure.

With the importance of the inclusion of the $J^P = \frac{5}{2}^-$ and $J^P = \frac{3}{2}^+$ partial waves in the fit demonstrated, it is now time to consider the effect of adding an additional wave to the fit. The $-ln(\mathcal{L})$ from a fit containing the $J^P = \frac{1}{2}^-, \frac{3}{2}^+, \frac{5}{2}^-$(fit #101) partial waves is subtracted from the $-ln(\mathcal{L})$ from a fit with $J^P = \frac{1}{2}^-, \frac{3}{2}^+, \frac{5}{2}^-, \frac{5}{2}^+$(fit #104). The plot of the likelihood difference as a function of W is shown in Figure 6.7(C). The plot indicates that there is essentially no benefit from including the $J^P = \frac{5}{2}^+$ partial wave in this fit. It does not appear to significantly improve the fit in any region of W.

Figure 6.7(D) demonstrates a comparison very similar to that shown in Figure 6.7(C). In this plot, the $-ln(\mathcal{L})$ from a fit containing the $J^P = \frac{1}{2}^-, \frac{3}{2}^+, \frac{5}{2}^-$(fit #101) partial waves is subtracted from the $-ln(\mathcal{L})$ from a fit with $J^P = \frac{1}{2}^-, \frac{3}{2}^+, \frac{5}{2}^-, \frac{7}{2}^+$(fit #105). $\Delta(-ln(\mathcal{L}))$ is generally negative across the entire range of center-of-mass energy. Most of the apparent improvement due to the additional wave is insignificant, however, there is a small systematically negative structure near $W = 2150 MeV$. This structure is small, but may imply a slight advantage to an additional $J^P = \frac{7}{2}^+$ partial wave in this region of W. It is interesting to note that in this case, the η' analysis appears to distinguish between the $J^P = \frac{5}{2}^+$ and $J^P = \frac{7}{2}^+$ partial waves.

There are a few conclusions which can be taken away from the plots contained in Figure 6.7. First, there is a strong indication that the $J^P = \frac{3}{2}^+$ and $J^P = \frac{5}{2}^-$ are important in describing the physics present in the data. Second, that the inclusion of a $J^P = \frac{5}{2}^+$ along with a base set of $J^P = \frac{1}{2}^-, \frac{3}{2}^+, \frac{5}{2}^-$(fit #101) waves seemed to have little to no effect on the fits ability to describe the data. Third, while the addition of a $J^P = \frac{5}{2}^+$ wave appeared to have no effect, there was a

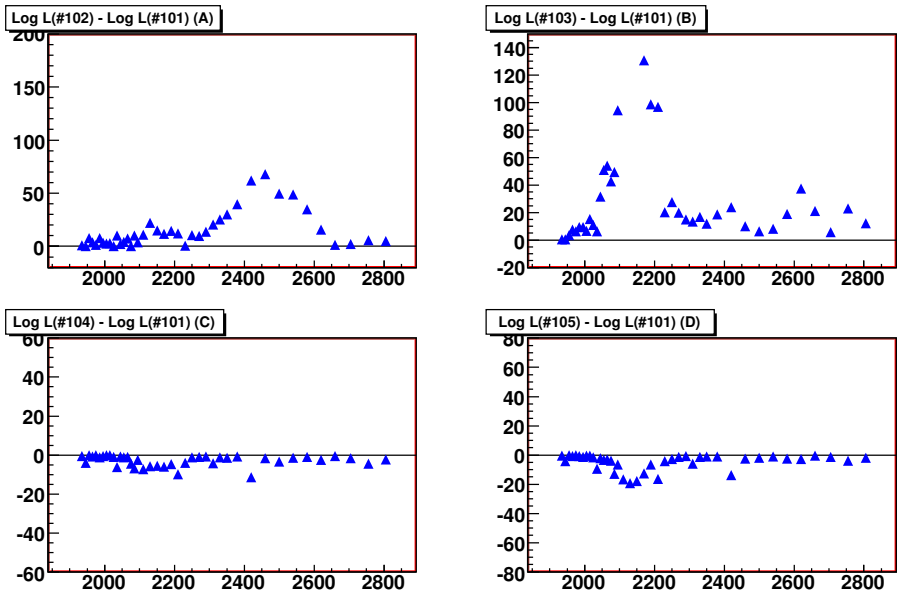

Figure 6.7: Plots of the difference in $-ln(\mathcal{L})$ between two η' fits on a bin by bin basis. A fit containing $J^P = \frac{1}{2}^-, \frac{3}{2}^+, \frac{5}{2}^-$ (fit #101) partial waves has been taken as a reference to which fits with alternate wave sets will be compared. The y-axis is the value of the $\Delta(-ln(\mathcal{L}))$, while the x-axis is center-of-mass energy(W). A positive result indicates that the reference fit is a better description of the data than the opposing fit. A negative result implies the opposite to be true. The significant positive peaks in plots (A) and (B) indicate the importance of the $J^P = \frac{5}{2}^-$ and $J^P = \frac{3}{2}^+$ partial waves in the fit. Plots (C) shows that there is essentially no benefit from including an extra $J^P = \frac{5}{2}^+$ partial wave when the fit already contains the $J^P = \frac{1}{2}^-, \frac{3}{2}^+, \frac{5}{2}^-$ partial waves. Plot (D) indicates that there is a small effect when an additional $J^P = \frac{7}{2}^+$ partial wave is included alongside the $J^P = \frac{1}{2}^-, \frac{3}{2}^+, \frac{5}{2}^-$ partial waves. This small benefit appears around $W = 2150 MeV$.

more noticeable effect with the addition of a $J^P = \frac{7}{2}^+$ partial wave. The improvement was not a large one, but the benefit was noticeable. Additionally the fit has the ability to distinguish between the $J^P = \frac{5}{2}^+$ and $J^P = \frac{7}{2}^+$ waves in the case of the η' analysis. There is a more clear systematic improvement in the fit containing the additional $J^P = \frac{7}{2}^+$ partial wave, in comparison to the fit with an additional $J^P = \frac{5}{2}^+$ wave.

Figure 6.8(A) is a plot showing the $\Delta(-ln(\mathcal{L}))$ between two fits. The $-ln(\mathcal{L})$ of the reference fit, containing $J^P = \frac{1}{2}^-, \frac{3}{2}^+, \frac{5}{2}^-$ (fit #101), is subtracted from the $-ln(\mathcal{L})$ of the other fit, containing $J^P = \frac{1}{2}^-, \frac{5}{2}^+$ (fit #106). The largely positive values of $\Delta(-ln(\mathcal{L}))$ indicate that the reference fit is considerably better at describing the data in comparison to the alternate fit. Additionally, the removal of the $J^P = \frac{3}{2}^+$, which is present in the reference fit, is clearly preventing the fit from describing the data well.

Along similar lines, Figure 6.8(B) displays the difference in $-ln(\mathcal{L})$ between the reference fit($J^P = \frac{1}{2}^-, \frac{3}{2}^+, \frac{5}{2}^-$ (fit #101)) and a fit containing only the $J^P = \frac{1}{2}^-, \frac{3}{2}^-$ (fit #107). The difference is positive across the whole range in W with a significant structure displayed centered at $W = 2150$ MeV. This is reminiscent of the structure seen in Figure 6.7(B) when the $J^P = \frac{3}{2}^+$ wave was removed from the reference fit. Differences beyond $W = 2400$ MeV are likely caused by the lack of higher-spin waves

in the fit containing only the $J^P = \frac{1}{2}^-, \frac{3}{2}^-$(fit #107) waves.

Figure 6.8(C) shows a plot of the difference in $-ln(\mathcal{L})$ between two fits which are of opposite parities to one another. The $-ln(\mathcal{L})$ for the reference fit, which contains the $J^P = \frac{1}{2}^-, \frac{3}{2}^+, \frac{5}{2}^-$(fit #101) waves, is subtracted from the $-ln(\mathcal{L})$ of the opposite parity wave set containing the $J^P = \frac{1}{2}^+, \frac{3}{2}^-, \frac{5}{2}^+$(fit #108) waves. As was seen in the η results the fit has the ability to distinguish between parity chains. The positive value of the difference in likelihoods indicates that the reference fit is preferred over the fit of opposite parity. At threshold, there is a clear indication that the fit can better describe the data with the $J^P = \frac{1}{2}^-$ partial wave compared with the $J^P = \frac{1}{2}^+$. The rest of the range in W, the $\Delta(-ln(\mathcal{L}))$ is generally positive, but the differences are small and thus at higher energy the fit has more trouble distinguishing between the two parity chains.

Figure 6.8(D) presents a plot of the likelihood difference between two fits which differ only by the identity of a single partial wave. The $-ln(\mathcal{L})$ for the reference fit, which contains the $J^P = \frac{1}{2}^-, \frac{3}{2}^+, \frac{5}{2}^-$(fit #101) waves, is subtracted from the $-ln(\mathcal{L})$ of the wave set containing the $J^P = \frac{1}{2}^-, \frac{5}{2}^-, \frac{5}{2}^+$(fit #109) partial waves. The positively-valued structure at $W = 2150MeV$ is indicative of the lack of the $J^P = \frac{3}{2}^+$ wave in the $J^P = \frac{1}{2}^-, \frac{5}{2}^-, \frac{5}{2}^+$(fit #109) fit. This is consistent with Figure 6.7(B) for the presence of the $J^P = \frac{3}{2}^+$ wave. The $J^P = \frac{5}{2}^+$ wave may compensate for the missing $J^P = \frac{3}{2}^+$, but ultimately it has a different angular structure and can only compensate so much. Other than that structure, there is really no difference between the two fits, again indicating that the $J^P = \frac{5}{2}^+$ wave does not influence the η' fits in a significant way.

A few conclusions can be taken away from the information presented in Figure 6.8. First, that the fit, like in the case of the η analysis, can distinguish between the $J^P = \frac{1}{2}^-$ and the $J^P = \frac{1}{2}^+$ partial waves, and it prefers the negative parity wave. Second, there is continuing support for the inclusion of the $J^P = \frac{3}{2}^+$ partial wave. When this wave is removed from a fit, there appears to be a significant structure in the likelihood difference plots centered around $W = 2150$ MeV. Third, the inclusion of the $J^P = \frac{5}{2}^+$ wave does not appear to be required for these fits. This is perhaps surprising because there was an apparent improvement to the fit when the $J^P = \frac{5}{2}^+$ wave was included in the fits to the η.

Figure 6.9(A) presents a plot of the difference in $-ln(\mathcal{L})$ between two fits for the η'. The $-ln(\mathcal{L})$ for the reference fit, which contains the $J^P = \frac{1}{2}^-, \frac{3}{2}^+, \frac{5}{2}^-$(fit #101) waves, is subtracted from the $-ln(\mathcal{L})$ of the wave set containing the $J^P = \frac{1}{2}^-, \frac{5}{2}^-, \frac{7}{2}^+$(fit #110) partial waves. The positive structure in the plot indicates the inability of the $J^P = \frac{1}{2}^-, \frac{5}{2}^-, \frac{7}{2}^+$ wave set to describe the physics present in the data around $W = 2150MeV$. As previously indicated this is the location in W where the $J^P = \frac{3}{2}^+$ partial wave appears essential. Across much of the rest of the W range, the two fits appear fairly similar. In the previous comparisons the only structure ever seen in the $J^P = \frac{7}{2}^+$ partial wave appeared around $W = 2150MeV$, the effect of which would be overshadowed by the lack of the $J^P = \frac{3}{2}^+$ partial wave.

The plot displayed in Figure 6.9(B) shows the $\Delta(-ln(\mathcal{L}))$ as a function of W comparing between the reference fit $J^P = \frac{1}{2}^-, \frac{3}{2}^+, \frac{5}{2}^-$(fit #101) and a fit containing the $J^P = \frac{1}{2}^-, \frac{3}{2}^-, \frac{5}{2}^-$(fit #111) partial waves. The two wave sets differ only in the parity of the $J = \frac{3}{2}$ partial wave. The positive structure around $W = 2150MeV$ demonstrates that the fit can provide a better description of the data with the positive parity $J = \frac{3}{2}$ partial wave than the negative parity wave. The importance of the $J^P = \frac{3}{2}^+$ partial wave appears clearly in this plot. Other than the single positive structure at $W = 2150MeV$, both fits are nearly identical in their ability to describe the data in other regions of W. This result appears entirely consistent with the other likelihood results previously presented.

As a summary to the results presented in Figure 6.9, these two plots offer clear indications of the necessity of the presence of the $J^P = \frac{3}{2}^+$ partial wave in the wave set. Fits run with several different combinations of partial waves have shown that it is an essential wave in describing the

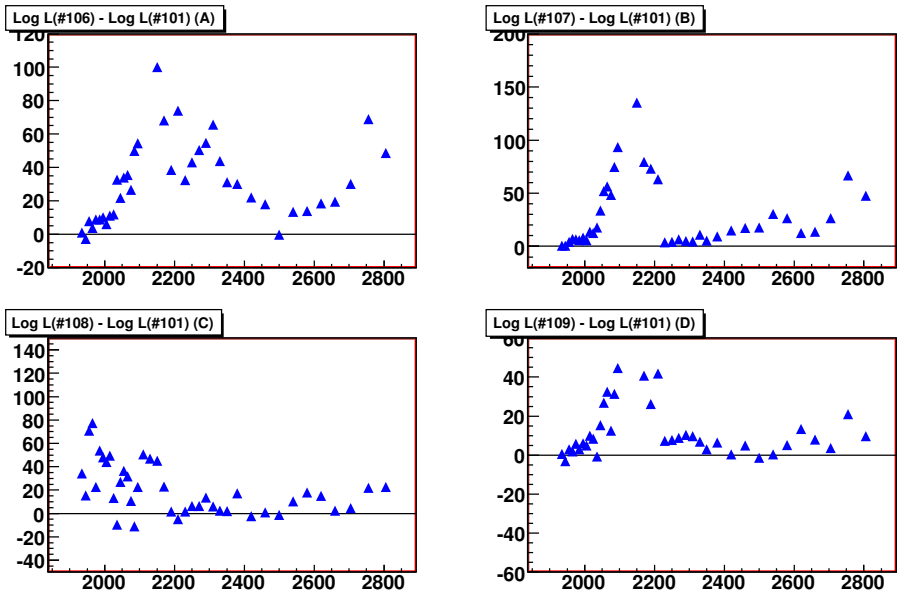

Figure 6.8: Plots of the difference in -ln($\mathcal{L}$) between two differing η' fits on a bin by bin basis. Plot (A) shows the difference in the $-ln(\mathcal{L})$ between a reference fit containing $J^P = \frac{1}{2}^-, \frac{3}{2}^+, \frac{5}{2}^-$(fit #101) partial waves and an alternate fit with $J^P = \frac{1}{2}^-, \frac{5}{2}^+$(fit #106) waves. The positive structure indicates the lack of the $J^P = \frac{3}{2}^+$ in the fit, and perhaps a slight preference for the $J^P = \frac{5}{2}^-$ over the $J^P = \frac{5}{2}^+$ partial wave. Plot (B) compares the reference fit to a fit containing only the $J^P = \frac{1}{2}^-, \frac{3}{2}^-$(fit #107) partial waves. The significant structure indicates that the fit prefers the $J^P = \frac{3}{2}^+$ to the $J^P = \frac{3}{2}^-$ partial wave. Plot (C) demonstrates the ability of the fit to distinguish between parity of differing waves. Comparing the reference fit to a fit containing the $J^P = \frac{1}{2}^+, \frac{3}{2}^-, \frac{5}{2}^+$(fit #108) partial waves, the fit at threshold clearly prefers the $J^P = \frac{1}{2}^-$ to the $J^P = \frac{1}{2}^+$. Plot (D) shows that the reference fit is still a better description of the data when compared to a fit containing $J^P = \frac{1}{2}^-, \frac{5}{2}^-, \frac{5}{2}^+$(fit #109). The fit clearly indicates that the $J^P = \frac{5}{2}^+$ partial wave is not beneficial in the η' analysis, while the $J^P = \frac{3}{2}^+$ partial wave appears essential.

physics present in the η' data. There was not a significant indication of the benefits of a higher-spin positive parity wave. The presence of the $J^P = \frac{7}{2}^+$ wave does not appear to be required in these fits.

In order to provide a slightly different perspective to the comparisons of different fits, several of the fits already described will be compared to a different "reference" fit, which is comprised of the $J^P = \frac{1}{2}^-, \frac{5}{2}^-$(fit #103) partial waves. The term "reference" is used here to indicate that the likelihood differences will now be determined relative to this fit. As this fit contains only two partial waves, it is not expected to describe the data well, merely to provide a different comparison for the fits already run. The motivation behind this choice of fits comes solely from the previous results and the apparently essential nature of the $J^P = \frac{1}{2}^-, \frac{5}{2}^-$ partial waves.

As a starting point, the reference fit, comprised of the $J^P = \frac{1}{2}^-, \frac{5}{2}^-$(fit #103) partial waves will be compared to a fit containing the $J^P = \frac{1}{2}^-, \frac{3}{2}^+$(fit #102) partial waves. A plot of the difference in the $-ln(\mathcal{L})$ between of the two fits is presented in Figure 6.10(A). The large negative value of the

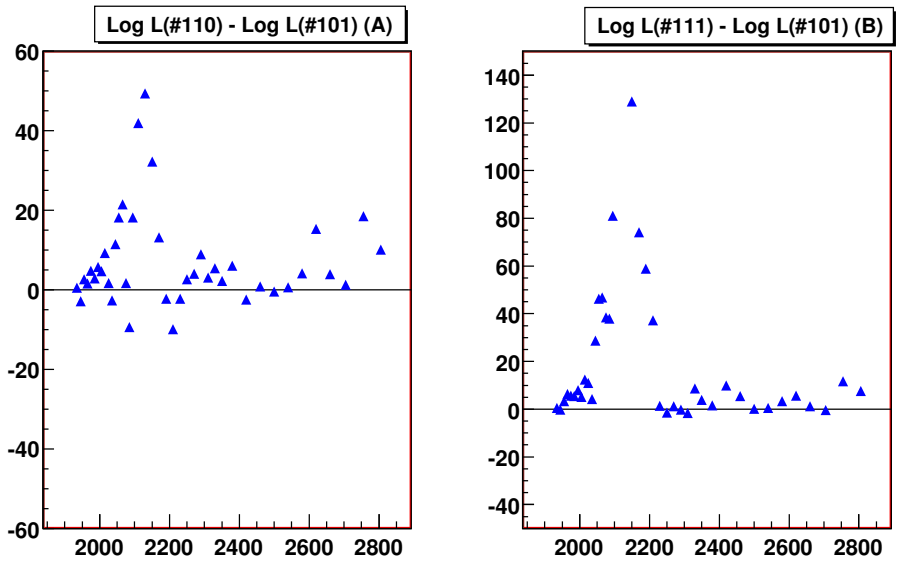

Figure 6.9: Plots of the difference in -ln($\mathcal{L}$) for η' fits. A $J^P = \frac{1}{2}^-, \frac{3}{2}^+, \frac{5}{2}^-$(fit #101) fit is used as the reference for this comparison. On the y-axis is the value of $\Delta(-ln(\mathcal{L}))$, while the x-axis is W. A positive value indicates that the reference fit better describes the data than the opposing fit. Neither of the fits compared here to the reference fit contain a $J^P = \frac{3}{2}^+$ partial wave, and the lack of this wave is evident in both plots (A) and (B). Both plots have a clear structure around $W = 2150 MeV$. Plot (B) is a comparison of the reference fit to a fit containing the $J^P = \frac{1}{2}^-, \frac{3}{2}^-, \frac{5}{2}^-$(fit #111), and the preference of the fit for a positive parity $J = \frac{3}{2}$ partial wave in the region of $W = 2150 MeV$ could not be more clear.

likelihood difference below $W = 2300$ MeV is demonstrates that the fit which includes the $J^P = \frac{3}{2}^+$ partial wave is a better description of the data in that region. Alternatively, above $W = 2300$ MeV the positive values indicate that the reference fit, containing the $J^P = \frac{5}{2}^-$, better represents the physics in the data.

Figure 6.10(B) shows a plot which is the difference in the $-ln(\mathcal{L})$ between the reference fit ($J^P = \frac{1}{2}^-, \frac{5}{2}^-$(fit #103)) and a fit containing only the $J^P = \frac{1}{2}^-, \frac{5}{2}^+$(fit #106) partial waves. This will provide a vary direct comparison as to the effect of including the $J^P = \frac{5}{2}^+$ wave over the $J^P = \frac{5}{2}^-$ partial wave. The negative values shown at threshold and up to $W \approx 2250$ MeV indicate that the fit with the $J^P = \frac{5}{2}^+$ wave(fit #106) provides a better description of the data in this region of W. From $W = 2250 \rightarrow 2400$ MeV there is an indication of the reference fit describing the data a bit better than the opposing fit. Beyond $W = 2400$ MeV, the fits are essentially equivalent. With a total lack of supporting evidence suggesting the importance of the $J^P = \frac{5}{2}^+$ up to this point, the apparent importance of the $J^P = \frac{5}{2}^+$ wave is likely an artifact of the fit using the positive parity wave to mock-up the $J^P = \frac{3}{2}^+$ wave which is known to be prevalent, but does not exist in these fits.

The plot displayed in Figure 6.10(C) shows the difference in the $-ln(\mathcal{L})$ as a function of W between the reference fit containing the $J^P = \frac{1}{2}^-, \frac{5}{2}^-$(fit #103) partial waves and a fit containing only the $J^P = \frac{1}{2}^-, \frac{3}{2}^-$(fit #107) partial waves. Across most of the plot, there is very little difference between the two fits. Both wave sets are apparently capable of describing the data in comparable

ways. The structure in the negative direction around $W = 2150$ MeV is likely the influence of the $J = \frac{3}{2}^+$ wave which is not present in the reference fit, and thus, in this region of W the fit containing only the $J^P = \frac{1}{2}^-, \frac{3}{2}^-$(fit #107) partial waves is a better description of the data. Clearly, previous evidence indicates that the fit prefers a positive parity $J = \frac{3}{2}$ wave at this W, but without such a wave present in the fit, clearly the negative parity state has been substituted.

The next two fits to be compared have significant differences from one another. The $-ln(\mathcal{L})$ of the reference fit, with the $J^P = \frac{1}{2}^-, \frac{5}{2}^-$(fit #103) partial waves is subtracted from the $-ln(\mathcal{L})$ of the a fit containing the $J^P = \frac{1}{2}^+, \frac{3}{2}^-, \frac{5}{2}^+$(fit #108) partial waves. A plot of the likelihood difference in Figure 6.10(D) demonstrates two significant features. First, the fit is once again clearly preferring the negative parity $J = \frac{1}{2}$ wave at threshold over the positive parity partial wave. Second, the apparent presence of a $J = \frac{3}{2}$ wave in the $W = 2150MeV$ region is again noted. As previously mentioned however, the fit appears to prefer a positive parity $J = \frac{3}{2}$ wave to the negative parity alternative. This structure is likely the fit trying to use the $J^P = \frac{3}{2}^-$ wave to compensate for a lack of the $J^P = \frac{3}{2}^+$ wave. At high W there appears to be no significant differences between the two fits.

On the whole, the plots present in Figure 6.10 demonstrate the importance of the $J^P = \frac{1}{2}^-$ partial wave at threshold, and the ability of the fit to distinguish between the two different parity $J = \frac{1}{2}$ waves. Additionally, the presence of a significant $J = \frac{3}{2}$ wave present in the fit around $W = 2150$ MeV appears to be a consistent result through all compared fits. There is also some hint that in the $W = 2450MeV$ region the $J^P = \frac{5}{2}^-$ partial wave is still an important contribution.

Figure 6.11(A) is a plot of the $-ln(\mathcal{L})$ of a reference fit, consisting of the $J^P = \frac{1}{2}^-, \frac{5}{2}^-$(fit #103) partial waves, subtracted from the $-ln(\mathcal{L})$ of an opposing fit, consisting of the $J^P = \frac{1}{2}^-, \frac{5}{2}^-, \frac{5}{2}^+$(fit #109) partial waves, on a Wbin by Wbin basis. The negative value of the $\Delta(-ln(\mathcal{L}))$ indicates that the reference fit is not as good at describing the data as the fit to which it has been compared. The influence of the $J^P = \frac{5}{2}^+$ partial wave is shown across the whole range in W. Generally the effect is small, but in the region around $W = 2150MeV$ there is a considerable improvement in the fit with the addition of the $J^P = \frac{5}{2}^+$ partial wave.

The plot displayed in Figure 6.11(B) is along a similar vein. The $-ln(\mathcal{L})$ of the reference fit, consisting of the $J^P = \frac{1}{2}^-, \frac{5}{2}^-$(fit #103) partial waves, is subtracted from the $-ln(\mathcal{L})$ of the opposing fit, consisting of the $J^P = \frac{1}{2}^-, \frac{5}{2}^-, \frac{7}{2}^+$(fit #110) partial waves. This plot looks very similar to Figure 6.11(A). There is a large negative peak at the same location in W indicating that the fit containing the $J^P = \frac{7}{2}^+$ partial wave provides a superior description of the data. Across the rest of the W range there is a slight improvement, but it is unlikely anything that could not be attributed to the additional freedom provided to the fit by the extra partial wave.

Figure 6.11(C) is a plot of the $\Delta(-ln(\mathcal{L}))$ determined by subtracting the $-ln(\mathcal{L})$ of a reference fit, consisting of the $J^P = \frac{1}{2}^-, \frac{5}{2}^-$(fit #103) partial waves, from the $-ln(\mathcal{L})$ of an opposing fit, consisting of the $J^P = \frac{1}{2}^-, \frac{3}{2}^-, \frac{5}{2}^-$(fit #111) partial waves. Again, the result of this comparison appears very similar to the plots shown in Figures 6.11(A) and 6.11(B). The additional wave in the fit, this time a $J^P = \frac{3}{2}^-$ partial wave, provides a general improvement across W in the ability of the fit to describe the data. The same negative peak appears at the appropriate W to indicate the specific region where an extra wave is really needed in the fit.

A few conclusions can be drawn from the plots contained in Figure 6.11. First, the fit is clearly benefiting from an additional partial wave around $W = 2150$ MeV. This improvement indicates that the simple $J^P = \frac{1}{2}^-, \frac{5}{2}^-$ wave set is insufficient at describing the data in that region. Second, there appears to be a general improvement in the fits when an additional partial wave is added, and there appears to be a slight preference for the additional wave to be of positive parity. An additional wave, or possibly two, is required to accurately describe the data. From previous comparisons, the inclusion of a $J^P = \frac{3}{2}^+$ partial wave is indicated.

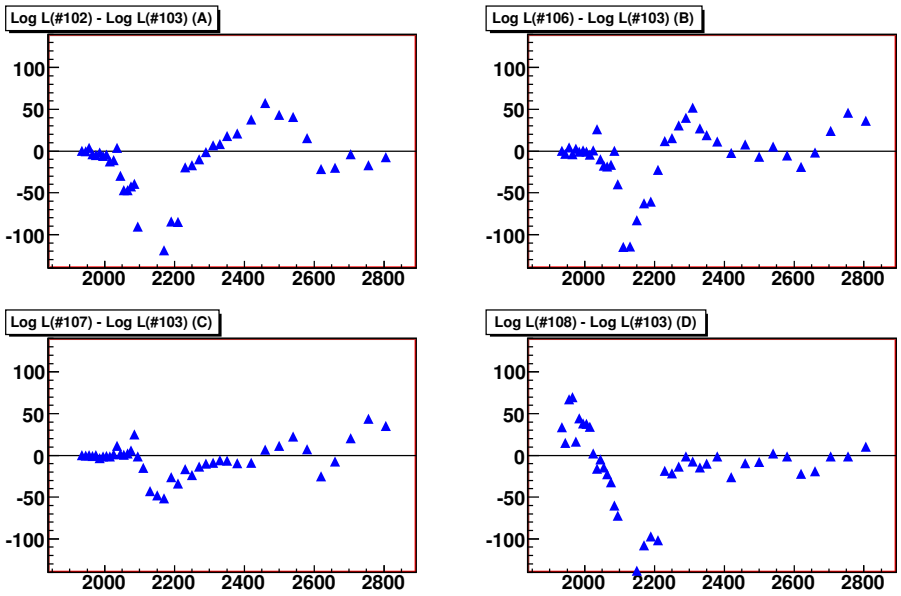

Figure 6.10: Plots of the difference in $-ln(\mathcal{L})$ for various combinations of η' fits. For these plots a fit containing the $J^P = \frac{1}{2}^-, \frac{5}{2}^-$(fit #103) partial waves is used as a reference. The $-ln(\mathcal{L})$ of this reference fit was subtracted from the $-ln(\mathcal{L})$ of an opposing fit on a Wbin by Wbin basis. The y-axis is the value of the $\Delta(-ln(\mathcal{L}))$, while the x-axis is W. A positive value indicates that the reference fit provides a better description of the data, while a negative value indicates that the opposing fit is better. The comparison shown in plot (A) between the reference fit with the $J^P = \frac{1}{2}^-, \frac{5}{2}^-$(fit #103) partial waves and an opposing fit with the $J^P = \frac{1}{2}^-, \frac{3}{2}^+$(fit #102) partial waves clearly indicates that both wave sets are missing something that the other wave set has. This lends more confidence to the need for a wave set comprised of the $J^P = \frac{1}{2}^-, \frac{3}{2}^+, \frac{5}{2}^-$ partial waves. Plot (B) demonstrates the preference of the fit for a $J^P = \frac{5}{2}^+$ wave, but this is likely a compensation for lack of a $J^P = \frac{3}{2}^+$ wave in the fit. Plot (C) then shows a preference for the presence of a $J^P = \frac{3}{2}^-$ wave, which given previous results is likely compensating for a $J^P = \frac{3}{2}^+$ wave which is not in the fit. Finally, plot (D) again demonstrates the fit's ability to distinguish between the parity of the $J = \frac{1}{2}$ partial wave, and selects the negative parity wave at threshold.

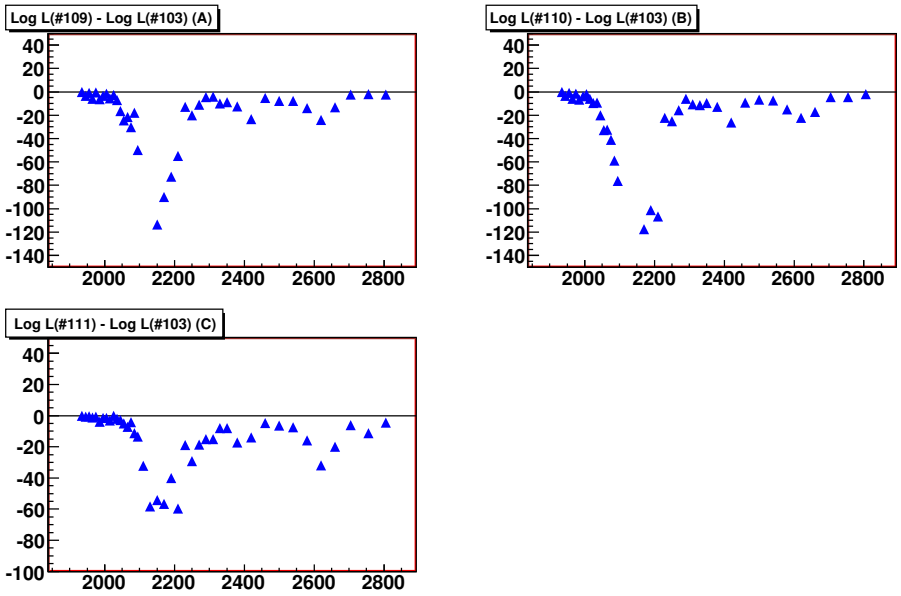

Figure 6.11: Plots of the difference in $-ln(\mathcal{L})$ as a function of W for differing wave sets in η' analysis. The value of $\Delta(-ln(\mathcal{L}))$ as a function of center-of-mass energy(W) is shown. A negative value indicates that the reference fit $J^P = \frac{1}{2}^-, \frac{5}{2}^-$(fit #103) is a less successful description of the data than the opposing wave set. In Plot (A) the reference wave set is compared to a $J^P = \frac{1}{2}^-, \frac{5}{2}^-, \frac{5}{2}^+$(fit #109) wave set. Plot (B) compares the reference wave set to a fit containing $J^P = \frac{1}{2}^-, \frac{5}{2}^-, \frac{7}{2}^+$(fit #110). Plot (C) compares the reference wave set to a wave set containing the $J^P = \frac{1}{2}^-, \frac{3}{2}^-, \frac{5}{2}^-$(fit #111) partial waves. On the whole the ability of the fit to describe the data is improved with an additional partial wave. All three of the fits compared here contain an extra partial wave in comparison to the reference fit. These additional partial waves allow for a better description of the data. Given the similarities of the results, there is no obvious way to tell which of the three is preferred, except that the addition of a positive-parity wave improves the fit more that a negative-parity wave. Although, the improvement in the likelihood appears to be of a larger scale when a positive parity wave is added. It is clear that around $W = 2150MeV$ an additional partial wave is required beyond the simple set of $J^P = \frac{1}{2}^-, \frac{5}{2}^-$.

Plots of the $\Delta(-ln(\mathcal{L}))$ as a function of center-of-mass energy are an important tool in the process of evaluating which partial waves are required to describe the data being analyzed. The η' analysis here has shown that some partial waves are very important, while other appear to not add much to the fits description of the data.

There are several conclusions which can be drawn from this exercise as a whole. First, the threshold region in W absolutely requires the $J^P = \frac{1}{2}^-$ partial wave. This is not a surprising conclusion as the result was similar in the η analysis. Additionally, very near threshold there is not much energy available to create a high-spin object.

Second, the inclusion of the $J^P = \frac{5}{2}^-$ appears to improve the fit, particularly above $W = 2300$ MeV. When removed from a set of partial waves there is a considerable effect on the likelihood of the fit. With the addition of this partial wave, a base set of waves can be constructed, which will now include: $J^P = \frac{1}{2}^-, \frac{5}{2}^-$. As the plots shown in Figure 6.11 indicate however, this is insufficient for fully describing the data.

Third, the effect of including the $J^P = \frac{3}{2}^+$ improves the likelihood in the $W = 2100 \rightarrow 2200$ MeV region. Other waves appear to have mocked-up the effect of this wave in different fits, but the $J^P = \frac{3}{2}^+$ appears to consistently improve the fit. The possible inclusion of the negative parity $J = \frac{3}{2}$ appeared to be a possibility from some of the likelihood difference plots. There was a simple test of this possibility presented in Figure 6.9(B) which clearly indicated a preference for the positive parity $J^P = \frac{3}{2}^+$ wave. Adding the $J^P = \frac{3}{2}^+$ partial wave, increases the base wave set to three partial waves: $J^P = \frac{1}{2}^-, \frac{3}{2}^+, \frac{5}{2}^-$.

Fourth, as plots (C) and (D) in Figure 6.7 indicate, there is a small, possibly negligible, benefit in the likelihood if a higher-spin positive parity wave is included in the fit. Specifically the $J^P = \frac{7}{2}^+$ appears to have a slight advantage over the $J^P = \frac{5}{2}^+$ partial wave. While plots of the likelihood differences may hint at the inclusion of a higher-spin positive parity wave, it is a relatively small change in likelihood and as such it is prudent to maintain the base set of three waves: $J^P = \frac{1}{2}^-, \frac{3}{2}^+, \frac{5}{2}^-$. The addition of these higher spin waves will be studied further to determine if what, if any, structure exists.

There are three fits which will be studied further for the η' analysis. Given the clear indications to include the base set of three waves, the fit containing the $J^P = \frac{1}{2}^-, \frac{3}{2}^+, \frac{5}{2}^-$(fit #101) waves will be given further study. Likewise, the fits containing $J^P = \frac{1}{2}^-, \frac{3}{2}^+, \frac{5}{2}^-, \frac{5}{2}^+$(fit #104) or $J^P = \frac{1}{2}^-, \frac{3}{2}^+, \frac{5}{2}^-, \frac{7}{2}^+$(fit #105) will warrant further scrutiny.

It is important to note that this set of partial waves was determined from looking at the results of fits run on the η' only. The fact that some of the same wave sets were selected for further scrutiny in the η and η' analysis is consistent with the assumption that the partial waves of a particular J^P which couple to $N\eta$ also couple to $N\eta'$. This appears to be somewhat in question however, as the influence of the $J^P = \frac{3}{2}^+$ wave appears much more obviously in the $N\eta'$ than in the $N\eta$.

6.4 Parity Chain Determination

One of the interesting features of the formalism which was used for this analysis, is that the kinematics are built into the amplitudes for the purposes of fitting. This allows for one partial wave to be distinguished from another seemingly identical partial wave. Consider, as an example, the $J^P = \frac{1}{2}^-$ and $J^P = \frac{1}{2}^+$ partial waves. For a given photon energy these two partial waves produce identical angular distributions, but in this analysis the data has been binned as a function of W. The assumption would ordinarily be that the physics does not change considerably over the $10MeV$ width of the majority of the bins. This assumption is not quite true for kinematics of the amplitudes. The energy varies enough over the range of W in the bin, that the amplitudes are slightly different and thus the fit prefers the state which allows a lower energy. The positive parity partial wave is an $L = 1$ state, while the negative parity wave is a $L = 0$ state. This difference in L provides a kinematic difference between the two waves which allows for the determination of a preference in the fit. As is shown in Figure 6.3(C), the fit prefers the negative parity state at threshold to the positive parity wave. It has been suggested that this effect is principally caused by the fact that no W dependence is included in the propagator when fitting. The investigation of this possibility is relegated to future work.

6.5 Comparison of η Fit Results to Data in $\cos(\theta_{CM})$

While a detailed and systematic analysis of the $\Delta(-ln(\mathcal{L}))$ plots may aid in determining which partial waves help most in describing the data, the question remains how well the fit is actually describing the data. This analysis has only one angle of interest, and as such can be subjected to a standard chi-square test to determine how closely the fit and the data match. The results of this check will be presented in this section for the η using the $J^P = \frac{1}{2}^-, \frac{3}{2}^+, \frac{5}{2}^-$ wave set in the fit. Displayed in alternating figures will be the histograms of the data events, the accepted Monte Carlo events, and the accepted Monte Carlo events weighted by the fit results. For each set of these histograms, a plot of the χ^2 for each bin as a function of $cos(\theta_{CM})$ of the η meson is presented. The Monte Carlo histograms have been scaled down to match the integral of the data histogram. The accepted Monte Carlo histogram is shown in gray criss-cross markers, and it indicates what phase space would look like in the data. The red open-diamonds is the accepted Monte Carlo weighted by the fit results. If the fit is a good representation of the data, then the weighted accepted Monte Carlo should line-up with the data. The data is reported in black. Figures 6.12 to 6.37 present these comparison plots. Each page contains the data and fit results for six bins, followed by a plot of the χ^2 for each of those six bins.

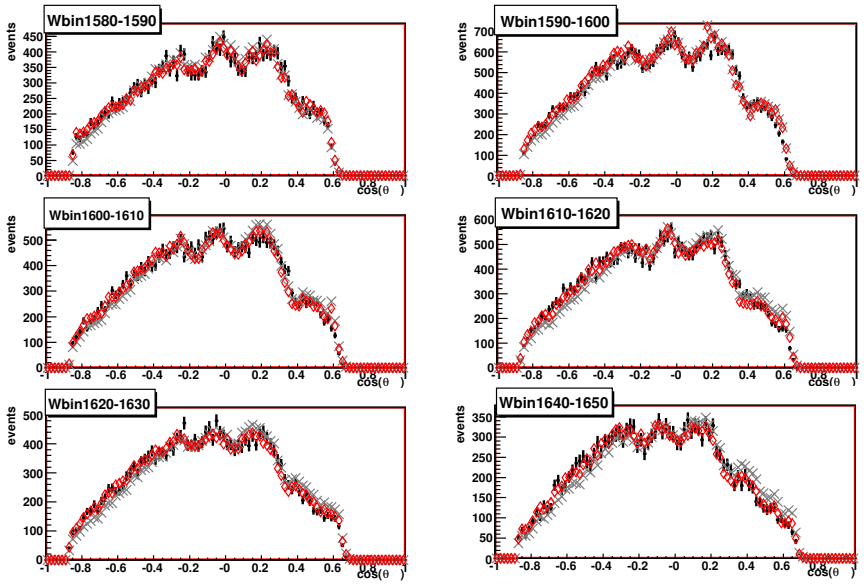

Figure 6.12: Plot to compare η fit results with data as a function of $\cos(\theta_{CM})$. The black points are the data events, the grey criss-cross markers represent the accepted Monte Carlo, and the red open diamonds is the accepted Monte Carlo weighted by the fit results.

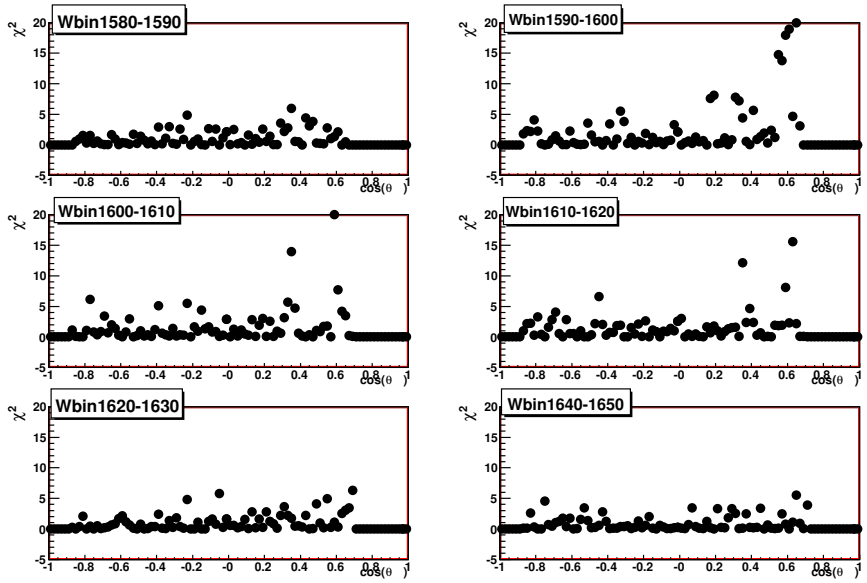

Figure 6.13: Plot of the χ^2 as a function of $\cos(\theta_{CM})$ for the η fits shown in Figure 6.12. As was evident in the comparisons of the event distributions, the χ^2 is low indicating that the fit is reproducing the data.

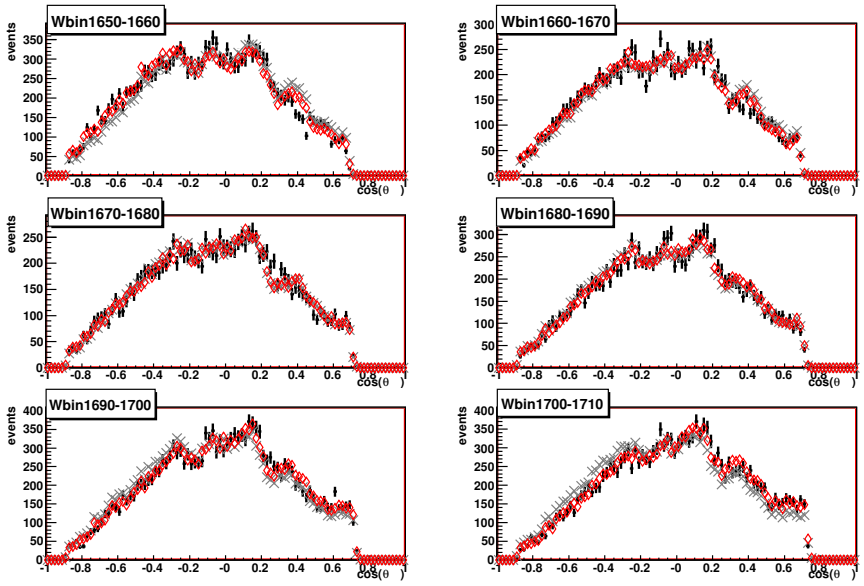

Figure 6.14: Plot to compare η fit results with data as a function of $\cos(\theta_{CM})$. The black points are the data events, the grey criss-cross markers represent the accepted Monte Carlo, and the red open diamonds is the accepted Monte Carlo weighted by the fit results.

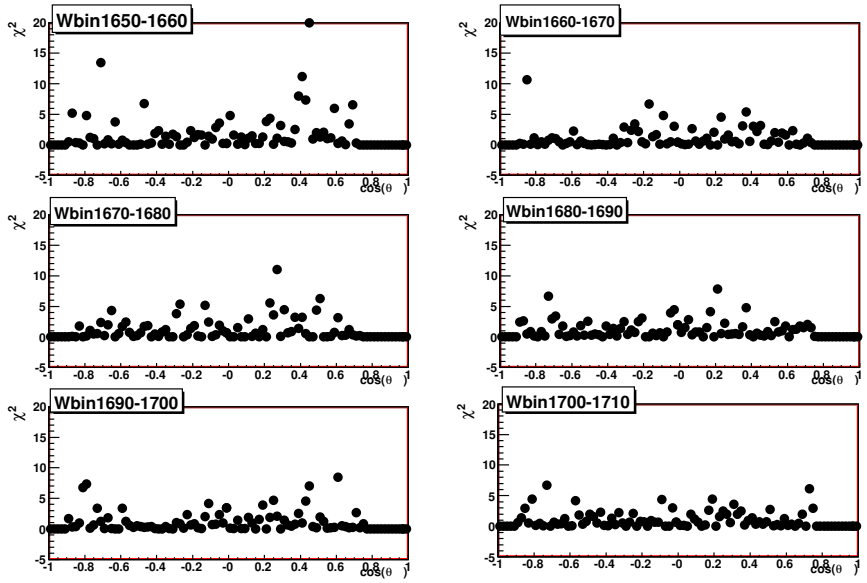

Figure 6.15: Plot of the χ^2 as a function of $\cos(\theta_{CM})$ for the η fits shown in Figure 6.14. As was evident in the comparisons of the event distributions, the χ^2 is low indicating that the fit is reproducing the data.

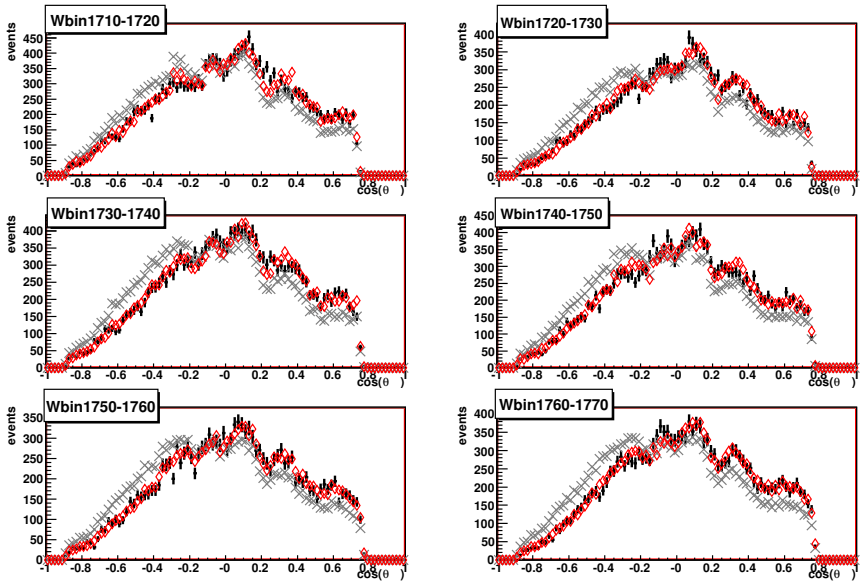

Figure 6.16: Plot to compare η fit results with data as a function of $\cos(\theta_{CM})$. The black points are the data events, the grey criss-cross markers represent the accepted Monte Carlo, and the red open diamonds is the accepted Monte Carlo weighted by the fit results.

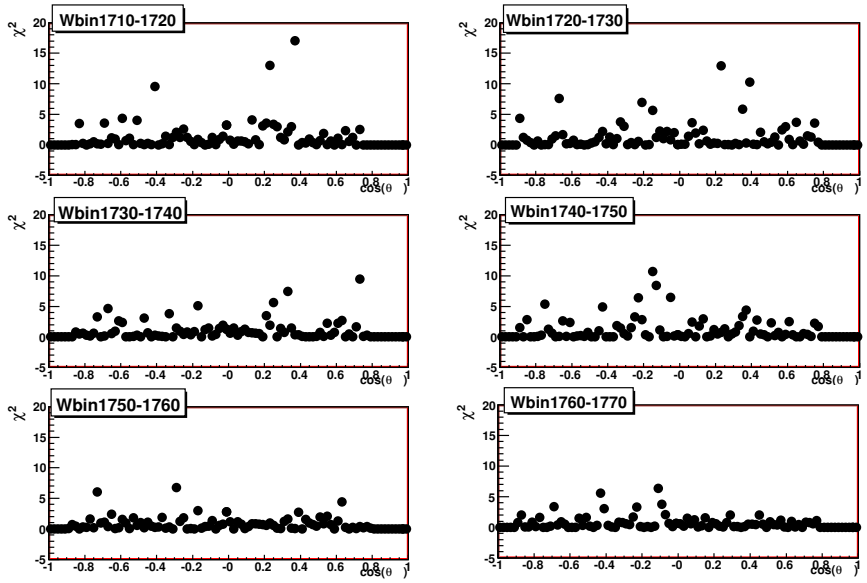

Figure 6.17: Plot of the χ^2 as a function of $\cos(\theta_{CM})$ for the η fits shown in Figure 6.16. As was evident in the comparisons of the event distributions, the χ^2 is low indicating that the fit is reproducing the data.

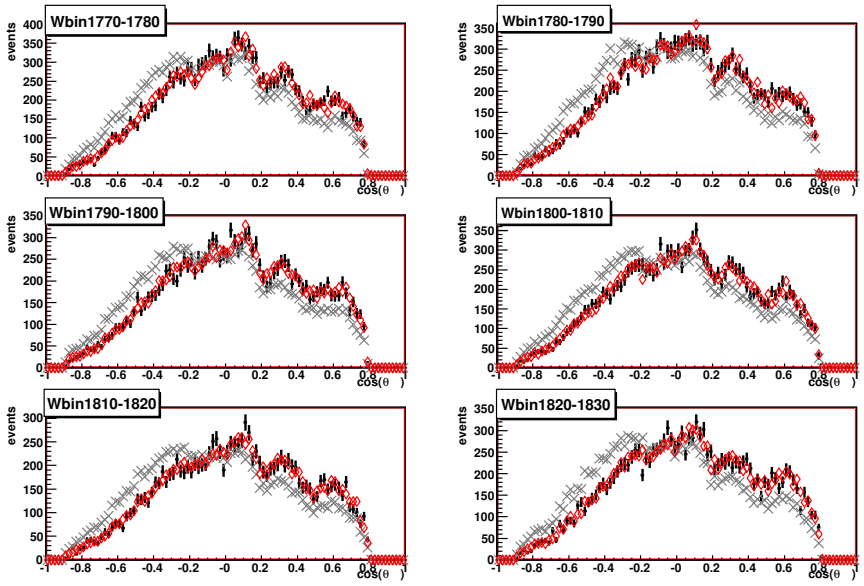

Figure 6.18: Plot to compare η fit results with data as a function of $\cos(\theta_{CM})$. The black points are the data events, the grey criss-cross markers represent the accepted Monte Carlo, and the red open diamonds is the accepted Monte Carlo weighted by the fit results.

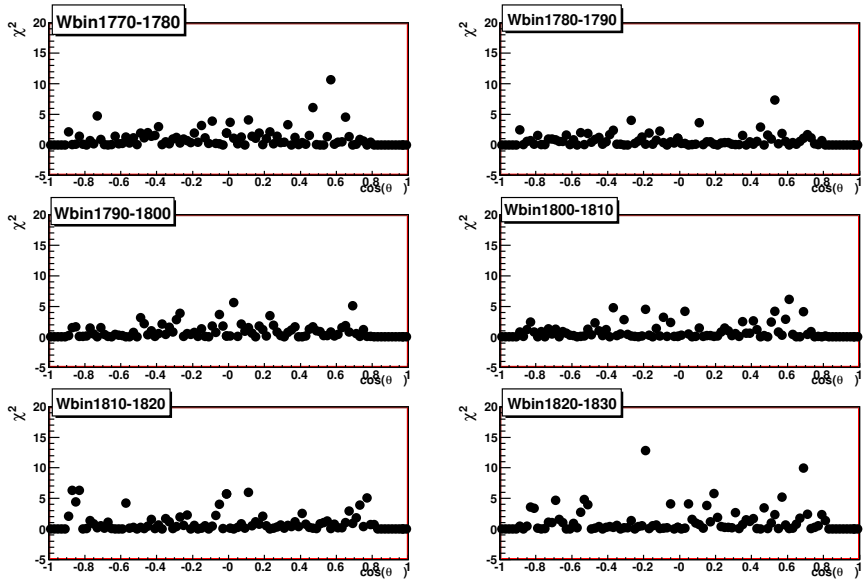

Figure 6.19: Plot of the χ^2 as a function of $\cos(\theta_{CM})$ for the η fits shown in Figure 6.18. As was evident in the comparisons of the event distributions, the χ^2 is low indicating that the fit is reproducing the data.

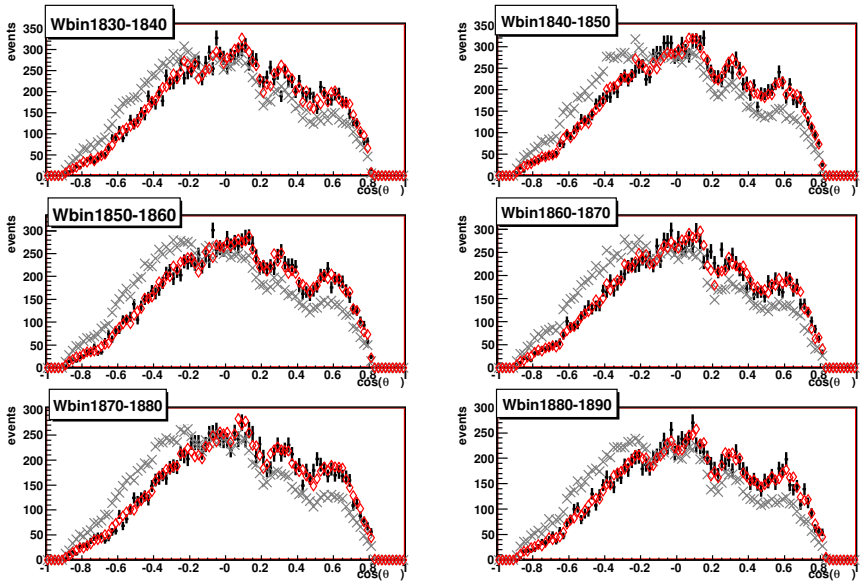

Figure 6.20: Plot to compare η fit results with data as a function of $\cos(\theta_{CM})$. The black points are the data events, the grey criss-cross markers represent the accepted Monte Carlo, and the red open diamonds is the accepted Monte Carlo weighted by the fit results.

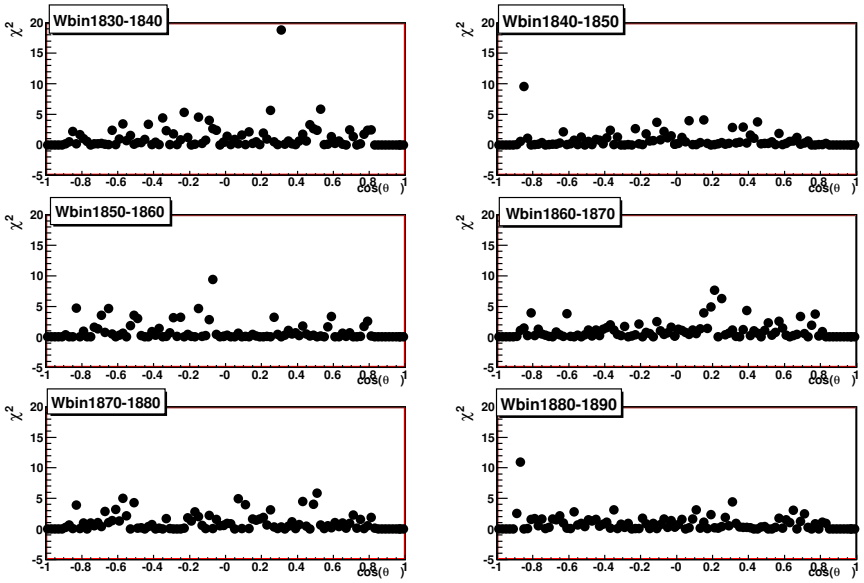

Figure 6.21: Plot of the χ^2 as a function of $\cos(\theta_{CM})$ for the η fits shown in Figure 6.20. As was evident in the comparisons of the event distributions, the χ^2 is low indicating that the fit is reproducing the data.

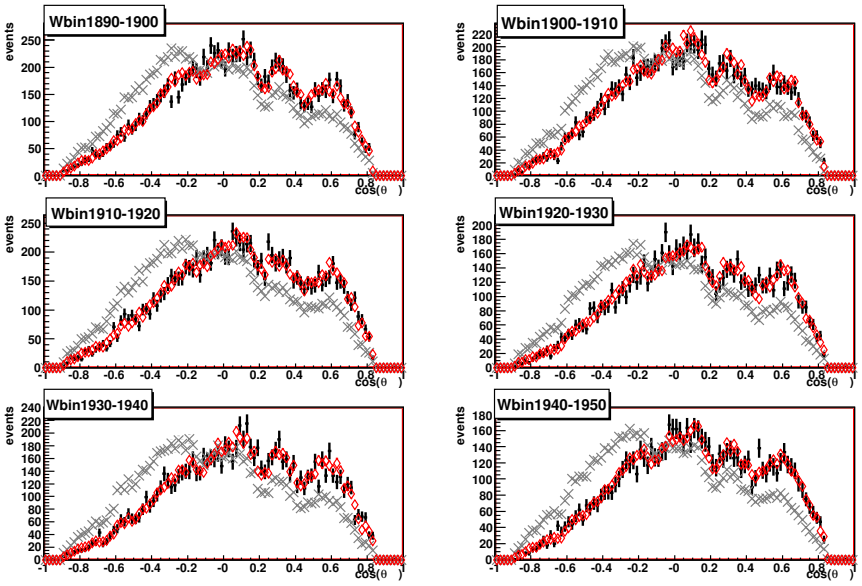

Figure 6.22: Plot to compare η fit results with data as a function of $\cos(\theta_{CM})$. The black points are the data events, the grey criss-cross markers represent the accepted Monte Carlo, and the red open diamonds is the accepted Monte Carlo weighted by the fit results.

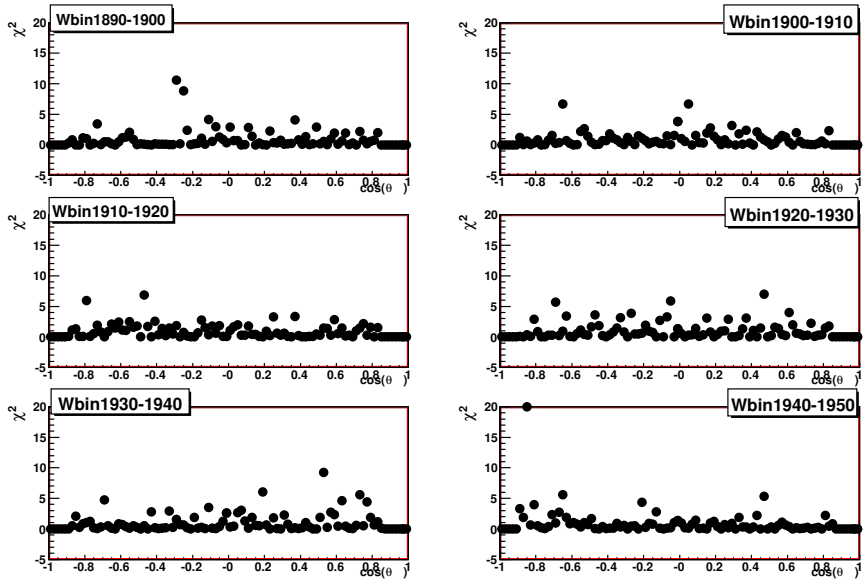

Figure 6.23: Plot of the χ^2 as a function of $\cos(\theta_{CM})$ for the η fits shown in Figure 6.22. As was evident in the comparisons of the event distributions, the χ^2 is low indicating that the fit is reproducing the data.

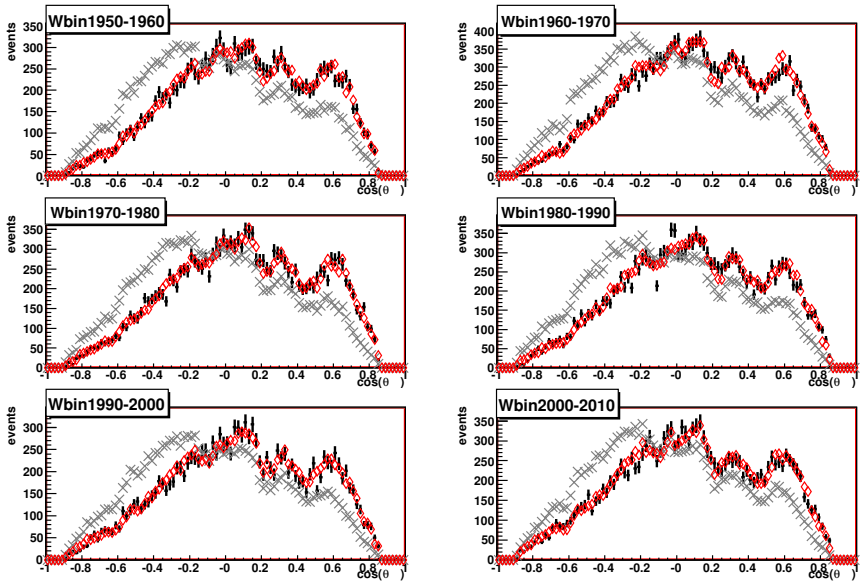

Figure 6.24: Plot to compare η fit results with data as a function of $\cos(\theta_{CM})$. The black points are the data events, the grey criss-cross markers represent the accepted Monte Carlo, and the red open diamonds is the accepted Monte Carlo weighted by the fit results.

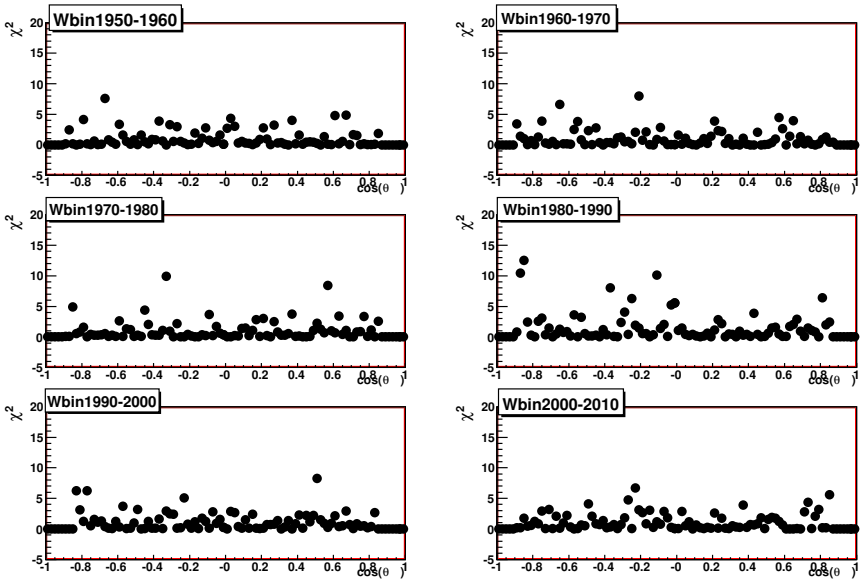

Figure 6.25: Plot of the χ^2 as a function of $\cos(\theta_{CM})$ for the η fits shown in Figure 6.24. As was evident in the comparisons of the event distributions, the χ^2 is low indicating that the fit is reproducing the data.

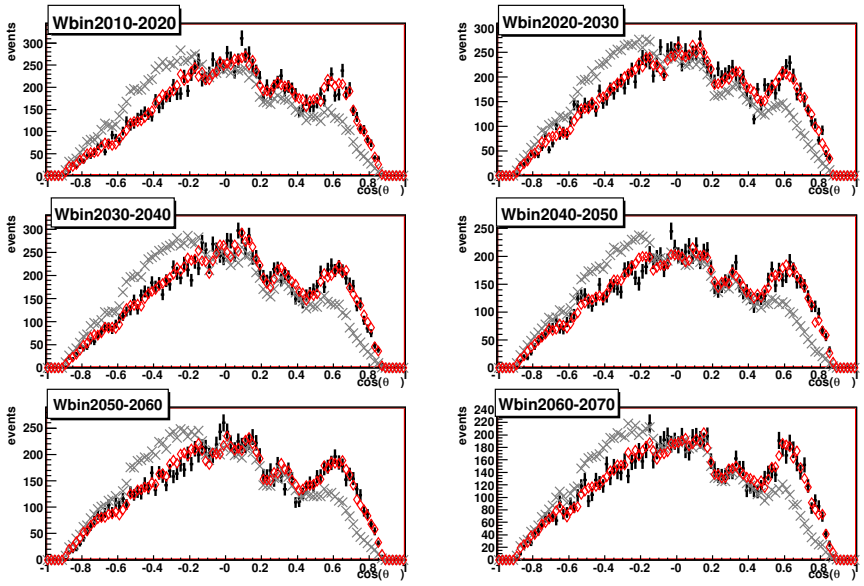

Figure 6.26: Plot to compare η fit results with data as a function of $\cos(\theta_{CM})$. The black points are the data events, the grey criss-cross markers represent the accepted Monte Carlo, and the red open diamonds is the accepted Monte Carlo weighted by the fit results.

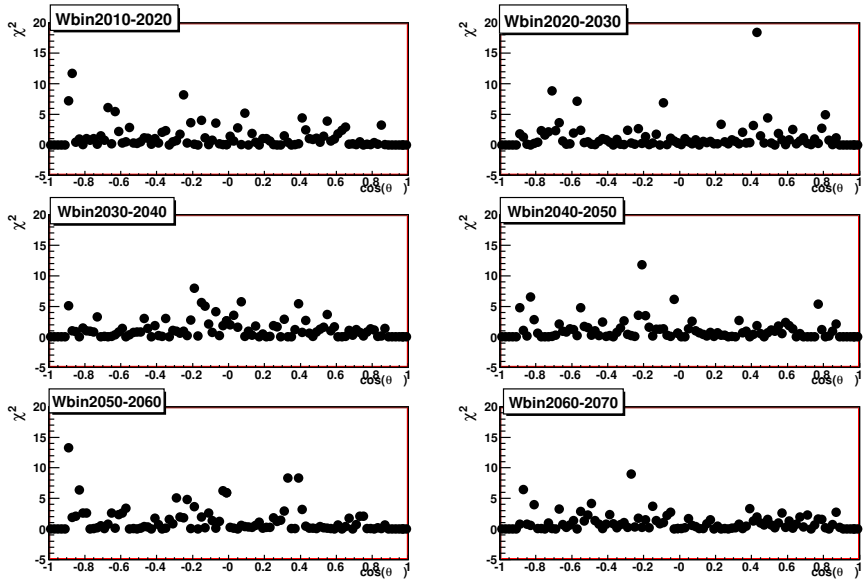

Figure 6.27: Plot of the χ^2 as a function of $\cos(\theta_{CM})$ for the η fits shown in Figure 6.26. As was evident in the comparisons of the event distributions, the χ^2 is low indicating that the fit is reproducing the data.

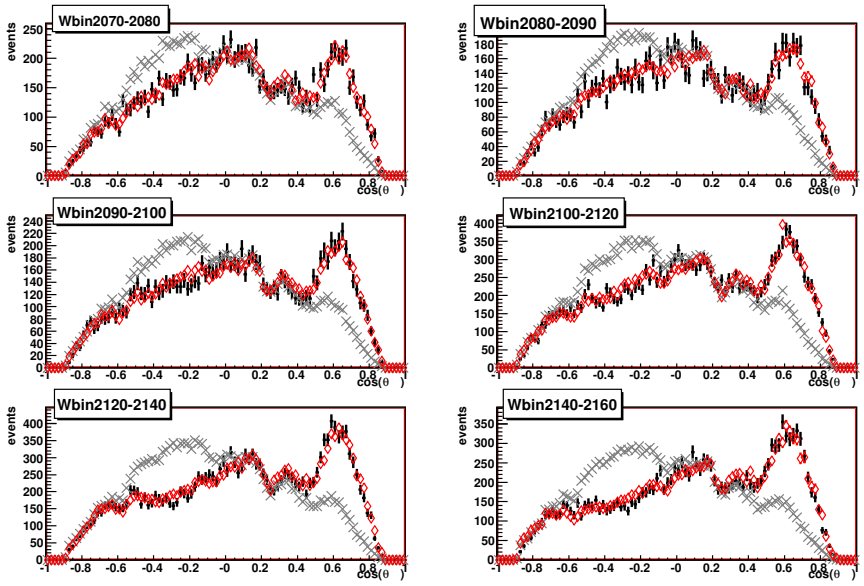

Figure 6.28: Plot to compare η fit results with data as a function of $\cos(\theta_{CM})$. The black points are the data events, the grey criss-cross markers represent the accepted Monte Carlo, and the red open diamonds is the accepted Monte Carlo weighted by the fit results.

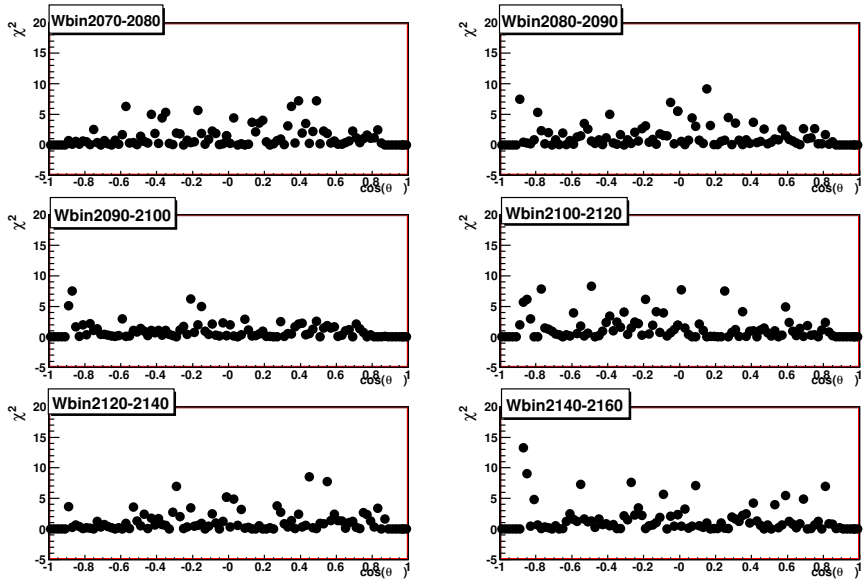

Figure 6.29: Plot of the χ^2 as a function of $\cos(\theta_{CM})$ for the η fits shown in Figure 6.29. As was evident in the comparisons of the event distributions, the χ^2 is low indicating that the fit is reproducing the data.

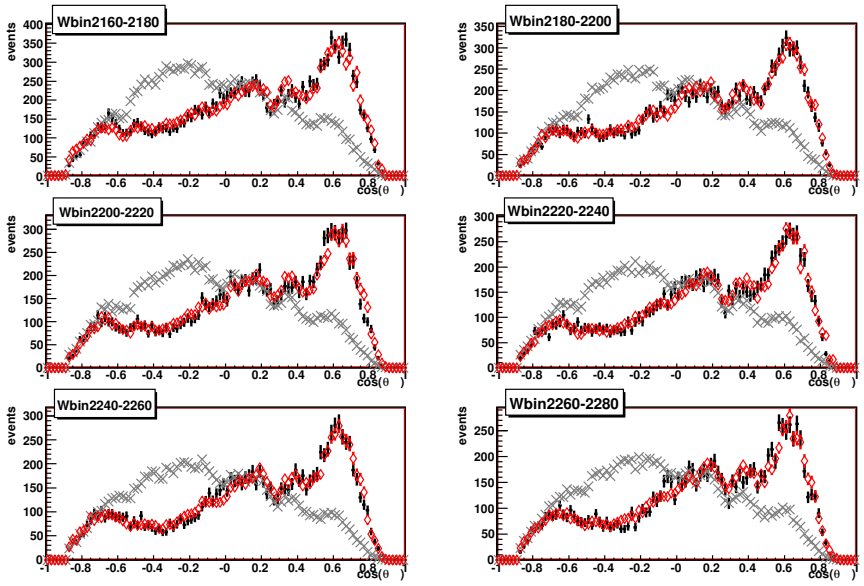

Figure 6.30: Plot to compare η fit results with data as a function of $\cos(\theta_{CM})$. The black points are the data events, the grey criss-cross markers represent the accepted Monte Carlo, and the red open diamonds is the accepted Monte Carlo weighted by the fit results.

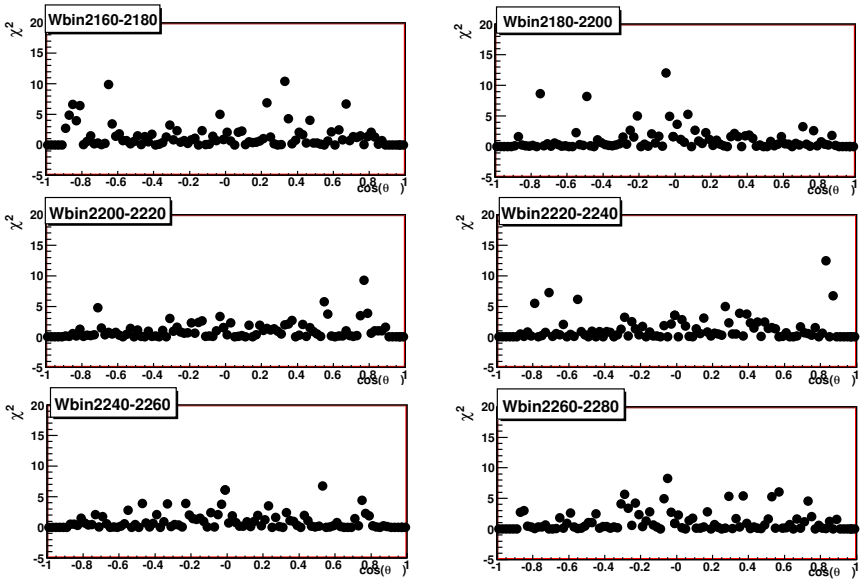

Figure 6.31: Plot of the χ^2 as a function of $\cos(\theta_{CM})$ for the η fits shown in Figure 6.30. As was evident in the comparisons of the event distributions, the χ^2 is low indicating that the fit is reproducing the data.

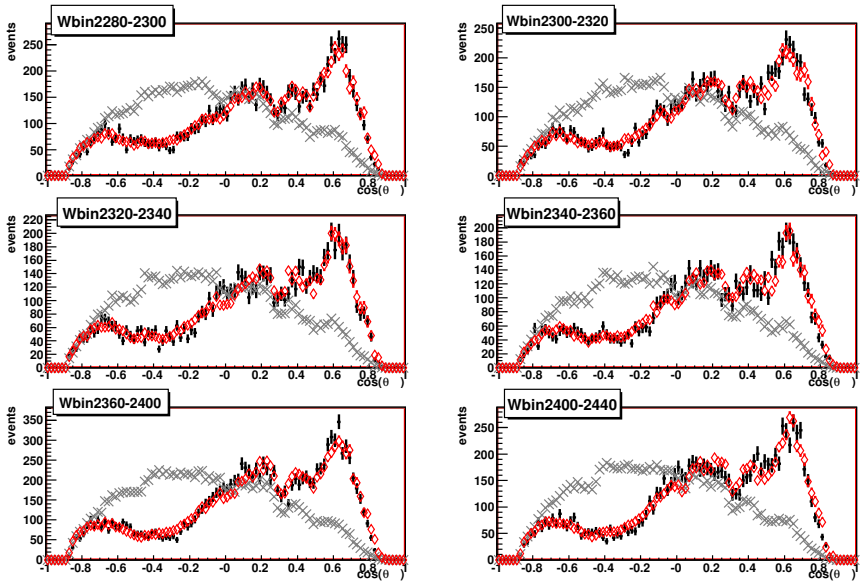

Figure 6.32: Plot to compare η fit results with data as a function of $\cos(\theta_{CM})$. The black points are the data events, the grey criss-cross markers represent the accepted Monte Carlo, and the red open diamonds is the accepted Monte Carlo weighted by the fit results.

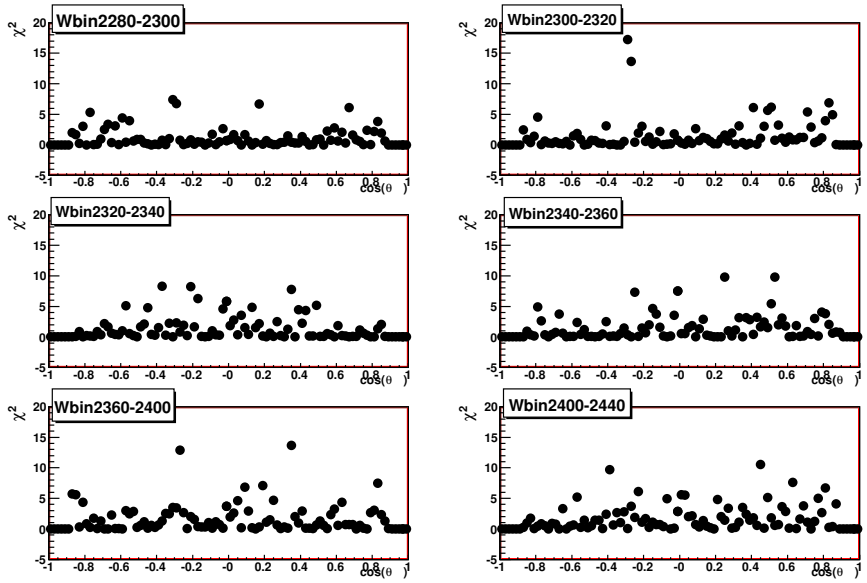

Figure 6.33: Plot of the χ^2 as a function of $\cos(\theta_{CM})$ for the η fits shown in Figure 6.32. As was evident in the comparisons of the event distributions, the χ^2 is low indicating that the fit is reproducing the data.

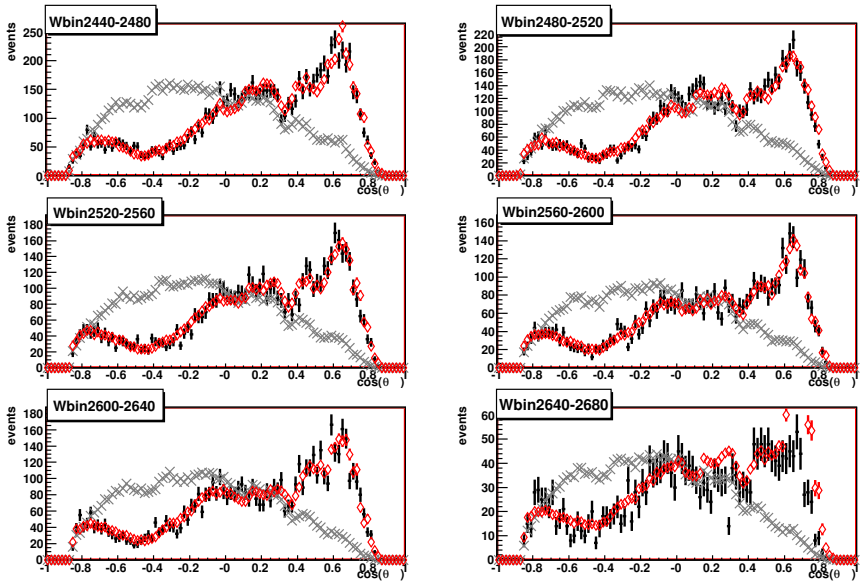

Figure 6.34: Plot to compare η fit results with data as a function of $\cos(\theta_{CM})$. The black points are the data events, the grey criss-cross markers represent the accepted Monte Carlo, and the red open diamonds is the accepted Monte Carlo weighted by the fit results. Plots are shown here for $2440 < W < 2680$ MeV.

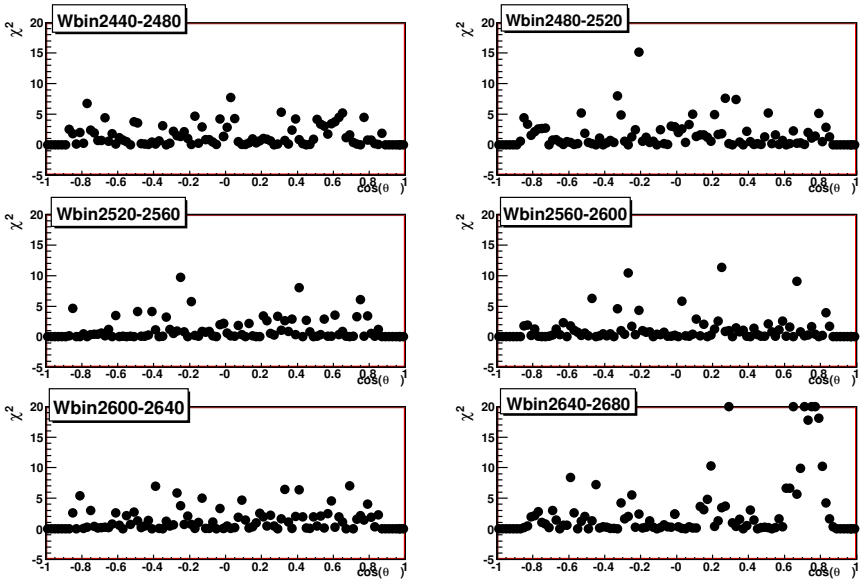

Figure 6.35: Plot of the χ^2 as a function of $\cos(\theta_{CM})$ for the η fits shown in Figure 6.34. As was evident in the comparisons of the event distributions, the χ^2 is low indicating that the fit is reproducing the data.

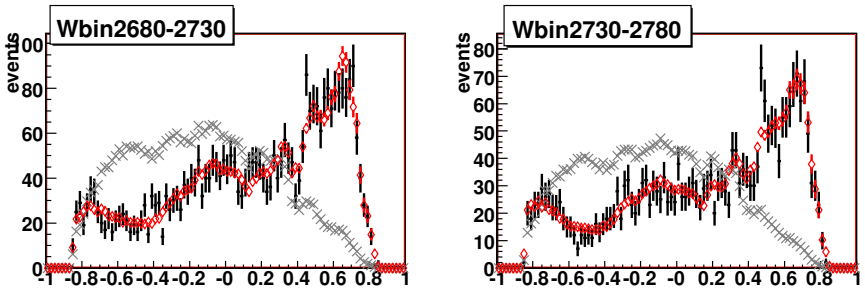

Figure 6.36: Plot to compare η fit results with data as a function of cos(θ_{CM}). The black points are the data events, the grey criss-cross markers represent the accepted Monte Carlo, and the red open diamonds is the accepted Monte Carlo weighted by the fit results. Plots are shown here for $2680 < W < 2780$ MeV.

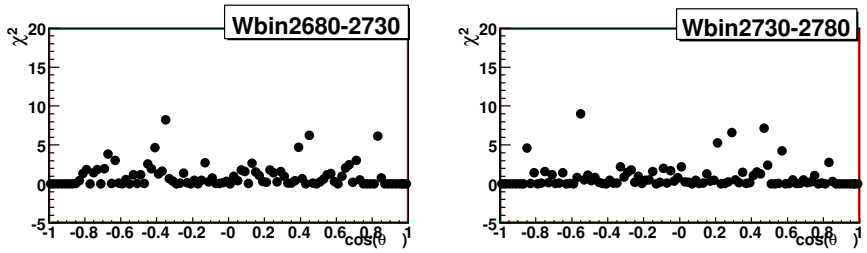

Figure 6.37: Plot of the χ^2 as a function of cos(θ_{CM}) for the η fits shown in Figure 6.36. As was evident in the comparisons of the event distributions, the χ^2 is low indicating that the fit is reproducing the data.

In general, the fit to the η using a relatively modest three partial wave set (containing $J^P = \frac{1}{2}^-, \frac{3}{2}^+, \frac{5}{2}^-$) appears to do a reasonable job describing the data. It is interesting to note the similarities between the accepted phase space Monte Carlo and the data at low W. Clearly at low W a partial wave with a "flat" angular distributions should describe the data well, which has been indicated by the preference of a $J^P = \frac{1}{2}^-$ partial wave in this region.

It is important to note that the calculated χ^2 is only relevant within the region where data is present. The very forward and backward angular bins contain no events, and as such the χ^2 results for these bins are not meaningful. Beyond the bins at the very edges, the agreement across most of the angular region is good.

Areas of discrepancy between the fit and the data typically appear near the very edges of acceptance, or near the location of a paddle cut. These paddle cuts are indicated by an abrupt drop in the event in a relatively small in range. For example, the saw-tooth like pattern present in the low W plots in Figure 6.12 in the middle of the angular distribution.

In the higher W region, for example Figure 6.32, the data is reproduced very well by the fit. Note the significant difference in the higher W region between the data and the phase space Monte Carlo.

Overall, the data appears to be reproduced well by this particular fit. Adding partial waves to this fit has been shown to be beneficial in some regions of W, but clearly a significant portion of the data is being described well by this three-wave fit.

6.6 Intensities and Phases of Best Fits

The difference in $ln(\mathcal{L})$ plots indicate that there are several fits to the η and η' datasets which merit further study. To determine if any resonance structure is present, plots of the modulus and phases of the complex number which serves as the propagator for the s-channel amplitudes are constructed. The modulus information for each partial wave is displayed as a function of W, and should map out a Breit-Wigner resonance shape if there is one present. The phase information is used in plots of the phase differences from one partial wave to another. In this section a brief overview of what resonance structures might look like will be presented. With an understanding of what the phase differences and modulus plots might look like, PWA results will be presented for both Nη and Nη' reaction channels.

6.6.1 Resonance Structure

Prior to looking at the results of the fits themselves, it is important to consider the results in an ideal case. Nominally, this means constructing two Breit-Wigner resonances with differing masses and widths, and seeing how the modulus and phase difference plots should look. This is a purely mathematical exercise, as there is no background and only two resonances with different J^Ps are included in this example. It is instructive however to consider what the plots might look like prior to seeing the experimental results. Insight can be gained by altering some of the available variables in this exercise. For example, resonances which are further apart, and thus less interfering, will have a significantly different phase difference plot than two resonances which appear very near to one another. The width of one or both of the resonances can be altered to observe the effect on the phase difference plot.

Figure 6.38 demonstrates the structure associated with two Breit-Wigner resonances a significant distance apart. When defining what is significant in terms of their separation, the natural scale to use is the widths of the resonances themselves. In the figure, there is a clear separation of the peaks of the resonances. Extraction of these resonances on the basis of the strength of the peak would be relatively straightforward in this case. The plot of the phase difference between the two resonances would also be a simple matter in the ideal case. Unfortunately, the ideal case is not typically found

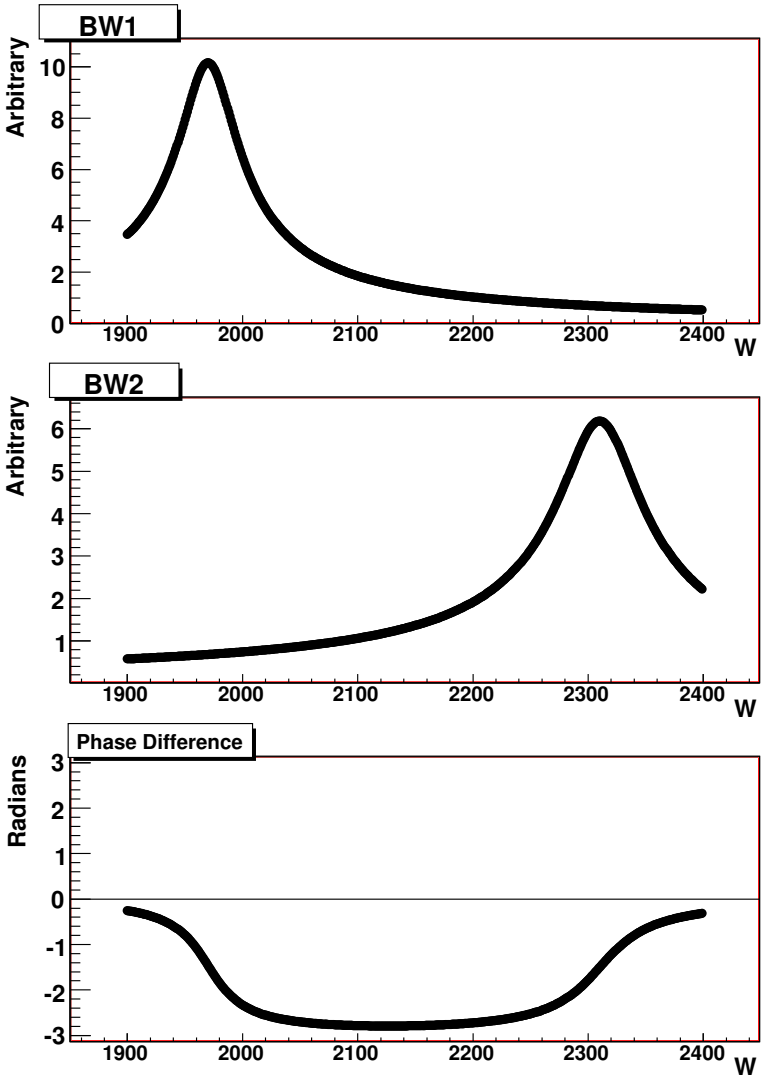

Figure 6.38: Two Breit-Wigner resonances of width $approx 90$ MeV separated by ≈ 300 MeV. The resonances are well separated for their width, and can be extracted through the modulus information in a straightforward way. The phase difference plot appears to clearly indicate the resonances present. In practice, this is not necessarily the case for widely separated resonances.

in nature, and the 'idea phase difference plot can only offer a hint at what structures may exist in the data. When two resonances are significantly separated, then their interference is not as strong and the phase difference is less well defined, and therefore more difficult to fit.

Figure 6.39 displays the structure associated with two Breit-Wigner resonances that are separated by a distance of similar order to their width. At similar order to the widths, the maximal interference appears in the phase difference plot, and the there is still reasonable separation of the strengths of the resonances structures.

Figure 6.40 demonstrates a complicated problem where two resonance states are lying very close to one another, within the width of the resonance. Note that the phase difference plot is considerably diminished in the detail it displays. The peaks are very near to one another, and difficult to separate.

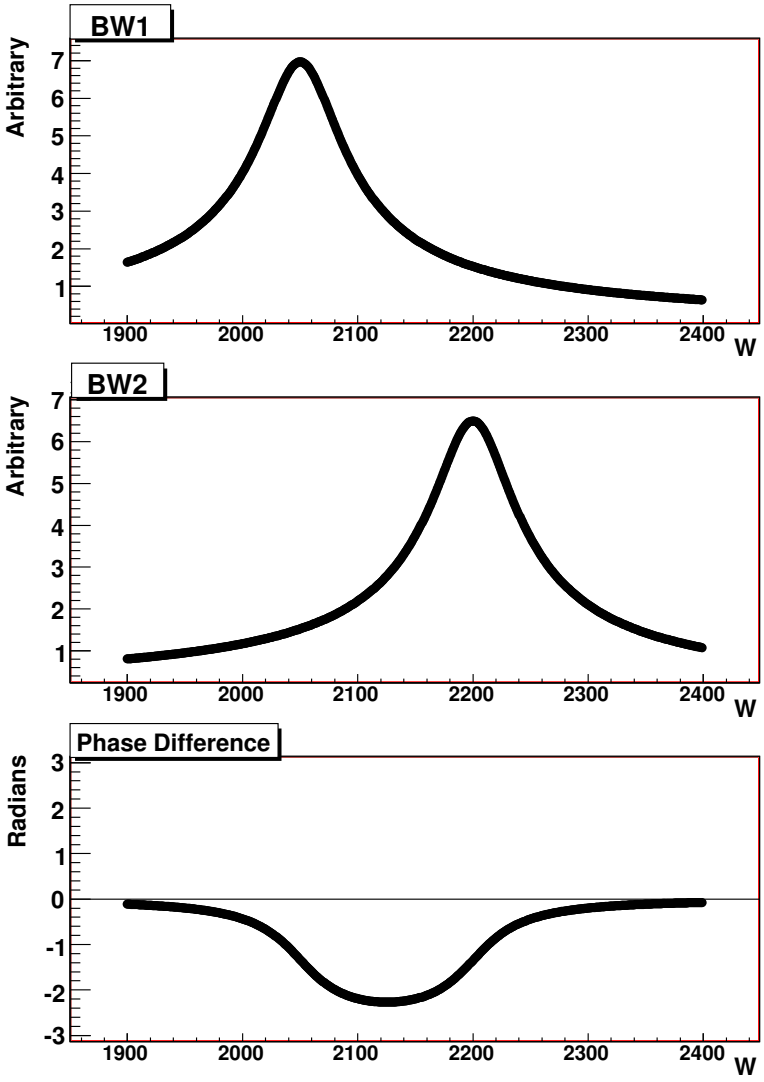

Figure 6.39: Two Breit-Wigner resonances of width $\approx$ 90 MeV separated by $\approx 150 MeV$. The modulus of the resonances appear well separated, and the phase difference passes from $0 \rightarrow -\pi \rightarrow 0$.

Together the strengths and phase difference might allow for the two resonances to be separated, and their properties to be determined.

While the idealized results are instructive, there is a question as to whether the phase difference between two partial waves is well defined in areas which are "far" from the two resonances. In practice, phase differences are well defined in regions where resonances overlap. In regions where there is almost no overlap, or no overlap at all, then the phase difference is not considered to be well defined. Still, the ideal case has allowed for a description of what might be seen in the PWA yield and phase difference results from this analysis. Clearly, the idea of the PWA fit results appearing exactly as the 'ideal case is absurd, but the general structures and shapes which have been shown in Figures 6.38 to 6.40 may still appear in the PWA results.

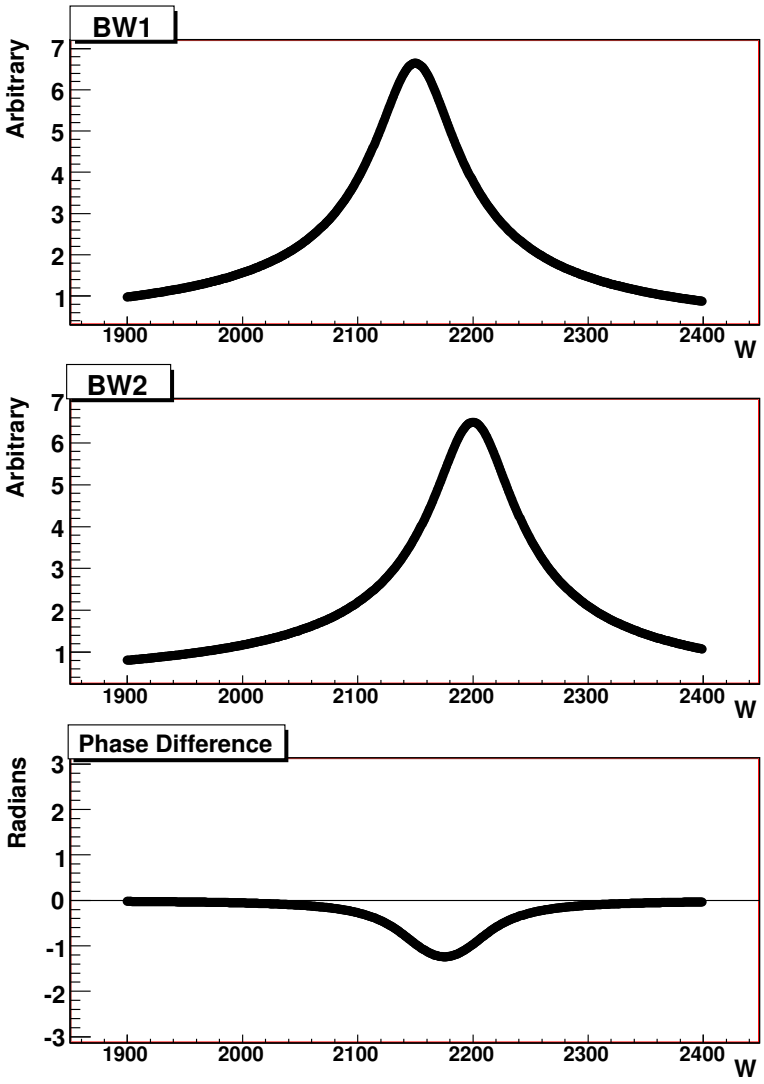

Figure 6.40: Two Breit-Wigner resonances of width $\approx$ 90 MeV separated by $\approx 50 MeV$ in mass are compared. When two resonances are so closely spaced, the phase difference grows smaller, making it more difficult to extract the resonances parameters.

6.6.2 η PWA Results

The PWA results for $\gamma p \to N^* \to p\eta$ will be reported here for a selected subset of fits. As a reminder, the fits which will be further scrutinized for η photoproduction are Fits #001, #004, #005, #009, and #010. In general, the modulus of the complex valued propagator which was determined in the fit for a particular partial wave will be used, along with kinematic factors to produce a yield for a particular partial wave. This yield will be plotted as a function of center of mass energy, W. Additionally, the phase difference between two partial waves will be plotted as a function of W. The results will be presented fit by fit.

The errors on these plots come directly from Minuit, and clearly appear to be underestimated given the spread and variation in the fit results from bin to bin. The wild variation of the points is discussed in Section 6.6.3. Beyond the actual values of the results, the errors are clearly correlated, and those correlations must be taken into account properly for the errors to be meaningful. However, at this point the larger problem is with the stability of the fit, and without a proper resolution to that issue, the errors presented in the PWA results will remain unphysical.

$J^P = \frac{1}{2}^-, \frac{3}{2}^+, \frac{5}{2}^-$ (fit #001)

Results from a PWA fit containing the wave set: $J^P = \frac{1}{2}^-, \frac{3}{2}^+, \frac{5}{2}^-$ (fit #001) will be presented here. This set of partial waves was influenced by previous results from Anisovich[8].

Perhaps the most obvious structure in all of the fits run on the η dataset, is the $J^P = \frac{1}{2}^-$ partial wave at low W near threshold. There is a very well known resonance which couples very strongly to $N\eta$ in this region called the $S_{11}(1535)$. Unfortunately, the dataset which is the base of this analysis does not contain photons of low enough energy to map out the whole threshold region. This means that only the high energy side of the resonance can be observed in this analysis. In 6.41 a plot of the modulus of the complex fit parameter is presented. The falling edge of the peak in this plot was fit to determine a mass of ≈ 1585 MeV with a width of ≈ 87 MeV. While the peak position is within the width of the $S_{11}(1535)$, the width is well off from the known value of ≈ 140 MeV. The determination of the mass and width of this resonance is severely limited by only fitting one half of the peak. The known mass and width of the $S_{11}(1535)$ resonance were tried, to determine how closely the fit results lined up with the known values. Unfortunately, the fit was not very good, most likely due to presence of an additional known resonance, the $S_{11}(1650)$. The $S_{11}(1650)$ is also a $J^P = \frac{1}{2}^-$ resonance which resides within the region of the "peak" and has a known branching fraction to $N\eta$. The strength of the $S_{11}(1650)$ appears to be dwarfed by the strength of the $S_{11}(1535)$, but the existence of the resonance at $W = 1650$ MeV may be another reason for the fit mass to come out higher than that of the $S_{11}(1535)$ mass.

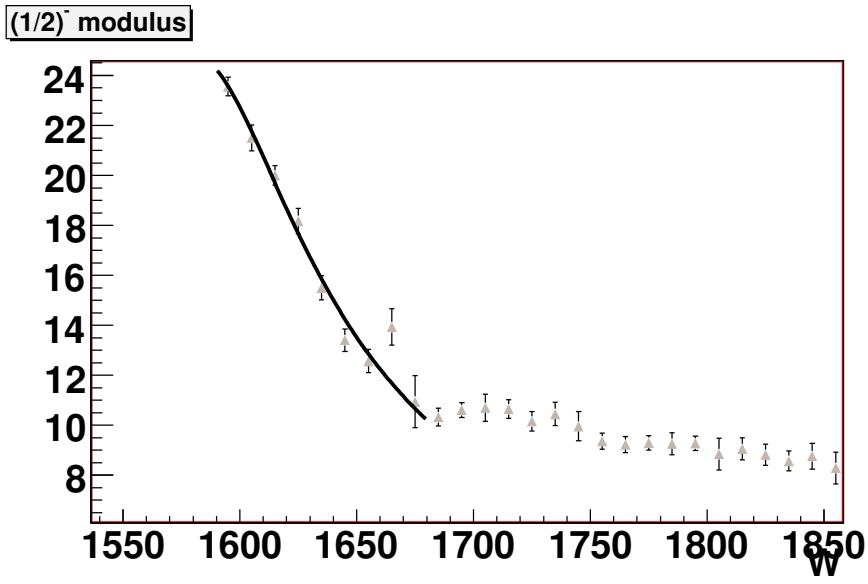

Figure 6.41: Modulus of the $J^P = \frac{1}{2}^-$ partial wave near threshold as seen in a fit with a wave set of $J^P = \frac{1}{2}^-, \frac{3}{2}^+, \frac{5}{2}^-$(fit #001). The fit to the modulus of the peak is indicative of a resonance with a mass at $W = 1585$ MeV with a width of $\Gamma = 87$ MeV. The mass and width are not accurate for either of the individual $J^P = \frac{1}{2}^-$ resonances known to be in this region. The fit suffers from the ability to only fit one side of the peak given the kinematics of the experiment. The horizontal axis is labeled in MeV.

The plots of the results from the partial wave analysis, which follow, are in the following format. Of the three plots for each pair of partial waves, there are plots of the yields of the two partial waves, and a plot of the phase difference between the two partial waves. As the phase difference is an angle, there are ambiguities. The phase difference plots are plotted several times on the same set of axis, with each iteration being separated by adding or subtracting π or 2π. This allows for the trends in the phase differences to be seen. For cases when the phase difference plot becomes too confused when displayed with all of the π and 2π rotations, and in those cases specific choices will be made to determine the appropriate plotting conditions.

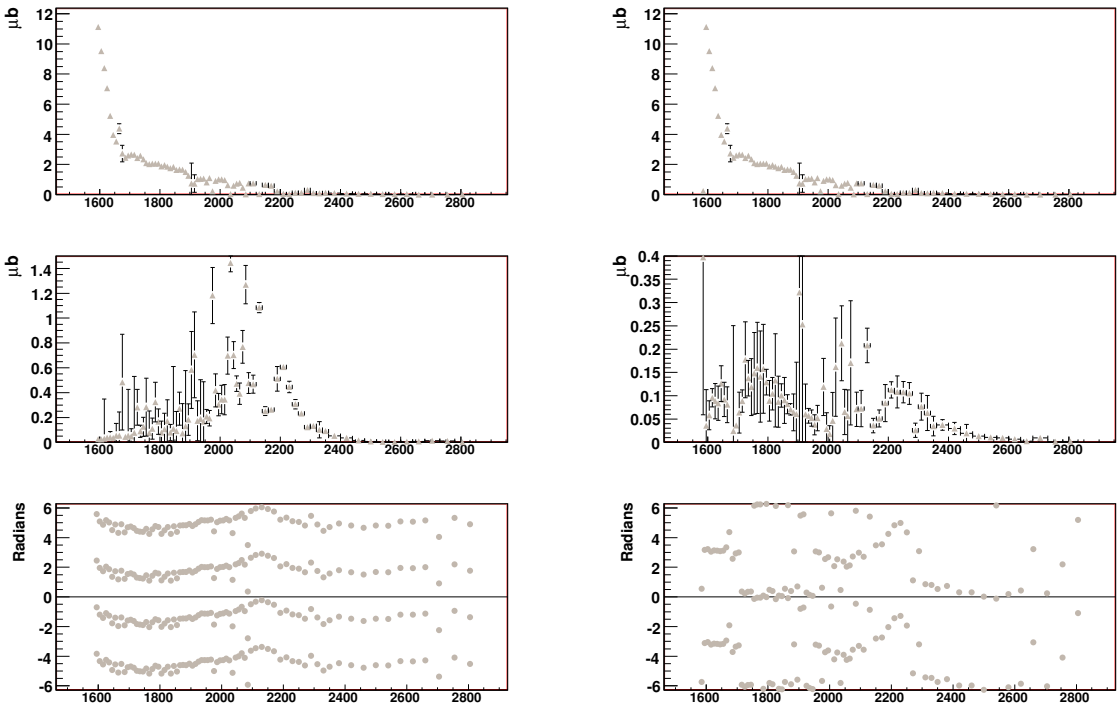

Figure 6.42: PWA results for the η with a fit which contains the $J^P = \frac{1}{2}^-, \frac{3}{2}^+, \frac{5}{2}^-$(fit #001) partial waves. Left: The yields for the $\frac{1}{2}^-$(top) and $\frac{5}{2}^-$(middle) partial waves, along with the phase difference between the two(bottom). The yield of the $\frac{1}{2}^-$ partial waves shows the large contribution at threshold and long tails, while the yield of the $\frac{5}{2}^-$ wave shows strength in the $W = 2000 \rightarrow 2250$ MeV region. Right: The yield for the $\frac{1}{2}^-$(top) and $\frac{3}{2}^+$(middle) partial waves, along with the phase difference between the two waves(bottom). The yield of the $\frac{3}{2}^+$ partial wave shows some strength in the $W = 1800$ MeV and $W = 2200$ MeV regions.

On the left hand side of Figure 6.42 the plots of the yields for the $J^P = \frac{1}{2}^-$(top) and the $J^P = \frac{5}{2}^-$(middle) partial waves are presented for a fit containing the $J^P = \frac{1}{2}^-, \frac{3}{2}^+, \frac{5}{2}^-$(fit #001) partial waves. As previously pointed out, the prominence of the threshold $J^P = \frac{1}{2}^-$ is quite clear. Additionally, the behavior of the $J^P = \frac{5}{2}^-$ partial wave is interesting. The fit effectively turned the $J^P = \frac{5}{2}^-$ wave off until $W \approx 1800 \rightarrow 1900$ MeV, indicating that it does not require that wave to fit the data. The strength of the $J^P = \frac{5}{2}^-$ partial wave appears to peak in the range between

$W \approx 2000 \rightarrow 2200$ MeV. The phase difference(bottom plot) between the two partial waves shows interesting structure in the $W = 2000 \rightarrow 2200$ MeV region. This structure is reminiscent of a phase difference between two resonances which overlap. The overall sign is dependent on the order of the phase difference.

On the right hand side of Figure 6.42 are plots of the yields from the $J^P = \frac{1}{2}^-$(top) and the $J^P = \frac{3}{2}^+$(middle) partial waves. The $J^P = \frac{3}{2}^+$ partial wave appears to show strength around $W = 1800$ MeV, as well as around $W = 2250$ MeV. The plot of the phase difference (bottom plot) between the two wave appears to show interesting motion in the broad region from $W = 1900 \rightarrow 2400$ MeV. The lack of interesting phase motion in the $W = 1800$ MeV region could be caused by two resonance structures which are very close to one another, causing the phase difference plot to be nearly flat.

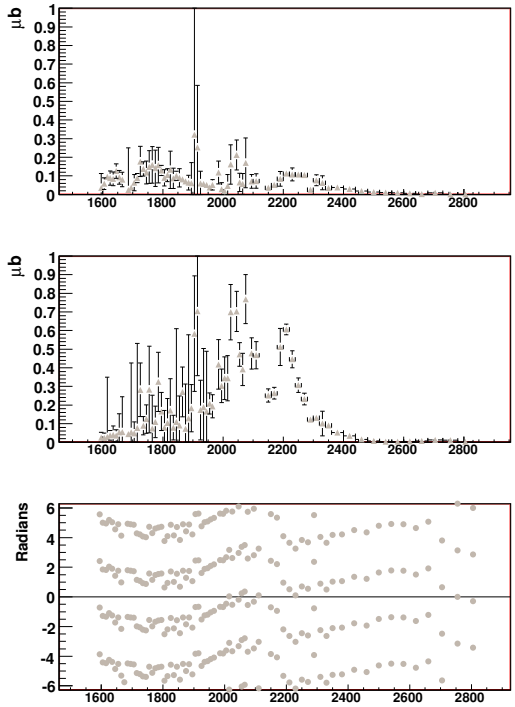

Figure 6.43: The PWA results for a fit containing the $J^P = \frac{1}{2}^-, \frac{3}{2}^+, \frac{5}{2}^-$(fit #001) partial waves. The results are presented here for the yields of the $\frac{3}{2}^+$ partial wave(top) and the $\frac{5}{2}^-$ partial wave(middle). The plot on the bottom is the phase difference between these two waves. There is interesting phase motion in the $W = 1900 \rightarrow 2200$ MeV region.

The plots in Figure 6.43 show the yields of the $J^P = \frac{3}{2}^+$(top) and the $J^P = \frac{5}{2}^-$(middle) partial waves, along with the phase difference plot(bottom). The strengths of these partial waves has been pointed out already, but there is interesting phase motion between the two waves in the region from $W = 1900 \rightarrow 2400$ MeV. It would appear to suggest the existence of a pair of resonances beating against each other. One broad state with a mass around $W = 2000$ MeV, and a second more narrow state near a mass of $W = 2200$ MeV.

$J^P = \frac{1}{2}^-, \frac{3}{2}^+, \frac{5}{2}^-, \frac{5}{2}^+$ (fit #004)

The waves present in this fit are: $J^P = \frac{1}{2}^-, \frac{3}{2}^+, \frac{5}{2}^-, \frac{5}{2}^+$(fit #004). As previously demonstrated in Figure 6.2(C) the addition of a higher-spin positive parity wave improves the fit somewhat in the higher W regions. This provides the motivation for further study of this partial wave set.

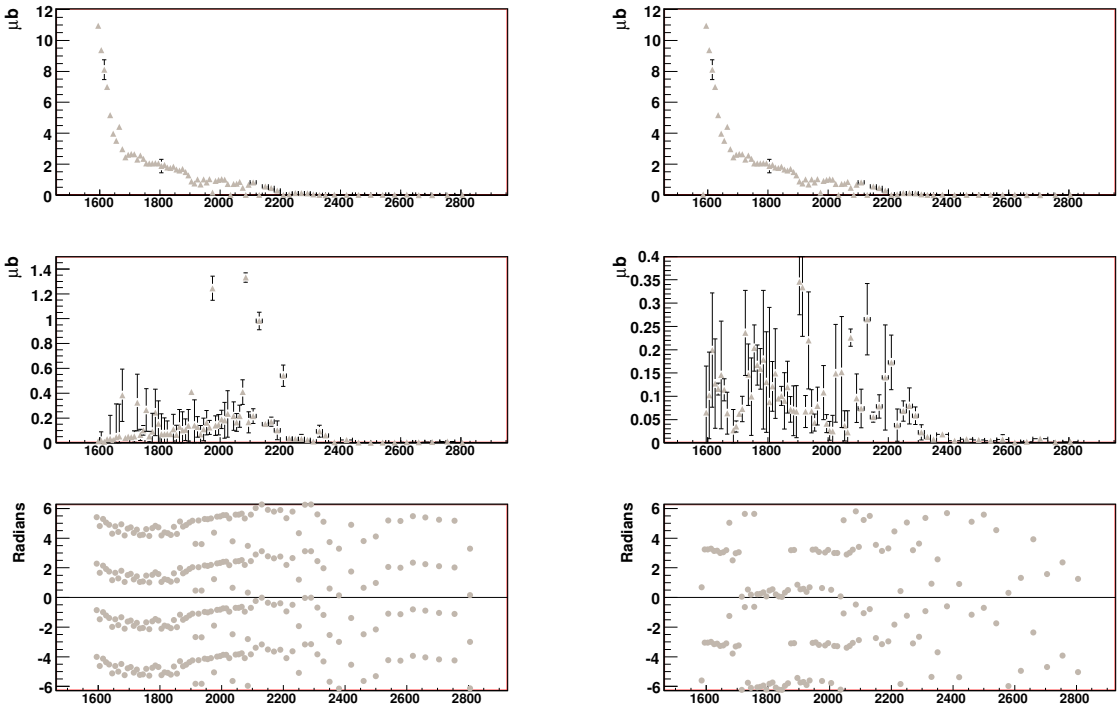

Figure 6.44: The PWA results for the η analysis fit with a $J^P = \frac{1}{2}^-, \frac{3}{2}^+, \frac{5}{2}^-, \frac{5}{2}^+$(fit #004) partial wave set. Left: Plots of the yield for the $\frac{1}{2}^-$(top) and $\frac{5}{2}^-$(middle) partial waves. The phase difference(bottom) between the two partial waves is shown as well. Right: The yield plots for the $\frac{1}{2}^-$(top) and $\frac{3}{2}^+$(middle) partial waves. The phase difference plot(bottom) between these two partial waves is also presented.

The plots on the left side of Figure 6.44 show the yields of the $J^P = \frac{1}{2}^-$(top) and the $J^P = \frac{5}{2}^-$(middle) partial waves. Displayed just below the yield plots is the phase difference plot(bottom) for the two waves. As previously seen the $J^P = \frac{1}{2}^-$ yield is dominating at threshold and then falls off slowly after $W \approx 1700$ MeV. The $J^P = \frac{5}{2}^-$ yield demonstrates a consistent result with fit #001 as it appears to peak around the same mass, $W = 2100$ MeV. The phase difference plot appears to slowly rise and fall through the regions where these two partial waves show structure. This may be indicative of the interference of very broad resonances. The yield plot for the $J^P = \frac{5}{2}^-$ appears to show structure over a very broad range in this fit.

The plots on the right side of Figure 6.44 show the yields of the $J^P = \frac{1}{2}^-$(top) and the $J^P = \frac{3}{2}^+$(middle) partial waves. Shown at the bottom of the right hand side is the phase difference between the $J^P = \frac{1}{2}^-$ and the $J^P = \frac{3}{2}^+$ partial waves. The yield plots appear to be reasonably consistent with the results from the $J^P = \frac{1}{2}^-, \frac{3}{2}^+, \frac{5}{2}^-$(fit #001) and there is strength in the $J^P = \frac{3}{2}^+$ wave

around $W = 1800$ MeV and around $W = 2200$ MeV. The phase difference plot shows several small amplitude wiggles below $W = 2100$ MeV. These small wiggles do not appear to contain structure.

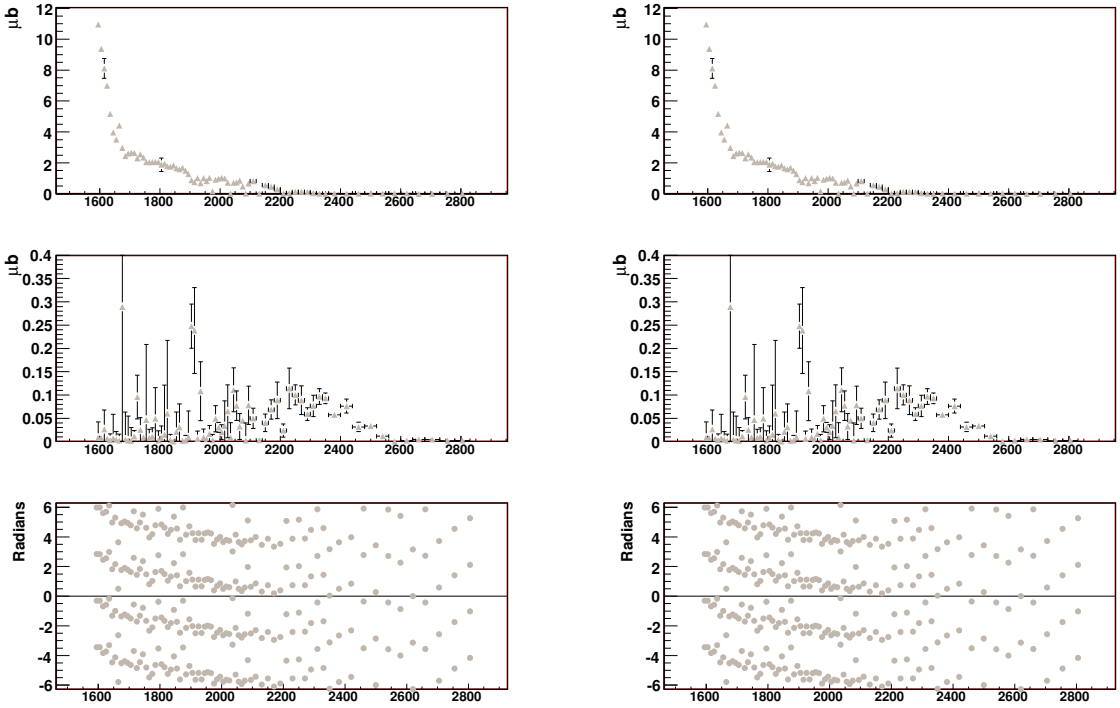

Figure 6.45: The PWA results for the η analysis fit with a $J^P = \frac{1}{2}^-, \frac{3}{2}^+, \frac{5}{2}^-, \frac{5}{2}^+$(fit #004) partial wave set. Left: Plots of the yield for the $\frac{1}{2}^-$(top) and $\frac{5}{2}^+$(middle) partial waves. The phase difference(bottom) between the two partial waves is shown as well. Right: The yield plots for the $\frac{5}{2}^-$(top) and $\frac{5}{2}^+$(middle) partial waves. The phase difference plot(bottom) between these two partial waves is also presented.

The plots displayed on the left hand side of Figure 6.45 show the yields of the $J^P = \frac{1}{2}^-$(top) and the $J^P = \frac{5}{2}^+$(middle) partial waves, along with the phase difference(bottom) between the two waves. The yield of the $J^P = \frac{5}{2}^+$ is significantly different from the yield of the $J^P = \frac{5}{2}^-$ yield. While the yield of the $J^P = \frac{5}{2}^-$ appears to be roughly centered around $W = 2100$ MeV, the positive parity state appears to have its yield strength centered more around $W = 2300$ MeV. It is notably higher in mass than the $J^P = \frac{5}{2}^-$ strength. The phase difference plots shows some phase motion at high W, but this may be meaningless as the strength of the $J^P = \frac{1}{2}^-$ has dropped off.

The plots displayed on the right hand side of Figure 6.45 show the yields of the $J^P = \frac{5}{2}^-$(top) and the $J^P = \frac{5}{2}^+$(middle) partial waves. At the bottom of the right hand is the phase difference plot between the $J^P = \frac{5}{2}^-$ and the $J^P = \frac{5}{2}^+$ waves. Having already examined the yield plots, the phase difference between these two waves requires scrutiny. The phase difference appears to be falling slowly from about $W = 1900$ MeV to $W = 2200$ MeV.

$J^P = \frac{1}{2}^-, \frac{3}{2}^+, \frac{5}{2}^-, \frac{7}{2}^+$(fit #005)

Along a similar vein to the previous wave set examined, this fit contains an additional higher-spin positive parity wave. In this case, that wave is the $J^P = \frac{7}{2}^+$. So the total wave set included in this fit is: $J^P = \frac{1}{2}^-, \frac{3}{2}^+, \frac{5}{2}^-, \frac{7}{2}^+$(fit #005). As previously pointed out in Figure 6.2(D) the addition of a high-spin positive parity partial wave to the base set of waves can improve the fit's ability to describe the data.

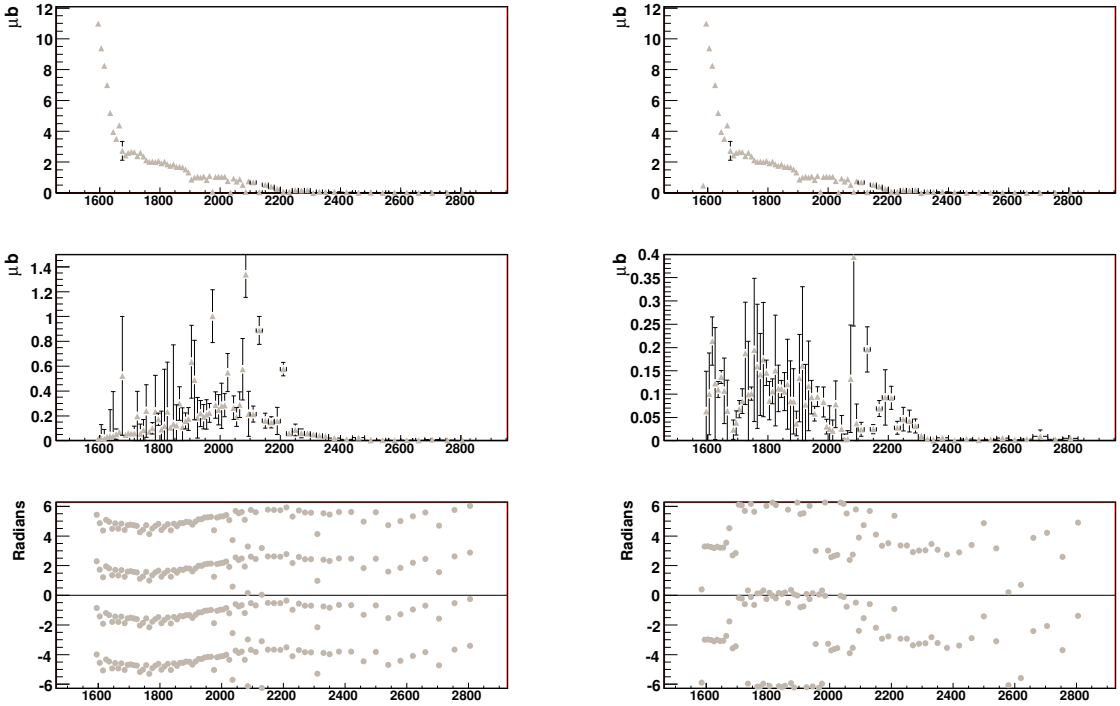

Figure 6.46: The PWA results for the η analysis fit with a $J^P = \frac{1}{2}^-, \frac{3}{2}^+, \frac{5}{2}^-, \frac{7}{2}^+$(fit #005) partial wave set. Left: Plots of the yield for the $\frac{1}{2}^-$(top) and $\frac{5}{2}^-$(middle) partial waves. The phase difference(bottom) between the two partial waves is shown as well. Right: The yield plots for the $\frac{1}{2}^-$(top) and $\frac{3}{2}^+$(middle) partial waves. The phase difference plot(bottom) between these two partial waves is also presented.

The plots on the left side of Figure 6.46 show the yields of the $J^P = \frac{1}{2}^-$(top) and the $J^P = \frac{5}{2}^-$(middle) partial waves. Displayed beneath the yield plots is the phase difference plot for the two waves. As previously seen the $J^P = \frac{1}{2}^-$ yield is dominating at threshold and then falls off slowly after $W \approx 1700$ MeV. The $J^P = \frac{5}{2}^-$ yield demonstrates a consistent result with the simpler wave set $J^P = \frac{1}{2}^-, \frac{3}{2}^+, \frac{5}{2}^-$(fit #001) as it appears to peak around the same mass, $W = 2050$ MeV, and be very broad. The phase difference plot appears to be varying smoothly as a function of W. If a resonance structure is present in the plot, then the state producing it is extremely broad. Through the regions in W where these two waves are strongest, the phase slowly falls and rises.

The plots on the right side of Figure 6.46 show the yields of the $J^P = \frac{1}{2}^-$(top) and the $J^P = \frac{3}{2}^+$(middle) partial waves. Shown at the bottom of the right hand side is the phase difference between

the $J^P = \frac{1}{2}^-$ and the $J^P = \frac{3}{2}^+$ partial waves. The yield plots again appear to be consistent with the results from fits to other wave sets and there is strength in the $J^P = \frac{3}{2}^+$ wave around $W = 1800$ MeV and around $W = 2200$ MeV. The phase difference plot shows generally smooth phase motion up to $W = 2000$ MeV. Above that, there appears to be a rapid drop in the phase difference roughly between $W = 2000 \rightarrow 2200$ MeV.

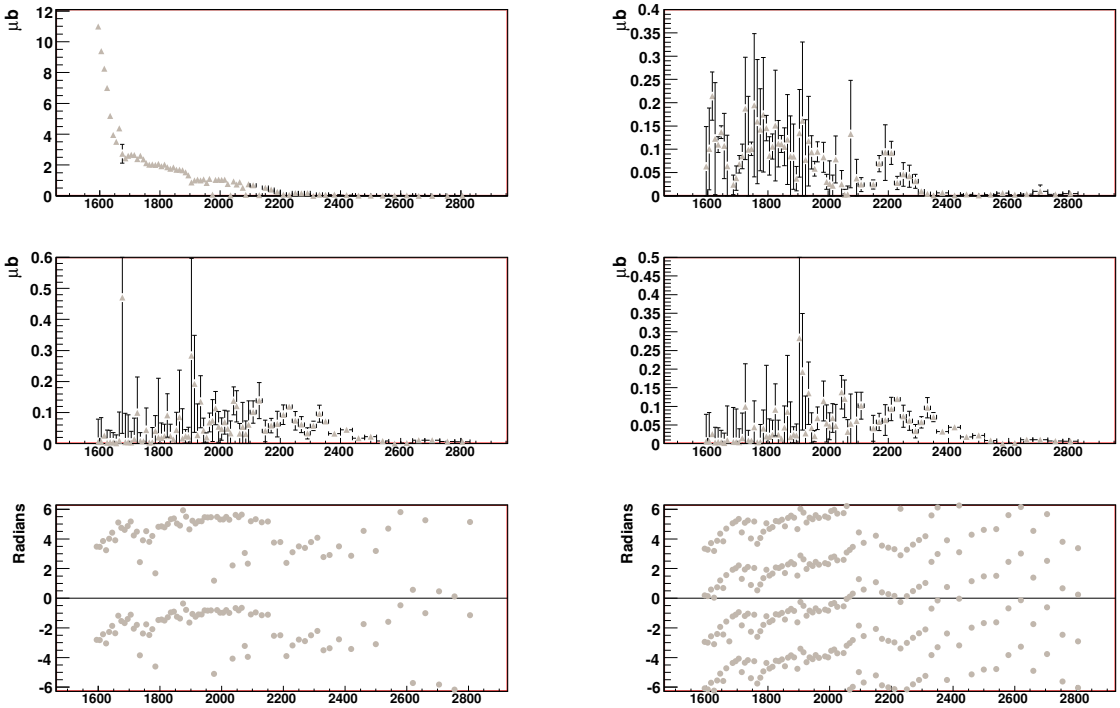

Figure 6.47: The PWA results for the η analysis fit with a $J^P = \frac{1}{2}^-, \frac{3}{2}^+, \frac{5}{2}^-, \frac{7}{2}^+$(fit #005) partial wave set. Left: Plots of the yield for the $\frac{1}{2}^-$(top) and $\frac{7}{2}^+$(middle) partial waves. The phase difference(bottom) between the two partial waves is shown as well. Right: The yield plots for the $\frac{3}{2}^+$(top) and $\frac{7}{2}^+$(middle) partial waves. The phase difference plot(bottom) between these two partial waves is also presented.

Displayed on the left hand side of Figure 6.47 are the plots for the yields from the $J^P = \frac{1}{2}^-$(top) and the $J^P = \frac{7}{2}^+$(middle) partial waves. At the bottom of the left hand column is the plot of the phase difference between the two partial waves. There is strength in the $J^P = \frac{7}{2}^+$ partial wave, but it is very broad structure. There is a small amount of strength in that wave going from $W = 2000$ MeV to $W = 2400$ MeV. The phase difference between the two partial waves appears to rise relatively slowly across most of the W range. The phase difference changes rapidly over the W range from $2200 \rightarrow 2300$ MeV. By itself the phase difference is not likely to be very meaningful, due to the lack of strength in the $J^P = \frac{1}{2}^-$ wave. When viewed in conjunction with the yield from the partial waves, it is perhaps a bit more convincing, while still not more than an indication of structure.

The left hand side of Figure 6.47 are the plots for the yields from the $J^P = \frac{3}{2}^+$(top) and the $J^P = \frac{7}{2}^+$(middle) partial waves, along with the phase difference between the two plotted at the bottom of the column. The yields have already been discussed, so the phase difference plot is really

the article of interest here. There is a slowly rising trend in the phase difference from threshold up to about 2100 MeV. There is a hint of possible structure in the phase difference from $W = 2100 \rightarrow 2300$ MeV.

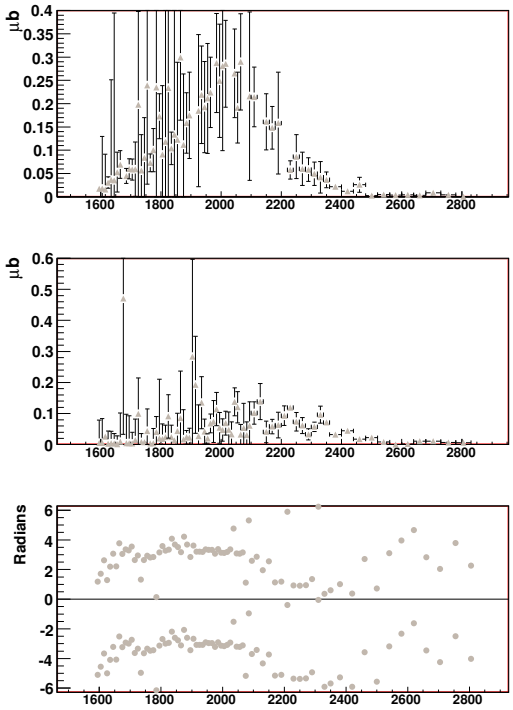

Figure 6.48: The PWA results for the η analysis fit with a $J^P = \frac{1}{2}^-, \frac{3}{2}^+, \frac{5}{2}^-, \frac{7}{2}^+$(fit #005) partial wave set. Presented here are plots of the yield for the $\frac{5}{2}^-$(top) and $\frac{7}{2}^+$(middle) partial waves. The phase difference(bottom) between the two partial waves is shown as well.

Figure 6.48 shows the yields of the $J^P = \frac{5}{2}^-$(top) and the $J^P = \frac{7}{2}^+$(middle) partial waves, along with the phase difference between the two plotted below. The phase difference plot is generally uninspiring, as it appears to move slowly, with perhaps a hint of structure at $W = 1950$ MeV and between $W = 2300 \rightarrow 2500$ MeV. It should be noted that the region $W = 2300 \rightarrow 2500$ MeV in Figure 6.2(D) is precisely where the additional $J^P = \frac{7}{2}^+$ partial wave improves the ability of the fit to describe the data. The relatively nice appearance of the $J^P = \frac{5}{2}^-$ in the yield certainly indicates a resonance structure, while the phase difference plot appear to lack the supporting argument in this case. It is possible that while the addition of the $J^P = \frac{7}{2}^+$ partial wave improved the fit, it only improved the fit and the additional wave lacks a real resonance structure.

$J^P = \frac{1}{2}^-, \frac{5}{2}^-, \frac{5}{2}^+$ (fit #009)

The wave set used in this fit contains three partial waves. The waves present are: $J^P = \frac{1}{2}^-, \frac{5}{2}^-, \frac{5}{2}^+$. The removal of the $J^P = \frac{3}{2}^+$ partial wave is primarily meant as a check on how essential the wave is when fitting the η data. The likelihood difference plots indicated that it was a required wave as demonstrated in Figure 6.2(B). Still, it is worthwhile to look at the results of a fit or two that leave this wave out.

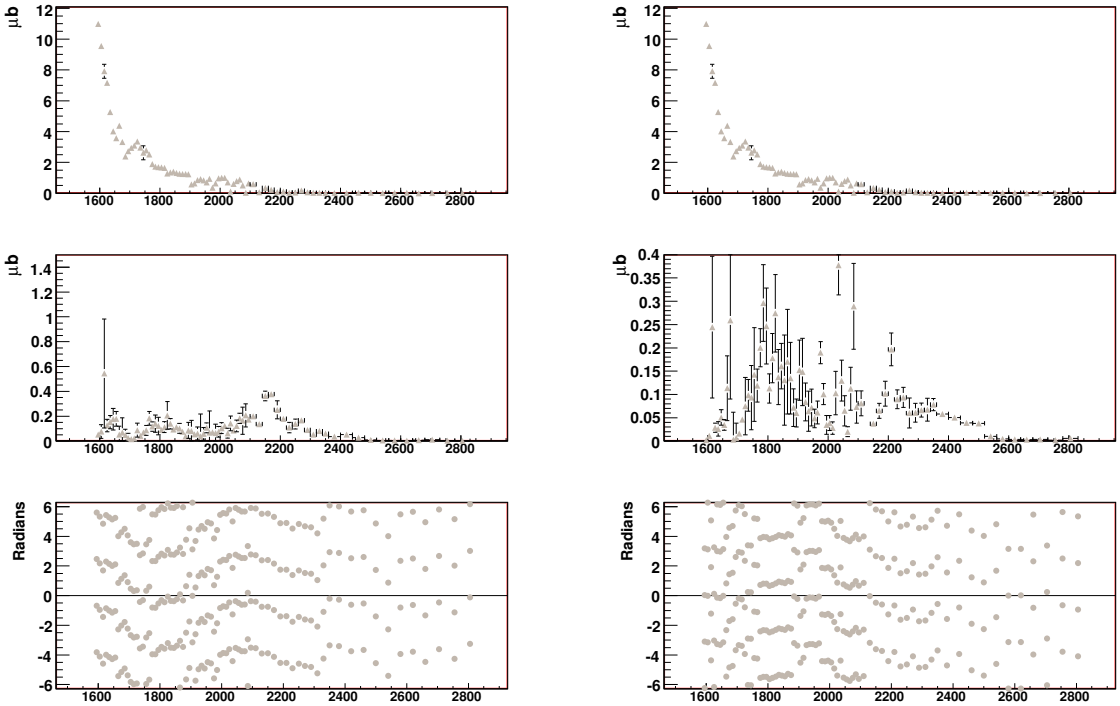

Figure 6.49: The PWA results for the η analysis fit with a $J^P = \frac{1}{2}^-, \frac{5}{2}^-, \frac{5}{2}^+$(fit #009) partial wave set. Left: Plots of the yield for the $\frac{1}{2}^-$(top) and $\frac{5}{2}^-$(middle) partial waves. The phase difference(bottom) between the two partial waves is shown as well. Right: The yield plots for the $\frac{1}{2}^-$(top) and $\frac{5}{2}^+$(middle) partial waves. The phase difference plot(bottom) between these two partial waves is also presented.

The plots on the left side of Figure 6.49 show the yields of the $J^P = \frac{1}{2}^-$(top) and the $J^P = \frac{5}{2}^-$(middle) partial waves. Displayed under the yield plots is the phase difference plot for the two waves. The $J^P = \frac{1}{2}^-$ yield is dominating at threshold and then falls off slowly after $W \approx 1700$ MeV. As an added feature, however, there is a small bump around $W = 1700$ MeV which appears in the $J^P = \frac{1}{2}^-$ yield which was not there when the $J^P = \frac{3}{2}^+$ wave was present. The $J^P = \frac{5}{2}^-$ yield demonstrates a slightly new behavior in the absence of the $J^P = \frac{3}{2}^+$ partial wave. There is strength in the $J^P = \frac{5}{2}^-$ as low as $W = 1800$ MeV and a separate peak in the yield at $W = 2200$ MeV. Prior to this test, this wave always presented as a single bump with its peak around $W = 2100$ MeV. The phase difference plot, is likewise affected by the absence of the $J^P = \frac{3}{2}^+$ wave. Large broad fluctuation in the phase between the $J^P = \frac{1}{2}^-$ and the $J^P = \frac{5}{2}^-$ waves begin at threshold

and continue to about $W = 2300$ MeV.

The plots on the right side of Figure 6.49 show the yields of the $J^P = \frac{1}{2}^-$(top) and the $J^P = \frac{5}{2}^+$(middle) partial waves. Displayed under the yield plots is the phase difference plot for the two waves. The $J^P = \frac{1}{2}^-$ yield has been described for this fit already. The $J^P = \frac{5}{2}^+$ yield demonstrates a very different behavior in the absence of the $J^P = \frac{3}{2}^+$ partial wave. There is strength in the $J^P = \frac{5}{2}^+$ as low as $W = 1700$ MeV. Prior to this test, this wave always presented as a single bump with its peak around $W = 2300$ MeV. The phase difference plot, is likewise affected by the absence of the $J^P = \frac{3}{2}^+$ wave. Large fluctuations in the phase between the $J^P = \frac{1}{2}^-$ and the $J^P = \frac{5}{2}^+$ waves begin at threshold and continue to about $W = 2300$ MeV. The region between $W = 1800 \rightarrow 2000$ MeV shows very interesting phase motion, in a region where there is significant strength in the $J^P = \frac{5}{2}^+$ partial wave.

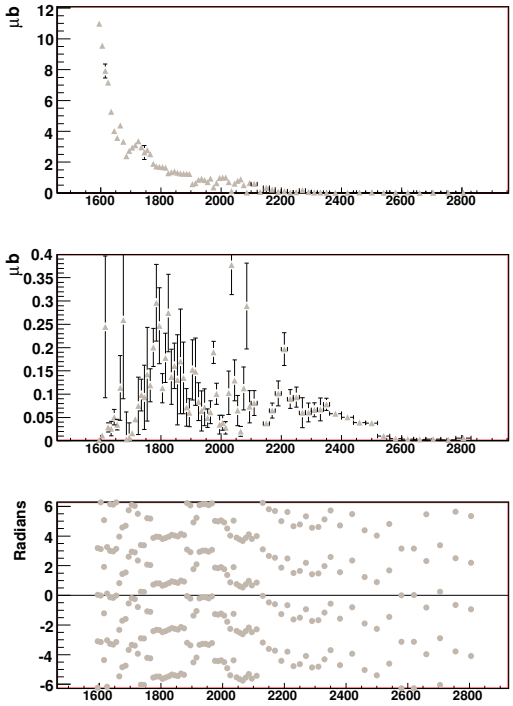

Figure 6.50: The PWA results for the η analysis fit with a $J^P = \frac{1}{2}^-, \frac{5}{2}^-, \frac{5}{2}^+$(fit #009) partial wave set. Plots of the yield for the $\frac{5}{2}^-$(top) and $\frac{5}{2}^+$(middle) partial waves. The phase difference(bottom) between the two partial waves is shown as well.

The plots contained in Figure 6.50 display the yields from the $J^P = \frac{5}{2}^-$(top) and $J^P = \frac{5}{2}^+$(middle) partial waves. The yields for these two waves have already been examined, but the phase motion between the two partial waves requires scrutiny. The phase motion is plotted at the bottom of the column of plots in Figure 6.50. The phase motion is somewhat erratic in the region below $W = 2200$ MeV. There is a radical change of phase between the two fits at $W = 2000$ MeV, which is near a minimum in the yields for both of the partial waves which may imply that the phase motion is not indicative of any type of resonance structure.

$J^P = \frac{1}{2}^-, \frac{5}{2}^-, \frac{7}{2}^+$(fit #010)

The waves present in this fit are the following: $J^P = \frac{1}{2}^-, \frac{5}{2}^-, \frac{7}{2}^+$. The removal of the $J^P = \frac{3}{2}^+$ partial wave is partly meant as a check on how important the wave is when fitting the η data. This fit also provides an additional check as to the ability of the fit to compensate for an important wave which may be missing from the fit. In examining the results from previous fits, all of which included the $J^P = \frac{3}{2}^+$ partial wave, it was decided to further study wave sets which did not contain this wave due to the relatively small contribution to the total yield. The likelihood difference plots indicated that the $J^P = \frac{3}{2}^+$ was a required wave as demonstrated in Figure 6.2(B). Still, it is worthwhile to spend time looking at the results of a fit or two that leave this wave out.

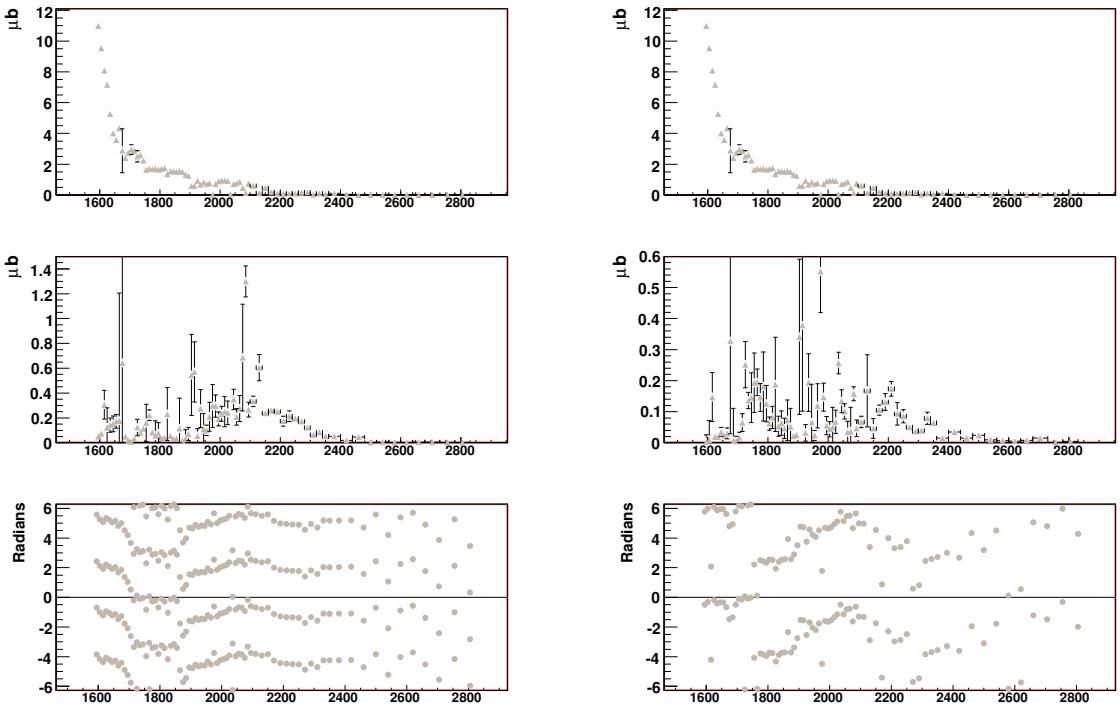

Figure 6.51: The PWA results for the η analysis fit with a $J^P = \frac{1}{2}^-, \frac{5}{2}^-, \frac{7}{2}^+$(fit #010) partial wave set. Left: Plots of the yield for the $\frac{1}{2}^-$(top) and $\frac{5}{2}^-$(middle) partial waves. The phase difference(bottom) between the two partial waves is shown as well. Right: The yield plots for the $\frac{1}{2}^-$(top) and $\frac{7}{2}^+$(middle) partial waves. The phase difference plot(bottom) between these two partial waves is also presented.

The plots on the left side of Figure 6.51 show the yields of the $J^P = \frac{1}{2}^-$(top) and the $J^P = \frac{5}{2}^-$(middle) partial waves. Displayed under the yield plots is the phase difference plot for the two waves. The $J^P = \frac{1}{2}^-$ yield is dominating at threshold and then falls off slowly after $W \approx 1700$ MeV. However, there is a small bump around $W = 1700$ MeV which appears in the $J^P = \frac{1}{2}^-$ yield which was not there when the $J^P = \frac{3}{2}^+$ wave was present. The $J^P = \frac{5}{2}^-$ yield demonstrates a slightly new behavior in the absence of the $J^P = \frac{3}{2}^+$ partial wave. There is strength in the $J^P = \frac{5}{2}^-$ as low as $W = 1750$ MeV and a separate broad peak in the yield at $W = 2100$ MeV. This wave had

previously presented as a single bump with its peak around $W = 2100$ MeV. It appears that the $J^P = \frac{5}{2}^-$ yield has absorbed some of the yield which would otherwise have gone into the $J^P = \frac{3}{2}^+$ wave. The phase difference plot, is likewise affected by the absence of the $J^P = \frac{3}{2}^+$ wave. There are rapid changes in the phase between the two waves, but only in regions of W where one of the waves or the other is effectively at zero strength. This makes the phase motion an effect of something other than a resonance structure.

The plots on the right hand side of Figure 6.51 show the yields of the $J^P = \frac{1}{2}^-$(top) and the $J^P = \frac{7}{2}^+$(middle) partial waves, along with the phase difference plot presented at the bottom of the column of plots. The yield of the $J^P = \frac{7}{2}^+$ partial wave demonstrates strength around $W = 1750$ MeV and $W = 2200$ MeV. This, again is unusual for the $J^P = \frac{7}{2}^+$ to demonstrate structure that low in W. Clearly the fit is using one positive parity state to compensate for another which is not present in the fit. The phase difference between the $J^P = \frac{1}{2}^-$ and the $J^P = \frac{7}{2}^+$ waves has structure between $W = 1950 \rightarrow 2300$ MeV. This phase motion takes place between two non-zero waves across a wide region in W, and as such it should be considered as a plausible result. Clearly, the only take-away lesson here may be that a positive-parity wave is useful in fitting the data in that W region.

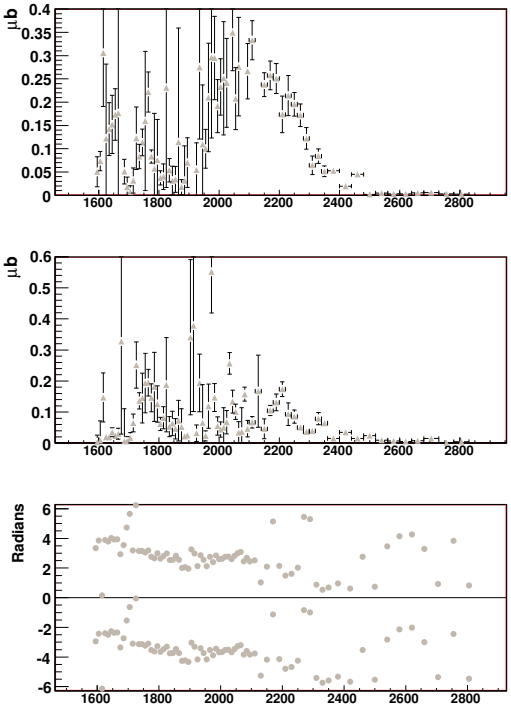

Figure 6.52: The PWA results for the η analysis fit with a $J^P = \frac{1}{2}^-, \frac{5}{2}^-, \frac{7}{2}^+$(fit #010) partial wave set. Plots of the yield for the $\frac{5}{2}^-$(top) and $\frac{7}{2}^-$(middle) partial waves. The phase difference(bottom) between the two partial waves is shown as well.

Figure 6.52 displays the yields from the $J^P = \frac{5}{2}^-$(top) and the $J^P = \frac{7}{2}^+$(middle) partial waves. Additionally at the bottom of the column of plots, there is a plot of the phase difference between the two waves. The yields have been previously discussed, but the phase difference plot warrants attention. The phase difference plot is unremarkable. In regions where both of the waves have a

significant yield, the phase is just slowly drifting. In regions where the yields of a partial wave go toward zero, then the phase demonstrates considerable motion. This is not surprising, as there are no real constraints on the phase if the overall strength of the partial wave is effectively zero.

Discussion of η PWA Results

Compiling the available solutions, there are structures within various partial waves which may indicate a resonance structure. If these structures appear consistently throughout several different fits, then further confidence is gained in calling them resonances. The structures which appear to be the most robust, are the threshold $J^P = \frac{1}{2}^-$ and a higher-mass $J^P = \frac{5}{2}^-$ near $W = 2200$ MeV. There is some indication of a $J^P = \frac{3}{2}^+$ partial wave contributing around $W = 1800$ MeV, as well as hints of a higher-spin positive-parity wave like $J^P = \frac{5}{2}^+$ or $J^P = \frac{7}{2}^+$ near $W = 2300$ MeV. In the case of the $\frac{5}{2}^+$ and $\frac{7}{2}^+$ partial wave results, there is no means to distinguish between the two waves in the analysis of the η.

There is a question as to whether the $J^P = \frac{1}{2}^-$ state observed near $W = 2000$ MeV is actually a separate resonance, or is part of a very long tail from the very strong and dominating $S_{11}(1535)$. The fall off of the $J^P = \frac{1}{2}^-$ partial wave as a function of W tends to be relatively gradual, which may indicate other weak resonance structures, or significant tails to the known structures.

Figures 6.53, 6.54, 6.55, and 6.56 demonstrate the contribution to the yield from the different s-channel partial waves of a fit when compared to the total yield. As a reminder, the t-channel and u-channel contributions to the yield are present in the fit, but not plotted in these figures. See Section 5.3 to view these non-resonant contributions.

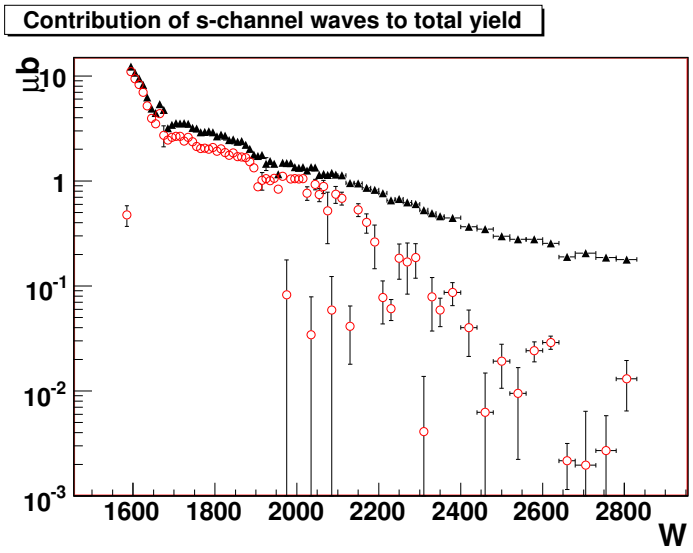

Figure 6.53: Plot of the yields from the $J^P = \frac{1}{2}^-$ partial wave compared to the total yield for the η analysis. The fit used to obtain these yields contained the $J^P = \frac{1}{2}^-, \frac{3}{2}^+, \frac{5}{2}^-, \frac{7}{2}^+$ partial waves. The threshold region is clearly dominated by the $J^P = \frac{1}{2}^-$ partial wave.

Combining the yield results, along with the likelihood difference results, a set of four partial waves is preferred in describing the physics present in the η dataset. There is a clear indication for the inclusion of either a $J^P = \frac{5}{2}^+$ or $J^P = \frac{7}{2}^+$ partial wave. The inclusion of the $J^P = \frac{3}{2}^+$ wave appears to benefit the ability of the fit to describe the data, but the structure in the yields and phase differences is generally lacking. The inclusion of the $J^P = \frac{3}{2}^+$ and the higher-spin positive parity waves are not as clear. The inclusion of the base $J^P = \frac{1}{2}^-$ and $J^P = \frac{5}{2}^-$ waves appear very clearly in the fit results.

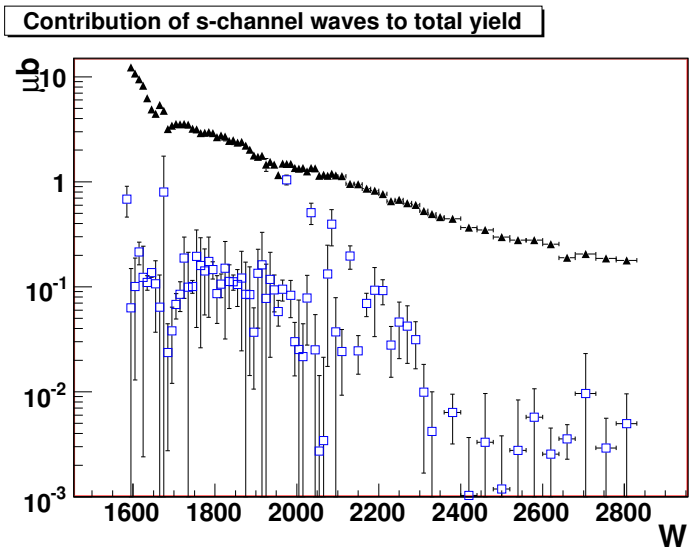

Figure 6.54: Plot of the yields from the $J^P = \frac{3}{2}^+$ partial wave compared to the total yield for the η analysis. The fit used to obtain these yields contained the $J^P = \frac{1}{2}^-, \frac{3}{2}^+, \frac{5}{2}^-, \frac{7}{2}^+$ partial waves.

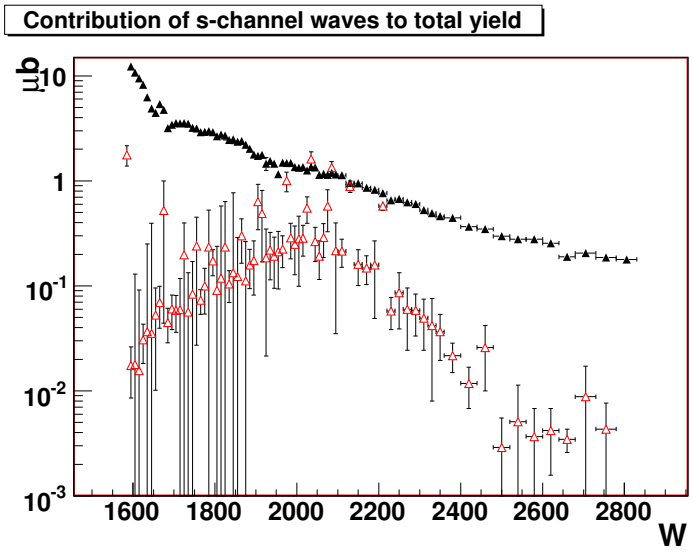

Figure 6.55: Plot of the yields from the $J^P = \frac{5}{2}^-$ partial wave compared to the total yield for the η analysis. The fit used to obtain these yields contained the $J^P = \frac{1}{2}^-, \frac{3}{2}^+, \frac{5}{2}^-, \frac{7}{2}^+$ partial waves.

6.6.3 Stability of Fit Results

In the plots of the yields presented as part of the fit results for the η analysis, there are clearly points which jump wildly and require investigation and explanation. This phenomenon has been observed in the fits since the first fits were run for the η and η' analyses. There have been several attempts to determine why these points are so wildly different than their neighboring points. First, recall that

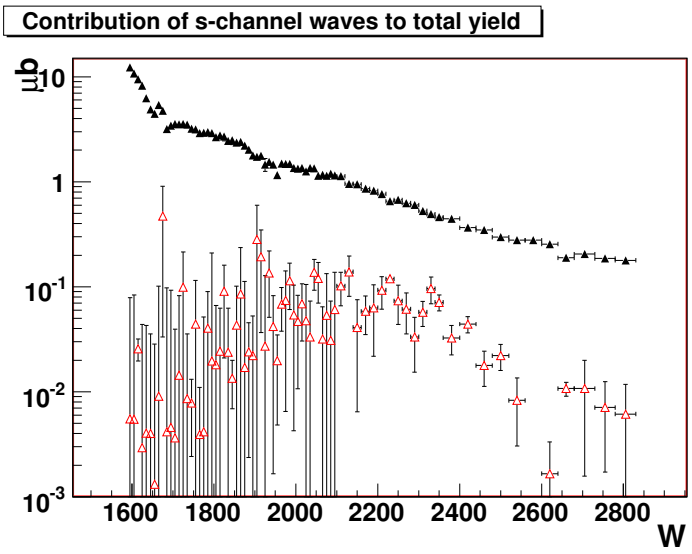

Figure 6.56: Plot of the yields from the $J^P = \frac{7}{2}^+$ partial wave compared to the total yield for the η analysis. The fit used to obtain these yields contained the $J^P = \frac{1}{2}^-, \frac{3}{2}^+, \frac{5}{2}^-, \frac{7}{2}^+$ partial waves.

each of the bins in W represents an independent fit. In all cases, the results presented are not the result of a single fit in a single bin. Multiple fits utilizing different starting values for the parameters were used for each of the points found in Figure 6.42. For example, the fit described in Section 6.6.2 demonstrates these wildly jumping points in several of the results. See Figures 6.42 and 6.43. The strangely high points in the yields of the $J^P = \frac{5}{2}^-$ or $J^P = \frac{3}{2}^+$ partial waves correspond directly to strangely low points in the $J^P = \frac{1}{2}^-$ yield. This is indicative of the fit replacing the contribution of one partial wave with another partial wave in a given bin. Which may indicate that the fit has reached a local minimum in likelihood space from which it can not escape.

If it were as simple as the fit locating a local minimum, then there are a couple of viable solutions. First, run a very large number of fits in a given bin starting from random locations. This should allow for the fit to locate the real minimum in likelihood space, causing the fit results to be more stable. This option was explored, sometimes running as many as 100 or more independent fits form different starting values in a given bin. This solution had no apparent effect on the fit results.

Another solution was considered, which tracked the solution from a previous W bin, and used the parameters from that previous solution as a starting point for the fit in a subsequent bin. The idea being that if you find a solution in one bin, and the physics is not significantly different from bin to bin, then that solution should be similar in the next bin. By starting near that solution, it is less likely that the fit will find very different solution. This technique showed no improvement over the original results.

Perhaps most interesting is that two bins next to each other in W can have wildly differing partial wave results from the fit, and still both describe the data well. Looking closely at the $J^P = \frac{5}{2}^-$ yield plot in Figure 6.42, it is evident that the two bins located at $W = 1900 \rightarrow 1910$ MeV and $W = 1910 \rightarrow 1920$ MeV are systematically high in comparison to the four or five bins on either side. While these bins represent a differing solution to the neighboring bins, the fit in those bins appears to describe the data very well. This is evident from Figure 6.22, which has been reproduced here for convenience as Figure 6.57. The bins on either side of these two anomalous bins appear nearly indistinguishable in their $cos(\theta_{CM})$ angular distributions. The fits appear to do a reasonable job

describing these bins, and yet return a yield in the $J^P = \frac{5}{2}^-$ partial wave which is considerably higher.

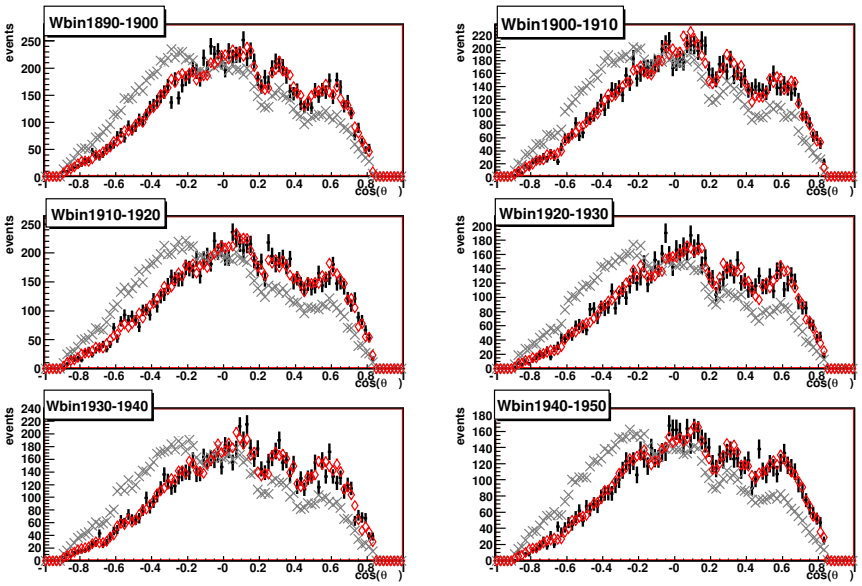

Figure 6.57: Plot to compare η fit results with data as a function of $\cos(\theta_{CM})$. The black points are the data events, the gray criss-cross markers represent the accepted Monte Carlo, and the red open diamond markers represents the accepted Monte Carlo weighted by the fit results. Note the similarities between the distributions across all of these bins, and that the fit reasonably describes the data.

For these few bins, Table 6.3 lists the final fit parameters for each bin. This fit contained the $J^P = \frac{1}{2}^-, \frac{3}{2}^+, \frac{5}{2}^-$ partial waves, and has a total of 8 free parameters. The final parameters do not appear to contain any single parameters which may obviously be causing the anomalous behavior of bins $1900 \rightarrow 1910$ and $1910 \rightarrow 1920$. For a more global perspective, Appendix 14 contains the yields, and fit parameters for this same fit across a larger region in W.

Parameter	$1890 \rightarrow 1900$	$1900 \rightarrow 1910$	$1910 \rightarrow 1920$	$1920 \rightarrow 1930$	$1930 \rightarrow 1940$
mod($\frac{1}{2}^-$)	-7.25 ± 0.25	-5.5 ± 5	5.5 ± 2.3	-6.6 ± 0.25	6.7 ± 0.30
phase($\frac{1}{2}^-$)	2.8 ± 0.4	2.4 ± 3.4	5.6 ± 0.9	3.1 ± 0.45	6.25 ± 0.5
mod($\frac{3}{2}^+$)	-11.5 ± 5	22 ± 24	19.5 ± 9.5	10.0 ± 4	8.8 ± 0.8
phase($\frac{3}{2}^+$)	2.0 ± 0.9	0.0 ± 1.5	0.0 ± 0.4	6 ± 0.6	3 ± 1.2
E/M($\frac{3}{2}^+$)	5.7 ± 0.7	5 ± 3.25	5.4 ± 1.2	2 ± 2.9	5.05 ± 0.8
mod($\frac{5}{2}^-$)	105 ± 40	-185 ± 115	-190 ± 40	-72 ± 28	74 ± 62
phase($\frac{5}{2}^-$)	4.15 ± 0.35	3.9 ± 2.25	3.85 ± 0.55	1.2 ± 0.23	4.23 ± 0.15
E/M($\frac{5}{2}^-$)	6.3 ± 0.1	3.07 ± 1.1	3.06 ± 0.15	6.3 ± 0.15	3.09 ± 0.09

Table 6.3: The final fit values for the free parameters in a series of five W bins. Bins $1900 \rightarrow 1910$ and $1910 \rightarrow 19290$ appear to be anomalous in the yield plots in comparison to neighboring bins.

In this case, the fit is clearly unable to distinguish between solutions for some bins in W. Exactly why this occurs in one bin, and not another just 10 MeV away, is a bit of a mystery at this point.

Clearly, the fit requires further constraints, which would allow it to determine the best solution in a given W bin.

6.6.4 PWA Fit Errors

As mentioned just previously, the fit was not always able to distinguish between two viable solutions when fitting the data. The values resulting from the fit were very different, and yet the comparison to the data was very difficult to distinguish. This raises the question of the errors assigned to these points. The errors reported throughout the PWA results chapter come from the fit itself. MINUIT reports the errors, and they are recorded and used. No additional source of error is used at this point.

There are a few outlying points fow which the error appears to be suprisingly low. Work was done to determine the nature of the points, as well as the correctness of the error associated with those points.

As an example, the middle plot in Figure 7.2 was used. This plot presents the yield of the $J^P = \frac{5}{2}^-$ partial wave for a fit which contains the $J^P = \frac{1}{2}^-, \frac{3}{2}^+, \frac{5}{2}^-$ waves. Also, it is important to note that this particular fit was done without the use of fiducial cuts, hence the location of the plot in Chapter 7. There are many points in the plot, but here the one of particular interest is located at $W = 2030 \rightarrow 2040$ MeV. The yield determined at this point is strangely high at 1.4 μb. Clearly, the error presented here is very low, which is cause for further examination. To look more systematically at the results, the points on either side of this one will be examined as well.

The yields determined for these three points are reported in Table 6.4.

Table 6.4: η Yield Results

W	yield($\frac{5}{2}^-$)(μb)	error
2025	0.81	0.11
2035	1.4	0.03
2045	0.65	0.10

Clearly the errors on the middle bin here are suspect. To determine the origin of these errors, and to assure that there is no mistake in calculating them from the fit parameters, the fit parameters for the $J^P = \frac{5}{2}^-$ partial wave will be reported for these three bins.

Table 6.5: η Parameter Fit Results

W	mod($\frac{5}{2}^-$)	phase($\frac{5}{2}^-$)	E/M($\frac{5}{2}^-$)
2025	137±9	4.75±0.1	6.27±0.04
2035	-173±1.5	1.47±0.1	6.25±0.02
2045	-114±8	1.78±0.06	6.26±0.03

As can be seen by Table 6.5 the errors on the fit parameters are likewise small for this point. This would indicate that the errors which are small in the yields are correctly determined from the fit parameters.

Additionally, it should be noted that another solution was determined in the process of analyzing this result. In the same bin where the error was being scrutinized, there was an additional solution

a little bit lower in yield. It was located at 1.12 ± 0.03 μb. While this point is more inline with the results in the neighboring bins, it is about 50 worse in -ln($\mathcal{L}$). While this may be an equivalent solution, and more inline with the nearby results, there was no effort made to "smooth" the solutions in this analysis. A smoothing of the results, requiring that the results do not vary by more than some amount may be utilized in future analyses to determine more consistent results.

As far as the errors are concerned, there are a few things which may be tried in future to improve the error measurement. The errors reported here result only from the fit itself. These can be explored using different calls to MINUIT, as there are a few options which may result in slightly different error determination. Additionally, in future, a systematic study of the fit output may allow for a systematic error to be determined for a given bin, which can then be combined with the fit error to yield a more reasonable error for a given point.

6.6.5 η' PWA Results

The PWA results for $\gamma p \to N^* \to p\eta'$ will be reported here for the selected subset of fits. The results will be presented as plots of the yields and phase differences between partial waves for the different fits. There are only three fits which are being examined for the η' analysis. The analysis of the likelihood difference plots indicated that the there were three partial waves which were necessary to describe the physics in the data. These partial waves form the base wave set for all of the fits to be further analyzed here. The base wave set of the η' analysis is the following: $J^P = \frac{1}{2}^-, \frac{3}{2}^+, \frac{5}{2}^-$. The results will be presented fit by fit for the three fits under continued study.

$J^P = \frac{1}{2}^-, \frac{3}{2}^+, \frac{5}{2}^-$ (fit #101)

The basic wave set for the η' contains: $J^P = \frac{1}{2}^-, \frac{3}{2}^+, \frac{5}{2}^-$ partial waves. There are clear reasons for selecting this set of waves as a point to further pursue the analysis of η' photoproduction. The plots of the likelihood differences are clear in their indications that the presence of these waves as seen in the plots in Figures 6.7,6.9. Additionally, in Figure 6.8 there is a comparison between two fits with wave sets which differ only by a global parity flip. This comparison allows for the identity of the $J^P = \frac{1}{2}^-$ partial wave at threshold to be established.

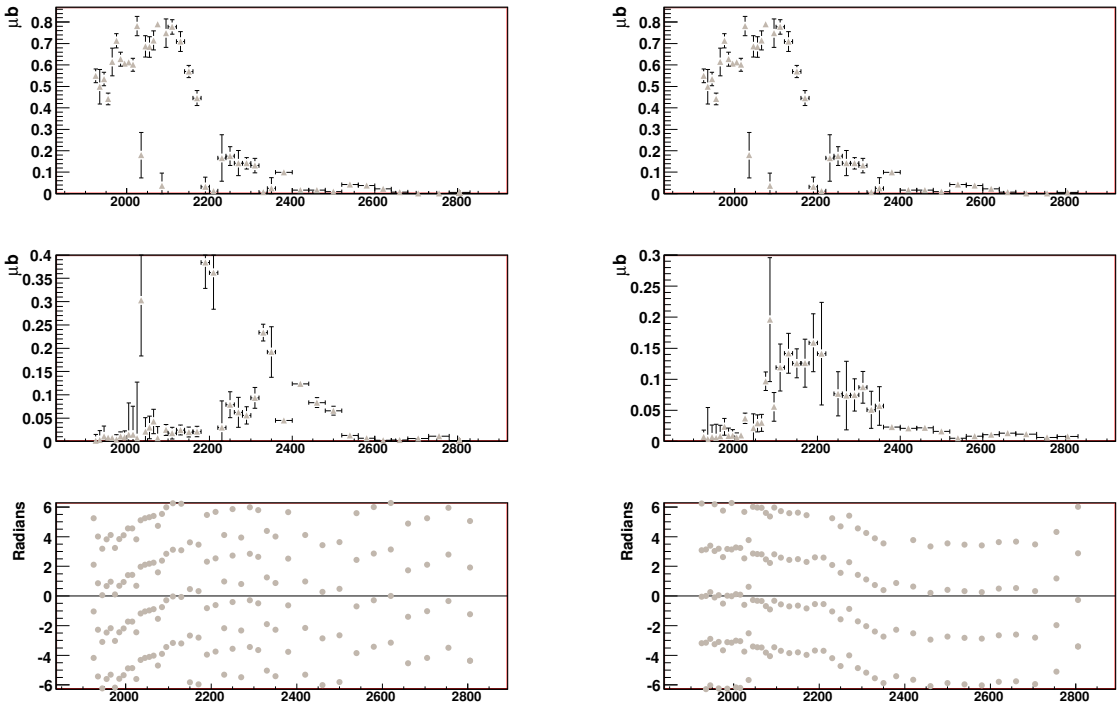

Figure 6.58: Plots of the PWA results for the η' analysis from a fit with $J^P = \frac{1}{2}^-, \frac{3}{2}^+, \frac{5}{2}^-$ partial waves. Left: Plots of the yield for the $\frac{1}{2}^-$(top) and $\frac{5}{2}^-$(middle) partial waves. The phase difference plot(bottom) is displayed. Right: Plots of the yield for the $\frac{1}{2}^-$(top) and $\frac{3}{2}^+$(middle) partial waves. The phase difference between the two waves is presented as well(bottom).

The plots on the left hand side of Figure 6.58 display the yields for the $J^P = \frac{1}{2}^-$(top) and

$J^P = \frac{5}{2}^-$(middle) partial waves. The yield of the $J^P = \frac{1}{2}^-$ wave clearly indicates the importance of this wave at threshold. It dominates the yield in scale from threshold up to $W \approx 2200$ MeV, after which is drops off. The yield of the $J^P = \frac{5}{2}^-$ wave is peaked just shy of $W = 2400$ MeV and appears to contribute almost nothing at threshold. This is reassuring because producing a high-spin object at threshold should be kinematically suppressed. The phase difference between the two fits is shown in the bottom plot on the left hand side of Figure 6.58. The phase difference between the $J^P = \frac{1}{2}^-$ and $J^P = \frac{5}{2}^-$ partial waves appears to drop off rapidly in the region around $W = 2200$ MeV where the yields of both partial waves are non-zero.

The plots on the right hand side of Figure 6.58 display the yields for the $J^P = \frac{1}{2}^-$(top) and $J^P = \frac{3}{2}^+$(middle) waves. The yield of the $J^P = \frac{3}{2}^+$ wave is broad and appears in the range $W = 2050 \rightarrow 2400$ MeV. Like the $J^P = \frac{5}{2}^-$ the $J^P = \frac{3}{2}^+$ appears to contribute almost nothing at threshold. The phase difference between the two fits is shown in the bottom plot on the right hand side of Figure 6.58. The phase difference between the $J^P = \frac{1}{2}^-$ and $J^P = \frac{3}{2}^+$ partial waves falls slowly until reaching the range of $W = 2200 \rightarrow 2400$ MeV where it appears to drop off rapidly.

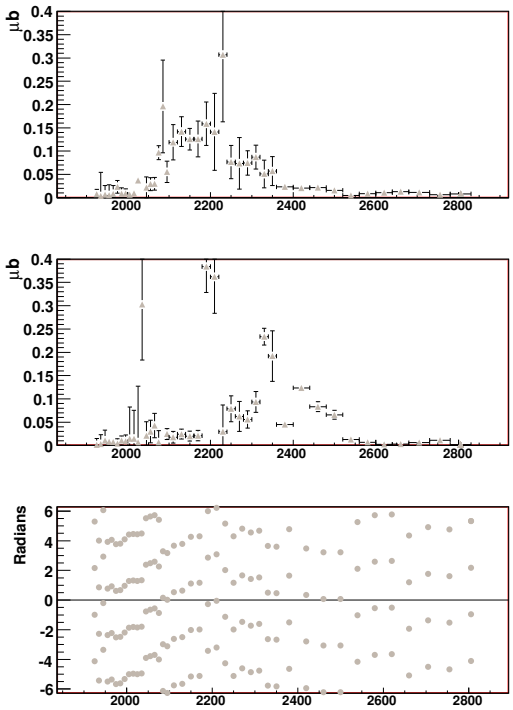

Figure 6.59: Plots of the PWA results for the η' analysis from a fit with $J^P = \frac{1}{2}^-, \frac{3}{2}^+, \frac{5}{2}^-$ partial waves. Plots of the yield for the $\frac{3}{2}^+$(top) and $\frac{5}{2}^-$(middle) partial waves. The phase difference plot(bottom) is displayed.

Figure 6.59 displays the plots of the yields of $J^P = \frac{3}{2}^+$(top) and $J^P = \frac{5}{2}^-$(middle) waves. The yields themselves have been discussed, but the phase difference between the two partial waves bears investigation. There is non-zero yield and an apparent overlap of strength in the yield of these two waves. The phase difference, as seen in the last plot in Figure 6.59 indicates that from $W = 2100 \rightarrow 2350$ MeV the phase is rising and the falling in a systematic way. This phase motion, along with the strength of the yield in the region of W may indicate the presence of a resonance.

$J^P = \frac{1}{2}^-, \frac{3}{2}^+, \frac{5}{2}^-, \frac{5}{2}^+$ (fit #104)

Adding to the base set of partial waves a $J^P = \frac{5}{2}^+$ wave, brings this fit up to four partial waves to describe the data. The waves included then are: $J^P = \frac{1}{2}^-, \frac{3}{2}^+, \frac{5}{2}^-, \frac{5}{2}^+$. The indications from the analyzing the likelihood difference plots was that the addition of a $J^P = \frac{5}{2}^+$ wave did not really improve the quality of fit when compared to the base set of waves. The conclusion was to further study this wave set to determine if any influences of the $J^P = \frac{5}{2}^+$ wave can be seen.

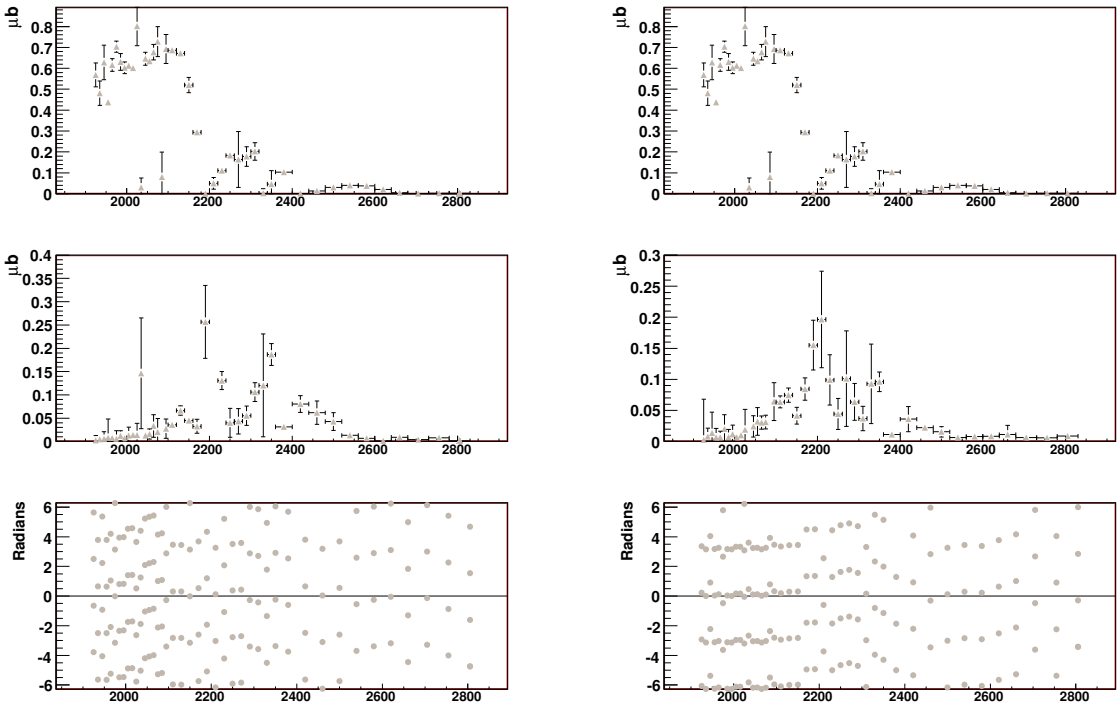

Figure 6.60: Plots of the PWA results for the η' analysis from a fit with $J^P = \frac{1}{2}^-, \frac{3}{2}^+, \frac{5}{2}^-, \frac{5}{2}^+$(fit #104) partial waves. Left: Plots of the yield for the $\frac{1}{2}^-$(top) and $\frac{5}{2}^-$(middle) partial waves. The phase difference plot(bottom) is displayed. Right: Plots of the yield for the $\frac{1}{2}^-$(top) and $\frac{3}{2}^+$(middle) partial waves. The phase difference between the two waves is presented as well(bottom).

The plots on the left hand side of Figure 6.60 display the yields for the $J^P = \frac{1}{2}^-$(top) and $J^P = \frac{5}{2}^-$(middle) waves. The yield of the $J^P = \frac{1}{2}^-$ wave clearly indicates the importance of this wave at threshold. It dominates the yield in scale from threshold up to $W \approx 2200$ MeV, after which is drops off. The yield of the $J^P = \frac{5}{2}^-$ wave is peaked just shy of $W = 2400$ MeV and appears to contribute almost nothing at threshold. This is reassuring because producing a high-spin object at threshold should be kinematically suppressed. There is, however a slight enhancement at $W = 2150$ MeV which appears in this fit, but was not present in the fit with only the $J^P = \frac{1}{2}^-, \frac{3}{2}^+, \frac{5}{2}^-$(fit #101) waves. The phase difference between the two waves is shown in the bottom plot on the left hand side of Figure 6.60. The phase difference between the $J^P = \frac{1}{2}^-$ and $J^P = \frac{5}{2}^-$ partial waves appears to drop off rapidly in the region around $W = 2200$ MeV where the yields of both partial waves are non-zero.

The plots on the right hand side of Figure 6.60 display the yields for the $J^P = \frac{1}{2}^-$(top) and $J^P = \frac{3}{2}^+$(middle) waves. The yield of the $J^P = \frac{3}{2}^+$ wave is broad and appears in the range $W = 2050 \rightarrow 2400$ MeV. Like the $J^P = \frac{5}{2}^-$ the $J^P = \frac{3}{2}^+$ appears to contribute almost nothing at threshold. The location of the strength in the $J^P = \frac{3}{2}^+$ may be the same, but the overall shape has become more rounded as compared to fit #101 which lacks the additional $J^P = \frac{5}{2}^+$ wave. The phase difference between the two waves is shown in the bottom plot on the right hand side of Figure 6.60. The phase difference between the $J^P = \frac{1}{2}^-$ and $J^P = \frac{3}{2}^+$ partial waves falls slowly until reaching the range of $W = 2200 \rightarrow 2400$ MeV where it appears to drop off.

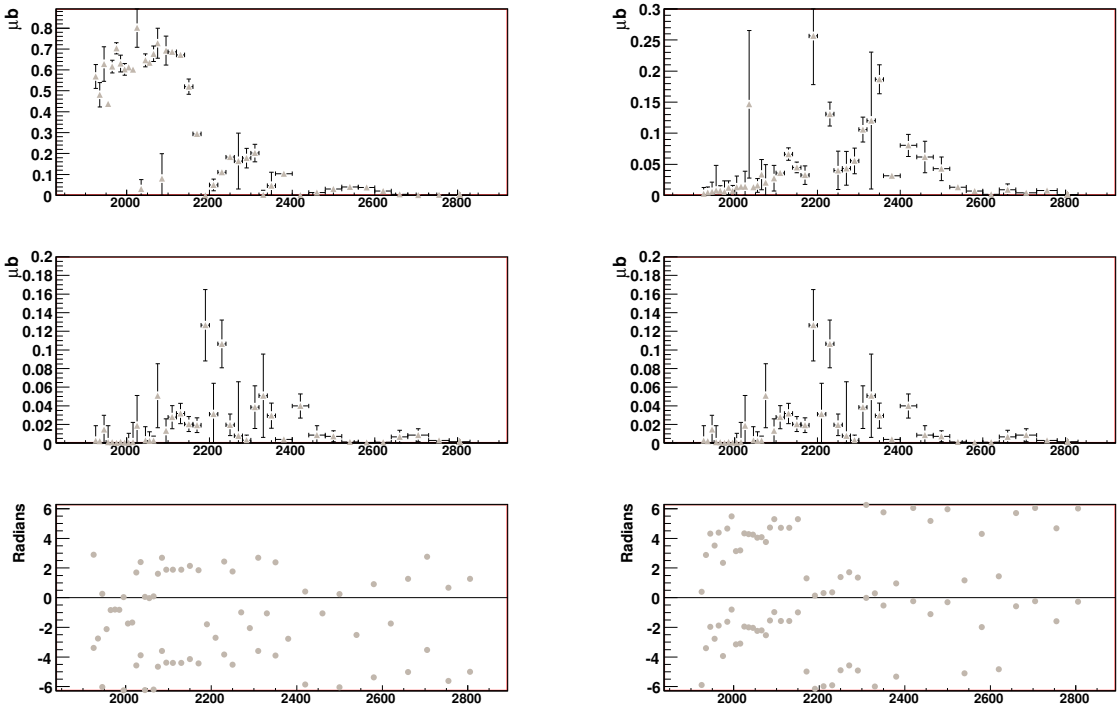

Figure 6.61: Plots of the PWA results for the η' analysis from a fit with $J^P = \frac{1}{2}^-, \frac{3}{2}^+, \frac{5}{2}^-, \frac{5}{2}^+$(fit #104) partial waves. Left: Plots of the yield for the $\frac{1}{2}^-$(top) and $\frac{5}{2}^+$(middle) partial waves. The phase difference plot(bottom) is displayed. Right: Plots of the yield for the $\frac{5}{2}^-$(top) and $\frac{5}{2}^+$(middle) partial waves. The phase difference between the two waves is presented as well(bottom).

The plots on the left hand side of Figure 6.61 display the yields for the $J^P = \frac{1}{2}^-$(top) and $J^P = \frac{5}{2}^+$(middle) waves. The yield of the $J^P = \frac{5}{2}^+$ wave is generally quite small, and appears significant around $W = 2350$ MeV. The phase difference between the two waves is shown in the bottom plot on the left hand side of Figure 6.61. The phase difference between the $J^P = \frac{1}{2}^-$ and $J^P = \frac{5}{2}^+$ partial waves appears to be relatively flat and featureless. The yields from the $J^P = \frac{5}{2}^+$ are likely too small to allow for proper interference with a much larger wave such as the $J^P = \frac{1}{2}^-$.

The plots on the right hand side of Figure 6.61 display the yields for the $J^P = \frac{5}{2}^-$(top) and $J^P = \frac{5}{2}^+$(middle) waves. The yields of these two partial waves have already been described, so the phase difference between the two waves will be examined. The phase difference between the $J^P = \frac{5}{2}^-$

and $J^P = \frac{5}{2}^+$ partial waves appears to oscillate up and down in the range between $W = 2000$ and $W = 2400$ MeV. The motion in the phase difference between the two waves could be an indication of a resonance state.

$J^P = \frac{1}{2}^-, \frac{3}{2}^+, \frac{5}{2}^-, \frac{7}{2}^+$ (fit #105)

Following along the previous fit, this fit adds a $J^P = \frac{7}{2}^+$ wave to the base set of waves, bringing the total number of partial waves in the fit to four. The waves included here are: $J^P = \frac{1}{2}^-, \frac{3}{2}^+, \frac{5}{2}^-, \frac{7}{2}^+$(fit #105). While the indications from the likelihood difference fits were better for the inclusion of a $J^P = \frac{7}{2}^+$ than for the $J^P = \frac{5}{2}^+$ the effect was not large. The general conclusion was to further study this wave set, to determine what structures, if any, might come out of the fit. This fit can also form a study of the effect of inclusion of a higher-spin positive parity wave on the results which had come out of the base set of waves: $J^P = \frac{1}{2}^-, \frac{3}{2}^+, \frac{5}{2}^-$(fit #101).

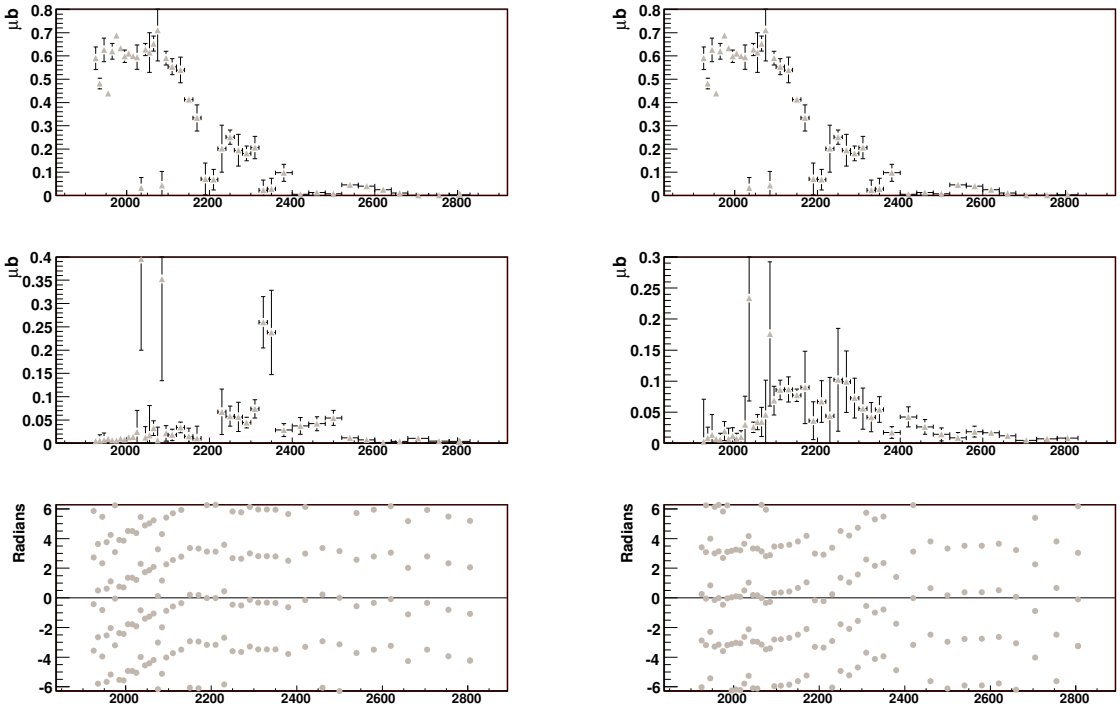

Figure 6.62: Plots of the PWA results for the η' analysis from a fit with $J^P = \frac{1}{2}^-, \frac{3}{2}^+, \frac{5}{2}^-, \frac{7}{2}^+$(fit #105) partial waves. Left: Plots of the yield for the $\frac{1}{2}^-$(top) and $\frac{5}{2}^-$(middle) partial waves. The phase difference plot(bottom) is displayed. Right: Plots of the yield for the $\frac{1}{2}^-$(top) and $\frac{3}{2}^+$(middle) partial waves. The phase difference between the two waves is presented as well(bottom).

The plots on the left hand side of Figure 6.62 display the yields for the $J^P = \frac{1}{2}^-$(top) and $J^P = \frac{5}{2}^-$(middle) waves. The yield of the $J^P = \frac{1}{2}^-$ wave clearly indicates the importance of this wave at threshold. It dominates the yield in scale from threshold up to $W \approx 2300$ MeV, after which is drops off. The yield of the $J^P = \frac{5}{2}^-$ wave appears to contribute broadly stretching to cover the range from $W = 2000 \rightarrow 2500$ MeV. The phase difference between the two waves is shown in the bottom plot on the left hand side of Figure 6.62. The phase difference between the $J^P = \frac{1}{2}^-$ and $J^P = \frac{5}{2}^-$ partial waves appears to change rapidly from threshold to ≈ 2200 MeV. Beyond this region, into higher W, there is very little phase motion evident between the $J^P = \frac{1}{2}^-$(top) and $J^P = \frac{5}{2}^-$ partial waves.

The plots on the right hand side of Figure 6.62 display the yields for the $J^P = \frac{1}{2}^-$(top) and $J^P = \frac{3}{2}^+$(middle) waves. The yield of the $J^P = \frac{3}{2}^+$ wave is broad and appears in the range $W = 2050 \rightarrow 2400$ MeV. The $J^P = \frac{3}{2}^+$ appears to contribute almost nothing at threshold. The location of the strength in the $J^P = \frac{3}{2}^+$ yield are roughly the same, and the overall shape of the yield is consistent with the results for the yield of the $J^P = \frac{3}{2}^+$ in fit #101. The phase difference between the two waves is shown in the bottom plot on the right hand side of Figure 6.62. The phase difference between the $J^P = \frac{1}{2}^-$ and $J^P = \frac{3}{2}^+$ partial waves rises slowly until reaching the range of $W = 2100 \rightarrow 2400$ MeV where it appears to change.

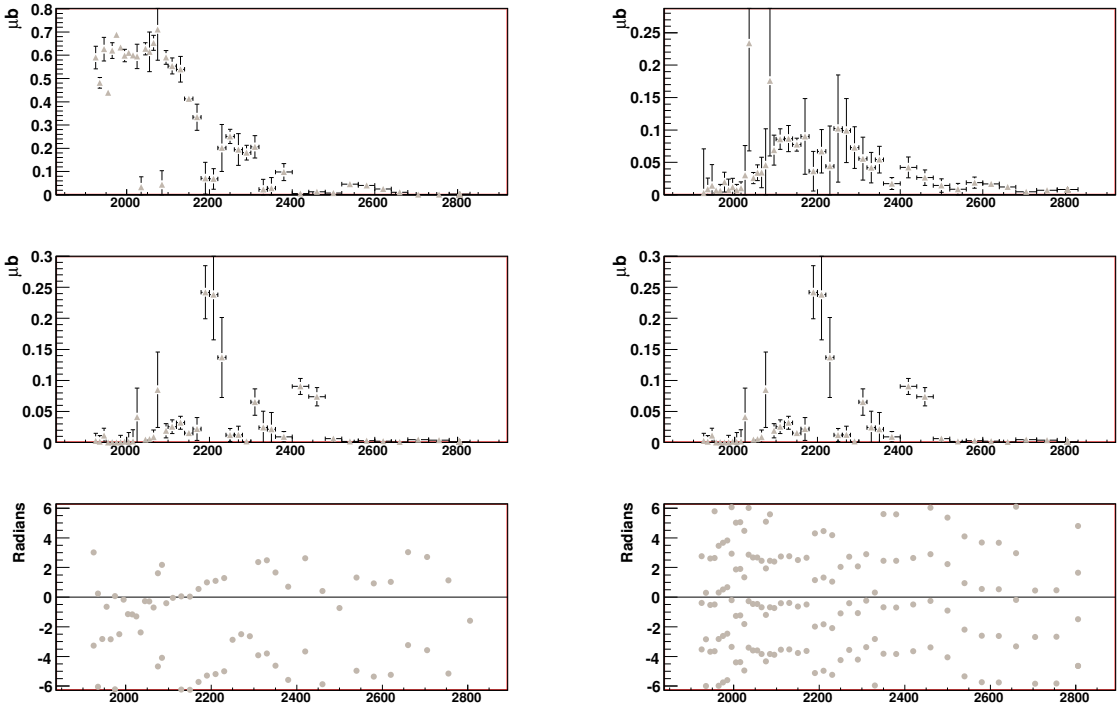

Figure 6.63: Plots of the PWA results for the η' analysis from a fit with $J^P = \frac{1}{2}^-, \frac{3}{2}^+, \frac{5}{2}^-, \frac{7}{2}^+$(fit #105) partial waves. Left: Plots of the yield for the $\frac{1}{2}^-$(top) and $\frac{7}{2}^-$(middle) partial waves. The phase difference plot(bottom) is displayed. Right: Plots of the yield for the $\frac{3}{2}^+$(top) and $\frac{7}{2}^+$(middle) partial waves. The phase difference between the two waves is presented as well(bottom).

On the left side of Figure 6.63 the plots for the yields of the $J^P = \frac{1}{2}^-$(top) and $J^P = \frac{7}{2}^+$(middle) partial waves are shown. The yield of the $J^P = \frac{1}{2}^-$ has been discussed, but the yield of the $J^P = \frac{7}{2}^+$ requires examination. The yield of the $J^P = \frac{7}{2}^+$ is very small across nearly the entire range in W. There is a non-zero yield in the region between $W = 2100$ MeV and $W = 2200$ MeV. The phase difference plot for these waves is generally non-informative. Where both partial waves have non-zero yield, there appears to be smooth phase motion from $W = 2100$ MeV to $W = 2200$ MeV. Aside from that, the phase information is likely meaningless as the fit does not really include the $J^P = \frac{7}{2}^+$ wave in the fit.

The plots on the right hand side of Figure 6.63 display the yields for the $J^P = \frac{3}{2}^+$(top) and

$J^P = \frac{7}{2}^+$(middle) waves. The yields of these partial waves have been described before. The phase difference plot may indicate something previously unnoticed. In the range of $W = 2100 \rightarrow 2300$ MeV there is noticeable phase motion between two waves which are both non-zero. The phase difference plot is shown at the bottom of Figure 6.63.

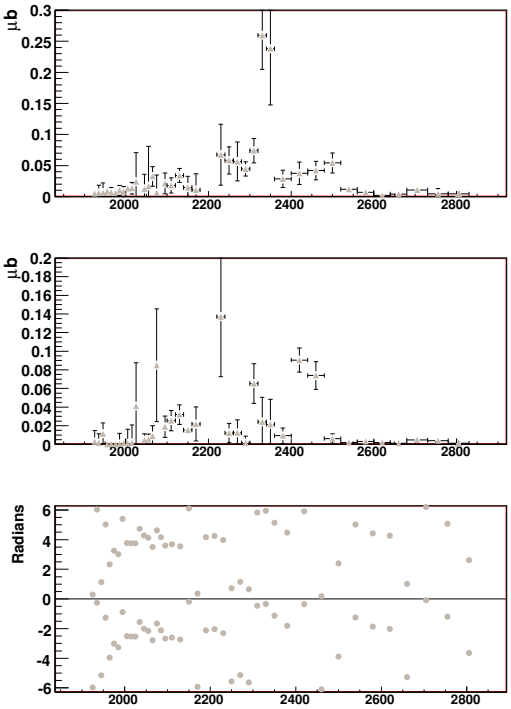

Figure 6.64: Plots of the PWA results for the η' analysis from a fit with $J^P = \frac{1}{2}^-, \frac{3}{2}^+, \frac{5}{2}^-, \frac{7}{2}^+$(fit #105) partial waves. Left: Plots of the yield for the $\frac{5}{2}^-$(top) and $\frac{7}{2}^-$(middle) partial waves. The phase difference plot(bottom) is displayed.

The plots in Figure 6.64 display the yields for the $J^P = \frac{5}{2}^-$(top) and $J^P = \frac{7}{2}^+$(middle) waves. The yields of these partial waves have been described before. The phase difference plot may indicate something previously unseen. In the range of $W = 2100 \rightarrow 2300$ MeV there is noticeable phase motion between two waves which are both non-zero. The phase difference plot is shown at the bottom of Figure 6.64.

Discussion of η' PWA results

It is difficult to assign any known resonance states to the η' results, as very few measurements have been made on this reaction channel. The PDG[4] does not list the η' separate from the η in the tables of N^* branching ratios. With the same quantum numbers as the η it is assumed that states which couple to $N\eta$ will also couple to the $N\eta'$. Unfortunately, there are no well established resonance states which couple to $N\eta$ which are above threshold for η' production. No attempt at assignment of these possible resonance states to known states will be made. There are relatively clear indications of a threshold $J^P = \frac{1}{2}^-$ partial wave. The fit clearly appears to require a $J^P = \frac{3}{2}^+$ partial wave around $W = 2150$ MeV. There is also a hint of strength in the $J^P = \frac{5}{2}^-$ in the higher W region around 2400 MeV.

The PWA on the photoproduced $N\eta'$ final state has a slightly different result when compared with the $N\eta$ final state. The $N\eta$ results appear to find evidence of a higher mass positive parity wave, which does not show up in the $N\eta'$ result. The reactions have slightly different angular acceptances and as such the $N\eta'$ fit is better able to distinguish between the $J^P = \frac{5}{2}^+$ and the $J^P = \frac{7}{2}^+$ partial waves than the $N\eta$. Although neither appear to contribute significantly. To determine the significance of a given state a bit further, the yield results from the $J^P = \frac{1}{2}^-, \frac{3}{2}^+, \frac{5}{2}^-$(fit# 101) reference fit are shown in Figures 6.65, 6.66, and 6.67. It is clear from the given plots that the three waves included contribute to the total yield. The $J^P = \frac{1}{2}^-$ partial wave clearly contributes at threshold, the $J^P = \frac{3}{2}^+$ partial wave at around $W = 2150$ MeV, and the $J^P = \frac{5}{2}^-$ partial wave at slightly higher masses. As a reminder, the non-resonant contribution to the total yield is not presented here, but can be seen in Section 5.3.

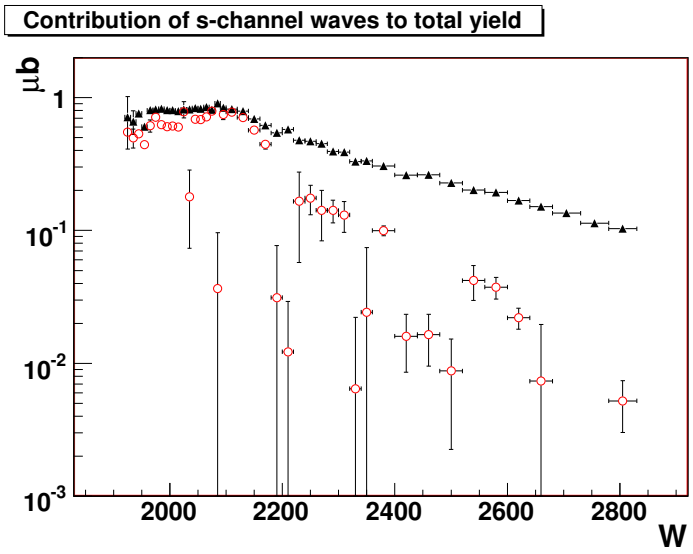

Figure 6.65: Plot of the yields from the $J^P = \frac{1}{2}^-$ partial wave compared to the total yield for the η' analysis. The fit used to obtain these yields contained the $J^P = \frac{1}{2}^-, \frac{3}{2}^+, \frac{5}{2}^-$ partial waves. The threshold region is clearly dominated by the $J^P = \frac{1}{2}^-$ partial wave.

These three wave best describe the physics present in the $N\eta'$ dataset. There is a possible hint of a $J^P = \frac{7}{2}^+$ partial wave, which shows up in the likelihood difference plots and a little bit in the yield, however those results are in no way definitive. Ultimately, in the case of the η' analysis, there is confidence in the structures seen in Figures 6.65, 6.66, and 6.67.

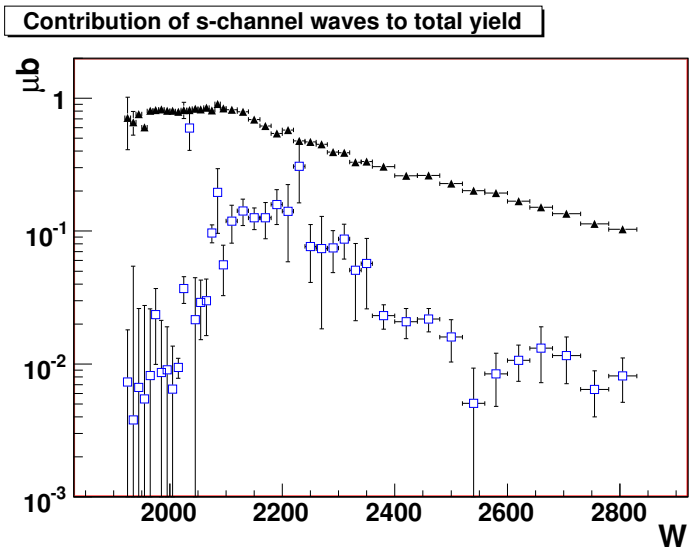

Figure 6.66: Plot of the yields from the $J^P = \frac{3}{2}^+$ partial wave compared to the total yield for the η' analysis. The fit used to obtain these yields contained the $J^P = \frac{1}{2}^-, \frac{3}{2}^+, \frac{5}{2}^-$ partial waves. The $J^P = \frac{3}{2}^+$ partial wave demonstrates clear structure in the $W = 2150$ MeV region, where other results, such as the likelihood differences, indicated that it should contribute significantly.

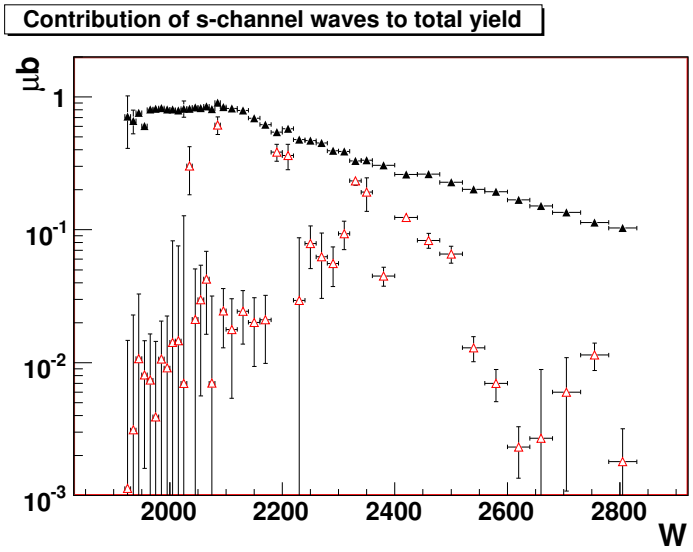

Figure 6.67: Plot of the yields from the $J^P = \frac{5}{2}^-$ partial wave compared to the total yield for the η' analysis. The fit used to obtain these yields contained the $J^P = \frac{1}{2}^-, \frac{3}{2}^+, \frac{5}{2}^-$ partial waves. There is a broad structure to the $J^P = \frac{5}{2}^-$ partial wave in its contribution to the total yield. This similar structure was indicated in the likelihood difference results previously described.

6.6.6 Coupled η and η' Fits

As a brief note regarding coupled fits to the η and η' datasets, it must be said that while fitting the datasets simultaneously was possible and even done at various points, the results were some-

what disappointing. The idea behind the coupled channel analysis was to utilize slightly different acceptances between the two reactions to include as much knowledge as possible in the fit, and thus further constrain the results. The major benefit is that the production pieces of the amplitudes for the coupled channel analysis are forced to be the same for both datasets, as the final state does not have knowledge about how the N^* was created. This provides a further constraint on the fit. Unfortunately, the outcome of the exercise was to essentially reproduce the results from the individual fits. While this improves the confidence which can be had in those results, the lack of substantive improvement in the fits was disappointing.

6.7 Summary

This chapter details the results obtained from PWA of η and η' photoproduction. A large number of PWA fits were run, and the results of those fits were scrutinized to determine if some kind of resonance structure was present in the results. Overall the results from the η analysis lined up relatively well with the previous results from Anisovich[8]. There were clear indications of the presence of a $J^P = \frac{1}{2}^-$ partial wave at threshold, along with a higher mass $J^P = \frac{5}{2}^-$ contribution. The evidence for a strong $J^P = \frac{3}{2}^+$ influence in between the threshold $J^P = \frac{1}{2}^-$ and the higher-mass $J^P = \frac{5}{2}^-$ seems less convincing. There was also a hint of a possible contribution of a higher-spin positive parity wave in the high-W region.

The results from the η' analysis appear to be a little bit different. Once again a threshold $J^P = \frac{1}{2}^-$ contribution appears to be clear. There are indications of a significant $J^P = \frac{3}{2}^+$ contribution at around $W = 2150$ MeV, and a higher-mass $J^P = \frac{5}{2}^-$ contribution, which appears weaker.

Overall, the results are interesting, even if they are only to be considered indications and hints of possible structure. For example, there are no known $J^P = \frac{3}{2}^+$ resonance states near a mass of $W = 2150$ MeV which couple to $N\eta$ or $N\eta'$ listed in the PDG[4].

Chapter 7

Systematics

This chapter describes the systematic studies performed on the PWA results for η and η' photoproduction. To make sure that the results of this analysis are representing the physics inherent in the data, and not an artifact from a cut that was made to select the data, several of the cuts were turned off or altered. By turning these cuts off or changing them, a determination can be made as to whether a particular cut has any effect on the analysis results. This chapter will briefly summarize the results of the analysis for η and η' reaction channels. With a reminder of the results of the analysis, the effect of turning off or altering selected cuts will be presented. The cuts which are being examined in this chapter have all been described in detail in Chapter 3. Refer to that chapter for a more in depth look at the cuts, and the motivation behind them.

7.1 Summary of η PWA Results

While the results of the partial wave analysis are only to be taken as indications or hints, there were structures which appeared consistently in the results. The structure most evident in the η analysis is the strength at threshold found in the $J^P = \frac{1}{2}^-$ partial wave. Additionally, a higher-mass structure was typically found in the $J^P = \frac{5}{2}^-$ partial wave around $W = 2200$ MeV. There were also indications of strength of the $J^P = \frac{3}{2}^+$ near $W = 1800$ MeV. Finally, at higher W, around 2300 MeV, there was an enhancement found in either the $J^P = \frac{5}{2}^+$ or the $J^P = \frac{7}{2}^+$ partial waves. While no resonance parameters were extracted from these structures, the consistent appearance of a structure in a given partial wave in fits with various combinations of waves is taken to be indicative of something physical.

7.2 Summary of η' PWA Results

A summary of the PWA results for the η' is given in this section. The structure most evident in the η' analysis is the threshold $J^P = \frac{1}{2}^-$ partial wave. Additionally, a slightly higher-mass structure was typically found in the $J^P = \frac{3}{2}^+$ partial wave around $W = 2150$ MeV. There was also some indication of the $J^P = \frac{5}{2}^-$ contributing near $W = 2400$ MeV. While no resonance parameters were extracted from these structures, the consistent appearance of a structure in a given partial wave in fits with various combinations of waves is taken to be indicative of something physical.

7.3 Systematic Check of PWA Results

With the results of the η and η' analysis reviewed, it is prudent to move on to the effect of cuts on the results which the analysis has rendered. In order to determine the effect of the cuts made on the partial wave analysis results, fits were run with differing sets of cuts on the data. To allow for a more methodical approach to the systematic analysis, three sets of partial waves were selected for the analysis of the η and η' reaction channels. All of the fits which were run here will utilize a base set of three partial waves. These waves are $J^P = \frac{1}{2}^-, \frac{3}{2}^+, \frac{5}{2}^-$, which correspond to Fit #001 for the η and Fit #101 for the η'. Additionally, two other sets will include either the $J^P = \frac{5}{2}^+$ or the $J^P = \frac{7}{2}^+$ partial wave. These fits correspond to Fit #004,005 or Fit #104,105 as described in Chapter 6.

The purpose of this exercise is to determine the stability of the PWA results under different event selection criteria. To determine if the structures observed in the results of the η and η' analyses are stable, different event inputs were used. Fits were run with cuts either removed completely, or altered, and the results should indicate how dependent the original results are on the event selection of the data and Monte Carlo. The cuts examined here were the fiducial cuts, the vertex timing cut, the confidence level cut, and an alteration of the t-channel parameterization. With each variation, a series of fits was run to determine the effect of the cut on the results. Each of the fits and the subsequent results will be described and compared to the original results.

It is important to note, that since the individual W bins are all fit independently, it is entirely likely that there will be changes in a given bin for the strength of different partial waves. The purpose of this systematic check is not to determine the effects of the cuts on a particular bin, but to examine the effect more globally. The objective is to see if the larger structures, which appear over many subsequent W bins, are still present when the cuts are altered or removed.

7.3.1 Performing Systematic Checks

The general process used in running the systematic checks described in this chapter, will be described here. It is important to note that the effect of changing a cut in this analysis, is not a simple process. The separation of various fit components into different files makes the process faster, but still non-trivial. The different files used are described in Section 5.10 With every change in the event selection, the background parameterization process must be repeated. A majority of the cuts made on the data are there to remove any possible background, and as such the parameterization of that background must be re-determined. The process by which the background is parameterized is given in Section 3.8. Once the background parameterization has been done for the altered cuts on the data, then the background amplitudes which represent the parameterization within the fit, must be regenerated. Every time new amplitudes are generated, the normalization integral files must be regenerated as well. Finally, new fit parameters for the background amplitudes must be determined. With all of those components available for the new version of the cuts, a fit must be created which then utilizes the appropriate cut files. With the fit created, a fit is run over the entire dataset using multiple iterations of the fit in each W bin. While this process is relatively easy to describe, it can be rather lengthy when it is being repeated systematically to determine the individual effects on the PWA results for a change in a single cut.

The advantage of this procedure is that at all times the background is being re-parameterized and correctly compensated for. For example, the vertex timing cut, which is described fully in Section 3.6.4, removes mostly background from the dataset. When this background is re-introduced to the dataset by removing this cut, the background parameterization procedure will compensate for that change. This should allow for the fit to reproduce the PWA results regardless of the presence of the fit.

7.3.2 Fiducial Cut

Producing cuts in the data to use only the efficient parts of the detector is a widely accepted practice in CLAS. There are obvious holes in the forward and backward directions of the detector, the very edges of which are traditionally removed. Additionally, there are the boundaries of the six sectors which are removed due to lack of ability to track through that region. In determining the effects of the fiducial cuts on the PWA results, the fiducial cuts were completely removed. This tested the most extreme change in the fiducial cuts, which in turn should provide for the maximal effect on the results. Additionally, there is always the possibility of making the fiducial cuts more severe, and determining the effect on the PWA results for η and η'. This option is not explored in this analysis due to the lack of support for more severe fiducial cuts in the systematic studies of the data and Monte Carlo. For further information about what specific cuts were made as part of the fiducial cuts, please see Section 3.6.5.

As the η and η' have slightly different angular acceptances, it is warranted that both analyses are subject to the this test of the effect of fiducial cuts. For the sake of comparison, the original fit results are plotted for the η and the η' along with the versions with the fiducial cuts removed. The original results will not be reproduced for the comparison to the versions with modified timing cut, or confidence level.

η $J^P = \frac{1}{2}^-, \frac{3}{2}^+, \frac{5}{2}^-$ (Fit #001)

The first sets of fits to be compared were Fit #001 for the η with and without the fiducial cuts. This set of partial waves was a starting place for the analysis and contains most of the partial waves with significant structure. Perhaps the most obvious starting points in this comparison are the $J^P = \frac{1}{2}^-$ and $J^P = \frac{5}{2}^-$ partial waves in the fit.

Comparison of the η results which utilize the fiducial cuts and the results which do not, indicates that the general shape and features of the $J^P = \frac{1}{2}^-$ and $J^P = \frac{5}{2}^-$ partial waves remain consistent. The plots of the strength of the partial wave, as well as the phase differences of the two, are in relatively good agreement, which indicates that for the η analysis, the fiducial cuts do not have a critical effect upon the results of the fit.

As an additional check, a comparison of the $J^P = \frac{1}{2}^-$ and $J^P = \frac{3}{2}^+$ partial waves indicates that the structures which are seen are present in both versions of the fit. The phase motion is very similar, and the general structures of the strengths of the partial waves are in agreement.

As a whole, the agreement between the fit with and without the fiducial cuts is very good. The same structures appear in both versions of the fit, and so for the η analysis, it appears that the systematic effect of the fiducial cuts on the results of Fit #001 is minimal.

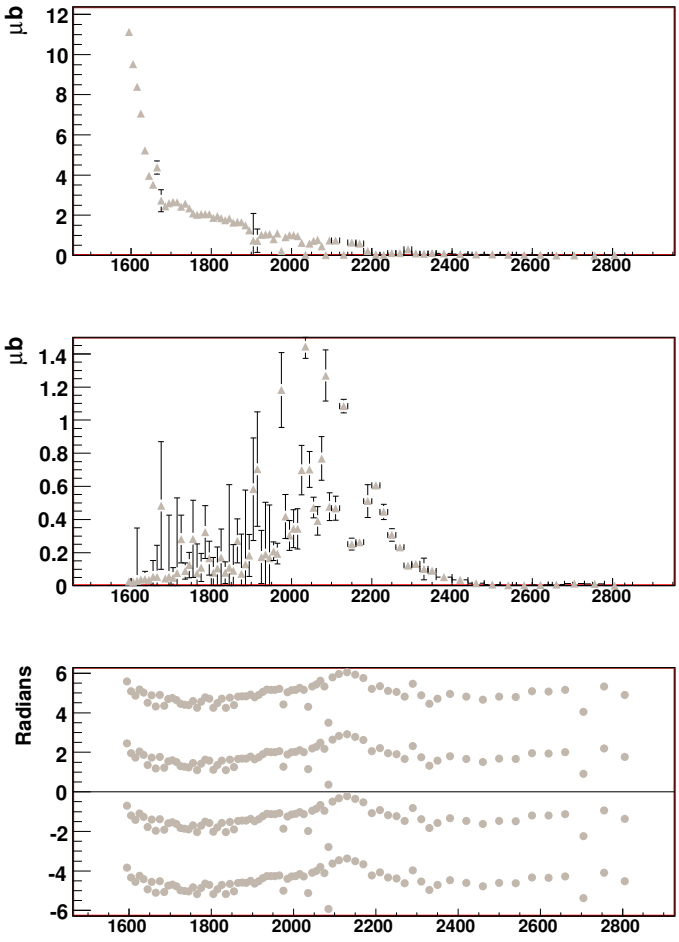

Figure 7.1: Plots of the yields and phase difference of the $J^P = \frac{1}{2}^-$(top) and $J^P = \frac{5}{2}^-$(middle) partial waves from the original set of cuts. This is given as a reference with which other versions of the fit can be compared.

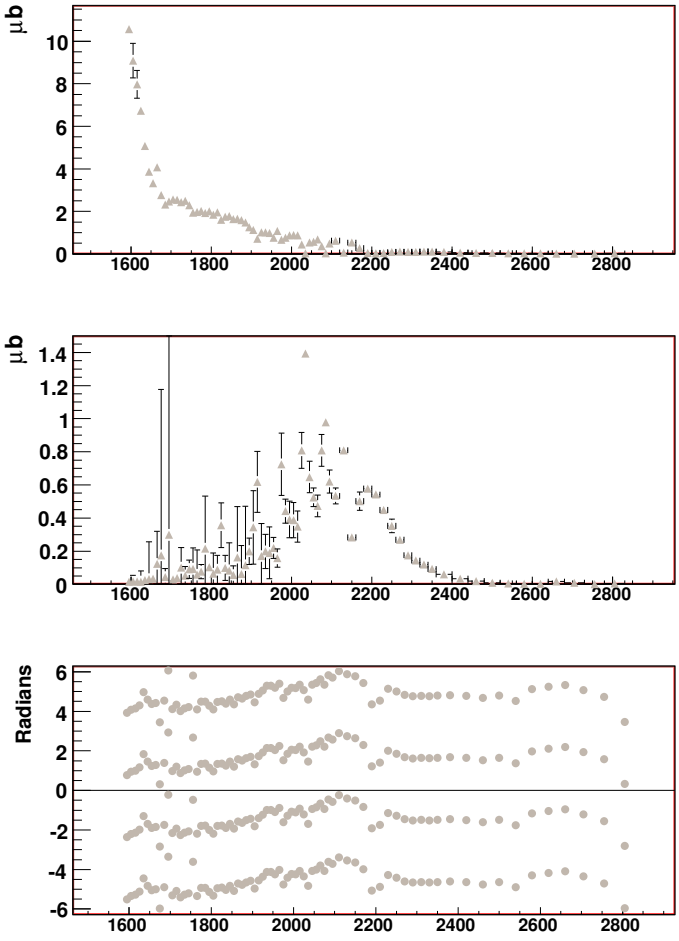

Figure 7.2: Plots of the yields and phase difference of the $J^P = \frac{1}{2}^-$ (top) and $J^P = \frac{5}{2}^-$ (middle) partial waves from the fits run without the fiducial cuts in place. Comparing this fit to 7.1 demonstrates how similar the results are.

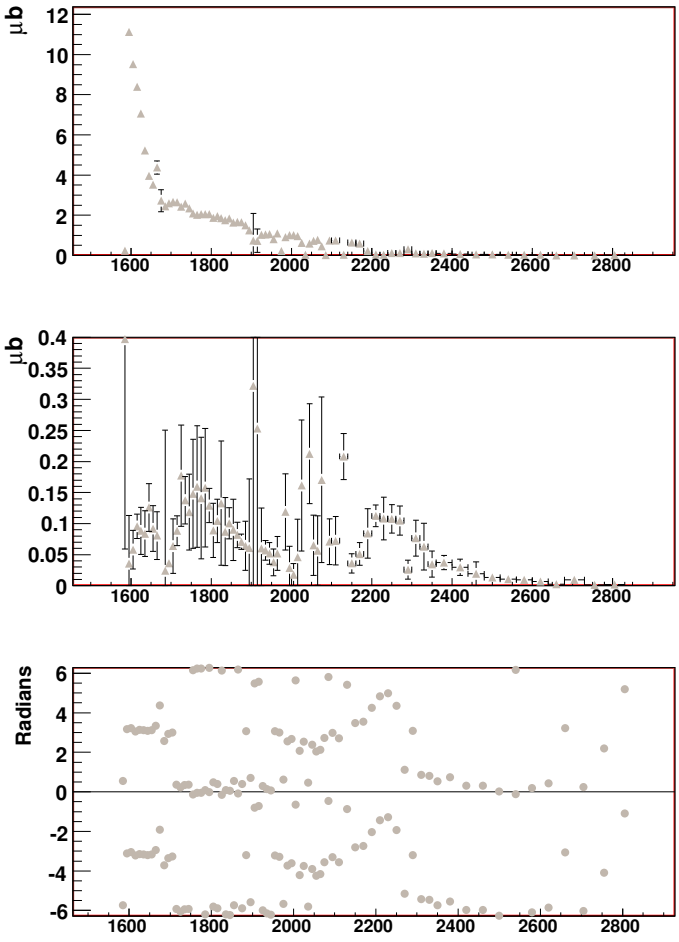

Figure 7.3: Plots of the yields and phase difference of the $J^P = \frac{1}{2}^-$(top) and $J^P = \frac{3}{2}^+$(middle) partial waves from the original set of cuts. This is given as a reference with which other versions of the fit can be compared.

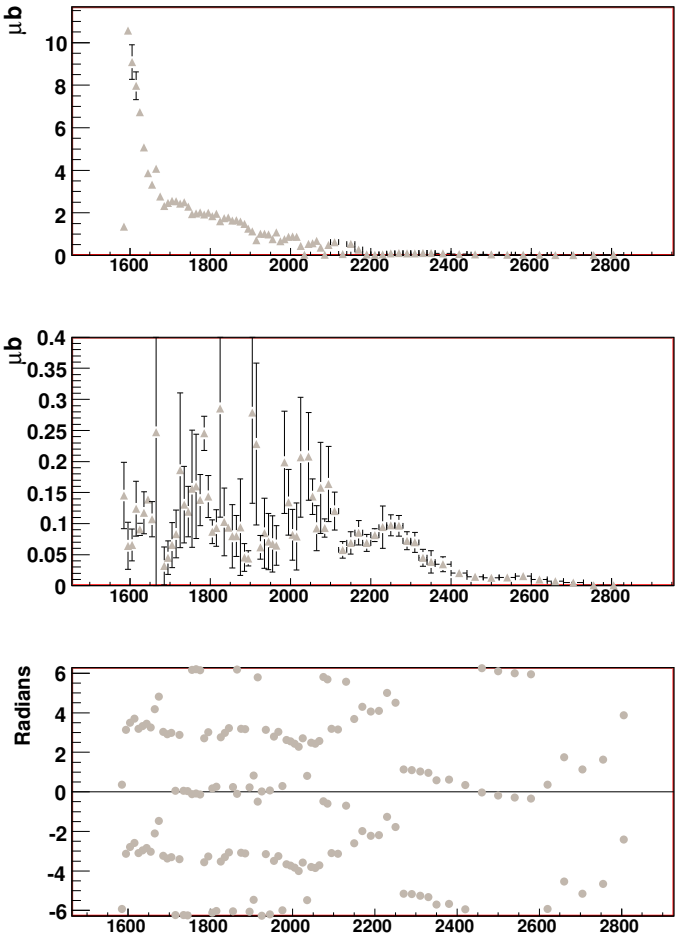

Figure 7.4: Plots of the yields and phase difference of the $J^P = \frac{1}{2}^-$(top) and $J^P = \frac{3}{2}^+$(middle) partial waves from the fits run without the fiducial cuts in place. This plot should be compared with 7.3. The comparison shows that the same structures exits in both versions of the fit.

η $J^P = \frac{1}{2}^-, \frac{3}{2}^+, \frac{5}{2}^-, \frac{5}{2}^+$ **(Fit #004)**

Fit #004 contains the three base partial waves which comprise Fit #001 but now adds a $J^P = \frac{5}{2}^+$ partial wave. As the η analysis is unable to distinguish between the $J^P = \frac{5}{2}^+$ and $J^P = \frac{7}{2}^+$(middle) partial waves, this will serve as a check on both Fit #004 and Fit #005. A comparison between the $J^P = \frac{1}{2}^-$ and $J^P = \frac{3}{2}^+$ waves will be made first (Figures 7.5 and 7.6), and then the $J^P = \frac{5}{2}^-$ and $J^P = \frac{5}{2}^+$ waves will be compared (Figures 7.7 and 7.8. This will yield a full picture of the effect the fiducial cuts have on the PWA η results for Fit #004.

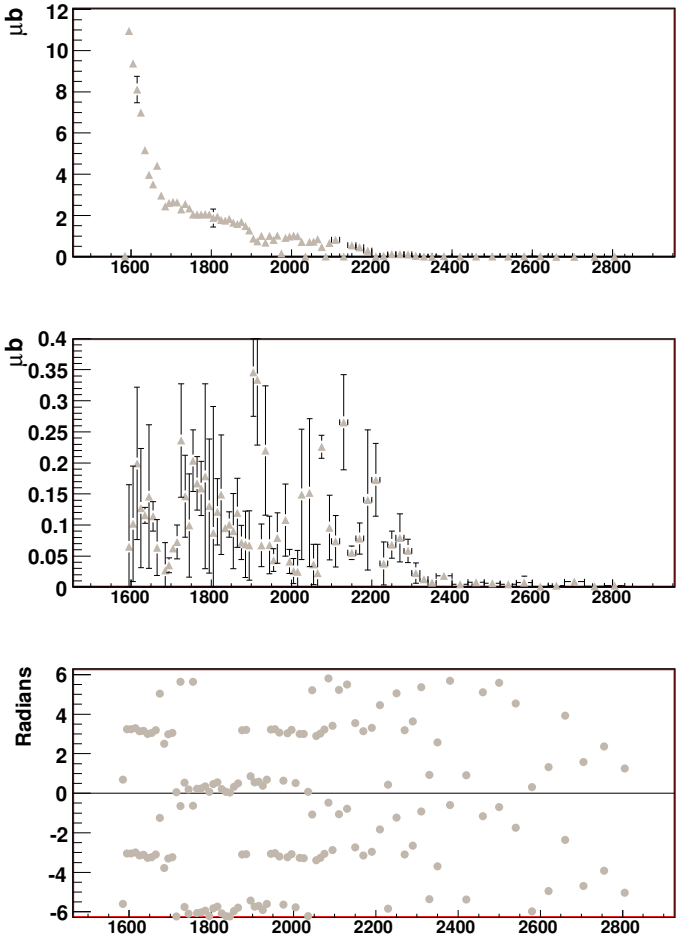

Figure 7.5: Plot of the yield of the $J^P = \frac{1}{2}^-$(top) and $J^P = \frac{3}{2}^+$(middle) partial waves for Fit #004 using the original cuts.

The same general structure exists in the $J^P = \frac{1}{2}^-$ and $J^P = \frac{3}{2}^+$ partial waves when compared. There is similar phase motion, and the strength of the partial waves are enhanced in similar regimes.

Comparison of the two $J = \frac{5}{2}$ partial waves is a more difficult task. See Figures 7.7,7.8. Clearly there is structure in each partial wave, and where the strength exists, the phase motion is consistent between the two version of the fit. Near threshold, or at very high center-of-mass energy (W) this comparison of phase appears to break down. There is a questions as to how strong the wave must

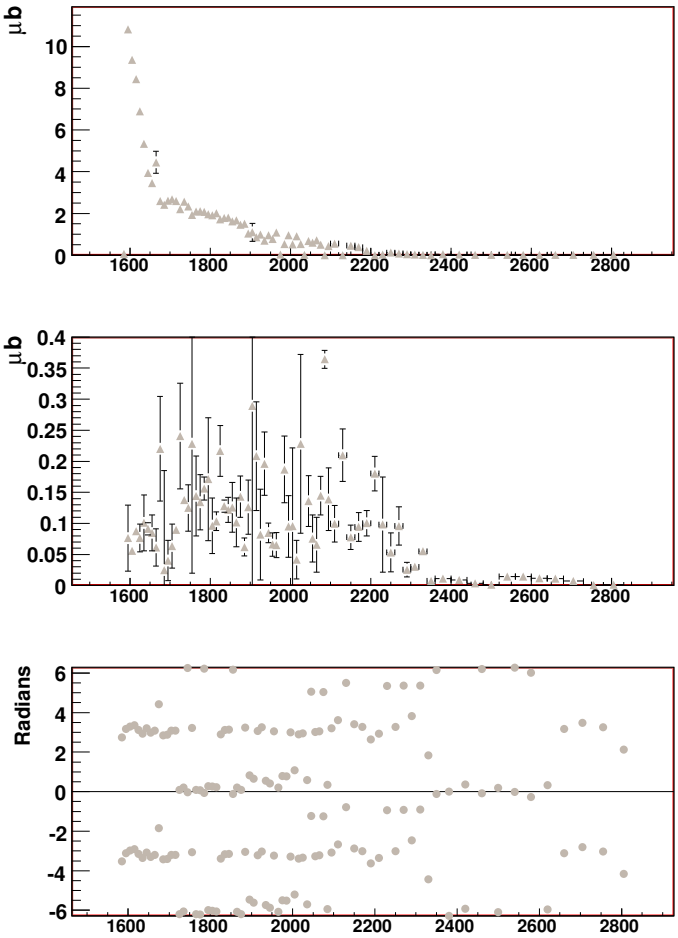

Figure 7.6: Plot of the yield of the $J^P = \frac{1}{2}^-$(top) and $J^P = \frac{3}{2}^+$(middle) partial waves for Fit #004 without the fiducial cuts. Comparing these to 7.5 demonstrates that the results are equivalent.

be to allow for reasonable wave motion. Simply put, the phase of a resonance structure is not well defined far from the peak, and thus the interference of the two, is likewise ill-defined. As can be observed in the Figures 7.7,7.8 the phase motion is somewhat chaotic below $\approx$ 1900 MeV. Overall the results present in the η analysis of Fit #004 with and without the fiducial cuts are consistent. It appears that the results are not strictly dependent on the fiducial cuts which were originally made.

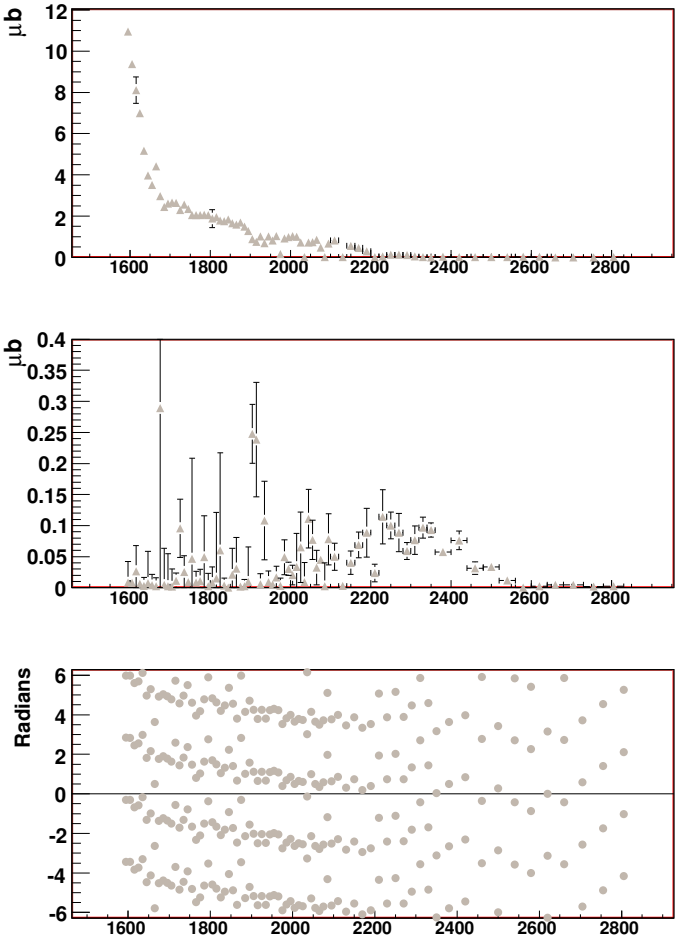

Figure 7.7: Plot of the yield of the $J^P = \frac{5}{2}^-$(top) and $J^P = \frac{5}{2}^+$(middle) partial waves for Fit #004 using the original cuts.

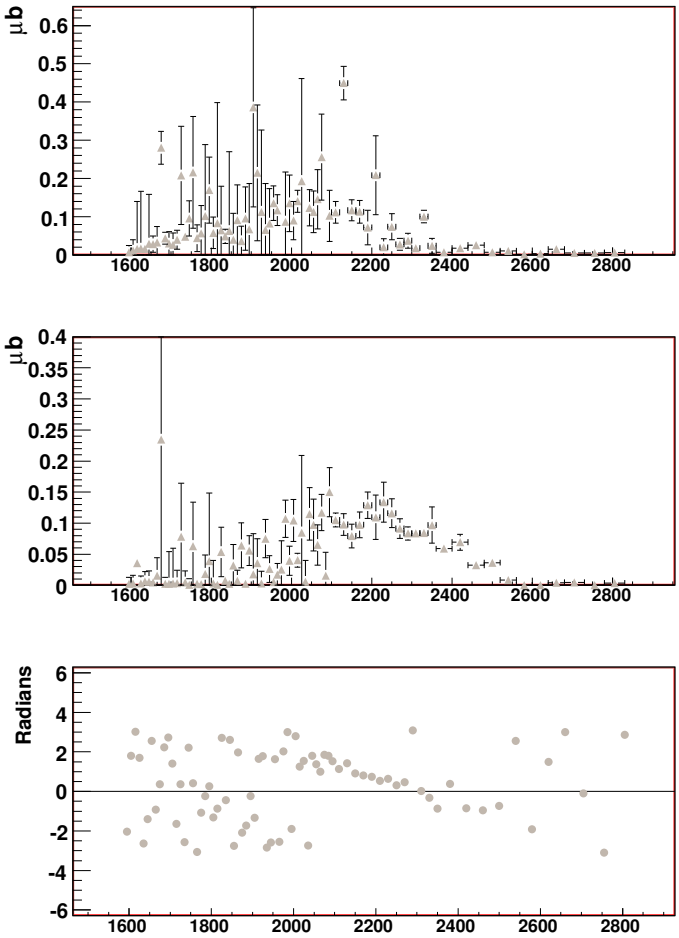

Figure 7.8: Plot of the yield of the $J^P = \frac{5}{2}^-$ (top) and $J^P = \frac{5}{2}^+$ (middle) partial waves for Fit #004 without the fiducial cuts.

η' $J^P = \frac{1}{2}^-, \frac{3}{2}^+, \frac{5}{2}^-$ (Fit #101)

Fit #101 is the starting point for comparison, and was the starting point for the study of the effect of the fiducial cuts on the PWA results for the η' analysis. The fiducial cuts can directly affect the angular acceptance of the particles in the final state, and as such are an important factor in determining if the fit results are stable.

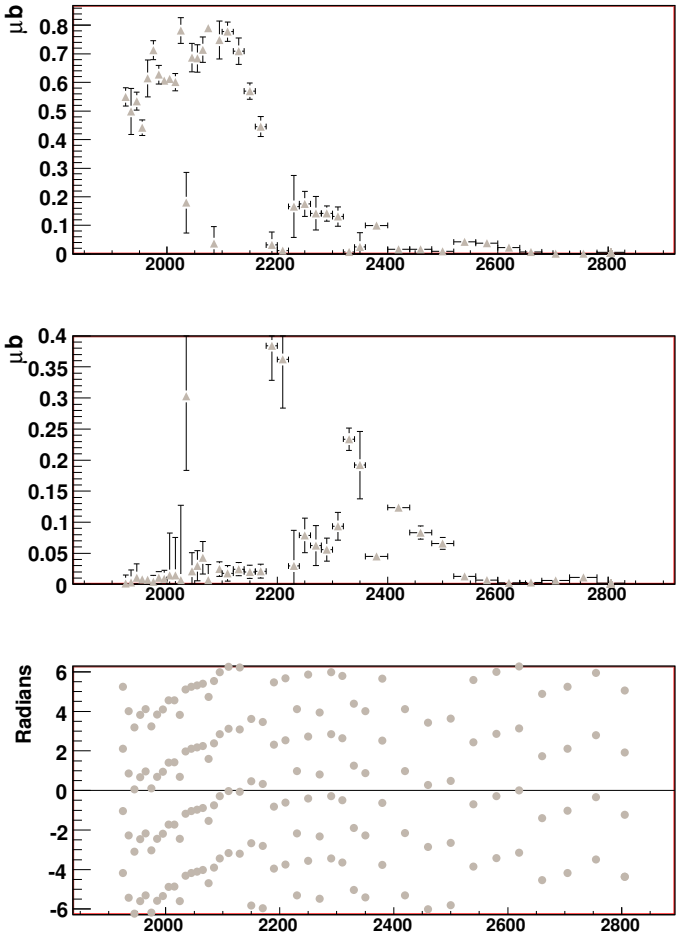

Figure 7.9: Plots of the yields and phase difference of the $J^P = \frac{1}{2}^-$(top) and $J^P = \frac{5}{2}^-$(middle) partial waves from the original set of cuts. This is given as a reference with which other versions of the fit can be compared.

The general shape and features of the $J^P = \frac{1}{2}^-$ and $J^P = \frac{5}{2}^-$ partial waves (See Figures 7.9 and 7.10) remain consistent between the two version of the fit for the η' analysis. The plots of the strength of the partial wave, as well as the phase differences of the two, are in relatively good agreement, which indicates that for the η' analysis, the fiducial cuts do not have a critical effect upon the results of the fit.

The $J^P = \frac{1}{2}^-$ and $J^P = \frac{3}{2}^+$ partial waves demonstrate similar structures (see Figures 7.11 and 7.12) if both versions of the fit. There is no indication of the strength of a partial wave diminishing

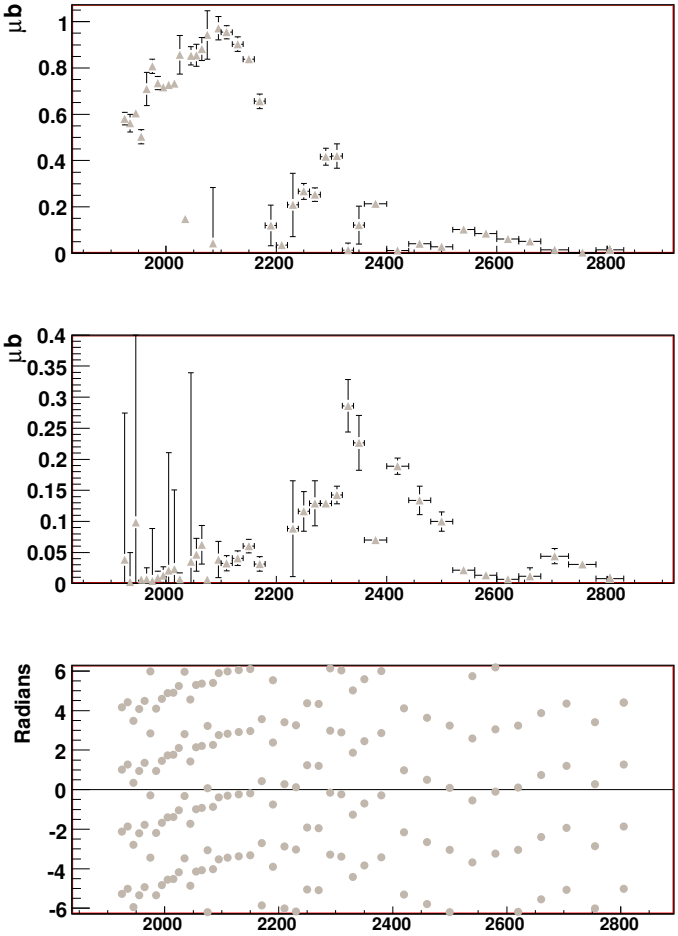

Figure 7.10: Plots of the yields and phase difference of the $J^P = \frac{1}{2}^-$(top) and $J^P = \frac{5}{2}^-$(middle) partial waves from the fits run without the fiducial cuts in place. Comparing this plot to 7.9 demonstrates the stability of the result, and indicates that the result is not an artifact of cuts made on the data.

due to the change in fiducial cuts. Additionally, there is no indication of significant change in phase motion.

Overall, Fit #101 is left generally unaffected by the removal of the fiducial cuts used in this analysis. There are several outlying points, but the general structure seen in the original results appears similarly to the results from the removal of the fiducial cuts. This indicates that the PWA results for this fit are largely independent of the specific fiducial cuts which have been employed.

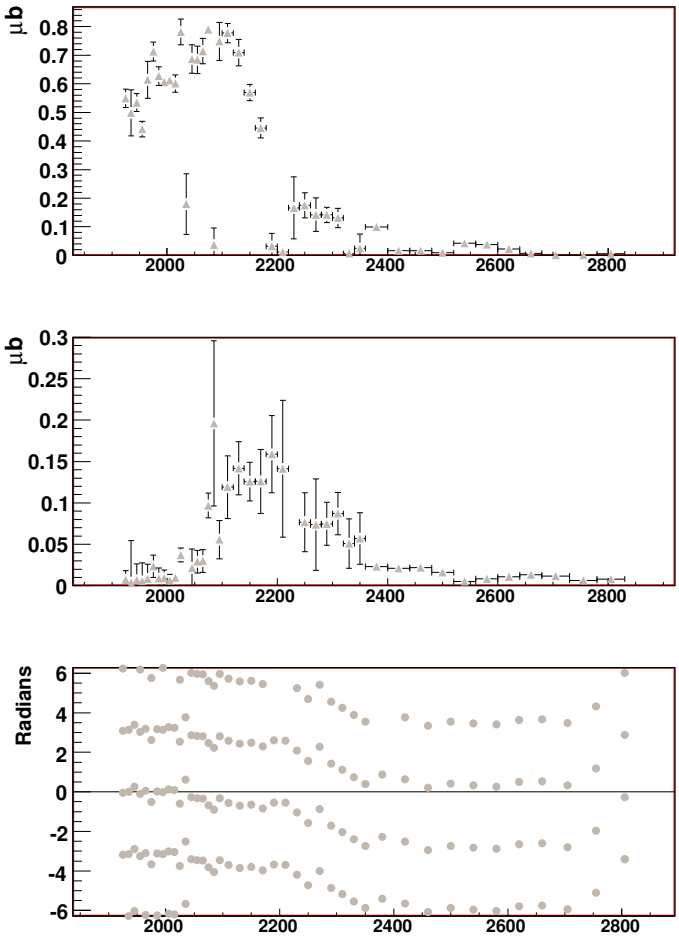

Figure 7.11: Plots of the yields and phase difference of the $J^P = \frac{1}{2}^-$(top) and $J^P = \frac{3}{2}^+$(middle) partial waves from the original set of cuts. This is given as a reference with which other versions of the fit can be compared.

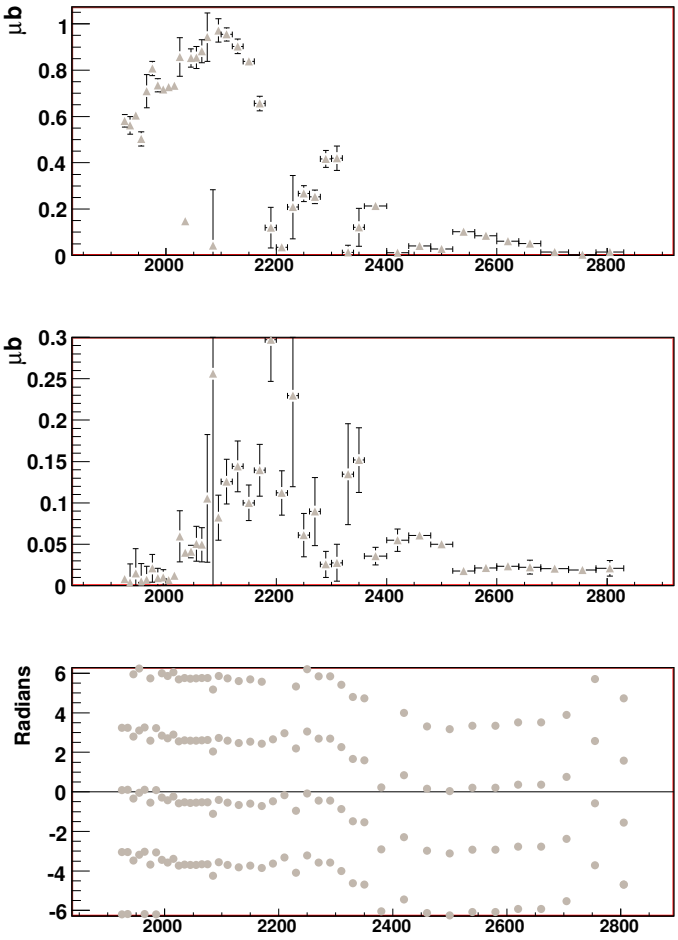

Figure 7.12: Plots of the yields and phase difference of the $J^P = \frac{1}{2}^-$(top) and $J^P = \frac{3}{2}^+$(middle) partial waves from the fits run without the fiducial cuts in place. Comparing 7.11 to this plot demonstrates the similarity in the two versions of the fit.

η' $J^P = \frac{1}{2}^-, \frac{3}{2}^+, \frac{5}{2}^-, \frac{7}{2}^+$ **(Fit #105)**

As the η' analysis appears to have a slight preference for the $J^P = \frac{7}{2}^+$ partial wave over the $J^P = \frac{5}{2}^+$ partial wave, Fit #105 will be used as the test bed for the effect of the fiducial cuts on the fits with additional higher-spin waves.

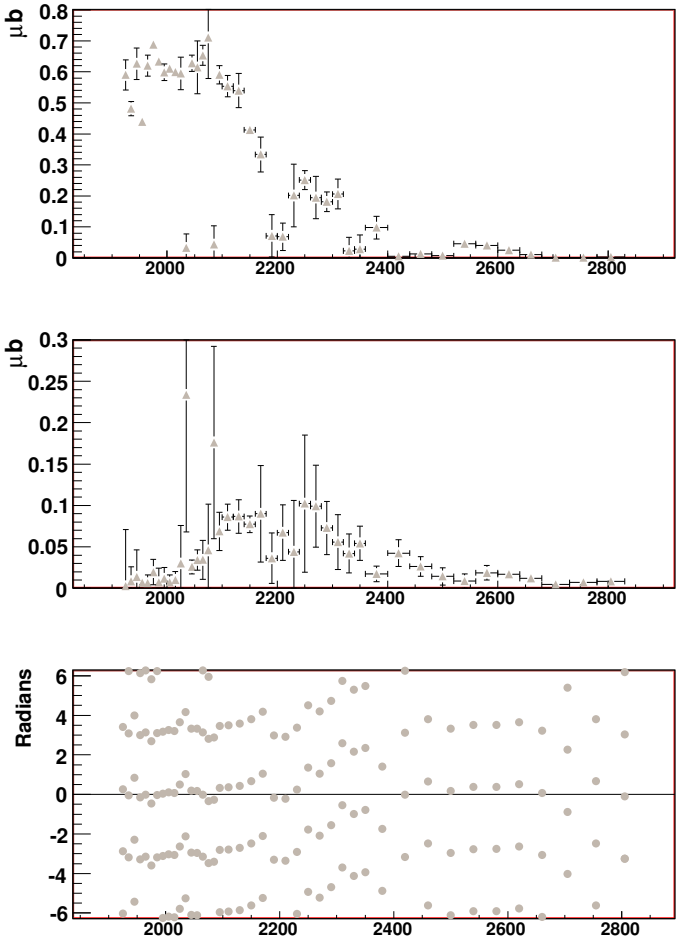

Figure 7.13: This is a plot of the yields of the $J^P = \frac{1}{2}^-$(top) and the $J^P = \frac{3}{2}^+$(middle) partial waves and their phase difference.

The same general structure exists in the $J^P = \frac{1}{2}^-$ and $J^P = \frac{3}{2}^+$ partial waves when compared, see Figures 7.13 and 7.14. There is similar phase motion, and the strengths of the partial waves are enhanced in similar regimes.

Similar structures appear in Figures 7.15 and 7.16 when comparing the results for the $J^P = \frac{1}{2}^-$ and $J^P = \frac{3}{2}^+$ partial waves with and without the fiducial cuts. To summarize, the general effect of the removal of fiducial cuts on this fit is minimal. The structures present in the partial waves persist, and there is no noticeable systematic change in phase motion. This fit appears to be fairly immune to changes in the fiducial cuts.

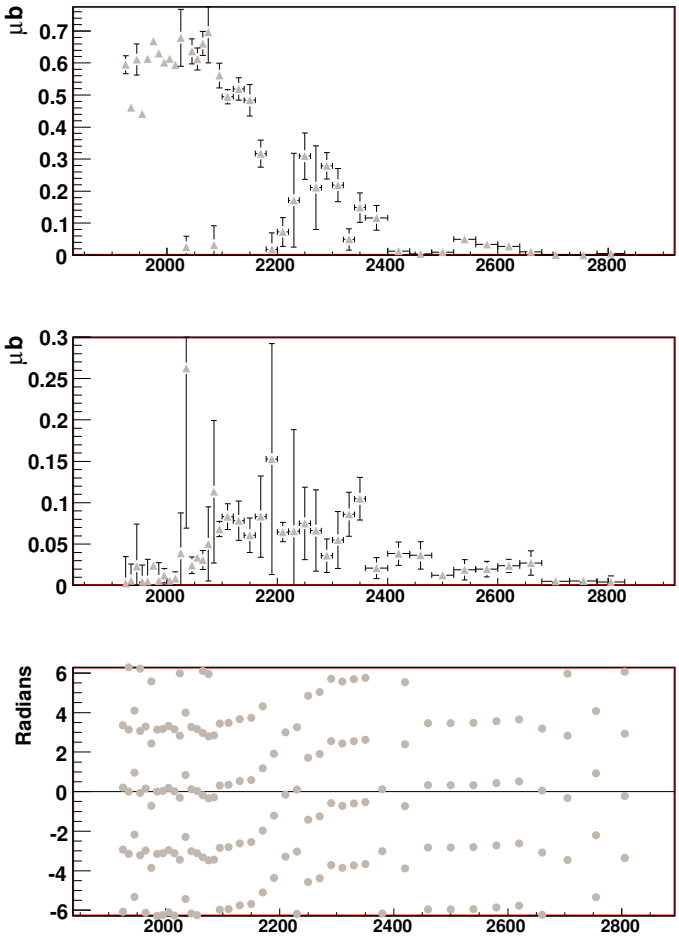

Figure 7.14: A plot of the yields of the $J^P = \frac{1}{2}^-$(top) and the $J^P = \frac{3}{2}^+$(middle) partial waves and their phase difference from Fit #105 without use of the fiducial cuts. Comparing this plot to 7.13 demonstrates that a change in the fiducial cuts will not have much of an effect on the results.

Conclusions Regarding Fiducial Cut

Overall, there studies here indicated that the PWA results of the η and η' analyses were relatively immune to changes in the fiducial cuts. If turning them off all together yields similar global structures, then smaller and more subtle changes are extremely likely to reproduce the results which were previously observed. Changes to the fiducial cuts which make them more severe could have an effect, but more severe cuts are not supported by any of the systematic studies of the data and Monte Carlo. Additionally, more severe cuts in the fiducial region would have to cut into the angular acceptance in $cos(\theta_{CM})$ of the η and η' mesons in order to have a significant effect.

7.3.3 Timing Cut

Event selection and particle identification are based on the vertex timing cut, and as such it was natural to determine what, if any, effect that cut has on the PWA results. To this end, the vertex

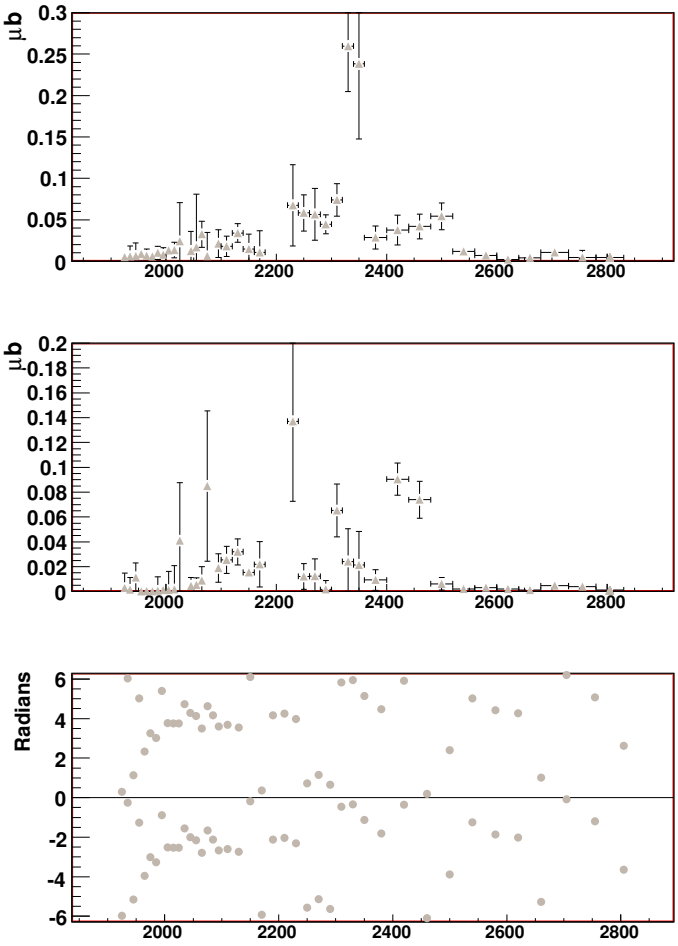

Figure 7.15: This is a plot of the yields of the $J^P = \frac{5}{2}^-$(top) and the $J^P = \frac{7}{2}^+$(middle) partial waves and their phase difference.

timing cut was simply loosened to the values of the initial data skim for the η and η' datasets. The initial cut placed on the event when skimming out event for analysis selected only events in which one of the three charged tracks was within 2.0 ns of the photon vertex time. By removing the vertex timing cut in the PWA fit, the timing criteria revert back to this initial condition. The effect of such a change is to increase the background contained in the data which is being analyzed in the PWA fitting process. Since the background presumably has different angular distributions from the η events, some effect is possible on the fit results. For more specific information regarding the timing cut, please refer to Section 3.6.4.

Only the plots of the new versions of the fits will be presented here. For comparison to the original solutions, refer back to the plots contained in the previous section on the effect of the fiducial cuts on fit results, or to the chapter describing the PWA results (Chapter 6.

Additionally, the fits for the η which will be presented contain the $J^P = \frac{1}{2}^-, \frac{3}{2}^+, \frac{5}{2}^-, \frac{5}{2}^+$ partial waves. The η' results will contain the $J^P = \frac{1}{2}^-, \frac{3}{2}^+, \frac{5}{2}^-, \frac{7}{2}^+$ partial waves. For the η comparison, please refer to Figures 7.5 and 7.7 for the original results. For the η' comparison, please refer to

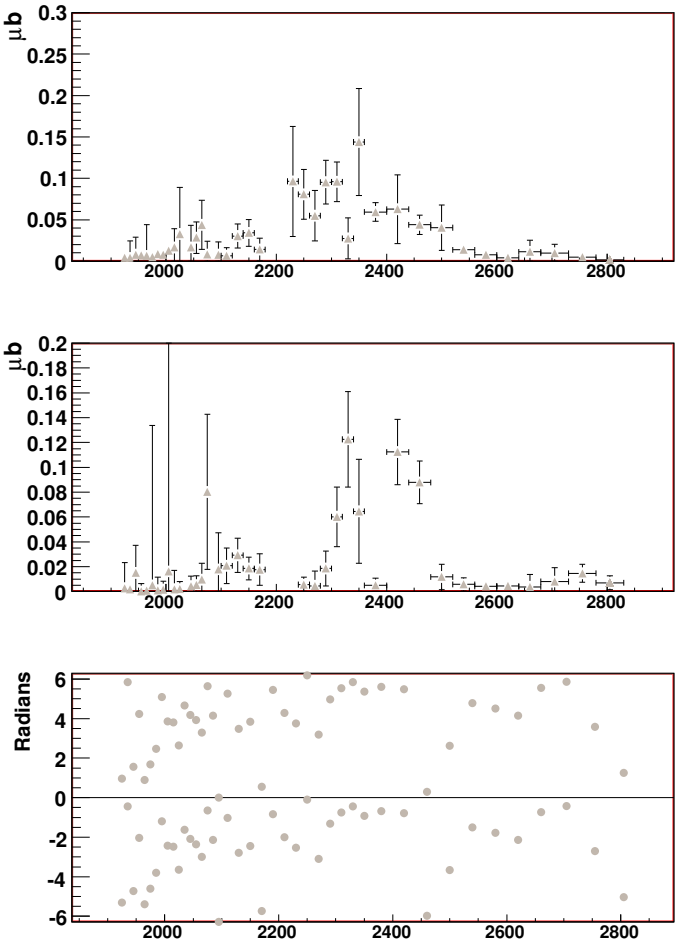

Figure 7.16: A plot of the yields of the $J^P = \frac{5}{2}^-$(top) and the $J^P = \frac{7}{2}^+$(middle) partial waves and their phase difference from Fit #105 without use of the fiducial cuts. Comparing this plot to 7.15 demonstrates that a change in the fiducial cuts will have some effect on the results, but that general location of strength in the partial waves remains similar.

Figures 7.13 and 7.15. The rational for presenting these results only, is that the fits with an additional partial wave have more freedom, and will therefore be more prone to adjust their solutions with the changing conditions. If a fit appears unchanged by an adjustment in a cut, then a fit with fewer partial waves, and thus less freedom, would be likewise unaffected. Additionally, in the description of the vertex timing cut, a study completed by Mike Williams[41] indicated that the events excluded by the cut were primarily background, with very little signal lost.

η $J^P = \frac{1}{2}^-, \frac{3}{2}^+, \frac{5}{2}^-, \frac{5}{2}^+$ (Fit #004)

Comparing the results from Fit #004 allows the fit to use an additional partial wave to fit to the data when compared to Fit #001. As structure has been noted in the $J^P = \frac{5}{2}^+$ partial wave, the effect of the alteration of the vertex timing cut shall be demonstrated for the waves in the fit. Comparing the

lower spin partial waves, the $J^P = \frac{1}{2}^-$ and $J^P = \frac{3}{2}^+$, there is equivalent structure in these results as in the original results previously reported. See Figure 7.17 in comparison to the original results in Figure 7.5.

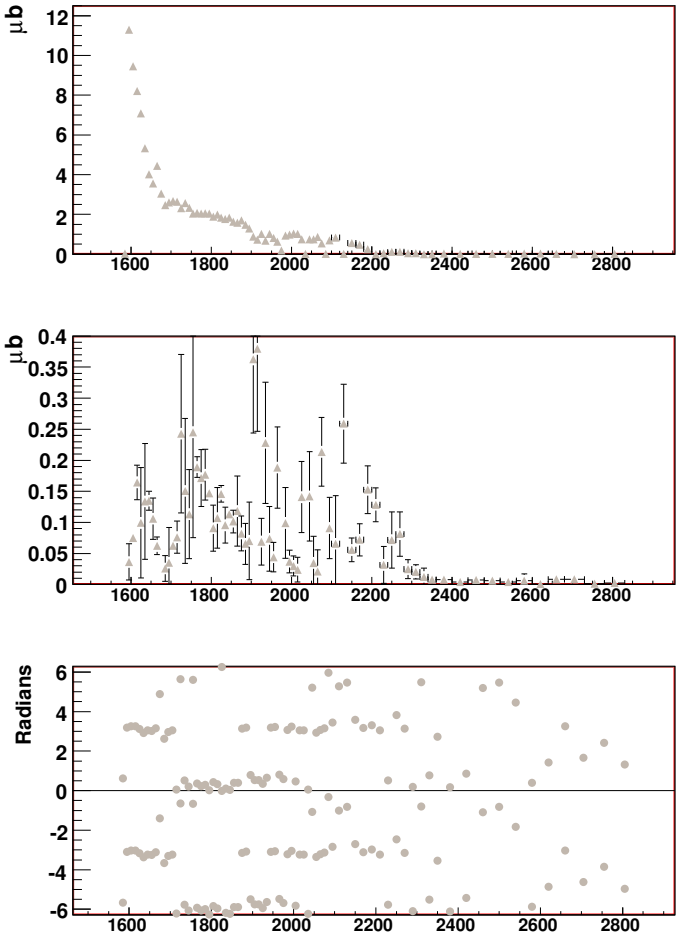

Figure 7.17: Plots of the yields and phase difference of the $J^P = \frac{1}{2}^-$(top) and $J^P = \frac{3}{2}^+$(middle) partial waves from the fits run without the vertex timing cut in place. Comparing this plot to 7.5, it is clearly seen that the removal of the vertex timing cut has a minimal effect.

Perhaps the more interesting is the effect of the timing cut on the higher-spin $J^P = \frac{5}{2}^-$ and $J^P = \frac{5}{2}^+$ partial waves. Refer to Figure 7.18 and to Figure 7.7 for the original result. The higher-spin waves are more dependent on the edges of the angular acceptance, and as such more sensitive to effects which might alter the background and acceptance. Clearly the effect is minimal, and structure which appears in the fit is consistent with previously reported results.

Overall, the effect of altering of the vertex timing cut on Fit #004 appears to be minimal, and the structures observed appear insensitive to changes in this cut.

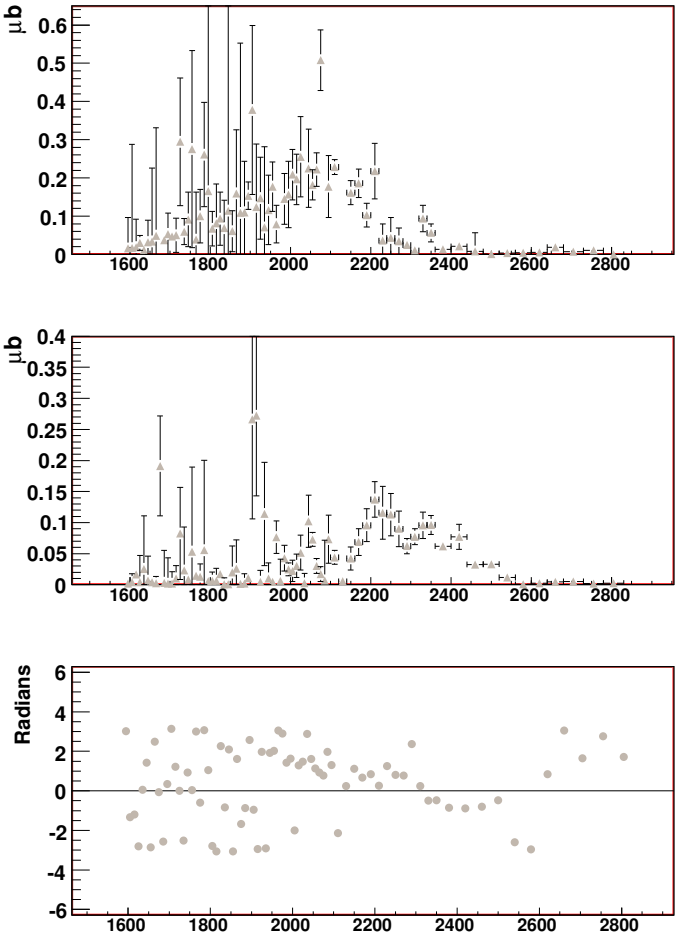

Figure 7.18: Plots of the yields and phase difference of the $J^P = \frac{5}{2}^-$(top) and $J^P = \frac{5}{2}^+$(middle) partial waves from the fits run without the vertex timing cut. This is to be compared with 7.7.

η' $J^P = \frac{1}{2}^-, \frac{3}{2}^+, \frac{5}{2}^-, \frac{7}{2}^+$ **(Fit #105)**

The effect of the modification of the vertex timing cut on the η' analysis appears to be minimal. The low-spin partial waves are consistent with the results previously reported. Comparing the $J^P = \frac{1}{2}^-$ and $J^P = \frac{3}{2}^+$ waves in this fit(see Figure 7.19 and Figure 7.13 for the original), it is clear that the overall structure of the results is consistent with the previously reported results. Equivalent solutions observed in the lower-spin resonances yields further confidence that the higher-spin waves will be consistent as well.

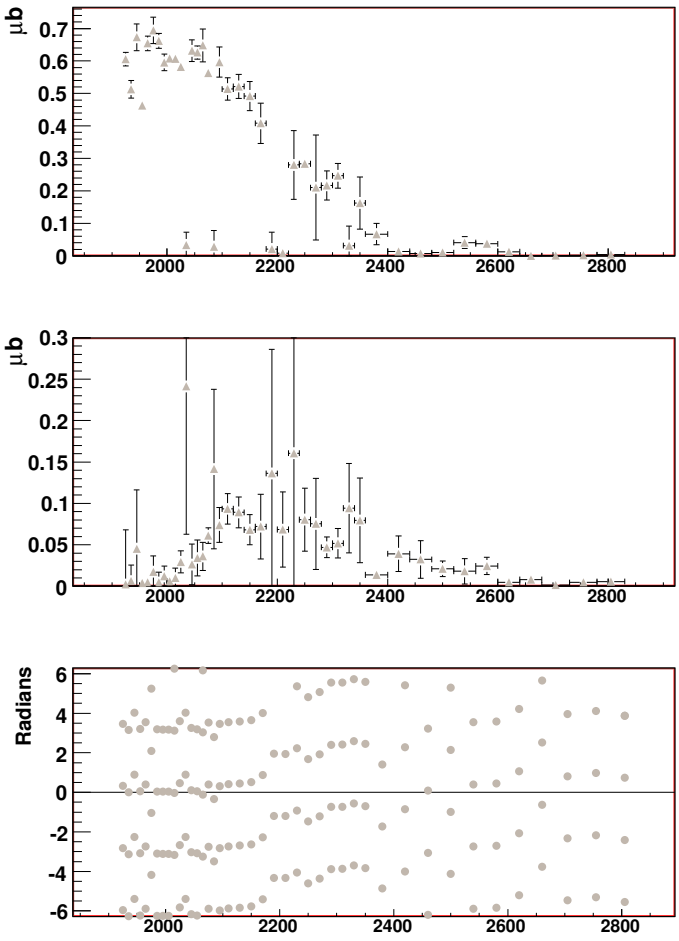

Figure 7.19: Plots of the yields and phase difference of the $J^P = \frac{1}{2}^-$(top) and $J^P = \frac{3}{2}^+$(middle) partial waves from the fit without the vertex timing cut in place. Comparing this to 7.13 demonstrates the minimal effect the vertex timing cut has on the overall results.

Turning attention to the higher-spin waves, as expected the $J^P = \frac{5}{2}^-$ and $J^P = \frac{7}{2}^+$ waves are consistent with the original fit results. Refer to Figure 7.20 and to Figure 7.15 for the original. There appears to be little effect on these partial waves when the vertex timing cut is tweaked, even by a substantial amount.

The structures present in the η' results appear regardless of the modification of the vertex timing

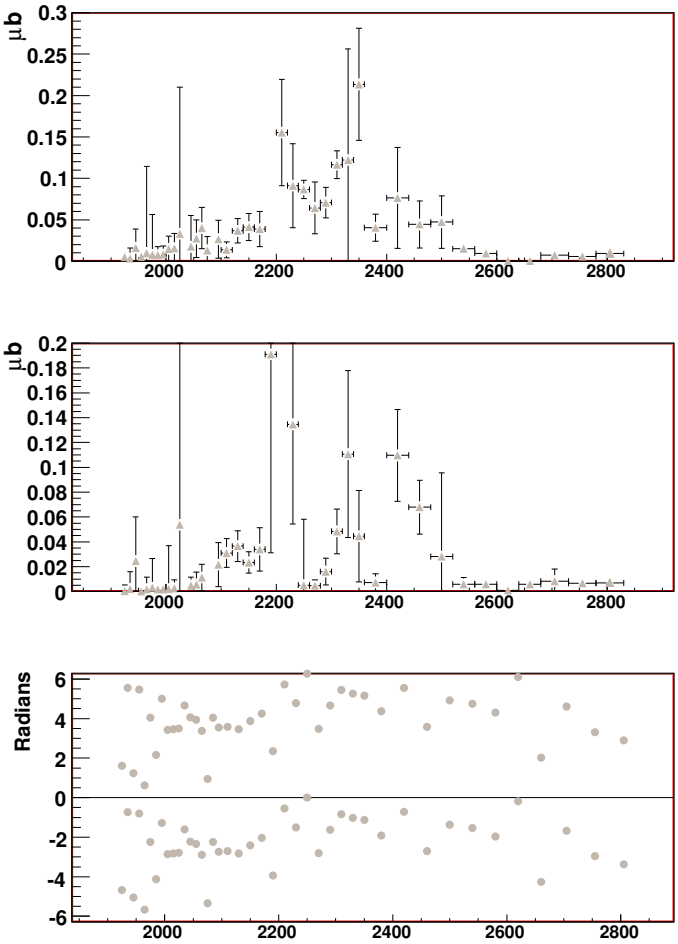

Figure 7.20: Plots of the yields and phase difference of the $J^P = \frac{5}{2}^-$(top) and $J^P = \frac{7}{2}^+$(middle) partial waves from the fits run without the vertex timing cut. Comparison of this plot to 7.15 demonstrates the similarities.

cut. The results of the η' analysis appear insensitive to the alteration of the vertex timing cut which was made to reduce background. The larger, more global structures still appear where they were previously observed, even with some of the individual points shifting around.

Conclusions Regarding Timing Cut

The η and η' PWA results appear to remain unaffected by a serious modification of the vertex timing cut. The results are generally consistent with those previously reported in Chapter 6. The timing cut was determined using the data and Monte Carlo, and any cut which is more severe is likely to cut into the signal events. This analysis demonstrates that loosening the cut considerably does not alter the global PWA results. Overall, the conclusion drawn is that the PWA results are generally not sensitive to the vertex timing cut.

7.3.4 Confidence Level Cut

The confidence level cut from the kinematic fit to the missing π° is a measure of how well the η is reconstructed. As it is so central to the analysis, it is natural that the stability of the PWA results when this cut is altered should be tested. To this end, the confidence level cut has been made more restrictive by increasing the cut from 10% to 20%. This provides a more restricted set of data to run through the PWA fits and determine what, if any, effect this change will have on the PWA results. Likewise, for the η' results the reconstruction of the η meson is vital to the selection of events, and will be tested similarly to the η analysis. The confidence level cut is described in Section 3.6.6.

Increasing the confidence level cut should essentially reduce the number of events in the analysis, but each of those events is more kinematically consistent with the hypothetical event. The PWA results should be stable to this change if the original cut of 10% was sufficient to aid in the selection of the events for analysis. Additionally, the background in the data sample created with a 20% cut should be lower, and thus the process of the background parameterization should compensate for this change. This demonstrates the robust nature of the fit process utilized in this analysis.

η $J^P = \frac{1}{2}^-, \frac{3}{2}^+, \frac{5}{2}^-, \frac{5}{2}^+$ (Fit #004)

The η results for Fit #004 when modified by a more stringent confidence level cut appear equivalent to the results from the previously reported results. Comparing the two fits, the lower-spin waves in the fit appear to be consistent with the results previously reported. While the strength of the $J^P = \frac{1}{2}^-$ partial wave has already been compared, the $J^P = \frac{3}{2}^+$ wave is now observed and the phase between the two waves is examined. See Figures 7.21 and Figure 7.5 for comparison. The agreement appears to be very good in general. The structures in the strength as a function of center-of-mass energy are consistent.

The $J^P = \frac{5}{2}^+$ and $J^P = \frac{5}{2}^-$ waves are the more interesting results in the analysis. See Figure 7.22 and Figure 7.7 for the original result. Comparing to the previously reported results indicates that the results for these partial waves are not affected by the more strict confidence level cut. There are differences in the results across the entire range in W, but the structures of importance in the higher W region appears to be present regardless of the change in the confidence level cut.

The η fits do not appear to be sensitive to the higher level of confidence level cut. This yields confidence in the results as a more strictly determined dataset does not alter the results.

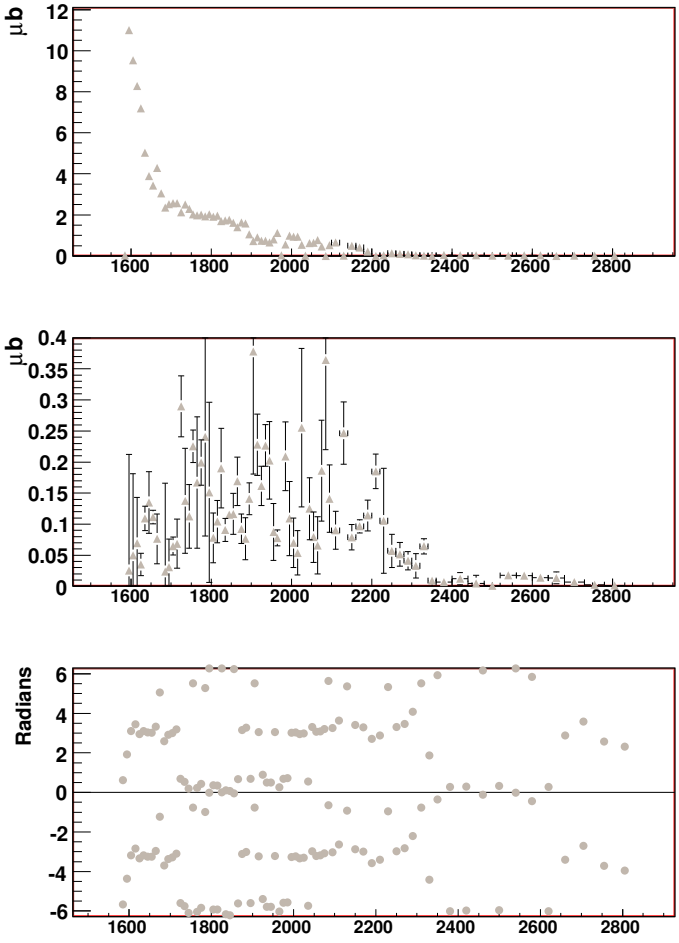

Figure 7.21: Plots of the yields and phase difference of the $J^P = \frac{1}{2}^-$(top) and $J^P = \frac{3}{2}^+$(middle) partial waves from a fit run with the confidence level cut set to 20%. Comparing this to 7.5 the similarities and differences in structure can be seen.

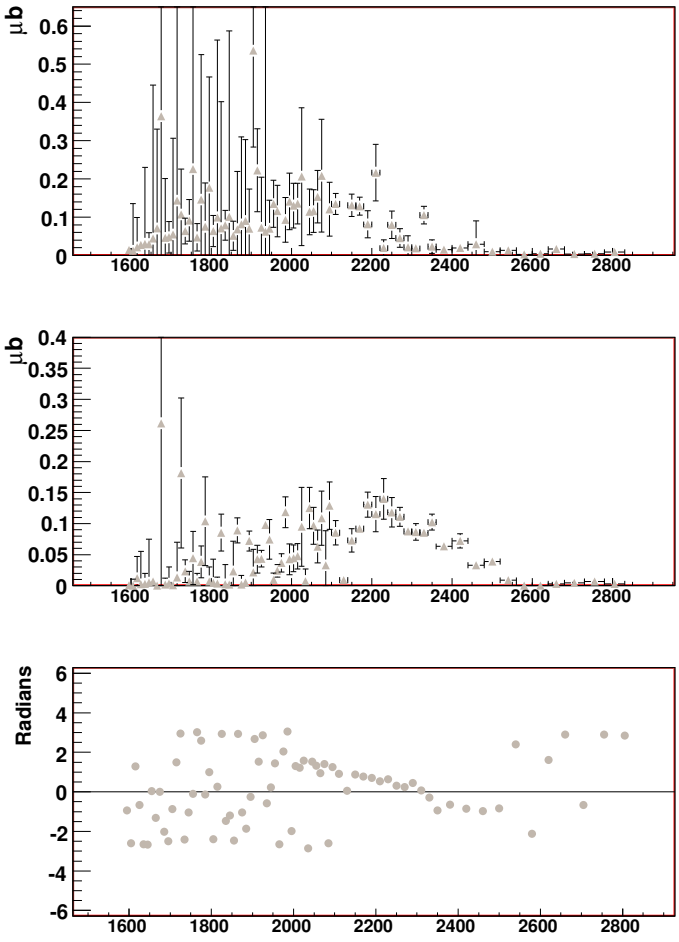

Figure 7.22: Plots of the yields and phase difference of the $J^P = \frac{5}{2}^-$(top) and $J^P = \frac{5}{2}^+$(middle) partial waves from a fit run with a 20% confidence level cut in place. Comparing this plot to 7.7 demonstrates the many similar features.

η' $J^P = \frac{1}{2}^-, \frac{3}{2}^+, \frac{5}{2}^-, \frac{7}{2}^+$ (Fit #105)

Fit #105 will now be compared used to compare the original fits with the fits run with a more strict confidence level cut. Ideally there will be little difference in the results, as that indicates the selection of the events with a 10% cut is sufficient. Comparing the lower-spin waves in the fit, the $J^P = \frac{1}{2}^-$ and $J^P = \frac{3}{2}^+$ waves appear consistent with the results previously reported. See Figure 7.23 and Figure 7.13 for the original result. The structures as a function of W are generally equivalent, and there is similar phase motion.

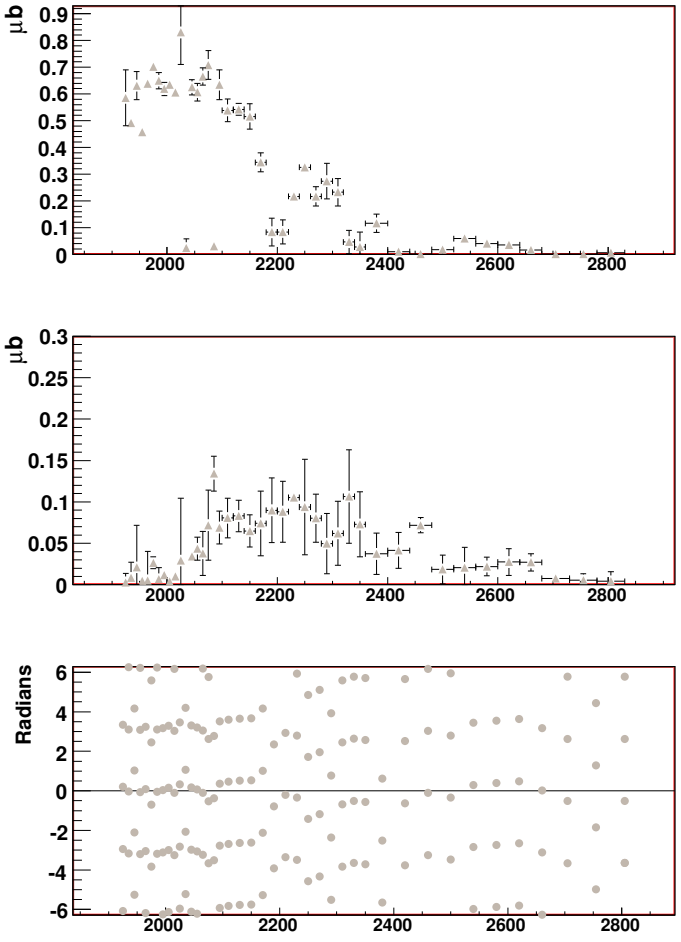

Figure 7.23: Plots of the yields and phase difference of the $J^P = \frac{1}{2}^-$(top) and $J^P = \frac{3}{2}^+$(middle) waves which come from a fit which utilized a 20% confidence level cut. The similarities and differences between this plot and the original analysis results can be seen by comparing to Figure 7.13.

The higher-spin waves are also consistent with the previously reported results. Figure 7.24 shows the plots of the $J^P = \frac{5}{2}^-$ and $J^P = \frac{7}{2}^+$ partial waves show strength in similar structure in center-of-mass energy and the features in the phase plot appear consistent as well. It should be compared to Figure 7.15 which is the original result.

The structures originally seen in the η' results appear to be relatively unaffected by a change in

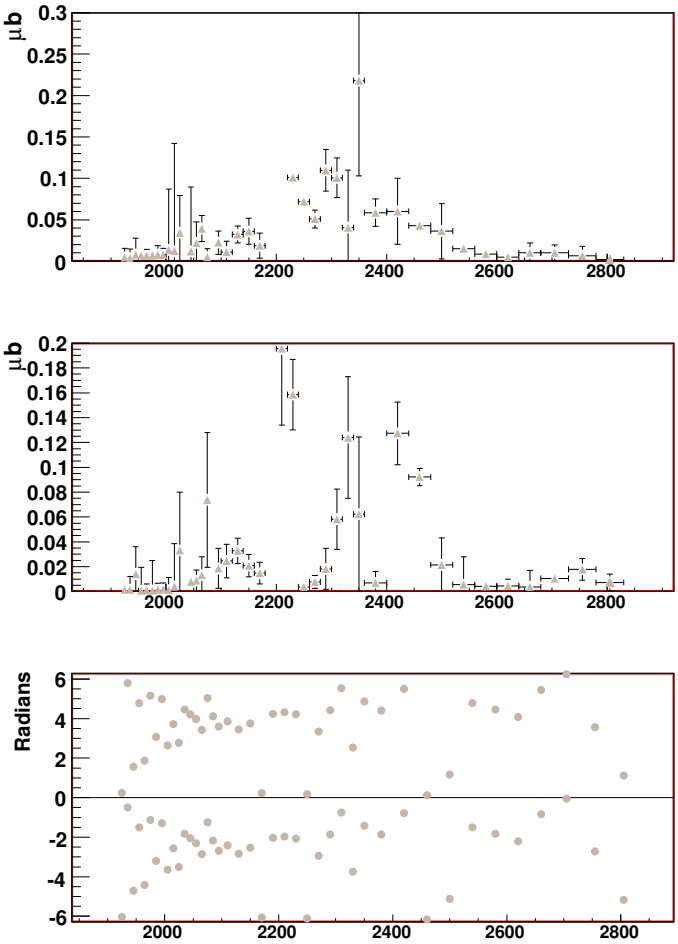

Figure 7.24: Plots of the yields and phase difference of the $J^P = \frac{5}{2}^-$(top) and $J^P = \frac{7}{2}^+$(middle) partial waves from a fit run with a 20% confidence level cut. The similarities between this plot and the previously reported results can be seen by comparing to 7.15.

the confidence level cut on the dataset. This is promising, as this indicates that the 10% cut yields an nearly equivalent dataset to the 20% cut.

Conclusions Regarding Confidence Level Cut

Overall, the structures seen across large sections of W appear to be reproduced in the analysis which utilizes a higher confidence level cut. Neither the η, nor the η' appear to yield significantly different PWA results with a different confidence level used to select the events. This is indicative of the fact that the 10% confidence level cut is similar in its ability to select the η and η' events as a 20% confidence level cut. If there was a significant difference, it would likely indicate that a significant amount of background was leaking through the confidence level cut at the 10% level. Since this does not appear to be the case, confidence can be had regarding the confidence level chosen for the cut.

7.3.5 Sensitivity to t-,u-channel parameters

It is important to account for the non-resonant contributions to η and η' photoproduction, so that the resonant contributions can be as cleanly separated as possible. As mentioned in a previous section, the contributions of the t- and u-channel diagrams was determined by fitting the high energy data, and extrapolating down through the range of energy in the data. It is clear from the differential cross sections that at high W there is a prominent forward peak in η photoproduction. Structure of this type is generally attributed to t-channel processes. With the values of the parameters for the t- and u-channel fixed in the fits, the question remains of how sensitive the results are to the values chosen.

First, a reminder of the contributions of the t- and u-channel processes to the total yield of the η and η' photoproduction. Starting with the η, as seen in Figure 7.25, the t-channel constitutes a majority of the yield at high W. It is clear that any results indicating resonance characteristics in the high W regime will be affected by a significant change in the t-channel parameters. The t-channel appears to begin contributing significantly in the vicinity of $W = 2200 \rightarrow 2300$MeV. Below this region, the sensitivity to the t-channel is likely to be more limited.

Alternatively, the u-channel appears to contribute very little to η photoproduction at the energies available in this analysis. It would therefore be highly unlikely that altering the u-channel would effect the results. The alteration of the u-channel, and it effects on the PWA results, is not investigated in this analysis.

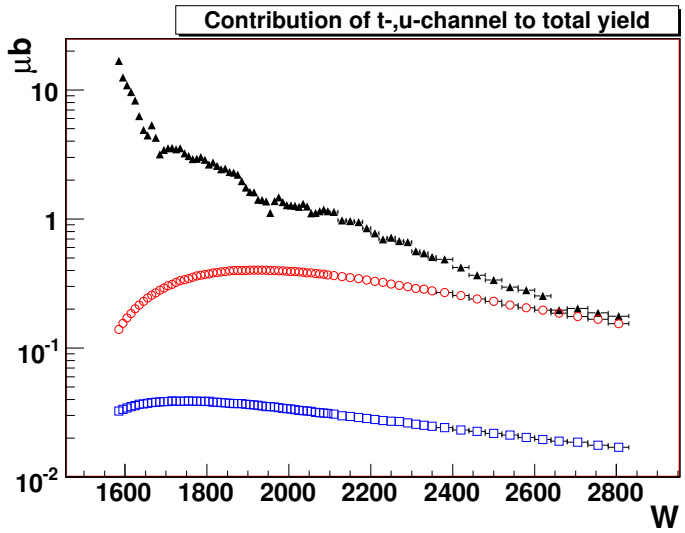

Figure 7.25: The contributions of the t- and u-channels to the η total yield. The t-channel is in the hollow circles, while the hollow squares denote the u-channel contribution. Note that this is plotted on a log scale. At high W the t-channel accounts for a large amount of the total η yield. This is not surprising, as this is where the contribution of the t-channel was determined. Note that in general, the u-channel does not make a significant contribution to the total yield.

The contributions to the total yield of the η' which come from the t- and u-channels are similar to those seen in the η analysis, and a shown in Figure 7.26. The u-channel contributes very little to the total yield of the η'. The t-channel on the other hand appears to contribute to a majority of the total yield at high W. The forward peak in the differential cross sections is present, but slightly less pronounced than in the η analysis. In the region of center-of-mass energy above $W = 2400$MeV,

the t-channel dominates in the η' photoproduction. Below this, however, the contribution is limited, and this the sensitivity to the parameters chosen to lock down the t-channel should be small.

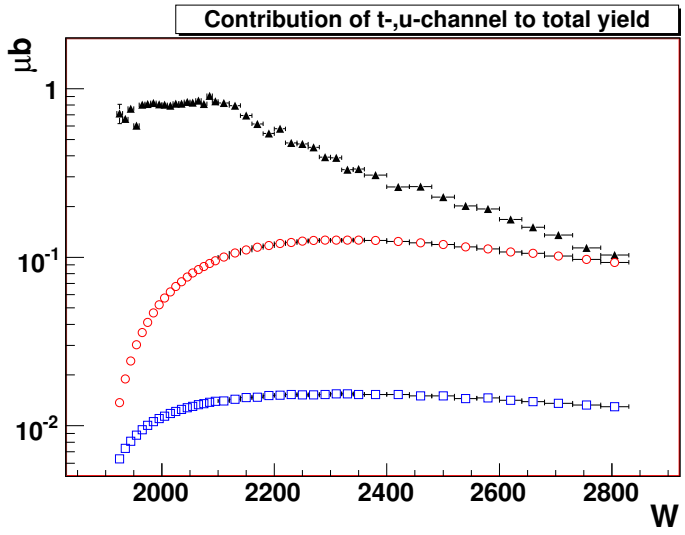

Figure 7.26: The contributions of the t- and u-channels to the η' total yield. The t-channel is in the hollow circles, while the hollow squares denote the u-channel contribution. Note that this is plotted on a log scale. At high W the t-channel accounts for a large amount of the total η' yield. This is not surprising, as this is where the contribution of the t-channel was determined. Note that in general, the u-channel does not make a significant contribution to the total yield.

With the contributions of the t- and u-channel pieces described, it is now prudent to vary the parameters to determine how sensitive the PWA results are to these values. The increasing contribution of the t-channel with energy would hint that any higher mass resonance states would be affected by a change in the t-channel. The u-channel appears to contribute very little to the overall yield of η and η' photoproduction, and as such the systematic effects of altering the parameters will not be studied.

η - $J^P = \frac{1}{2}^-, \frac{3}{2}^+, \frac{5}{2}^-, \frac{5}{2}^+$ (Fit #004)

The η results for the $J^P = \frac{1}{2}^-, \frac{3}{2}^+, \frac{5}{2}^-, \frac{5}{2}^+$(Fit #004) fit with altered t-channel parameters will be presented here. The t-channel parameters have been scaled down arbitrarily by a factor of 2, to determine the effect on the previously reported results. Comparing the lower-spin waves between the two fits, they appear to be consistent with the results previously reported.

Looking at the $J^P = \frac{1}{2}^-$ and $J^P = \frac{3}{2}^+$ partial waves, see Figure 7.27 and Figure 7.5 for the original result, there are similarities in the global structure across most of W. The agreement appears to be very good in general. The structures in the strength as a function of center-of-mass energy are consistent.

The $J^P = \frac{5}{2}^+$ and $J^P = \frac{5}{2}^-$ waves are the more interesting results in the analysis, see Figure 7.28 and Figure 7.7 for the original result. Comparing to the previously reported results indicates that the results for these partial waves are not effected by the more strict confidence level cut.

The η fits do not appear to be sensitive to the higher level of confidence level cut. This yields confidence in the results as a more strictly determined dataset does not alter the results.

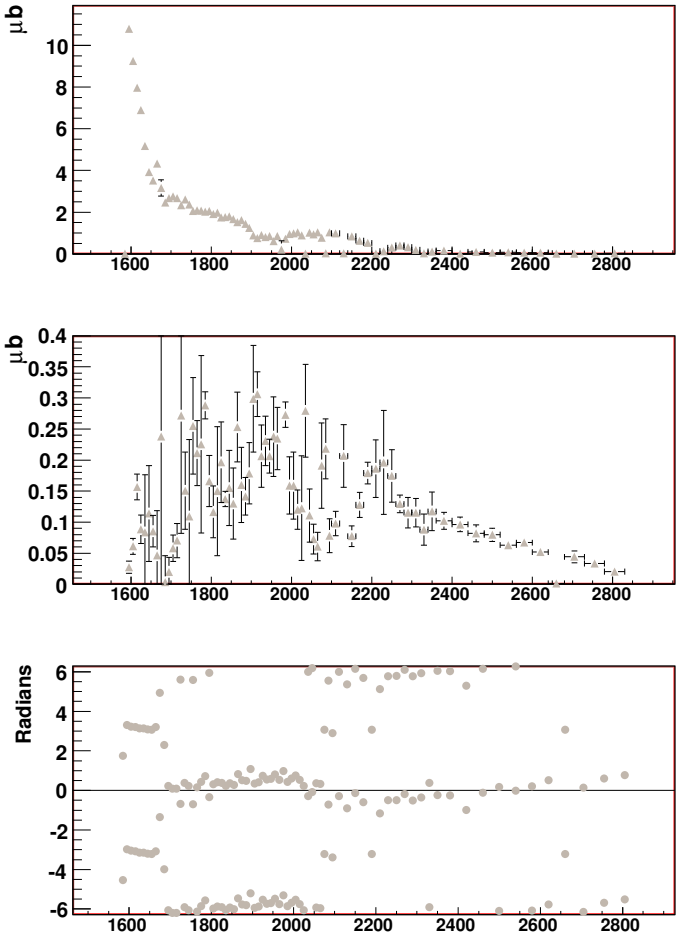

Figure 7.27: Plots of the yields and phase difference of the $J^P = \frac{1}{2}^-$(top) and $J^P = \frac{3}{2}^+$(middle) partial waves from a fit run with the t-channel parameters scaled down by a factor of 2. Comparing this to 7.5 the similarities in structure can be seen.

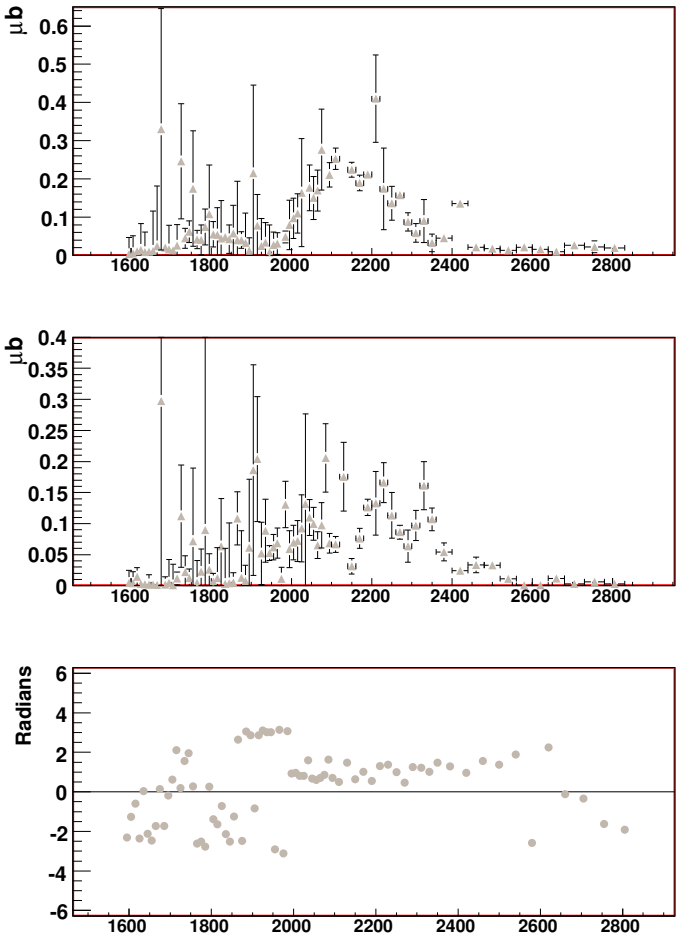

Figure 7.28: Plots of the yields and phase difference of the $J^P = \frac{5}{2}^-$(top) and $J^P = \frac{5}{2}^+$(middle) partial waves from a fit run with the t-channel parameters scaled down by a factor of 2. Comparing this plot to 7.7 demonstrates the many similar features.

η' - $J^P = \frac{1}{2}^-, \frac{3}{2}^+, \frac{5}{2}^-$ (Fit #101)

The η' results for the $J^P = \frac{1}{2}^-, \frac{3}{2}^+, \frac{5}{2}^-$ (Fit #101) fit with altered t-channel parameters will be presented here. The t-channel parameters have been scaled down arbitrarily by a factor of 2, to determine the effect on the previously reported results. Looking at the $J^P = \frac{1}{2}^-$ and $J^P = \frac{5}{2}^-$ partial waves, there appears to be....

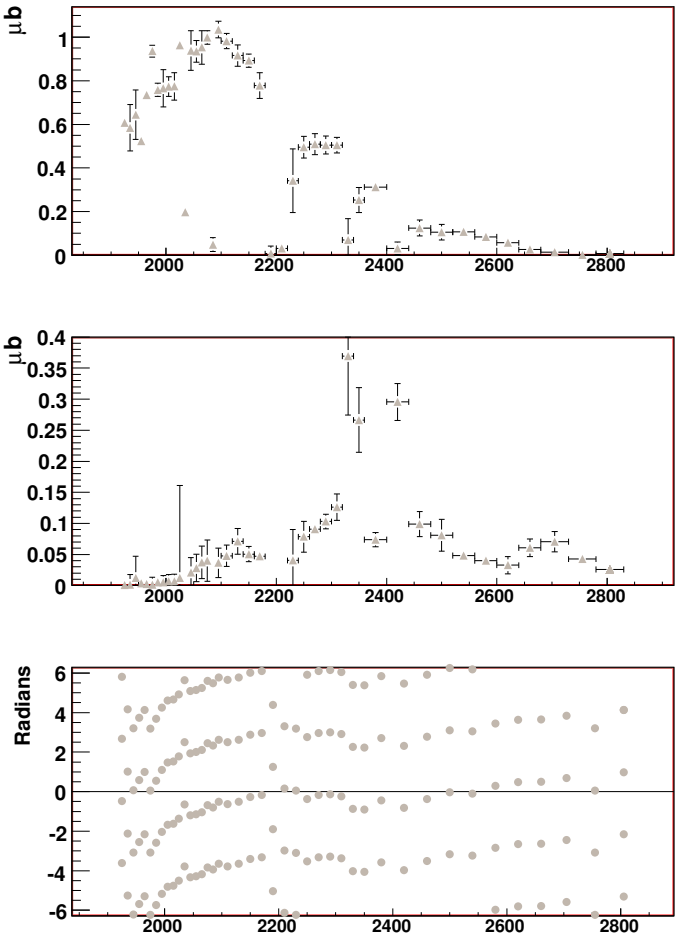

Figure 7.29: Plots of the yields and phase difference of the $J^P = \frac{1}{2}^-$(top) and $J^P = \frac{5}{2}^-$(middle) partial waves from a fit run with the confidence level cut set at 20% instead of the standard 10%. This plot should be compared with 6.58 to note all the similarities.

Turning attention to the lower-spin waves in the fit, the $J^P = \frac{1}{2}^-$ and $J^P = \frac{3}{2}^+$ waves appear consistent with the results previously reported, see Figure 7.30 and Figure 7.13 for the original result. The structures as a function of W are generally equivalent, and there is similar phase motion.

Conclusions regarding t-channel parameters

The alteration of the t-channel parameters used for the fits in both the η and η' analysis are relatively unsurprising. At low-W there appears to be very little difference between the original results and

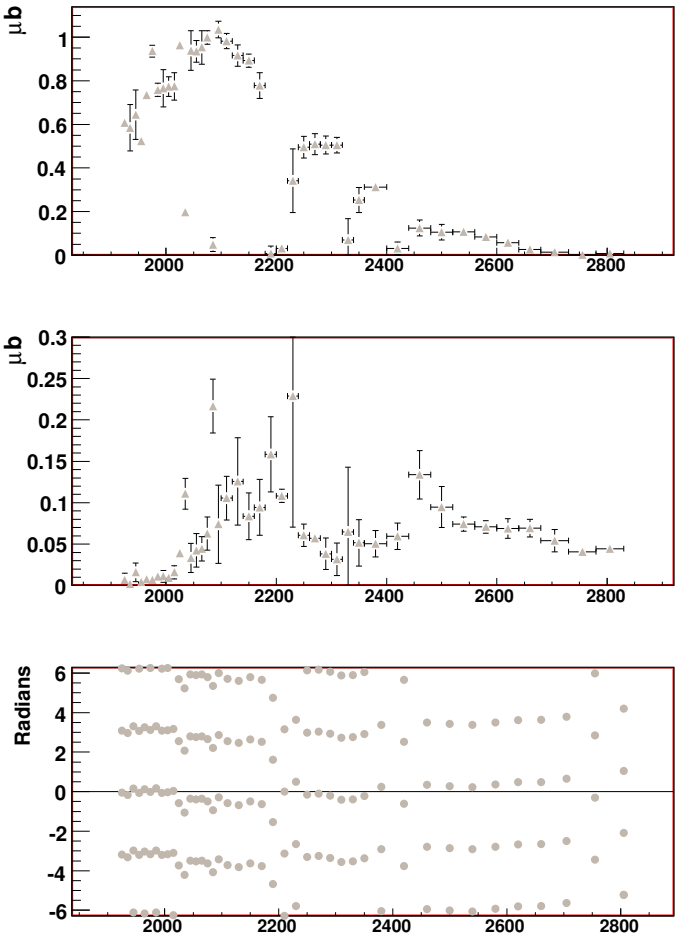

Figure 7.30: Plots of the yields and phase difference of the $J^P = \frac{1}{2}^-$(top) and $J^P = \frac{3}{2}^+$(middle) waves which come from a fit which utilized a 20% confidence level cut. The similarities between this plot and the original analysis results can be seen in 7.13.

the results determined with half of the t-channel contribution. The maximal effect is clearly in the high W region, where the s-channel partial waves are clearly trying to account for the reduction in the t-channel contribution. The partial waves which are most affected appear to be the higher-spin positive-parity waves, such as the $J^P = \frac{5}{2}^+$ and the $J^P = \frac{7}{2}^+$. Still, below ≈ 2300 MeV the structures previously seen in the PWA are reproduced relatively well.

7.4 Summary

In order to determine how stable the results from the PWA analysis of the η and η' were, a study of the most significant cuts made on the data and the Monte Carlo was done. The overall conclusion to this study was that the results were stable with respect to changing conditions of the fiducial cuts, the vertex timing cut, and the confidence level cut. These cuts were varied within reasonable limits, and as such there are regimes where the results are likely not stable with respect to these

cuts. As an example, severe fiducial cuts could hinder the PWA in distinguishing between different J^P partial waves. This would be likely to occur if the fiducial cuts significantly reduced the range of the relevant angular distributions involved. For the purposes of this analysis the fiducial cuts were driven by the comparison between the data and the Monte Carlo, and there was no need for extreme cuts to satisfy that criteria.

The timing cut was significantly relaxed in favor of a very basic cut which required only one particle to lie within 2.0 ns of the photon vertex time, and the results from the PWA were not affected. The timing cut, as demonstrated in the Chapter 3 primarily selects the signal events and removes background from the dataset. The inclusion of this background did not affect the results of the analysis. Most likely, the background which was included without the vertex timing cut was simply parameterized, and accounted for, in the fit itself. The background parameterization has been described in Chapter 3.

The confidence level cut is used to refine the dataset and remove background. By increasing the level of the confidence level cut, a more refined dataset is available for study. Since the results from both sets of fits are equivalent, the only real difference in the two is the statistics are higher with a 10% cut than with a 20% cut. This also indicates that the events selected by a 10% cut are essentially equivalent to those selected with a 20% cut. The background parameterization was necessarily changed for the dataset with a 20 % confidence level, and the consistency of the PWA results indicate the overall robust nature of the fitting procedure used in this analysis.

The systematic check of the sensitivity of the PWA results to the t-channel parameterization was completed. Unlike the previous systematic checks, this did not change the cuts, or require a re-parameterization of the background. It was determined that the change in the t-channel parameters did not significantly alter the structures seen in the PWA results. In some cases the widths appeared to have changed, but the global structures remained similar. It was also clear that the lack of strength in the t-channel was being compensated for by a higher-spin wave in the fit.

Due to the fact that resonance parameters were not able to be extracted in this analysis, a quantitative determination of the systematic error is not possible in this analysis. The objective of this systematic analysis was to determine if the structures seen in the PWA results were insensitive to the cuts which selected the dataset. It appears that the results are relatively robust to the data selection process. While it would be foolish to attempt to measure a differential cross section without fiducial cuts, this systematic analysis has indicated that a PWA may still be able to produce viable results without the fiducial cuts. This is not to say that the cuts should not be used, just that the PWA results are relatively insensitive to their existence.

This chapter describes the systematic adjustment of cuts made on the data and the effects of those cuts on the PWA results reported earlier in 6. The conclusion of this study is that the PWA results of η and η' photoproduction are stable within the cuts described. None of the results presented are inherently dependent on a particular cut on the data or Monte Carlo.

Chapter 8

Conclusion

This analysis has taken advantage of one of the largest datasets for photoproduction off of a proton target available. There was considerable work done throughout the analysis process from writing code, to developing tools to transfer large amounts of data over distance and storing that data efficiently. This document has attempted to review and describe all of the salient details of both the results and the analysis process.

This chapter will briefly review the main results of this analysis. First, a review of this analysis within Carnegie Mellon University's PWA program will be given. Then, a review of the results from the differential cross section measurement for the η and η' photoproduction. Followed by a review of the partial wave analysis results for both reaction channels will be given. Finally, a proposal will be presented for future work in this area of analysis.

8.1 The Data

The data used in this analysis were taken from May to July of 2004. This dataset is the largest photoproduction dataset for multiple charged final states available in the world. With such a large dataset, considerable effort was put into calibrating and correcting the data for this analysis. This process was neither quick, nor simple as very detailed studies were conducted to determine what cuts and corrections were required. It is important to note, that in many cases the detail of the studies done required a statistically significant dataset. It was because of the large statistics that detailed corrections could be made. Overall, the quality of the dataset was very good, and it has allowed for a variety of analysis with tremendous statistics.

8.2 Review of Differential Cross Section Results

The primary results from this analysis are the differential cross section measurements made for η and η' photoproduction. Considerable time and effort was put into determining the systematics of the dataset to produce reliable measurements of the differential cross sections. The overall result is a measurement of the η' differential cross section which is in very good agreement with the world data. The result for the η differential cross section, however, is a bit confusing. The η results extend the kinematic range, and give slightly better statistics, as compared to world data. There are, however, systematic differences between the results of this analysis and the Crede[12] results in the region of high-W and forward-angles. The exact nature of this discrepancy is currently unknown, but the relatively large nature of the discrepancy rules out many of the typical sources. Systematic checks of the fiducial cuts and the background both indicated that even radical changes in the cuts could not account for the large size of the discrepancy. Adjustments to the cuts could produce changes in the

differential cross section measurement on the order of $10 \rightarrow 20\%$ but would not yield the factor of 2 required to resolve the discrepancy in the forward-angle high-W region. The same systematic checks led to the inclusion of an additional systematic error of 10% for the measurement of the η. It is important to note that the results of this analysis are in reasonable agreement with the preliminary results from another CLAS analysis from Ball[9]. The earlier CLAS measurement from Dugger[6] is systematically low by about 20% in comparison to this analysis in the low-W region. In the high-W region the Dugger result is systematically high by roughly 20%. While these discrepancies exist, it is important to note that generally, in the lower-W and backward-angle regions, the results of this analysis line up reasonably well with all three of the other results to which they are compared.

Plots of the results for the differential cross section measurement for η photoproduction are presented in Figures 8.1 to 8.3. The results are presented here as a function of W binned in $cos(\theta_{CM})$ of the η meson. Plotting the differential cross sections in this manner allows for comparison to many other measurements and demonstrates the discrepancy between the results of this analysis and the Crede[12] analysis in a clear way. The black cross markers are the results of this analysis. The red criss-cross markers are the Crede[12] results, the blue circles are the Dugger[6] results, and the green empty cross markers are the Ball[9] results. In Figure 8.3 there are two additional lines indicating the t-channel contribution to the differential cross section. The magenta line, which is systematically lower than the blue line, indicate the result from this analysis. The blue line indicates the result from Chiang[54] in a fit to data from DESY[53] data taken in 1970. It should be noted that the Ball[9] results are very preliminary, and are only being displayed here to allow for a comparison to an additional CLAS measurement.

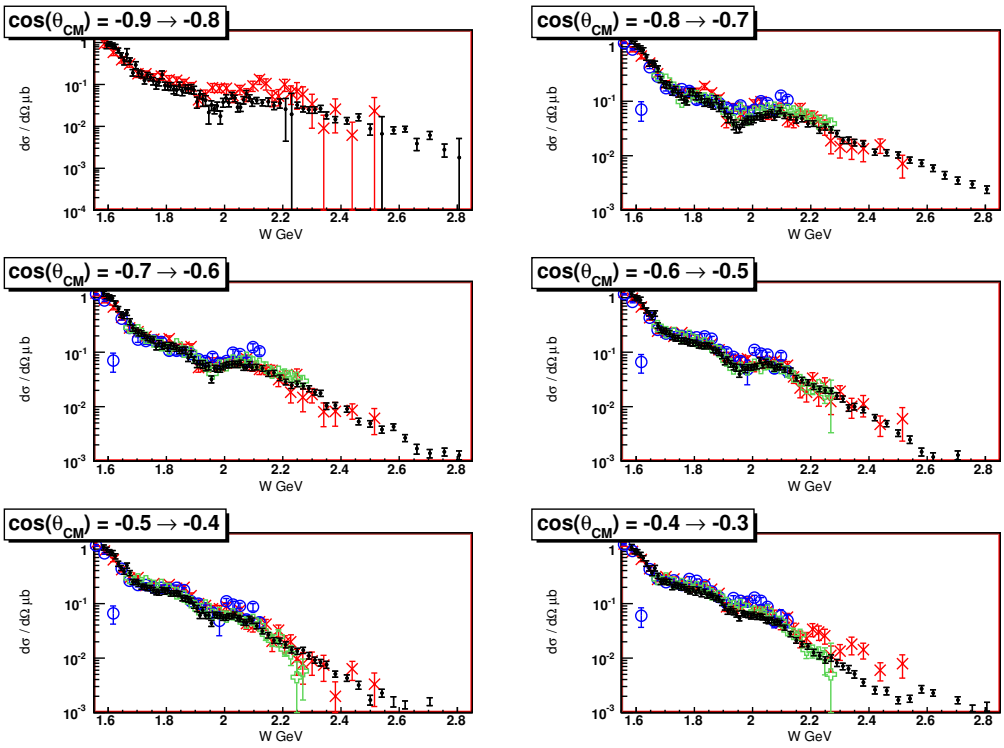

Figure 8.1: Differential cross section results for η photoproduction. The bins presented here are in $\cos(\theta_{CM})$, with results plotted as a function of W. The width of the bins is $\cos(\theta_{CM}) = 0.1$. The black points are the Krahn results. The red criss-cross markers are the Crede[12] results, the blue circles are the Dugger[6] results, and the green empty cross markers are the Ball[9] results. Through most of the backward angles, across W the results from the Krahn analysis and the Crede, Dugger, and Ball analyses appear to be in good agreement. Maximal disagreement appears to occur around $W = 2000 \rightarrow 2200$ MeV.

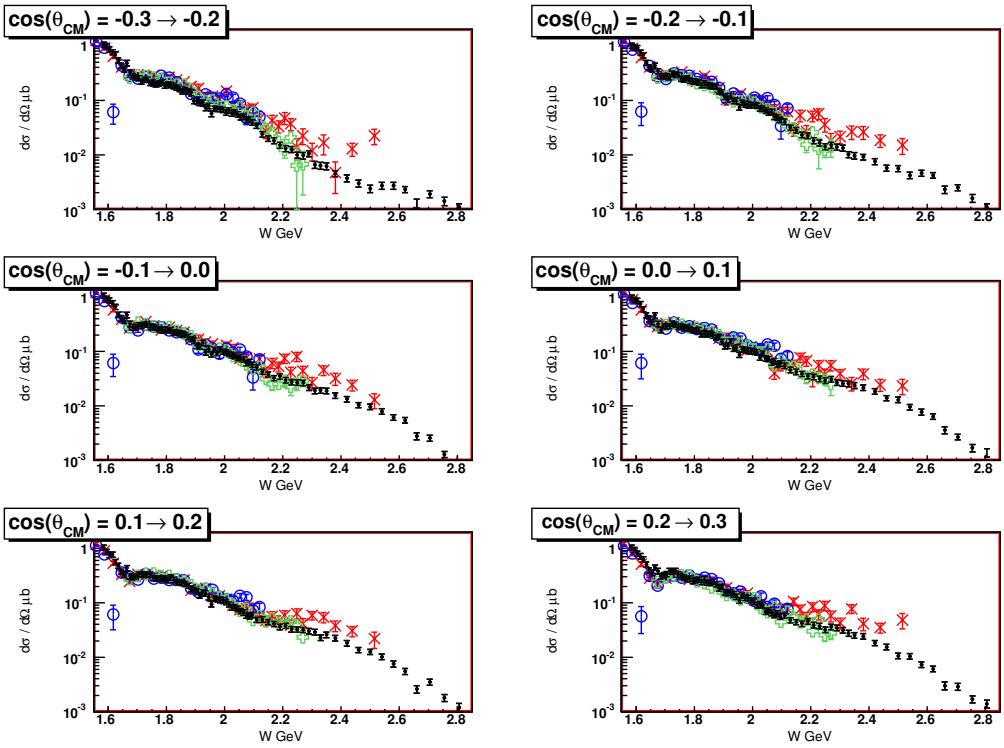

Figure 8.2: Differential cross section results for η photoproduction. The bins presented here are in $\cos(\theta_{CM})$, with results plotted as a function of W. The width of the bins is $\cos(\theta_{CM}) = 0.1$. The black points are the Krahn results. The red criss-cross markers are the Crede[12] results, the blue circles are the Dugger[6] results, and the green empty crosses denote the preliminary Ball[9] results. Up to $\approx$ 2000 MeV the agreement at these angles is good between the three results. Above this W range, however, the Krahn result appears systematically low in comparison to the Dugger and Crede results. Worth noting however, is that the Ball results and the Krahn results still appear to be in good agreement.

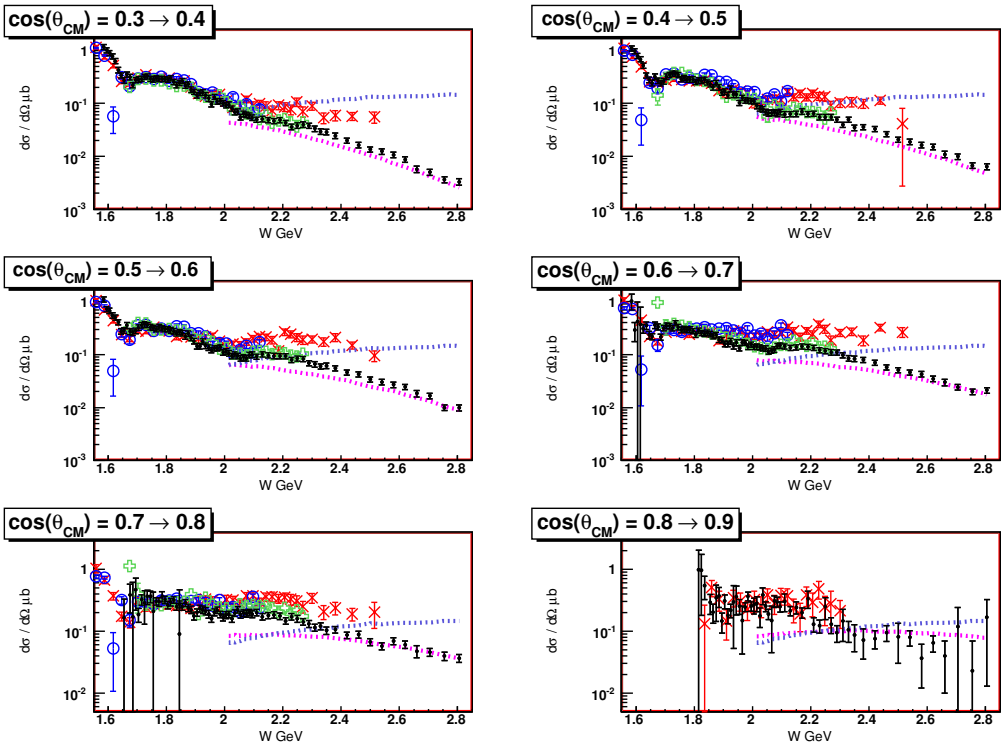

Figure 8.3: Differential cross section results for η photoproduction. The bins presented here are in $\cos(\theta_{CM})$, with results plotted as a function of W. The width of the bins is $\cos(\theta_{CM}) = 0.1$. The black points are the Krahn results. The red criss-cross markers are the Crede[12] results, the blue circles are the Dugger[6] results, and the green empty cross markers indicate the Ball[9] preliminary results. Again, for $W < 2000$ MeV the agreement between the results appears to be pretty good, while above this value the results diverge with the Krahn result systematically low. Again, the Ball result and the Krahn result appear to agree fairly well, despite the divergence from the Crede and Dugger results.

The η' measurement is a drastic improvement over current world data, of which the best dataset was a previous CLAS result. The statistics are improved, as well as the kinematic range. The differential cross section results will now allow theorists to develop models, and test them. This has never been readily available up to this point, as the differential cross section measurements have been very limited.

The results of the differential cross section measurements for η' photoproduction are presented here as a function of W binned in $\cos(\theta_{CM})$ of the η' meson. The black cross markers are the results of this analysis, while the red triangular markers are the previously published results from Dugger[7]. Displaying the results in this way allow for the demonstration of the vast improvement in the statistics and kinematic range that these results represent. While there are known discrepancies between the results from the η analysis and previous results, there is only limited data with which to compare the η' results. Thus, it is unclear at this point if the discrepancies noted in the η measurement carry over to the η' measurement. The results can be seen in Figures 8.4 to 8.6. The results of the η' measurment have included a 10% systematic error, due to the additional analysis work done on the η in determining the measured cross sections.

8.3 Review of PWA Results

The PWA results from this analysis represent a new approach to η and η' partial wave analysis. Until now, PWA results on the η were fits to differential cross sections, and typically they were run coupled to single-pion reaction channel. Previous resonance analysis of η' photoproduction was only done through fits to models which incorporated certain resonance contributions. The analysis presented here is a drastic improvement in the analysis of η' photoproduction.

It is important to note that this analysis was essentially exploratory in terms of the PWA results. This was the first analysis to emerge from the CMU PWA program, and if many ways this analysis was used to drive the development of the PWA program. Due to the exploratory nature of this analysis within the framework of the CMU PWA program, the results presented here are not to be taken with confidence. While analysis of this channel may require considerable future work, there is no doubt that this analysis helped drive the program at CMU in PWA.

Fits were run on the η, the η', and as a coupled-channel η with η'. A tremendous amount of time and effort went into setting-up and running these PWA fits. Unfortunately, given the difficulties with the cross section measurements and the lack of additional information to further constrain the fit, it is premature to claim observation of resonance structure. It should be noted that both the η and the η' both appear to favor the $J^P = \frac{1}{2}^-$ partial wave near threshold. For the η, at least, this is in line with previous results from Anisovich et al[8].

8.4 Future Work

There is considerable work to be done to continue this analysis in the future. In the more immediate time frame, the inclusion of beam polarization asymmetry information in the fit is a primary goal. Analyses of other reaction channels($N\omega$,ΛK) have indicated that polarization information is a powerful tool in PWA, and the $N\eta$ and $N\eta'$ should benefit from additional information. It is hoped that the additional information may provide some constraints on the fit, which would allow for improved fit stability.

The discrepancies in the differential cross section measurements need to be resolved, at least to within the experiment in order that they can be published. It is still unclear as to the nature of such a large discrepancy between the results of this analysis and the results from Crede et al.[12]. If, or when, this discrepancy is finally resolved, then the applicability of the solution will be determined for the η' measurement.

Further in the future, the η and η' reaction channels will be coupled with other reaction channels to provide even more information for the fit. Combining a whole series of photoproduced datasets, including $N\pi$, $N\omega$, $K\Lambda$,and $K\Sigma$, should allow for greater resolving power when searching for baryon resonances. Each of these channels has slightly different kinematics and acceptances, and combining these reaction channels should allow for a comprehensive study of the baryon resonance spectrum. With a well mapped spectrum for baryon excitations, there is the opportunity for a deeper understanding of QCD and of confinement. It is the eventual goal of this analysis program to help provide that well mapped baryon resonances spectrum.

8.5 Summary

This analysis is the first of several in progress in the PWA program at CMU. There is currently work being done on several other final states, which should allow for the production of a coherent picture of the baryon resonances available in photoproduction off of the proton. The goal of this analysis was to look for baryon resonance structures which couple to $N\eta$ and $N\eta'$ in photoproduction data. An additional goal was to extract differential cross section measurements for η and η' photoproduction. Further, there was an extra goal for this analysis, as it is the first to emerge from the PWA program.

This analysis was to function as a driving force for the entire development of the analysis procedure and techniques. The analysis was the test bed for nearly every piece of code that was written, and without this analysis the entire program would not be as advanced as it is today. Overall, this analysis accomplished its goals to measure cross sections, search for indications of possible resonance states, and advance the entire PWA program at CMU.

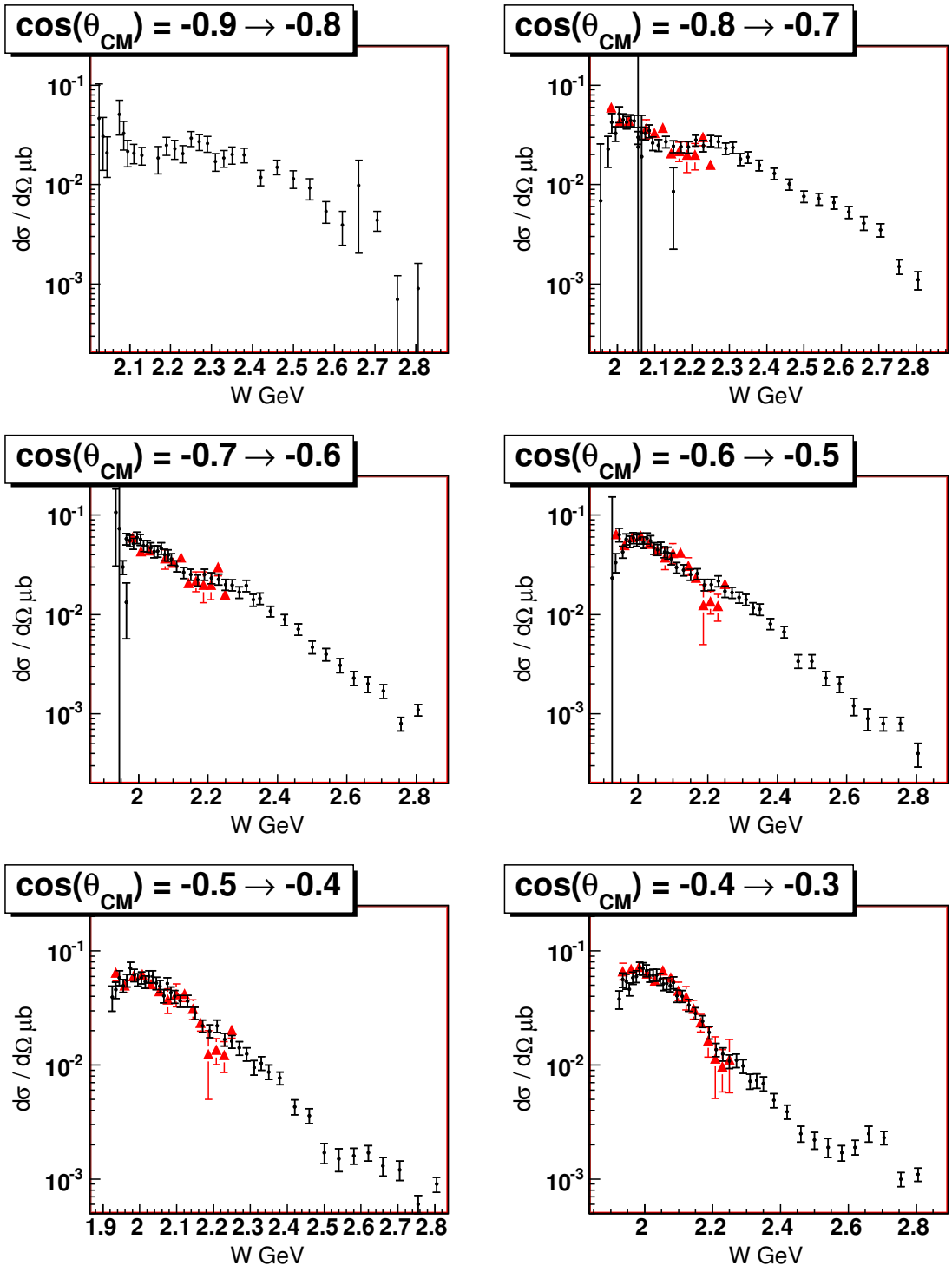

Figure 8.4: Differential cross section results for η' photoproduction. The bins presented here are in $\cos(\theta_{CM})$, with results plotted as a function of W. The width of the bins is $\cos(\theta_{CM}) = 0.1$. The black points are the Krahn results, and the red triangular markers are the Dugger[7] results. The Krahn results appear to line up reasonably well with the Dugger results as a function of W. These bins are in the most backward angles.

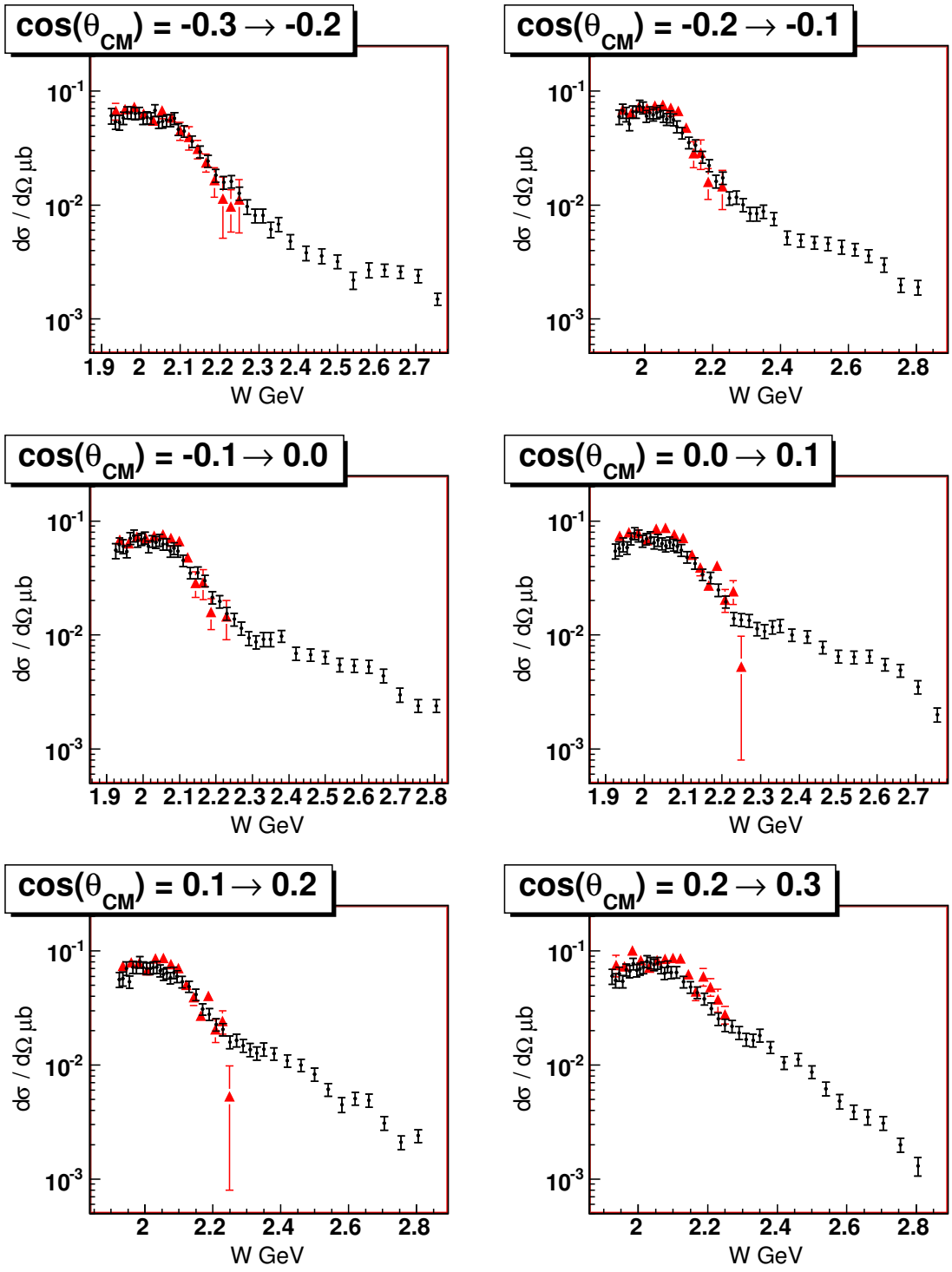

Figure 8.5: Differential cross section results for η' photoproduction. The bins presented here are in $\cos(\theta_{CM})$, with results plotted as a function of W. The width of the bins is $\cos(\theta_{CM}) = 0.1$. The black points are the Krahn results, and the red triangular markers are the Dugger[7] results. The results from the Krahn and Dugger analyses appear to be consistent within errors. These bins are in backward angles.

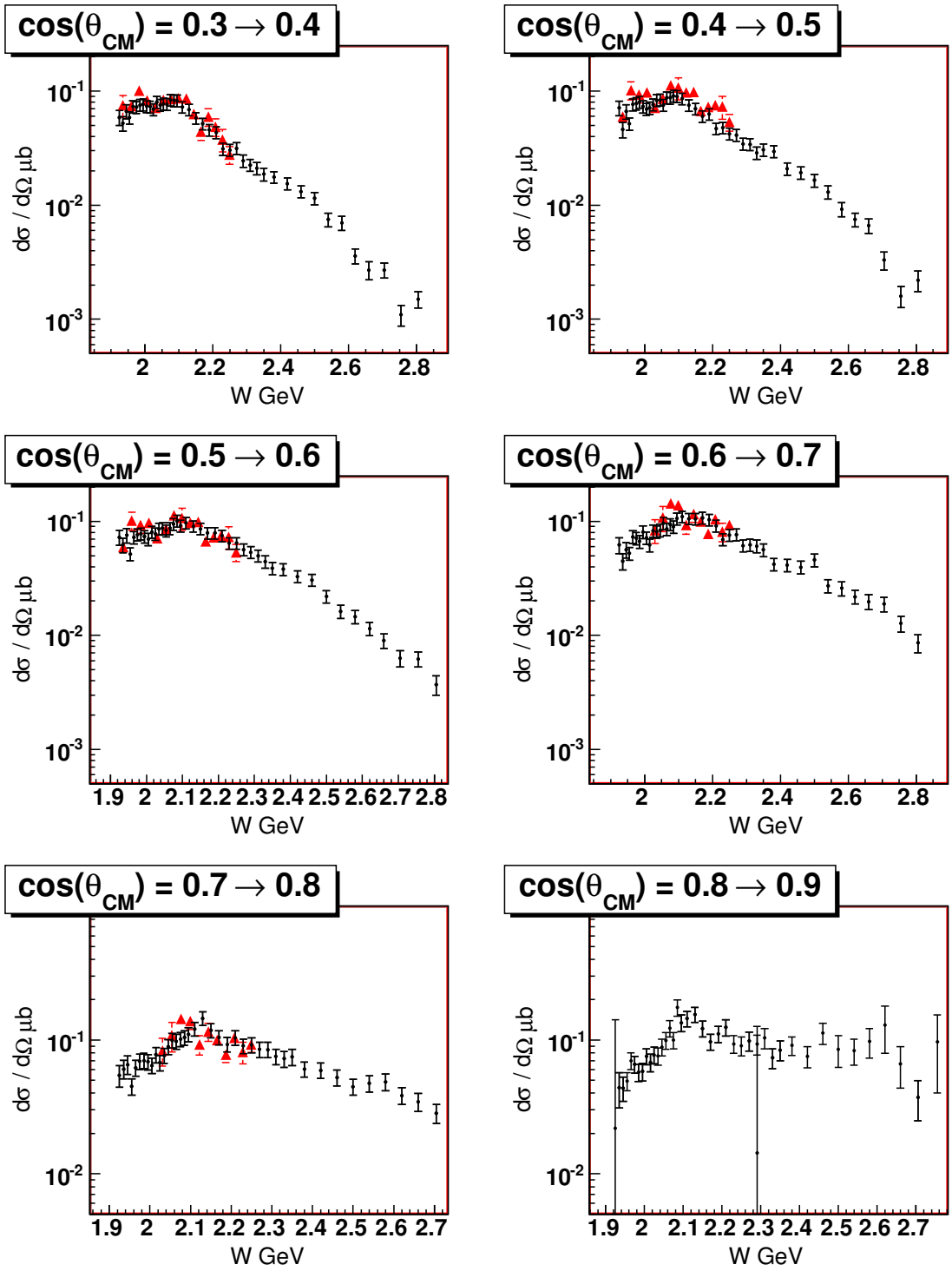

Figure 8.6: Differential cross section results for η' photoproduction. The bins presented here are in $\cos(\theta_{CM})$, with results plotted as a function of W. The width of the bins is $\cos(\theta_{CM}) = 0.1$. The black points are the Krahn results, and the red triangular markers are the Dugger[7] results. In the middle of the angular binning, the results from Krahn and Dugger appear here to be reasonably consistent. These bins are in the middle of the angular binning.

Bibliography

[1] Capstick, Simon and Roberts, Winston. *$N\pi$ decays of baryons in a relativized model.* Phys. Rev. D. 47 (1993).

[2] Koniuk, R. and Isgur, N. *Baryon decays in a quark model with chromodynamics.* Phys. Rev. D 21, 1868 - 1886 (1980).

[3] Lichtenberg, D.B. and Tassie, L.J. and Keleman, P.J. *Quark-Diquark Model of Baryons and SU(6).* Phys. Rev. 167, 1535 - 1542 (1968).

[4] W.-M. Yao, et al. *Review of Particle Physics.* Journal of Physics G 33, 1 (2006).

[5] Capstick, Simon and Roberts, Winston. *Quasi-two-body decays of nonstrange baryons.* Phys. Rev. D. 49 (1994).

[6] M. Dugger, B.G. Ritchie, J. Ball, and E. Pasyuk. *η Photoproduction on the Proton for Photon Energies from 0.75 to 1.95 GeV.* Phys. Rev. Lett.89 (2002) 222002.

[7] M. Dugger, B.G. Ritchie, J. Ball, and E. Pasyuk. *η' Photoproduction on the Proton for Photon Energies from 1.527 to 2.227 GeV.* Phys. Rev. Lett.96 (2006) 062001.

[8] A.V. Anisovich, A. Sarantsev, O. Bartholomy, E. Klempt, V.A. Nikonov and U. Thoma. *Photoproduction of Baryons Decaying into $N\pi$ and $N\eta$.* European Physical Journal A. 25 (2005).

[9] J. Ball. Private Communication. Arizona State University.

[10] A. Sibirtsev, Ch. Elster, S. Krewald, and J. Speth, *Photoproduction of η' mesons from the Proton.* AIP Conf. Proc.717, 837 (2004). For more detail see: nucl-th/0303044.

[11] K. Nakayama and H. Haberzettl, *Consistent analysis of the reactions $\gamma p \to p\eta'$ and $\gamma p \to pp\eta'$.* Phys. Rev. C 69, 065212 (2004).

[12] V. Crede, and O. Bartholomy. *Photoproduction of η Mesons off Protons for 0.75 GeV $< E_\gamma <$ 3GeV.* Phys. Rev. Lett.94 (2005) 012004.

[13] M. Crofford, C. Hovater, G. Lahti, C. Piller, and M. Poelker. *The RF system for the CEBAF polarized photoinjector.* Thomas Jefferson National Accelerator Facility, 1993. Posted online at: http://www.jlab.org/accel/inj_group/docs/TU4067.pdf

[14] Posted online at http://www.jlab.org/news/facts/works.html

[15] C. Sinclair. *Polarized Electrons at Jefferson Laboratory.* JLAB-ACT-97-11. Thomas Jefferson National Accelerator Facliity, 1997.

[16] B.M. Dumham. *Jefferson Lab, a status report* Thomas Jefferson National Accelerator Facility, 1997. Posted online at: http://www.jlab.org/accel/inj_group/pdf/Paper.pdf

[17] S. Gagnon. *Jefferson Lab Guided Tour* http://education.jlab.org/sitetour/guidedtour05.html. Thomas Jefferson National Accelerator Facility, Newport News, VA.

[18] D.I. Sober, et al. *The bremsstrahlung tagged photon beam in Hall B at JLab*, Nucl Inst Meth A 440, 263 (2000).

[19] Details of the g11a target are posted at: http://www.jlab.org/ christo/g11a%20final.pdf

[20] Sharabian, Y.G.; Battaglieri, M.;Burkert, V.D.;Devita, R.;Elouadrhiri, L.; Guo, L.; Kashy,D.;Kubarovsky, V; Mutchler, G.S.; Ostrick, M.; Ripani, M.; Rossi, P.;Rottura, A.; Pasyuk, E.; Weygand, D. *A new highly segmented start counter for the CLAS detector.* Nucl. Phys. A 556 246 (2006)

[21] Alan J. Street, et al. *Final site assembly and testing of the superconducting toroidal magnet for the CEBAF Larege Acceptance Spectrometer (CLAS)* IEEE Trans. Mag. Vol. 32, No. 4, 2074 (1996).

[22] David S. Armstrong. *CLAS Magnet.* Posted online at: http://www.physics.wm.edu/ armd/clas_photo.html.

[23] M.D. Mestayer, et al. *The CLAS drift chamber system*, Nucl Inst Meth A 449, 81 (2000).

[24] D.S. Carman, et al. *The Region One drift chamber for the CLAS spectrometer*, Nucl Inst Meth A 419, 315 (1998).

[25] L.M. Qin, et al. *Prototype studies and design considerations for the CLAS Region Two drift chambers*, Nucl Inst Meth A 367, 316 (1995).

[26] F.J. Barbosa, et al. *A drift chamber system for a toroidal detector*, Nucl Inst Meth A 323, 19 (1992).

[27] E. Smith, et al. *The time-of-flight system for CLAS*, Nucl Inst Meth A 432, 265 (1999).

[28] Rok Ursic, Roger Flood, Chip Piller, Edward Strong, and Larry Turlington. *1 nA beam position monitoring system.* Proceedings of the 1997 Particle Accelerator Conference, (1998) 2131.

[29] B. Mecking, et al. *The CEBAF Large Acceptance Spectrometer (CLAS)*, Nucl Inst Meth A 503, 513 (2003).

[30] Battaglieri, M.et al. *Spectroscopy of Exotic Baryons with CLAS:Search for ground and first excited states* CLAS Analysis Proposal PR04-021

[31] Williams, M. and Meyer, C.A. *Kinematic Fitting in CLAS.* CLAS-Note 03-017 (2003).

[32] *Statistical and Computational Methods in DAta Analysis.* North Holland Publishing Company, (1970).

[33] A. G. Fordesen and O. Skjeggstad. *Probability and Statistics in Particle Physics.* Columbia University Press (1979).

[34] M. Holtrop A webpage is maintained to keep track of gsim software. It is currently located: $http://www.physics.unh.edu/maurik/Gsim/gsim_current_code_dev.shtml$

[35] E. Pasyuk. The CLAS ELOSS package.

[36] S. Stepanyan, B. Mecking, L. Guo, D. Dale, I. Nakagawa, A. Teymurazyan, M. Gabrielyan, M. Wood, A Glamazdin. *Energy calibration of the Hall B bremsstrahung tagging system using a magnetic pair spectrometer.* CLAS-note 2005-012 (2005).

[37] M. Williams, C.A. Meyer, and D. Applegate. *Determining momentum and energy corrections for g1c using the kinematic fitter.* CLAS note: 04-017 (2003).

[38] Dan Sober Private Comminucation

[39] D. Applegate, M. Bellis, Z. Krahn, C.A. Meyer, Williams, M. *A Detailed Study of the Sources of itstematic Errors in the CLAS g11a Data.* CLAS-Note 06-017 (2006).

[40] Private communications with Dr. Matthew Bellis at Carnegie Mellon University

[41] Private communications with Mike Williams at Carnegie Mellon University

[42] *Photon Flux Determination Through Sampling of "out-of-time" Hits with the Hall B Photon Tagger* CLAS-note 2005-002 (2005).

[43] *Photon Attenuation in the CLAS Beam Line* CLAS-note 2001-010 (2001).

[44] M. Williams PhD Thesis (currently unpublished) Carnegie Mellon University

[45] W. Rarita, J. S. Schwinger. *On a theory of particles with half integral spin.* Phys Rev. 60:61, 1941.

[46] S. U. Chung *Helicity-coupling amplitudes in tensor formalism.* Phys. Rev. D48:1225-1239,1993.

[47] M. E. Peskin, D. V. Schroeder *An Introduction to Quantum Field Theory.* Harper Collins Publishers (1995).

[48] A. V. Anisovich, E. Klempt, A. V. Sarantsev, U. Thoma. *Partial-wave decomposition of pion and photoproduction amplitudes.* Eur. Phys. J. A 24 111-128 (2005).

[49] M. Guidal, J. M. Laget, and M. Vanderhaeghen. *Pion and kaon photoproduction at high energies: Forward and intermediate angles.* Nucl. Phys., A627:645678, 1997.

[50] S. U. Chung. *Formulas for Partial-Wave Analysis* Brookhaven BNL-QGS-93-05, unpublished (1993).

[51] D.H. Perkins *Introduction to High energy Physics.* 4th edition (2000), Addison-Wesley, Reading, MA.

[52] MINUIT Manual available from CERN website at: http://wwwasdoc.web.cern.ch/wwwasdoc/minuit/minmain.ht

[53] W. Braunschweig et al. *SINGLE PHOTOPRODUCTION OF eta-MESONS ON HYDROGEN IN FORWARD DIRECTION AT 4 AND 6 GeV.* Phys. Lett. B 33 236 (1970).

[54] W. T. Chiang, S. N. Yang, L. Tiator, M. Vanderhaeghen, D. Drechsel. *Reggeized model for η and η' photoproduction.* Phys. Rev. C 68 045202 (2003).

[55] A. Sibirtsev, Ch. Elster, S. Krewald, J. Speth. AIP Conf. Proc. 717, 837 (2004).

[56] K. Nakayama, H. Haberzettl Private communication with M. Dugger at ASU.

[57] JLAB Picture Exchange http://www.jlab.org

[58] Bersani, Andrea Personal Website: http://www.ge.infn.it/ bersani/img/clas.jpg

[59] Perkins, Donald H. *Introduction to High Energy Physics* Cambridge University Press; 4 edition (April 24, 2000).

[60] Fletcher, Roger *Practical Methods of Optimization* Wiley Interscience Publication, Chichester, NY: Wiley, 1987

Chapter 9

Appendix A

This appendix describes kinematic fitting and its uses in determining momentum corrections for the g11a dataset in CLAS. The information contained within this appendix is taken from two sources. The first is the the CLAS-NOTE written by Williams, Meyer, and Applegate entitled "Determining momentum and energy corrections for g1c using the kinematic fitter" [37]. The second is from the cuts and corrections section of the PhD thesis of Mike Williams[44].

9.1 Kinematic Fitting Formulas

In this section, the formulas needed to perform the kinematic fits described in this chapter are presented. Kinematic fitting is used for improving the data by enforcing energy and momentum conservation and for deriving tagger and momentum corrections.

9.1.1 Least Squares Fitting with Lagrangian Multipliers

When performing a least squares fit with a set of constraint equations, each equation can be used to reduce the number of fit quantities. In order to treat each unknown equally, the method of Lagrangian multipliers was used instead. This section follows the work of [32].

Before going into the details, some notation must be established. The m unknown parameters are denoted $\vec{x}$, the n measurable quantities are $\vec{y}$. The actual measured quantities and their errors are the n-vectors $\vec{\eta}$ and $\vec{\epsilon}$ respectively. Therefore,

$$\vec{\eta} = \vec{y} + \vec{\epsilon}. \tag{9.1}$$

The vectors $\vec{x}$ and $\vec{y}$ are related by the r constraint functions,

$$f_k(\vec{x}, \vec{y}) = 0, \qquad k = 1, 2, ..., r. \tag{9.2}$$

The first approximation of the unknowns is labeled $\vec{x}_0$. Using $\vec{y}_0 = \vec{\eta}$ and require the constraint functions to be approximately linear near $(\vec{x}_0, \vec{y}_0)$. A Taylor expansion of the constraint functions in this region is taken to first order,

$$f_k(\vec{x}, \vec{y}) \approx f_k(\vec{x}_0, \vec{y}_0) + \sum_i^m A_{ki}(x^i - x_0^i) + \sum_i^n B_{ki}(y^i - y_0^i), \tag{9.3}$$

where,

$$A_{ij} = \left(\frac{\partial f_i}{\partial x_j}\right)(\vec{x}_0, \vec{y}_0), \qquad B_{ij} = \left(\frac{\partial f_i}{\partial y_j}\right)(\vec{x}_0, \vec{y}_0), \tag{9.4}$$

Define the r-vector $\vec{c}$ with $c_k = f_k(\vec{x}_0, \vec{y}_0)$, the m-vector $\vec{\xi} = \vec{x} - \vec{x}_0$ and the n-vector $\vec{\delta} = \vec{y} - \vec{y}_0$. Then Eqn.(9.3) can be rewritten as,

$$A\vec{\xi} + B\vec{\delta} + \vec{c} = 0. \tag{9.5}$$

Write the minimization quantity as the following: $\vec{\delta}^T C_\eta^{-1} \vec{\delta}$ where C_η is the covariance matrix of the measured quantities.

The Lagrangian is now introduced,

$$L = \vec{\delta}^T C_\eta^{-1} \vec{\delta} + 2\vec{\mu}^T \left(A\vec{\xi} + B\vec{\delta} + \vec{c} \right), \tag{9.6}$$

where $\vec{\mu}$ is the r-vector of Lagrangian multipliers. Using the fact that $\vec{\delta}$ and $\vec{\xi}$ are independent variables, setting the total differential of L to zero yields,

$$\frac{\partial L}{\partial \delta_i} = \frac{\partial L}{\partial \xi_i} = 0. \tag{9.7}$$

Substituting the solutions to Eqn.(9.7) into Eqn.(9.5) gives,

$$\vec{\xi} = -\left(A^T C_B A\right)^{-1} A^T C_B \vec{c} \tag{9.8}$$

$$\vec{\delta} = -C_\eta B^T C_B \left(\vec{c} - A\vec{\xi} \right), \tag{9.9}$$

where $C_B = (BC_\eta B^T)^{-1}$. The least squares estimates for the parameters $\vec{x}$ and improved measurements $\vec{y}$ are then,

$$\vec{x} = \vec{x}_0 + \vec{\xi} \tag{9.10}$$

$$\vec{y} = \vec{y}_0 + \vec{\delta}. \tag{9.11}$$

When the constraint equations are nonlinear, these results should be considered better approximations and the process should be iterated.

The estimates of the measurement errors are the n-vector,

$$\vec{\epsilon} = \vec{\eta} - \vec{y}, \tag{9.12}$$

where $\vec{y}$ are the improved measurements obtained form the final iteration and $\vec{\eta}$ are the measured values. If the errors are normally distributed and the constraint functions are sufficiently linear near $(\vec{x}_0, \vec{y}_0)$, then $\vec{\epsilon}^T C_\eta^{-1} \vec{\epsilon}$ follows a χ^2 distribution with $r - m$ degrees of freedom.

Finally, propagation of errors can be used to write the covariance matrix for the improved measurements as,

$$C_y = C_\eta - C_\eta B^T C_B B C_\eta + C_\eta B^T C_B A (A^T C_B A)^{-1} A^T C_B B C_\eta, \tag{9.13}$$

and the covariance matrix for the parameters as,

$$C_x = (A^T C_B A)^{-1}. \tag{9.14}$$

9.1.2 Confidence Levels and Pull Distributions

The primary measure of the goodness of fit for the least squares method is the called the confidence level.

$$CL = \int_{\chi^2}^{\infty} f(z; n) dz, \tag{9.15}$$

where $f(z;n)$ is the χ^2 probability density function with n degrees of freedom. It is a measure of the probability that a χ^2 from the theoretical distribution is greater than the χ^2 obtained from the fit. For a dataset consisting entirely of events which satisfy the fit hypothesis with normally distributed errors, the confidence level distribution is flat on the interval of $0 \rightarrow 1$. Events that do not satisfy the fit hypothesis, background for example, have small value confidence levels. Cutting events with a low confidence level provides a means of eliminating the majority of the background events while losing a well defined amount of the signal.

To effectively use the confidence level to cut background, an understanding of each fit quantity's errors is necessary. The quality of the error estimation can be examined using the pull distributions. The pull of the i^{th} fit quantity is defined as [33],

$$z_i = \frac{\epsilon_i}{\sigma(\epsilon_i)}, \tag{9.16}$$

where $\epsilon_i = \eta_i - y_i$ with standard deviation σ_{ϵ_i}. The pulls are written using $\vec{\epsilon}$ since it is the only quantity for which the true mean value of each measurement is known. The i^{th} pull can be rewritten as,

$$z_i = \frac{\eta_i - y_i}{\sqrt{\sigma^2(\eta_i) - \sigma^2(y_i)}}. \tag{9.17}$$

The z_i's should be normally distributed about zero with $\sigma = 1$. A systematic error in the measured quantity η_i, can be seen as an overall shift in the distribution of the corresponding z_i away from zero. Similarly, if the error of η_i has been consistently overestimated (underestimated), then the corresponding pull distribution will be too narrow (broad).

9.2 Energy and Momentum Corrections

9.2.1 Tagger Corrections

Gravitational sag in the photon tagger's focal plane were first discovered in 2003 [36, 37, 38]. This leads to an inaccurate photon energy constructed from the raw tagger information. We can obtain an empirical correction for this affect using the $\gamma p \rightarrow p\pi^+\pi^-$ channel.

To start, events are selected with only one proton, π^+ and π^- and no other charged tracks. Energy loss and momentum corrections are then applied, to the final state particles. Then event is kinematically fit to an event hypothesis of $(\gamma)p \rightarrow p\pi^+\pi^-$ while ignoring the measured photon energy. A 10% confidence level cut from the kinematic fit excludes event which are not consistent with the event hypothesis. For each event included in calculating the correction, the kinematic fit produces a calculated photon energy(E_γ^{kfit}) for the photon in the event. This can then be compared to the measured value of the photon energy(E_γ^{meas}) to deermine what, if any, correction is required.

For each event, the kinematic fit estimate for the tagger energy correction is,

$$\Delta E_\gamma = E_\gamma^{kfit} - E_\gamma^{meas}. \tag{9.18}$$

The corrections are binned in tagger E-counter as seen in Figure 9.1(a). From each bin the Gaussian mean is extracted as seen in Figure 9.1(b). Then, for each g11 run r the beam offset is calculated by fitting each run's individual corrections to,

$$\Delta E_{\gamma,r} = \Delta E_{\gamma,tot} + B_r, \tag{9.19}$$

where B_r is the beam offset for run r (Figure 9.1(c)). Thus, for an event from run r with a photon from E-counter e, the correction applied to the photon energy is,

$$\Delta E_{\gamma,e,r} = \Delta E_{\gamma,e} + B_r, \tag{9.20}$$

where $\Delta E_{\gamma,e}$ is the Gaussian mean for E-counter e.

9.2.2 Momentum Corrections

Discrepancies in the toroidal magnetic field map and/or in the drift chamber survey information can lead to inaccuracies in the reconstructed momenta. Following the procedure described for the determination of the tagger correction, the inclusive channel $\gamma p \to p\pi^+\pi^-$ is used to empirically obtain corrections for the reconstructed momenta. Events are selected which contain only a single proton, π^+ and π^-. Energy loss corrections are applied to the particles, along with the tagger corrections from the previous iteration. The event is kinematically fit to the series of hypotheses $\gamma p \to p\pi^+(\pi^-)$, $\gamma p \to p(\pi^+)\pi^-$ and $\gamma p \to (p)\pi^+\pi^-$. The parentetical notation used here indicates a particle which is reconstructred, instead of directly measured. The series of hypotheses systematically checks each particle, allowing for the comparison between a reconstructed missing particle and the detected measured particle. As with the tagger correction, only events with a confidence level of greater than 10% are used for determining the momentum corrections.

The kinematic fit estimate for the corrections to the tracking parameters is then,

$$\Delta p_x = p_x^{kfit} - p_x^{meas} \tag{9.21}$$
$$\Delta \lambda_x = \lambda_x^{kfit} - \lambda_x^{meas} \tag{9.22}$$
$$\Delta \phi_x = \phi_x^{kfit} - \phi_x^{meas}, \tag{9.23}$$

where $x = (p, \pi^+, \pi^-)$ is the excluded particle. For example, Δp_p is obtained using p_p^{kfit} from the kinematic fit to $\gamma p \to (p)\pi^+\pi^-$, whereas Δp_{π^-} is obtained using $p_{\pi^-}^{kfit}$ from the fit to $\gamma p \to p\pi^+(\pi^-)$ and so on.

Each of the quantities defined in Eqn.(9.21) is, in principle, a function of the particle's momentum magnitude p, orientation (θ, ϕ) in the lab coordinates , CLAS sector number and charge. Thus, to obtain our momentum corrections, we have divided each of the 6 CLAS sectors into 180 (θ, ϕ) bins. A correction is then obtained for the quantities Eqn.(9.21)—as a polynomial function of p—in each bin for both charges. The binning in each sector and charge is the same. The azimuthal angle ϕ is divided into twelve 5° bins in each θ bin. The polar angle θ is divided into nine 5° bins for $\theta\epsilon[5°, 50°)$, four 10° bins for $\theta\epsilon[50°, 90°)$ and two 20° bins for $\theta\epsilon[90°, 140°)$.

In each bin, histograms are built of ΔX_q vs. p_q where X_q denotes the quantities (9.21) for both charges. The momentum magnitude p is binned in equal sized $1/p$ bins, since the tracking is done in terms of q/p. The Gaussian means are extracted for each p bin and fit to a polynomial function of p. Figure 9.2 shows an example of this process in a single $(sector, \theta, \phi)$ bin for Δp. The size of the corrections in this particular $(sector, \theta, \phi)$ bin are atypically large. Most bins have much smaller, if not negligible, momentum corrections. This particular bin was chosen because the size of the corrections aids in illustrating how the process works. Notice that at higher momenta $\Delta p_+(p) \approx -\Delta p_-(p)$. Thus, the correction to the tracking quantity q/p is independent of which way the track bends. The same process is followed to obtain the corrections $\Delta\lambda$ and $\Delta\phi$.

Figure 9.2.2 shows the size of the corrections for all detected protons and π's in the $2-positive/1-negative$ track skim for run 43582. The corrections to the magnitude of the momenta is generally less than $10 MeV/c$, as seen in Figures 9.2.2(a) and (d). The corrections to the tracking angles are typically on the order of a few milliradians as shown in Figures 9.2.2(b),(c),(e),(f).

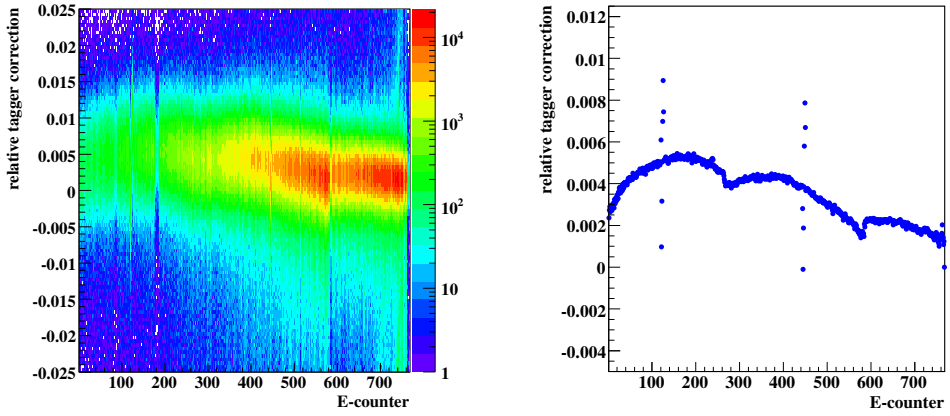

(a) (b)

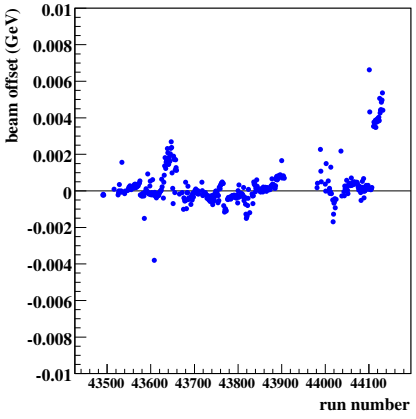

(c)

Figure 9.1: Tagger Corrections: (a) $\Delta E_\gamma / E_{beam}$ vs E-counter for $(\gamma)p \rightarrow p\pi^+\pi^-$ events. (b) Gaussian mean extracted for each E-counter from (a). The two sets of six E-counter corrections which do not fall on the curve are the result of swapped cables during cooking. (c) beam offset in GeV vs run number.

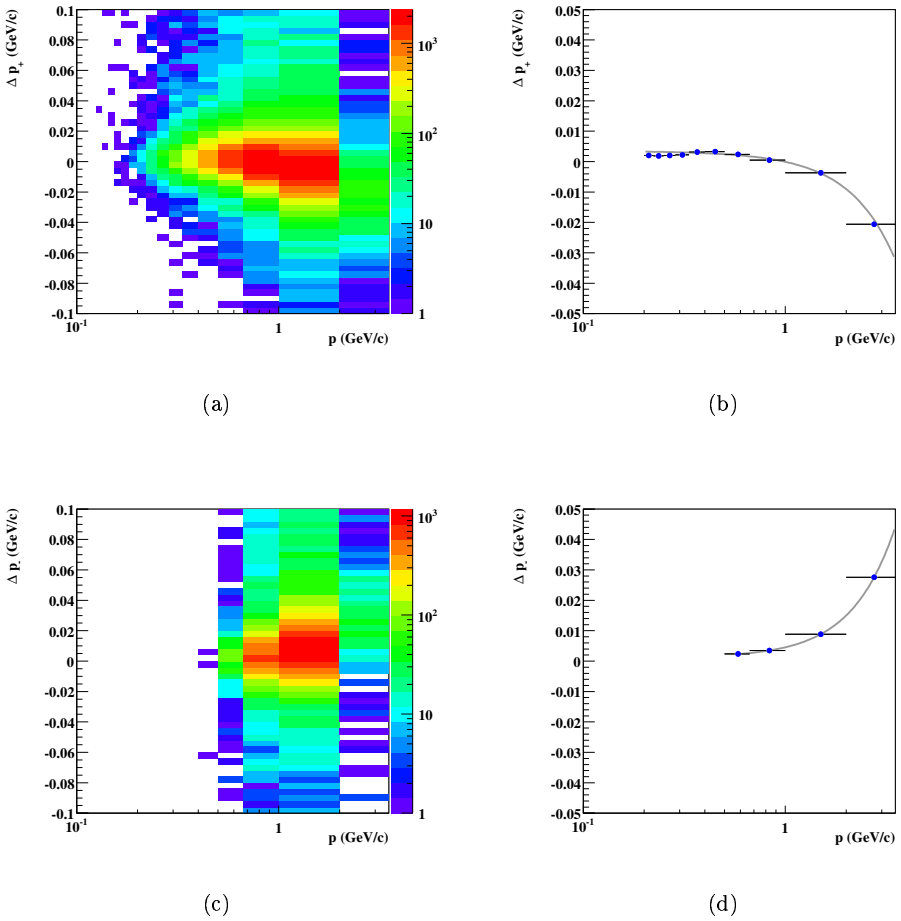

Figure 9.2: Momentum Corrections: Sector 1, $\theta\epsilon(20°, 25°)$, $\phi\epsilon(-15°, -10°)$: (a) $\Delta p(GeV/c)$ vs. $p(GeV/c)$ for positively charged particles in this $(sector, \theta, \phi)$ bin. (b) Gaussian mean extracted for each p bin from (a). The line is from a polynomial fit which is used as the correction to p. (c) $\Delta p(GeV/c)$ vs. $p(GeV/c)$ for negatively charged particles in this $(sector, \theta, \phi)$ bin. The lack of events with $p < 0.5 GeV/c$ is an artifact of the detector acceptance. (d) Gaussian mean extracted for each p bin from (c). The line is from a polynomial fit which is used as the correction to p. The size of the corrections in this particular $(sector, \theta, \phi)$ bin are atypically large, which aids in displaying how the corrections are obtained. Most bins have much smaller, if not negligible, momentum corrections.

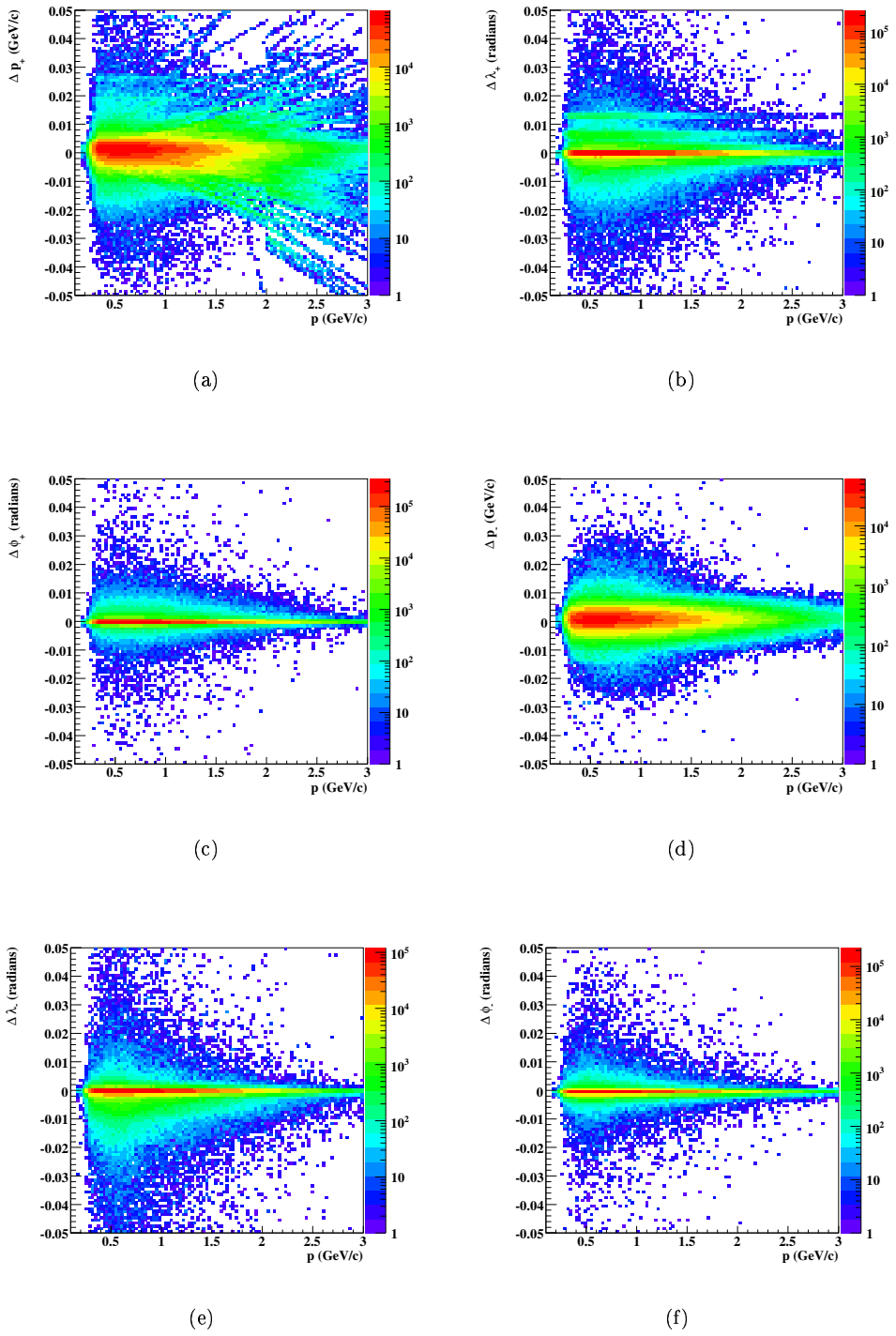

Figure 9.3: Momentum corrections for all protons and pions in the $++-$ skim for run 43582. (a) $\Delta p(GeV/c)$ vs $p(GeV/c)$ for positively charged particles. (b) $\Delta\lambda(radians)$ vs $p(GeV/c)$ for positively charged particles. (c) $\Delta\phi(radians)$ vs $p(GeV/c)$ for positively charged particles. (d) $\Delta p(GeV/c)$ vs $p(GeV/c)$ for negatively charged particles. (e) $\Delta\lambda(radians)$ vs $p(GeV/c)$ for negatively charged particles. (f) $\Delta\phi(radians)$ vs $p(GeV/c)$ for negatively charged particles. Note that the majority of the corrections are small.

Chapter 10

Appendix B

This appendix provides the cuts on the missing mass off of the proton which were used to select the η and the η' mesons in this analysis. The cut, as mentioned in the chapter on data selection, is made at $2.5 \times \sigma$. For each W bin, there will be a Mean and Sigma listed.

Table 10.1: Mean and Sigma by bin for the η data.

W bin (MeV)	mean	sigma
1570-1580	0.550223516992811	0.00364813382354159
1580-1590	0.549400840776225	0.00379695957098705
1590-1600	0.54940985492498	0.00400083019154546
1600-1610	0.549377915591922	0.00411671113722731
1610-1620	0.549425187100754	0.00422638241006233
1620-1630	0.54939220393782	0.0043041533760627
1630-1640	0.549341322543059	0.00438447928594424
1640-1650	0.549310732009855	0.00442423698334149
1650-1660	0.549310238068569	0.00456793335920109
1660-1670	0.549320412075166	0.00461312243774945
1670-1680	0.549203611934113	0.00478646517068872
1680-1690	0.549150106383443	0.00484809738415417
1690-1700	0.549230140690223	0.00495339044577116
1700-1710	0.549204170089726	0.00504393755648632
1710-1720	0.549196255996356	0.00510775871556488
1720-1730	0.549101892481516	0.0052513187580105
1730-1740	0.549055554260655	0.00534738601891459
1740-1750	0.549248400947348	0.0053651524836839
1750-1760	0.54908560147212	0.0054362241430172
1760-1770	0.549055752526909	0.0055359577940049
1770-1780	0.549054539511971	0.00549950226785681
1780-1790	0.548905249759288	0.00572001148802607
1790-1800	0.548981706788961	0.00550061564570973
1800-1810	0.548963625817338	0.00569109014877133
1810-1820	0.549117612429655	0.00561324233705258
1820-1830	0.548970953388673	0.00576744396256997
1830-1840	0.548885893553233	0.00577194147690603
1840-1850	0.54899549383149	0.00594107907590183
1850-1860	0.548943794233924	0.00580295928778349
1860-1870	0.548761711902662	0.00592120215975448
1870-1880	0.548869480993396	0.00571265059953935
1880-1890	0.548768656993587	0.00589366910676453
1890-1900	0.548997015945412	0.00598764950349622
1900-1910	0.548713930994143	0.00596315613934172
1910-1920	0.548710011492504	0.0059852241819052
1920-1930	0.548691978257132	0.0056920633616464
1930-1940	0.548776009057112	0.00593838724532993
1940-1950	0.548629580025633	0.00573462548680739
1950-1960	0.548792940169215	0.00586422184563614
1960-1970	0.548703691323976	0.00592948282091199
1970-1980	0.548620143021711	0.00600477116476093
1980-1990	0.548704473759866	0.00602441142754368
1990-2000	0.548537022204685	0.00583085295401428
2000-2010	0.548757836418592	0.006073082865443
2010-2020	0.548716241719254	0.0060006442350202
2020-2030	0.548712637937526	0.00597278945984622

Table 10.2: Mean and Sigma by bin for the η data continued

W bin (MeV)	mean	sigma
2030-2040	0.548642471651948	0.00601240584740765
2040-2050	0.548583794737918	0.00582854519734847
2050-2060	0.548673794293115	0.00590771335559037
2060-2070	0.548603788906829	0.00580137989918916
2070-2080	0.548707451754063	0.006013610637344
2080-2090	0.548597040992893	0.005993954942049
2090-2100	0.548741151781067	0.00596959211000215
2100-2120	0.548588161419716	0.0061123289343874
2120-2140	0.548442856726612	0.00611419370602401
2140-2160	0.54840566693302	0.00609932233082509
2160-2180	0.548590074775776	0.00616719316324634
2180-2200	0.54846129485419	0.00606574676211222
2200-2220	0.548562117389172	0.0058671024387282
2220-2240	0.548347037919835	0.00603311087332121
2240-2260	0.548390861122249	0.00597141301252752
2260-2280	0.54834614057654	0.00618269770603894
2280-2300	0.5485363955121	0.00602692883610744
2300-2320	0.548318628856367	0.0058804417054413
2320-2340	0.548429008158517	0.006120964509278
2340-2360	0.548337897126437	0.00588312964971138
2360-2400	0.548398776376967	0.00585334582498621
2400-2440	0.548239019818664	0.00606033917724366
2440-2480	0.548235378488556	0.00584575631786736
2480-2520	0.548114398158868	0.00598830468413537
2520-2560	0.548282627353658	0.00598183285591894
2560-2600	0.548267665948636	0.00628891098118543
2600-2640	0.548486108838916	0.00601925293894723
2640-2680	0.54825239814897	0.00607670280213778
2680-2730	0.548554569099104	0.00613195439951944
2730-2780	0.548081055102469	0.00584009108283091
2780-2830	0.54810099735367	0.00625118120979543
2830-2880	0.547287577448386	0.00594424352783033

Table 10.3: Mean and Sigma by bin for the η accepted Monte Carlo.

W bin (MeV)	mean	sigma
1570-1580	0.547315276567578	0.00372139515271224
1580-1590	0.547631535497163	0.00384667234040817
1590-1600	0.547626434325115	0.0040085556029628
1600-1610	0.547631973319808	0.00415707266148637
1610-1620	0.547666563484778	0.00427701445142495
1620-1630	0.547661392589732	0.00442668468482839
1630-1640	0.547725981480847	0.00452723225591571
1640-1650	0.547688796051179	0.0047184976909077
1650-1660	0.547712729049105	0.00482886679115067
1660-1670	0.547720311089632	0.00493172907554116
1670-1680	0.547743176310694	0.00502373836963728
1680-1690	0.547757806149292	0.0051794371447258
1690-1700	0.547740609111277	0.00528216712353245
1700-1710	0.547737030260248	0.00537576601880255
1710-1720	0.547734691266298	0.00548679429911333
1720-1730	0.547761595315072	0.00559080144853494
1730-1740	0.547777944115532	0.00565811674560133
1740-1750	0.547768268064358	0.00579216495240394
1750-1760	0.547783478346416	0.0058724146755267
1760-1770	0.54780017320649	0.00590634907919841
1770-1780	0.547806180038422	0.0060196333668618
1780-1790	0.547866134336944	0.00608066496457941
1790-1800	0.547798637541306	0.00613139740862875
1800-1810	0.547858005157796	0.00617237690651726
1810-1820	0.547865101000312	0.00627585957174923
1820-1830	0.547881641526259	0.00631986002041647
1830-1840	0.547943051851081	0.00635028675150181
1840-1850	0.547894964873586	0.00642403546179332
1850-1860	0.54785365089657	0.00650110936463145
1860-1870	0.54793020967644	0.00649584377834257
1870-1880	0.547910290039878	0.00653663532146284
1880-1890	0.547938505447095	0.00656980058283341
1890-1900	0.547902781014008	0.00653088188429684
1900-1910	0.5479634080005	0.00663063276440508
1910-1920	0.547837384523949	0.00666356581136939
1920-1930	0.547873737265458	0.00665080302485877
1930-1940	0.547954824110605	0.00678977290295363
1940-1950	0.547834670519027	0.00668923421534909
1950-1960	0.547946240477835	0.00673849564981913
1960-1970	0.548019074196336	0.00679634548083799
1970-1980	0.547901015565603	0.00676131719343288
1980-1990	0.547869656624583	0.00675512491187467
1990-2000	0.547832200830037	0.00663183738100326
2000-2010	0.547887875303592	0.00670644429198271
2010-2020	0.547938688743215	0.00667046318342005

Table 10.4: Mean and Sigma by bin for the η accepted Monte Carlo continued

W bin (MeV)	mean	sigma
2020-2030	0.547871195122761	0.00677869985056509
2030-2040	0.547908603884882	0.00673016669179552
2040-2050	0.547891713395303	0.00672250218480449
2050-2060	0.547904123054492	0.00678690889267882
2060-2070	0.547902407289727	0.00670415612014411
2070-2080	0.547888511425389	0.00674389359232558
2080-2090	0.547894770914942	0.00670100852983963
2090-2100	0.547860846307102	0.00681824333705012
2100-2120	0.547907156102821	0.00673478792804685
2120-2140	0.547812617172463	0.00665008964601442
2140-2160	0.54784632368955	0.00673850382050394
2160-2180	0.547826862850319	0.00666900479929578
2180-2200	0.547875318452737	0.00672798490024148
2200-2220	0.547817704846572	0.00668162355936569
2220-2240	0.547783470503856	0.00666861065001774
2240-2260	0.54777501404537	0.00658081703165538
2260-2280	0.547792843821425	0.00664491283856222
2280-2300	0.547762034822248	0.00656346993552253
2300-2320	0.547760257639008	0.0066481063547025
2320-2340	0.547723593593152	0.00664519625613817
2340-2360	0.547750305971762	0.00665895385218332
2360-2400	0.547730931269065	0.0065808426823254
2400-2440	0.547714813446105	0.00658734254586773
2440-2480	0.547698019925068	0.00659453194329781
2480-2520	0.547668540049297	0.00660288143358287
2520-2560	0.547700829080192	0.0065648253437921
2560-2600	0.547673954350513	0.00651147620909765
2600-2640	0.547671935408847	0.00663954929261213
2640-2680	0.547619384479076	0.00661783159623489
2680-2730	0.547588516135646	0.00666043139292513
2730-2780	0.547602728718536	0.00672822534210718
2780-2830	0.547615323391233	0.00674222480076646
2830-2880	0.547671620722792	0.00685175737073517

Table 10.5: Mean and Sigma by bin for the η' data.

W bin (MeV)	mean	sigma
1900-1910	0.941374662825976	0.00616763450019399
1910-1920	0.958128937535538	0.00170133422419114
1920-1930	0.958390703247244	0.00184136839862599
1930-1940	0.958514448394653	0.0021415087157139
1940-1950	0.958668814329792	0.00232052180693012
1950-1960	0.958446789455353	0.00245918326309311
1960-1970	0.958565424203316	0.0026062381033833
1970-1980	0.958561798308268	0.00270949723933152
1980-1990	0.958508673825906	0.00280682195007998
1990-2000	0.958463931881894	0.00289097155797524
2000-2010	0.958532687934024	0.00291438193532168
2010-2020	0.958460390926075	0.00318662948184978
2020-2030	0.958483355160293	0.00331617512662148
2030-2040	0.958512034092772	0.00342543407125028
2040-2050	0.958477762323713	0.00343524852996338
2050-2060	0.958348272583438	0.00355311807292771
2060-2070	0.958437867789629	0.00359922918161235
2070-2080	0.958536377788176	0.00370713299327101
2080-2090	0.95853211163313	0.00385865347951193
2090-2100	0.958356064106647	0.00383552089095649
2100-2120	0.958504550262478	0.00398009884089177
2120-2140	0.958508595737583	0.00415735779407419
2140-2160	0.958470784294255	0.00419187514151332
2160-2180	0.958535298509516	0.00438925279327113
2180-2200	0.958425660017592	0.00448748792251584
2200-2220	0.958503902242139	0.0045154382626015
2220-2240	0.958317566225443	0.0045405127413982
2240-2260	0.958399193030659	0.00463465160448205
2260-2280	0.958341082751924	0.00488833795192906
2280-2300	0.958155355302951	0.00476318227084746
2300-2320	0.958206457218631	0.00469433519571873
2320-2340	0.958091824839775	0.00483407108616774
2340-2360	0.958253075357839	0.00495439436700493
2360-2400	0.958304612630131	0.00505049993931474
2400-2440	0.958230678556387	0.00512633633748891
2440-2480	0.958229705666848	0.00497631535179249
2480-2520	0.958153598215889	0.00515525852386758
2520-2560	0.958225237377298	0.00476247940552843
2560-2600	0.958266709844339	0.00477620741468039
2600-2640	0.957992523938861	0.00498283424002982
2640-2680	0.958309047133718	0.00507375482743781
2680-2730	0.958091279536493	0.00502779165220682
2730-2780	0.957806708077491	0.00457668323301147
2780-2830	0.958210661044549	0.00488811994048273
2830-2880	0.95800732354873	0.00478133065050891

Table 10.6: Mean and Sigma by bin for the η' accepted Monte Carlo.

W bin (MeV)	mean	sigma
1900-1910	0.943493086380049	0.000290030723653147
1910-1920	0.957179214995768	0.00146296595490561
1920-1930	0.957481707157154	0.00177325528750237
1930-1940	0.957587239175579	0.00192203295934925
1940-1950	0.957619168738203	0.00211264157114987
1950-1960	0.957636990402288	0.00227859626769695
1960-1970	0.957696283118557	0.00242249781786181
1970-1980	0.957684977732212	0.00254953065780945
1980-1990	0.957736319279203	0.00268873668041437
1990-2000	0.957781555069352	0.00276952718990512
2000-2010	0.957796646983496	0.00291112455813869
2010-2020	0.95781841948726	0.00303417741682633
2020-2030	0.957817685607627	0.00309833587916209
2030-2040	0.957850706376063	0.00321661914278763
2040-2050	0.957854975300044	0.0033318801562961
2050-2060	0.957886582684087	0.00341854722426635
2060-2070	0.95790351959501	0.00355234275836414
2070-2080	0.957916738874367	0.00360268030793336
2080-2090	0.957983732873834	0.00373171104914191
2090-2100	0.957958059834938	0.00382565313943307
2100-2120	0.957982074890447	0.00386169337727592
2120-2140	0.958041800292048	0.00405877476972545
2140-2160	0.958049591559775	0.00419582722014086
2160-2180	0.958078647633685	0.00432426136896442
2180-2200	0.958123857735058	0.00445952128929345
2200-2220	0.958167898455267	0.00454960291434591
2220-2240	0.95816573599744	0.004685875732909
2240-2260	0.958169195434437	0.00477760246471028
2260-2280	0.958187940827304	0.00481588385985232
2280-2300	0.958178419881091	0.00487271115353254
2300-2320	0.958151586309151	0.00493912525183324
2320-2340	0.958189032002816	0.0050621875360258
2340-2360	0.958180984638388	0.00500980550579796
2360-2400	0.958134928085551	0.00493307600450446
2400-2440	0.958157713799008	0.00510632600034872
2440-2480	0.958080524375915	0.00508759786758179
2480-2520	0.958078956683415	0.00502456182639437
2520-2560	0.958005461292338	0.00488071714277086
2560-2600	0.958043204134958	0.00487578201965735
2600-2640	0.958016972902086	0.00472879215352929
2640-2680	0.95798162278075	0.00476115688474866
2680-2730	0.957929082866047	0.00475572296903078
2730-2780	0.957914525711312	0.00468493573286445
2780-2830	0.957936902332801	0.00470277301747406
2830-2880	0.957831223105934	0.00473683088630191

Chapter 11

Appendix C

This appendix describes the production of amplitudes used in this fit, within the covariant tensor formalism. This appendix was taken from the formalism section of the PhD thesis of Mike Williams[44] to document the construction of the amplitudes.

11.1 Integral Spin Formalism

In this section, polarization tensors for relativistic integral spin particles will be constructed. The technique used will be to embed each spin-J system, with $(2J+1)$ independent elements, into the higher dimension space of rank-J tensors, with 4^J independent elements. Supplementary conditions, known as the Rarita-Schwinger conditions [45], will then be needed to reduce the number of independent elements to the proper number. The reason for using this embeddings process, is that the transformation properties of the spin-J system become those of the rank-J tensor. Thus, coupling the spin-J system to any 4-momenta or other spin tensors (including the half-integral spin tensors discussed below) to form a Lorentz scalar becomes a straight forward process.

11.1.1 Spin-1 Polarization 4-Vectors

Massive Particles

Construction of the polarization vector for a massive spin-1 particle with momentum p, mass w and canonical spin projection m will be described here. The constraint equation,

$$p_\mu \epsilon^\mu(p,m) = 0 \tag{11.1}$$

reduces the number of independent components of the 4-vector to 3 (the correct number for a spin-1 state). In the particle's rest frame, (11.1) implies that the energy component is 0. The spatial components are then chosen to be the eigenvectors of the S^2 and S_z angular momentum operators,

$$\vec{\epsilon}(\pm 1) = \mp\frac{1}{\sqrt{2}}(1, \pm i, 0), \qquad \vec{\epsilon}(0) = (0,0,1). \tag{11.2}$$

Thus, in the particle's rest frame, $\epsilon^\mu(p,m)$ transforms under spatial rotations as,

$$R^\mu{}_\nu(\alpha,\beta,\gamma)\epsilon^\nu(p,m) \xrightarrow[rf]{} R_{ij}(\alpha,\beta,\gamma)\epsilon_j(m) = \sum_{m'} D^{(1)}_{m'm}(\alpha,\beta,\gamma)\epsilon_j(m') \tag{11.3}$$

where $R_{ij}(\alpha,\beta,\gamma)$ is the rotation matrix for Euler angles α, β and γ. To get the polarization 4-vector in an arbitrary frame, we simply boost it from the rest-frame,

$$\epsilon^\mu(p,m) = \Lambda^\mu{}_\nu(p)\epsilon^\nu(p_{rf},m), \tag{11.4}$$

where $\Lambda^{\mu}{}_{\nu}(p)$ performs the Lorentz transformation that boosts p_{rf} to p. The spin-1 projection operator is defined as,

$$P^{(1)}_{\mu\nu}(p) = \sum_{m} \epsilon_{\mu}(p,m)\epsilon^{*}_{\nu}(p,m) = -g_{\mu\nu} + \frac{p_{\mu}p_{\nu}}{w^2} \equiv -\tilde{g}_{\mu\nu}. \tag{11.5}$$

When $P^{(1)}_{\mu\nu}(p)$ is contracted with an arbitrary 4-vector, y^{ν}, the resulting 4-vector, $\tilde{y}_{\mu} = P^{(1)}_{\mu\nu}(p)y^{\nu}$, is orthogonal to p. Therefore, it projects any 4-vector into the space spanned by the spin-1 states.

Photons

Since the photon doesn't have a rest frame, construction of its polarization 4-vectors are necessarily different from the massive particle case. Constructing the photon polarization 4-vectors,

$$A \equiv A^{\mu}\epsilon_{\mu}(k,m), \tag{11.6}$$

where A is the Lorentz invariant amplitude for some process $\gamma X \to Y$. Under the gauge transformation, $\epsilon_{\mu} \to \epsilon_{\mu} + \lambda k_{\mu}$, (11.6) becomes,

$$A^{\mu}\epsilon_{\mu}(k,m) \to A^{\mu}(\epsilon_{\mu} + \lambda k_{\mu}) = A + \lambda A^{\mu}k_{\mu}. \tag{11.7}$$

Therefore, gauge invariance requires $A^{\mu}k_{\mu} = 0$ (known as the Ward Identity). The following is required,

$$k^{\mu}\epsilon_{\mu}(k,m) = 0, \tag{11.8}$$

then only the gauge invariant piece of A^{μ}, the component orthogonal to k, will contribute to A once we've chosen a gauge to work in. The Coulomb gauge is chosen,

$$\vec{k} \cdot \vec{\epsilon} = 0. \tag{11.9}$$

Equations (11.8) and (11.9) reduce the number of independent elements of ϵ_{μ} to 2, corresponding to helicities ± 1.

As an example, consider a photon with $\vec{k} = k\hat{z}$. Equations (11.8) and (11.9) require $\epsilon_0 = \epsilon_3 = 0$. The photon polarization vectors can then be written as,

$$\epsilon^{\mu}(k\hat{z}, \pm 1) = \mp\frac{1}{\sqrt{2}}(0, 1, \pm i, 0). \tag{11.10}$$

11.1.2 Spin-2 (and higher) Polarization Tensors

The spin-2 polarization tensors are constructed from the spin-1 polarization 4-vectors as [46],

$$\epsilon_{\mu\nu}(p,m) = \sum_{m_1,m_2} (1m_1 1m_2|2m)\epsilon_{\mu}(p,m_1)\epsilon_{\nu}(p,m_2), \tag{11.11}$$

where $(1m_1 1m_2|2m)$ is the Clebsch-Gordon coefficient coupling two spin-1 states to a spin-2 state. The transformation properties of the spin-1 states (11.3) along with the properties of the D-functions can be used to show that, in the particle's rest frame, $\epsilon_{\mu\nu}(p,m)$ does transform under spatial rotations as a spin-2 state,

$$R^{\mu}{}_{\rho}R^{\nu}{}_{\pi}\epsilon_{\mu\nu}(p,m) \xrightarrow[rf]{} R_{ik}R_{jl}\epsilon_{ij}(m) = \sum_{m'} D^{(2)}_{m'm}(R)\epsilon_{\rho\pi}(m'). \tag{11.12}$$

A general 2nd rank tensor has 16 independent elements, however, a spin-2 state only has 5 ($m_z = \pm 2, \pm 1, 0$). The Rarita-Schwinger conditions,

$$\begin{aligned} p^\mu \epsilon_{\mu\nu}(p,m) &= 0 && (11.13)\\ \epsilon_{\mu\nu}(p,m) &= \epsilon_{\nu\mu}(p,m) && (11.14)\\ g^{\mu\nu}\epsilon_{\mu\nu}(p,m) &= 0, && (11.15) \end{aligned}$$

which follow directly from (11.11) and (11.1), reduce the number of independent elements to 5.

The spin-2 projection operator is defined as [46],

$$\begin{aligned} P^{(2)}_{\mu_1\mu_2\nu_1\nu_2}(p) &= \sum_m \epsilon_{\mu_1\mu_2}(p,m)\epsilon^*_{\nu_1\nu_2}(p,m) && (11.16)\\ &= \frac{1}{2}(\tilde{g}_{\mu_1\nu_1}\tilde{g}_{\mu_2\nu_2} + \tilde{g}_{\mu_1\nu_2}\tilde{g}_{\mu_2\nu_1}) - \frac{1}{3}\tilde{g}_{\mu_1\mu_2}\tilde{g}_{\nu_1\nu_2}, && (11.17) \end{aligned}$$

where $\tilde{g}_{\mu\nu}$ is defined in (11.5). When $P^{(2)}_{\mu_1\mu_2\nu_1\nu_2}(p)$ is contracted with an arbitrary 2nd rank tensor, the resulting tensor satisfies the spin-2 Rarita-Schwinger conditions (11.1.2). Therefore, it projects any 2nd rank tensor into the space spanned by the pure spin-2 states.

The technique used to build the spin-2 state can now be generalized to arbitrary integer spin-J. The spin-J state is described by a rank-J polarization tensor given by [46],

$$\epsilon_{\mu_1\mu_2\ldots\mu_J}(p,m) = \sum_{m_{J-1},m_1} ((J-1)m_{J-1}1m_1|Jm)\epsilon_{\mu_1\mu_2\ldots\mu_{J-1}}(p,m_{J-1})\epsilon_{\mu_J}(p,m_1). \qquad (11.18)$$

Therefore, using the spin-1 and spin-2 states, the spin-3 states can be built using (11.18). Then, the spin-1 and spin-3 states, along with (11.18), give the spin-4 states, and so on up to any spin-J.

The rotational properties of the spin-1 states (11.3) along with the properties of the D-functions can be used to show that, in the particle's rest frame, $\epsilon_{\mu_1\mu_2\ldots\mu_J}(p,m)$ does transform under spatial rotations as a spin-J state,

$$R^{\mu_1}{}_{\nu_1}\ldots R^{\mu_n}{}_{\nu_n}\epsilon^{\nu_1\ldots\ldots\nu_J}(p,m) \xrightarrow[rf]{} R_{i_1j_1}\ldots R_{i_Jj_J}\epsilon_{j_1\ldots j_J}(m) = \sum_{m'} D^{(J)}_{m'm}(R)\epsilon_{j_1\ldots j_J}(m'). \qquad (11.19)$$

The Rarita-Schwinger conditions for integer spin-J are,

$$\begin{aligned} p^{\mu_i}\epsilon_{\mu_1\mu_2\ldots\mu_i\ldots\mu_J}(p,m) &= 0 && (11.20)\\ \epsilon_{\mu_1\mu_2\ldots\mu_i\ldots\mu_j\ldots\mu_J}(p,m) &= \epsilon_{\mu_1\mu_2\ldots\mu_j\ldots\mu_i\ldots\mu_J}(p,m) && (11.21)\\ g^{\mu_i\mu_j}\epsilon_{\mu_1\mu_2\ldots\mu_i\ldots\mu_j\ldots\mu_J}(p,m) &= 0, && (11.22) \end{aligned}$$

for any μ_i, μ_j, and reduce the number of independent elements from 4^J to $(2J+1)$.

The spin-J projection operator can then be defined as,

$$P^{(J)}_{\mu_1\mu_2\ldots\mu_J\nu_1\nu_2\ldots\nu_J}(p) = \sum_m \epsilon_{\mu_1\mu_2\ldots\mu_J}(p,m)\epsilon^*_{\nu_1\nu_2\ldots\nu_J}(p,m), \qquad (11.23)$$

and simply projects out the piece of an arbitrary rank-J tensor that satisfies the Rarita-Schwinger conditions for spin-J, (11.1.2). Thus, it projects any rank-J tensor into the space spanned by the states of pure spin-J.

Similar techniques can be employed to build spin-J projection operators whose rank is not $2J$. These operators will be useful when writing N^* photoproduction amplitudes using the multipole formalism. Start by constructing a state with spin-J and rank r, $r-2 \leq J < r$,

$$\epsilon^J_{\mu_1\mu_2\ldots\mu_r}(p,m) = \sum_{m_{r-1},m_1} ((r-1)m_{r-1}1m_1|Jm)\epsilon_{\mu_1\mu_2\ldots\mu_{r-1}}(p,m_{r-1})\epsilon_{\mu_J}(p,m_1). \tag{11.24}$$

The projection operator is then formed as before,

$$P^{(J)}_{\mu_1\mu_2\ldots\mu_r\nu_1\nu_2\ldots\nu_r}(p) = \sum_m \epsilon^J_{\mu_1\mu_2\ldots\mu_r}(p,m)\epsilon^{J*}_{\nu_1\nu_2\ldots\nu_r}(p,m). \tag{11.25}$$

11.2 Half-Integral Spin Formalism

In this section, the polarization spinors for relativistic half-integer spin particles will be constructed. The 4-component spinor formalism of Dirac will be used for spin-1/2. The polarization tensors from the previous section will be coupled to the relativistic spin-1/2 spinors to form spinors of higher half-integer spin.

11.2.1 Spin-1/2 Dirac Spinors

The Dirac formalism uses a 4-component spinor, $u(p,m)$, to describe the polarization of a spin-1/2 particle. However, a spin-1/2 particle only has 2 independent elements ($m = \pm\frac{1}{2}$). The Dirac equation in momentum space is written as,

$$(\gamma^\mu p_\mu - w)u(p,m) = 0, \tag{11.26}$$

where the 4 x 4 matrices, γ^μ, satisfy,

$$\gamma^\mu\gamma^\nu + \gamma^\nu\gamma^\mu = 2g^{\mu\nu}, \tag{11.27}$$

reduces the number of independent components of $u(p,m)$ to 2. Choosing the following representation, in 2 x 2 block form, for the γ matrices,

$$\gamma^0 = \begin{pmatrix} 1 & 0 \\ 0 & -1 \end{pmatrix} \tag{11.28}$$

$$\gamma^i = \begin{pmatrix} 0 & \sigma_i \\ -\sigma_i & 0 \end{pmatrix}, \tag{11.29}$$

where σ_i are the Pauli matrices, the Dirac equation in the particle's rest frame is,

$$\begin{pmatrix} 0 & 0 \\ 0 & -2w \end{pmatrix} u(p_{rf},m) = 0. \tag{11.30}$$

Therefore, the lower 2 components of $u(p_{rf},m)$ are zero. Thus, the 4 component spinor takes the form,

$$u(p_{rf},m) = 2w \begin{pmatrix} \chi(m) \\ 0 \end{pmatrix}, \tag{11.31}$$

where,

$$\chi(+\frac{1}{2}) = \begin{pmatrix} 1 \\ 0 \end{pmatrix}, \quad \chi(-\frac{1}{2}) = \begin{pmatrix} 0 \\ 1 \end{pmatrix}, \tag{11.32}$$

are the non-relativistic 2-component spinors. Under spatial rotations in the rest frame, $u(p_{rf}, m)$ transforms as,

$$\Lambda_{\frac{1}{2}}(R)u(p,m) \xrightarrow[rf]{} 2wR_{ij}\chi_j(m) = 2w\sum_{m'} D^{(\frac{1}{2})}_{m'm}(R)\chi(m'). \tag{11.33}$$

To get the 4-component spinor in an arbitrary frame, simply boost it from the rest frame to yield [47],

$$u(p,m) = \Lambda_{\frac{1}{2}}(p)u(p_{rf},m) = \sqrt{E+w}\begin{pmatrix} \chi(m) \\ \frac{\vec{\sigma}\cdot\vec{p}}{E+w}\chi(m) \end{pmatrix}, \tag{11.34}$$

where $\Lambda_{\frac{1}{2}}(p)$ is the boost operator that takes a spin-1/2 particle from p_{rf} to p.

When writing out amplitudes, it is common to multiply 2 Dirac spinors together to form a Lorentz scalar. Define the following quantity,

$$\bar{u} \equiv u^\dagger\gamma^0, \tag{11.35}$$

which transforms as $\bar{u} \to \bar{u}\Lambda^{-1}_{\frac{1}{2}}$, then $\bar{u}u$ is a Lorentz scalar.

Now define the spin-1/2 projection operator to be,

$$P^{(\frac{1}{2})}(p) = \frac{1}{2w}\sum_m u(p,m)\bar{u}(p,m) = \frac{1}{2w}(\gamma^\mu p_\mu + w). \tag{11.36}$$

When $P^{(\frac{1}{2})}(p)$ operates on an arbitrary spinor, Π, it projects out the piece that is a solution to the Dirac equation with 4-momentum p,

$$(\gamma^\mu p_\mu - w)P^{(\frac{1}{2})}(p)\Pi = \frac{1}{2w}(p^2 - w^2)\Pi = 0. \tag{11.37}$$

Therefore, Π has been projected into the space spanned by $u(p,m)$ $(m = \pm\frac{1}{2})$.

Here one more important point must be introduced prior to moving on to higher half-integer spins. The γ matrices have the following property [47],

$$\Lambda^{-1}_{\frac{1}{2}}\gamma^\mu\Lambda_{\frac{1}{2}} = \Lambda^\mu{}_\nu\gamma^\nu. \tag{11.38}$$

So the combination $\bar{u}\gamma^\mu u$ transforms under Lorentz transformations as,

$$\bar{u}\gamma^\mu u \to \bar{u}\Lambda^{-1}_{\frac{1}{2}}\gamma^\mu\Lambda_{\frac{1}{2}}u = \Lambda^\mu{}_\nu\bar{u}\gamma^\nu u. \tag{11.39}$$

Therefore, $\bar{u}\gamma^\mu u$ transforms like a 4-vector. Thus, even though the μ-index on γ^μ isn't a true 4-vector index, it can be safely treated as one when contracting a γ matrix with any tensor. Using property (11.38), it's easy to derive the transformation properties of $\bar{u}\Gamma u$ found in Table (11.2.1), where an additional γ matrix is introduced, $\gamma^5 \equiv i\gamma^0\gamma^1\gamma^2\gamma^3$.

11.2.2 Spin-3/2 (and higher) Dirac Spinor-Tensors

With the polarization tensors constructed for any integer spin-n and spin-1/2 spinors, they can be coupled to build a spinor-tensor for any half-integer spin-J, where $J = n + 1/2$, according to [46],

$$u_{\mu_1\mu_2.....\mu_n}(p,m) = \sum_{m_n m_{\frac{1}{2}}} (nm_n\frac{1}{2}m_{\frac{1}{2}}|Jm)\epsilon_{\mu_1\mu_2.....\mu_n}(p,m_n)u(p,m_{\frac{1}{2}}), \tag{11.40}$$

where $\epsilon_{\mu_1\mu_2.....\mu_n}(p,m_n)$ is the spin-n polarization tensor defined in (11.18). The rotational transformation properties (11.33) and (11.19) along with the properties of the D-functions can be used to

Table 11.1: Transformation properties of $\bar{u}\Gamma u$.

Γ	Transforms As
1	scalar
γ^5	pseudo-scalar
γ^μ	vector
$\gamma^\mu\gamma^5$	pseudo-vector
$\gamma^\mu\gamma^\nu$	tensor

show that, in the particle's rest frame, $u_{\mu_1\mu_2.....\mu_n}(p,m)$ transforms as a spin-J state under spatial rotations,

$$R^{\mu_1}{}_{\nu_1}\dots R^{\mu_n}{}_{\nu_n}u^{\nu_1.....\nu_n}(p,m)\xrightarrow[rf]{}R_{i_1j_1}\dots R_{i_nj_n}u_{j_1\dots j_n}(m)=\sum_{m'}D^{(J)}_{m'm}(R)u_{j_1\dots j_n}(m'). \quad (11.41)$$

A general 4-component spinor of n-th rank tensors has 4^{n+1} independent elements, but a spin-J state only has $(2J+1)$. The Rarita-Schwinger conditions [45], which follow from (11.40), are,

$$\begin{aligned}
(\gamma^\mu p_\mu - w)u_{\mu_1\mu_2.....\mu_n}(p,m) &= 0 && (11.42)\\
u_{\mu_1\mu_2\dots\mu_i\dots\mu_j\dots\mu_n}(p,m) &= u_{\mu_1\mu_2\dots\mu_j\dots\mu_i\dots\mu_n}(p,m) && (11.43)\\
p^{\mu_i}u_{\mu_1\mu_2\dots\mu_i\dots\mu_n}(p,m) &= 0 && (11.44)\\
\gamma^{\mu_i}u_{\mu_1\mu_2\dots\mu_i\dots\mu_n}(p,m) &= 0 && (11.45)\\
g^{\mu_i\mu_j}u_{\mu_1\mu_2\dots\mu_i\dots\mu_j\dots\mu_n}(p,m) &= 0, && (11.46)
\end{aligned}$$

and reduce the number of independent elements to $(2J+1)$. Of the 5 Rarita-Schwinger conditions, all but (11.2.2d) follow directly from the properties of $\epsilon_{\mu_1\mu_2.....\mu_n}(p,m_n)$ and $u(p,m_{\frac{1}{2}})$. Property (11.2.2d) can be understood by considering the Dirac equation of the spinor $\gamma^5\gamma^{\mu_i}v_{\mu_1\mu_2\dots\mu_i\dots\mu_n}(p,m)$, where,

$$v_{\mu_1\mu_2\dots\mu_i\dots\mu_n}=\epsilon_{\mu_1\mu_2.....\mu_n}\otimes u. \quad (11.47)$$

Clearly v satisfies all of the Rarita-Schwinger conditions except (11.2.2d). It then follows that,

$$\begin{aligned}
(\gamma^\nu p_\nu - w)\gamma^5\gamma^{\mu_i}v_{\mu_1\mu_2\dots\mu_i\dots\mu_n}(p,m) &= \gamma^5(\gamma^{\mu_i}(\gamma^\nu p_\nu - w) - 2p^{\mu_i})v_{\mu_1\mu_2\dots\mu_i\dots\mu_n}(p,m) && (11.48)\\
&= \gamma^5\gamma^{\mu_i}(\gamma^\nu p_\nu - w)v_{\mu_1\mu_2\dots\mu_i\dots\mu_n}(p,m) && (11.49)\\
&= 0. && (11.50)
\end{aligned}$$

Therefore, $\gamma^5\gamma^{\mu_i}v_{\mu_1\mu_2\dots\mu_i\dots\mu_n}(p,m)$ satisfies the Rarita-Schwinger conditions (except (11.2.2d)) for a spin-$(J-1)$ state (since v was built from a tensor product of a spin-n and spin-1/2 state, it has both spin-$(n+1/2)$ and spin-$(n-1/2)$ components). So (11.2.2d) must hold for a state of pure spin-J, which we've insured through the use of the Clebsch-Gordon coefficients in (11.40).

The spin-$J=n+1/2$ projection operator can be written as,

$$P^{(J)}_{\mu_1\mu_2\dots\mu_n\nu_1\nu_2\dots\nu_n}(p)=\frac{1}{2w}\sum_m u_{\mu_1\mu_2.....\mu_n}(p,m)\bar{u}_{\nu_1\nu_2.....\nu_n}(p,m) \quad (11.51)$$

When $P^{(J)}_{\mu_1\mu_2\dots\mu_n\nu_1\nu_2\dots\nu_n}(p)$ operates on an arbitrary 4-component spinor of rank-n tensors, it projects out the piece that satisfies the Rarita-Schwinger conditions (11.2.2) for spin-J Thus, it projects any

4-component spinor of rank-n tensors into the space spanned by the states of pure spin-J.

As an example, the spin-3/2 projection operator is [46],

$$P^{(\frac{3}{2})}_{\mu\nu}(P) = P^{(\frac{1}{2})}(P)(\left(\tilde{g}_{\mu\nu} - \frac{1}{3}\tilde{g}_{\mu\alpha}\gamma^{\alpha}\tilde{g}_{\nu\beta}\gamma^{\beta}\right). \tag{11.52}$$

Notice that the 2nd term in (11.52) enforces (11.2.2d). If follows directly from the arguments above concerning this Rarita-Schwinger condition that the spin-1/2 projection operator in rank-2 space is,

$$P^{(\frac{1}{2})}_{\mu\nu}(P) = P^{(\frac{1}{2})}(P)\frac{1}{3}\tilde{g}_{\mu\alpha}\gamma^{\alpha}\tilde{g}_{\nu\beta}\gamma^{\beta}. \tag{11.53}$$

Both (11.52) and (11.53) will be used heavily in all of the s-channel amplitudes for this analysis.

11.3 Orbital Angular Momentum Tensors

Now, two particles will be coupled to a state of pure orbital angular momentum ℓ. Let the momenta of the 2 particles be p_a and p_b, then define $P = p_a + p_b$ and $p_{ab} = \frac{1}{2}(p_a - p_b)$ to be the total and relative momentum respectively. A state of pure orbital angular momentum can be constructed out of the measured momenta using the integer spin projection operators $P^{(\ell)}_{\mu_1\mu_2\ldots\mu_\ell\nu_1\nu_2\ldots\nu_\ell}(P)$, defined in equation (11.23). This is done by building a rank-ℓ tensor out of the relative momentum, $p^{\nu_1}_{ab}p^{\nu_2}_{ab}\ldots p^{\nu_\ell}_{ab}$, then projecting it to a state of pure spin-ℓ which yields,

$$L^{(\ell)}_{\mu_1\mu_2\ldots\mu_\ell}(p_{ab}) = (-)^{\ell}P^{(\ell)}_{\mu_1\mu_2\ldots\mu_\ell\nu_1\nu_2\ldots\nu_\ell}(P)p^{\nu_1}_{ab}p^{\nu_2}_{ab}\ldots p^{\nu_\ell}_{ab}. \tag{11.54}$$

The properties of the integer spin projection operators guarantee that the states $L^{(\ell)}_{\mu_1\mu_2\ldots\mu_\ell}(p_{ab})$ satisfy the Rarita-Schwinger conditions,

$$P^{\mu_i}L^{(\ell)}_{\mu_1\mu_2\ldots\mu_i\ldots\mu_\ell}(p_{ab}) = 0 \tag{11.55}$$

$$L^{(\ell)}_{\mu_1\mu_2\ldots\mu_i\ldots\mu_j\ldots\mu_\ell}(p_{ab}) = L^{(\ell)}_{\mu_1\mu_2\ldots\mu_j\ldots\mu_i\ldots\mu_\ell}(p_{ab}) \tag{11.56}$$

$$g^{\mu_i\mu_j}L^{(\ell)}_{\mu_1\mu_2\ldots\mu_i\ldots\mu_j\ldots\mu_\ell}(p_{ab}) = 0, \tag{11.57}$$

for any μ_i, μ_j, which insures that they have $(2\ell+1)$ independent elements.

The states of pure orbital angular momentum for $\ell = 0, 1, 2, 3$ are [48],

$$L^{(0)}(p_{ab}) = 1 \tag{11.58}$$

$$L^{(1)}_{\mu}(p_{ab}) = \tilde{p}^{ab}_{\mu} \tag{11.59}$$

$$L^{(2)}_{\mu_1\mu_2}(p_{ab}) = \tilde{p}^{ab}_{\mu_1}\tilde{p}^{ab}_{\mu_2} - \frac{1}{3}\tilde{p}^2_{ab}\tilde{g}_{\mu_1\mu_2} \tag{11.60}$$

$$L^{(3)}_{\mu_1\mu_2\mu_3}(p_{ab}) = \tilde{p}^{ab}_{\mu_1}\tilde{p}^{ab}_{\mu_2}\tilde{p}^{ab}_{\mu_3} - \frac{1}{5}\tilde{p}^2_{ab}(\tilde{g}_{\mu_1\mu_2}\tilde{p}^{ab}_{\mu_3} + \tilde{g}_{\mu_1\mu_3}\tilde{p}^{ab}_{\mu_2} + \tilde{g}_{\mu_2\mu_3}\tilde{p}^{ab}_{\mu_1}), \tag{11.61}$$

where $\tilde{g}_{\mu_1\mu_2} = g_{\mu_1\mu_2} - \frac{P_{\mu_1}P_{\mu_2}}{P^2}$ and $\tilde{p}^{ab}_{\mu} = \tilde{g}_{\mu\nu}p^{\nu}_{ab}$.

In the previous sections, demonstration of the rotational properties of the spin-J states were the same as in *traditional* non-relativistic quantum mechanics. A similar connection can be made in this case. Consider the inner product of the $\ell = 2$ orbital tensor with a state of pure $m = 2$ in the rest frame of the system,

$$\begin{aligned} L^{(2)}_{\mu\nu}(p_{ab})\epsilon^{\mu\nu}(P,+2) &\xrightarrow[rf]{} (\vec{p}_{ab}\cdot\vec{\epsilon}(+))(\vec{p}_{ab}\cdot\vec{\epsilon}(+)) - \frac{1}{3}|\vec{p}_{ab}|^2(\vec{\epsilon}(+)\cdot\vec{\epsilon}(+)) \\ &= (p\sin(\theta)e^{i\phi})^2 \propto p^2Y^2_2(\theta,\phi). \end{aligned} \tag{11.62}$$

Thus, the non-relativistic quantum mechanics solution, within a reasonable energy scale, is again preserved in the rest frame of the system.

11.4 $\eta \to \pi^+\pi^-\pi^0$ Amplitude

The amplitude for $\eta \to \pi^+\pi^-\pi^0$ must be constructed. The η is an iso-scalar, while the three π's are iso-vectors. There is only one way to form an iso-scalar from three iso-vectors that conserves isospin, $(\vec{I}_{\pi^+} \times \vec{I}_{\pi^-}) \cdot \vec{I}_{\pi^0}$. With the convention $\vec{I}_{\pi^+} = -\frac{1}{\sqrt{2}}(1, i, 0)$, $\vec{I}_{\pi^-} = \frac{1}{\sqrt{2}}(1, -i, 0)$ and $\vec{I}_{\pi^0} = (0, 0, 1)$ gives,

$$(\vec{I}_{\pi^+} \times \vec{I}_{\pi^-}) \cdot \vec{I}_{\pi^0} = i, \tag{11.63}$$

thus, isospin conservation contributes an overall phase factor to the amplitude. If we now consider just spin and parity, the decay can be written as $\eta(0^-) \to \pi^+(0^-)\pi^-(0^-)\pi^0(0^-)$. The 3π system has negative intrinsic parity and spin-0. Therefore, the angular dependent piece describing the 3π system must have $\ell = 0$ and positive parity. The amplitude can then be written as,

$$A_{\eta\to\pi^+\pi^-\pi^0} = N\left((\vec{I}_{\pi^+} \times \vec{I}_{\pi^0}) \cdot \vec{I}_{\pi^-}\right) \epsilon_{\mu\nu\alpha\beta} p^{\nu}_{\pi^+} p^{\alpha}_{\pi^-} p^{\beta}_{\pi^0} \epsilon^{\mu}(q, m_\eta), \tag{11.64}$$

which is totally symmetric in the 3 π's. N is a normalization factor defined as following,

$$\int |A_{\eta\to\pi^+\pi^-\pi^0}|^2 d\Phi_{3\pi} = 1. \tag{11.65}$$

The mean path of the η prior to its decay is $\approx 150pm$. For the CLAS detector to track the decay π^+ and π^-, required for the events used in this analysis, the η must decay prior to traveling $\approx 1m$. Thus, η's produced in this experiment, all decay within the detector. The normalization condition (11.65) enforces this condition at the amplitude level.

The quantity $\epsilon_{\mu\nu\alpha\beta} p^{\nu}_{\pi^+} p^{\alpha}_{\pi^-} p^{\beta}_{\pi^0}$ can be rewritten as $\epsilon_{\mu\nu\alpha\beta} p^{\nu}_{\pi^+} p^{\alpha}_{\pi^-} q^{\beta}$ using conservation of 4-momentum. In the η rest frame, (11.64) simplifies to,

$$\begin{aligned} A_{\eta\to\pi^+\pi^-\pi^0} &= iN\epsilon_{\mu\nu\alpha 0} p^{\nu}_{\pi^+} p^{\alpha}_{\pi^-} w_\omega \epsilon^{\mu}(q, m_\omega) && (11.66)\\ &= iN w_\eta \epsilon^{i}(q, m_\eta) \epsilon_{ijk} p^{j}_{\pi^+} p^{k}_{\pi^-} && (11.67)\\ &= iN w_\eta \, (\vec{p}_{\pi^+} \times \vec{p}_{\pi^-}) \cdot \vec{\epsilon}(q, m_\eta), && (11.68) \end{aligned}$$

where w_η is the mass of the η. In subsequent sections amplitudes will be constructed for different processes which go from a γp initial state to the ηp final state. The amplitudes, aside from the masses of the particles involved, are of the same construction for the $\eta' p$ final state.

11.4.1 $J^P \to p\eta$

Consider a baryon with spin-parity J^P, 4-momentum P and spin projection M decaying to $p\eta$. Since the η is an iso-scalar, $p\eta$ only couples to J^P states with $I = \frac{1}{2}$. Thus, J^P must be an N^* state and isospin will only contribute a factor of 1 at this vertex. The work presented in this section loosely follows that of Anisovich [8].

J^P States with $P = (-)^{J-\frac{1}{2}}$ $\left(\frac{1}{2}^+, \frac{3}{2}^-, \frac{5}{2}^+ \ldots\right)$

First, consider $J^P = \frac{1}{2}^+$ which decays to $p\eta$ in P-wave only. The $p\eta$ system can be coupled to either $s = \frac{1}{2}$ or $s = \frac{3}{2}$. Therefore, there are 2 independent amplitudes for the decay of $J^P = \frac{1}{2}^+ \to p\eta$ which can be written as,

$$A^{\ell=1, s=\frac{1}{2}, \frac{3}{2}}_{\frac{1}{2}^+\to p\eta} = \bar{u}(p_p, m_p) \epsilon^{*\mu}(p_\eta, m_\eta) P^{(s)}_{\mu\nu}(P) L^{(1)\nu}(p_{p\eta}) u(P, M). \tag{11.69}$$

Generalizing (11.69) to construct the amplitudes for $J = \ell - \frac{1}{2}$ states,

$$A^{\ell=J+\frac{1}{2},s=\frac{1}{2},\frac{3}{2}}_{J^P\to p\eta} = \bar{u}(p_p,m_p)\epsilon^{*\mu}(p_\eta,m_\eta)P^{(s)}_{\mu\nu}(P)L^{(\ell)\nu\mu_1\mu_2\ldots\mu_{\ell-1}}(p_{p\eta})u_{\mu_1\mu_2\ldots\mu_{\ell-1}}(P,M). \quad (11.70)$$

Therefore, (11.70) can be used to obtain amplitudes for $\frac{1}{2}^+ \to p\eta$ in P-wave, $\frac{3}{2}^- \to p\eta$ in D-wave, $\frac{5}{2}^+ \to p\eta$ in F-wave, etc.

To build the remaining amplitudes for these states, first consider $\frac{3}{2}^- \to p\eta$ in S-wave. The $p\eta$ system must couple to $s = \frac{3}{2}$, so there's only 1 amplitude which can be written as,

$$A^{\ell=0,s=\frac{3}{2}}_{\frac{3}{2}^-\to p\eta} = \bar{u}(p_p,m_p)\epsilon^{*\mu}(p_\eta,m_\eta)u_\mu(P,M), \quad (11.71)$$

which can be generalized for $J = \ell + \frac{3}{2}$ states to,

$$A^{\ell=J-\frac{3}{2},s=\frac{3}{2}}_{J^P\to p\eta} = \bar{u}(p_p,m_p)\epsilon^*_\nu(p_\eta,m_\eta)L^{(\ell)}_{\mu_1\mu_2\ldots\mu_\ell}u^{\nu\mu_1\mu_2\ldots\mu_\ell}(P,M). \quad (11.72)$$

Therefore, (11.72) can be used to obtain amplitudes for $\frac{3}{2}^- \to p\eta$ in S-wave, $\frac{5}{2}^+ \to p\eta$ in P-wave, $\frac{7}{2}^- \to p\eta$ in D-wave, etc. Thus, (11.70) and (11.72) together yield all of the $J^P \to p\eta$ amplitudes for the $P = (-)^{J-\frac{1}{2}}$ states.

J^P States with $P = (-)^{J+\frac{1}{2}}$ $\left(\frac{1}{2}^-, \frac{3}{2}^+, \frac{5}{2}^- \ldots\right)$

For the remaining J^P states, consider $\frac{1}{2}^- \to p\eta$ which can proceed in either S-wave (with $s = \frac{1}{2}$) or D-wave (with $s = \frac{3}{2}$). Therefore, there are two amplitudes for this process which can be written as,

$$A^{\ell=0,s=\frac{1}{2}}_{\frac{1}{2}^-\to p\eta} = \bar{u}(p_p,m_p)\epsilon^*_\mu(p_\eta,m_\eta)\gamma^\mu\gamma^5 u(P,M) \quad (11.73)$$

$$A^{\ell=2,s=\frac{3}{2}}_{\frac{1}{2}^-\to p\eta} = \bar{u}(p_p,m_p)\epsilon^*_\mu(p_\eta,m_\eta)L^{(2)\mu\nu}(p_{p\eta})\gamma_\nu\gamma^5 u(P,M), \quad (11.74)$$

where γ^5 has to be added to conserve parity.

Next consider $\frac{3}{2}^+ \to p\eta$ where the $p\eta$ system can be in either P-wave (with $s = \frac{3}{2}$ or $s = \frac{1}{2}$) or F-wave (with $s = \frac{3}{2}$). The amplitudes for the P-wave decay can be written as,

$$A^{\ell=1,s=\frac{1}{2}}_{\frac{3}{2}^+\to p\eta} = \bar{u}(p_p,m_p)\epsilon^{*\mu}(p_\eta,m_\eta)P^{(s)}_{\mu\nu}(P)\gamma^\nu\gamma^5 L^{(1)}_\alpha u^\alpha(P,M) \quad (11.75)$$

$$A^{\ell=1,s=\frac{3}{2}}_{\frac{3}{2}^+\to p\eta} = \bar{u}(p_p,m_p)\epsilon^{*\mu}(p_\eta,m_\eta)P^{(s)}_{\mu\nu}(P)\gamma^\alpha\gamma^5 L^{(1)}_\alpha u^\nu(P,M) \quad (11.76)$$

which can be generalized for $J = \ell + \frac{1}{2}$ to,

$$A^{\ell=J-\frac{1}{2},s=\frac{1}{2}}_{J^P\to p\eta} = \bar{u}(p_p,m_p)\epsilon^{*\mu}(p_\eta,m_\eta)P^{(s)}_{\mu\nu}(P)\gamma^\nu\gamma^5 L^{(\ell)\alpha_1\alpha_2\ldots\alpha_\ell}(p_{p\eta})u_{\alpha_1\alpha_2\ldots\alpha_\ell}(P) \quad (11.77)$$

$$A^{\ell=J-\frac{1}{2},s=\frac{3}{2}}_{J^P\to p\eta} = \bar{u}(p_p,m_p)\epsilon^*_\mu(p_\eta,m_\eta)P^{(s)\mu\nu}(P)\gamma_{\alpha_1}\gamma^5 L^{(\ell)\alpha_1\alpha_2\ldots\alpha_\ell}(p_{p\eta})u_{\nu\alpha_2\ldots\alpha_\ell}(P) \quad (11.78)$$

The F-wave decay of the $\frac{3}{2}^+$ to $p\eta$ has amplitude,

$$A^{\ell=3,s=\frac{3}{2}}_{\frac{3}{2}^+\to p\eta} = \bar{u}(p_p,m_p)\epsilon^{*\nu}(p_\eta,m_\eta)L^{(3)}_{\mu\nu\alpha}(p_{p\eta})\gamma^\alpha\gamma^5 u^\mu(P,M), \quad (11.79)$$

which can be generalized for $J = \ell - \frac{3}{2}$ to,

$$A^{\ell=J+\frac{3}{2},s=\frac{3}{2}}_{J^P\to p\eta} = \bar{u}(p_p,m_p)\epsilon^{*\mu_1}(p_\eta,m_\eta)L^{(\ell)}_{\mu_1\mu_2\ldots\mu_\ell}(p_{p\eta})\gamma^{\mu_2}\gamma^5 u^{\mu_3\ldots\mu_\ell}(P,M). \quad (11.80)$$

Therefore, (11.77) and (11.80) can be used to obtain all of the $J^P \to p\eta$ amplitudes for the $P = (-)^{J+\frac{1}{2}}$ states.

11.4.2 $\gamma p \to J^P$ Amplitudes

In this section, amplitude construction for photoproduction of a baryon with spin-parity J^P off of a proton target. In the previous sections, amplitudes were constructed in terms of specific $L-S$ states. However, the presence of a real photon in these amplitudes makes $L-S$ states not the best choice. To illustrate this, consider $\gamma p \to \frac{1}{2}^-$. To conserve parity and angular momentum, the γp system must be in either $\ell = 0$ or 2. This leads to two Lorentz invariant amplitudes, which can be written as,

$$A^{\ell=0}_{\gamma p \to \frac{1}{2}^-} = \bar{u}(P,M)\gamma^\mu\gamma^5 u(p_p,m_p)\epsilon_\mu(p_\gamma,m_\gamma) \tag{11.81}$$

$$A^{\ell=2}_{\gamma p \to \frac{1}{2}^-} = \bar{u}(P,M)L^{(2)}_{\mu\nu}(p_{p\gamma})\gamma^\mu\gamma^5 u(p_p,m_p)\epsilon^\nu(p_\gamma,m_\gamma), \tag{11.82}$$

which are both Dirac scalars, Lorentz scalars and conserve parity. Notice that $A^{\ell=2}_{\gamma p \to \frac{1}{2}^-}$ can be reduced to,

$$\begin{aligned}
\bar{u}L^{(2)}_{\mu\nu}(p_{p\gamma})\gamma^\mu\gamma^5 u\epsilon^\nu &= \bar{u}(\tilde{p}^{p\gamma}_\mu \tilde{p}^{p\gamma}_\nu - \frac{1}{3}\tilde{p}^2_{p\gamma}\tilde{g}_{\mu\nu})\gamma^\mu\gamma^5 u\epsilon^\nu && (11.83)\\
&= \bar{u}(-\frac{1}{3}\tilde{p}^2_{p\gamma}\epsilon_\mu)\gamma^\mu\gamma^5 u && (11.84)\\
&= -\frac{1}{3}\tilde{p}^2_{p\gamma}A^0_{\gamma p \to \frac{1}{2}^-}, && (11.85)
\end{aligned}$$

using $\tilde{p}^\mu_{p\gamma}\epsilon_\mu = 0$ and $\tilde{g}_{\mu\nu}\epsilon^\nu = \epsilon_\mu$ for a real photon. Since the analysis bins in $W(\sqrt{s})$, there is no way to distinguish between $A^{\ell=0}_{\gamma p \to \frac{1}{2}^-}$ and $A^{\ell=2}_{\gamma p \to \frac{1}{2}^-}$. So, instead of writing the $\gamma p \to J^P$ amplitudes in terms of $L-S$ states, multipoles will be used where the number of ways of coupling the states matches the number of angularly independent amplitudes.

In the multipole representation, the spin of the photon is coupled to the orbital angular momentum of the γp system ℓ, to form a state of definite spin-parity j^p. This j^p state is then coupled to the proton to form a state of definite total J^P. The real photon only has $m_\gamma = \pm 1$ states and ℓ only contributes from its $m_\ell = 0$ state (in the J^P rest frame, where ℓ is defined, the quantization axis is chosen to be $\hat{p}_\gamma$, since the physical states of γ are helicity states, therefore $\ell_z = 0$), thus, $m_j = \pm 1$ and $j \neq 0$. Two classes of multipoles are defined, electric states are those with $p = (-)^j$, while magnetic states have $p = (-)^{j+1}$. Thus, the states $1^-, 2^+, \ldots$ are given the designation $E1, E2, \ldots$ and the states $1^+, 2^-, \ldots$ are called $M1, M2, \ldots$ (there are no 0 states).

J^P States with $P = (-)^{J+\frac{1}{2}}$ $\left(\frac{1}{2}^-, \frac{3}{2}^+, \frac{5}{2}^- \ldots\right)$

Returning to $\gamma p \to \frac{1}{2}^-$ where $\ell = 0$ or 2. The photon can be coupled to $\ell = 0$ to get $j^p = 1^-$ and to $\ell = 2$ to get $1^-, 2^-, 3^-$. But only the 1^- state can then be coupled to the proton to get $J^P = \frac{1}{2}^-$. Thus, $J^P = \frac{1}{2}^-$ only couples to the $E1$ multipole with amplitude,

$$A^{mp=1^-}_{\gamma p \to \frac{1}{2}^-} = \bar{u}(P,M)\gamma^\mu\gamma^5 u(p_p,m_p)\left(P^{(1)}_{\mu\nu}(P)\epsilon^\nu(p_\gamma,m_\gamma)\right), \tag{11.86}$$

which reduces to,

$$A^{mp=1^-}_{\gamma p \to \frac{1}{2}^-} = \bar{u}(P,M)\gamma^\mu\gamma^5 u(p_p,m_p)\epsilon_\mu(p_\gamma,m_\gamma). \tag{11.87}$$

Moving on to $A_{\gamma p \to \frac{3}{2}^+}$. The reaction $\gamma p \to \frac{3}{2}^+$ can proceed with the γp system in P-wave or F-wave. The photon couples to $\ell = 1$ giving $j^p = 1^+, 2^+$ and to $\ell = 3$ giving $j^p = 2^+, 3^+, 4^+$,

however, only the 1^+ and 2^+ states can couple with the proton to get $J^P = \frac{3}{2}^+$. Thus, $J^P = \frac{3}{2}^+$ couples to the $E2$ and $M1$ multipoles, which can both be built with $\ell = 1$ according to,,

$$A^{mp=j^+}_{\gamma p \to \frac{3}{2}^+} = \bar{u}^\mu(P,M)\gamma^\nu\gamma^5 P^{(j)}_{\mu\nu\alpha\beta}(P)L^{(1)\alpha}(p_{p\gamma})\epsilon^\beta(p_\gamma,m_\gamma)u(p_p,m_p), \tag{11.88}$$

where $j = 1,2$. This can then be generalized for any of the $P = (-)^{J+\frac{1}{2}}$ states ($J > \frac{1}{2}$). Each J^P will couple to 2 multipoles (1 electric and 1 magnetic) with the following amplitudes,

$$A^{mp=j^p}_{\gamma p \to J^P} = \bar{u}^{\mu_1\mu_2\ldots\mu_\ell}(P,M)\gamma^\nu\gamma^5 P^{(j)}_{\mu_1\mu_2\ldots\mu_\ell\nu\alpha_1\alpha_2\ldots\alpha_\ell\beta}(P)L^{(\ell)\alpha_1\alpha_2\ldots\alpha_\ell}(p_{p\gamma})\epsilon^\beta(p_\gamma,m_\gamma)u(p_p,m_p), \tag{11.89}$$

where $j = J - \frac{1}{2}, J + \frac{1}{2}$,$p = (-)^{J+\frac{1}{2}}$ and $\ell = J - \frac{1}{2}$.

J^P States with $P = (-)^{J-\frac{1}{2}}$ $\left(\frac{1}{2}^+, \frac{3}{2}^-, \frac{5}{2}^+ \ldots\right)$

Now for the multipole amplitudes for the photoproduction of the states with $P = (-)^{J-\frac{1}{2}}$. Starting with $\gamma p \to \frac{1}{2}^+$ where $\ell = 1$ is the only possibility. The photon couples to $\ell = 1$ giving $j^p = 1^+, 2^+$ but only the 1^+ state can couple with the proton to $J^P = \frac{1}{2}^+$, thus only the $M1$ multipole will contribute. This amplitude can be written as,

$$A^{mp=1^+}_{\gamma p \to \frac{1}{2}^+} = \bar{u}(P,M)\gamma^\alpha L^{(1)}_\alpha(p_{p\gamma})\gamma^\mu\epsilon_\mu(p_\gamma,m_\gamma)u(p_p,m_p). \tag{11.90}$$

Examine the reaction $\gamma p \to \frac{3}{2}^-$ which can proceed with γp in S-wave or D-wave. The photon couples to $\ell = 0$ giving $j^p = 1^-$ and to $\ell = 2$ giving $j^p = 1^-, 2^-, 3^-$, however, only the 1^- and 2^- states couple with the proton to give $J^P = \frac{3}{2}^-$. Thus, $J^P = \frac{3}{2}^-$ couples to the $M2$ and $E1$ multipoles with amplitudes,

$$A^{mp=j^-}_{\gamma p \to \frac{3}{2}^-} = \bar{u}^\mu(P,M)\gamma^\nu\gamma^\alpha P^{(j)}_{\mu\nu\alpha\mu'\nu'\alpha'}(P)L^{(2)\mu'\nu'}(p_{p\gamma})\epsilon^{\alpha'}(p_\gamma,m_\gamma)u(p_p,m_p), \tag{11.91}$$

where $j = 1,2$. Generalizing this for all $P = (-)^{J-\frac{1}{2}}$ states ($J > \frac{1}{2}$) as,

$$A^{mp=j^p}_{\gamma p \to J^P} = \bar{u}^{\mu_1\mu_2\ldots\mu_{\ell-1}}(P,M)\gamma^{\mu_\ell}\gamma^{\mu_{\ell+1}}P^{(j)}_{\mu_1\mu_2\ldots\mu_{\ell+1}\nu_1\nu_2\ldots\nu_{\ell+1}}(P)L^{(\ell)\nu_1\nu_2\ldots\nu_\ell}(p_{p\gamma})\epsilon^{\nu_{\ell+1}}(p_\gamma,m_\gamma)u(p_p,m_p), \tag{11.92}$$

where $j = J - \frac{1}{2}, J + \frac{1}{2}$,$p = (-)^{J-\frac{1}{2}}$ and $\ell = J + \frac{1}{2}$.

11.4.3 $\gamma p \to J^P \to p\eta$ Amplitudes

With amplitudes written for $\gamma p \to J^P$ and $J^P \to p\eta$, they must be combined to construct $A_{\gamma p \to J^P \to p\eta}$. First define generic versions of the N^* amplitudes defined in the previous 2 sections,

$$A_{\gamma p \to J^P} \equiv \bar{u}_{\mu_1\mu_2\ldots\mu_{J-\frac{1}{2}}}(P,M)X^{\nu\mu_1\mu_2\ldots\mu_{J-\frac{1}{2}}}_{PROD}\epsilon_\nu(p_\gamma,m_\gamma)u(p_{p_i},m_{p_i}) \tag{11.93}$$

$$A_{J^P \to p\eta} \equiv \bar{u}(p_{p_f},m_{p_f})\epsilon^*_\nu(p_\eta,m_\eta)X^{\nu\mu_1\mu_2\ldots\mu_{J-\frac{1}{2}}}_{DECAY}u_{\mu_1\mu_2\ldots\mu_{J-\frac{1}{2}}}(P,M), \tag{11.94}$$

where X_{PROD}, X_{DECAY} depend on the initial and final state quantum numbers respectively. Since the N^* state is an intermediate particle (we can not observe it), its spin projections must be summed over coherently,

$$\begin{aligned} A_{\gamma p \to J^P \to p\eta} = \sum_M \bar{u}(p_{p_f},m_{p_f})\epsilon^*_\alpha(p_\eta,m_\eta)X^{\alpha\mu_1\mu_2\ldots\mu_{J-\frac{1}{2}}}_{DECAY}u_{\mu_1\mu_2\ldots\mu_{J-\frac{1}{2}}}(P,M)\bar{u}_{\nu_1\nu_2\ldots\nu_{J-\frac{1}{2}}}(P,M) \\ \times X^{\beta\nu_1\nu_2\ldots\nu_{J-\frac{1}{2}}}_{PROD}\epsilon_\beta(p_\gamma,m_\gamma)u(p_{p_i},m_{p_i}) \end{aligned} \tag{11.95}$$

which can be written using (11.51) as,

$$A_{\gamma p\to J^P\to p\eta} = \bar{u}(p_{p_f},m_{p_f})\epsilon^*_\alpha(p_\eta,m_\eta)X_{DECAY}^{\alpha\mu_1\mu_2\ldots\mu_{J-\frac{1}{2}}}P^{(J)}_{\mu_1\mu_2\ldots\mu_{J-\frac{1}{2}}\nu_1\nu_2\ldots\nu_{J-\frac{1}{2}}}(P) \times X_{PROD}^{\beta\nu_1\nu_2\ldots\nu_{J-\frac{1}{2}}}\epsilon_\beta(p_\gamma,m_\gamma)u(p_{p_i},m_{p_i}). \quad (11.96)$$

This is the prescription followed to combine all $\gamma p \to J^P$ amplitudes with $J^P \to p\eta$ amplitudes when constructing $\gamma p \to J^P \to p\eta$ amplitudes.

Chapter 12

Appendix D

This appendix provides the values of the measured differential cross sections for the η analysis.

Table 12.1: η Differential Cross Section Results

W bin (MeV)	$\cos(\theta_{CM})$	$\cos(\theta_{CM})$ Error	$d\sigma/d\Omega$ μb	$d\sigma/d\Omega$ Error
1580→1590	-0.83	0.03	1.433	0.187
1580→1590	-0.75	0.05	1.281	0.146
1580→1590	-0.65	0.05	1.190	0.132
1580→1590	-0.55	0.05	1.168	0.129
1580→1590	-0.45	0.05	1.074	0.117
1580→1590	-0.34	0.05	1.085	0.118
1580→1590	-0.24	0.05	1.052	0.114
1580→1590	-0.15	0.05	1.002	0.109
1580→1590	-0.05	0.05	1.059	0.114
1580→1590	0.04	0.05	0.980	0.106
1580→1590	0.15	0.05	1.040	0.113
1580→1590	0.25	0.05	1.037	0.112
1580→1590	0.34	0.05	1.169	0.128
1580→1590	0.44	0.05	1.098	0.122
1580→1590	0.54	0.05	1.111	0.126
1580→1590	0.62	0.03	1.035	0.341
1590→1600	-0.83	0.04	0.858	0.134
1590→1600	-0.74	0.05	1.122	0.124
1590→1600	-0.65	0.05	1.089	0.119
1590→1600	-0.55	0.05	1.026	0.111
1590→1600	-0.44	0.05	0.979	0.105
1590→1600	-0.35	0.05	0.913	0.098
1590→1600	-0.24	0.05	0.977	0.104
1590→1600	-0.14	0.05	0.927	0.099
1590→1600	-0.05	0.05	0.917	0.098
1590→1600	0.04	0.05	0.889	0.095
1590→1600	0.14	0.05	0.857	0.092
1590→1600	0.25	0.05	0.935	0.100
1590→1600	0.34	0.05	1.013	0.109
1590→1600	0.44	0.05	0.963	0.105
1590→1600	0.54	0.05	0.728	0.080
1590→1600	0.62	0.04	0.292	0.115
1600→1610	-0.83	0.04	0.947	0.130
1600→1610	-0.74	0.05	1.007	0.113
1600→1610	-0.65	0.05	1.026	0.113
1600→1610	-0.55	0.05	0.982	0.107
1600→1610	-0.45	0.05	0.885	0.096
1600→1610	-0.34	0.05	0.883	0.095
1600→1610	-0.25	0.05	0.856	0.092
1600→1610	-0.15	0.05	0.917	0.099

Table 12.2: η Differential Cross Section Results

W bin (MeV)	$\cos(\theta_{CM})$	$\cos(\theta_{CM})$ Error	$d\sigma/d\Omega$ μb	$d\sigma/d\Omega$ Error
1600→1610	-0.04	0.05	0.863	0.092
1600→1610	0.05	0.05	0.849	0.091
1600→1610	0.14	0.05	0.755	0.081
1600→1610	0.25	0.05	0.805	0.086
1600→1610	0.34	0.05	0.899	0.098
1600→1610	0.45	0.05	0.784	0.086
1600→1610	0.54	0.05	0.675	0.075
1600→1610	0.63	0.05	0.424	0.558
1610→1620	-0.83	0.04	0.862	0.111
1610→1620	-0.74	0.05	0.921	0.103
1610→1620	-0.65	0.05	0.981	0.108
1610→1620	-0.55	0.05	0.916	0.100
1610→1620	-0.44	0.05	0.853	0.092
1610→1620	-0.35	0.05	0.788	0.085
1610→1620	-0.24	0.05	0.761	0.082
1610→1620	-0.15	0.05	0.754	0.081
1610→1620	-0.05	0.05	0.779	0.084
1610→1620	0.04	0.05	0.748	0.080
1610→1620	0.14	0.05	0.775	0.083
1610→1620	0.25	0.05	0.717	0.077
1610→1620	0.35	0.05	0.770	0.084
1610→1620	0.44	0.05	0.680	0.075
1610→1620	0.54	0.05	0.551	0.062
1610→1620	0.63	0.05	0.369	0.415
1620→1630	-0.84	0.04	0.805	0.103
1620→1630	-0.75	0.05	0.857	0.097
1620→1630	-0.65	0.05	0.791	0.088
1620→1630	-0.54	0.05	0.721	0.079
1620→1630	-0.44	0.05	0.741	0.080
1620→1630	-0.34	0.05	0.680	0.074
1620→1630	-0.24	0.05	0.686	0.074
1620→1630	-0.14	0.05	0.664	0.072
1620→1630	-0.04	0.05	0.667	0.072
1620→1630	0.04	0.05	0.604	0.065
1620→1630	0.15	0.05	0.563	0.061
1620→1630	0.24	0.05	0.625	0.068
1620→1630	0.34	0.05	0.627	0.069
1620→1630	0.44	0.05	0.517	0.058
1620→1630	0.54	0.05	0.500	0.057
1620→1630	0.63	0.05	0.310	0.058

Table 12.3: η Differential Cross Section Results

W bin (MeV)	$\cos(\theta_{CM})$	$\cos(\theta_{CM})$ Error	$d\sigma/d\Omega$ μb	$d\sigma/d\Omega$ Error
1630→1640	-0.84	0.04	0.655	0.085
1630→1640	-0.75	0.05	0.637	0.073
1630→1640	-0.65	0.05	0.625	0.069
1630→1640	-0.55	0.05	0.587	0.064
1630→1640	-0.45	0.05	0.537	0.058
1630→1640	-0.35	0.05	0.544	0.059
1630→1640	-0.25	0.05	0.538	0.058
1630→1640	-0.14	0.05	0.485	0.052
1630→1640	-0.05	0.05	0.476	0.051
1630→1640	0.04	0.05	0.465	0.050
1630→1640	0.15	0.05	0.479	0.052
1630→1640	0.25	0.05	0.505	0.055
1630→1640	0.34	0.05	0.426	0.047
1630→1640	0.44	0.05	0.339	0.038
1630→1640	0.54	0.05	0.412	0.047
1630→1640	0.65	0.05	0.355	0.058
1630→1640	0.71	0.01	-0.09	-0.66
1640→1650	-0.84	0.04	0.506	0.068
1640→1650	-0.75	0.05	0.496	0.058
1640→1650	-0.65	0.05	0.499	0.056
1640→1650	-0.54	0.05	0.519	0.057
1640→1650	-0.44	0.05	0.453	0.050
1640→1650	-0.35	0.05	0.442	0.048
1640→1650	-0.25	0.05	0.434	0.047
1640→1650	-0.14	0.05	0.401	0.044
1640→1650	-0.05	0.05	0.408	0.044
1640→1650	0.05	0.05	0.387	0.042
1640→1650	0.14	0.05	0.373	0.041
1640→1650	0.24	0.05	0.395	0.044
1640→1650	0.34	0.05	0.337	0.038
1640→1650	0.44	0.05	0.280	0.032
1640→1650	0.54	0.05	0.275	0.033
1640→1650	0.65	0.05	0.236	0.038
1640→1650	0.71	0.01	-0.09	-0.14
1650→1660	-0.84	0.05	0.377	0.082
1650→1660	-0.74	0.05	0.503	0.059
1650→1660	-0.64	0.05	0.472	0.054
1650→1660	-0.55	0.05	0.445	0.050
1650→1660	-0.45	0.05	0.390	0.043
1650→1660	-0.35	0.05	0.364	0.040

Table 12.4: η Differential Cross Section Results

W bin (MeV)	$\cos(\theta_{CM})$	$\cos(\theta_{CM})$ Error	$d\sigma/d\Omega$ μb	$d\sigma/d\Omega$ Error
1650→1660	-0.25	0.05	0.370	0.040
1650→1660	-0.15	0.05	0.373	0.041
1650→1660	-0.05	0.05	0.364	0.040
1650→1660	0.04	0.05	0.347	0.038
1650→1660	0.15	0.05	0.332	0.036
1650→1660	0.24	0.05	0.353	0.039
1650→1660	0.34	0.05	0.273	0.031
1650→1660	0.45	0.05	0.240	0.029
1650→1660	0.54	0.05	0.288	0.034
1650→1660	0.64	0.05	0.219	0.029
1650→1660	0.71	0.01	0.163	0.162
1660→1670	-0.85	0.05	0.537	0.182
1660→1670	-0.75	0.05	0.480	0.061
1660→1670	-0.65	0.05	0.538	0.063
1660→1670	-0.55	0.05	0.519	0.059
1660→1670	-0.45	0.05	0.500	0.056
1660→1670	-0.35	0.05	0.445	0.050
1660→1670	-0.24	0.05	0.480	0.053
1660→1670	-0.14	0.05	0.434	0.049
1660→1670	-0.05	0.05	0.468	0.052
1660→1670	0.05	0.05	0.462	0.051
1660→1670	0.15	0.05	0.432	0.048
1660→1670	0.24	0.05	0.443	0.050
1660→1670	0.34	0.05	0.352	0.041
1660→1670	0.45	0.05	0.321	0.039
1660→1670	0.54	0.05	0.355	0.045
1660→1670	0.64	0.05	0.361	0.049
1660→1670	0.81	0.02	-0.01	-0.35
1670→1680	-0.85	0.05	0.369	0.068
1670→1680	-0.74	0.05	0.391	0.049
1670→1680	-0.65	0.05	0.366	0.043
1670→1680	-0.54	0.05	0.308	0.036
1670→1680	-0.45	0.05	0.363	0.041
1670→1680	-0.34	0.05	0.324	0.036
1670→1680	-0.25	0.05	0.326	0.036
1670→1680	-0.15	0.05	0.340	0.038
1670→1680	-0.04	0.05	0.324	0.036
1670→1680	0.04	0.05	0.323	0.036
1670→1680	0.15	0.05	0.312	0.035
1670→1680	0.24	0.05	0.383	0.043

Table 12.5: η Differential Cross Section Results

W bin (MeV)	$\cos(\theta_{CM})$	$\cos(\theta_{CM})$ Error	$d\sigma/d\Omega$ μb	$d\sigma/d\Omega$ Error
1670→1680	0.34	0.05	0.314	0.036
1670→1680	0.44	0.05	0.265	0.032
1670→1680	0.55	0.05	0.274	0.034
1670→1680	0.64	0.05	0.334	0.042
1670→1680	0.72	0.02	0.381	0.185
1680→1690	-0.84	0.05	0.192	0.034
1680→1690	-0.74	0.05	0.250	0.032
1680→1690	-0.65	0.05	0.278	0.033
1680→1690	-0.55	0.05	0.258	0.029
1680→1690	-0.45	0.05	0.250	0.028
1680→1690	-0.35	0.05	0.251	0.028
1680→1690	-0.24	0.05	0.277	0.030
1680→1690	-0.14	0.05	0.275	0.030
1680→1690	-0.05	0.05	0.282	0.031
1680→1690	0.05	0.05	0.249	0.028
1680→1690	0.15	0.05	0.294	0.032
1680→1690	0.24	0.05	0.305	0.034
1680→1690	0.34	0.05	0.221	0.025
1680→1690	0.44	0.05	0.241	0.028
1680→1690	0.55	0.05	0.261	0.031
1680→1690	0.64	0.05	0.214	0.027
1680→1690	0.71	0.03	0.169	0.448
1690→1700	-0.85	0.05	0.294	0.056
1690→1700	-0.74	0.05	0.208	0.027
1690→1700	-0.65	0.05	0.250	0.029
1690→1700	-0.54	0.05	0.248	0.028
1690→1700	-0.45	0.05	0.249	0.028
1690→1700	-0.34	0.05	0.262	0.029
1690→1700	-0.25	0.05	0.264	0.029
1690→1700	-0.14	0.05	0.274	0.030
1690→1700	-0.05	0.05	0.276	0.030
1690→1700	0.04	0.05	0.294	0.032
1690→1700	0.15	0.05	0.306	0.033
1690→1700	0.25	0.05	0.320	0.036
1690→1700	0.34	0.05	0.276	0.031
1690→1700	0.45	0.05	0.263	0.030
1690→1700	0.55	0.05	0.283	0.033
1690→1700	0.64	0.05	0.319	0.037
1690→1700	0.73	0.03	0.468	0.251
1700→1710	-0.84	0.05	0.189	0.033

Table 12.6: η Differential Cross Section Results

W bin (MeV)	$\cos(\theta_{CM})$	$\cos(\theta_{CM})$ Error	$d\sigma/d\Omega$ μb	$d\sigma/d\Omega$ Error
1700→1710	-0.75	0.05	0.200	0.026
1700→1710	-0.65	0.05	0.229	0.027
1700→1710	-0.54	0.05	0.239	0.027
1700→1710	-0.45	0.05	0.233	0.026
1700→1710	-0.35	0.05	0.251	0.028
1700→1710	-0.24	0.05	0.253	0.028
1700→1710	-0.14	0.05	0.281	0.031
1700→1710	-0.05	0.05	0.303	0.033
1700→1710	0.04	0.05	0.291	0.032
1700→1710	0.15	0.05	0.331	0.036
1700→1710	0.24	0.05	0.337	0.037
1700→1710	0.35	0.05	0.284	0.032
1700→1710	0.45	0.05	0.322	0.036
1700→1710	0.55	0.05	0.323	0.038
1700→1710	0.65	0.05	0.351	0.041
1700→1710	0.71	0.03	0.185	0.047
1710→1720	-0.85	0.05	0.176	0.033
1710→1720	-0.74	0.05	0.195	0.025
1710→1720	-0.65	0.05	0.222	0.026
1710→1720	-0.54	0.05	0.221	0.025
1710→1720	-0.45	0.05	0.206	0.023
1710→1720	-0.34	0.05	0.247	0.027
1710→1720	-0.24	0.05	0.222	0.024
1710→1720	-0.14	0.05	0.266	0.029
1710→1720	-0.05	0.05	0.294	0.032
1710→1720	0.05	0.05	0.297	0.032
1710→1720	0.15	0.05	0.335	0.036
1710→1720	0.24	0.05	0.381	0.042
1710→1720	0.34	0.05	0.290	0.032
1710→1720	0.44	0.05	0.344	0.039
1710→1720	0.55	0.05	0.359	0.041
1710→1720	0.64	0.05	0.346	0.040
1710→1720	0.72	0.03	0.321	0.059
1720→1730	-0.84	0.05	0.126	0.024
1720→1730	-0.74	0.05	0.149	0.021
1720→1730	-0.65	0.05	0.203	0.025
1720→1730	-0.54	0.05	0.192	0.022
1720→1730	-0.45	0.05	0.204	0.023
1720→1730	-0.35	0.05	0.203	0.023
1720→1730	-0.25	0.05	0.239	0.026

Table 12.7: η Differential Cross Section Results

W bin (MeV)	$\cos(\theta_{CM})$	$\cos(\theta_{CM})$ Error	$d\sigma/d\Omega$ μb	$d\sigma/d\Omega$ Error
1720→1730	-0.14	0.05	0.309	0.034
1720→1730	-0.05	0.05	0.314	0.034
1720→1730	0.05	0.05	0.324	0.035
1720→1730	0.15	0.05	0.325	0.036
1720→1730	0.24	0.05	0.372	0.041
1720→1730	0.34	0.05	0.316	0.035
1720→1730	0.44	0.05	0.366	0.041
1720→1730	0.55	0.05	0.376	0.043
1720→1730	0.65	0.05	0.319	0.037
1720→1730	0.73	0.04	0.287	0.157
1730→1740	-0.84	0.05	0.165	0.029
1730→1740	-0.74	0.05	0.164	0.022
1730→1740	-0.65	0.05	0.185	0.022
1730→1740	-0.54	0.05	0.181	0.021
1730→1740	-0.44	0.05	0.194	0.022
1730→1740	-0.34	0.05	0.220	0.024
1730→1740	-0.24	0.05	0.239	0.026
1730→1740	-0.14	0.05	0.298	0.032
1730→1740	-0.04	0.05	0.314	0.034
1730→1740	0.05	0.05	0.313	0.034
1730→1740	0.15	0.05	0.335	0.036
1730→1740	0.24	0.05	0.384	0.042
1730→1740	0.35	0.05	0.325	0.036
1730→1740	0.45	0.05	0.367	0.041
1730→1740	0.55	0.05	0.365	0.041
1730→1740	0.64	0.05	0.393	0.045
1730→1740	0.74	0.04	0.363	0.097
1740→1750	-0.84	0.05	0.148	0.026
1740→1750	-0.74	0.05	0.138	0.019
1740→1750	-0.64	0.05	0.175	0.021
1740→1750	-0.55	0.05	0.183	0.021
1740→1750	-0.45	0.05	0.193	0.022
1740→1750	-0.34	0.05	0.212	0.023
1740→1750	-0.25	0.05	0.209	0.023
1740→1750	-0.14	0.05	0.291	0.032
1740→1750	-0.04	0.05	0.291	0.032
1740→1750	0.05	0.05	0.284	0.031
1740→1750	0.14	0.05	0.330	0.036
1740→1750	0.24	0.05	0.333	0.037
1740→1750	0.35	0.05	0.294	0.033

Table 12.8: η Differential Cross Section Results

W bin (MeV)	$\cos(\theta_{CM})$	$\cos(\theta_{CM})$ Error	$d\sigma/d\Omega$ μb	$d\sigma/d\Omega$ Error
1740→1750	0.44	0.05	0.346	0.039
1740→1750	0.54	0.05	0.332	0.038
1740→1750	0.64	0.05	0.331	0.038
1740→1750	0.74	0.04	0.364	0.076
1750→1760	-0.84	0.05	0.121	0.024
1750→1760	-0.75	0.05	0.124	0.019
1750→1760	-0.65	0.05	0.170	0.021
1750→1760	-0.54	0.05	0.162	0.019
1750→1760	-0.45	0.05	0.176	0.020
1750→1760	-0.34	0.05	0.200	0.022
1750→1760	-0.24	0.05	0.212	0.023
1750→1760	-0.14	0.05	0.249	0.027
1750→1760	-0.04	0.05	0.282	0.031
1750→1760	0.05	0.05	0.289	0.032
1750→1760	0.15	0.05	0.287	0.032
1750→1760	0.24	0.05	0.307	0.034
1750→1760	0.34	0.05	0.284	0.032
1750→1760	0.45	0.05	0.287	0.033
1750→1760	0.55	0.05	0.322	0.037
1750→1760	0.65	0.05	0.294	0.034
1750→1760	0.73	0.05	0.210	0.215
1760→1770	-0.85	0.05	0.098	0.021
1760→1770	-0.74	0.05	0.107	0.016
1760→1770	-0.64	0.05	0.126	0.016
1760→1770	-0.54	0.05	0.164	0.019
1760→1770	-0.45	0.05	0.163	0.018
1760→1770	-0.34	0.05	0.199	0.022
1760→1770	-0.24	0.05	0.197	0.022
1760→1770	-0.14	0.05	0.239	0.026
1760→1770	-0.04	0.05	0.275	0.030
1760→1770	0.04	0.05	0.268	0.029
1760→1770	0.15	0.05	0.282	0.031
1760→1770	0.24	0.05	0.290	0.032
1760→1770	0.34	0.05	0.298	0.033
1760→1770	0.44	0.05	0.305	0.034
1760→1770	0.55	0.05	0.305	0.035
1760→1770	0.65	0.05	0.305	0.035
1760→1770	0.73	0.04	0.303	0.039
1770→1780	-0.84	0.05	0.115	0.021
1770→1780	-0.75	0.05	0.099	0.015

Table 12.9: η Differential Cross Section Results

W bin (MeV)	$\cos(\theta_{CM})$	$\cos(\theta_{CM})$ Error	$d\sigma/d\Omega$ μb	$d\sigma/d\Omega$ Error
1770→1780	-0.64	0.05	0.146	0.018
1770→1780	-0.54	0.05	0.159	0.019
1770→1780	-0.44	0.05	0.159	0.018
1770→1780	-0.34	0.05	0.184	0.020
1770→1780	-0.24	0.05	0.205	0.022
1770→1780	-0.14	0.05	0.254	0.028
1770→1780	-0.05	0.05	0.256	0.028
1770→1780	0.04	0.05	0.275	0.030
1770→1780	0.15	0.05	0.282	0.031
1770→1780	0.24	0.05	0.272	0.030
1770→1780	0.35	0.05	0.288	0.032
1770→1780	0.44	0.05	0.284	0.032
1770→1780	0.55	0.05	0.330	0.037
1770→1780	0.64	0.05	0.291	0.033
1770→1780	0.74	0.05	0.299	0.049
1780→1790	-0.85	0.05	0.173	0.035
1780→1790	-0.75	0.05	0.149	0.020
1780→1790	-0.65	0.05	0.129	0.016
1780→1790	-0.54	0.05	0.151	0.018
1780→1790	-0.44	0.05	0.179	0.020
1780→1790	-0.34	0.05	0.171	0.019
1780→1790	-0.24	0.05	0.212	0.023
1780→1790	-0.14	0.05	0.230	0.025
1780→1790	-0.04	0.05	0.245	0.027
1780→1790	0.04	0.05	0.261	0.028
1780→1790	0.15	0.05	0.274	0.030
1780→1790	0.24	0.05	0.279	0.031
1780→1790	0.35	0.05	0.294	0.033
1780→1790	0.45	0.05	0.280	0.032
1780→1790	0.55	0.05	0.314	0.036
1780→1790	0.64	0.05	0.299	0.034
1780→1790	0.75	0.05	0.364	0.071
1790→1800	-0.84	0.05	0.094	0.020
1790→1800	-0.74	0.05	0.146	0.020
1790→1800	-0.64	0.05	0.133	0.017
1790→1800	-0.54	0.05	0.147	0.017
1790→1800	-0.44	0.05	0.168	0.019
1790→1800	-0.34	0.05	0.183	0.020
1790→1800	-0.24	0.05	0.187	0.021
1790→1800	-0.14	0.05	0.223	0.024

Table 12.10: η Differential Cross Section Results

W bin (MeV)	$\cos(\theta_{CM})$	$\cos(\theta_{CM})$ Error	$d\sigma/d\Omega$ μb	$d\sigma/d\Omega$ Error
1790→1800	-0.05	0.05	0.254	0.028
1790→1800	0.04	0.05	0.248	0.027
1790→1800	0.15	0.05	0.283	0.031
1790→1800	0.24	0.05	0.253	0.028
1790→1800	0.34	0.05	0.289	0.032
1790→1800	0.44	0.05	0.283	0.032
1790→1800	0.54	0.05	0.302	0.034
1790→1800	0.64	0.05	0.278	0.032
1790→1800	0.74	0.05	0.320	0.045
1800→1810	-0.84	0.05	0.092	0.019
1800→1810	-0.75	0.05	0.124	0.017
1800→1810	-0.64	0.05	0.120	0.015
1800→1810	-0.54	0.05	0.150	0.017
1800→1810	-0.45	0.05	0.175	0.020
1800→1810	-0.34	0.05	0.159	0.018
1800→1810	-0.24	0.05	0.198	0.022
1800→1810	-0.15	0.05	0.221	0.024
1800→1810	-0.05	0.05	0.245	0.027
1800→1810	0.05	0.05	0.243	0.027
1800→1810	0.14	0.05	0.262	0.029
1800→1810	0.25	0.05	0.264	0.029
1800→1810	0.34	0.05	0.282	0.031
1800→1810	0.45	0.05	0.255	0.029
1800→1810	0.55	0.05	0.304	0.035
1800→1810	0.64	0.05	0.239	0.028
1800→1810	0.74	0.05	0.264	0.035
1800→1810	0.81	0.01	-0.13	-0.84
1810→1820	-0.84	0.05	0.091	0.020
1810→1820	-0.75	0.05	0.124	0.018
1810→1820	-0.65	0.05	0.135	0.017
1810→1820	-0.54	0.05	0.136	0.016
1810→1820	-0.44	0.05	0.153	0.018
1810→1820	-0.35	0.05	0.178	0.020
1810→1820	-0.24	0.05	0.190	0.021
1810→1820	-0.14	0.05	0.212	0.024
1810→1820	-0.05	0.05	0.246	0.027
1810→1820	0.04	0.05	0.245	0.027
1810→1820	0.15	0.05	0.291	0.032
1810→1820	0.25	0.05	0.265	0.030
1810→1820	0.35	0.05	0.298	0.033

Table 12.11: η Differential Cross Section Results

W bin (MeV)	$\cos(\theta_{CM})$	$\cos(\theta_{CM})$ Error	$d\sigma/d\Omega$ μb	$d\sigma/d\Omega$ Error
1810→1820	0.45	0.05	0.274	0.032
1810→1820	0.54	0.05	0.289	0.033
1810→1820	0.64	0.05	0.284	0.033
1810→1820	0.75	0.05	0.294	0.040
1810→1820	0.81	0.01	0.982	1.052
1820→1830	-0.85	0.05	0.078	0.017
1820→1830	-0.74	0.05	0.108	0.016
1820→1830	-0.65	0.05	0.129	0.016
1820→1830	-0.54	0.05	0.133	0.016
1820→1830	-0.44	0.05	0.153	0.017
1820→1830	-0.34	0.05	0.151	0.017
1820→1830	-0.24	0.05	0.184	0.020
1820→1830	-0.14	0.05	0.190	0.021
1820→1830	-0.04	0.05	0.224	0.024
1820→1830	0.04	0.05	0.209	0.023
1820→1830	0.15	0.05	0.263	0.029
1820→1830	0.24	0.05	0.240	0.027
1820→1830	0.35	0.05	0.254	0.028
1820→1830	0.44	0.05	0.267	0.031
1820→1830	0.54	0.05	0.276	0.032
1820→1830	0.64	0.05	0.257	0.030
1820→1830	0.75	0.05	0.319	0.040
1820→1830	0.81	0.01	0.962	0.784
1830→1840	-0.85	0.05	0.073	0.017
1830→1840	-0.74	0.05	0.093	0.014
1830→1840	-0.64	0.05	0.120	0.015
1830→1840	-0.54	0.05	0.129	0.015
1830→1840	-0.44	0.05	0.155	0.018
1830→1840	-0.34	0.05	0.166	0.018
1830→1840	-0.24	0.05	0.170	0.019
1830→1840	-0.14	0.05	0.209	0.023
1830→1840	-0.05	0.05	0.225	0.025
1830→1840	0.05	0.05	0.217	0.024
1830→1840	0.15	0.05	0.239	0.026
1830→1840	0.24	0.05	0.267	0.030
1830→1840	0.35	0.05	0.222	0.025
1830→1840	0.45	0.05	0.281	0.032
1830→1840	0.54	0.05	0.253	0.029
1830→1840	0.64	0.05	0.247	0.029
1830→1840	0.75	0.05	0.250	0.033

Table 12.12: η Differential Cross Section Results

W bin (MeV)	$\cos(\theta_{CM})$	$\cos(\theta_{CM})$ Error	$d\sigma/d\Omega$ μb	$d\sigma/d\Omega$ Error
1830→1840	0.81	0.01	0.545	0.224
1840→1850	-0.84	0.05	0.094	0.018
1840→1850	-0.74	0.05	0.097	0.014
1840→1850	-0.64	0.05	0.108	0.014
1840→1850	-0.54	0.05	0.135	0.016
1840→1850	-0.44	0.05	0.150	0.017
1840→1850	-0.34	0.05	0.141	0.016
1840→1850	-0.24	0.05	0.162	0.018
1840→1850	-0.14	0.05	0.190	0.021
1840→1850	-0.05	0.05	0.217	0.024
1840→1850	0.05	0.05	0.209	0.023
1840→1850	0.15	0.05	0.242	0.027
1840→1850	0.24	0.05	0.236	0.026
1840→1850	0.35	0.05	0.245	0.027
1840→1850	0.45	0.05	0.249	0.028
1840→1850	0.55	0.05	0.267	0.030
1840→1850	0.65	0.05	0.260	0.030
1840→1850	0.75	0.05	0.272	0.034
1840→1850	0.79	0.02	0.089	0.377
1850→1860	-0.84	0.05	0.070	0.016
1850→1860	-0.74	0.05	0.090	0.014
1850→1860	-0.64	0.05	0.109	0.014
1850→1860	-0.54	0.05	0.130	0.015
1850→1860	-0.44	0.05	0.127	0.014
1850→1860	-0.34	0.05	0.145	0.016
1850→1860	-0.24	0.05	0.147	0.016
1850→1860	-0.14	0.05	0.184	0.020
1850→1860	-0.05	0.05	0.209	0.023
1850→1860	0.04	0.05	0.215	0.024
1850→1860	0.15	0.05	0.230	0.025
1850→1860	0.24	0.05	0.231	0.026
1850→1860	0.35	0.05	0.265	0.030
1850→1860	0.45	0.05	0.231	0.027
1850→1860	0.54	0.05	0.254	0.029
1850→1860	0.64	0.05	0.244	0.028
1850→1860	0.74	0.05	0.247	0.032
1850→1860	0.81	0.01	0.289	0.103
1860→1870	-0.85	0.05	0.080	0.017
1860→1870	-0.74	0.05	0.083	0.012
1860→1870	-0.64	0.05	0.111	0.014

Table 12.13: η Differential Cross Section Results

W bin (MeV)	$\cos(\theta_{CM})$	$\cos(\theta_{CM})$ Error	$d\sigma/d\Omega$ μb	$d\sigma/d\Omega$ Error
1860→1870	-0.54	0.05	0.112	0.013
1860→1870	-0.44	0.05	0.125	0.014
1860→1870	-0.34	0.05	0.135	0.015
1860→1870	-0.24	0.05	0.154	0.017
1860→1870	-0.14	0.05	0.182	0.020
1860→1870	-0.04	0.05	0.204	0.022
1860→1870	0.04	0.05	0.197	0.022
1860→1870	0.15	0.05	0.222	0.025
1860→1870	0.24	0.05	0.245	0.027
1860→1870	0.34	0.05	0.218	0.025
1860→1870	0.44	0.05	0.203	0.024
1860→1870	0.54	0.05	0.220	0.026
1860→1870	0.64	0.05	0.227	0.027
1860→1870	0.75	0.05	0.285	0.037
1860→1870	0.81	0.01	0.202	0.070
1870→1880	-0.85	0.05	0.080	0.017
1870→1880	-0.74	0.05	0.109	0.016
1870→1880	-0.65	0.05	0.079	0.011
1870→1880	-0.54	0.05	0.107	0.013
1870→1880	-0.44	0.05	0.120	0.014
1870→1880	-0.34	0.05	0.127	0.014
1870→1880	-0.25	0.05	0.145	0.016
1870→1880	-0.15	0.05	0.179	0.020
1870→1880	-0.05	0.05	0.186	0.020
1870→1880	0.05	0.05	0.180	0.020
1870→1880	0.15	0.05	0.206	0.023
1870→1880	0.24	0.05	0.218	0.025
1870→1880	0.35	0.05	0.231	0.026
1870→1880	0.45	0.05	0.240	0.028
1870→1880	0.54	0.05	0.251	0.029
1870→1880	0.65	0.05	0.236	0.028
1870→1880	0.75	0.05	0.237	0.032
1870→1880	0.82	0.02	0.346	0.203
1880→1890	-0.85	0.05	0.080	0.020
1880→1890	-0.74	0.05	0.076	0.012
1880→1890	-0.65	0.05	0.092	0.012
1880→1890	-0.55	0.05	0.100	0.012
1880→1890	-0.44	0.05	0.112	0.013
1880→1890	-0.35	0.05	0.119	0.013
1880→1890	-0.24	0.05	0.137	0.015

Table 12.14: η Differential Cross Section Results

W bin (MeV)	$\cos(\theta_{CM})$	$\cos(\theta_{CM})$ Error	$d\sigma/d\Omega$ μb	$d\sigma/d\Omega$ Error
1880→1890	-0.14	0.05	0.148	0.016
1880→1890	-0.05	0.05	0.170	0.019
1880→1890	0.05	0.05	0.187	0.021
1880→1890	0.15	0.05	0.180	0.020
1880→1890	0.24	0.05	0.185	0.021
1880→1890	0.35	0.05	0.182	0.021
1880→1890	0.45	0.05	0.201	0.024
1880→1890	0.55	0.05	0.207	0.024
1880→1890	0.64	0.05	0.192	0.023
1880→1890	0.74	0.05	0.221	0.029
1880→1890	0.82	0.02	0.373	0.131
1890→1900	-0.85	0.05	0.074	0.016
1890→1900	-0.74	0.05	0.085	0.013
1890→1900	-0.64	0.05	0.072	0.010
1890→1900	-0.55	0.05	0.086	0.011
1890→1900	-0.44	0.05	0.093	0.011
1890→1900	-0.34	0.05	0.104	0.012
1890→1900	-0.24	0.05	0.097	0.011
1890→1900	-0.14	0.05	0.141	0.016
1890→1900	-0.05	0.05	0.159	0.018
1890→1900	0.05	0.05	0.151	0.017
1890→1900	0.14	0.05	0.172	0.019
1890→1900	0.25	0.05	0.198	0.022
1890→1900	0.34	0.05	0.166	0.019
1890→1900	0.44	0.05	0.160	0.019
1890→1900	0.55	0.05	0.181	0.021
1890→1900	0.65	0.05	0.187	0.022
1890→1900	0.74	0.05	0.177	0.025
1890→1900	0.81	0.02	0.144	0.052
1900→1910	-0.84	0.05	0.039	0.011
1900→1910	-0.75	0.05	0.062	0.010
1900→1910	-0.64	0.05	0.061	0.009
1900→1910	-0.55	0.05	0.068	0.009
1900→1910	-0.44	0.05	0.081	0.010
1900→1910	-0.34	0.05	0.086	0.010
1900→1910	-0.24	0.05	0.098	0.011
1900→1910	-0.14	0.05	0.116	0.013
1900→1910	-0.05	0.05	0.127	0.014
1900→1910	0.05	0.05	0.126	0.014
1900→1910	0.15	0.05	0.161	0.018

Table 12.15: η Differential Cross Section Results

W bin (MeV)	$\cos(\theta_{CM})$	$\cos(\theta_{CM})$ Error	$d\sigma/d\Omega$ μb	$d\sigma/d\Omega$ Error
1900→1910	0.24	0.05	0.156	0.018
1900→1910	0.35	0.05	0.142	0.017
1900→1910	0.45	0.05	0.169	0.020
1900→1910	0.54	0.05	0.144	0.017
1900→1910	0.65	0.05	0.159	0.019
1900→1910	0.75	0.05	0.202	0.027
1900→1910	0.82	0.02	0.307	0.079
1910→1920	-0.84	0.05	0.058	0.013
1910→1920	-0.74	0.05	0.049	0.008
1910→1920	-0.64	0.05	0.061	0.009
1910→1920	-0.54	0.05	0.073	0.009
1910→1920	-0.44	0.05	0.061	0.007
1910→1920	-0.34	0.05	0.072	0.008
1910→1920	-0.25	0.05	0.089	0.010
1910→1920	-0.14	0.05	0.103	0.012
1910→1920	-0.05	0.05	0.124	0.014
1910→1920	0.05	0.05	0.127	0.014
1910→1920	0.15	0.05	0.137	0.015
1910→1920	0.24	0.05	0.155	0.018
1910→1920	0.34	0.05	0.158	0.018
1910→1920	0.44	0.05	0.143	0.017
1910→1920	0.54	0.05	0.144	0.017
1910→1920	0.65	0.05	0.161	0.019
1910→1920	0.75	0.05	0.232	0.031
1910→1920	0.81	0.02	0.180	0.048
1920→1930	-0.85	0.05	0.045	0.015
1920→1930	-0.74	0.05	0.049	0.009
1920→1930	-0.64	0.05	0.060	0.009
1920→1930	-0.54	0.05	0.062	0.008
1920→1930	-0.44	0.05	0.075	0.009
1920→1930	-0.34	0.05	0.076	0.009
1920→1930	-0.24	0.05	0.089	0.010
1920→1930	-0.14	0.05	0.119	0.014
1920→1930	-0.05	0.05	0.143	0.016
1920→1930	0.05	0.05	0.154	0.017
1920→1930	0.14	0.05	0.156	0.018
1920→1930	0.24	0.05	0.152	0.018
1920→1930	0.35	0.05	0.160	0.019
1920→1930	0.45	0.05	0.190	0.023
1920→1930	0.55	0.05	0.177	0.021

Table 12.16: η Differential Cross Section Results

W bin (MeV)	$\cos(\theta_{CM})$	$\cos(\theta_{CM})$ Error	$d\sigma/d\Omega$ μb	$d\sigma/d\Omega$ Error
1920→1930	0.65	0.05	0.178	0.022
1920→1930	0.74	0.05	0.221	0.030
1920→1930	0.81	0.02	0.218	0.052
1930→1940	-0.85	0.05	0.042	0.012
1930→1940	-0.74	0.05	0.037	0.007
1930→1940	-0.65	0.05	0.054	0.008
1930→1940	-0.54	0.05	0.055	0.007
1930→1940	-0.44	0.05	0.060	0.007
1930→1940	-0.34	0.05	0.071	0.008
1930→1940	-0.24	0.05	0.073	0.008
1930→1940	-0.14	0.05	0.097	0.011
1930→1940	-0.05	0.05	0.098	0.011
1930→1940	0.05	0.05	0.113	0.013
1930→1940	0.15	0.05	0.147	0.017
1930→1940	0.24	0.05	0.144	0.017
1930→1940	0.34	0.05	0.142	0.016
1930→1940	0.45	0.05	0.146	0.018
1930→1940	0.55	0.05	0.148	0.018
1930→1940	0.65	0.05	0.146	0.018
1930→1940	0.75	0.05	0.211	0.029
1930→1940	0.83	0.03	0.297	0.244
1940→1950	-0.85	0.05	0.021	0.010
1940→1950	-0.74	0.05	0.033	0.007
1940→1950	-0.64	0.05	0.056	0.008
1940→1950	-0.55	0.05	0.052	0.007
1940→1950	-0.45	0.05	0.060	0.008
1940→1950	-0.34	0.05	0.064	0.008
1940→1950	-0.25	0.05	0.078	0.009
1940→1950	-0.14	0.05	0.098	0.011
1940→1950	-0.04	0.05	0.110	0.013
1940→1950	0.04	0.05	0.117	0.013
1940→1950	0.15	0.05	0.126	0.014
1940→1950	0.24	0.05	0.130	0.015
1940→1950	0.35	0.05	0.125	0.015
1940→1950	0.45	0.05	0.147	0.018
1940→1950	0.54	0.05	0.136	0.017
1940→1950	0.64	0.05	0.168	0.020
1940→1950	0.75	0.05	0.189	0.026
1940→1950	0.83	0.03	0.360	0.177
1950→1960	-0.85	0.05	0.032	0.008

Table 12.17: η Differential Cross Section Results

W bin (MeV)	$\cos(\theta_{CM})$	$\cos(\theta_{CM})$ Error	$d\sigma/d\Omega$ μb	$d\sigma/d\Omega$ Error
1950→1960	-0.74	0.05	0.031	0.005
1950→1960	-0.64	0.05	0.031	0.004
1950→1960	-0.55	0.05	0.039	0.005
1950→1960	-0.44	0.05	0.043	0.005
1950→1960	-0.35	0.05	0.053	0.006
1950→1960	-0.24	0.05	0.056	0.006
1950→1960	-0.14	0.05	0.074	0.008
1950→1960	-0.04	0.05	0.090	0.010
1950→1960	0.05	0.05	0.087	0.009
1950→1960	0.15	0.05	0.094	0.010
1950→1960	0.24	0.05	0.110	0.012
1950→1960	0.34	0.05	0.096	0.011
1950→1960	0.45	0.05	0.101	0.011
1950→1960	0.55	0.05	0.122	0.014
1950→1960	0.65	0.05	0.132	0.015
1950→1960	0.75	0.05	0.158	0.019
1950→1960	0.83	0.03	0.253	0.067
1960→1970	-0.84	0.05	0.026	0.006
1960→1970	-0.74	0.05	0.038	0.005
1960→1970	-0.64	0.05	0.051	0.006
1960→1970	-0.54	0.05	0.053	0.006
1960→1970	-0.45	0.05	0.062	0.007
1960→1970	-0.34	0.05	0.066	0.007
1960→1970	-0.25	0.05	0.070	0.008
1960→1970	-0.14	0.05	0.091	0.010
1960→1970	-0.05	0.05	0.108	0.012
1960→1970	0.04	0.05	0.110	0.012
1960→1970	0.15	0.05	0.121	0.013
1960→1970	0.24	0.05	0.135	0.015
1960→1970	0.35	0.05	0.132	0.014
1960→1970	0.45	0.05	0.128	0.014
1960→1970	0.54	0.05	0.132	0.015
1960→1970	0.65	0.05	0.170	0.019
1960→1970	0.75	0.05	0.202	0.024
1960→1970	0.81	0.04	0.147	0.104
1970→1980	-0.84	0.05	0.030	0.007
1970→1980	-0.74	0.05	0.042	0.006
1970→1980	-0.64	0.05	0.049	0.006
1970→1980	-0.54	0.05	0.048	0.005
1970→1980	-0.44	0.05	0.061	0.007

Table 12.18: η Differential Cross Section Results

W bin (MeV)	$\cos(\theta_{CM})$	$\cos(\theta_{CM})$ Error	$d\sigma/d\Omega$ μb	$d\sigma/d\Omega$ Error
1970→1980	-0.35	0.05	0.063	0.007
1970→1980	-0.24	0.05	0.069	0.007
1970→1980	-0.14	0.05	0.085	0.009
1970→1980	-0.04	0.05	0.095	0.010
1970→1980	0.04	0.05	0.107	0.011
1970→1980	0.15	0.05	0.116	0.013
1970→1980	0.25	0.05	0.124	0.014
1970→1980	0.34	0.05	0.110	0.012
1970→1980	0.45	0.05	0.114	0.013
1970→1980	0.54	0.05	0.132	0.015
1970→1980	0.65	0.05	0.167	0.019
1970→1980	0.75	0.05	0.217	0.026
1970→1980	0.82	0.03	0.246	0.041
1980→1990	-0.83	0.05	0.017	0.006
1980→1990	-0.74	0.05	0.046	0.006
1980→1990	-0.64	0.05	0.049	0.006
1980→1990	-0.55	0.05	0.052	0.006
1980→1990	-0.44	0.05	0.059	0.006
1980→1990	-0.34	0.05	0.062	0.007
1980→1990	-0.24	0.05	0.069	0.007
1980→1990	-0.15	0.05	0.085	0.009
1980→1990	-0.04	0.05	0.110	0.012
1980→1990	0.05	0.05	0.103	0.011
1980→1990	0.14	0.05	0.113	0.012
1980→1990	0.24	0.05	0.122	0.013
1980→1990	0.34	0.05	0.110	0.012
1980→1990	0.45	0.05	0.113	0.013
1980→1990	0.55	0.05	0.138	0.015
1980→1990	0.65	0.05	0.142	0.016
1980→1990	0.75	0.05	0.187	0.022
1980→1990	0.83	0.03	0.365	0.061
1990→2000	-0.85	0.05	0.037	0.008
1990→2000	-0.74	0.05	0.044	0.006
1990→2000	-0.65	0.05	0.054	0.007
1990→2000	-0.54	0.05	0.052	0.006
1990→2000	-0.45	0.05	0.055	0.006
1990→2000	-0.35	0.05	0.059	0.006
1990→2000	-0.24	0.05	0.066	0.007
1990→2000	-0.14	0.05	0.081	0.009
1990→2000	-0.04	0.05	0.100	0.011

Table 12.19: η Differential Cross Section Results

W bin (MeV)	$\cos(\theta_{CM})$	$\cos(\theta_{CM})$ Error	$d\sigma/d\Omega$ μb	$d\sigma/d\Omega$ Error
1990→2000	0.05	0.05	0.103	0.011
1990→2000	0.14	0.05	0.112	0.012
1990→2000	0.25	0.05	0.111	0.012
1990→2000	0.34	0.05	0.101	0.011
1990→2000	0.45	0.05	0.111	0.013
1990→2000	0.55	0.05	0.111	0.013
1990→2000	0.64	0.05	0.154	0.018
1990→2000	0.75	0.05	0.168	0.021
1990→2000	0.82	0.03	0.252	0.044
2000→2010	-0.85	0.05	0.047	0.009
2000→2010	-0.75	0.05	0.046	0.006
2000→2010	-0.64	0.05	0.058	0.007
2000→2010	-0.54	0.05	0.054	0.006
2000→2010	-0.44	0.05	0.055	0.006
2000→2010	-0.34	0.05	0.062	0.007
2000→2010	-0.24	0.05	0.059	0.006
2000→2010	-0.14	0.05	0.081	0.009
2000→2010	-0.05	0.05	0.096	0.010
2000→2010	0.04	0.05	0.100	0.011
2000→2010	0.14	0.05	0.102	0.011
2000→2010	0.24	0.05	0.104	0.011
2000→2010	0.34	0.05	0.093	0.010
2000→2010	0.45	0.05	0.108	0.012
2000→2010	0.54	0.05	0.115	0.013
2000→2010	0.65	0.05	0.140	0.016
2000→2010	0.75	0.05	0.182	0.022
2000→2010	0.84	0.04	0.265	0.075
2010→2020	-0.83	0.05	0.037	0.007
2010→2020	-0.74	0.05	0.052	0.007
2010→2020	-0.64	0.05	0.059	0.007
2010→2020	-0.55	0.05	0.055	0.006
2010→2020	-0.45	0.05	0.059	0.006
2010→2020	-0.34	0.05	0.057	0.006
2010→2020	-0.25	0.05	0.065	0.007
2010→2020	-0.14	0.05	0.080	0.009
2010→2020	-0.05	0.05	0.090	0.010
2010→2020	0.05	0.05	0.097	0.010
2010→2020	0.15	0.05	0.094	0.010
2010→2020	0.25	0.05	0.090	0.010
2010→2020	0.34	0.05	0.094	0.010

Table 12.20: η Differential Cross Section Results

W bin (MeV)	$\cos(\theta_{CM})$	$\cos(\theta_{CM})$ Error	$d\sigma/d\Omega$ μb	$d\sigma/d\Omega$ Error
2010→2020	0.45	0.05	0.090	0.010
2010→2020	0.55	0.05	0.107	0.012
2010→2020	0.65	0.05	0.142	0.016
2010→2020	0.75	0.05	0.187	0.023
2010→2020	0.84	0.04	0.282	0.074
2020→2030	-0.84	0.05	0.055	0.009
2020→2030	-0.74	0.05	0.053	0.007
2020→2030	-0.65	0.05	0.059	0.007
2020→2030	-0.55	0.05	0.070	0.008
2020→2030	-0.44	0.05	0.058	0.006
2020→2030	-0.34	0.05	0.059	0.006
2020→2030	-0.24	0.05	0.057	0.006
2020→2030	-0.14	0.05	0.071	0.008
2020→2030	-0.05	0.05	0.086	0.009
2020→2030	0.05	0.05	0.077	0.008
2020→2030	0.14	0.05	0.082	0.009
2020→2030	0.24	0.05	0.095	0.010
2020→2030	0.34	0.05	0.080	0.009
2020→2030	0.45	0.05	0.081	0.009
2020→2030	0.55	0.05	0.093	0.011
2020→2030	0.65	0.05	0.137	0.015
2020→2030	0.75	0.05	0.159	0.019
2020→2030	0.82	0.04	0.175	0.060
2030→2040	-0.84	0.05	0.047	0.008
2030→2040	-0.74	0.05	0.049	0.006
2030→2040	-0.64	0.05	0.061	0.007
2030→2040	-0.55	0.05	0.057	0.006
2030→2040	-0.44	0.05	0.062	0.007
2030→2040	-0.35	0.05	0.056	0.006
2030→2040	-0.25	0.05	0.060	0.006
2030→2040	-0.14	0.05	0.070	0.007
2030→2040	-0.05	0.05	0.083	0.009
2030→2040	0.04	0.05	0.091	0.010
2030→2040	0.15	0.05	0.081	0.009
2030→2040	0.25	0.05	0.090	0.010
2030→2040	0.34	0.05	0.068	0.008
2030→2040	0.45	0.05	0.077	0.009
2030→2040	0.55	0.05	0.101	0.011
2030→2040	0.65	0.05	0.131	0.015
2030→2040	0.75	0.05	0.195	0.023

Table 12.21: η Differential Cross Section Results

W bin (MeV)	$\cos(\theta_{CM})$	$\cos(\theta_{CM})$ Error	$d\sigma/d\Omega$ μb	$d\sigma/d\Omega$ Error
2030→2040	0.84	0.04	0.381	0.113
2040→2050	-0.84	0.05	0.028	0.006
2040→2050	-0.74	0.05	0.056	0.007
2040→2050	-0.65	0.05	0.060	0.007
2040→2050	-0.54	0.05	0.066	0.007
2040→2050	-0.44	0.05	0.054	0.006
2040→2050	-0.35	0.05	0.050	0.005
2040→2050	-0.25	0.05	0.055	0.006
2040→2050	-0.14	0.05	0.064	0.007
2040→2050	-0.04	0.05	0.076	0.008
2040→2050	0.04	0.05	0.075	0.008
2040→2050	0.15	0.05	0.077	0.008
2040→2050	0.25	0.05	0.069	0.008
2040→2050	0.34	0.05	0.070	0.008
2040→2050	0.45	0.05	0.069	0.008
2040→2050	0.55	0.05	0.095	0.011
2040→2050	0.65	0.05	0.130	0.015
2040→2050	0.75	0.05	0.222	0.027
2040→2050	0.83	0.04	0.251	0.045
2050→2060	-0.83	0.05	0.028	0.006
2050→2060	-0.74	0.05	0.056	0.007
2050→2060	-0.64	0.05	0.064	0.007
2050→2060	-0.55	0.05	0.060	0.007
2050→2060	-0.44	0.05	0.052	0.006
2050→2060	-0.34	0.05	0.048	0.005
2050→2060	-0.24	0.05	0.049	0.005
2050→2060	-0.14	0.05	0.060	0.006
2050→2060	-0.04	0.05	0.079	0.008
2050→2060	0.05	0.05	0.073	0.008
2050→2060	0.15	0.05	0.071	0.008
2050→2060	0.24	0.05	0.072	0.008
2050→2060	0.34	0.05	0.055	0.006
2050→2060	0.45	0.05	0.065	0.008
2050→2060	0.55	0.05	0.085	0.010
2050→2060	0.65	0.05	0.115	0.013
2050→2060	0.75	0.05	0.185	0.022
2050→2060	0.83	0.04	0.189	0.035
2060→2070	-0.84	0.05	0.042	0.008
2060→2070	-0.75	0.05	0.061	0.008
2060→2070	-0.64	0.05	0.053	0.006

Table 12.22: η Differential Cross Section Results

W bin (MeV)	$\cos(\theta_{CM})$	$\cos(\theta_{CM})$ Error	$d\sigma/d\Omega$ μb	$d\sigma/d\Omega$ Error
2060→2070	-0.54	0.05	0.059	0.007
2060→2070	-0.44	0.05	0.046	0.005
2060→2070	-0.35	0.05	0.050	0.005
2060→2070	-0.24	0.05	0.050	0.005
2060→2070	-0.14	0.05	0.061	0.007
2060→2070	-0.05	0.05	0.071	0.008
2060→2070	0.04	0.05	0.063	0.007
2060→2070	0.15	0.05	0.066	0.007
2060→2070	0.24	0.05	0.065	0.007
2060→2070	0.34	0.05	0.063	0.007
2060→2070	0.45	0.05	0.066	0.008
2060→2070	0.55	0.05	0.089	0.010
2060→2070	0.65	0.05	0.119	0.014
2060→2070	0.75	0.05	0.197	0.024
2060→2070	0.83	0.05	0.149	0.104
2070→2080	-0.85	0.05	0.060	0.012
2070→2080	-0.74	0.05	0.051	0.006
2070→2080	-0.64	0.05	0.052	0.006
2070→2080	-0.55	0.05	0.050	0.006
2070→2080	-0.45	0.05	0.044	0.005
2070→2080	-0.34	0.05	0.045	0.005
2070→2080	-0.24	0.05	0.044	0.005
2070→2080	-0.14	0.05	0.049	0.005
2070→2080	-0.05	0.05	0.061	0.007
2070→2080	0.04	0.05	0.066	0.007
2070→2080	0.15	0.05	0.058	0.006
2070→2080	0.24	0.05	0.059	0.007
2070→2080	0.35	0.05	0.060	0.007
2070→2080	0.45	0.05	0.068	0.008
2070→2080	0.55	0.05	0.085	0.010
2070→2080	0.65	0.05	0.125	0.014
2070→2080	0.75	0.05	0.191	0.023
2070→2080	0.84	0.04	0.305	0.063
2080→2090	-0.83	0.05	0.048	0.008
2080→2090	-0.74	0.05	0.058	0.007
2080→2090	-0.65	0.05	0.060	0.007
2080→2090	-0.54	0.05	0.053	0.006
2080→2090	-0.44	0.05	0.052	0.006
2080→2090	-0.34	0.05	0.046	0.005
2080→2090	-0.25	0.05	0.045	0.005

Table 12.23: η Differential Cross Section Results

W bin (MeV)	$\cos(\theta_{CM})$	$\cos(\theta_{CM})$ Error	$d\sigma/d\Omega$ μb	$d\sigma/d\Omega$ Error
2080→2090	-0.14	0.05	0.048	0.005
2080→2090	-0.04	0.05	0.064	0.007
2080→2090	0.05	0.05	0.057	0.006
2080→2090	0.14	0.05	0.057	0.006
2080→2090	0.25	0.05	0.063	0.007
2080→2090	0.35	0.05	0.058	0.007
2080→2090	0.45	0.05	0.064	0.008
2080→2090	0.55	0.05	0.098	0.011
2080→2090	0.65	0.05	0.145	0.016
2080→2090	0.75	0.05	0.201	0.025
2080→2090	0.84	0.04	0.297	0.053
2090→2100	-0.83	0.05	0.037	0.007
2090→2100	-0.75	0.05	0.066	0.008
2090→2100	-0.65	0.05	0.052	0.006
2090→2100	-0.55	0.05	0.054	0.006
2090→2100	-0.45	0.05	0.048	0.005
2090→2100	-0.35	0.05	0.044	0.005
2090→2100	-0.25	0.05	0.039	0.004
2090→2100	-0.14	0.05	0.043	0.005
2090→2100	-0.05	0.05	0.057	0.006
2090→2100	0.05	0.05	0.061	0.007
2090→2100	0.15	0.05	0.059	0.006
2090→2100	0.24	0.05	0.056	0.006
2090→2100	0.34	0.05	0.053	0.006
2090→2100	0.45	0.05	0.069	0.008
2090→2100	0.55	0.05	0.100	0.011
2090→2100	0.65	0.05	0.148	0.017
2090→2100	0.75	0.05	0.189	0.023
2090→2100	0.83	0.04	0.250	0.046
2100→2120	-0.84	0.05	0.042	0.007
2100→2120	-0.74	0.05	0.054	0.006
2100→2120	-0.65	0.05	0.053	0.006
2100→2120	-0.55	0.05	0.048	0.005
2100→2120	-0.45	0.05	0.038	0.004
2100→2120	-0.35	0.05	0.036	0.004
2100→2120	-0.24	0.05	0.034	0.003
2100→2120	-0.14	0.05	0.040	0.004
2100→2120	-0.04	0.05	0.051	0.005
2100→2120	0.04	0.05	0.054	0.006
2100→2120	0.15	0.05	0.049	0.005

Table 12.24: η Differential Cross Section Results

W bin (MeV)	$\cos(\theta_{CM})$	$\cos(\theta_{CM})$ Error	$d\sigma/d\Omega$ μb	$d\sigma/d\Omega$ Error
2100→2120	0.25	0.05	0.058	0.006
2100→2120	0.35	0.05	0.049	0.005
2100→2120	0.45	0.05	0.062	0.007
2100→2120	0.55	0.05	0.091	0.010
2100→2120	0.65	0.05	0.143	0.015
2100→2120	0.75	0.05	0.200	0.023
2100→2120	0.84	0.05	0.303	0.095
2120→2140	-0.83	0.05	0.037	0.005
2120→2140	-0.75	0.05	0.051	0.006
2120→2140	-0.65	0.05	0.050	0.005
2120→2140	-0.55	0.05	0.045	0.005
2120→2140	-0.45	0.05	0.031	0.003
2120→2140	-0.35	0.05	0.027	0.003
2120→2140	-0.24	0.05	0.023	0.002
2120→2140	-0.14	0.05	0.031	0.003
2120→2140	-0.04	0.05	0.043	0.004
2120→2140	0.05	0.05	0.046	0.005
2120→2140	0.14	0.05	0.049	0.005
2120→2140	0.24	0.05	0.047	0.005
2120→2140	0.35	0.05	0.050	0.005
2120→2140	0.45	0.05	0.062	0.007
2120→2140	0.55	0.05	0.102	0.011
2120→2140	0.65	0.05	0.134	0.014
2120→2140	0.75	0.05	0.171	0.019
2120→2140	0.83	0.04	0.212	0.035
2140→2160	-0.85	0.05	0.039	0.009
2140→2160	-0.75	0.05	0.045	0.005
2140→2160	-0.65	0.05	0.041	0.004
2140→2160	-0.55	0.05	0.033	0.003
2140→2160	-0.45	0.05	0.026	0.003
2140→2160	-0.35	0.05	0.021	0.002
2140→2160	-0.24	0.05	0.019	0.002
2140→2160	-0.14	0.05	0.028	0.003
2140→2160	-0.04	0.05	0.038	0.004
2140→2160	0.05	0.05	0.042	0.004
2140→2160	0.15	0.05	0.044	0.005
2140→2160	0.25	0.05	0.044	0.005
2140→2160	0.35	0.05	0.048	0.005
2140→2160	0.45	0.05	0.063	0.007
2140→2160	0.55	0.05	0.096	0.010

Table 12.25: η Differential Cross Section Results

W bin (MeV)	$\cos(\theta_{CM})$	$\cos(\theta_{CM})$ Error	$d\sigma/d\Omega$ μb	$d\sigma/d\Omega$ Error
2140→2160	0.65	0.05	0.138	0.015
2140→2160	0.75	0.05	0.178	0.021
2140→2160	0.85	0.05	0.241	0.052
2160→2180	-0.84	0.05	0.031	0.006
2160→2180	-0.75	0.05	0.047	0.005
2160→2180	-0.64	0.05	0.042	0.004
2160→2180	-0.55	0.05	0.030	0.003
2160→2180	-0.45	0.05	0.021	0.002
2160→2180	-0.35	0.05	0.018	0.002
2160→2180	-0.24	0.05	0.018	0.002
2160→2180	-0.14	0.05	0.023	0.002
2160→2180	-0.04	0.05	0.032	0.003
2160→2180	0.05	0.05	0.038	0.004
2160→2180	0.15	0.05	0.041	0.004
2160→2180	0.25	0.05	0.041	0.004
2160→2180	0.35	0.05	0.046	0.005
2160→2180	0.45	0.05	0.070	0.007
2160→2180	0.55	0.05	0.094	0.010
2160→2180	0.65	0.05	0.143	0.016
2160→2180	0.75	0.05	0.182	0.021
2160→2180	0.84	0.04	0.199	0.038
2180→2200	-0.84	0.05	0.036	0.009
2180→2200	-0.75	0.05	0.038	0.004
2180→2200	-0.65	0.05	0.034	0.004
2180→2200	-0.55	0.05	0.028	0.003
2180→2200	-0.45	0.05	0.020	0.002
2180→2200	-0.35	0.05	0.016	0.002
2180→2200	-0.25	0.05	0.015	0.001
2180→2200	-0.14	0.05	0.022	0.002
2180→2200	-0.04	0.05	0.035	0.004
2180→2200	0.04	0.05	0.035	0.004
2180→2200	0.15	0.05	0.036	0.004
2180→2200	0.25	0.05	0.045	0.005
2180→2200	0.35	0.05	0.048	0.005
2180→2200	0.45	0.05	0.063	0.007
2180→2200	0.55	0.05	0.094	0.010
2180→2200	0.65	0.05	0.139	0.015
2180→2200	0.75	0.05	0.175	0.021
2180→2200	0.85	0.05	0.335	0.102
2200→2220	-0.83	0.05	0.025	0.021

Table 12.26: η Differential Cross Section Results

W bin (MeV)	$\cos(\theta_{CM})$	$\cos(\theta_{CM})$ Error	$d\sigma/d\Omega$ μb	$d\sigma/d\Omega$ Error
2200→2220	-0.74	0.05	0.038	0.004
2200→2220	-0.65	0.05	0.028	0.003
2200→2220	-0.55	0.05	0.023	0.002
2200→2220	-0.45	0.05	0.017	0.002
2200→2220	-0.35	0.05	0.012	0.001
2200→2220	-0.24	0.05	0.013	0.001
2200→2220	-0.14	0.05	0.018	0.002
2200→2220	-0.04	0.05	0.029	0.003
2200→2220	0.05	0.05	0.034	0.003
2200→2220	0.15	0.05	0.037	0.004
2200→2220	0.25	0.05	0.038	0.004
2200→2220	0.35	0.05	0.042	0.004
2200→2220	0.45	0.05	0.064	0.007
2200→2220	0.55	0.05	0.094	0.010
2200→2220	0.65	0.05	0.133	0.015
2200→2220	0.74	0.05	0.146	0.017
2200→2220	0.82	0.05	0.129	0.033
2220→2240	-0.83	0.05	0.019	0.042
2220→2240	-0.75	0.05	0.029	0.003
2220→2240	-0.65	0.05	0.024	0.003
2220→2240	-0.55	0.05	0.021	0.002
2220→2240	-0.45	0.05	0.014	0.001
2220→2240	-0.35	0.05	0.011	0.001
2220→2240	-0.24	0.05	0.012	0.001
2220→2240	-0.14	0.05	0.016	0.002
2220→2240	-0.04	0.05	0.027	0.003
2220→2240	0.05	0.05	0.031	0.003
2220→2240	0.14	0.05	0.032	0.003
2220→2240	0.25	0.05	0.037	0.004
2220→2240	0.35	0.05	0.036	0.004
2220→2240	0.45	0.05	0.055	0.006
2220→2240	0.55	0.05	0.079	0.008
2220→2240	0.65	0.05	0.122	0.013
2220→2240	0.75	0.05	0.170	0.020
2220→2240	0.83	0.04	0.122	0.028
2240→2260	-0.84	0.04	0.032	0.005
2240→2260	-0.75	0.05	0.033	0.004
2240→2260	-0.65	0.05	0.026	0.003
2240→2260	-0.55	0.05	0.020	0.002
2240→2260	-0.45	0.05	0.013	0.001

Table 12.27: η Differential Cross Section Results

W bin (MeV)	$\cos(\theta_{CM})$	$\cos(\theta_{CM})$ Error	$d\sigma/d\Omega$ μb	$d\sigma/d\Omega$ Error
2240→2260	-0.34	0.05	0.009	0.001
2240→2260	-0.24	0.05	0.009	0.001
2240→2260	-0.14	0.05	0.014	0.001
2240→2260	-0.04	0.05	0.027	0.003
2240→2260	0.04	0.05	0.029	0.003
2240→2260	0.14	0.05	0.032	0.003
2240→2260	0.25	0.05	0.032	0.003
2240→2260	0.35	0.05	0.038	0.004
2240→2260	0.45	0.05	0.055	0.006
2240→2260	0.55	0.05	0.084	0.009
2240→2260	0.65	0.05	0.117	0.013
2240→2260	0.75	0.05	0.158	0.019
2240→2260	0.85	0.05	0.249	0.095
2260→2280	-0.83	0.04	0.026	0.004
2260→2280	-0.75	0.05	0.029	0.003
2260→2280	-0.65	0.05	0.024	0.002
2260→2280	-0.55	0.05	0.019	0.002
2260→2280	-0.45	0.05	0.013	0.001
2260→2280	-0.35	0.05	0.010	0.001
2260→2280	-0.24	0.05	0.009	0.001
2260→2280	-0.14	0.05	0.015	0.001
2260→2280	-0.04	0.05	0.026	0.003
2260→2280	0.05	0.05	0.031	0.003
2260→2280	0.15	0.05	0.031	0.003
2260→2280	0.24	0.05	0.036	0.004
2260→2280	0.34	0.05	0.039	0.004
2260→2280	0.45	0.05	0.055	0.006
2260→2280	0.55	0.05	0.082	0.009
2260→2280	0.65	0.05	0.111	0.012
2260→2280	0.75	0.05	0.141	0.017
2260→2280	0.83	0.05	0.128	0.037
2280→2300	-0.83	0.04	0.024	0.004
2280→2300	-0.74	0.05	0.025	0.003
2280→2300	-0.65	0.05	0.021	0.002
2280→2300	-0.55	0.05	0.015	0.002
2280→2300	-0.45	0.05	0.011	0.001
2280→2300	-0.35	0.05	0.008	0.001
2280→2300	-0.24	0.05	0.010	0.001
2280→2300	-0.14	0.05	0.013	0.001
2280→2300	-0.04	0.05	0.022	0.002

Table 12.28: η Differential Cross Section Results

W bin (MeV)	$\cos(\theta_{CM})$	$\cos(\theta_{CM})$ Error	$d\sigma/d\Omega$ μb	$d\sigma/d\Omega$ Error
2280→2300	0.05	0.05	0.026	0.003
2280→2300	0.14	0.05	0.030	0.003
2280→2300	0.24	0.05	0.034	0.004
2280→2300	0.35	0.05	0.037	0.004
2280→2300	0.45	0.05	0.049	0.005
2280→2300	0.55	0.05	0.069	0.007
2280→2300	0.65	0.05	0.109	0.012
2280→2300	0.75	0.05	0.131	0.016
2280→2300	0.83	0.04	0.094	0.028
2300→2320	-0.84	0.04	0.025	0.004
2300→2320	-0.74	0.05	0.019	0.002
2300→2320	-0.65	0.05	0.018	0.002
2300→2320	-0.55	0.05	0.013	0.001
2300→2320	-0.44	0.05	0.009	0.001
2300→2320	-0.35	0.05	0.007	0.001
2300→2320	-0.23	0.05	0.006	0.000
2300→2320	-0.14	0.05	0.013	0.001
2300→2320	-0.04	0.05	0.019	0.002
2300→2320	0.05	0.05	0.025	0.003
2300→2320	0.15	0.05	0.029	0.003
2300→2320	0.25	0.05	0.031	0.003
2300→2320	0.35	0.05	0.033	0.003
2300→2320	0.45	0.05	0.039	0.004
2300→2320	0.54	0.05	0.065	0.007
2300→2320	0.65	0.05	0.098	0.011
2300→2320	0.75	0.05	0.113	0.014
2300→2320	0.83	0.04	0.146	0.078
2320→2340	-0.84	0.04	0.026	0.004
2320→2340	-0.75	0.05	0.019	0.002
2320→2340	-0.65	0.05	0.017	0.002
2320→2340	-0.54	0.05	0.009	0.001
2320→2340	-0.45	0.05	0.008	0.001
2320→2340	-0.34	0.05	0.006	0.000
2320→2340	-0.25	0.05	0.006	0.000
2320→2340	-0.14	0.05	0.010	0.001
2320→2340	-0.04	0.05	0.019	0.002
2320→2340	0.05	0.05	0.025	0.003
2320→2340	0.14	0.05	0.022	0.002
2320→2340	0.24	0.05	0.027	0.003
2320→2340	0.35	0.05	0.029	0.003

Table 12.29: η Differential Cross Section Results

W bin (MeV)	$\cos(\theta_{CM})$	$\cos(\theta_{CM})$ Error	$d\sigma/d\Omega$ μb	$d\sigma/d\Omega$ Error
2320→2340	0.45	0.05	0.049	0.005
2320→2340	0.55	0.05	0.060	0.007
2320→2340	0.65	0.05	0.085	0.009
2320→2340	0.75	0.05	0.119	0.015
2320→2340	0.83	0.04	0.105	0.039
2340→2360	-0.84	0.04	0.018	0.003
2340→2360	-0.75	0.05	0.017	0.002
2340→2360	-0.64	0.05	0.010	0.001
2340→2360	-0.55	0.05	0.010	0.001
2340→2360	-0.44	0.05	0.007	0.001
2340→2360	-0.35	0.05	0.005	0.000
2340→2360	-0.24	0.05	0.006	0.000
2340→2360	-0.14	0.05	0.009	0.001
2340→2360	-0.04	0.05	0.019	0.002
2340→2360	0.05	0.05	0.023	0.002
2340→2360	0.15	0.05	0.026	0.003
2340→2360	0.25	0.05	0.025	0.003
2340→2360	0.34	0.05	0.028	0.003
2340→2360	0.45	0.05	0.034	0.004
2340→2360	0.55	0.05	0.061	0.007
2340→2360	0.65	0.05	0.084	0.009
2340→2360	0.74	0.05	0.102	0.013
2340→2360	0.83	0.05	0.086	0.039
2360→2400	-0.83	0.04	0.014	0.002
2360→2400	-0.75	0.05	0.016	0.002
2360→2400	-0.65	0.05	0.010	0.001
2360→2400	-0.55	0.05	0.008	0.001
2360→2400	-0.45	0.05	0.005	0.000
2360→2400	-0.35	0.05	0.003	0.000
2360→2400	-0.24	0.05	0.004	0.000
2360→2400	-0.14	0.05	0.009	0.001
2360→2400	-0.04	0.05	0.015	0.001
2360→2400	0.05	0.05	0.021	0.002
2360→2400	0.14	0.05	0.022	0.002
2360→2400	0.25	0.05	0.024	0.002
2360→2400	0.35	0.05	0.024	0.002
2360→2400	0.45	0.05	0.035	0.004
2360→2400	0.55	0.05	0.055	0.006
2360→2400	0.65	0.05	0.079	0.008
2360→2400	0.75	0.05	0.106	0.012

Table 12.30: η Differential Cross Section Results

W bin (MeV)	$\cos(\theta_{CM})$	$\cos(\theta_{CM})$ Error	$d\sigma/d\Omega$ μb	$d\sigma/d\Omega$ Error
2360→2400	0.84	0.05	0.072	0.036
2400→2440	-0.84	0.04	0.013	0.002
2400→2440	-0.75	0.05	0.011	0.001
2400→2440	-0.65	0.05	0.009	0.001
2400→2440	-0.55	0.05	0.006	0.000
2400→2440	-0.45	0.05	0.004	0.000
2400→2440	-0.34	0.05	0.002	0.000
2400→2440	-0.24	0.05	0.003	0.000
2400→2440	-0.14	0.05	0.007	0.000
2400→2440	-0.04	0.05	0.013	0.001
2400→2440	0.04	0.05	0.018	0.002
2400→2440	0.15	0.05	0.018	0.002
2400→2440	0.25	0.05	0.018	0.002
2400→2440	0.35	0.05	0.019	0.002
2400→2440	0.45	0.05	0.032	0.003
2400→2440	0.55	0.05	0.045	0.005
2400→2440	0.65	0.05	0.070	0.007
2400→2440	0.74	0.05	0.086	0.010
2400→2440	0.83	0.04	0.076	0.024
2440→2480	-0.84	0.04	0.016	0.003
2440→2480	-0.75	0.05	0.011	0.001
2440→2480	-0.65	0.05	0.005	0.000
2440→2480	-0.55	0.05	0.004	0.000
2440→2480	-0.45	0.05	0.003	0.000
2440→2480	-0.34	0.05	0.002	0.000
2440→2480	-0.24	0.05	0.003	0.000
2440→2480	-0.14	0.05	0.005	0.000
2440→2480	-0.04	0.05	0.010	0.001
2440→2480	0.04	0.05	0.014	0.001
2440→2480	0.15	0.05	0.013	0.001
2440→2480	0.25	0.05	0.015	0.001
2440→2480	0.35	0.05	0.016	0.001
2440→2480	0.45	0.05	0.026	0.003
2440→2480	0.55	0.05	0.042	0.004
2440→2480	0.65	0.05	0.057	0.006
2440→2480	0.75	0.05	0.088	0.011
2440→2480	0.83	0.04	0.094	0.027
2480→2520	-0.84	0.04	0.008	0.002
2480→2520	-0.75	0.05	0.010	0.001
2480→2520	-0.65	0.05	0.004	0.000

Table 12.31: η Differential Cross Section Results

W bin (MeV)	$\cos(\theta_{CM})$	$\cos(\theta_{CM})$ Error	$d\sigma/d\Omega$ μb	$d\sigma/d\Omega$ Error
2480→2520	-0.54	0.05	0.003	0.000
2480→2520	-0.45	0.05	0.001	0.000
2480→2520	-0.35	0.05	0.001	0.000
2480→2520	-0.25	0.05	0.002	0.000
2480→2520	-0.14	0.05	0.005	0.000
2480→2520	-0.04	0.05	0.009	0.001
2480→2520	0.05	0.05	0.013	0.001
2480→2520	0.14	0.05	0.012	0.001
2480→2520	0.25	0.05	0.010	0.001
2480→2520	0.35	0.05	0.013	0.001
2480→2520	0.45	0.05	0.020	0.002
2480→2520	0.55	0.05	0.034	0.003
2480→2520	0.65	0.05	0.051	0.005
2480→2520	0.74	0.05	0.067	0.008
2480→2520	0.84	0.04	0.081	0.051
2520→2560	-0.82	0.04	0.006	0.010
2520→2560	-0.75	0.05	0.008	0.001
2520→2560	-0.65	0.05	0.003	0.000
2520→2560	-0.55	0.05	0.002	0.000
2520→2560	-0.45	0.05	0.002	0.000
2520→2560	-0.35	0.05	0.001	0.000
2520→2560	-0.24	0.05	0.002	0.000
2520→2560	-0.14	0.05	0.004	0.000
2520→2560	-0.04	0.05	0.008	0.000
2520→2560	0.05	0.05	0.009	0.001
2520→2560	0.15	0.05	0.010	0.001
2520→2560	0.24	0.05	0.010	0.001
2520→2560	0.35	0.05	0.012	0.001
2520→2560	0.45	0.05	0.018	0.002
2520→2560	0.55	0.05	0.030	0.003
2520→2560	0.65	0.05	0.046	0.005
2520→2560	0.75	0.05	0.057	0.007
2520→2560	0.82	0.03	0.079	0.022
2560→2600	-0.82	0.03	0.008	0.001
2560→2600	-0.75	0.05	0.007	0.001
2560→2600	-0.65	0.05	0.004	0.000
2560→2600	-0.55	0.05	0.001	0.000
2560→2600	-0.44	0.05	0.001	0.000
2560→2600	-0.34	0.05	0.002	0.000
2560→2600	-0.24	0.05	0.002	0.000

Table 12.32: η Differential Cross Section Results

W bin (MeV)	$\cos(\theta_{CM})$	$\cos(\theta_{CM})$ Error	$d\sigma/d\Omega$ μb	$d\sigma/d\Omega$ Error
2560→2600	-0.14	0.05	0.004	0.000
2560→2600	-0.05	0.05	0.006	0.000
2560→2600	0.04	0.05	0.007	0.000
2560→2600	0.14	0.05	0.007	0.000
2560→2600	0.25	0.05	0.007	0.000
2560→2600	0.35	0.05	0.010	0.001
2560→2600	0.45	0.05	0.016	0.001
2560→2600	0.55	0.05	0.027	0.003
2560→2600	0.65	0.05	0.042	0.005
2560→2600	0.75	0.05	0.069	0.009
2560→2600	0.80	0.03	0.036	0.024
2600→2640	-0.82	0.03	0.008	0.001
2600→2640	-0.75	0.05	0.005	0.000
2600→2640	-0.65	0.05	0.002	0.000
2600→2640	-0.55	0.05	0.001	0.000
2600→2640	-0.44	0.05	0.001	0.000
2600→2640	-0.35	0.05	0.002	0.000
2600→2640	-0.24	0.05	0.002	0.000
2600→2640	-0.14	0.05	0.004	0.000
2600→2640	-0.04	0.05	0.005	0.000
2600→2640	0.05	0.05	0.006	0.000
2600→2640	0.14	0.05	0.005	0.000
2600→2640	0.25	0.05	0.006	0.000
2600→2640	0.35	0.05	0.008	0.001
2600→2640	0.45	0.05	0.015	0.001
2600→2640	0.55	0.05	0.024	0.002
2600→2640	0.65	0.05	0.035	0.004
2600→2640	0.75	0.05	0.060	0.008
2600→2640	0.81	0.03	0.064	0.018
2640→2680	-0.83	0.03	0.003	0.001
2640→2680	-0.75	0.05	0.004	0.000
2640→2680	-0.65	0.05	0.001	0.000
2640→2680	-0.54	0.05	0.000	0.000
2640→2680	-0.44	0.05	0.000	0.000
2640→2680	-0.35	0.05	0.000	0.000
2640→2680	-0.24	0.05	0.001	0.000
2640→2680	-0.14	0.05	0.002	0.000
2640→2680	-0.05	0.05	0.002	0.000
2640→2680	0.05	0.05	0.003	0.000
2640→2680	0.14	0.05	0.002	0.000

Table 12.33: η Differential Cross Section Results

W bin (MeV)	$\cos(\theta_{CM})$	$\cos(\theta_{CM})$ Error	$d\sigma/d\Omega$ μb	$d\sigma/d\Omega$ Error
2640→2680	0.23	0.05	0.003	0.000
2640→2680	0.35	0.05	0.005	0.000
2640→2680	0.45	0.05	0.010	0.001
2640→2680	0.55	0.05	0.018	0.002
2640→2680	0.65	0.05	0.029	0.004
2640→2680	0.75	0.05	0.047	0.010
2640→2680	0.81	0.02	0.039	0.029
2680→2730	-0.82	0.03	0.006	0.001
2680→2730	-0.74	0.05	0.003	0.000
2680→2730	-0.65	0.05	0.001	0.000
2680→2730	-0.55	0.05	0.001	0.000
2680→2730	-0.44	0.05	0.001	0.000
2680→2730	-0.35	0.05	0.001	0.000
2680→2730	-0.24	0.05	0.001	0.000
2680→2730	-0.15	0.05	0.002	0.000
2680→2730	-0.04	0.05	0.002	0.000
2680→2730	0.04	0.05	0.002	0.000
2680→2730	0.14	0.05	0.003	0.000
2680→2730	0.25	0.05	0.002	0.000
2680→2730	0.35	0.05	0.005	0.000
2680→2730	0.45	0.05	0.009	0.001
2680→2730	0.55	0.05	0.016	0.002
2680→2730	0.65	0.05	0.024	0.002
2680→2730	0.75	0.05	0.046	0.006
2680→2730	0.84	0.03	0.118	0.122
2730→2780	-0.82	0.03	0.002	0.000
2730→2780	-0.75	0.05	0.003	0.000
2730→2780	-0.65	0.05	0.001	0.000
2730→2780	-0.55	0.05	0.000	0.000
2730→2780	-0.44	0.05	0.000	0.000
2730→2780	-0.34	0.05	0.001	0.000
2730→2780	-0.25	0.05	0.001	0.000
2730→2780	-0.15	0.05	0.001	0.000
2730→2780	-0.05	0.05	0.001	0.000
2730→2780	0.04	0.05	0.001	0.000
2730→2780	0.15	0.05	0.001	0.000
2730→2780	0.25	0.05	0.001	0.000
2730→2780	0.35	0.05	0.003	0.000
2730→2780	0.46	0.05	0.006	0.000
2730→2780	0.55	0.05	0.010	0.001

Table 12.34: η Differential Cross Section Results

W bin (MeV)	$\cos(\theta_{CM})$	$\cos(\theta_{CM})$ Error	$d\sigma/d\Omega$ μb	$d\sigma/d\Omega$ Error
2730→2780	0.65	0.05	0.020	0.002
2730→2780	0.75	0.05	0.039	0.006
2730→2780	0.80	0.03	0.022	0.046
2780→2830	-0.81	0.03	0.001	0.003
2780→2830	-0.74	0.05	0.002	0.000
2780→2830	-0.65	0.05	0.001	0.000
2780→2830	-0.54	0.05	0.000	0.000
2780→2830	-0.44	0.05	0.000	0.000
2780→2830	-0.34	0.05	0.001	0.000
2780→2830	-0.25	0.05	0.001	0.000
2780→2830	-0.15	0.05	0.001	0.000
2780→2830	-0.04	0.05	0.000	0.000
2780→2830	0.05	0.05	0.001	0.000
2780→2830	0.14	0.05	0.001	0.000
2780→2830	0.25	0.05	0.001	0.000
2780→2830	0.35	0.05	0.003	0.000
2780→2830	0.44	0.05	0.006	0.000
2780→2830	0.55	0.05	0.009	0.001
2780→2830	0.65	0.05	0.021	0.002
2780→2830	0.75	0.05	0.036	0.005
2780→2830	0.83	0.03	0.166	0.154

Chapter 13

Appendix E

This appendix provides the values of the measured differential cross sections for the η' analysis.

Table 13.1: η' Differential Cross Section Results

W bin (MeV)	$\cos(\theta_{CM})$	$\cos(\theta_{CM})$ Error	$d\sigma/d\Omega$ μb	$d\sigma/d\Omega$ Error
1920→1930	-0.51	0.03	0.023	0.129
1920→1930	-0.44	0.05	0.039	0.009
1920→1930	-0.34	0.05	0.037	0.006
1920→1930	-0.24	0.05	0.060	0.009
1920→1930	-0.14	0.05	0.059	0.008
1920→1930	-0.04	0.05	0.055	0.008
1920→1930	0.04	0.05	0.054	0.008
1920→1930	0.14	0.05	0.056	0.008
1920→1930	0.24	0.05	0.060	0.008
1920→1930	0.35	0.05	0.058	0.008
1920→1930	0.45	0.05	0.071	0.010
1920→1930	0.55	0.05	0.072	0.010
1920→1930	0.65	0.05	0.062	0.009
1920→1930	0.74	0.05	0.054	0.009
1920→1930	0.80	0.04	0.021	0.119
1930→1940	-0.62	0.02	0.107	0.076
1930→1940	-0.54	0.05	0.033	0.007
1930→1940	-0.44	0.05	0.045	0.007
1930→1940	-0.35	0.05	0.056	0.008
1930→1940	-0.24	0.05	0.053	0.007
1930→1940	-0.14	0.05	0.067	0.009
1930→1940	-0.05	0.05	0.062	0.008
1930→1940	0.05	0.05	0.057	0.008
1930→1940	0.14	0.05	0.057	0.008
1930→1940	0.24	0.05	0.055	0.007
1930→1940	0.35	0.05	0.052	0.007
1930→1940	0.44	0.05	0.046	0.007
1930→1940	0.55	0.05	0.062	0.009
1930→1940	0.64	0.05	0.044	0.007
1930→1940	0.74	0.05	0.060	0.009
1930→1940	0.84	0.05	0.043	0.013
1930→1940	0.91	0.01	0.774	1.113
1940→1950	-0.65	0.05	0.072	0.180
1940→1950	-0.55	0.05	0.063	0.009
1940→1950	-0.45	0.05	0.058	0.009
1940→1950	-0.35	0.05	0.054	0.008
1940→1950	-0.25	0.05	0.053	0.008
1940→1950	-0.15	0.05	0.062	0.008
1940→1950	-0.05	0.05	0.060	0.008
1940→1950	0.04	0.05	0.062	0.008

Table 13.2: η' Differential Cross Section Results

W bin (MeV)	$\cos(\theta_{CM})$	$\cos(\theta_{CM})$ Error	$d\sigma/d\Omega$ μb	$d\sigma/d\Omega$ Error
1940→1950	0.14	0.05	0.070	0.009
1940→1950	0.25	0.05	0.063	0.008
1940→1950	0.34	0.05	0.066	0.009
1940→1950	0.44	0.05	0.066	0.009
1940→1950	0.55	0.05	0.075	0.010
1940→1950	0.64	0.05	0.056	0.008
1940→1950	0.75	0.05	0.065	0.010
1940→1950	0.84	0.05	0.043	0.009
1940→1950	0.92	0.02	0.131	0.101
1950→1960	-0.71	0.01	0.006	0.018
1950→1960	-0.64	0.05	0.030	0.004
1950→1960	-0.54	0.05	0.042	0.005
1950→1960	-0.44	0.05	0.049	0.006
1950→1960	-0.35	0.05	0.046	0.005
1950→1960	-0.24	0.05	0.058	0.007
1950→1960	-0.14	0.05	0.051	0.006
1950→1960	-0.05	0.05	0.054	0.006
1950→1960	0.05	0.05	0.058	0.007
1950→1960	0.14	0.05	0.053	0.006
1950→1960	0.24	0.05	0.054	0.006
1950→1960	0.34	0.05	0.058	0.007
1950→1960	0.44	0.05	0.051	0.006
1950→1960	0.54	0.05	0.051	0.006
1950→1960	0.65	0.05	0.052	0.006
1950→1960	0.74	0.05	0.045	0.006
1950→1960	0.85	0.05	0.049	0.007
1950→1960	0.90	0.03	0.020	0.111
1960→1970	-0.70	0.02	0.013	0.007
1960→1970	-0.64	0.05	0.057	0.007
1960→1970	-0.54	0.05	0.057	0.007
1960→1970	-0.44	0.05	0.055	0.007
1960→1970	-0.34	0.05	0.058	0.007
1960→1970	-0.25	0.05	0.065	0.007
1960→1970	-0.14	0.05	0.065	0.008
1960→1970	-0.05	0.05	0.070	0.008
1960→1970	0.04	0.05	0.069	0.008
1960→1970	0.15	0.05	0.072	0.008
1960→1970	0.25	0.05	0.068	0.008
1960→1970	0.34	0.05	0.073	0.008
1960→1970	0.44	0.05	0.076	0.009

Table 13.3: η' Differential Cross Section Results

W bin (MeV)	$\cos(\theta_{CM})$	$\cos(\theta_{CM})$ Error	$d\sigma/d\Omega$ μb	$d\sigma/d\Omega$ Error
1960→1970	0.54	0.05	0.072	0.008
1960→1970	0.65	0.05	0.073	0.009
1960→1970	0.74	0.05	0.062	0.008
1960→1970	0.85	0.05	0.070	0.010
1960→1970	0.93	0.03	0.065	0.017
1970→1980	-0.71	0.03	0.022	0.007
1970→1980	-0.64	0.05	0.055	0.007
1970→1980	-0.54	0.05	0.054	0.007
1970→1980	-0.45	0.05	0.070	0.008
1970→1980	-0.34	0.05	0.060	0.007
1970→1980	-0.25	0.05	0.064	0.007
1970→1980	-0.15	0.05	0.065	0.007
1970→1980	-0.04	0.05	0.074	0.008
1970→1980	0.05	0.05	0.077	0.009
1970→1980	0.15	0.05	0.071	0.008
1970→1980	0.25	0.05	0.066	0.008
1970→1980	0.35	0.05	0.072	0.008
1970→1980	0.45	0.05	0.077	0.009
1970→1980	0.54	0.05	0.076	0.009
1970→1980	0.65	0.05	0.071	0.008
1970→1980	0.75	0.05	0.069	0.009
1970→1980	0.84	0.05	0.065	0.009
1970→1980	0.93	0.04	0.057	0.091
1980→1990	-0.73	0.04	0.042	0.009
1980→1990	-0.64	0.05	0.051	0.006
1980→1990	-0.54	0.05	0.059	0.007
1980→1990	-0.44	0.05	0.061	0.007
1980→1990	-0.35	0.05	0.070	0.008
1980→1990	-0.24	0.05	0.063	0.007
1980→1990	-0.15	0.05	0.074	0.008
1980→1990	-0.04	0.05	0.067	0.008
1980→1990	0.05	0.05	0.074	0.008
1980→1990	0.15	0.05	0.080	0.009
1980→1990	0.25	0.05	0.077	0.009
1980→1990	0.34	0.05	0.075	0.009
1980→1990	0.45	0.05	0.080	0.009
1980→1990	0.54	0.05	0.078	0.009
1980→1990	0.64	0.05	0.066	0.008
1980→1990	0.74	0.05	0.070	0.009
1980→1990	0.84	0.05	0.057	0.008

Table 13.4: η' Differential Cross Section Results

W bin (MeV)	$\cos(\theta_{CM})$	$\cos(\theta_{CM})$ Error	$d\sigma/d\Omega$ μb	$d\sigma/d\Omega$ Error
1980→1990	0.92	0.04	0.039	0.011
1990→2000	-0.73	0.04	0.032	0.005
1990→2000	-0.64	0.05	0.059	0.007
1990→2000	-0.54	0.05	0.056	0.007
1990→2000	-0.45	0.05	0.056	0.007
1990→2000	-0.35	0.05	0.070	0.008
1990→2000	-0.24	0.05	0.064	0.007
1990→2000	-0.15	0.05	0.071	0.008
1990→2000	-0.05	0.05	0.069	0.008
1990→2000	0.05	0.05	0.066	0.008
1990→2000	0.15	0.05	0.071	0.008
1990→2000	0.25	0.05	0.067	0.008
1990→2000	0.34	0.05	0.076	0.009
1990→2000	0.44	0.05	0.073	0.008
1990→2000	0.55	0.05	0.073	0.009
1990→2000	0.64	0.05	0.080	0.010
1990→2000	0.74	0.05	0.068	0.009
1990→2000	0.84	0.05	0.058	0.008
1990→2000	0.93	0.04	0.065	0.016
2000→2010	-0.75	0.05	0.051	0.009
2000→2010	-0.65	0.05	0.057	0.007
2000→2010	-0.55	0.05	0.058	0.007
2000→2010	-0.45	0.05	0.058	0.007
2000→2010	-0.35	0.05	0.067	0.008
2000→2010	-0.24	0.05	0.057	0.006
2000→2010	-0.14	0.05	0.060	0.007
2000→2010	-0.05	0.05	0.071	0.008
2000→2010	0.04	0.05	0.069	0.008
2000→2010	0.15	0.05	0.070	0.008
2000→2010	0.25	0.05	0.069	0.008
2000→2010	0.35	0.05	0.073	0.008
2000→2010	0.44	0.05	0.069	0.008
2000→2010	0.54	0.05	0.069	0.008
2000→2010	0.65	0.05	0.071	0.008
2000→2010	0.74	0.05	0.064	0.008
2000→2010	0.84	0.05	0.075	0.010
2000→2010	0.92	0.04	0.044	0.012
2010→2020	-0.74	0.05	0.044	0.006
2010→2020	-0.64	0.05	0.049	0.006
2010→2020	-0.55	0.05	0.053	0.006

Table 13.5: η' Differential Cross Section Results

W bin (MeV)	$\cos(\theta_{CM})$	$\cos(\theta_{CM})$ Error	$d\sigma/d\Omega$ μb	$d\sigma/d\Omega$ Error
2010→2020	-0.44	0.05	0.053	0.006
2010→2020	-0.35	0.05	0.060	0.007
2010→2020	-0.24	0.05	0.058	0.007
2010→2020	-0.15	0.05	0.064	0.007
2010→2020	-0.05	0.05	0.059	0.007
2010→2020	0.04	0.05	0.071	0.008
2010→2020	0.15	0.05	0.070	0.008
2010→2020	0.24	0.05	0.071	0.008
2010→2020	0.35	0.05	0.073	0.008
2010→2020	0.45	0.05	0.071	0.008
2010→2020	0.55	0.05	0.080	0.009
2010→2020	0.65	0.05	0.062	0.007
2010→2020	0.75	0.05	0.077	0.010
2010→2020	0.84	0.05	0.068	0.010
2010→2020	0.93	0.04	0.075	0.022
2020→2030	-0.81	0.01	0.046	0.056
2020→2030	-0.75	0.05	0.042	0.005
2020→2030	-0.64	0.05	0.049	0.006
2020→2030	-0.55	0.05	0.058	0.007
2020→2030	-0.44	0.05	0.059	0.007
2020→2030	-0.35	0.05	0.061	0.007
2020→2030	-0.25	0.05	0.057	0.006
2020→2030	-0.14	0.05	0.062	0.007
2020→2030	-0.04	0.05	0.066	0.007
2020→2030	0.05	0.05	0.064	0.007
2020→2030	0.15	0.05	0.071	0.008
2020→2030	0.24	0.05	0.081	0.009
2020→2030	0.35	0.05	0.069	0.008
2020→2030	0.45	0.05	0.076	0.009
2020→2030	0.55	0.05	0.077	0.009
2020→2030	0.65	0.05	0.082	0.010
2020→2030	0.74	0.05	0.067	0.008
2020→2030	0.84	0.05	0.077	0.011
2020→2030	0.93	0.04	0.116	0.035
2030→2040	-0.81	0.01	0.030	0.016
2030→2040	-0.74	0.05	0.044	0.006
2030→2040	-0.64	0.05	0.046	0.006
2030→2040	-0.55	0.05	0.054	0.006
2030→2040	-0.44	0.05	0.059	0.007
2030→2040	-0.35	0.05	0.061	0.007

Table 13.6: η' Differential Cross Section Results

W bin (MeV)	$\cos(\theta_{CM})$	$\cos(\theta_{CM})$ Error	$d\sigma/d\Omega$ μb	$d\sigma/d\Omega$ Error
2030→2040	-0.25	0.05	0.067	0.008
2030→2040	-0.14	0.05	0.064	0.007
2030→2040	-0.04	0.05	0.065	0.007
2030→2040	0.05	0.05	0.068	0.008
2030→2040	0.14	0.05	0.072	0.008
2030→2040	0.25	0.05	0.078	0.009
2030→2040	0.35	0.05	0.080	0.009
2030→2040	0.45	0.05	0.083	0.009
2030→2040	0.54	0.05	0.085	0.010
2030→2040	0.64	0.05	0.081	0.010
2030→2040	0.74	0.05	0.076	0.009
2030→2040	0.85	0.05	0.075	0.011
2030→2040	0.93	0.04	0.078	0.085
2040→2050	-0.81	0.01	0.021	0.009
2040→2050	-0.75	0.05	0.043	0.006
2040→2050	-0.64	0.05	0.043	0.005
2040→2050	-0.54	0.05	0.046	0.006
2040→2050	-0.44	0.05	0.052	0.006
2040→2050	-0.34	0.05	0.056	0.006
2040→2050	-0.25	0.05	0.053	0.006
2040→2050	-0.15	0.05	0.066	0.007
2040→2050	-0.05	0.05	0.068	0.008
2040→2050	0.04	0.05	0.063	0.007
2040→2050	0.15	0.05	0.067	0.008
2040→2050	0.25	0.05	0.075	0.008
2040→2050	0.34	0.05	0.075	0.009
2040→2050	0.45	0.05	0.083	0.010
2040→2050	0.54	0.05	0.086	0.010
2040→2050	0.64	0.05	0.083	0.010
2040→2050	0.75	0.05	0.089	0.011
2040→2050	0.85	0.05	0.088	0.012
2040→2050	0.95	0.04	0.224	0.179
2050→2060	-0.80	0.02	0.023	0.185
2050→2060	-0.74	0.05	0.029	0.004
2050→2060	-0.64	0.05	0.043	0.005
2050→2060	-0.55	0.05	0.044	0.005
2050→2060	-0.44	0.05	0.049	0.006
2050→2060	-0.34	0.05	0.051	0.006
2050→2060	-0.24	0.05	0.054	0.006
2050→2060	-0.14	0.05	0.060	0.007

Table 13.7: η' Differential Cross Section Results

W bin (MeV)	$\cos(\theta_{CM})$	$\cos(\theta_{CM})$ Error	$d\sigma/d\Omega$ μb	$d\sigma/d\Omega$ Error
2050→2060	-0.04	0.05	0.062	0.007
2050→2060	0.05	0.05	0.060	0.007
2050→2060	0.15	0.05	0.062	0.007
2050→2060	0.25	0.05	0.078	0.009
2050→2060	0.35	0.05	0.077	0.009
2050→2060	0.44	0.05	0.075	0.009
2050→2060	0.55	0.05	0.083	0.010
2050→2060	0.64	0.05	0.096	0.011
2050→2060	0.74	0.05	0.099	0.012
2050→2060	0.85	0.05	0.099	0.014
2050→2060	0.91	0.02	0.102	0.034
2060→2070	-0.80	0.02	0.019	0.030
2060→2070	-0.75	0.05	0.033	0.004
2060→2070	-0.65	0.05	0.046	0.006
2060→2070	-0.55	0.05	0.047	0.006
2060→2070	-0.45	0.05	0.040	0.005
2060→2070	-0.34	0.05	0.052	0.006
2060→2070	-0.24	0.05	0.055	0.006
2060→2070	-0.15	0.05	0.056	0.006
2060→2070	-0.05	0.05	0.062	0.007
2060→2070	0.05	0.05	0.064	0.007
2060→2070	0.15	0.05	0.064	0.007
2060→2070	0.25	0.05	0.071	0.008
2060→2070	0.35	0.05	0.076	0.009
2060→2070	0.45	0.05	0.087	0.010
2060→2070	0.55	0.05	0.087	0.010
2060→2070	0.64	0.05	0.085	0.010
2060→2070	0.74	0.05	0.097	0.012
2060→2070	0.85	0.05	0.122	0.017
2060→2070	0.91	0.03	0.167	0.168
2070→2080	-0.82	0.02	0.051	0.019
2070→2080	-0.75	0.05	0.032	0.004
2070→2080	-0.64	0.05	0.040	0.005
2070→2080	-0.55	0.05	0.042	0.005
2070→2080	-0.44	0.05	0.052	0.006
2070→2080	-0.34	0.05	0.049	0.006
2070→2080	-0.24	0.05	0.055	0.006
2070→2080	-0.14	0.05	0.059	0.007
2070→2080	-0.05	0.05	0.054	0.006
2070→2080	0.05	0.05	0.061	0.007

Table 13.8: η' Differential Cross Section Results

W bin (MeV)	$\cos(\theta_{CM})$	$\cos(\theta_{CM})$ Error	$d\sigma/d\Omega$ μb	$d\sigma/d\Omega$ Error
2070→2080	0.14	0.05	0.058	0.006
2070→2080	0.25	0.05	0.063	0.007
2070→2080	0.35	0.05	0.083	0.009
2070→2080	0.44	0.05	0.087	0.010
2070→2080	0.55	0.05	0.094	0.011
2070→2080	0.65	0.05	0.093	0.011
2070→2080	0.74	0.05	0.101	0.012
2070→2080	0.85	0.05	0.099	0.014
2070→2080	0.93	0.03	0.240	0.167
2080→2090	-0.82	0.02	0.032	0.010
2080→2090	-0.74	0.05	0.034	0.005
2080→2090	-0.64	0.05	0.039	0.005
2080→2090	-0.55	0.05	0.041	0.005
2080→2090	-0.44	0.05	0.042	0.005
2080→2090	-0.35	0.05	0.052	0.006
2080→2090	-0.25	0.05	0.057	0.006
2080→2090	-0.14	0.05	0.056	0.006
2080→2090	-0.04	0.05	0.057	0.006
2080→2090	0.05	0.05	0.060	0.007
2080→2090	0.15	0.05	0.064	0.007
2080→2090	0.25	0.05	0.073	0.008
2080→2090	0.35	0.05	0.082	0.009
2080→2090	0.45	0.05	0.091	0.010
2080→2090	0.55	0.05	0.100	0.012
2080→2090	0.64	0.05	0.089	0.010
2080→2090	0.75	0.05	0.104	0.013
2080→2090	0.85	0.05	0.174	0.024
2080→2090	0.92	0.02	0.245	0.150
2090→2100	-0.81	0.02	0.021	0.006
2090→2100	-0.75	0.05	0.026	0.003
2090→2100	-0.64	0.05	0.036	0.004
2090→2100	-0.55	0.05	0.036	0.004
2090→2100	-0.45	0.05	0.039	0.005
2090→2100	-0.34	0.05	0.040	0.005
2090→2100	-0.24	0.05	0.046	0.005
2090→2100	-0.14	0.05	0.048	0.005
2090→2100	-0.04	0.05	0.054	0.006
2090→2100	0.05	0.05	0.055	0.006
2090→2100	0.15	0.05	0.059	0.007
2090→2100	0.25	0.05	0.064	0.007

Table 13.9: η' Differential Cross Section Results

W bin (MeV)	$\cos(\theta_{CM})$	$\cos(\theta_{CM})$ Error	$d\sigma/d\Omega$ μb	$d\sigma/d\Omega$ Error
2090→2100	0.34	0.05	0.082	0.009
2090→2100	0.44	0.05	0.090	0.010
2090→2100	0.55	0.05	0.091	0.010
2090→2100	0.65	0.05	0.105	0.012
2090→2100	0.74	0.05	0.110	0.013
2090→2100	0.84	0.05	0.134	0.019
2090→2100	0.91	0.02	0.213	0.104
2100→2120	-0.81	0.02	0.020	0.004
2100→2120	-0.74	0.05	0.025	0.003
2100→2120	-0.64	0.05	0.030	0.003
2100→2120	-0.54	0.05	0.029	0.003
2100→2120	-0.44	0.05	0.036	0.004
2100→2120	-0.35	0.05	0.040	0.004
2100→2120	-0.24	0.05	0.044	0.005
2100→2120	-0.14	0.05	0.043	0.004
2100→2120	-0.05	0.05	0.045	0.005
2100→2120	0.05	0.05	0.048	0.005
2100→2120	0.15	0.05	0.053	0.006
2100→2120	0.25	0.05	0.065	0.007
2100→2120	0.35	0.05	0.072	0.008
2100→2120	0.45	0.05	0.085	0.009
2100→2120	0.55	0.05	0.096	0.011
2100→2120	0.64	0.05	0.109	0.012
2100→2120	0.75	0.05	0.120	0.014
2100→2120	0.84	0.05	0.144	0.018
2100→2120	0.92	0.02	0.362	0.271
2120→2140	-0.81	0.02	0.019	0.003
2120→2140	-0.74	0.05	0.027	0.003
2120→2140	-0.64	0.05	0.026	0.003
2120→2140	-0.54	0.05	0.028	0.003
2120→2140	-0.44	0.05	0.036	0.004
2120→2140	-0.34	0.05	0.033	0.003
2120→2140	-0.24	0.05	0.036	0.004
2120→2140	-0.15	0.05	0.035	0.004
2120→2140	-0.04	0.05	0.035	0.004
2120→2140	0.04	0.05	0.042	0.004
2120→2140	0.15	0.05	0.048	0.005
2120→2140	0.25	0.05	0.053	0.006
2120→2140	0.35	0.05	0.068	0.007
2120→2140	0.45	0.05	0.075	0.008

Table 13.10: η' Differential Cross Section Results

W bin (MeV)	$\cos(\theta_{CM})$	$\cos(\theta_{CM})$ Error	$d\sigma/d\Omega$ μb	$d\sigma/d\Omega$ Error
2120→2140	0.55	0.05	0.090	0.010
2120→2140	0.65	0.05	0.105	0.012
2120→2140	0.75	0.05	0.145	0.016
2120→2140	0.84	0.05	0.154	0.019
2120→2140	0.91	0.02	0.106	0.069
2140→2160	-0.80	0.03	0.008	0.006
2140→2160	-0.75	0.05	0.024	0.003
2140→2160	-0.65	0.05	0.025	0.003
2140→2160	-0.55	0.05	0.025	0.003
2140→2160	-0.45	0.05	0.028	0.003
2140→2160	-0.34	0.05	0.028	0.003
2140→2160	-0.25	0.05	0.029	0.003
2140→2160	-0.15	0.05	0.033	0.003
2140→2160	-0.05	0.05	0.035	0.004
2140→2160	0.05	0.05	0.034	0.003
2140→2160	0.15	0.05	0.041	0.004
2140→2160	0.25	0.05	0.048	0.005
2140→2160	0.35	0.05	0.057	0.006
2140→2160	0.45	0.05	0.069	0.008
2140→2160	0.55	0.05	0.086	0.009
2140→2160	0.65	0.05	0.104	0.012
2140→2160	0.74	0.05	0.118	0.014
2140→2160	0.84	0.05	0.121	0.016
2140→2160	0.92	0.02	0.413	0.440
2160→2180	-0.82	0.03	0.018	0.005
2160→2180	-0.75	0.05	0.024	0.003
2160→2180	-0.64	0.05	0.022	0.002
2160→2180	-0.55	0.05	0.025	0.003
2160→2180	-0.45	0.05	0.022	0.002
2160→2180	-0.34	0.05	0.024	0.002
2160→2180	-0.25	0.05	0.024	0.002
2160→2180	-0.15	0.05	0.026	0.003
2160→2180	-0.05	0.05	0.029	0.003
2160→2180	0.04	0.05	0.031	0.003
2160→2180	0.15	0.05	0.030	0.003
2160→2180	0.25	0.05	0.043	0.005
2160→2180	0.35	0.05	0.051	0.005
2160→2180	0.44	0.05	0.060	0.006
2160→2180	0.55	0.05	0.079	0.009
2160→2180	0.65	0.05	0.107	0.012

Table 13.11: η' Differential Cross Section Results

W bin (MeV)	$\cos(\theta_{CM})$	$\cos(\theta_{CM})$ Error	$d\sigma/d\Omega$ μb	$d\sigma/d\Omega$ Error
2160→2180	0.74	0.05	0.104	0.012
2160→2180	0.84	0.05	0.097	0.013
2160→2180	0.91	0.01	0.265	0.087
2180→2200	-0.82	0.03	0.024	0.005
2180→2200	-0.74	0.05	0.023	0.003
2180→2200	-0.64	0.05	0.025	0.003
2180→2200	-0.55	0.05	0.019	0.002
2180→2200	-0.45	0.05	0.019	0.002
2180→2200	-0.34	0.05	0.019	0.002
2180→2200	-0.24	0.05	0.018	0.002
2180→2200	-0.15	0.05	0.022	0.002
2180→2200	-0.05	0.05	0.021	0.002
2180→2200	0.05	0.05	0.024	0.003
2180→2200	0.15	0.05	0.027	0.003
2180→2200	0.25	0.05	0.038	0.004
2180→2200	0.34	0.05	0.045	0.005
2180→2200	0.45	0.05	0.063	0.007
2180→2200	0.55	0.05	0.079	0.009
2180→2200	0.65	0.05	0.103	0.012
2180→2200	0.74	0.05	0.092	0.011
2180→2200	0.84	0.05	0.110	0.015
2180→2200	1.15	0.02	-0.00	-0.20
2200→2220	-0.83	0.03	0.023	0.005
2200→2220	-0.74	0.05	0.028	0.003
2200→2220	-0.64	0.05	0.023	0.003
2200→2220	-0.55	0.05	0.020	0.002
2200→2220	-0.45	0.05	0.022	0.002
2200→2220	-0.35	0.05	0.013	0.001
2200→2220	-0.24	0.05	0.015	0.002
2200→2220	-0.15	0.05	0.016	0.002
2200→2220	-0.05	0.05	0.019	0.002
2200→2220	0.05	0.05	0.019	0.002
2200→2220	0.15	0.05	0.022	0.002
2200→2220	0.25	0.05	0.031	0.003
2200→2220	0.35	0.05	0.043	0.005
2200→2220	0.45	0.05	0.046	0.005
2200→2220	0.55	0.05	0.074	0.008
2200→2220	0.65	0.05	0.091	0.010
2200→2220	0.75	0.05	0.104	0.012
2200→2220	0.84	0.05	0.124	0.017

Table 13.12: η' Differential Cross Section Results

W bin (MeV)	$\cos(\theta_{CM})$	$\cos(\theta_{CM})$ Error	$d\sigma/d\Omega$ μb	$d\sigma/d\Omega$ Error
2200→2220	0.91	0.01	0.179	0.063
2220→2240	-0.82	0.03	0.020	0.004
2220→2240	-0.74	0.05	0.024	0.003
2220→2240	-0.65	0.05	0.022	0.002
2220→2240	-0.54	0.05	0.021	0.002
2220→2240	-0.45	0.05	0.016	0.002
2220→2240	-0.35	0.05	0.012	0.001
2220→2240	-0.24	0.05	0.016	0.002
2220→2240	-0.15	0.05	0.017	0.002
2220→2240	-0.04	0.05	0.015	0.001
2220→2240	0.05	0.05	0.013	0.001
2220→2240	0.15	0.05	0.020	0.002
2220→2240	0.25	0.05	0.025	0.003
2220→2240	0.34	0.05	0.031	0.003
2220→2240	0.45	0.05	0.047	0.005
2220→2240	0.55	0.05	0.064	0.007
2220→2240	0.65	0.05	0.069	0.008
2220→2240	0.75	0.05	0.090	0.011
2220→2240	0.85	0.05	0.093	0.013
2220→2240	0.91	0.01	0.191	0.075
2240→2260	-0.83	0.03	0.029	0.005
2240→2260	-0.75	0.05	0.027	0.003
2240→2260	-0.65	0.05	0.020	0.002
2240→2260	-0.55	0.05	0.017	0.002
2240→2260	-0.45	0.05	0.016	0.002
2240→2260	-0.35	0.05	0.010	0.001
2240→2260	-0.25	0.05	0.012	0.001
2240→2260	-0.14	0.05	0.011	0.001
2240→2260	-0.05	0.05	0.013	0.001
2240→2260	0.05	0.05	0.013	0.001
2240→2260	0.15	0.05	0.015	0.002
2240→2260	0.25	0.05	0.022	0.002
2240→2260	0.35	0.05	0.030	0.003
2240→2260	0.45	0.05	0.042	0.005
2240→2260	0.55	0.05	0.064	0.007
2240→2260	0.65	0.05	0.075	0.009
2240→2260	0.75	0.05	0.092	0.011
2240→2260	0.85	0.05	0.090	0.014
2240→2260	0.91	0.01	0.088	0.043
2260→2280	-0.83	0.03	0.026	0.004

Table 13.13: η' Differential Cross Section Results

W bin (MeV)	$\cos(\theta_{CM})$	$\cos(\theta_{CM})$ Error	$d\sigma/d\Omega$ μb	$d\sigma/d\Omega$ Error
2260→2280	-0.75	0.05	0.027	0.003
2260→2280	-0.65	0.05	0.019	0.002
2260→2280	-0.55	0.05	0.016	0.002
2260→2280	-0.45	0.05	0.014	0.001
2260→2280	-0.34	0.05	0.011	0.001
2260→2280	-0.25	0.05	0.009	0.001
2260→2280	-0.14	0.05	0.011	0.001
2260→2280	-0.04	0.05	0.011	0.001
2260→2280	0.04	0.05	0.013	0.001
2260→2280	0.14	0.05	0.016	0.002
2260→2280	0.25	0.05	0.021	0.002
2260→2280	0.35	0.05	0.031	0.003
2260→2280	0.45	0.05	0.041	0.004
2260→2280	0.55	0.05	0.056	0.006
2260→2280	0.65	0.05	0.076	0.009
2260→2280	0.74	0.05	0.084	0.011
2260→2280	0.84	0.05	0.098	0.015
2260→2280	0.91	0.01	0.024	0.031
2280→2300	-0.83	0.03	0.025	0.004
2280→2300	-0.75	0.05	0.023	0.003
2280→2300	-0.64	0.05	0.016	0.002
2280→2300	-0.55	0.05	0.014	0.001
2280→2300	-0.45	0.05	0.012	0.001
2280→2300	-0.36	0.05	0.009	0.001
2280→2300	-0.24	0.05	0.008	0.001
2280→2300	-0.15	0.05	0.010	0.001
2280→2300	-0.04	0.05	0.009	0.001
2280→2300	0.05	0.05	0.011	0.001
2280→2300	0.14	0.05	0.014	0.001
2280→2300	0.24	0.05	0.019	0.002
2280→2300	0.35	0.05	0.024	0.003
2280→2300	0.45	0.05	0.034	0.004
2280→2300	0.54	0.05	0.053	0.006
2280→2300	0.65	0.05	0.061	0.007
2280→2300	0.75	0.05	0.084	0.011
2280→2300	0.85	0.05	0.092	0.015
2280→2300	0.85	0.02	0.014	0.111
2300→2320	-0.82	0.03	0.017	0.003
2300→2320	-0.75	0.05	0.023	0.003
2300→2320	-0.65	0.05	0.019	0.002

Table 13.14: η' Differential Cross Section Results

W bin (MeV)	$\cos(\theta_{CM})$	$\cos(\theta_{CM})$ Error	$d\sigma/d\Omega$ μb	$d\sigma/d\Omega$ Error
2300→2320	-0.54	0.05	0.014	0.001
2300→2320	-0.45	0.05	0.009	0.001
2300→2320	-0.35	0.05	0.007	0.001
2300→2320	-0.24	0.05	0.008	0.001
2300→2320	-0.14	0.05	0.008	0.001
2300→2320	-0.05	0.05	0.008	0.001
2300→2320	0.05	0.05	0.010	0.001
2300→2320	0.15	0.05	0.013	0.001
2300→2320	0.25	0.05	0.016	0.002
2300→2320	0.34	0.05	0.022	0.002
2300→2320	0.45	0.05	0.034	0.004
2300→2320	0.54	0.05	0.050	0.006
2300→2320	0.65	0.05	0.062	0.007
2300→2320	0.74	0.05	0.075	0.010
2300→2320	0.85	0.05	0.103	0.017
2300→2320	0.91	0.01	0.150	0.066
2320→2340	-0.82	0.03	0.018	0.003
2320→2340	-0.74	0.05	0.018	0.002
2320→2340	-0.65	0.05	0.014	0.001
2320→2340	-0.55	0.05	0.011	0.001
2320→2340	-0.45	0.05	0.010	0.001
2320→2340	-0.34	0.05	0.007	0.001
2320→2340	-0.24	0.05	0.006	0.000
2320→2340	-0.14	0.05	0.008	0.001
2320→2340	-0.04	0.05	0.009	0.001
2320→2340	0.04	0.05	0.011	0.001
2320→2340	0.15	0.05	0.012	0.001
2320→2340	0.25	0.05	0.016	0.002
2320→2340	0.35	0.05	0.021	0.002
2320→2340	0.45	0.05	0.028	0.003
2320→2340	0.55	0.05	0.044	0.005
2320→2340	0.65	0.05	0.060	0.007
2320→2340	0.75	0.05	0.072	0.009
2320→2340	0.84	0.05	0.073	0.012
2320→2340	0.91	0.01	0.093	0.041
2340→2360	-0.82	0.03	0.020	0.003
2340→2360	-0.74	0.05	0.018	0.002
2340→2360	-0.65	0.05	0.014	0.001
2340→2360	-0.55	0.05	0.011	0.001
2340→2360	-0.45	0.05	0.008	0.001

Table 13.15: η' Differential Cross Section Results

W bin (MeV)	$\cos(\theta_{CM})$	$\cos(\theta_{CM})$ Error	$d\sigma/d\Omega$ μb	$d\sigma/d\Omega$ Error
2340→2360	-0.35	0.05	0.006	0.001
2340→2360	-0.24	0.05	0.006	0.001
2340→2360	-0.15	0.05	0.008	0.001
2340→2360	-0.05	0.05	0.009	0.001
2340→2360	0.05	0.05	0.012	0.001
2340→2360	0.15	0.05	0.013	0.001
2340→2360	0.25	0.05	0.018	0.002
2340→2360	0.35	0.05	0.018	0.002
2340→2360	0.45	0.05	0.030	0.003
2340→2360	0.55	0.05	0.038	0.004
2340→2360	0.65	0.05	0.056	0.007
2340→2360	0.75	0.05	0.074	0.010
2340→2360	0.84	0.05	0.084	0.014
2340→2360	0.92	0.02	0.106	0.104
2360→2400	-0.83	0.03	0.019	0.003
2360→2400	-0.75	0.05	0.015	0.002
2360→2400	-0.64	0.05	0.010	0.001
2360→2400	-0.55	0.05	0.008	0.001
2360→2400	-0.45	0.05	0.007	0.001
2360→2400	-0.35	0.05	0.004	0.000
2360→2400	-0.24	0.05	0.004	0.000
2360→2400	-0.14	0.05	0.007	0.000
2360→2400	-0.04	0.05	0.009	0.001
2360→2400	0.04	0.05	0.010	0.001
2360→2400	0.15	0.05	0.012	0.001
2360→2400	0.24	0.05	0.014	0.001
2360→2400	0.35	0.05	0.017	0.002
2360→2400	0.45	0.05	0.029	0.003
2360→2400	0.55	0.05	0.038	0.004
2360→2400	0.65	0.05	0.041	0.005
2360→2400	0.75	0.05	0.060	0.007
2360→2400	0.85	0.05	0.091	0.014
2360→2400	0.91	0.02	0.056	0.038
2400→2440	-0.82	0.03	0.011	0.002
2400→2440	-0.75	0.05	0.012	0.001
2400→2440	-0.65	0.05	0.008	0.001
2400→2440	-0.55	0.05	0.006	0.000
2400→2440	-0.44	0.05	0.004	0.000
2400→2440	-0.35	0.05	0.003	0.000
2400→2440	-0.24	0.05	0.003	0.000

Table 13.16: η' Differential Cross Section Results

W bin (MeV)	$\cos(\theta_{CM})$	$\cos(\theta_{CM})$ Error	$d\sigma/d\Omega$ μb	$d\sigma/d\Omega$ Error
2400→2440	-0.14	0.05	0.005	0.000
2400→2440	-0.04	0.05	0.006	0.000
2400→2440	0.05	0.05	0.009	0.001
2400→2440	0.15	0.05	0.010	0.001
2400→2440	0.25	0.05	0.010	0.001
2400→2440	0.35	0.05	0.015	0.001
2400→2440	0.45	0.05	0.020	0.002
2400→2440	0.54	0.05	0.032	0.004
2400→2440	0.65	0.05	0.041	0.005
2400→2440	0.74	0.05	0.059	0.007
2400→2440	0.85	0.05	0.075	0.013
2400→2440	0.92	0.02	0.058	0.038
2440→2480	-0.82	0.03	0.015	0.002
2440→2480	-0.74	0.05	0.010	0.001
2440→2480	-0.65	0.05	0.007	0.000
2440→2480	-0.55	0.05	0.003	0.000
2440→2480	-0.45	0.05	0.003	0.000
2440→2480	-0.35	0.05	0.002	0.000
2440→2480	-0.24	0.05	0.003	0.000
2440→2480	-0.15	0.05	0.004	0.000
2440→2480	-0.04	0.05	0.006	0.000
2440→2480	0.05	0.05	0.007	0.001
2440→2480	0.15	0.05	0.010	0.001
2440→2480	0.24	0.05	0.011	0.001
2440→2480	0.35	0.05	0.013	0.001
2440→2480	0.45	0.05	0.019	0.002
2440→2480	0.55	0.05	0.030	0.003
2440→2480	0.65	0.05	0.039	0.005
2440→2480	0.75	0.05	0.052	0.007
2440→2480	0.86	0.05	0.113	0.020
2440→2480	0.91	0.02	0.050	0.030
2480→2520	-0.83	0.03	0.011	0.002
2480→2520	-0.75	0.05	0.007	0.001
2480→2520	-0.65	0.05	0.004	0.000
2480→2520	-0.55	0.05	0.003	0.000
2480→2520	-0.44	0.05	0.001	0.000
2480→2520	-0.34	0.05	0.002	0.000
2480→2520	-0.24	0.05	0.003	0.000
2480→2520	-0.15	0.05	0.004	0.000
2480→2520	-0.04	0.05	0.006	0.000

Table 13.17: η' Differential Cross Section Results

W bin (MeV)	$\cos(\theta_{CM})$	$\cos(\theta_{CM})$ Error	$d\sigma/d\Omega$ μb	$d\sigma/d\Omega$ Error
2480→2520	0.05	0.05	0.006	0.000
2480→2520	0.14	0.05	0.008	0.001
2480→2520	0.24	0.05	0.008	0.001
2480→2520	0.35	0.05	0.011	0.001
2480→2520	0.45	0.05	0.016	0.002
2480→2520	0.55	0.05	0.021	0.002
2480→2520	0.65	0.05	0.045	0.005
2480→2520	0.74	0.05	0.044	0.006
2480→2520	0.86	0.05	0.085	0.022
2480→2520	0.92	0.02	0.183	0.131
2520→2560	-0.82	0.03	0.009	0.002
2520→2560	-0.75	0.05	0.007	0.001
2520→2560	-0.65	0.05	0.004	0.000
2520→2560	-0.55	0.05	0.002	0.000
2520→2560	-0.44	0.05	0.001	0.000
2520→2560	-0.34	0.05	0.001	0.000
2520→2560	-0.24	0.05	0.002	0.000
2520→2560	-0.14	0.05	0.004	0.000
2520→2560	-0.04	0.05	0.005	0.000
2520→2560	0.05	0.05	0.006	0.000
2520→2560	0.14	0.05	0.006	0.000
2520→2560	0.24	0.05	0.006	0.000
2520→2560	0.35	0.05	0.007	0.001
2520→2560	0.45	0.05	0.013	0.001
2520→2560	0.55	0.05	0.016	0.002
2520→2560	0.65	0.05	0.027	0.003
2520→2560	0.74	0.05	0.047	0.006
2520→2560	0.85	0.05	0.083	0.018
2520→2560	0.91	0.02	0.099	0.111
2560→2600	-0.81	0.03	0.005	0.001
2560→2600	-0.75	0.05	0.006	0.000
2560→2600	-0.65	0.05	0.003	0.000
2560→2600	-0.55	0.05	0.002	0.000
2560→2600	-0.45	0.05	0.001	0.000
2560→2600	-0.34	0.05	0.001	0.000
2560→2600	-0.24	0.05	0.002	0.000
2560→2600	-0.15	0.05	0.004	0.000
2560→2600	-0.04	0.05	0.005	0.000
2560→2600	0.05	0.05	0.006	0.000
2560→2600	0.15	0.05	0.004	0.000

Table 13.18: η' Differential Cross Section Results

W bin (MeV)	$\cos(\theta_{CM})$	$\cos(\theta_{CM})$ Error	$d\sigma/d\Omega$ μb	$d\sigma/d\Omega$ Error
2560→2600	0.24	0.05	0.004	0.000
2560→2600	0.35	0.05	0.007	0.000
2560→2600	0.45	0.05	0.009	0.001
2560→2600	0.55	0.05	0.014	0.002
2560→2600	0.65	0.05	0.025	0.003
2560→2600	0.75	0.05	0.048	0.006
2560→2600	0.86	0.05	0.097	0.024
2560→2600	0.91	0.01	0.052	0.063
2600→2640	-0.82	0.03	0.003	0.001
2600→2640	-0.75	0.05	0.005	0.000
2600→2640	-0.65	0.05	0.002	0.000
2600→2640	-0.54	0.05	0.001	0.000
2600→2640	-0.45	0.05	0.001	0.000
2600→2640	-0.33	0.05	0.001	0.000
2600→2640	-0.24	0.05	0.002	0.000
2600→2640	-0.14	0.05	0.004	0.000
2600→2640	-0.04	0.05	0.005	0.000
2600→2640	0.04	0.05	0.005	0.000
2600→2640	0.14	0.05	0.005	0.000
2600→2640	0.24	0.05	0.003	0.000
2600→2640	0.35	0.05	0.003	0.000
2600→2640	0.45	0.05	0.007	0.001
2600→2640	0.55	0.05	0.011	0.001
2600→2640	0.65	0.05	0.021	0.002
2600→2640	0.75	0.05	0.038	0.005
2600→2640	0.86	0.05	0.129	0.049
2640→2680	-0.83	0.03	0.009	0.007
2640→2680	-0.75	0.05	0.004	0.000
2640→2680	-0.65	0.05	0.002	0.000
2640→2680	-0.54	0.05	0.000	0.000
2640→2680	-0.44	0.05	0.001	0.000
2640→2680	-0.35	0.05	0.002	0.000
2640→2680	-0.24	0.05	0.002	0.000
2640→2680	-0.14	0.05	0.003	0.000
2640→2680	-0.04	0.05	0.004	0.000
2640→2680	0.05	0.05	0.004	0.000
2640→2680	0.15	0.05	0.004	0.000
2640→2680	0.24	0.05	0.003	0.000
2640→2680	0.36	0.05	0.002	0.000
2640→2680	0.45	0.05	0.006	0.001

Table 13.19: η' Differential Cross Section Results

W bin (MeV)	$\cos(\theta_{CM})$	$\cos(\theta_{CM})$ Error	$d\sigma/d\Omega$ μb	$d\sigma/d\Omega$ Error
2640→2680	0.55	0.05	0.009	0.001
2640→2680	0.65	0.05	0.019	0.003
2640→2680	0.74	0.05	0.034	0.005
2640→2680	0.85	0.05	0.066	0.022
2640→2680	0.91	0.01	0.227	0.263
2680→2730	-0.82	0.02	0.004	0.001
2680→2730	-0.75	0.05	0.003	0.000
2680→2730	-0.66	0.05	0.001	0.000
2680→2730	-0.55	0.05	0.000	0.000
2680→2730	-0.45	0.05	0.001	0.000
2680→2730	-0.35	0.05	0.002	0.000
2680→2730	-0.25	0.05	0.002	0.000
2680→2730	-0.14	0.05	0.003	0.000
2680→2730	-0.05	0.05	0.003	0.000
2680→2730	0.05	0.05	0.003	0.000
2680→2730	0.14	0.05	0.003	0.000
2680→2730	0.25	0.05	0.003	0.000
2680→2730	0.34	0.05	0.002	0.000
2680→2730	0.44	0.05	0.003	0.000
2680→2730	0.55	0.05	0.006	0.001
2680→2730	0.65	0.05	0.018	0.002
2680→2730	0.76	0.05	0.028	0.004
2680→2730	0.84	0.05	0.037	0.012
2680→2730	0.91	0.01	0.032	0.077
2730→2780	-0.81	0.02	0.000	0.000
2730→2780	-0.75	0.05	0.001	0.000
2730→2780	-0.65	0.05	0.000	0.000
2730→2780	-0.54	0.05	0.000	0.000
2730→2780	-0.45	0.05	0.000	0.000
2730→2780	-0.34	0.05	0.001	0.000
2730→2780	-0.24	0.05	0.001	0.000
2730→2780	-0.14	0.05	0.002	0.000
2730→2780	-0.05	0.05	0.002	0.000
2730→2780	0.04	0.05	0.002	0.000
2730→2780	0.14	0.05	0.002	0.000
2730→2780	0.24	0.05	0.002	0.000
2730→2780	0.35	0.05	0.001	0.000
2730→2780	0.46	0.05	0.001	0.000
2730→2780	0.55	0.05	0.006	0.000
2730→2780	0.66	0.05	0.012	0.002

Table 13.20: η' Differential Cross Section Results

W bin (MeV)	$\cos(\theta_{CM})$	$\cos(\theta_{CM})$ Error	$d\sigma/d\Omega$ μb	$d\sigma/d\Omega$ Error
2730→2780	0.75	0.05	0.023	0.003
2730→2780	0.87	0.05	0.096	0.056
2780→2830	-0.82	0.02	0.000	0.000
2780→2830	-0.75	0.05	0.001	0.000
2780→2830	-0.65	0.05	0.001	0.000
2780→2830	-0.55	0.05	0.000	0.000
2780→2830	-0.44	0.05	0.000	0.000
2780→2830	-0.34	0.05	0.001	0.000
2780→2830	-0.24	0.05	0.001	0.000
2780→2830	-0.14	0.05	0.001	0.000
2780→2830	-0.04	0.05	0.002	0.000
2780→2830	0.04	0.05	0.002	0.000
2780→2830	0.14	0.05	0.002	0.000
2780→2830	0.25	0.05	0.001	0.000
2780→2830	0.35	0.05	0.001	0.000
2780→2830	0.45	0.05	0.002	0.000
2780→2830	0.54	0.05	0.003	0.000
2780→2830	0.65	0.05	0.008	0.001
2780→2830	0.75	0.05	0.022	0.003
2780→2830	0.86	0.05	0.059	0.035
2780→2830	0.93	0.01	-0.03	-0.07

Chapter 14

Appendix F

This appendix provides the values of the fit parameters and their respective errors from MINUIT, along with the calculated yields and errors. Table 14.1 presents the determined fit parameters and errors. This is for a representative fit in the η analysis containing the $J^P = \frac{1}{2}^-, \frac{3}{2}^+, \frac{5}{2}^-$ partial waves. With the non-resonant pieces of the fit locked, there are only 8 free parameters in the fit, the results of which are reported here for bins in the range of $1900 < W < 2300$ MeV.

For this same representative fit, the calculated yields as a function of W in MeV is presented is presented in Table 14.2. The yields for the three partial waves with errors are reported for bins in the range of $1900 < W < 2300$ MeV.

NOTE: The errors on the calculated yields which appear here, are actually the square of the real error. The errors, when properly calculated, are considerably larger. The proper errors are presented in the plots of the results, and systematics.

Table 14.1: η Parameter Fit Results

W	mod($\frac{1}{2}^-$)	phase($\frac{1}{2}^-$)	mod($\frac{3}{2}^+$)	phase($\frac{3}{2}^+$)	E/M($\frac{3}{2}^+$)	mod($\frac{5}{2}^-$)	phase($\frac{5}{2}^-$)	E/M($\frac{5}{2}^-$)
1895	-7.25±0.25	2.78±0.38	-13.0±7.33	2.07±0.76	5.70±0.73	104.5±39.1	4.14±0.35	6.16±0.096
1905	-5.57±5.07	2.41±3.36	22.0±24.3	0.08±1.37	5.0±4.20	-184.4±112.5	3.90±2.25	3.07±1.0
1915	5.54±2.20	5.60±0.91	20.0±9.91	0.04±0.35	5.17±0.61	-192.2±39.6	3.84±0.57	3.06±0.18
1925	-6.58±0.26	3.10±0.44	-9.5±3.91	5.95±0.49	2.02±2.9	-90.7±46.9	1.19±0.24	6.19±0.15
1935	6.64±0.27	6.25±0.51	-8.75±0.75	2.97±1.26	5.0±0.41	-92.6±79.5	4.22±0.11	3.09±0.09
1945	6.68±0.21	0.27±0.46	8.1±0.94	3.34±1.47	1.82±0.43	-82.8±85.5	4.54±0.16	3.07±0.15
1955	-5.8±0.20	3.4±0.16	6.61±2.04	3.53±0.48	1.52±0.82	85.7±12.9	1.44±0.11	3.01±0.07
1965	6.8±0.19	0.37±0.15	-7.64±2.0	3.65±0.40	4.7±0.55	-82.3±13.8	1.45±0.09	6.21±0.06
1975	-3.09±1.04	5.49±0.32	-51.1±4.91	1.74±0.19	3.03±0.11	-198.8±18.9	4.21±0.18	3.11±0.02
1985	6.22±0.44	0.25±0.14	-11.1±2.92	0.84±0.36	1.53±0.41	-111.8±19.8	1.50±0.08	6.20±0.07
1995	6.58±0.27	0.47±0.15	5.36±3.48	4.07±0.53	1.48±0.91	-90.9±14.7	1.60±0.092	6.19±0.07
2005	-6.61±0.24	3.6±0.11	4.14±1.79	1.19±0.50	4.86±1.22	-91.6±18.5	4.80±0.08	3.02±0.073
2015	-6.44±0.39	3.93±0.18	7.19±5.65	1.85±0.41	4.17±0.52	88.7±17.3	4.95±0.12	6.17±0.05
2025	-5.21±0.58	3.57±0.13	13.0±5.47	1.03±0.41	4.2±0.47	-125.9±14.3	1.55±0.11	6.22±0.05
2035	-1.06±1.29	5.71±0.54	-36.9±2.29	2.1±0.09	2.98±0.05	-175.7±3.7	1.41±0.17	6.23±0.03
2045	5.06±0.35	0.78±0.14	13.6±3.22	4.68±0.21	1.34±0.47	117.3±9.9	1.7±0.08	3.08±0.040
2055	-5.64±0.36	4.22±0.16	8.97±4.65	2.18±0.31	3.91±0.41	92.4±6.3	1.94±0.09	3.01±0.03
2065	5.82±0.40	1.42±0.20	8.14±4.52	2.43±0.43	3.93±0.32	81.4±9.3	5.2±0.11	6.21±0.04
2075	4.4±1.1	0.93±0.12	-12.3±6.3	4.49±0.55	4.23±0.47	109.6±10.6	1.89±0.11	3.05±0.54
2085	-0.71±0.55	5.2±1.0	-31.1±5.0	5.62±0.16	6.14±0.10	139.9±8.4	4.85±0.10	6.26±0.02
2095	-5.70±0.46	4.76±0.32	-8.35±2.53	1.78±0.52	0.88±0.38	82.5±7.4	5.25±0.14	6.2±0.02
2110	5.75±0.31	1.79±0.25	-7.28±2.22	5.35±0.42	4.39±0.33	77.2±6.56	2.10±0.097	3.08±0.03
2130	1.32±0.23	1.72±0.29	-20.0±1.77	2.58±0.08	3.11±0.07	-111.1±2.45	5.09±0.046	3.18±0.02
2150	-5.36±0.17	5.15±0.13	5.68±1.52	4.81±0.34	0.80±0.24	46.6±5.03	2.37±0.10	2.98±0.05
2170	-5.15±0.23	5.09±0.13	7.59±1.58	1.54±0.29	3.68±0.16	-44.1±3.83	2.47±0.098	6.10±0.04
2190	-3.14±0.76	4.64±0.19	7.58±1.19	0.40±0.56	4.1±0.43	64.0±5.9	5.72±0.10	0.035±0.04
2210	-1.40±0.30	4.70±0.19	10.4±0.99	6.14±0.09	3.72±0.1	64.2±1.85	2.49±0.04	3.23±0.02
2230	1.09±0.92	1.49±0.85	8.21±1.49	2.78±0.14	0.96±0.29	51.7±2.7	2.67±0.09	3.2±0.04
2250	-2.30±0.50	4.81±0.17	7.11±0.73	0.46±0.32	4.57±0.19	41.8±2.56	2.9±0.082	3.17±0.03
2270	-2.27±0.39	4.65±0.21	7.18±1.00	0.39±0.28	5.11±0.18	-33.9±2.39	6.13±0.10	3.22±0.03
2290	3.77±0.35	2.30±0.17	4.5±1.42	5.49±0.33	0.55±0.20	21.9±1.93	6.2±0.16	6.11±0.04

Table 14.2: η Yield Fit Results

W	Yield($\frac{1}{2}^-$)	Yield($\frac{3}{2}^+$)	Yield($\frac{5}{2}^-$)
1895	1.250±0.007538	0.0607±0.0124214	0.1831±0.016105
1905	0.738±1.80286	0.3216±1.15126	0.5827±0.096129
1915	0.727±0.335133	0.2531±0.110714	0.7037±0.119692
1925	1.027±0.006660	0.0603±0.0041604	0.1734±0.025601
1935	1.042±0.007234	0.0568±0.0002467	0.1887±0.098800
1945	1.052±0.004457	0.0520±0.0002993	0.1657±0.103885
1955	0.8126±0.00322	0.0376±0.0004716	0.2078±0.003209
1965	1.094±0.003727	0.0522±0.0007453	0.1934±0.003864
1975	0.2248±0.02314	0.8269±0.0280124	1.1816±0.051331
1985	0.904±0.016503	0.1188±0.0037491	0.4180±0.017666
1995	1.009±0.007103	0.0285±0.0012144	0.3029±0.008017
2005	1.015±0.005718	0.0174±0.0003283	0.3439±0.013104
2015	0.9624±0.01359	0.0458±0.0037666	0.3435±0.014692
2025	0.6292±0.01999	0.1613±0.011082	0.6980±0.022069
2035	0.0260±0.00401	0.5454±0.0055321	1.4439±0.005081
2045	0.5882±0.00696	0.2125±0.0064582	0.7023±0.011592
2055	0.7293±0.00873	0.0651±0.0023714	0.4720±0.003998
2065	0.7737±0.01158	0.0566±0.0030992	0.3912±0.007411
2075	0.4511±0.04953	0.1705±0.0177976	0.7683±0.017370
2085	0.0116±0.00032	0.4501±0.0214094	1.2692±0.023917
2095	0.7371±0.01467	0.0708±0.0013558	0.4774±0.007003
2110	0.7467±0.00650	0.0724±0.0015237	0.4675±0.005308
2130	0.0391±0.00019	0.2080±0.0013762	1.0847±0.001674
2150	0.6401±0.00177	0.0360±0.0002450	0.2511±0.001267
2170	0.5877±0.00289	0.0511±0.0003330	0.2631±0.000989
2190	0.2172±0.01108	0.0841±0.0015863	0.5113±0.009948
2210	0.0428±0.00034	0.1124±0.0003073	0.6057±0.000787
2230	0.0260±0.00193	0.1085±0.0011883	0.4458±0.002104
2250	0.1145±0.00255	0.1076±0.0005360	0.3067±0.001480
2270	0.1104±0.00146	0.1049±0.0005481	0.2323±0.001017
2290	0.3021±0.00330	0.0258±0.0002391	0.1223±0.000342